Effect of Web-Flange Interaction on the Buckling Behaviour of Slender Girders

By

ABDEL-RAHIM BADAWY ABDEL-RAHIM

A Thesis

Submitted to the Faculty of Graduate Studies

in Partial Fulfilment of the Requirements

for the Degree of

Doctor of Philosophy

Department of Civil and Geological Engineering

The University of Manitoba

Winnipeg, Manitoba, Canada, February 1996

©ABDEL-RAHIM BADAWY ABDEL-RAHIM 1996

National Library
of Canada

Acquisitions and
Bibliographic Services Branch

395 Wellington Street
Ottawa, Ontario
K1A 0N4

Bibliothèque nationale
du Canada

Direction des acquisitions et
des services bibliographiques

395, rue Wellington
Ottawa (Ontario)
K1A 0N4

Your file *Votre référence*

Our file *Notre référence*

The author has granted an irrevocable non-exclusive licence allowing the National Library of Canada to reproduce, loan, distribute or sell copies of his/her thesis by any means and in any form or format, making this thesis available to interested persons.

L'auteur a accordé une licence irrévocable et non exclusive permettant à la Bibliothèque nationale du Canada de reproduire, prêter, distribuer ou vendre des copies de sa thèse de quelque manière et sous quelque forme que ce soit pour mettre des exemplaires de cette thèse à la disposition des personnes intéressées.

The author retains ownership of the copyright in his/her thesis. Neither the thesis nor substantial extracts from it may be printed or otherwise reproduced without his/her permission.

L'auteur conserve la propriété du droit d'auteur qui protège sa thèse. Ni la thèse ni des extraits substantiels de celle-ci ne doivent être imprimés ou autrement reproduits sans son autorisation.

ISBN 0-612-12942-X

Canada

THE UNIVERSITY OF MANITOBA

FACUTY OF GRADUATE STUDIES

COPYRIGHT PERMISSION

EFFECT OF WEB-FLANGE INTERACTION ON THE BUCKLING BEHAVIOUR OF SLENDER GIRDERS

BY

ABDEL-RAHIM BADAWY ABDEL-RAHIM

A Thesis/Practicum submitted to the Faculty of Graduate Studies of the University of Manitoba in partial fulfillment of the requirements for the degree of

DOCTOR OF PHILOSOPHY

Abdel-Rahim Badawy Abdel-Rahim © 1996

Permission has been granted to the LIBRARY OF THE UNIVERSITY OF MANITOBA to lend or sell copies of this thesis/practicum, to the NATIONAL LIBRARY OF CANADA to microfilm this thesis/practicum and to lend or sell copies of the film, and to UNIVERSITY MICROFILMS INC. to publish an abstract of this thesis/practicum..

This reproduction or copy of this thesis has been made available by authority of the copyright owner solely for the purpose of private study and research, and may only be reproduced and copied as permitted by copyright laws or with express written authorization from the copyright owner.

I hereby declare that I am the sole author of this thesis.

I authorize the University of Manitoba to lend this thesis to other institutions or individuals for the purpose of scholarly research.

ABSTRACT

In 1983, the collapse of an industrial steel building roof in Freeport, Texas, due to local buckling of the compression flange of slender plate girders, had raised a question about the validity of the design standards and specifications. Thus, both experimental and theoretical studies were conducted at the Structural Engineering and Construction Research and Development Facility of the Civil and Geological Engineering Department, the University of Manitoba to study the effect of web-flange interaction on the behaviour of slender girders subjected to bending about the major axis,. In the experimental phase of this study, nine full-scale girders were tested. The girders had a span of 4.5 m and a variable web height ranging from 798 mm to 1200 mm, giving a range in height-to-thickness ratios (h/w) of 170 to 257. The flange widths ranged from 201 mm to 352 mm, giving a range in width-to-thickness ratios (b/2t) of 12.5 to 21.9.

The specimens were subjected to two concentrated loads located at equal distances from the end supports causing a uniform bending moment between the loads. The portion of the girders between the applied loads constituted the test region and was designed separately from the end portions which were heavily reinforced to prevent failure within these regions.

To prevent failure by lateral-torsional buckling, the tested girders were laterally supported at the load points as well as at supports.

Standard tension tests were performed on coupons cut from the component plates of these tested girders to determine the actual mechanical properties, which showed that the flange plates were made from CAN/CSA-G40.21-300W steel and the web plates may made

from different grades of ASTM A607 steel.

In the theoretical phase of this study, a finite element model was developed to simulate the behaviour of such tested girders. The postbuckling behaviour as well as the web-flange interaction were taken into account. To include the effect of large displacements on the behaviour, a nonlinear geometric analysis was performed. A bilinear elasto-plastic response of the material was considered. The Newton-Raphson iterative method was used to perform these nonlinear analyses and the load was applied in increments.

The results from the developed finite element model showed excellent agreement with the experimental results. Once the validity of this model was verified, it was used to conduct a parametric study with the flange width-to-thickness ratio (b/2t) varied from 12.5 to 40.6 and the web height-to-thickness ratio (h/w) varied from 138 to 427.

A design model based on the results developed from the finite element analysis and the obtained experimental results is proposed. The ultimate moment capacities of such girders computed according to many standards and specifications as well as the proposed design model were compared to those obtained experimentally from the tests performed in this study and another study. The comparison showed that the proposed design model results had excellent agreement with the experimental results. The ultimate moment capacities obtained through the developed model were within 4% of those obtained experimentally. At the same time, the comparison showed that the ultimate moment capacities computed according to the current standards and specifications varied from overconservative to unconservative depending on the cross-sectional dimensions and the level of yield strength.

ACKNOWLEDGEMENT

The author wishes to express his gratitude and appreciation to Dr. D. Polyzois, Civil and Geological Engineering Department, for his guidance, advice and encouragement throughout this investigation.

The author also wishes to thank the members of his committee, Drs. G. Morris, R. K. N. D. Rajapakse and M. L. Ayari for their comments and suggestions.

The experimental program of this study, was conducted at the Structural Engineering and Construction Research and Development Facility, Civil and Geological Engineering Department, the University of Manitoba. The author wishes to express his appreciation for the technical assistance of its staff.

This research was funded by the Natural Science and Engineering Research Council of Canada (NSERC).

TABLE OF CONTENTS

LIST OF TABLES

LIST OF FIGURES

Figure **Page**

NOTATION

A_{feff} = effective area of compression flange;

A_f = flange area;

A_{gf} = gross area of flange;

A_w = web area;

a = distance between transverse stiffeners;

B = coefficient = $40000/\lambda_{fg}$;

b = width of flange;

b_e = effective width of compression flange;

b_{ineff} = ineffective width of compression flange;

b_p = end plate width;

b_1 = effective width of web adjacent to the compression flange;

b_2 = effective width of web above the neutral axis;

c = flange warpage;

d_p = end plate depth;

E = elastic modulus;

E_t = tangent modulus;

(F^a) = vector of applied load;

F_{cr} = critical stress;

F_{max} = maximum compressive stress in a plate;

(F^{nr}) = vector of restoring loads corresponding to the element internal load;

$(F^{nr})_{i-1}$ = load vector based on the displacement resulted from iteration (i-1);

F_{pl} = proportional limit of the stress;

F_t = ultimate strength at the tension flange;

F_u = ultimate strength;

F_y = yield strength;

F_{yf} = yield strength of compression flange;

F_1 = maximum compressive stress of web;

F_2 = maximum tensile stress of web;

G = shear modulus;

h = height of web;

h_e = web effective-width in compression;

h_{ineff} = ineffective height of web;

h_t = web effective-width in tension;

I_{xeff} = moment of inertia of the effective section about the major axis;

$[K]_{i-1}$ = deformed stiffness matrix resulted from the deformed geometry of iteration (i-1);

$[K_T]$ = tangent stiffness matrix;

k = buckling coefficient;

k_f = buckling coefficient of compression flange;

k_w = buckling coefficient of web;

M = applied moment;

M_{CSA} = ultimate moment capacity according to the CAN/CSA-S136-94 Standard (1994);

M_{ECCS} = ultimate moment capacity according to the ECCS Recommendations (1986);

M_{exp} = ultimate moment capacity obtained from testing;

$M_{F.E.}$ = ultimate moment capacity resulted from the finite element analysis;

M_{Mod} = ultimate moment capacity according to the proposed design model;

M_{sp} = ultimate moment capacity when $\lambda_w = \lambda_{wp}$;

M_{sr} = ultimate moment capacity when $\lambda_w = \lambda_{wr}$;

M_u = ultimate moment capacity;

M_y = yielding moment;

M_{y330} = ultimate moment capacity using yield strength of 330 MPa;

M_{y500} = ultimate moment capacity using yield strength of 500 MPa;

P = applied load;

P_u = ultimate load;

P_y = yielding load;

Q = function of stress termed the plastic potential determining the direction of plastic straining;

Rot_x, Rot_y, Rot_z = rotations about the nodal X, Y and Z axes;

[S] = stiffening stiffness matrix;

S_x = section modulus about the strong axis;

S_{xeff} = effective section modulus about the strong axis;

t = thickness of flange;

U_x, U_y, U_z, = translations in the nodal X, Y and Z directions;

(u) = displacement vector;

$(u)_i$ = displacement vector at the current iteration (i);

$(u)_{i-1}$ = displacement vector resulted from iteration (i-1);

w = thickness of web;

z = variation between flange centreline and web centreline;

α = angle between web and flange;

(Δu) = nodal displacement increment vector;

$(\Delta u)_i$ = nodal displacement increment vector of iteration (i-1);

δ = maximum percent elongation;

λ = plastic multiplier determining the amount of plastic straining;

λ_f = flange width-to-thickness ratio (b/2t);

λ_p = maximum limit allowing to a plate subjected to axial compressive stress to reach one half of its plastic strain without buckling = $65/\sqrt{F_{yf}}$ (ksi);

λ_r = minimum limit allowing to a plate subjected to axial compressive stress to buckle in the elastic range = $150/\sqrt{F_{yf}}$ (ksi);

λ_w = web height-to-thickness ratio (h/w);

θ = angle of rotation;

μ = Poisson's ratio;

σ_{eq} = single equivalent stress;

$\sigma_1, \sigma_2, \sigma_3$ = principle stresses; and

ψ = absolute ratio of maximum tensile stress to maximum compressive stress in the web;

CHAPTER 1

INTRODUCTION

1.1 GENERAL

The use of built-up structural members has increased significantly in the recent years. Improvements in welding quality combined with better automated welding equipment have resulted in built-up section becoming economically competitive. Now, when the range of rolled shapes has been exceeded, a designer can turn to built-up shapes as a possible option (Kulak et. al, 1995).

A plate girder is a beam built up from plate elements to achieve a more efficient arrangement of material than is possible with rolled beams (Salmon and Johnson, 1990). Plate girders have generally found their greatest application in spanning distances in the order of 25 m to 45 m (Kulak et. al, 1995).

In most cases, the plate elements used in such girder are slender. The main problem in using these plates is that local buckling of one of the component plates may take place before overall buckling of the member occurs.

1.2 LOCAL BUCKLING

Local buckling is defined as a bifurcation phenomenon. A component plate subjected to in-

plane stresses may be in equilibrium either in its original planar configuration or in a neighbouring deflected configuration (Galambos, 1968). Local buckling may occur either in the elastic or in the inelastic range of the material response. This local buckling is dependent upon width-to-thickness ratio, boundary conditions and yield strength of the plate (Bleich, 1952, Haaijer and Thürlimann, 1958, Timoshenko and Gere, 1961 and Galambos, editor, 1988).

Slender plates used as basic elements of a structural member may fail by local instability before overall instability of the member takes a place. Local buckling of such plates, subjected to axial compression and/or in-plane bending stresses, is recognized as a limit state by most of the current standards and specifications.

The current CAN/CSA-S16.1-94 Standard (1994) classifies sections for which local buckling is the ultimate limit state as Class 4 sections. The current AISC-LRFD Specification (1993), classifies such sections as slender sections. The classification, in both specifications, depends on the width-to-thickness ratio and the yield strength of the component plates.

1.3 POSTBUCKLING STRENGTH

Postbuckling strength was first observed by Wilson (1886). He had noticed that railroad plate-girder bridges with webs 3/16 in. (4.76 mm) thick and stiffeners at intervals of 5 ft (1.524 m) were "*bearing up well under use*".

It has been recognized that a critical buckling load of a plate is not satisfactory measure of plate strength for design purposes. To study the true behaviour of a built-up structural member composed of slender plates, it is important to extend the small deflection

plate equations to include the effect of out-of-plane deformations on the in-plane stress state of these plates. The out-of-plane plate buckling causes a stretching of the plate and develops a membrane action in both directions. The tensile stresses developed after buckling result in higher compressive stresses near the plate edges (supported edges), which are the stiffest parts of the plate (Dubas and Gehri, editors, 1986).

1.4 SCOPE

In this section, the statement of the problem and the objectives of this research program are presented. Highlights on the current study program and layout of the report are also presented in this section.

1.4.1 Statement of the Problem

In 1983, the collapse of an industrial steel building roof in Freeport, Texas, due to local buckling of the compression flange, had raised a question about the validity of the design standards and specifications for slender plate girders in bending. Thus, an experimental investigation was conducted at Butler Research Centre by Johnson (1985) to determine the ultimate moment capacity of such girders. The ranges of the investigated parameters, such as the flange width-to-thickness ratio (b/2t), the web height-to-thickness ratio (h/w) and the yield strength, were limited. Moreover, the study focussed on the ultimate moment capacity without studying the behaviour of such girders.

As a direct result of this experimental program, a variable buckling coefficient for the compression flange, as a function of the web height-to-thickness ratio (h/w), was suggested.

The experimental results of that study were incorporated in the latest editions of the AISC-Specifications (WSD, 1989 and LRFD, 1993).

Due to the lack of research in the field of bending of slender plate girders, many of the current standards recommend or specify that the design of such girders may or should be according to the standards of Cold-Formed Steel Members, for example, the CAN/CSA-S16.1-94 Standard (1994). In the standards of the Cold-Formed Steel Members, the web-flange interaction is not considered and for laterally supported girders the ultimate stress at the compression flange is assumed to reach the yield strength, regardless of the cross-sectional dimensions.

Due to these differences in the assumptions from standard to another, the difference in the design moment capacity computed according to standard is different than that computed according to another, sometimes, by as much as 400%.

1.4.2 Objectives

The main objectives of this study program are:

i) to study experimentally and theoretically the parameters that may affect the behaviour or the capacity of slender plate girders in bending;

ii) to use the experimental and the theoretical results to develop a new design model for such girders. The model should take into account the effect of web-flange interaction, the postbuckling strength and to be based on more realistic member behaviour;

iii) to compare the proposed model results to those of the current standards and specifications; and

iv) to suggest modifications for the current design guidelines.

1.4.3 Current Study Program

In this program, experimental and theoretical investigations to study the effect of web-flange interaction on the behaviour and the capacity of slender plate girders are discussed. An evaluation of the current standards and specifications is also included.

In the experimental investigation, nine full-scale slender plate girders were tested. Their cross sections were doubly-symmetric I-sections. The plate girders were simply supported at the ends and loaded at the third points. To prevent failure by lateral-torsional buckling, they were laterally supported at the ends and at the loaded points. Both the compression flange and the tension flange were laterally supported at these locations. The tested plate girders had a 4.5 m span. The heights of the webs ranged from 798 mm to 1200 mm, and their height (h)-to-thickness (w) ratios (h/w) ranged from 170 to 257. The widths of the flanges ranged from 201 mm to 352 mm, and their width (b)-to-thickness (t) ratios (b/2t) ranged from 12.5 to 21.9.

The mechanical properties of the material used for the component plates were determined in accordance with the ASTM Standards. A total number of 27 standard tension coupons were cut from these plates. The mechanical properties measured were: the yield strength (F_y); the ultimate strength (F_u); the elastic modulus (E); the maximum percent elongation (δ); and the Poisson's ratio (μ).

In the theoretical investigation, a finite element model was developed using the ANSYS finite element program (Swanson Analysis System, Inc., 1992). The finite element

results showed excellent agreement with the experimental results. Thus, the finite element analysis was extended to include a parametric study to determine the effects of different parameters on the buckling behaviour and the capacity of such girders.

In the finite element analysis, the heights of webs ranged from 650 mm to 2000 mm, and their height-to-thickness ratios (h/w) ranged from 139 to 427. The widths of the flanges ranged from 200 mm to 650 mm, and their width-to-thickness ratios (b/2t) ranged from 12.5 to 40.6. In addition, other cases were analyzed in which the thicknesses of the flange and the web were the variables. The parametric study and the experimental results were used to develop a design model for slender girders. The postbuckling strength and the web-flange interaction were considered in the design model.

A comparison of the experimental results, the computed values based on current standards and specifications and the results obtained using the proposed design model has also been presented in this study.

1.4.4 Layout of Report

Chapter one has presented an introduction in addition to the scope and the objectives of this study.

Chapter two presents the state of knowledge of the behaviour of plates subjected to axial compressive stresses or bending stresses. This behaviour includes the effect of local buckling and postbuckling on the behaviour of these plates and the plate girders. A review of the available design standards and specifications, that deal with the design of slender sections, is also presented.

Chapter three describes the experimental program. This includes a description of the specimens, test setup, test preparation, dimensions and variables of tested plate girders, instrumentation and test procedure. In addition, it includes a description of the tests to determine the mechanical properties of the steel.

The results obtained from the tests performed on the plate-girder specimens are presented in Chapter four. The observed behaviour of the plate-girder specimens is also discussed.

Chapter five presents the finite element model that was developed and used in this study. A comparison between the finite element results and the test results is also presented to show the correlation between them. The different variables considered in the parametric study and their effects on the behaviour and the capacities of the slender plate-girders are also discussed.

A design model of such girders in bending is proposed in Chapter six. A comparison between the test results, the values obtained using different standards and specifications and the results obtained using the proposed design model, is also discussed in Chapter six.

Chapter seven gives a summary of conclusions and suggestions for future work to continue this investigation.

Finally, some of the experimental results are presented in Appendices A, B, C, D, E, F and G, while results obtained from the finite element analysis and the proposed design model are presented in Appendices H and I.

CHAPTER 2

LITERATURE SURVEY

2.1 INTRODUCTION

A plate girder is a beam with a slender web. It behaves like a deep beam (Salmon and Johnson, 1990). Failure of a plate girder may be due to lateral-torsional buckling, local buckling of the compression flange, or yielding. In design, vertical buckling of the compression flange is prevented by limiting the web height-to-thickness ratio (h/w). Based on experimental and theoretical work by Basler and Thürlimann (1961 and 1963), a maximum limit of h/w ratio was given as follows:

$$\frac{h}{w} \leq \frac{13800}{\sqrt{F_{yf}\,(F_{yf} + 16.5)}} \qquad (2.1)$$

where,

h = height of web;

w = thickness of web; and

F_{yf} = yield strength of compression flange (ksi).

Equation 2.1 is given in the AISC-LRFD Specification (1993) as:

$$\frac{h}{w} \leq \frac{14000}{\sqrt{F_{yf}\,(F_{yf} + 16.5)}} \qquad for \quad \frac{a}{h} > 1.5 \tag{2.2}$$

where,

a = distance between transverse stiffeners.

If transverse stiffeners on the web are arranged, so that $\frac{a}{h} \leq 1.5$, the following higher limit of web height-to-thickness ratio (h/w) is allowed by the AISC-LRFD Specification (1993), as recommended by the ASCE-AASHO, Joint Committee, Subcommittee 1 on Hybrid Girder Design (1968):

$$\frac{h}{w} \leq \frac{2000}{\sqrt{F_{yf}\ (ksi)}} \qquad for \quad \frac{a}{h} \leq 1.5 \tag{2.3}$$

In deriving the preceding equations, it was assumed that E, the elastic modulus, is 29000 ksi; μ, the Poisson's ratio, is 0.30; the web area-to-compression flange area ratio (A_w/A_f) is equal to 0.50; and the maximum residual compressive stress is 16.5 ksi.

The CAN/CSA-S16.1-94 Standard (1994) gives the following limit for the web height-to-thickness ratio(h/w):

$$\frac{h}{w} \leq \frac{12000}{F_{yf}\ (ksi)}$$

or in SI units:

$$\frac{h}{w} \leq \frac{83138}{F_{yf}\ (MPa)} \tag{2.4}$$

In both AISC-LRFD Specification (1993) and CAN/CSA-S16.1-94 Standard (1994), these limits are based on the assumption that the maximum compressive residual stress is 1/3 of the

yield strength and they are considered to be conservative limits because they ignore the postbuckling strength of the girder.

2.2 WEB BUCKLING

Until the early 1960s, local web buckling was not considered critical in plate-girder design. The postbuckling strength was taken into account by assuming a factor of safety for web buckling smaller than that used for yielding or any other type of failure (Galambos, editor, 1988). Based on the results of an extensive theoretical and experimental investigation by Basler et. al (1960, 1961 and 1963), the limit of the web height-to-thickness ratio (h/w) was established as $980/\sqrt{F_{yf}}$ (ksi) to allow the girder to reach its yielding moment (M_y). A limit of $970/\sqrt{F_{yf}}$ (ksi) was adopted by the AISC Specifications (LRFD, 1986, LRFD, 1993, WSD, 1978 and WSD, 1989).

According to the AISC Specifications (LRFD, 1986, LRFD, 1993, WSD, 1978 and WSD, 1989), the flanges are assumed to provide some rotational restraint to the web. The web buckling coefficient (k_w) is assumed to have a value of 36.25, which is closer to 39.6, the value corresponding to plates with fixed unloaded edges than to 23.9, the value for a plate under stress gradient with hinged unloaded edges. The value of 36.25 corresponds to approximately 80% of fixity along the unloaded edges.

A limit of $1810/\sqrt{F_{yf}}$ (MPa) was used in the CAN/CSA-S16.1-M84 Standard (1984), based on the test results of two beams with Class 3 webs tested by Holtz and Kulak (1975). This limit had been increased to $1900/\sqrt{F_{yf}}$ (MPa) in the CAN/CSA-S16.1-M89 Standard (1989), based on an analytical study by Dawe and Kulak (1981).

Thus, according to the AISC Specifications (LRFD, 1986, LRFD, 1993, WSD, 1978 and WSD, 1989), the web is defined as slender if its height-to-thickness ratio (h/w) is larger than $970/\sqrt{F_{yf}}$ (ksi). It is classified as a Class 4 web (slender web) by the CAN/CSA-S16.1-94 Standard (1994) if its height-to-thickness ratio (h/w) is larger than $1900/\sqrt{F_{yf}}$ (MPa). The specified limit given by the CAN/CSA-S16.1-94 Standard (1994) is more conservative than that given by the AISC Specifications (LRFD, 1986, LRFD, 1993, WSD, 1978 and WSD, 1989).

To account for the postbuckling capacity of a slender plate girder, most researchers have assumed that part of the web in compression becomes ineffective after local buckling. Basler and Thürlimann (1961 and 1963) considered that only a part of the web equal to 30 times the web thickness located adjacent to the compression flange, was effective in compression while the remainder of the web in compression was considered ineffective, as shown in Figure 2.1.

Assuming a linear reduction in the bending capacity of slender girders due to local buckling, the following expression was developed by Basler and Thürlimann (1961 and 1963):

$$\frac{M_u}{M_y} = 1 - 0.0005 \frac{A_w}{A_f}\left(\frac{h}{w} - 5.7\sqrt{\frac{E}{F_y}} \right) \qquad \leq 1 \qquad (2.5)$$

where,

M_u = ultimate moment capacity;

M_y = yielding moment;

A_w = cross-sectional area of web;

A_f = cross-sectional area of compression flange;

E = elastic modulus; and

F_y = yield strength.

The second term on the right side of Equation 2.5 represents the effect of local buckling but includes the postbuckling capacity as shown in Figure 2.2.

In developing Equation 2.5, it was assumed that the term $5.7\sqrt{E/F_y}$ was the maximum limit for web height-to-thickness ratio (h/w) corresponding to web yielding without buckling. For F_y = 33 ksi and E = 29000 ksi, Equation 2.5 gives h/w = 170.

Experimental results obtained by Basler and Thürlimann (1963), Maeda (1971) and Cooper (1971), were in good agreement with the results obtained from Equation 2.5. The AISC-LRFD Specification (1986) as well as the AISC-WSD Specifications (1978 and 1989) have adopted Equation 2.5 for the design of plate girders.

In the AISC-LRFD Specification (1993), Equation 2.5 has been modified to:

$$\frac{M_u}{M_y} = 1 - \frac{A_w/A_f}{1200 + 300\, A_w/A_f}\left(\frac{h}{w} - 5.7\sqrt{\frac{E}{F_y}}\right) \leq 1 \qquad (2.6)$$

The reduction in bending capacity obtained through Equation 2.6 was similar to that obtained through Equation 2.5. Except when a slender web and low flange width-to-thickness ratio (b/2t) were used, a higher reduction in the bending capacity is obtained from Equation 2.5.

Högland (1973) proposed a different effective section shown in Figure 2.3 for computing the postbuckling capacity of plate girders. In this model, Högland assumed that the effective width of the web in compression is made up of two parts. The first located

adjacent to the compression flange with a width,

$$b_1 = 0.76\ w \sqrt{\frac{E}{F_{yf}}} \tag{2.7}$$

and the second located just above the neutral axis with a width,

$$b_2 = 1.64\ w \sqrt{\frac{E}{F_{yf}}} \tag{2.8}$$

where,

F_{yf} = yield strength of the compression flange.

(This section has also been adopted by the Swedish Specification, 1973).

This may lead to the following reduction in the section modulus:

$$\frac{S_{xeff}}{S_x} = 1 - 0.15 \frac{A_w}{A_f} \left(1 - 4.8 \frac{w}{h} \sqrt{\frac{E}{F_{yf}}} \right) \quad for \quad \frac{h}{w} \geq 4.8 \sqrt{\frac{E}{F_{yf}}} \tag{2.9}$$

where,

S_{xeff} = effective section modulus about the major axis; and

S_x = section modulus about the major axis.

Equation 2.9 gives a slightly larger reduction in the section properties than does of Equation 2.5 (Galambos, editor, 1988).

An approach similar to that developed by Högland was proposed by the ECCS-Technical Committee 8 (Dubas and Gehri, editors, 1986). In this case b_1 and b_2 were defined as follows:

$$b_1 = 0.87\ w\sqrt{\frac{E}{F_y}} \tag{2.10}$$

and,

$$b_2 = 1.30\ w\sqrt{\frac{E}{F_y}} \tag{2.11}$$

The CAN/CSA-S16.1-94 Standard (1994), gives an ultimate moment capacity for a plate girder section with Class 4 web and Class 1, Class 2 or Class 3 flange as follows:

$$\frac{M_u}{M_y} = 1 - 0.0005\ \frac{A_w}{A_f}\left(\frac{h}{w} - \frac{1900}{\sqrt{F_{yf}\ (MPa)}}\right) \tag{2.12}$$

The only difference between Equation 2.12 and Equation 2.5, is the term $1900/\sqrt{F_{yf}\ (MPa)}$, which corresponds to the maximum limit for the web slenderness ratio for which yielding without local buckling takes a place.

According to the CAN/CSA-S16.1-94 Standard (1994), if the width-to-thickness ratio of the compression flange (b/2t) is greater than $200/\sqrt{F_{yf}\ (MPa)}$ (Class 4 flange), the section should be designed according to the CAN/CSA-S136-94 Standard (1994), for the design of Cold-Formed Steel Structural Members. The effective section for the web in this case is similar to that proposed by the ECCS-Technical Committee 8 (Dubas and Gehri, editors, 1986). The effective widths b_1 and b_2, shown in Figure 2.3 are as follows:

$$b_1 = \frac{h_e}{(3 + \psi)} \tag{2.13}$$

and,

$$b_2 = \frac{h_e}{(1 + \psi)} - b_1 \qquad (2.14)$$

where,

h_e = effective width of web in compression defined as:

$$h_e = 0.95\, w \sqrt{\frac{k_w E}{F_1}} \left(1 - \frac{0.208}{h/w} \sqrt{\frac{k_w E}{F_1}} \right) \qquad (2.15)$$

ψ = absolute ratio of maximum tensile stress (F_2) to maximum compressive stress (F_1) in the web = $\left| \frac{F_2}{F_1} \right|$; and

k_w = web buckling coefficient:

$= 4 + 2(1 + \psi)^3 + 2(1 + \psi)$ $\qquad 0 \le \psi \le 1$

$= 6(1 + \psi)^2$ $\qquad 1 < \psi \le 3$

Equation 2.15, is the general form of Winter's equation, which was developed from experimental investigation (1947 and 1968). It was a modification of Von-Kármán's equation (1932) and included the effect of imperfections.

Gerard (1957) suggested the following effective portion of the web in compression:

$$h_e = 0.787 \left(\sqrt{\frac{k_w E}{F_{max}}} \frac{w}{h} \right)^{-0.85} \qquad (2.16)$$

and, Faulkner (1977) recommended:

$$h_e = w \sqrt{\frac{k_w E}{F_{max}}} \left(1 - \frac{0.248}{h/w} \sqrt{\frac{k_w E}{F_{max}}} \right) \qquad (2.17)$$

where,

F_{max} = maximum compressive stress in the plate.

Winter's equation is currently used by both the AISI Specification (1989) and the CAN/CSA-S136-94 Standard (1994) for computing the effective area of the section.

2.3 COMPRESSION FLANGE BUCKLING

The compression flange of a plate girder is considered by most researchers to be a plate simply supported along the web with or without some rotational restraint and subjected to an axial compressive stress.

There are two approaches to determine the torsional-buckling behaviour of the compression flange in a plate girder. In first approach, the full section of the compression flange is assumed to be effective while a reduced compressive stress is used to compute the buckling strength, defined as:

$$P_u = A_{gf} F_{cr} \tag{2.18}$$

where,

A_{gf} = gross area of compression flange;

F_{cr} = reduced critical stress; and

P_u = ultimate force capacity of compression flange.

In the second approach, the full yield strength of the plate is multiplied by an effective area of the compression flange to compute the buckling strength, that is:

$$P_u = A_{feff} F_{yf} \tag{2.19}$$

where,

A_{feff} = effective area of compression flange; and

F_{yf} = yield strength of compression flange.

The AISC-LRFD Specifications (1986 and 1993) as well as the AISC-WSD Specifications (1978 and 1989) follow the first approach. The AISC-LRFD Specification (1986) classifies the compression flange into three categories:

Category (1) For : $\lambda_f \leq \lambda_p$ (stocky flange):

$$F_{cr} = F_{yf} \tag{2.20}$$

No reduction in the stresses is considered in this Category

Category (2) For : $\lambda_p < \lambda_f \leq \lambda_r$:

$$F_{cr} = F_{yf}\left[1 - \frac{1}{2}\left(\frac{\lambda_f - \lambda_p}{\lambda_r - \lambda_p}\right)\right] \leq F_{yf} \tag{2.21}$$

A linear reduction from the yield strength is considered in Category 2 to take into account the inelastic behaviour of the plate.

Category (3) For : $\lambda_f > \lambda_r$ (slender flange):

$$F_{cr} = \frac{11200}{\lambda_f^2} \qquad (2.22)$$

The behaviour in Category 3 is considered to be elastic.

In Equations 2.20, 2.21 and 2.22,

λ_f = compression flange width-to-thickness ratio = $\frac{b}{2t}$;

λ_P = maximum limit allowing to a plate subjected to axial compressive stress to reach one-half of its plastic strain without buckling = $\frac{65}{\sqrt{F_{yf}}}$;

λ_r = the minimum limit allowing to a plate subjected to axial compressive stress to buckle in the elastic range = $\frac{150}{\sqrt{F_{yf}}}$; and

F_{cr} = reduced critical stress (ksi).

The same approach was used in the AISC-WSD Specification (1978). The three Categories in that specification were:

Category (1) For : $\lambda_f \leq \frac{95}{\sqrt{F_{yf}}}$:

Equation 2.20 was used.

Category (2) For : $\frac{95}{\sqrt{F_{yf}}} < \lambda_f < \frac{176}{\sqrt{F_{yf}}}$:

$$F_{cr} = F_{yf}\left(1.415 - 0.00437\,\lambda_f\sqrt{F_{yf}}\right) \leq F_{yf} \qquad (2.23)$$

Category (3) For : $\lambda_f \geq \frac{176}{\sqrt{F_{yf}}}$:

$$F_{cr} = \frac{20000}{\lambda_f^2} \qquad (2.24)$$

The main differences between the AISC-LRFD Specification (1986) and the AISC-WSD Specification (1978) are:

i) The AISC-LRFD Specification (1986) assumes that the web provides no rotational restraint to the compression flange, so a value of 0.43 for the buckling coefficient (k_f) of the compression flange is considered. In the AISC-WSD Specification (1978), however, a value of 0.70 was considered. This value falls midway between the case of a simply supported flange where $k_f = 0.43$ and a fixed flange where $k_f = 1.277$, i.e. a partial rotational restraint was assumed.

ii) Different transition equations which account for the inelastic behaviour of the compression flange are used (Equations 2.21 and 2.23).

iii) The proportional limit of the stress is given by the AISC-LRFD Specification (1986) as one-half the yield strength ($F_{pl} = 0.50\ F_{yf}$). While it is given by the AISC-WSD Specification (1978) as $0.66\ F_{yf}$.

Because of the preceding differences, the limits which classify the type of the compression flanges, are not the same for the two specifications, as shown in Figure 2.4.

Based on an analytical study by Dawe and Kulak (1981), the maximum limit for the compression flange width-to-thickness ratio (b/2t) to yield without local buckling, was reduced from $250/\sqrt{F_{yf}}\ (MPa)$, as given by the CAN/CSA-S16.1-M79 Standard (1979) to $200/\sqrt{F_{yf}}\ (MPa)$ in the CAN/CSA-S16.1-M84 Standard (1984), the CAN/CSA-S16.1-M89 Standard (1989) and the CAN/CSA-S16.1-94 Standard (1994). An experimental study by Lukey and Adams (1969) showed that a limit of $170/\sqrt{F_{yf}}\ (MPa)$ was required for the flange width-to-thickness ratio (b/2t) to reach the full plastic moment. Studies by Lay (1965),

McDermott (1969) and Culver and Nasir (1971), showed that a limit of $145/\sqrt{F_{yf}}$ (MPa) was required for the flange width-to-thickness ratio (b/2t) to reach strain-hardening. All of these limits are included in the current CAN/CSA-S16.1-94 Standard (1994).

According to the CAN/CSA-S16.1-94 Standard (1994), the design of a plate girder with Class 4 web and Class 4 flange is conducted according to the CAN/CSA-S136-94 Standard (1994), Cold-Formed Steel Structural Members. In this case the standard uses the full yield strength of the compression flange multiplied by an effective area. The width of the compression flange is reduced using Winter's equation, as follows:

$$b_e = 0.95(2t)\sqrt{\frac{k_f E}{F_{yf}}}\left(1 - \frac{0.208}{b/2t}\sqrt{\frac{k_f E}{F_{yf}}}\right) \quad for \quad \frac{b}{2t} \geq 0.644\sqrt{\frac{k_f E}{F_{yf}}} \qquad (2.25)$$

where,

b_e = effective width of compression flange;

b = total width of compression flange;

t = thickness of compression flange; and

k_f = buckling coefficient of compression flange.

A value of 0.43 is used for the buckling coefficient of the compression flange.

The effective width of the compression flange adopted by the ECCS-Technical Committee 8 (1986), is almost identical to that used in the CAN/CSA-S136-94 Standard (1994). The only difference is in the reduction term, which accounts for the effect of imperfections, where a factor of 0.190 is used instead of 0.208. This results in a slightly larger capacity than that predicted by the CAN/CSA-S136-94 Standard (1994).

2.4 WEB-FLANGE INTERACTION

The AISC-WSD Specification (1989) has introduced the following stress equations which account for the web-flange interaction:

Category (1) For : $\lambda_f \leq \dfrac{95}{\sqrt{F_{yf} / k_f}}$:

Equation 2.20 was used.

Category (2) For : $\dfrac{95}{\sqrt{F_{yf} / k_f}} \prec \lambda_f \prec \dfrac{195}{\sqrt{F_{yf} / k_f}}$:

$$F_{cr} = F_{yf}\left(1.293 - 0.00309\ \lambda_f \sqrt{F_{yf} / k_f} \right) \leq F_{yf} \qquad (2.26)$$

Category (3). For : $\lambda_f \geq \dfrac{195}{\sqrt{F_{yf} / k_f}}$:

$$F_{cr} = \frac{26200\ k_f}{\lambda_f^2} \qquad (2.27)$$

In Equations 2.26 and 2.27, k_f is the buckling coefficient of compression flange, defined as:

$$k_f = \frac{4.05}{(h/w)^{0.46}} \qquad for \qquad (h/w) > 70 \qquad (2.28)$$

otherwise $k_f = 1.0$.

Equations 2.26, 2.27 and 2.28 were based on results of an experimental investigation conducted at the Butler Research Center by Johnson (1985). Ten welded-wide-flange beams were tested. The beams were 15'-8" (4.775 m) long and were loaded by concentrated loads applied on the tension flanges at a distance of 60 in. (1.524 m) from each support. The heights of webs were approximately 12 in. (305 mm), and their height-to-thickness ratios

(h/w) ranged from 73.2 to 176.3. The widths of the flanges ranged from 5.23 in. (133 mm) to 6.42 in. (163 mm), and their width-to-thickness ratios (b/2t) ranged from 11.5 to 14.3. To prevent failure by lateral-torsional buckling, the compression flanges were laterally supported.

Johnson (1985) reported that premature flange buckling failure was observed in the tested specimens. The flange and the web rotated about a longitudinal axis coinciding with the web-flange intersection and they retained their 90° relationship. As a result of this phase of the study, the following variable buckling coefficient (k_f), which is a function of the web height-to-thickness ratio (h/w), was suggested:

$$k_f = \frac{4.44}{\sqrt{(h/w)}} \tag{2.29}$$

Johnson (1985) tested nine more welded wide-flange beams. These beams were 30 ft (9.144 m) long and were loaded at four points of 5 ft (1.52 m) interval distances. The heights of the webs ranged from 19.87 in. (505 mm) to 23.97 in. (609 mm), and their height-to-thickness ratios (h/w) ranged from 107 to 245. The width-to-thickness ratios of the flanges (b/2t) ranged from 7.1 to 15.5. Based on the results from these tests, the modification of the compression flange buckling coefficient, as presented in Equation 2.28, was suggested.

The buckling coefficient of the compression flange (k_f) used by various standards and specifications, is shown in Figure 2.5, as a function of web height-to-thickness ratio (h/w).

In the 1993 edition, the AISC-LRFD Specification has modified the stress equations, presented in the 1986 edition and discussed in Section 2.3, to account for the web-flange interaction in a way similar to that used in the AISC-WSD Specification (1989). The critical stress (F_{cr}) can be calculated according to Equations 2.20 and 2.21, while Equation 2.22,

which account for the elastic behaviour was modified as follows,

$$F_{cr} = \frac{26200\ k_f}{\lambda_f^2} \qquad (2.27)$$

which is identical to the equation representing the elastic behaviour in the AISC-WSD Specification (1989), except that:

$$k_f = \frac{4}{\sqrt{(h/w)}} \qquad where \qquad 0.35 \le k_f \le 0.763 \qquad (2.30)$$

Equation 2.30 is similar to those obtained by Johnson (1985). Finally, the limit λ_r is changed from $150/\sqrt{F_{yf}}$ in the 1986 edition to $230/\sqrt{F_{yf}/k_f}$ in the 1993 edition.

A theoretical model for computing the bending capacity of slender plate girders subjected to pure bending was also developed by Polyzois (1990). A series of 35 doubly symmetric I-sections was analyzed using finite element analysis software. The height-to-thickness ratios of the webs (h/w) ranged from 48 to 260 and the width-to-thickness ratios of the flanges (b/2t) ranged from 4 to 16. To prevent lateral-torsional buckling failure, the compression flanges were assumed to be laterally supported. In this model the effective widths of the compression flanges and the webs, as shown in Figure 2.2, were used. These are identical to those in the CAN/CSA-S136-94 Standard (1994), except that variable buckling coefficients for both the web and the compression flange were used to take into account the effect of web-flange interaction. The buckling coefficients are as follows:

For $\lambda_w \le \lambda_1$:

$$k_w = \left[1.277 - 0.827 \frac{(\lambda_l + B)}{\lambda_l (\lambda_w + B)} \right] \left(\frac{\lambda_w}{\lambda_f} \right)^2 \qquad (2.31)$$

For $\lambda_w > \lambda_l$:

$$k_w = 39.6 - \frac{29115}{(\lambda_w - \lambda_l + 76.6)^2} \tag{2.32}$$

and,

$$k_f = k_w \left(\frac{\lambda_f}{\lambda_w} \right)^2 \tag{2.33}$$

where,

λ_f = compression flange width-to-thickness ratio = $\frac{b}{2t}$;

λ_w = web height-to-thickness ratio = $\frac{h}{w}$;

$\lambda_l = 7.288\ \lambda_f$;

$B = \frac{40000}{\lambda_f^3}$;

k_f = buckling coefficient of compression flange; and

k_w = buckling coefficient of web.

A comparison between a limited number of experimental results and the results obtained from the theoretical model, showed that the theoretical model was conservative in estimating the ultimate moment capacity of the plate girders whose web height-to-thickness ratios (h/w) varied from 150 to 200 (Polyzois, 1990). Polyzois (1990) suggested that additional experimental tests were required to verify the current design criteria for girders with both slender webs and flanges.

2.5 THEORETICAL STUDIES

Plate buckling behaviour has been studied by many researchers since the nineteenth century.

Two major types of analysis have been used since: solving the governing differential equations, and introducing ultimate state models which depend only on the failure mechanisms (Dubas and Gehri, editors, 1986). The latter analysis is easier to use than the first. However, to use these simple models, calibration with test results or with finite element method simulations is important. Appropriate choice of failure mechanism by observing the buckling and postbuckling behaviour, if possible, of the tested plate or member is also important.

The methods, which depend on solving the governing differential equation, can be classified into two major categories, solving the Von-Kármán's differential equation (1932) (for example, using Fourier series or the finite difference method) and using the variational methods which can be classified as:

i) Analytical procedures: the most important analytical method used is the Ritz energy method (1908), (Chou and Pagano, 1967), where the displacements are expressed by polynomial functions whose coefficients are obtained by minimizing the potential energy of the plate.

ii) Folded plate theory: this approach was basically derived by Skaloud and Kristek (1977 and 1981) to study and analyze the postbuckling behaviour of box girders. The approach uses the folded plate theory, taking into account the large deflection effect of the plate and the interaction between different plates.

iii) Finite element method: it is the most powerful tool in the field of plate buckling (Dubas and Gehri, editors, 1986). Usually the principles of virtual work are used in this method. To account for the nonlinearity, an iterative procedure is needed

(generally, Newton-Raphson) and the load is applied in increments. To deal with the postbuckling behaviour of plates, the effects of plastic behaviour of the material and the influence of initial imperfection of the plates should also be included in the analysis.

The inelastic buckling for columns and rectangular plates has been investigated by Bleich (1952). He suggested the use of a reduced elastic modulus above the proportional limit in the direction of the longitudinal stresses, while no reduction was suggested for the elastic modulus in the transverse direction. Ros and Eichineger (1932) used the reduced elastic modulus above the proportional limit in both directions. Test results showed better agreement with Bleich (1952) assumptions.

To include the elasto-plastic material behaviour of the plate, Ilyushin (1947), Stowell (1948) and Bijlaard (1949) used the deformation theory of plasticity (Fung, 1965). On the other hand, the incremental theory was used in the plastic analysis of plate buckling by Handelman and Prager (1948) and Onat and Drucker (1953) (Fung, 1965). The latter method is mathematically correct (Drucker, 1949, Onat and Drucker, 1953, Haaijer and Thürlimann, 1958 and Dubay, 1978-79). However, the former method showed a better agreement with test results. The use of a shear modulus in the inelastic range equal to the shear modulus in the elastic range was the main reason for poor correlation between the incremental theory and test results (Drucker, 1949, Onat and Drucker, 1953, Haaijer and Thürlimann, 1958 and Lay, 1965). A reduction in the shear modulus in the inelastic range resulted in better correlation between the incremental theory and the test results (Haaijer and Thürlimann, 1958 and Lay, 1965).

The incremental theory was used by Haaijer and Thürlimann (1958) along with a reduction of 80% in the shear modulus. This was used in the inelastic range to determine the maximum plate width-to-thickness ratios of wide I-shapes for plastic design. The study presented analytical solutions for single web or flange assuming simple or rigid support at the web-flange junctions. They did not include the residual stress effects directly in the analysis. On the other hand, they suggested an empirical transition curve for the range above the proportional limit in the analysis of plate columns subjected to uniaxial compression.

Goldberg et. al (1964) presented a study of lateral and torsional buckling of thin-walled beams. The study included sectional distortion and proposed a strip analysis method depending on solving the strip differential equations of equilibrium. This method was used to study lateral and torsional buckling of channels subjected to bending. Elastic material behaviour was assumed and the effects of residual stresses were not included in the investigation.

Another finite strip method was presented by Graves-Smith and Sridharan (1978) to investigate the postbuckling analysis of perfect plates and sections. To include the nonlinear behaviour of imperfected plate, Hancock (1981) extended this method by using different displacement functions to study box and I-sections in compression.

Gallagher et. al (1971) used the finite element method successfully to simulate the nonlinear and postbuckling behaviour of plates. Rajasekaren and Murray (1973) investigated the coupled buckling in wide flange beam-columns by the finite element method. Deformational modes associated with distortion of the cross-section were included in the analysis. The effects of residual stresses were not included and a linear elastic material

behaviour was assumed. The model presented by Rajasekaren and Murray (1973) gave good results in predicting the flange local buckling, while it could not predict the web local buckling accurately.

A study of lateral-torsional buckling of I-beams was presented by Johnson and Will (1974). The finite element method was used to model the problem using plate elements for the web and line elements for the flanges. The cross sectional distortion was included in the study. In a later study Akey et. al (1977) extended this approach by isolating the out-of-plane buckling analysis from the in-plane stress analysis, which allowed them to use fewer equations. This method was also applied to gable frames. In both studies linear elastic behaviour of the material was assumed and the effects of residual stresses were not included.

Hancock (1978) used the finite strip technique to study the local, distortional and lateral buckling of wide I-shape beams. Linear material response was assumed and the effects of residual stresses were not included in the study. He reported that this method was more efficient than, but not as general as, the finite element method used by Johnson and Will (1974) and it was simpler to implement than the method developed by Goldberg et. al (1971).

Dawe and Kulak (1984a and 1984b) presented an energy-based plate buckling formulation to predict local buckling behaviour of wide I-shape members used as columns, beams and beam-columns. The web-flange interaction, residual stresses, elastic and inelastic behaviour of the material were included in the study. The method was limited to Class 1, Class 2 and Class 3 (according to the CAN/CSA-S16.1-M79 Standard, 1979) wide I-shapes. As mentioned earlier, the limits used in the CAN/CSA-S16.1-M89 Standard (1989) and CAN/CSA-S16.1-94 Standard (1994) to classify the sections are based on this study.

In 1981, Bradford and Trahair presented a finite element method to analyze the elastic distortional buckling of I-beams with flexible webs. The flanges were assumed to be rigid, so the local buckling behaviour of short-length beams was not predicted. This method was used to analyze particular cases of loading and end supports.

Pi and Trahair (1994a and 1994b) used the finite element method to investigate the nonlinear inelastic behaviour of thin-walled steel beam-columns subjected to biaxial bending and torsion. The method was based on the principles of virtual work and was extended to investigate the elastic and inelastic strengths of steel I-beams. The effects of residual stresses and initial crookedness of the I-beams were taken into account, but the loading cases were limited in analyzing the I-beams. The main objective of the study was to compare its proposed model to another model (small-rotation model) which ignored the high order terms and proved that the lateral-buckling load was overestimated, the postbuckling behaviour can not be performed and the maximum local capacities of slender beams were not correctly predicted using the small-rotation model.

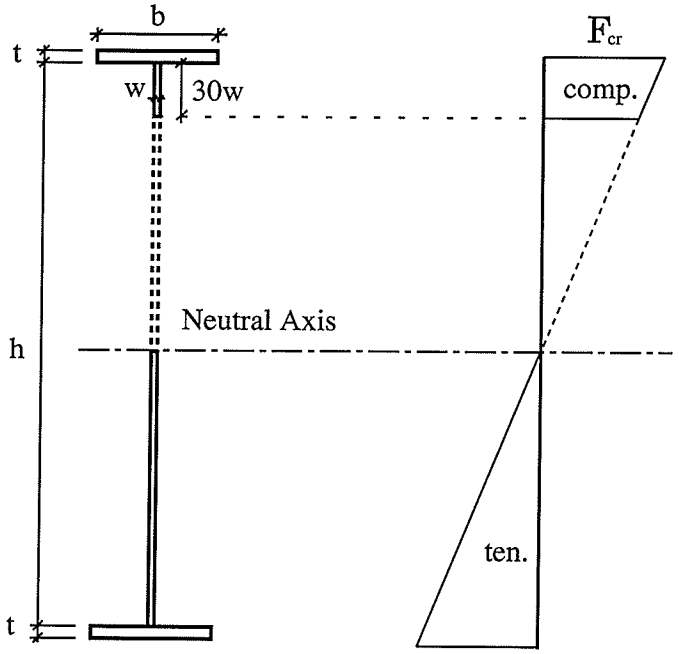

Figure 2.1 Effective Web Area and Stress Distribution as Presented by Basler and Thürlimann (1963)

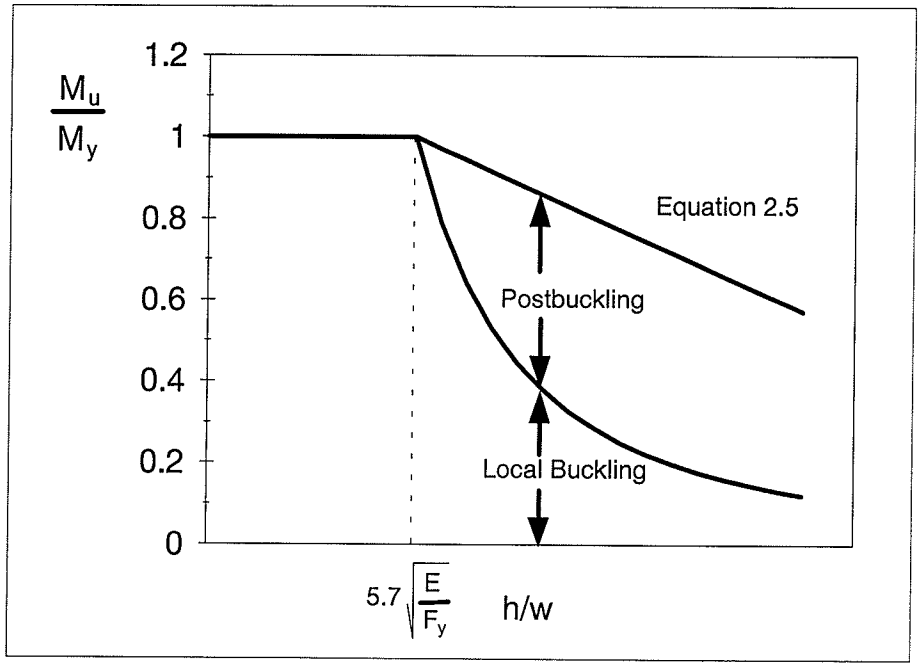

Figure 2.2 Effect of h/w on the Ultimate Moment Capacity

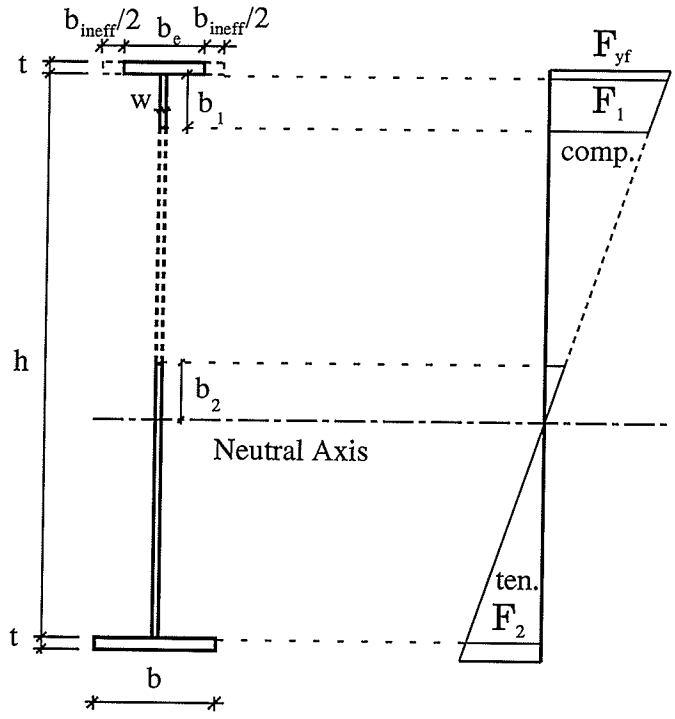

Figure 2.3 Effective Section and Stress Distribution According to the CAN/CSA-S136-94 Standard (1994)

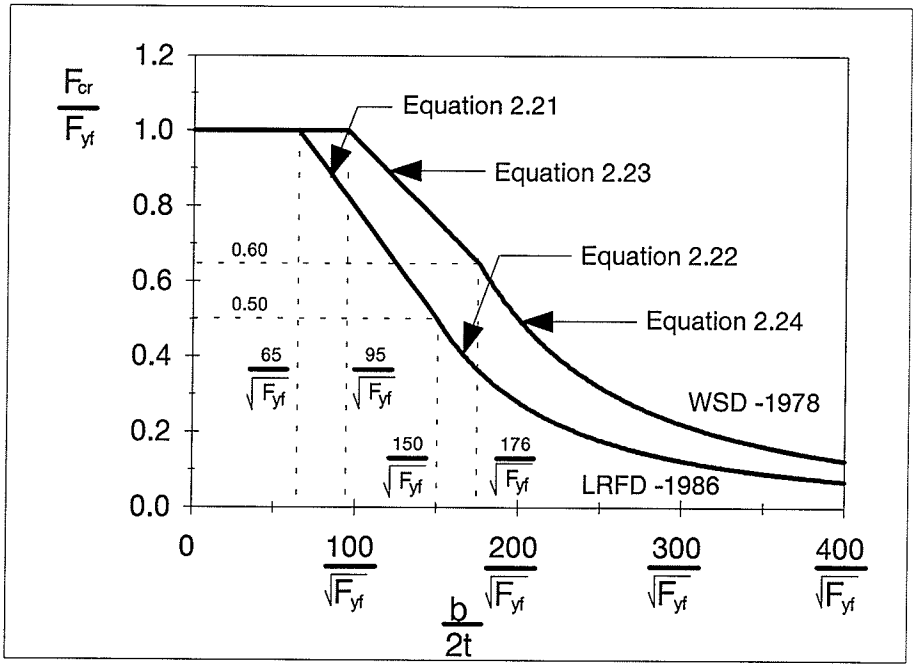

Figure 2.4 Effect of b/2t on the Reduced Critical Stress

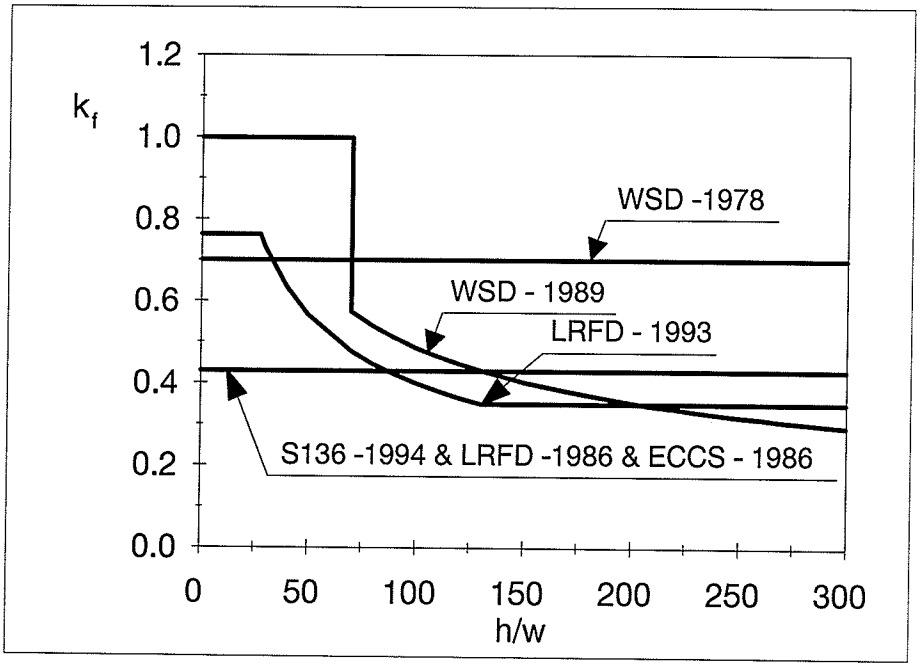

Figure 2.5 Effect of h/w on the Buckling Coefficient of Compression Flange

CHAPTER 3

EXPERIMENTAL PROGRAM

3.1 INTRODUCTION

As discussed in Chapter 1, one of the objectives of this research program was to study experimentally the parameters that may affect the behaviour and the capacity of slender plate girders subjected to bending about the major axis. Thus, nine full-scale specimens were tested. The web heights of these specimens ranged from 798 mm to 1200 mm to have h/w ratios range of 170 to 257. The flange widths of these specimens ranged from 201 mm to 352 mm to have b/2t ratios range of 12.5 to 21.9. To apply uniform bending moment to the specimens, the girders were simply supported at the ends and loaded by applying upward vertical loads at the third points, as shown in Figure 3.1. To prevent lateral-torsional buckling failure, the girders were laterally supported at the ends and at the loading locations. Both the compression flange and the tension flange were laterally supported. The ends of the girders were designed so that no failure would occur outside the middle third of the girders and to be re-used. The girder ends were stiff enough to produce uniform stress distributions on the loaded edges of the flange plates and linear stress distributions on the loaded edges of the web plate of the tested specimens.

A description of the test specimens, the tests to determine the mechanical properties

of the steel, the instrumentation used, the test setup, the test preparation and the test procedure, are presented in this Chapter.

3.2 TEST SPECIMENS

Nine full-scale specimens were tested at the Structural Engineering and Construction Research and Development Facility, the University of Manitoba. The specimens as well as the girder ends were fabricated in the Winnipeg plant of the Dominion Bridge Co. Ltd. The component plates were cut from larger plates by burning them mechanically (oxygen cut), so that the direction of applied stress was parallel to the direction of rolling. The flange plates were welded to the web plate using two sided fillet weld (size of weld = 4 mm), while these plates, flange and web plates, were welded to the end plates using groove welds. The welding procedure was according to the CAN/CSA-W59-M89 Standard (1989).

The specified thickness of the flange plates was 8 mm and that of the web plates was 5 mm. The thicknesses of the plates were kept constant while the flange width and the web height varied from one specimen to another. The specified dimensions and the slenderness ratios of the component plates of the specimens as well as the girder ends are listed in Table 3.1 and shown in Figure 3.2. Steel type CAN/CSA-G40.21-300W was specified. The minimum specified yield strength (F_y) of this type of steel is 300 MPa.

The dimensions of the component plates, such as web height and flange width were measured using a tape measure to an accuracy of 0.5 mm. The thicknesses of the plates were measured using a digital calliper to an accuracy of 0.01 mm.

The specimen depth and flange width as well as the distance from the web surface to

the edge of the flange, were measured in seven different locations on each side. Also, the specimen length was measured in five different locations on each side. The dimensions of the end-plates, the distances between the bolt holes and the hole diameters were also measured and recorded. The thickness of each flange was measured at seven different locations along its edges. The web thickness was determined from the standard tension coupon. All the dimensions were measured after removing the rust and cleaning the surfaces of the specimen. A similar procedure was used to measure the dimensions of the girder ends.

Table 3.2 lists the average measured dimensions of the cross sections of all specimens and girder ends. Also, in this table, the measured width-to-thickness ratios of the component plates are listed.

An initial check of all specimens showed that the flanges of the specimens were bent as shown in Figure 3.3. The warpage of the flange (c) and the lateral variations between the centreline of the flange and the centreline of the web (z) were measured and listed in Table 3.3. These measured values were less than the permissible limits given by the ANSI/AWS D1.1-88 Standard (1988).

The variations from flatness of webs, shown in Figure 3.4, were measured and the maximum value (Δ) for each specimen is listed in Table 3.4. The webs of the girders were initially imperfect, forming a half sin-wave in both directions, longitudinally and transversely, except for specimens G1, G2 and G3, where a reverse sin-wave was observed at the top part of the web. In other words, the initial distortion of the webs of these specimens was forming a half sin-wave at the mid-span sections, while it was forming two halves of sin-wave at the quarter-span sections, in the transverse direction. Longitudinally, it was forming a half sin-

wave at the bottom half of the webs of these specimens, while it was forming one and a half sin-waves at the top half of the webs, as shown in Figure 3.4. Also, the profile of the initial distortion of the web at mid-span and quarter-span sections of each specimen, in the transverse direction, is presented in Chapter 4.

The permissible limits of the variations from flatness of the webs, given by the ANSI/AWS D1.1-88 Standard (1988) and the CAN/CSA-W59-M89 Standard (1989), are also listed in Table 3.4, which shows that the maximum measured values of the variations from flatness of the webs of the tested specimens G1, G2 and G3 were lower than the permissible limits. However, they were higher than the permissible limits in specimens G4 to G9.

The permissible limits of the variations from flatness of the web are not a mandatory part of the CAN/CSA-W59-M89 Standard (1989), while they are a mandatory part of the ANSI/AWS D1.1-88 Standard (1988). Also, the permissible limits tabulated in both standards are for 8 mm web-thick and thicker webs.

Finally, as recommended by the ANSI/AWS D1.1-88 Standard (1988), the web-flange intersection edges were used as references for measuring the variations from flatness of the webs.

3.3 MATERIAL MECHANICAL-PROPERTIES

To conduct proper analysis of the results, it was important to determine the mechanical properties of the steel. The mechanical properties determined were: the yield strength (F_y); the elastic modulus (E); and the Poisson's ratio (μ). The ultimate strength (F_u) and the

maximum percent elongation (δ), were also determined. In total, 27 standard tension coupons were cut from the component plates of the specimens and tested according to the ASTM A 370-90a (1990) and the ASTM E 8M-90a (1990) Standards. The determination of the elastic modulus was made according to the ASTM E 111-82 Standard (1982) while the determination of the Poisson's ratio was made according to the ASTM E 132-86 Standard (1986).

To determine the mechanical properties of the steel, three standard tension coupons were cut from each specimen; one from the compression flange, one from the tension flange and one from the web. The locations from where the coupons were cut are shown in Figure 3.5. In some cases the location was altered to avoid damaged area. The portions of the flanges and web were flame cut. The coupons were cut as far as possible from the flame cut sides and machined to the nearest 0.01 mm.

Plate-type coupons, with a 200 mm gage length, were used as specified by the ASTM A 370-90a (1990) and the CAN/CSA-G40.21-M92 (1992) Standards. A digital calliper, with an accuracy of 0.01 mm, was used to measure the cross-sectional dimensions of the coupons. These dimensions were measured at the ends of the gage length of each coupon and at 20 mm interval distance, then the average values were considered.

The tension coupons were tested in a 267 kN capacity testing machine. A 5 mm strain gage was placed in the longitudinal direction at the mid-length of the coupon as shown in Figure 3.6. Another 5 mm strain gage was placed on the back side of the coupon in the transverse direction, as shown in Figure 3.7, to determine the Poisson's ratio. An MTS extensometer with a gage length of 100 mm, was mounted on the coupon to obtain its

elongation, as shown in Figure 3.8.

All data signals were fed into Data Acquisition System to monitor and record these data onto a hard disk of a 286 PC Computer.

The coupons were properly aligned in the machine to avoid any bending stresses. The rate of loading was 1.5 kN/min. which was slow enough to avoid any thermal effect on the obtained results. The data were stored during testing at one second interval time.

The interpretation of data was carried out by a combination of regression analysis and the 0.2% offset method, according to the ASTM E 111-82 Standard (1982). The longitudinal strain gage was used to determine the yield strength and the elastic modulus, while the extensometer was used to determine the ultimate strength. The extensometer was removed from the coupon, once the neck had appeared, as shown in Figure 3.9. The regression analysis was also used to determine the Poisson's ratio.

A typical stress-strain curve of a coupon cut from the compression flange of specimen G4, is presented in Figure 3.10(a). The regression analysis and the 0.2% offset method were used to obtain the yield strength and the elastic modulus of the same coupon presented in Figure 3.10(b). Figure 3.10(c) presents the longitudinal vs transverse strain curve of the same tested coupon. The regression analysis was used here to obtain the Poisson's ratio. Typical stress-strain curves of coupons cut from the tension flange of specimen G4 and the compression flange of specimen G8 are presented in Figures 3.11 and 3.12, respectively.

Typical stress-strain curves of coupons cut from the web of specimen G4 and the web of specimen G8 are also presented in Figures 3.13 and 3.14, respectively.

The mechanical properties of all coupons, as well as the averages and the standard

divisions, are summarized in Table 3.5. The average yield strength of the flanges was 330 MPa. This was higher than the minimum specified yield strength of 300 MPa. The average yield strength of the web, as obtained from coupons cut from specimens G1, G2 and G3, was 384 MPa, while the yield strength of the coupons cut from the web plates of specimens G4 to G8 was 434 MPa. A yield strength of 479 MPa, was obtained from a coupon cut from the web of specimen G9. These results indicate that the 1000 mm and 1200 mm webs were cut from different plates than the 800 mm web.

By comparing the mechanical properties listed in Table 3.5 to those specified by the CAN/CSA-G40.21-M92 (1992) and the ASTM A607-90a (1990) Standards, it was found that the flange plates were made of steel type CAN/CSA-G40.21-300W (equivalent to steel type ASTM A607 Grade 45). According to the ASTM A607-90a Standard (1990), it was found that the web plates of specimens G1, G2 and G3 may made of steel type ASTM A607 Grade 55, while the web plates of specimens G4 to G8 may made of steel type ASTM A607 Grade 60. Finally, the web of specimen G9 may made from steel type ASTM A607 Grade 65.

3.4 INSTRUMENTATION

The instrumentation used in the experimental investigation was designed to measure:

i) the applied loads at the third points of the girders and the reaction forces at the end supports;

ii) the vertical displacements of the specimens and the end supports of the girders;

iii) the lateral deformations of the specimens and the lateral supports; and

iv) the strains in different sections and locations of the specimens.

3.4.1 Load Measurements

The loads were applied through hydraulic jacks with capacities of 200 Ton (2000 kN) and 100 Ton (1000 kN), as shown in Figure 3.15. To monitor and control the applied loads and to measure the reaction forces, the following pre-calibrated load cells were used, as shown in Figures 3.15 and 3.16:

i) a 200 Ton (2000 kN) capacity Wagezelle-type 66 load cell was used at the first point of loading;

ii) a 200 kip (900 kN) capacity Strain Sert compression flat load cell FL-200C-35 GK was used at the second point of loading;

iii) a 200 kip (900 kN) capacity SR-4 type CXX load cell was used at the first end support; and

iv) a 220 kip (1000 kN) capacity MTS-661.31A-02 load cell was used at the second end support.

3.4.2 Vertical Displacement Measurements

Linear Motion Transducers (LMTs), Linear Variable Differential Transducers (LVDTs) and dial gages were used to measure the vertical displacement of the specimens at various locations along their spans.

The LMT is a stainless steel cable attached to the moving object and the body of the transducer, as shown in Figure 3.17. Extension of the cable rotates a spring loaded shaft,

coupled to a sensing circuits. The constant force spring provides torque for cable retraction. Cable retraction velocity is limited by torque generated by the spring.

To monitor the vertical displacement and the rotation of the bottom flange (compression flange), four LMTs with a range of 10 in. (500 mm), were clamped to the flange edges. Two of these were located at the mid-span section of the specimen and the other two were located at a distance of 375 mm from the mid-span section of the specimen (the quarter-span section), as shown in Figure 3.17, with the exception of specimen G1, where the LMTs were located at a distance of 250 mm from the mid-span section.

Two LVDTs with a range of 2 in. (51 mm), were also used . They were placed at the mid-width points of the top flange (tension flange), as shown in Figure 3.17. To observe the rotation of the tension flange a vertical dial gage with 2 in. (51 mm) range and 0.001 in. (0.0254 mm) accuracy, was placed vertically at 20 mm from the flange edge at the mid-section of the specimen. In addition, similar two vertical dial gages were placed at the end supports to measure the vertical movement of the end supports, as shown in Figure 3.18.

The instrumentation used for measuring the displacements and the strains is shown schematically in Figure 3.19.

3.4.3 Lateral Displacement Measurements

A series of 15 dial gages with a range of 1 in. (25.4 mm) and accuracy of 0.001 in. (0.0254 mm), was used in each test to record the lateral displacements at various locations of the specimen.

Five horizontal dial gages were placed along the web height at the mid-span section

of the specimen, as shown in Figures 3.19 and 3.20. Four gages were placed along the web height at a distance of 375 mm from the mid-span section. In addition, two horizontal dial gages were used to measure the lateral displacement of the compression flange and the tension flange at the mid-span section of the specimen.

A group of four dial gages was placed horizontally on both flanges very close to the locations of the lateral supports, as shown in Figure 3.19, to monitor the lateral displacement at these locations.

3.4.4 Strain Measurements

To measure the longitudinal strains at the mid-span and the quarter-span sections, 20 electrical resistance strain gages were used in each specimen. The strain gages had 5 mm gage length and 120 ohm resistance. The gages were mounted according to the specified procedures. The locations, where the strain gages were to be mounted, were cleaned from any rust, oil or grease prior to mounting, as shown in Figure 3.21.

A series of eight strain gages was placed along the web height at the mid-span section of each specimen, as shown in Figure 3.19. They were placed on both the front and the back of the web so that each pair measured the strain at the same point of the web. This arrangement was adopted to monitor the membrane strains and to observe any web buckling. Another series of six strain gages was placed along the web height at the quarter-span section of each specimen, in a way similar to that used at the mid-span section.

At the mid-span section of each specimen, four strain gages were placed on both sides of the compression flange, 20 mm from the edges, to record the strains and observe the

buckling of this flange. Another two strain gages were placed on the top of the tension flange at a distance of 20 mm from the edges.

Figure 3.19 shows, schematically, the locations of all strain gages used. These location of the strain gages in specimen G1 was slightly different from the other specimens. The decision to change the location was made after observing the results from the testing of the first specimen G1.

The load cells, the LMTs, the LVDTs, and the strain gages were connected to a 50-channel Data Acquisition System which monitored and recorded all data onto a hard drive of a 286 PC Computer. The data was recorded at two seconds interval time. The readings obtained from the dial gages were recorded manually at a load increment of 25 kN.

3.5 TEST SETUP

A great deal of effort and time was spent in designing and constructing the test setup. All specimens were tested using the setup shown in Figures 3.22 and 3.23. The girders were loaded upward at the third points by pushing the bottom flange (compression flange) up. The girders were 4.5 m long. The actual specimens were 1.5 m long and were connected to stiffer ends with 26 mm thick end plates. Each specimen was connected to the girder ends using two groups of 12-1 in. (25.4 mm) diameter A490-bolts, as shown in Figure 3.23. The girder ends were designed to prevent failure during testing at these ends and also to be reused. All bolted and welded connections were designed so that no failure in these parts could take place during testing.

3.5.1 Load Equipment

An Enerpac RR-2006 hydraulic jack of 200 Ton (2000 kN) capacity and 6.625 in. (168 mm) stroke range, was used at one loading-point. The jack reacted was placed against the structural floor and load was applied to the bottom flange of the girder at the locations of the end-plates. The loading was applied by an Enerpac hydraulic pump PAM1022. The Wagezelle-type 66 load cell was placed between the hydraulic jack and the girder, using two 0.75 in. (19 mm) plates, as shown in Figures 3.15(a) and 3.23. A support consisting of two plates and cylinder was welded to the top load-cell plate. The cylinder allowed the top plate to be in full contact with the bottom flange of the girder and at the same time allowed the girder to rotate at the loading point.

A group of three Enerpac RLC-1002 hydraulic jacks with a capacity of 100 Ton (1000 kN) and stroke range 2.25 in. (57 mm) each, was used to apply the load at the second third-point, as shown in Figures 3.15(b) and 3.23. The jacks were placed on top of each others to have a combined stroke range of 6.75 in. (171 mm). The three jacks were controlled by using another hydraulic pump PAM1022, which was connected to the three jacks at the same time. The Strain Sert compression flat FL-200C-35GK load cell, was placed at the top of the jacks and the load was applied in the same way as that at the first point of loading.

To avoid any stress concentration and to allow for the rotation at the end supports, additional plates and cylinders were welded to the top flanges of the girder ends. Load cells were placed between these units and the supporting frames to measure the reaction forces, as shown in Figures 3.16 and 3.23.

3.5.2 Supporting Frames

Two frames were constructed to provide supports for the girder, as shown in Figures 3.24 and 3.25. Each frame consisted of two columns and a rafter connected to the columns with two 1 in. (25.4 mm) end plates. The rafter was connected to each column using 10-1 in. (25.4 mm) A490-bolts. Each column was welded to base plate. This base plate was then connected to the structural floor using four 1 in. (25.4 mm) prestressed dwyidag bars.

Each supporting frame provided the girder with lateral supports, as shown in Figures 3.24 and 3.25. Both the compression and the tension flanges were laterally supported. Teflon sheets were placed between the supports and the girder to allow the girder to displace vertically without friction.

3.5.3 Lateral-Supporting Frames

In addition to the lateral supports provided at the ends of the girder, lateral supports were also placed at the loading positions, as shown in Figures 3.22 and 3.26. Both top and bottom flanges were supported. The supports consisted of columns located on both sides of the girder and braced by back-to-back angles. The columns were welded to a base plate while the back-to-back angles were connected to the column using a gusset plate and connected to the structural floor using a base plate, as shown in Figure 3.26. The base plates were connected to the structural floor using prestressed dwyidag bars with a diameter of 1 in. (25.4 mm).

Adjustable brackets were attached to each column, as shown in Figure 3.26, to brace the top and the bottom flanges of the girders. Teflon sheets, similar to those at the end

support sections, were used to allow the girder to move with respect to the bracket supports.

3.6 TEST PROCEDURE

It took, approximately, two weeks to prepare and test each specimen.

3.6.1 Specimen Preparation

The following procedure was followed in preparing each specimen for testing:

i) The specimens were cleaned from rust.

ii) The dimensions of the specimens were measured, as discussed in Section 3.2.

iii) The specimens were positioned in the test setup using an overhead crane.

iv) The specimens were attached to the girder ends.

v) The specimens were levelled and aligned.

vi) The Teflon sheets were placed on the brackets to allow the girders to deflect vertically.

vii) The locations of the instrumentation were marked.

viii) A grid was marked on the web of each specimen to assist visual observation of the buckling distortion.

ix) The strain gages were mounted at the desired locations, as shown in Figure 3.21.

x) The specimens were whitewashed.

xi) The imperfection of the flanges and the web were measured.

xii) All dial gages, LMTs and LVDTs were positioned at the desired locations using magnetic bases and metal stands, as shown in Figure 3.17.

xiii) All instrumentation was connected to the Data Acquisition System.

3.6.2 Testing the Specimen

Each test started by adjusting the loading jacks so that contact with the bottom flange of the girder was achieved. The load cells at the load positions and at the ends were checked. Initial readings of all used instrumentation were then recorded.

The specimens were loaded using an increment load of 25 kN to allow for the readings of the dial gages to be recorded. Readings were recorded at two seconds interval time. The readings of the dial gages were recorded manually. Visual observations were also made during the test. The loads were controlled by using two hydraulic pumps, one for each point of loading. Loading of the girders was terminated after the maximum load was achieved and the recorded load was 10% below the maximum load achieved.

Once the recorded load started to drop, it was difficult to maintain load control. This was due to the failure of the specimen.

The testing of seven specimens was videotaped.

Table 3.1 Specified Dimensions of Specimens and Girder Ends*

Specimen	h (mm)	w (mm)	b (mm)	t (mm)	h/w	b/2t	b_p (mm)	d_p (mm)
G1	800	5	200	8	160	12.50	270	816
G2	800	5	270	8	160	16.88	270	816
G3	800	5	350	8	160	21.88	350	816
G4	1000	5	200	8	200	12.50	270	1016
G5	1000	5	270	8	200	16.88	270	1016
G6	1000	5	350	8	200	21.88	350	1016
G7	1200	5	200	8	240	12.50	270	1216
G8	1200	5	270	8	240	16.88	270	1216
G9	1200	5	350	8	240	21.88	350	1216
Girder Ends	1178	12	350	19	98	9.21	350	1216

*These dimensions are illustrated in Figure 3.2

Table 3.2 Average Measured Dimensions of Specimens and Girder Ends

Specimen	Web			Compression Flange			Tension Flange		
	h (mm)	w (mm)	h/w	b (mm)	t (mm)	b/2t	b (mm)	t (mm)	b/2t
G1	799.10	4.68	170.75	201.67	8.05	12.53	201.20	8.07	12.47
G2	798.40	4.70	169.87	270.71	8.10	16.71	270.64	8.10	16.71
G3	802.62	4.65	172.61	351.71	8.13	21.63	351.78	8.08	21.77
G4	1000.50	4.68	213.78	201.36	8 .00	12.59	201.18	8.03	12.53
G5	1000.00	4.71	212.31	270.50	8.03	16.84	270.50	8.03	16.84
G6	1000.00	4.70	212.77	351.50	8.05	21.83	351.50	8.07	21.78
G7	1200.50	4.74	253.27	200.93	8.04	12.50	201.00	7.96	12.63
G8	1200.00	4.67	256.96	270.50	8.04	16.82	270.00	7.99	16.90
G9	1196.00	4.65	257.20	352.00	8.07	21.81	351.00	8.01	21.91
Girder End 1	1177.88	12.56	93.78	349.80	18.55	9.43	350.83	18.57	9.45
Girder End 2	1176.27	12.57	93.58	351.40	18.77	9.36	350.00	18.73	9.34

Table 3.3 Dimensional Tolerances and Flanges Imperfection

Specimen	c (mm)*+		z (mm)**+	
	Mid-Span	Quarter-Span	Top Flange	Bottom Flange
G1	1.7	1.3	0.5	0.5
G2	3.0	1.5	0.5	0.5
G3	2.8	2.5	1.3	0.8
G4	1.5	1.0	1.8	1.0
G5	3.3	2.8	1.0	0.8
G6	2.8	2.3	1.0	1.0
G7	1.8	1.3	1.3	3.8
G8	2.8	2.0	0.3	1.0
G9	5.5	3.5	1.5	1.8

*c is sketched in Figure 3.3
**z is sketched in Figure 3.3
+According to the ANSI/AWS D1.1-88 Standard (1988), c and z should be less or equal to 6.4 mm

Table 3.4 Maximum Web Imperfection

Specimen	Δ^*	Δ_{all}^{**}		
		AWS Clause 8.13.2	AWS App. VI	CSA-W59***
G1	2.9	10.0	8.0	8.0
G2	2.6	10.0	8.0	8.0
G3	4.3	10.0	8.0	10.0
G4	17.8	12.5	9.5	12.0
G5	14.5	12.5	9.5	10.0
G6	17.7	12.5	9.5	10.0
G7	20.4	15.0	14.3	16.0
G8	20.1	15.0	14.3	16.0
G9	20.9	15.0	11.1	12.0

*Δ is the maximum measured imperfection of the web as shown in Figure 3.4

**Δ_{all} is the maximum allowable imperfection of the web According to the ANSI/AWS D1.1-88 Standard (1988) and the CAN/CSA-W59-M89 Standard (1989)

***According to the CAN/CSA-W59-M89 Standard (1989) these values are not a mandatory part of the standard

Table 3.5(a) Mechanical Properties of Coupons Cut from the Compression Flanges

Specimen	F_y (MPa)	F_u (MPa)	E (GPa)	δ (%)	μ
G1	327	506	235	21.5	0.282
G2*			Not Available		
G3	330	512	198	21.5	0.289
G4	332	522	211	21.5	0.308
G5	325	505	226	22.5	0.317
G6	327	511	211	22.5	0.290
G7	333	510	204	22.0	0.284
G8	332	509	221	21.0	0.313
G9	330	510	212	23.0	0.306
Average Values	330	511	215	21.9	0.299
Standard Divisions	2.88	5.18	12.00	0.68	0.014

*This compression flange was distorted to obtain flat coupons

Table 3.5(b) Mechanical Properties of Coupons Cut from the Tension Flanges

Specimen	F_y (MPa)	F_u (MPa)	E (GPa)	δ (%)	μ
G1	333	504	220	24.0	0.293
G2	330	509	215	21.5	0.282
G3	328	508	239	22.5	0.318
G4	335	517	207	21.8	0.182*
G5	327	505	227	21.5	0.293
G6	327	505	212	22.5	0.295
G7	327	505	214	24.0	0.293
G8	329	511	199	22.5	0.270
G9*	Not Available				
Average Values	330	508	216	22.5	0.292
Standard Divisions	3.02	4.38	12.27	1.00	0.015

*This value was not considered

Table 3.5(c) Mechanical Properties of Coupons Cut from the Webs

Specimen	h (mm)	F_y (MPa)	F_u (MPa)	E (GPa)	δ (%)	μ
G1	800	381	465	231	20.0	0.294
G2	800	388	469	218	21.0	0.278
G3	800	382	468	212	22.0	0.265
Average Values		384	467	220	21.0	0.279
Standard Divisions		3.79	2.08	9.71	1.00	0.015
G4	1000	432	507	224	18.0	0.282
G5	1000	437	503	209	18.0	0.240
G6	1000	440	503	211	17.0	0.280
G7	1200	432	489	208	19.0	0.260
G8	1200	430	492	224	22.5*	0.293
Average Values		434	499	215	18.0	0.266
Standard Divisions		4.15	7.82	8.11	0.82	0.021
G9	1200	479	527	222	20.0	0.281

*This value was considered

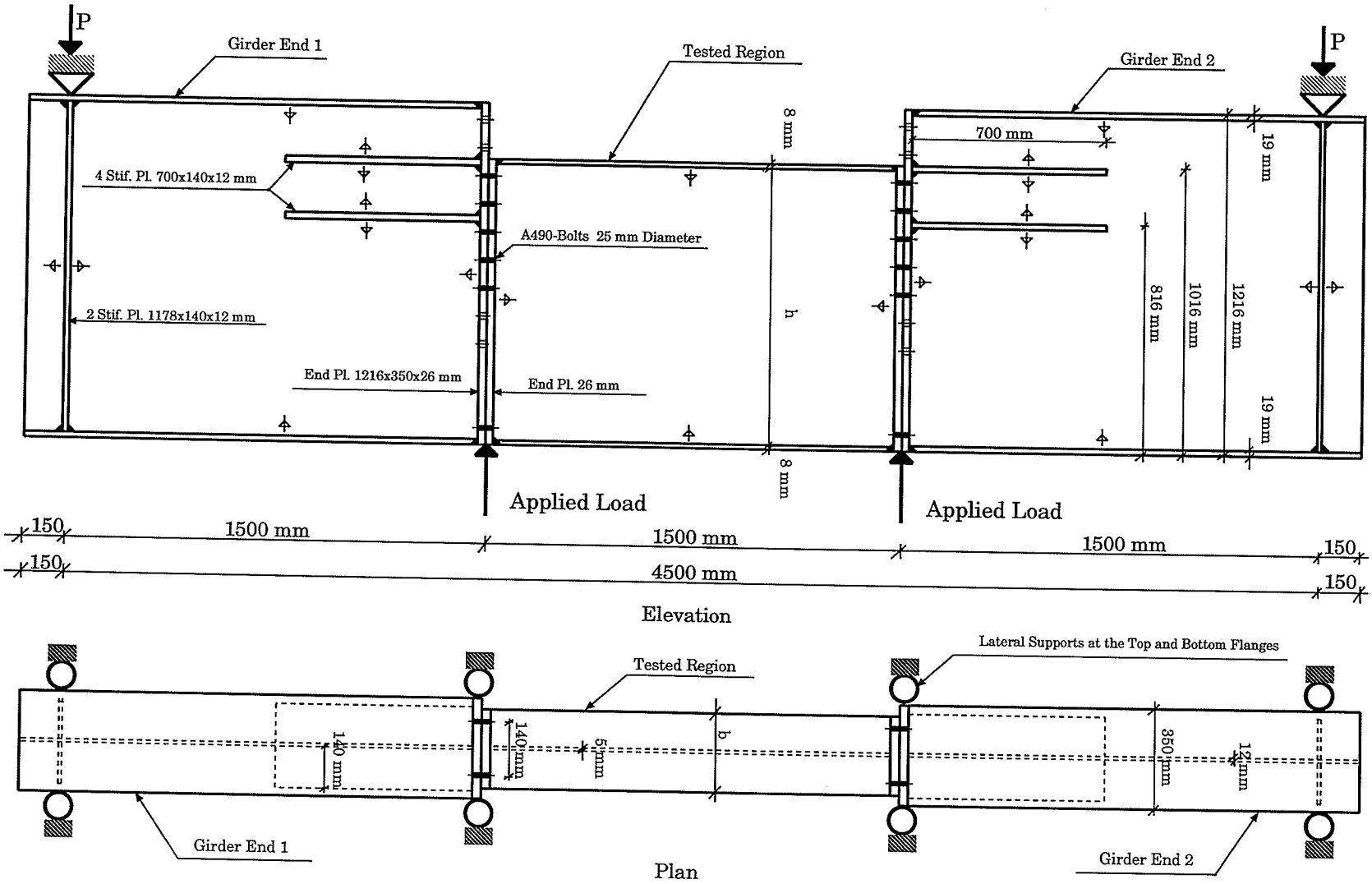

Figure 3.1 Statical System of the Tested Girder

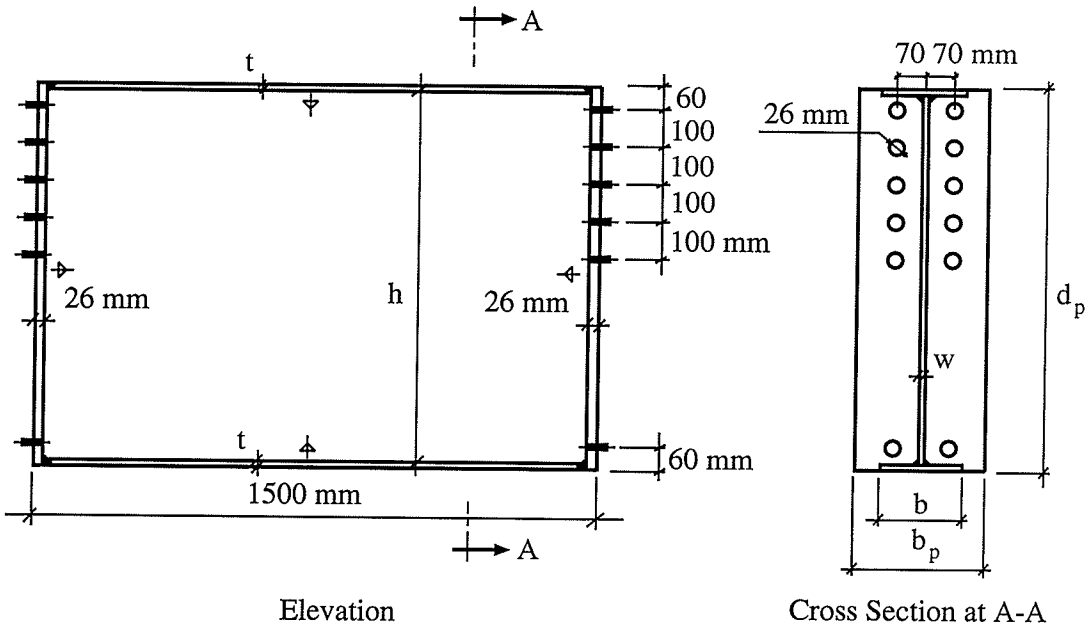

Figure 3.2 Specified Dimensions of Specimens

(a) Warpage of Flange

(b) Variation Between Flange and Web Centrelines

Figure 3.3 Initial Distortion of Flange

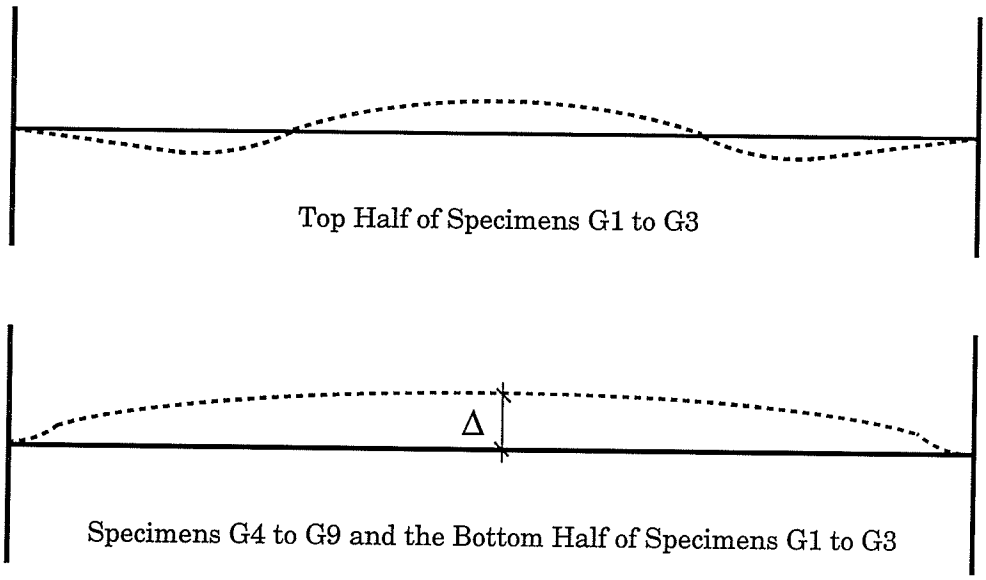

(a) Longitudinal Direction

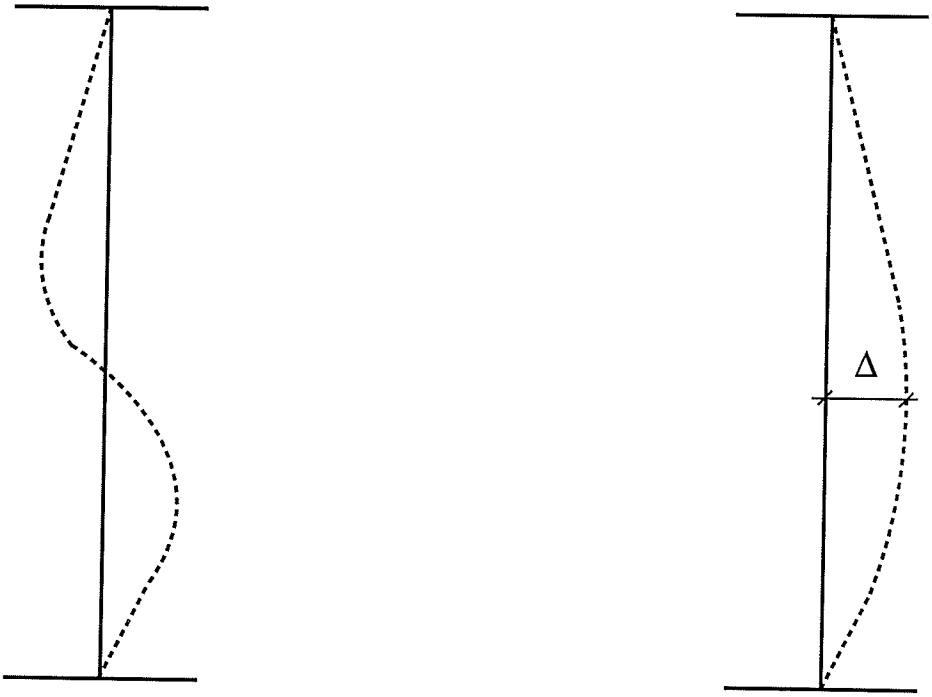

Quarter-Span Sections of Specimens G1 to G3

Specimens G4 to G9 and Mid-Span Sections of Specimens G1 to G3

(b) Transverse Direction

Figure 3.4 Variations from Flatness of Tested Specimens Webs

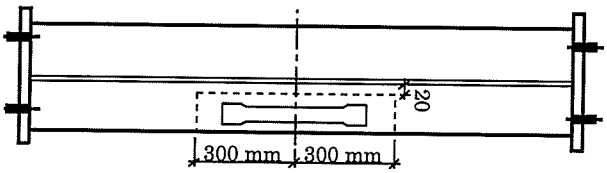

(a) Coupon Cut from the Tension Flange of the Specimen

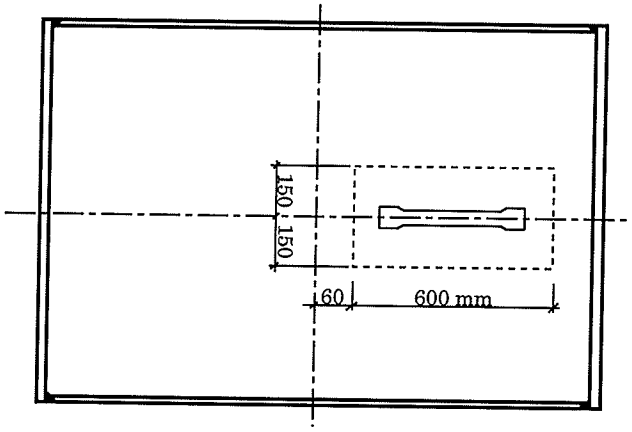

(b) Coupon Cut from the Web of the Specimen

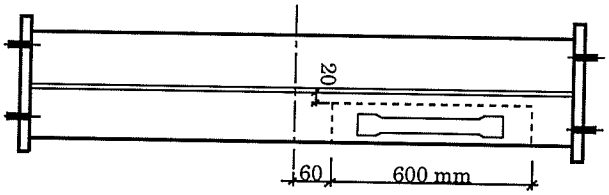

(c) Coupon Cut from the Compression Flange of the Specimen

Figure 3.5 Relative Coupon Locations in their Respective Plates

Figure 3.6 Strain Gage Placed on the Tested Coupon in the Longitudinal Direction

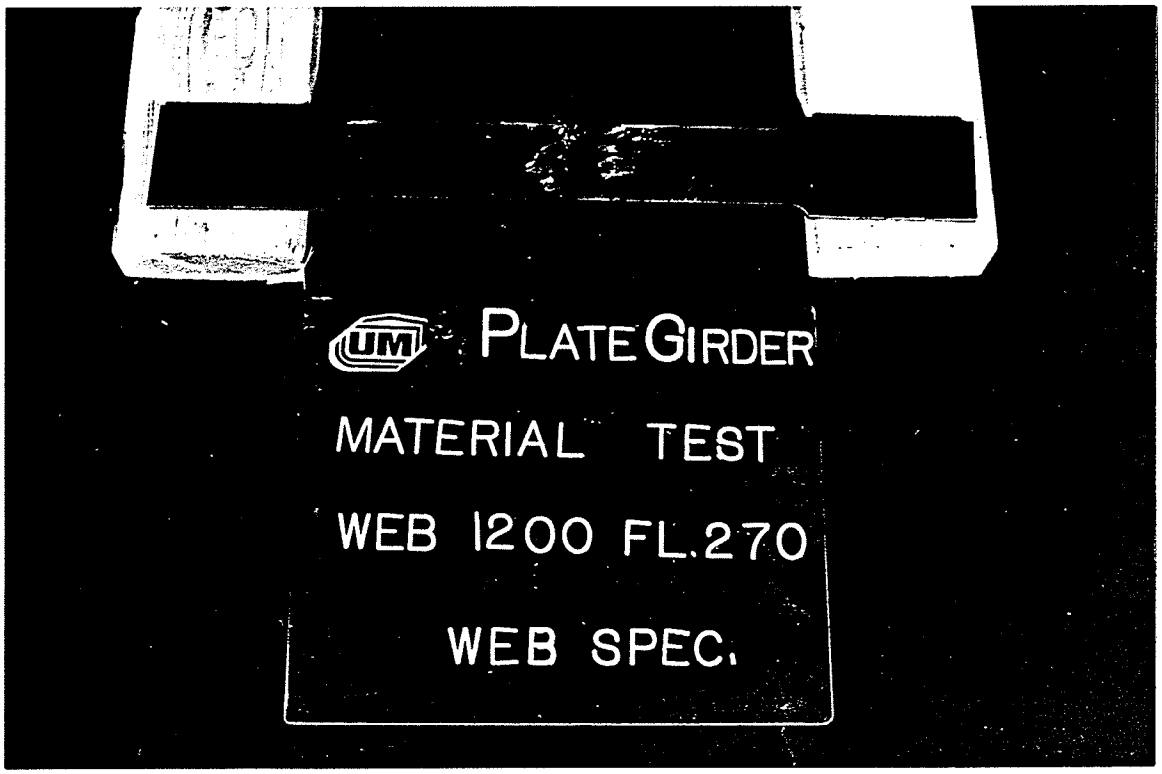

Figure 3.7 Strain Gage Placed on the Tested Coupon in the Transverse Direction

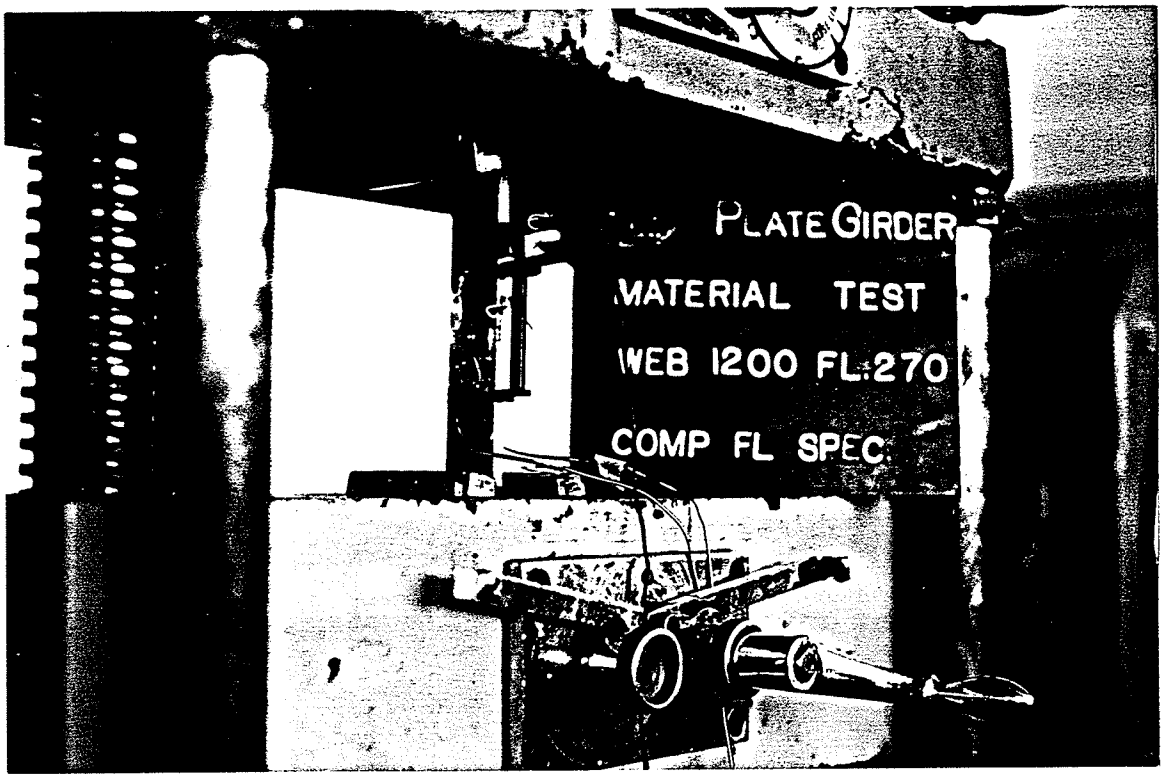

Figure 3.8 MTS Extensometer Placed on a Tested Coupon

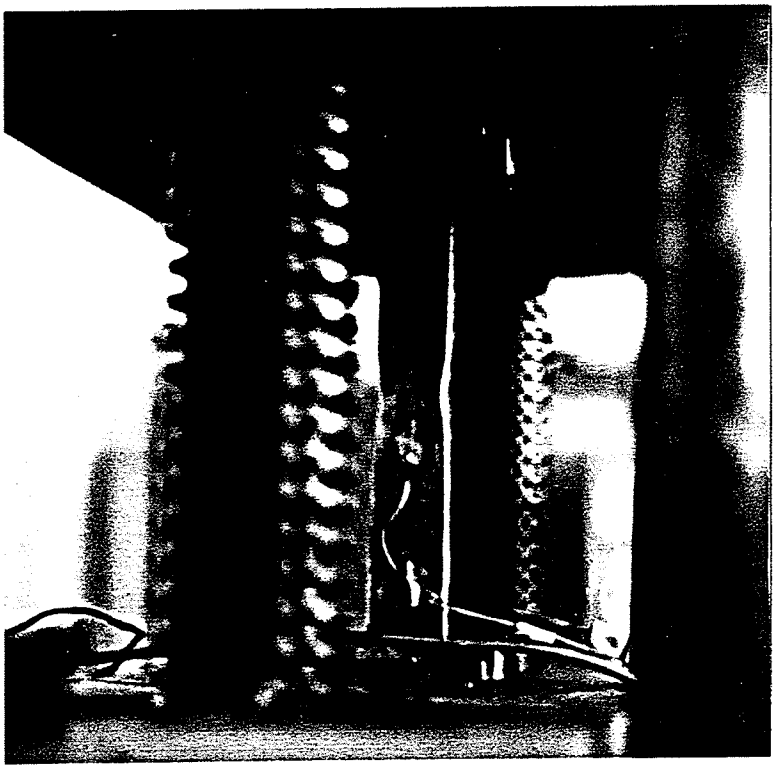

Figure 3.9 A Necked Coupon before Failure

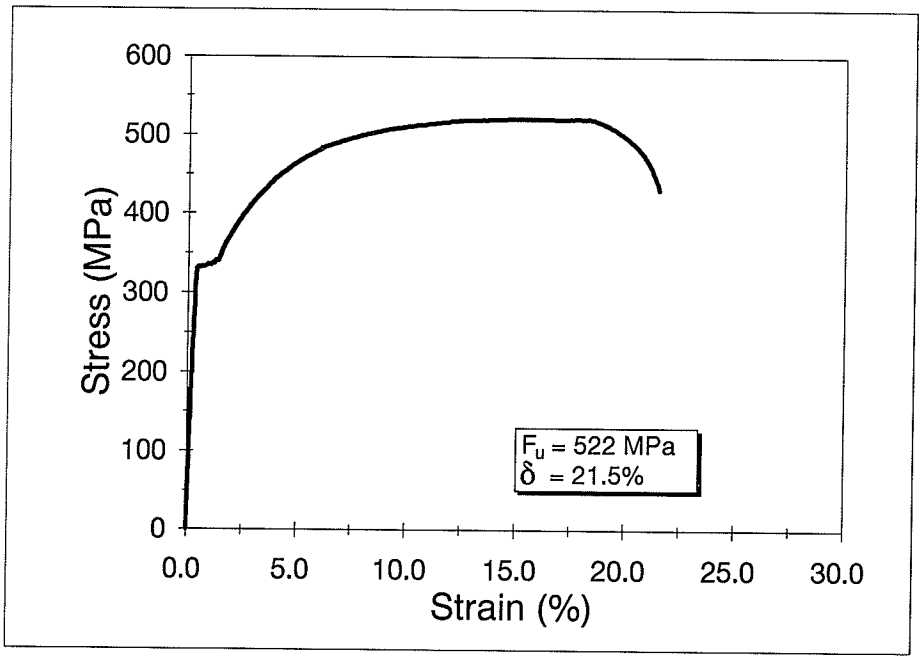

Figure 3.10(a) Typical Stress-Strain Curve of a Tested Coupon Cut from the Compression Flange of Specimen G4

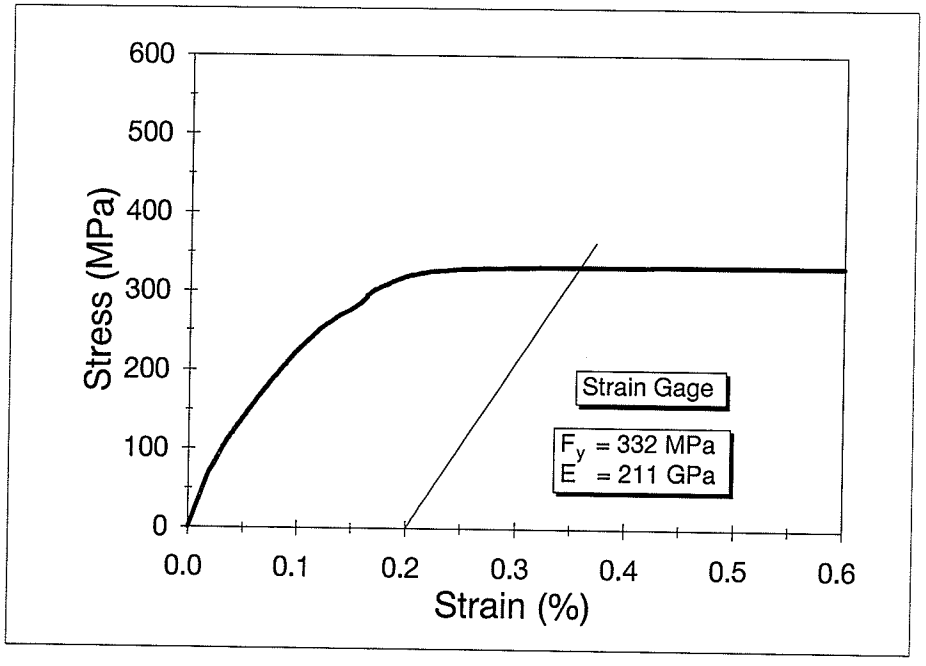

Figure 3.10(b) Regression Analysis and 0.2% Offset Method of a Tested Coupon Cut from the Compression Flange of Specimen G4

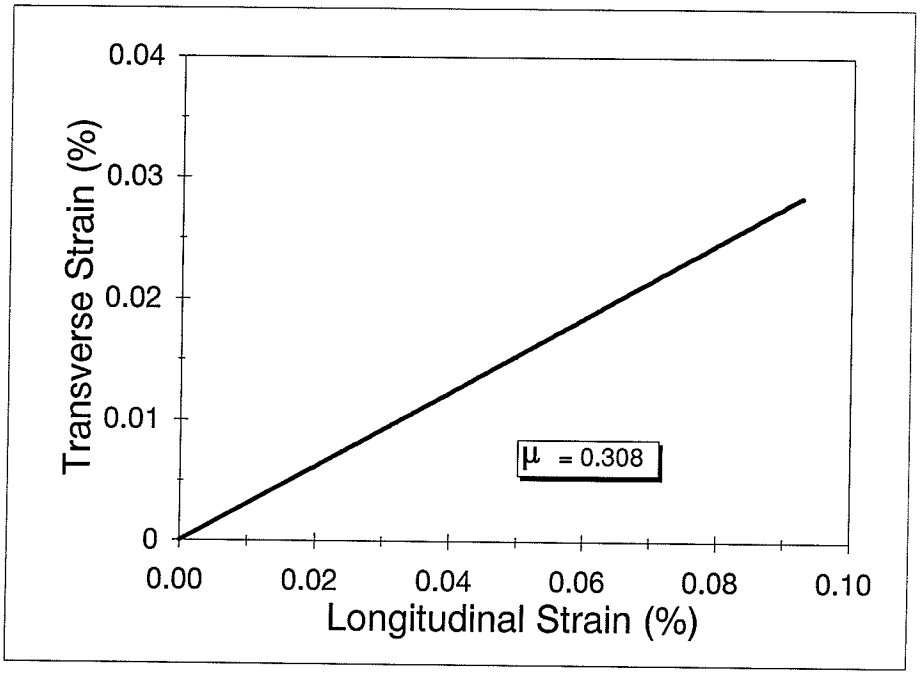

Figure 3.10(c) Typical Longitudinal-Transverse Strains of a Tested Coupon Cut from the Compression Flange of Specimen G4

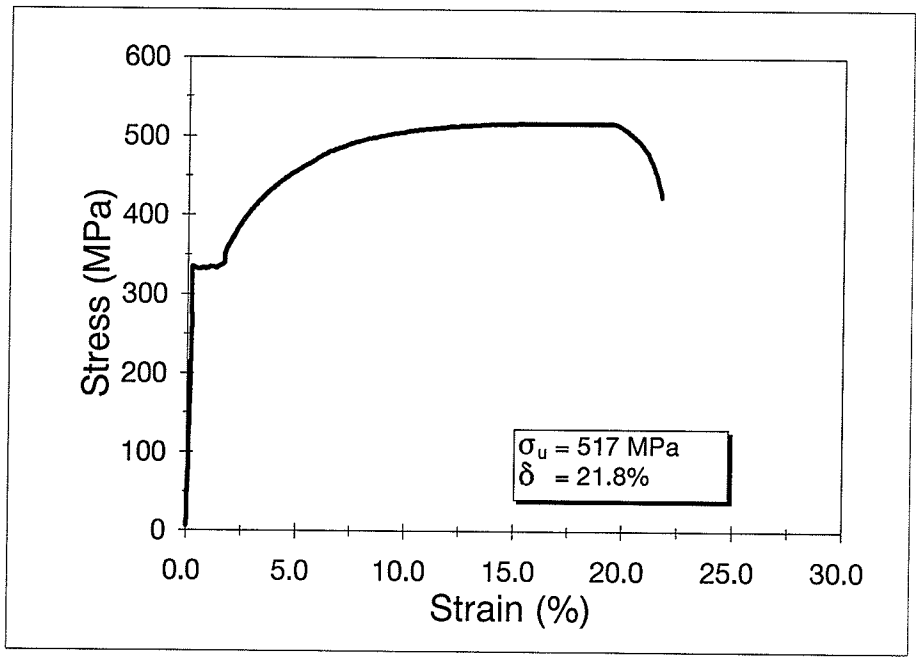

Figure 3.11(a) Typical Stress-Strain Curve of a Tested Coupon Cut from the Tension Flange of Specimen G4

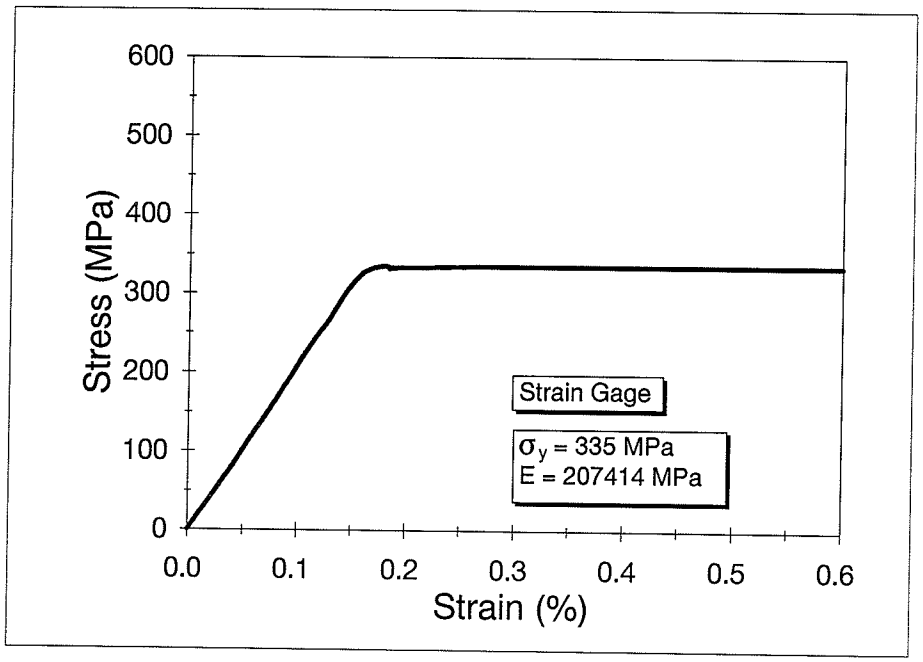

Figure 3.11(b) Regression Analysis and 0.2% Offset Method of a Tested Coupon Cut from the Tension Flange of Specimen G4

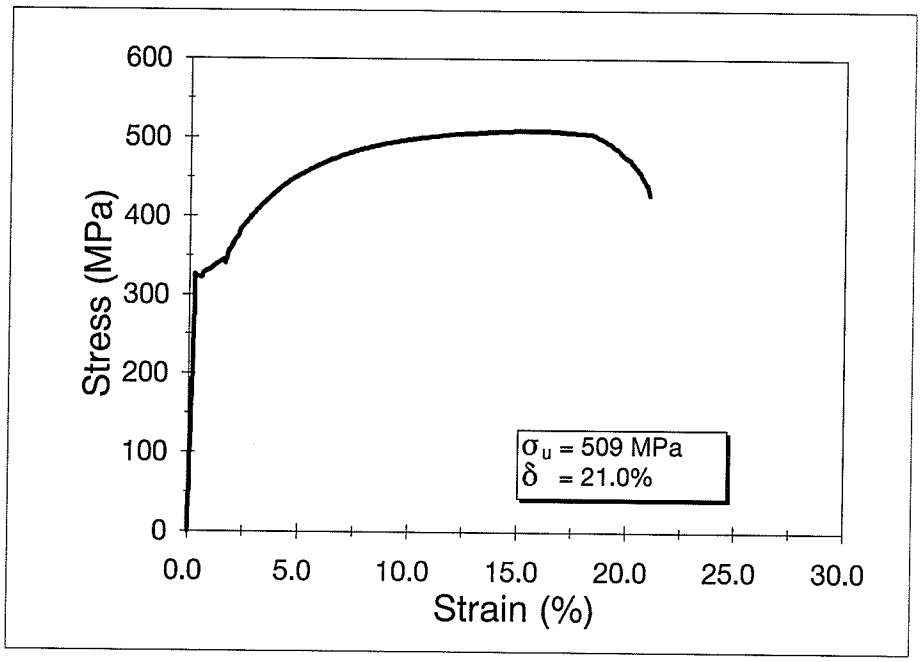

Figure 3.12(a) Typical Stress-Strain Curve of a Tested Coupon Cut from the Compression Flange of Specimen G8

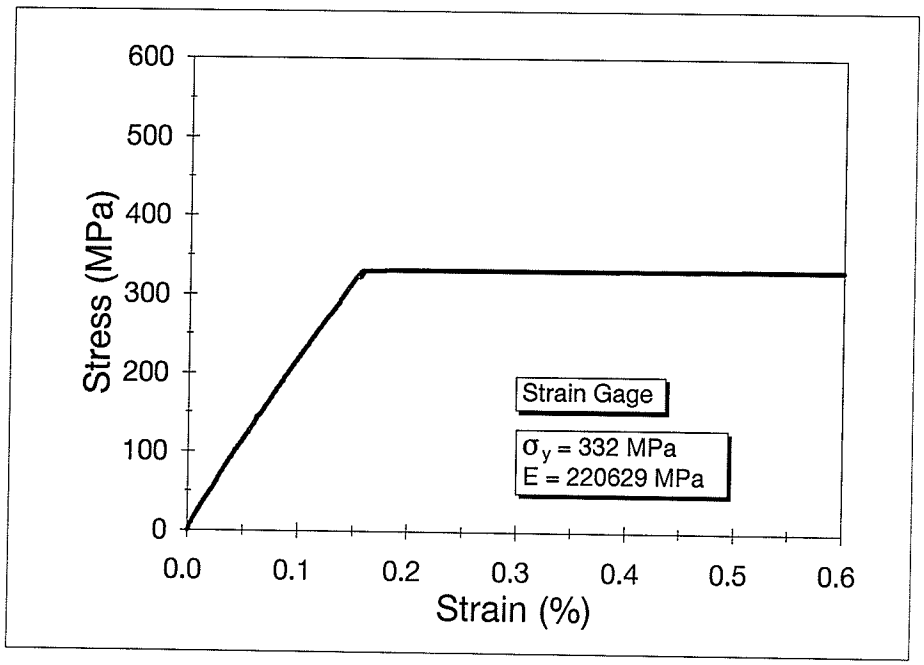

Figure 3.12(b) Regression Analysis and 0.2% Offset Method of a Tested Coupon Cut from the Compression Flange of Specimen G8

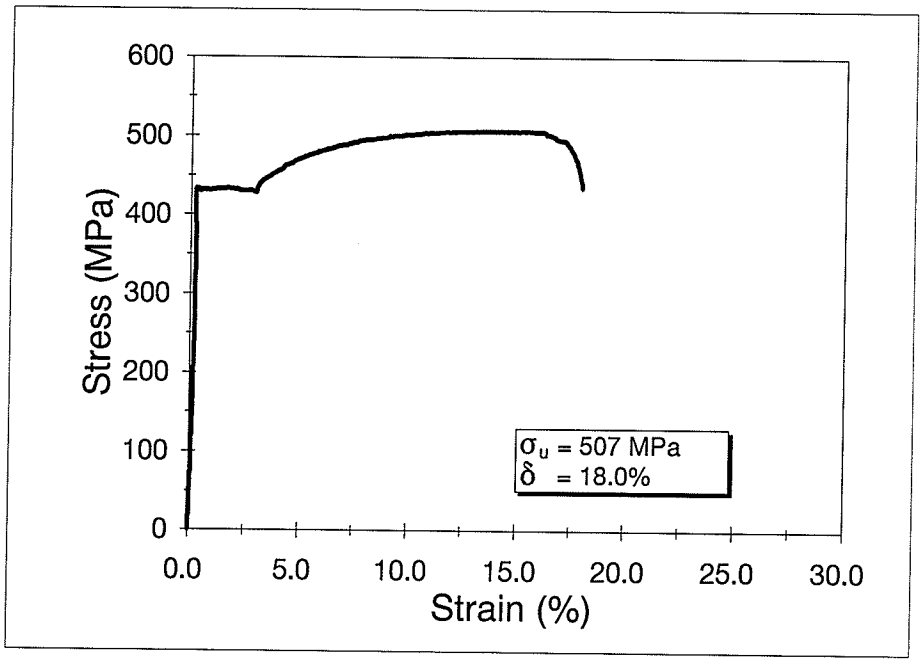

Figure 3.13(a) Typical Stress-Strain Curve of a Tested Coupon Cut from the Web of Specimen G4

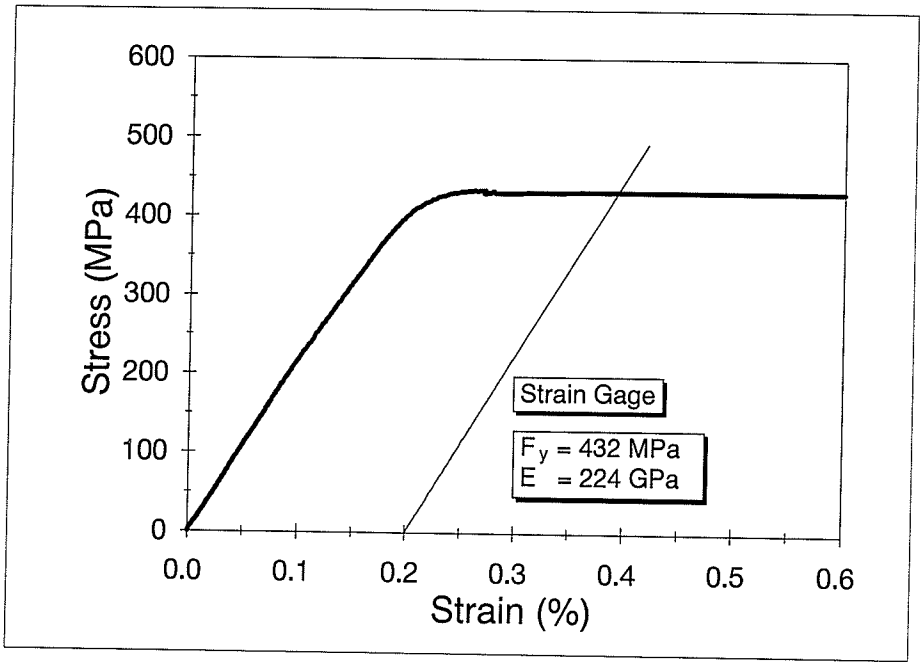

Figure 3.13(b) Regression Analysis and 0.2% Offset Method of a Tested Coupon Cut from the Web of Specimen G4

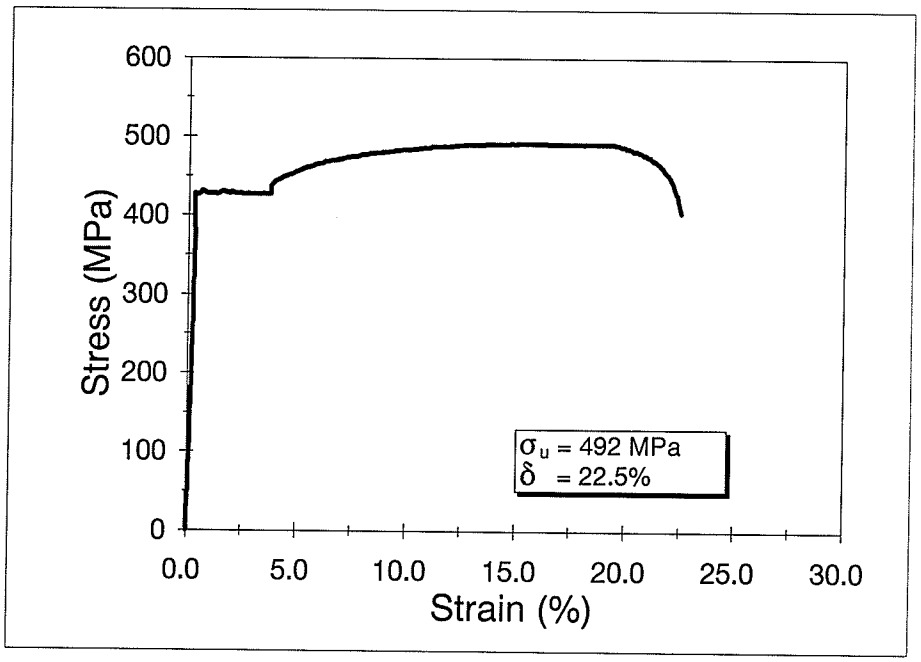

Figure 3.14(a) Typical Stress-Strain Curve of a Tested Coupon Cut from the Web of Specimen G8

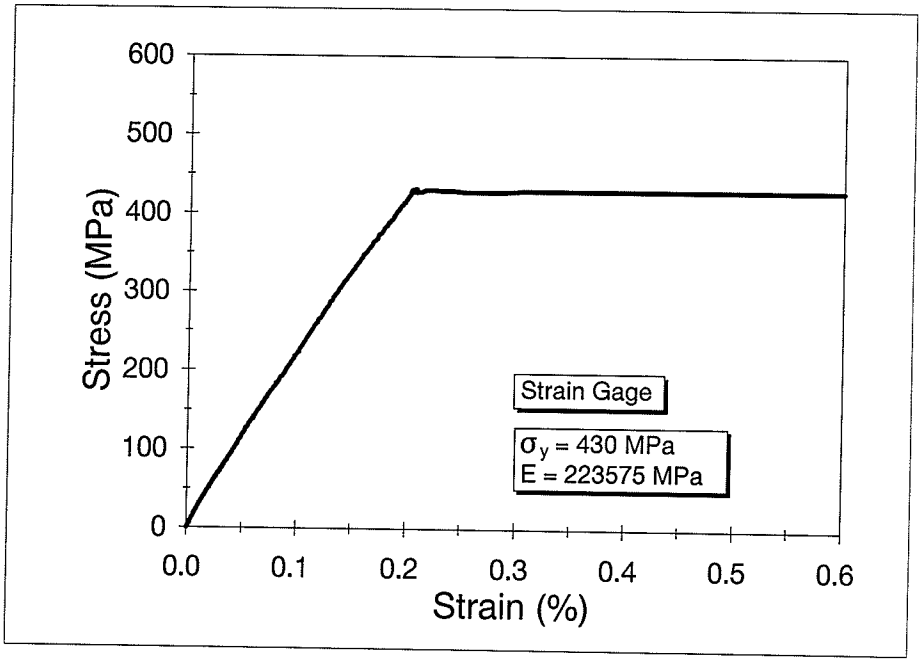

Figure 3.14(b) Regression Analysis and 0.2% Offset Method of a Tested Coupon Cut from the Web of Specimen G8

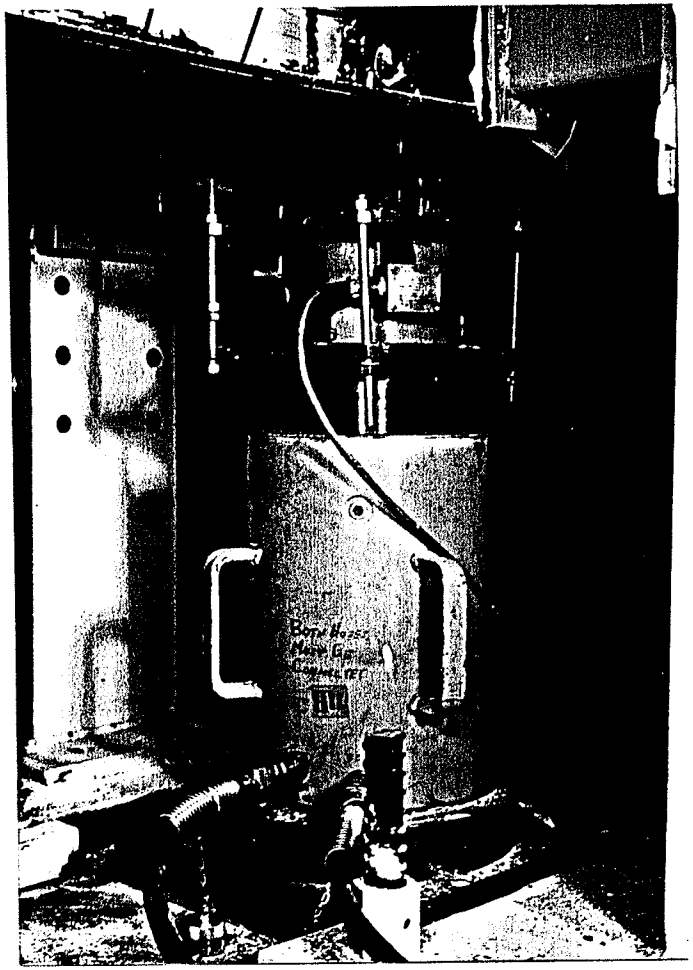

(a) First Point of Loading

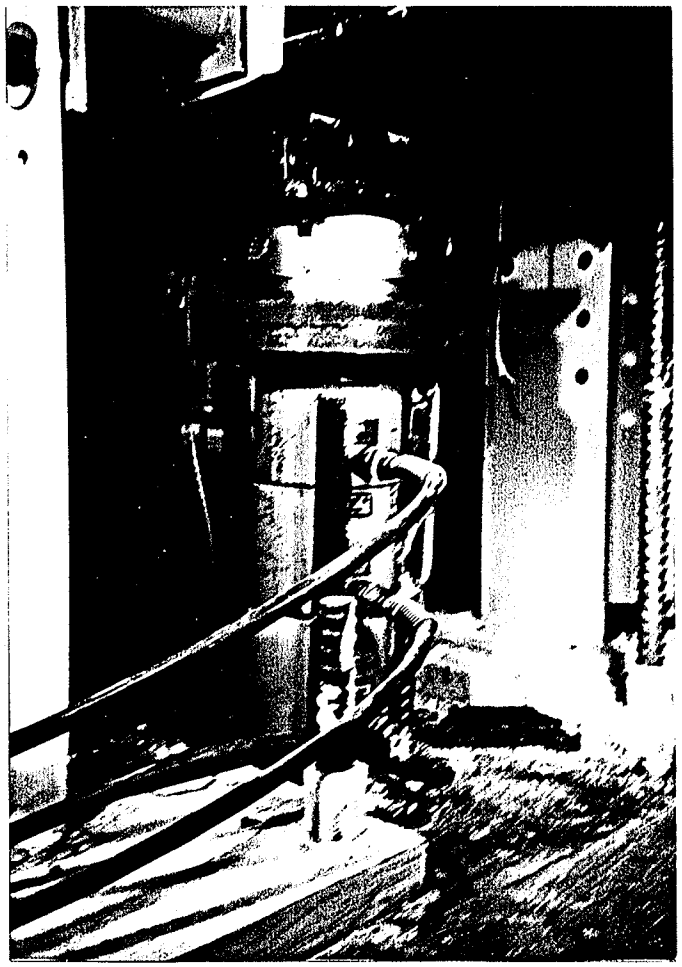

(b) Second Point of Loading

Figure 3.15 The Used Enerpac Hydraulic Jacks and Load Cells

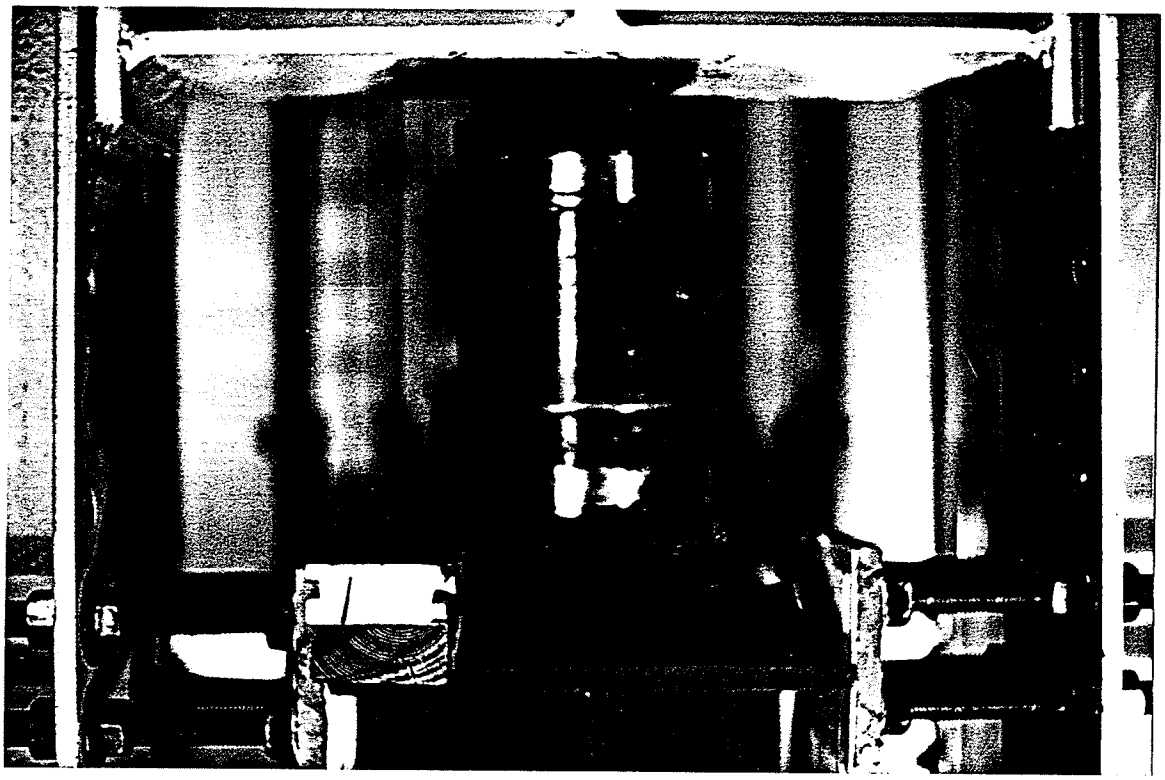

Figure 3.16 Load Cell Placed at the End-Support Section

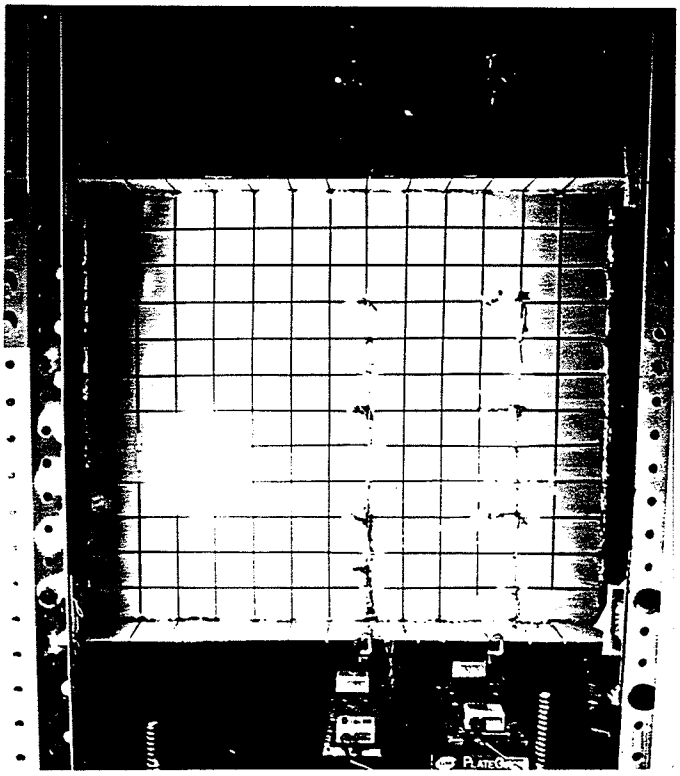

Figure 3.17 LMTs and LVDTs Placed on the Specimen before Testing

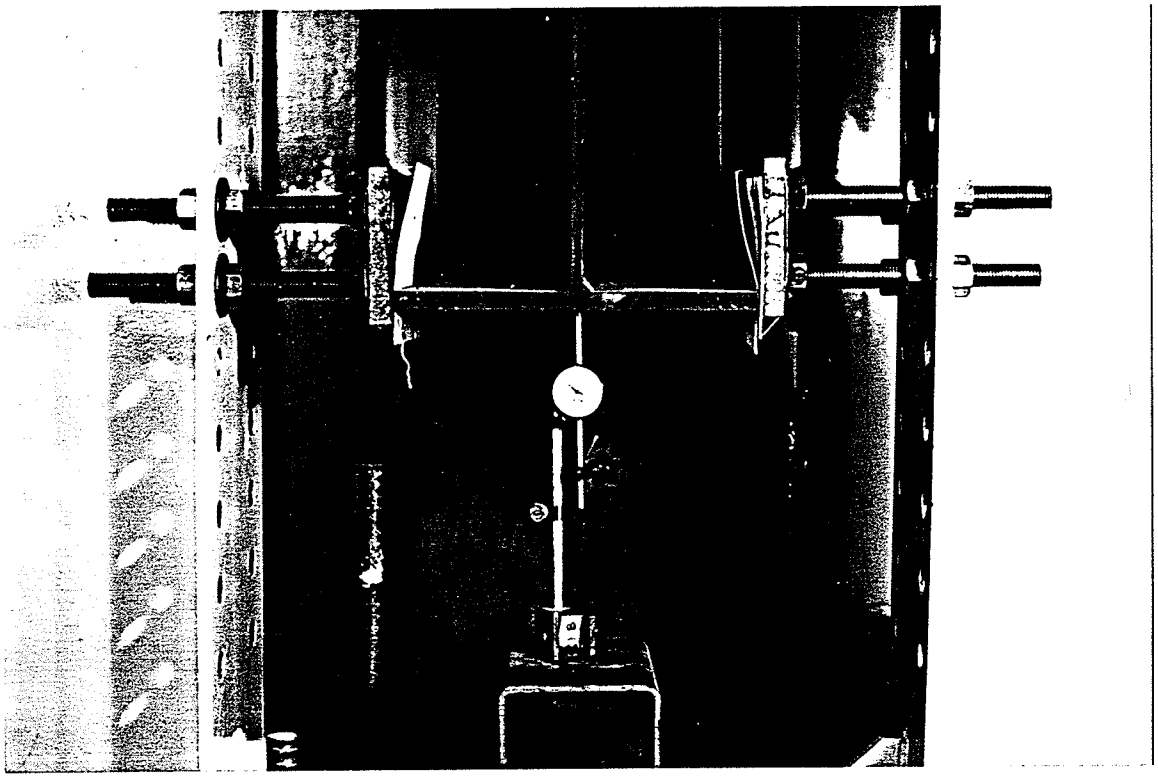

Figure 3.18 Dial Gage Placed at the End-Support Section

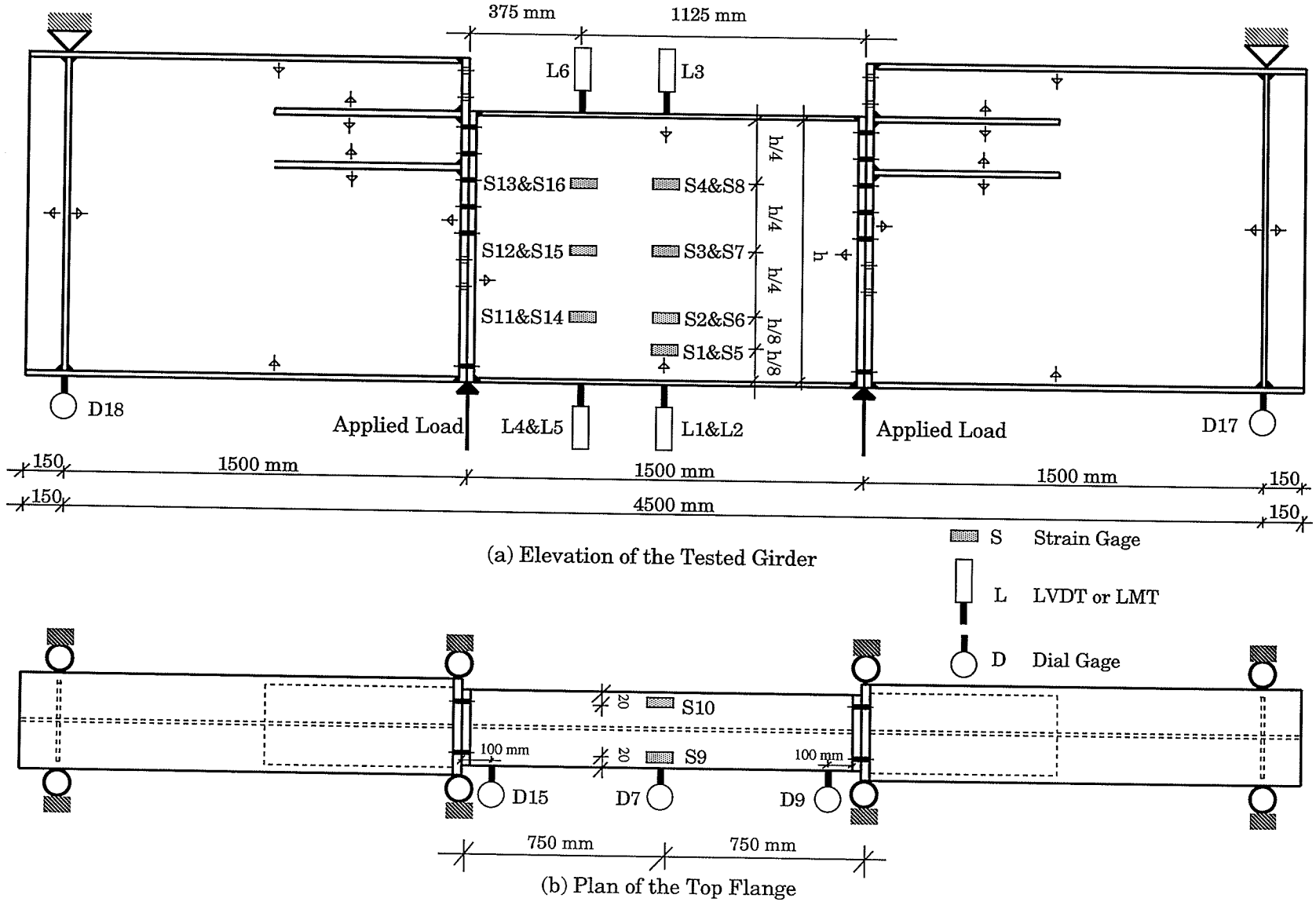

(a) Elevation of the Tested Girder

(b) Plan of the Top Flange

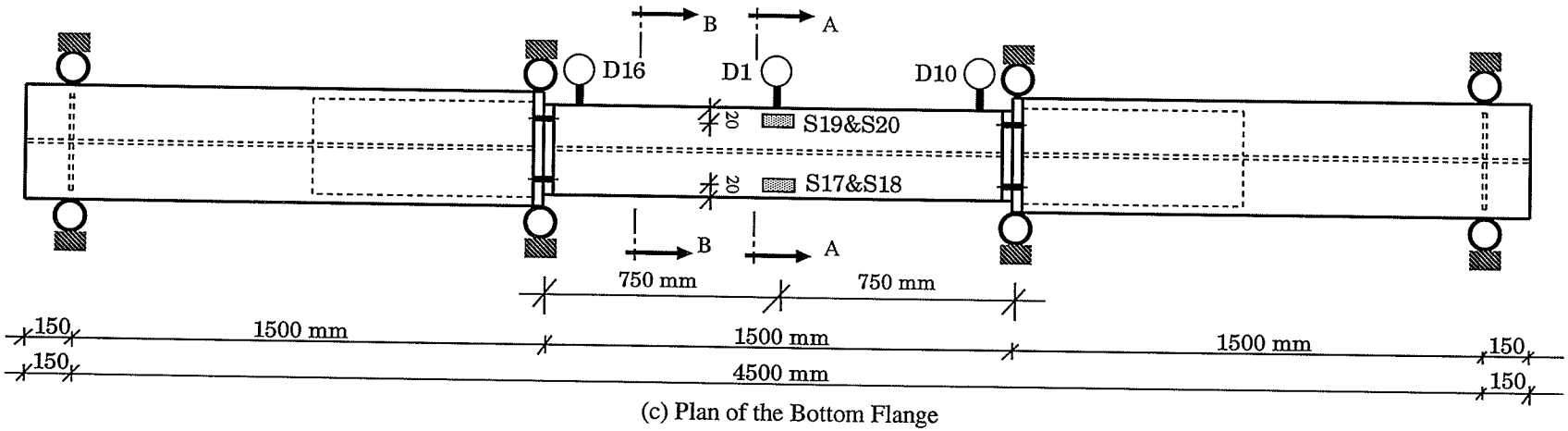

(c) Plan of the Bottom Flange

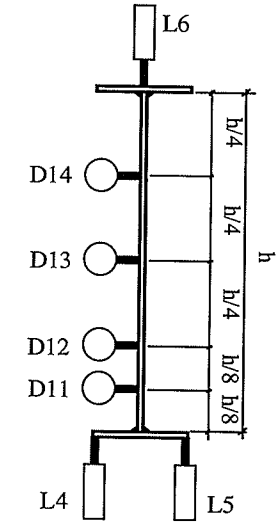

(d) Cross Section at B-B

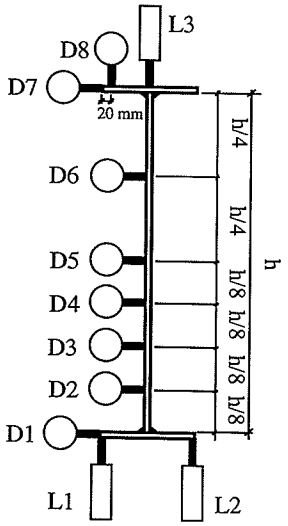

(e) Cross-Section at A-A

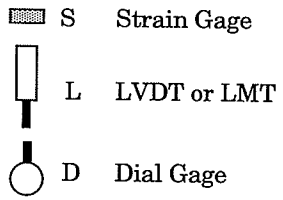

Figure 3.19 Instrumentation Placed on the Tested Girder

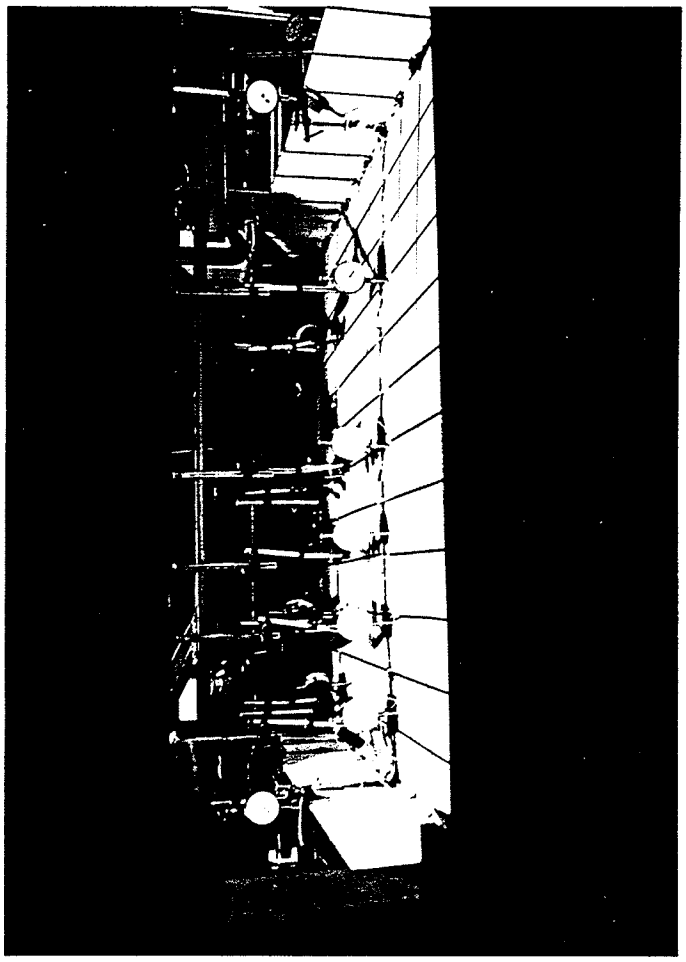

Figure 3.20 Dial Gages Placed Horizontally at the Mid-Span Section

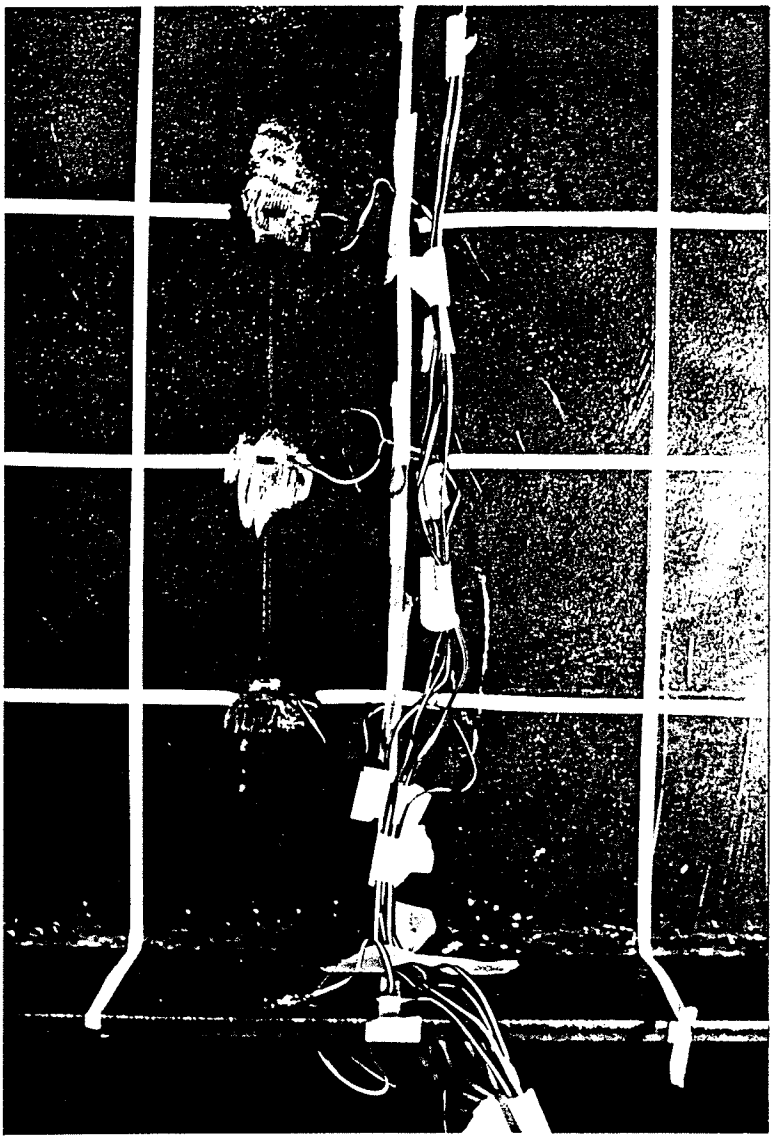

Figure 3.21 Strain Gages Mounted on the Specimen

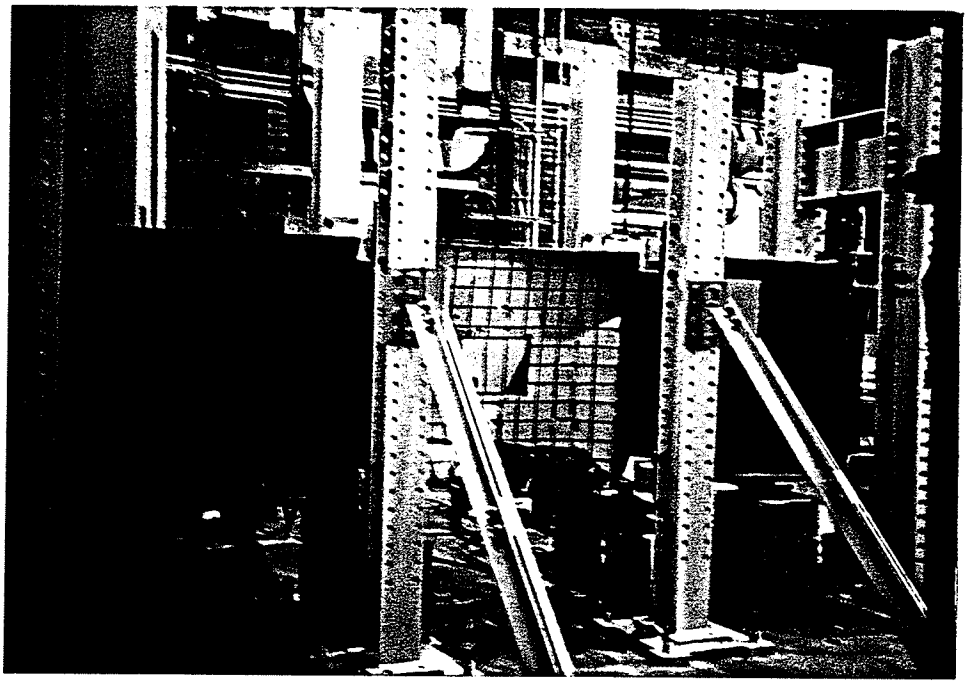

Figure 3.22 Test Setup

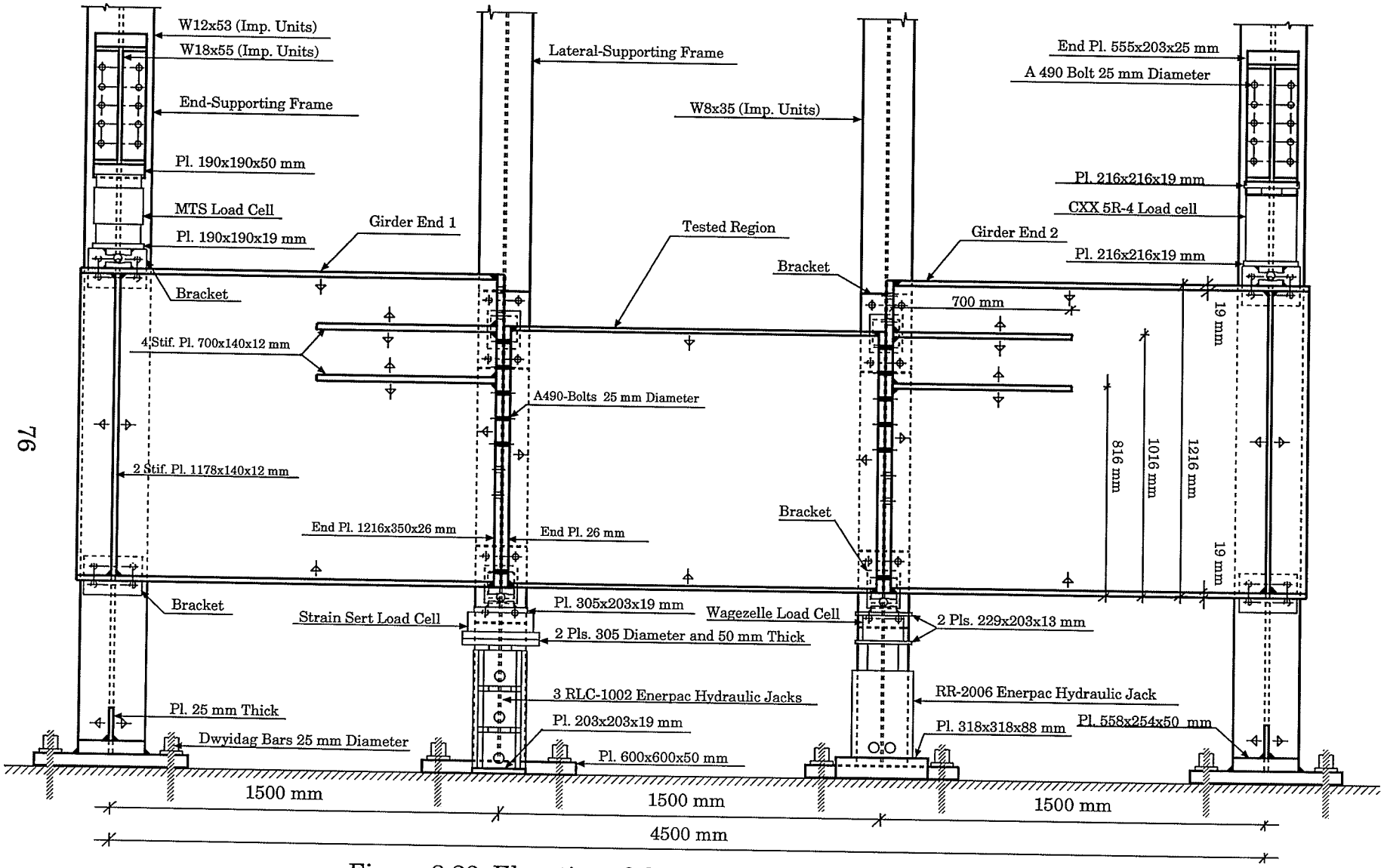

Figure 3.23 Elevation of the Test Setup and the Tested Girder

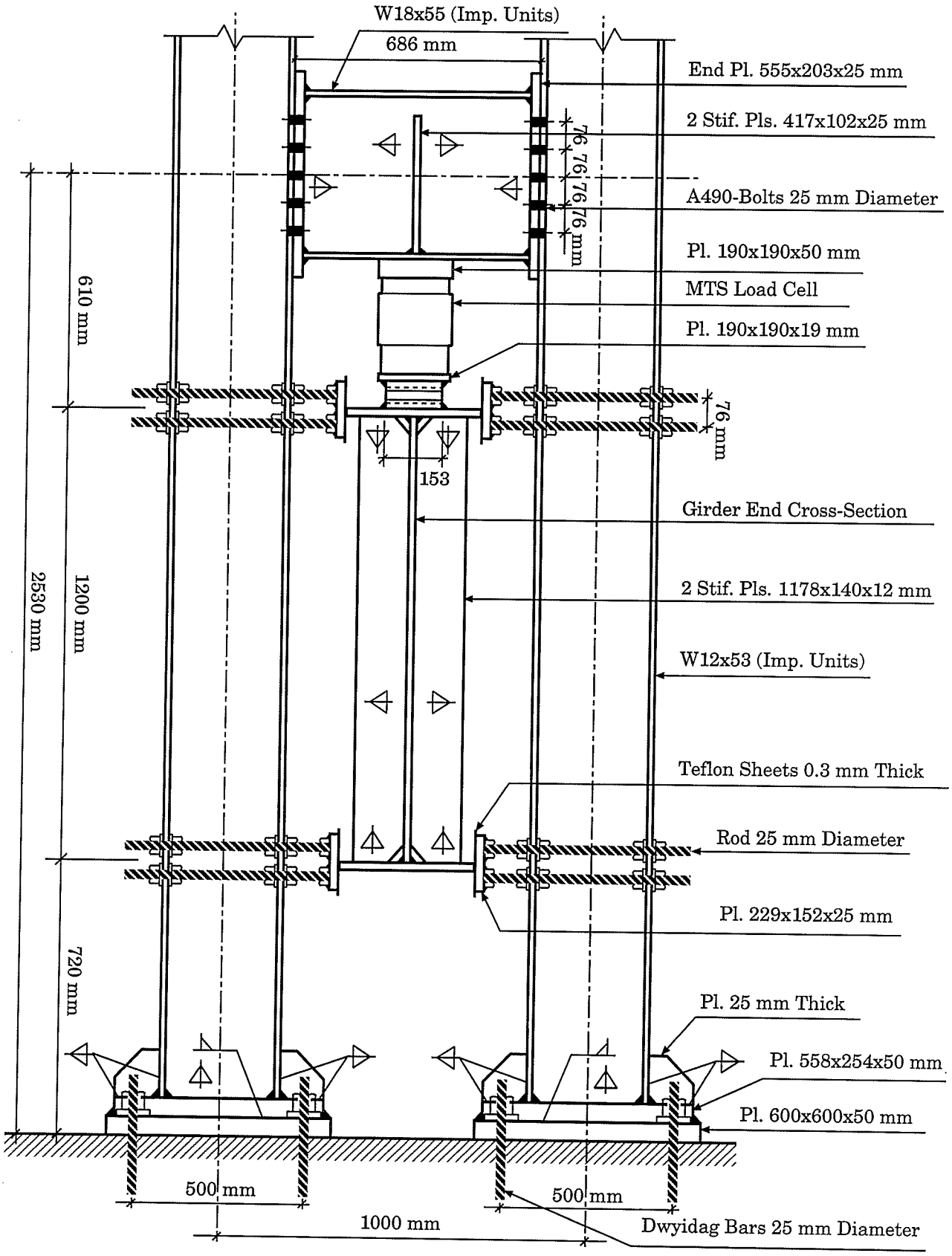

Figure 3.24 Side View at the End-Supporting Frame

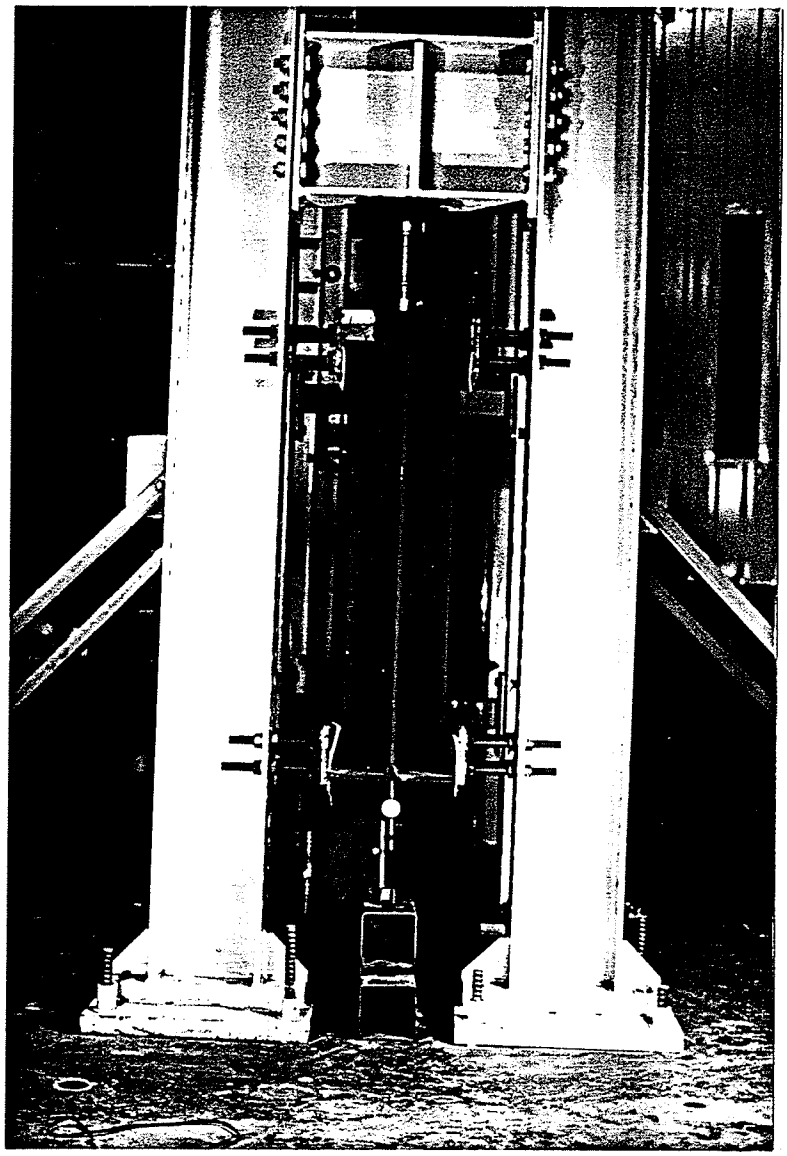

Figure 3.25 End-Supporting Frame

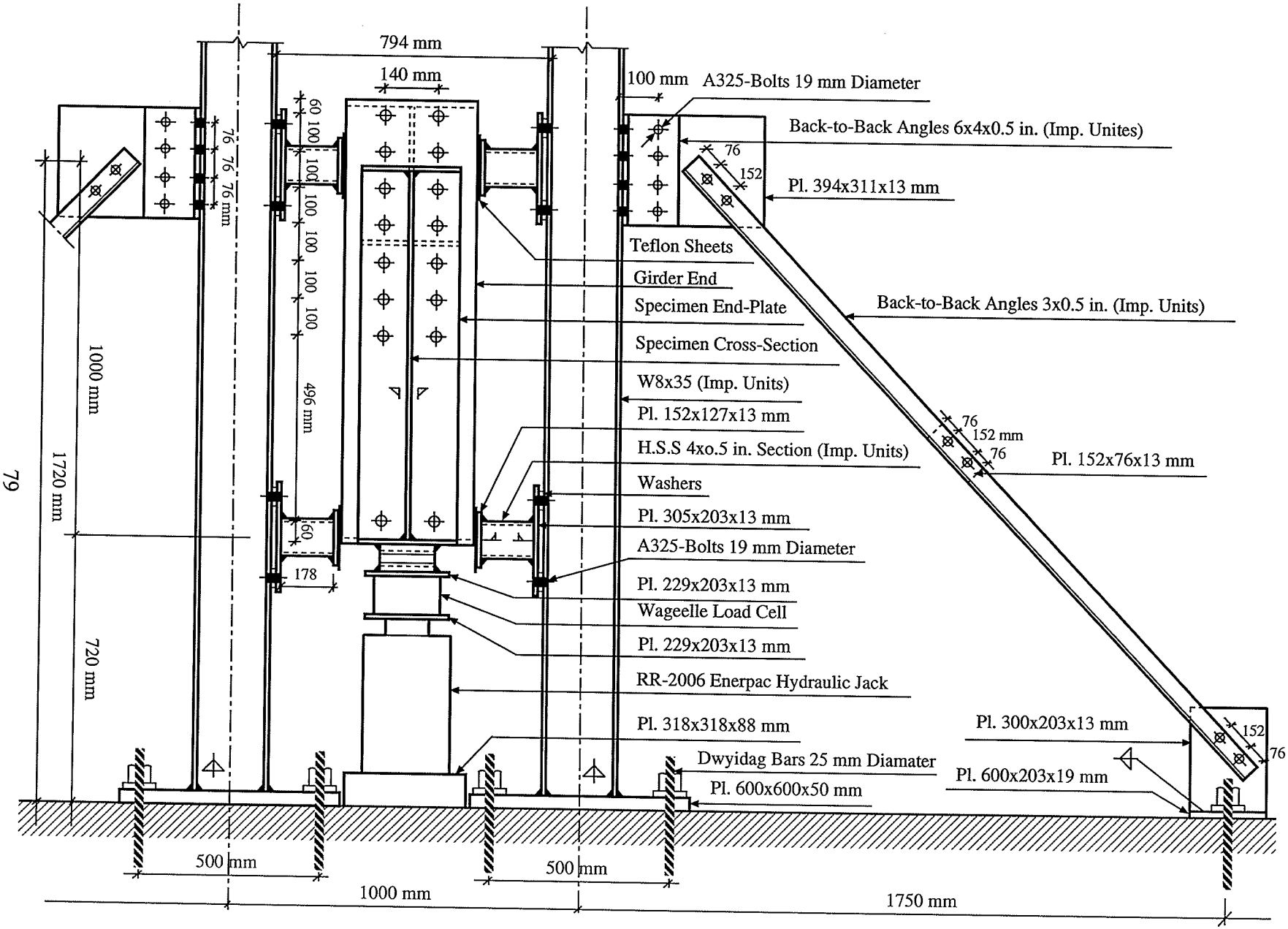

Figure 3.26 Side View at the Lateral-Supporting Frame

CHAPTER 4

DISCUSSION OF THE EXPERIMENTAL RESULTS

4.1 INTRODUCTION

In this chapter, the behaviour of the tested specimens is analyzed and the experimental results are discussed. These include:

i) the vertical deflections of the tested specimens;

ii) the lateral displacements of the webs; and

iii) the strains at mid-span and quarter-span sections.

Due to the large amount of data collected, the discussion will focus on three typical specimens, one for each range of the flange to width-to-thickness ratios (b/2t) and each range of the web height-to-thickness ratios (h/w). More specifically, specimen G2 was chosen to represent the low values of b/2t ratio and the intermediate values of the h/w ratio, specimen G4 was chosen to represent the intermediate values of b/2t ratio and the low values of h/w ratio, and specimen G9 was chosen to represent the high values of b/2t ratio and h/w ratio. In addition, the compression flange of each of these specimens buckled forming a different mode, which provides another aspect of the experimental results.

The results from the other tested specimens are presented in the appendices.

4.2 VERTICAL DEFLECTION

Two sets of LMTs and LVDTs were used to monitor the vertical deflections of each tested specimen. The first set was placed at mid-span section, while the second was placed at quarter-span section, as described in Chapter 3. The vertical deflections at mid-flange point of the tension flange were monitored using two LVDTs identified as L3 at mid-span section and as L6 at quarter-span section of the specimen, as shown in Figure 3.19. The deflections at these points were obtained by computing the difference between the LVDT readings and the vertical deflection readings at the end supports of the girder. Typical load-deflection curves at mid-span and at quarter-span sections of specimens G2, G4 and G9, are presented in Figures 4.1 to 4.3, respectively.

The vertical deflections of the compression flange were monitored by LMTs located at the edges of both the mid-span and the quarter-span sections. Two LMTs were used at each section in order to compute the rotation of the compression flange. The vertical deflections were obtained in the same way as that used in computing the vertical deflections of the tension flanges. The results are also shown in Figures 4.1 to 4.3 for specimens G2, G4 and G9, respectively.

Specimen G2

A linear behaviour was observed for the load-deflection curves for LVDT L3, until a load P = 173 kN was reached, as shown in Figure 4.1. This corresponds to $P/P_u = 0.503$ and $P/P_y = 0.351$, where P_u and P_y are the failure (ultimate) and the yielding loads, respectively. Then nonlinear behaviour was observed until failure occurred. The same change in behaviour was

observed at a load of 124 kN for LVDT L6. This load corresponds to $P/P_u = 0.361$ and $P/P_y = 0.252$. Table 4.1 lists the levels of load or moment, as a function of the ultimate moment capacity of the tested specimens, where the change in behaviour, from linear to nonlinear, took a place.

Specimen G4

During testing, a sudden change in the web profile was observed in specimen G4 as it changed its profile in the transverse direction from a half sine-wave to a sine-wave pattern. This sudden change in profile was accompanied by a loud noise and was observed at an applied load of 20 kN. This reversal of the web profile could explain the change in the slope of the load-deflection curves shown in Figure 4.2 at this load level. The same behaviour was obtained during the testing of specimens G1, G3 and G8 at load levels of 170, 36 and 305 kN, respectively.

A linear behaviour is observed in the load-deflection curves for LVDTs L3 and L6 up to a load of 298 kN, as shown in Figure 4.2. This level corresponds to $P/P_u = 0.773$ and $P/P_y = 0.565$, as listed in Table 4.1.

Specimen G9

As evident in Figure 4.3(a), linear behaviour of the load-deflection curve for LVDT L3 was observed until an applied load of 568 kN was reached, which corresponds to $P/P_u = 0.878$ and $P/P_y = 0.577$, then nonlinear behaviour was observed until failure was reached. This change in behaviour was also noticed at load level of 497 kN for LVDT L6, which corresponds to

$P/P_u = 0.769$, and $P/P_y = 0.505$.

The load-deflection curves of the other tested specimens are presented in Appendix A. The change in behaviour of the vertical deflection at mid-span sections took place when the P/P_u ratios ranged from 0.750 to 0.936 for specimens G3 to G9, as listed in Table 4.1. The lower P/P_u ratios obtained for specimens G1 and G2 were due to the buckling mode of these two specimens at failure. In these specimens, the compression flange and the adjacent portion of web buckled forming a one and a half sine-waves, sketched in Figure 4.4(a), while these of the other tested specimens either buckled forming a sine-wave or a half sine-wave, as sketched in Figures 4.4(b) and 4.4(c), respectively.

4.2.1 Rotation of Compression Flange

The rotation of compression flange (θ) about its longitudinal axis was obtained from the deflection readings of LMTs L1 and L2 at the mid-span section and LMTs L4 and L5 at the quarter-span section of each specimen. Typical curves of this rotation, as a function of the applied moment at the mid-span and the quarter-span sections, are presented in Figures 4.5 to 4.7 for specimens G2, G4 and G9, respectively. The results are discussed below.

Specimen G2

As shown in Figure 4.5, the rotation angle of the compression flange increased gradually at a low rate until an applied moment (M) of 222 kN.m at mid-span section and 446 kN.m at quarter-span section was reached. These moment levels correspond to $M/M_u = 0.430$ and 0.866 at mid-span and quarter-span, respectively, and $M/M_y = 0.300$ and 0.603, respectively,

where M_u and M_y are the ultimate (failure) and the yielding moments.

Comparing the results in Figure 4.5(a) to these in Figure 4.5(b), it was noticed that the rate of increase of the rotation angle at quarter-span section was higher than that at the mid-span section up to the point where nonlinear behaviour began. After this load, the rate of increase was higher at the mid-span section than that at the quarter-span section and failure took place at the mid-span section of this specimen.

The rotation of the compression flange at the mid-span section was in the opposite direction to those at the quarter-span sections due to the fact that the compression flange and the adjacent portion of the web buckled in a one and a half sine-waves pattern, as shown in Figure 4.8.

Specimen G4

A nonlinear relationship between the rotation angle of the compression flange and the applied bending moment was observed at the mid-span section of specimen G4, as shown in Figure 4.6(a). While a linear relationship at the quarter-span section was observed until an applied moment of 300 kN.m was reached, as shown in Figure 4.6(b), which corresponds to $M/M_u = 0.519$ and $M/M_y = 0.379$, as listed in Table 4.1.

The linear behaviour was not observed at the mid-span section of this specimen because of the initial-imperfection shape (mode) of the web, which caused the sudden change in the web profile as discussed earlier. The same behaviour was observed at the mid-span and the quarter-span sections of specimen G3.

When the compression flange reached the ultimate moment capacity (M_u), the rotation

at the quarter-span section of the specimen continue to increase without any additional load applied, as shown in Figure 4.6(b). This was due to the fact that failure of this specimen had occurred at or very close to the quarter-span section of the specimen, as shown in Figure 4.9.

Specimen G9

The nonlinear relationship of the moment-rotation of the compression flange started when the applied moment reached 431 kN.m at the mid-span section and 506 kN.m at the quarter-span section of specimen G9. These values correspond to $M/M_u = 0.444$ and 0.522, respectively, and $M/M_y = 0.292$ and 0.343, respectively. In this specimen, the compression flange buckled in a half sine-wave mode, as shown in Figure 4.10.

In all specimens, it was observed that the compression flange began to rotate from the onset of first load and continued in a gradual manner until failure took place. Except for the sudden change in the web profile in specimens G1, G3, G4 and G8, no sudden change in behaviour was observed. The maximum rotation angle of the compression flanges was smaller than 5° at both the mid-span and the quarter-span sections when failure took place, as shown in Figures 4.5 and 4.6, except for specimen G9 where the angle of rotation was 10° at failure. The compression flange and the adjacent web portion buckled in a half sine-wave pattern, as shown in Figures 4.10. This buckling mode allowed the compression flange to rotate with higher rate and value than these of the other specimens, which buckled in different patterns.

In all specimens, except specimens G3 and G4, the range of M/M_u ratio, where the change in behaviour from linear to nonlinear took place, was between 0.331 to 0.537 at the

mid-span sections. These moment levels, which may reflect local buckling and the beginning of postbuckling behaviour of the compression flanges, are affected by:

i) the flange width-to-thickness ratio (b/2t) as well as the web height-to-thickness ratio (h/w); and

ii) the initial imperfection shape (mode) of the web.

4.2.2 Rotation of Tension Flange

Typical curves of the rotation of the tension flange at mid-span section, as a function of the applied moment, are presented in Figures 4.11 to 4.13 for specimens G2, G4 and G9, respectively. These rotations were obtained from the deflection readings of LVDT L3, located at the mid-flange point, and those of dial gage D8, located at the edge of the flange. In all specimens, small rotations of the tension flange were observed, as shown in Figure 4.14. These rotations were less than 3°, as shown in Figures 4.11 to 4.13.

The sudden change in the web profile in specimen G4, shown in Figure 4.12, had a greater effect on the rotation of the tension flange than on the rotation of the compression flange because the lateral deformation of the web recorded in the tension region was larger than that recorded in the compression region of the web.

4.3 LATERAL DISPLACEMENT OF WEB

Two groups of dial gages were placed along the depth of the web at mid-span and quarter-span sections of each specimen. Initial readings were taken to establish the initial imperfection of the web, as discussed in Chapter 3. The largest initial out-of-straightness

(initial imperfection) values of the web are listed in Table 3.4 and the modes of this imperfection are sketched in Figure 3.4. These initial imperfections for the webs in the transverse direction at both the mid-span and the quarter-span sections of specimens G2, G4 and G9 are shown in Figures 4.15 to 4.17 as the deflection corresponding to an M/M_u ratio equal to zero. These figures also show the web profiles at different moment levels.

The lateral displacement curves of the webs are shown in Figures 4.18 to 4.20 for specimens G2, G4 and G9, respectively, as a function of the applied moment. A discussion of the lateral-displacement results for the web specimens is presented in the following sections.

Specimen G2

The initial out-of-straightness of the web of this specimen was in the form of a half sine-wave, in the transverse direction. However, once the load was applied, the web started to deflect laterally, in a gradual manner, towards a sine-wave pattern at mid-span section, until failure was reached, as shown in Figure 4.15(a).

A linear behaviour of the lateral displacement of the web versus the applied moment was observed until an applied moment of 259 kN.m was reached at mid-span section. Then a nonlinear behaviour was observed, as shown in Figure 4.18(a). The moment of 259 kN.m, which corresponds to $M/M_u = 0.502$ and $M/M_y = 0.348$, may reflect the limit at which the postbuckling strength of the web started to take place.

The maximum recorded lateral displacement of the web was 6.73 mm at a height of 190 mm from the compression flange at mid-span.

Specimen G4

As discussed earlier, a sudden change in the web profile occurred when the applied moment was 30 kN.m. This level corresponds to $M/M_u = 0.05$. This can be noticed by comparing the web profiles at $M/M_u = 0$ and at $M/M_u = 0.06$ in Figure 4.16. As shown in this figure, the web profile suddenly changed from a half sine-wave to a sine-wave pattern, in the transverse direction.

At higher loads, the web tried to recover from this sudden change in its profile and gradually returned to the original half sine-wave pattern, as shown in Figure 4.16.

The maximum recorded lateral displacement of the web was 13.51 mm at a height of 240 mm from the compression flange at quarter-span, as shown in Figure 4.19.

Specimen G9

As shown in Figure 4.17, the initial out-of-straightness of the web was in the form of half sine-wave in the transverse direction. The web deflected laterally, in a gradual manner, once the load was applied into the sine-wave form, as shown in Figure 4.17.

The maximum recorded lateral displacement of the web was 19.86 mm at a height of 290 mm from the compression flange at mid-span, as shown in Figure 4.20.

Due to the high values of initial out-of-straightness of the webs of specimens G4 to G9, the linear behaviour of the lateral displacement was not observed. Instead, nonlinear behaviour of these lateral displacement took place from the beginning. The same behaviour was observed for the lateral displacement of the web of specimen G1 because of the initial imperfection shape (mode) of the web which also caused the sudden change in the web profile

as discussed earlier.

4.3.1 Web-Flange Angle

The angle between the web and the flanges (α) was plotted as a function of the applied moment in Figures 4.21 to 4.23, for both the mid-span and the quarter-span sections of specimens G2, G4 and G9, respectively. Theoretically, this angle is supposed to be 90° and stay constant if there is no relative distortion between the flanges and the web. As shown in these figures, the maximum distortion of this angle from 90° at failure was 6°. It occurred in the compression side at mid-span section of specimen G9.

The sudden change in the web profile had affected the web-flange angle in the tension side of specimen G4 at mid-span section. At the same time, the maximum distortion of the web-flange angle had occurred due to this sudden changes in the web profile did not exceed 3°.

4.4 STRAIN DISTRIBUTION

To evaluate the strain distribution along the depth and along the span of the specimen, 20 electrical resistance strain gages were mounted on the web and on the flanges at mid-span and at quarter-span of each tested specimen. As discussed in Section 3.4.4, the strain gages were placed in pairs, one on either side of each plate, to monitor the plate bending strains, except for the strain gages on the tension flange which were placed on one side only.

The strain distribution along the depth of the sections at mid-span and at quarter-span sections of the specimens, are presented in Figures 4.24 to 4.26 for specimens G2, G4 and

G9, respectively. The membrane strains were computed by averaging the results obtained from each pair of strain gages. The strain distribution for each specimen was plotted for various moment levels including the moment at failure. The strain distribution according to the beam theory at failure is also presented in these figures.

The strain distributions presented in these figures show that the strains over one-quarter of the web, just below the mid-height point were very small and in some, small values of tensile strains were observed in these areas instead of compressive strains. Consequently, the compressive strains at the compression flange, except for specimen G9, were considerably higher than those obtained by the beam theory. However, the strains of the top half of the webs and in the tension flanges were very close to those predicted by the beam theory.

From the strain distributions, shown in Figures 4.24 to 4.27, and the lateral displacements, shown in Figures 4.15 to 4.17 for specimens G2, G4 and G9, respectively, it may be observed that the compression portions of webs that had least strains were those with highest lateral-displacement values. These high values of lateral displacement reduced the stiffness, which may result in a reduction in their capability to resist the applied bending moment, which may lead to these low values of the strains at these portions of the web.

The strain curves at mid-span and quarter-span sections of specimen G2, as a function of the applied moment, are presented in Figures 4.27 to 4.30. The strains predicted by beam theory are also shown in these figures. The web bending strains observed by each back-to-back pair of strain gages as well as their average values (membrane strains) at the mid-span and the quarter-span sections are shown in Figure 4.27 and 4.28, respectively, while the strains for the compression and the tension flanges are presented in Figures 4.29 and 4.30,

respectively. Comparing the strain results of the compression flange in Figure 4.29(a) to those in Figure 4.29(b), the strains at S17 and S18 locations were increased as the applied moment was increased with a lower rate than that at S19 and S20 locations. This resulted from the rotation of the compression flange, which caused vertical deflection at S17 and S18 locations in the opposite direction of the initial warpage of the flange, while it caused a vertical deflection in the direction of this warpage at S19 and S20 locations.

The strain results, as a function of the applied moment, at mid-span and quarter span sections for the web of specimen G4 are presented in Figures 4.31 and 4.32, while these results for the compression and the tension flanges are presented in Figures 4.33 and 4.34. Due to the sudden change in the web profile, from half sine-wave to sine-wave pattern at a moment of 30 kN.m, a horizontal shift in these strain readings was recorded, as shown in Figures 4.31 to 4.34. At the same time, it had an insignificant effect on the membrane strains. When the web buckled, the bending resistance contribution provided by the compression flange increased as indicated by the rate of increase of the strains in the compression flange shown in Figure 4.33(c).

The strain results versus the applied moment are shown in Figures 4.35 and 4.36 for the web of specimen G9 at mid-span and quarter-span sections, respectively. Figures 4.37 and 4.38 presents the strain results of the compression and the tension flanges, respectively. As evident in these figures, the bending strains in the web were very small, while these strains in the compression flange were high, especially when the specimen was close to failure. This may indicate that the failure of this specimen was due to the distortion of the compression flange and the adjacent portion of the web.

In all specimens, no sudden change in the strains was observed at the critical buckling moment of the web or the compression flange.

4.5 FAILURE MODE

In all specimens, the failure was due to the distortion of the compression flange. The compression flange started to distort and rotate gradually once a moment was applied. In Figure 4.39, the rotation of the compression flange of specimen G9 at a moment of 450 kN.m ($M/M_u = 0.464$) and at a moment of 825 kN.m ($M/M_u = 0.858$), is shown. As evident in this figure, once the load was applied the flange buckled forming a half sine-wave, as shown in Figure 4.10, and sketched in Figure 4.4(c). The web also buckled forming a half sine-wave, longitudinally and transversely.

As evident in Figure 4.40, the compression flange of specimen G8 started to rotate, in a gradual manner, forming a sine-wave, once the moment was applied and until failure was reached, as shown in Figure 4.40(c). The top portion of the web has buckled, longitudinally, in a half sine-wave pattern, while its bottom portion has buckled in a sine-wave pattern. Transversely, a portion of the web buckled in a half sine-wave pattern, as sketched in Figure 4.41(b), and the other portion has buckled forming a sine-wave, as sketched in Figure 4.41(a). The yield-line pattern, shown in Figure 4.41, is distinguishing between the two portions. This mode of failure was typical of those observed in testing specimens G3 to G7.

The distorted compression flange of specimen G2 at failure is shown in Figure 4.8. This compression flange and the bottom portion of the web buckled, longitudinally, forming a one and a half sine-waves, as sketched in Figure 4.4(a). At the same time, the top portion

of the web buckled, longitudinally, forming a half sine-wave. Transversely, the centre portion of the web buckled forming a half sine-wave, as sketched in Figure 4.41(b) while the end portions buckled forming a sine-wave, as sketched in Figure 4.41(a). This also was the typical failure mode of specimen G1.

Table 4.1 Linear Behaviour Limits

Specimen	Vertical Deflection		Rotation of Comp. Fl.		Lateral Disp. of Web	
	Mid-Span	Quarter-Span	Mid-Span	Quarter-Span	Mid-Span	Quarter-Span
G1	0.638	0.638	0.486	0.879	-*	-*
G2	0.503	0.361	0.430	0.868	0.502	-*
G3	0.750	0.786	-*	-*	0.505	0.628
G4	0.773	0.773	-*	0.519	-*	-*
G5	0.855	0.482	0.427	0.482	-*	-*
G6	0.872	0.783	0.455	0.502	-*	-*
G7	0.823	0.823	0.331	0.331	-*	-*
G8	0.936	0.936	0.537	0.537	-*	-*
G9	0.878	0.769	0.444	0.522	-*	-*

*Nonlinear behaviour started at zero moment

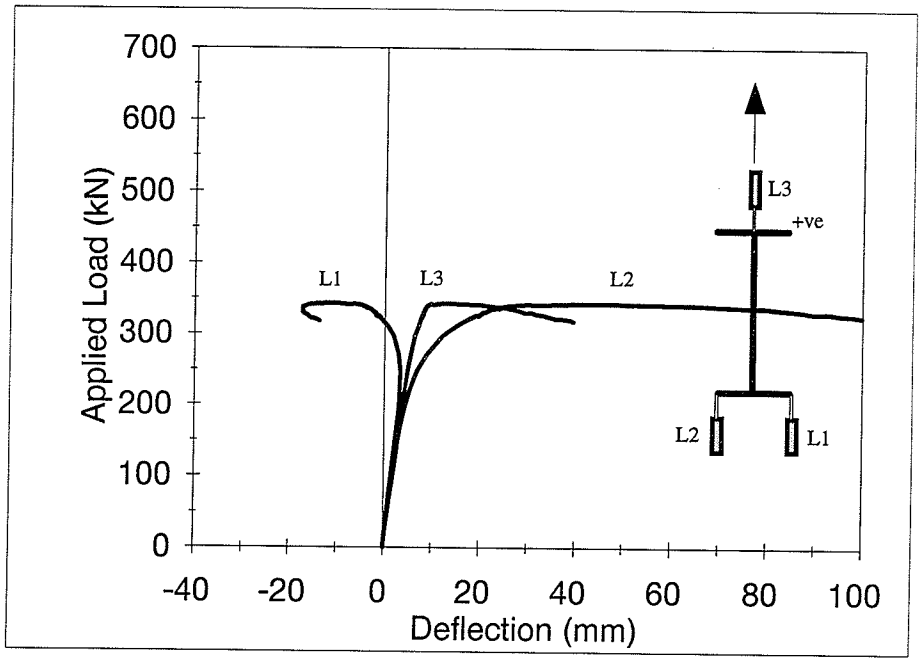

(a) Mid Span

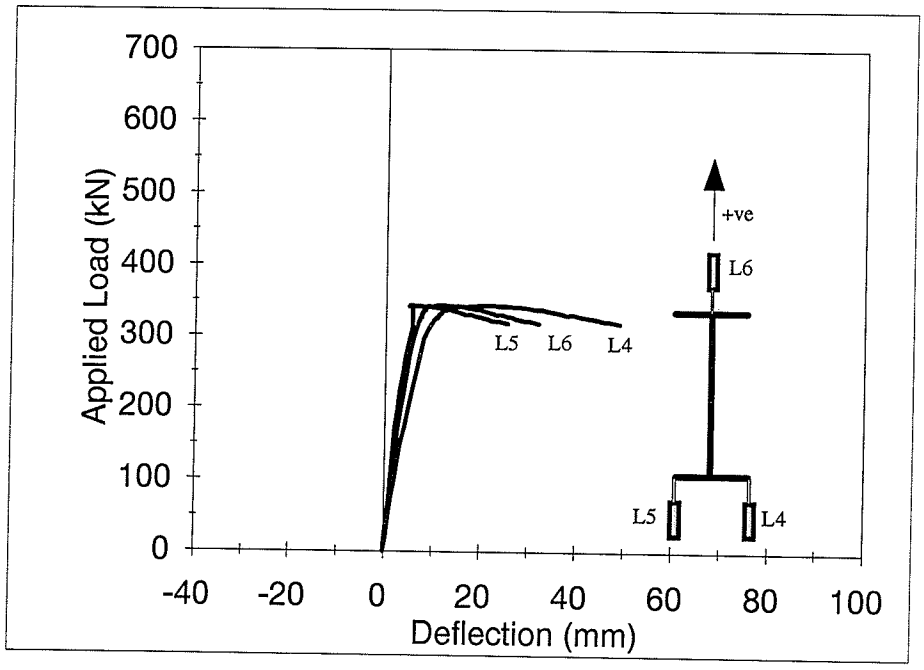

(b) Quarter Span

Figure 4.1 Load-Deflection Curves of Specimen G2

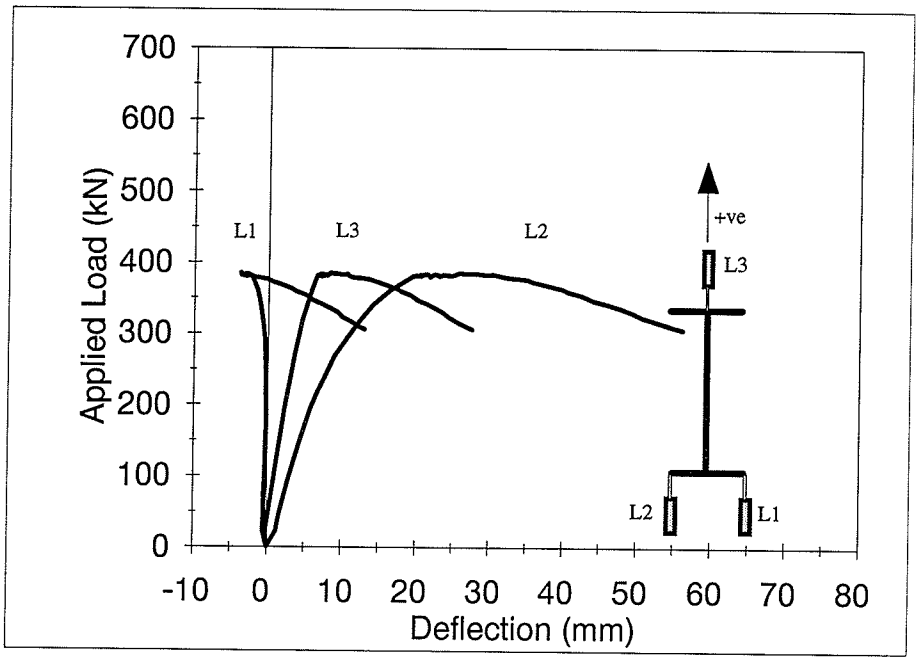

(a) Mid Span

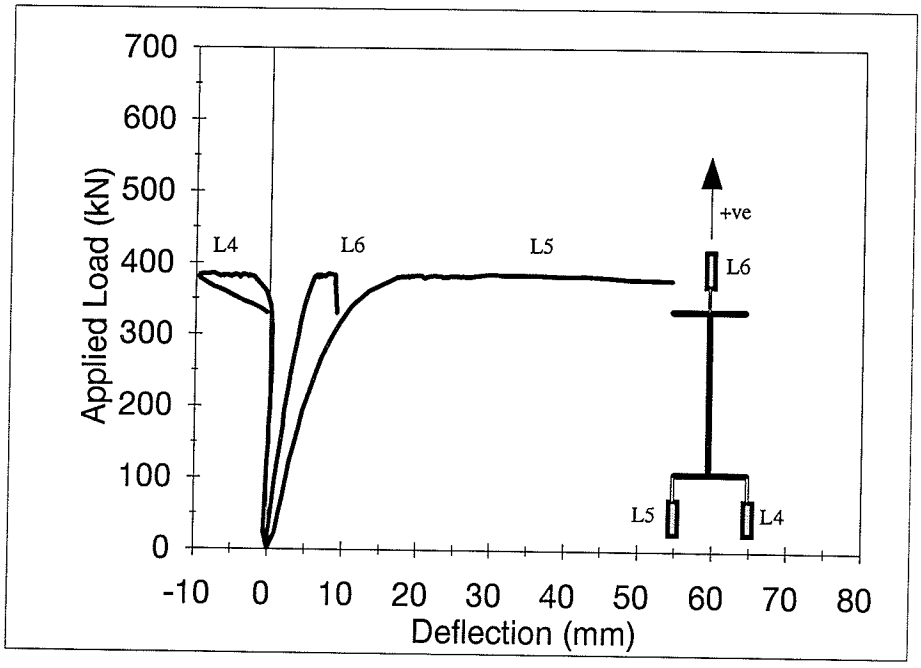

(b) Quarter Span

Figure 4.2 Load-Deflection Curves of Specimen G4

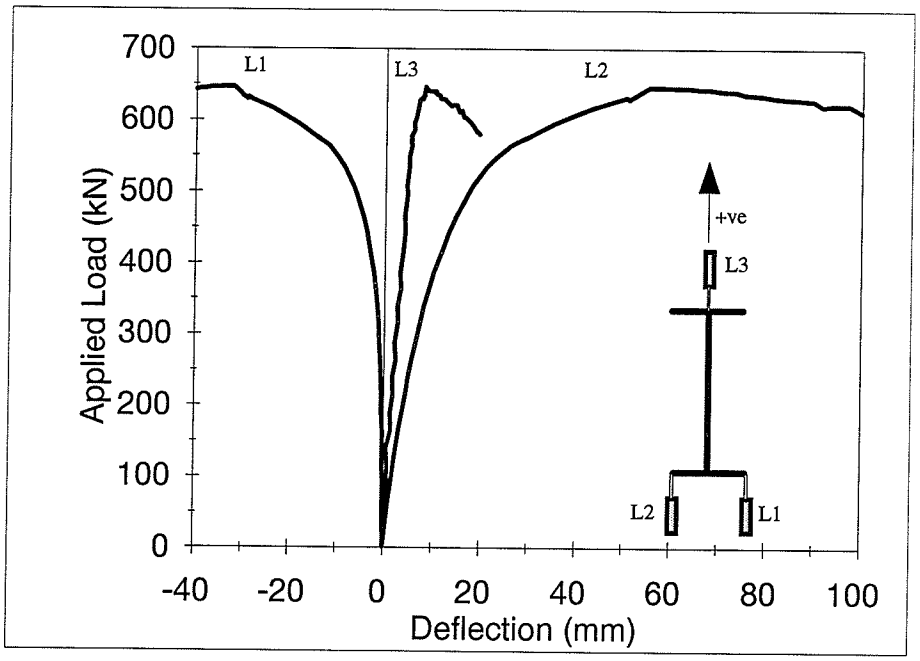

(a) Mid Span

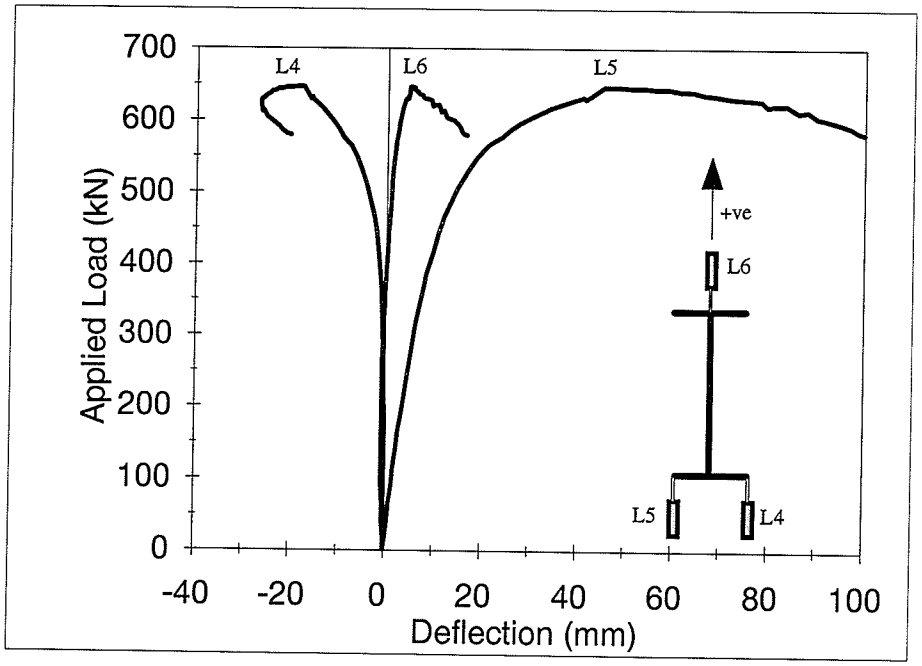

(b) Quarter Span

Figure 4.3 Load-Deflection Curves of Specimen G9

(a) One and a Half Sine-Wave Pattern (Specimens G1 & G2)

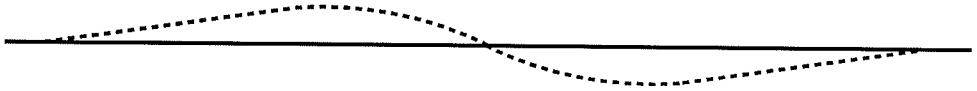

(b) Sine-Wave Pattern (Specimens G3 to G8)

(c) Half Sine-Wave Pattern (Specimen G9)

Figure 4.4 Summary the Buckling Modes of the Compression Flange

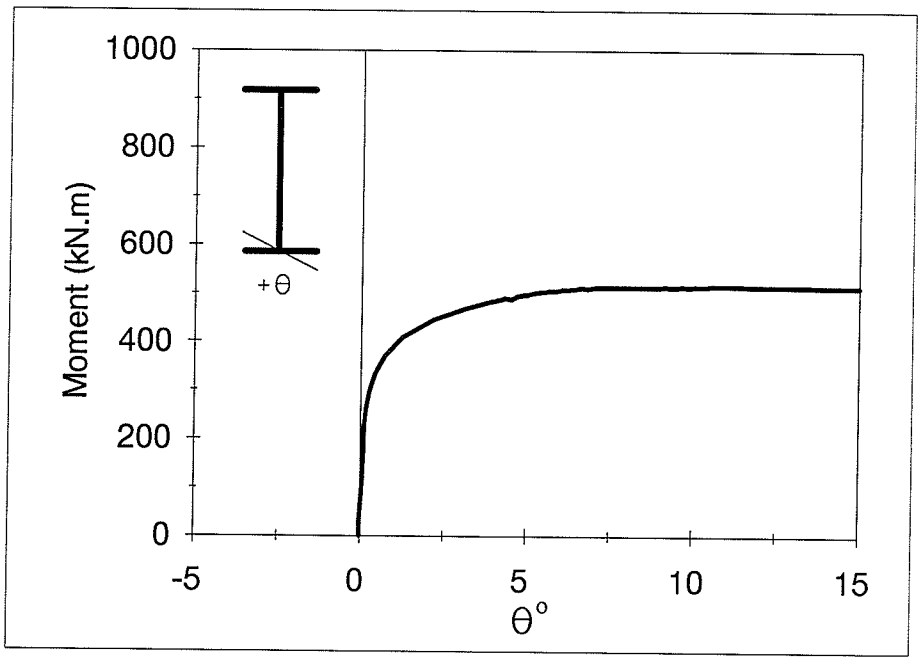

(a) Mid Span

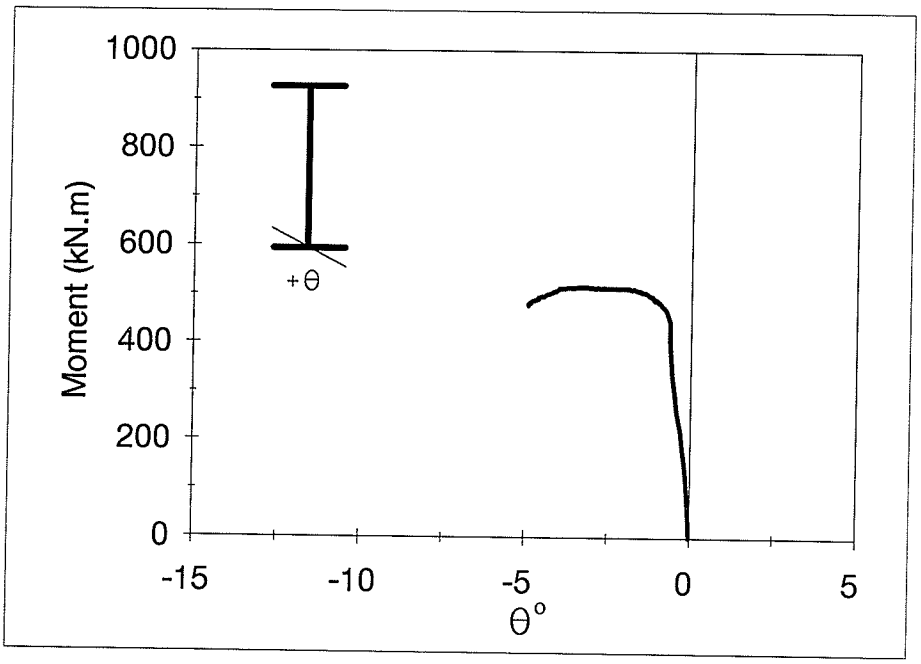

(b) Quarter Span

Figure 4.5 Rotation of Compression Flange of Specimen G2

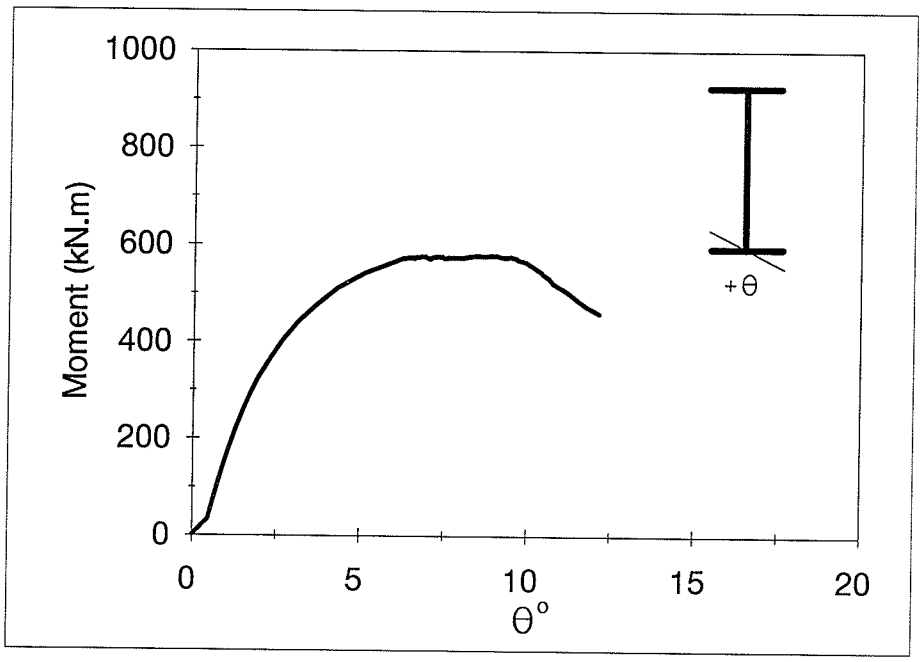

(a) Mid Span

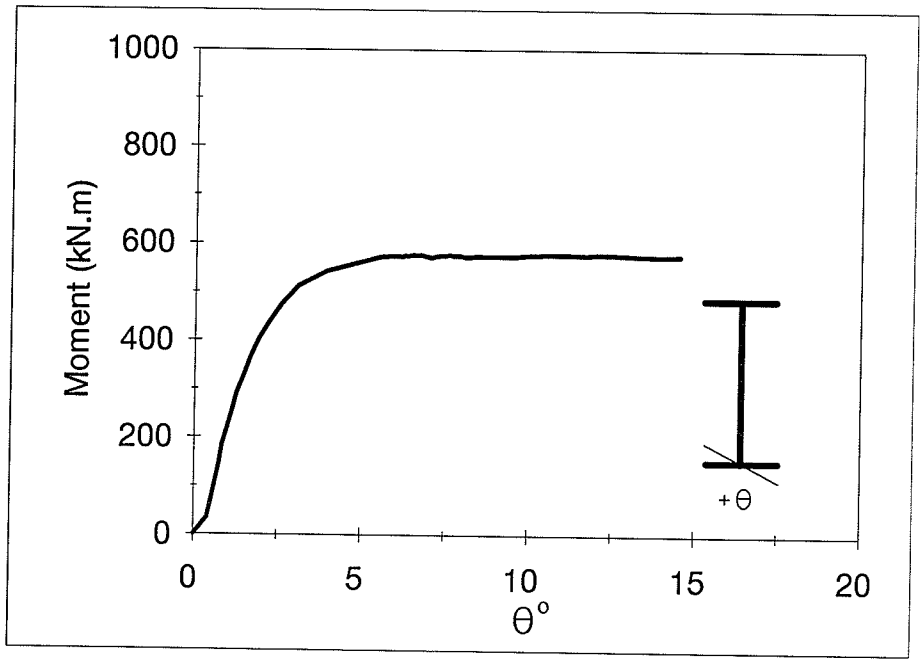

(b) Quarter Span

Figure 4.6 Rotation of Compression Flange of Specimen G4

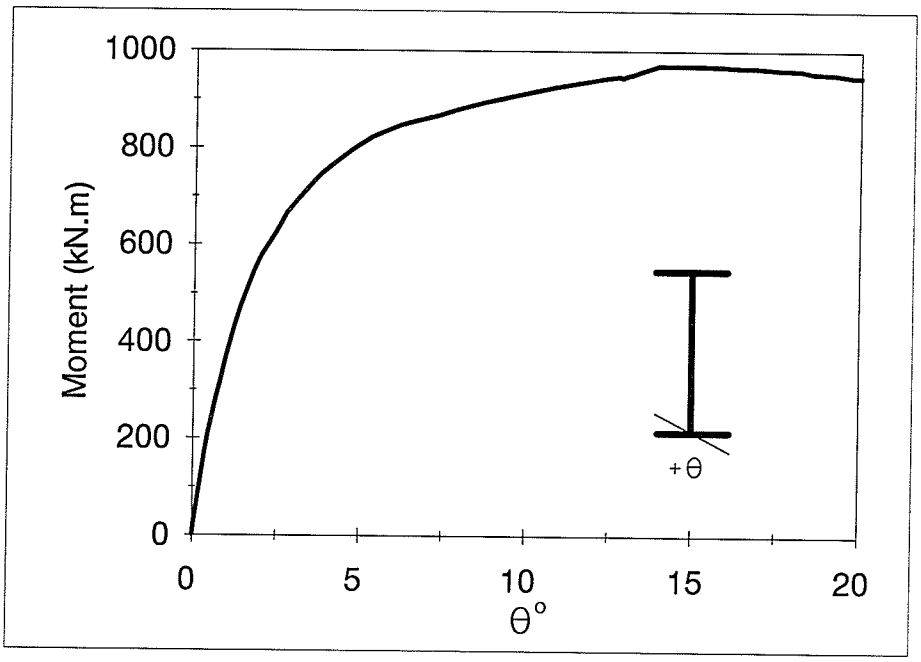

(a) Mid Span

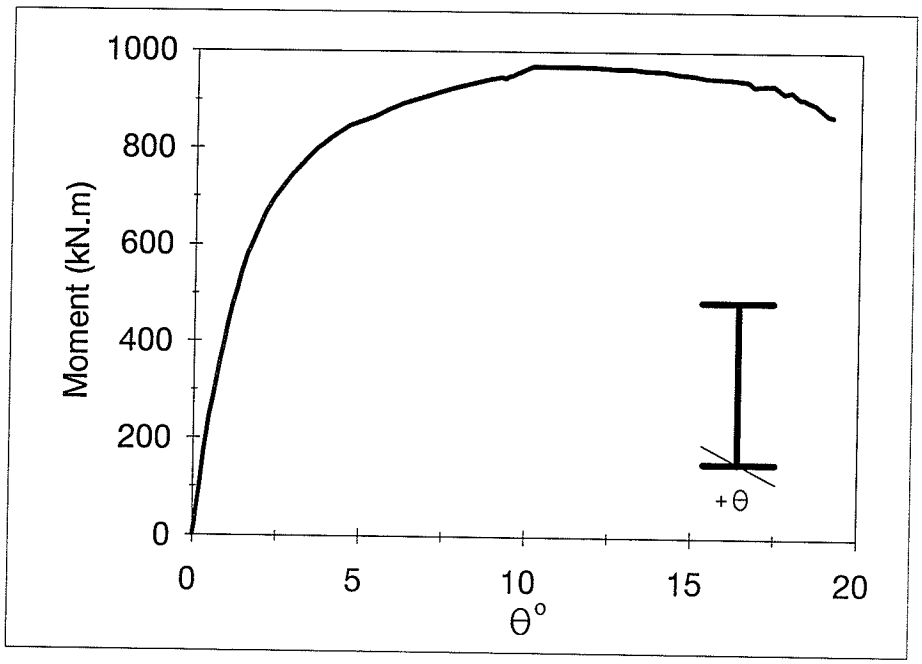

(b) Quarter Span

Figure 4.7 Rotation of Compression Flange of Specimen G9

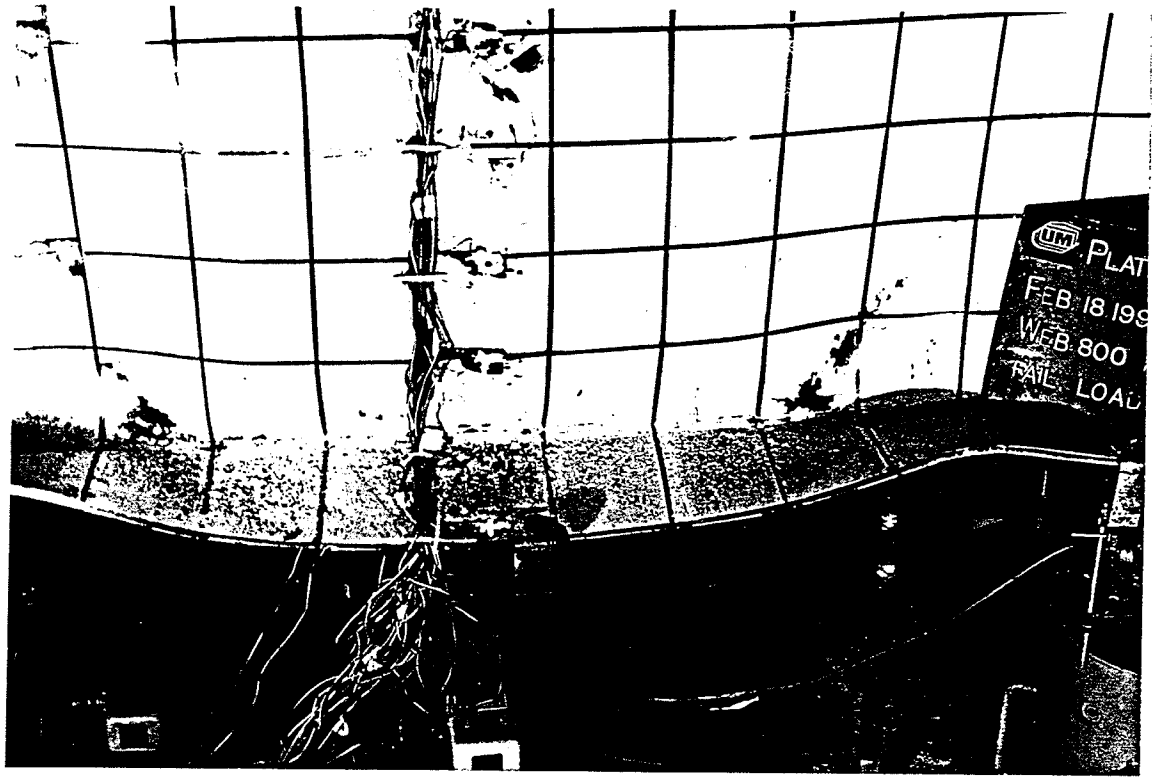

Figure 4.8 Rotated Compression Flange of Specimen G2 at Failure

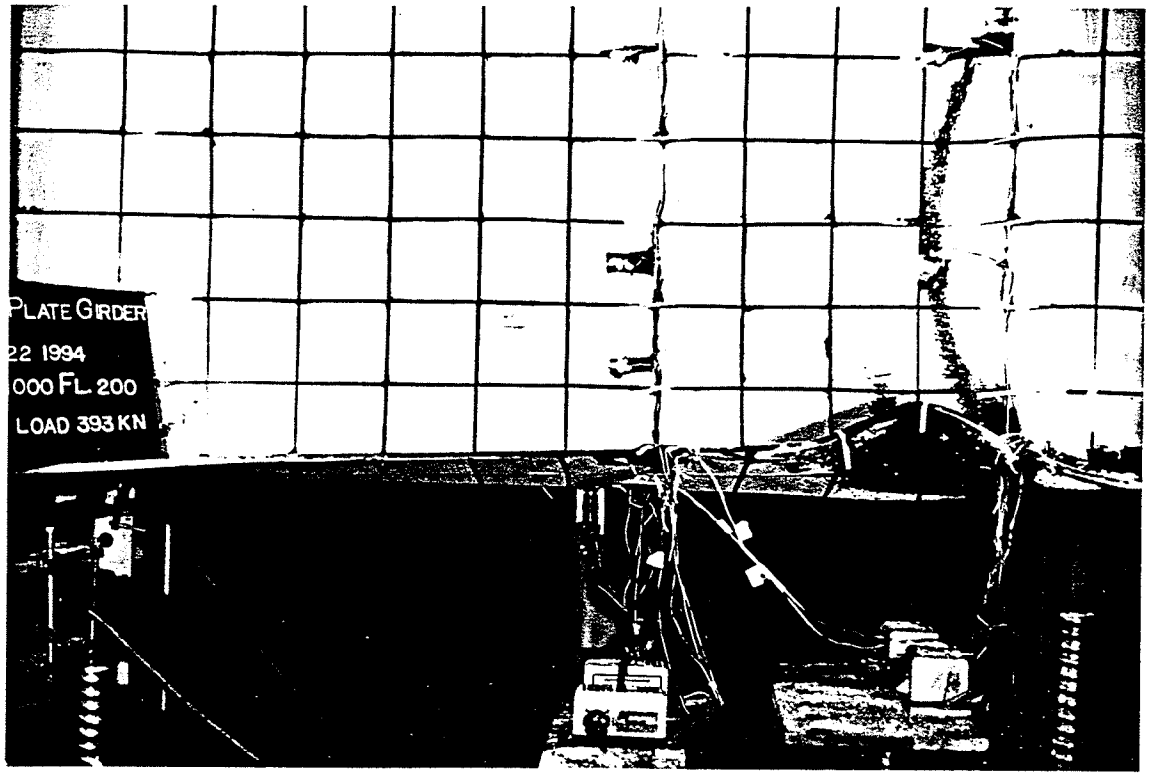

Figure 4.9 Rotated Compression Flange of Specimen G4 at Failure

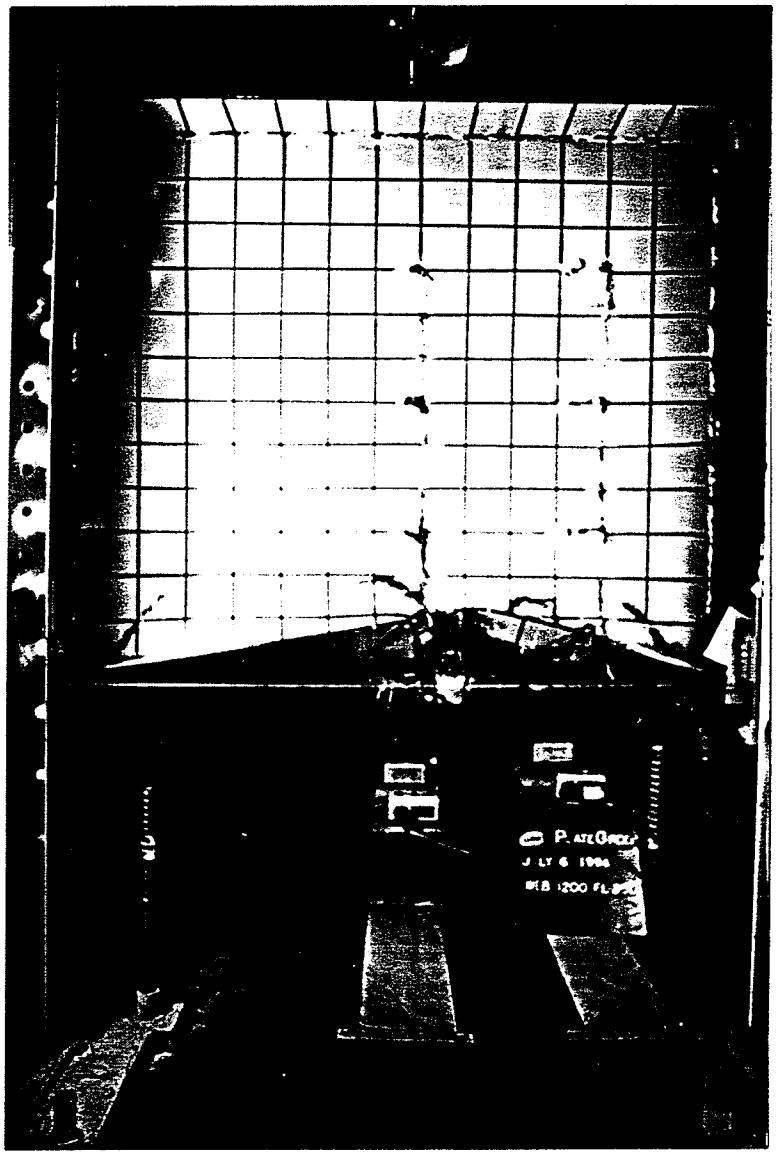

Figure 4.10 Rotated Compression Flange of Specimen G9 at Failure

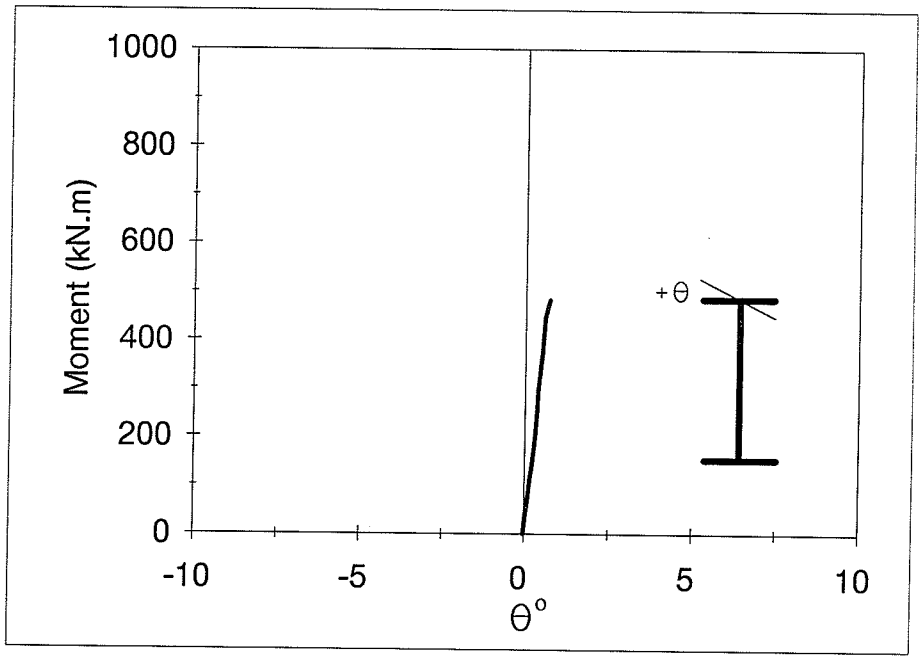

Figure 4.11 Rotation of Tension Flange at Mid-Span of Specimen G2

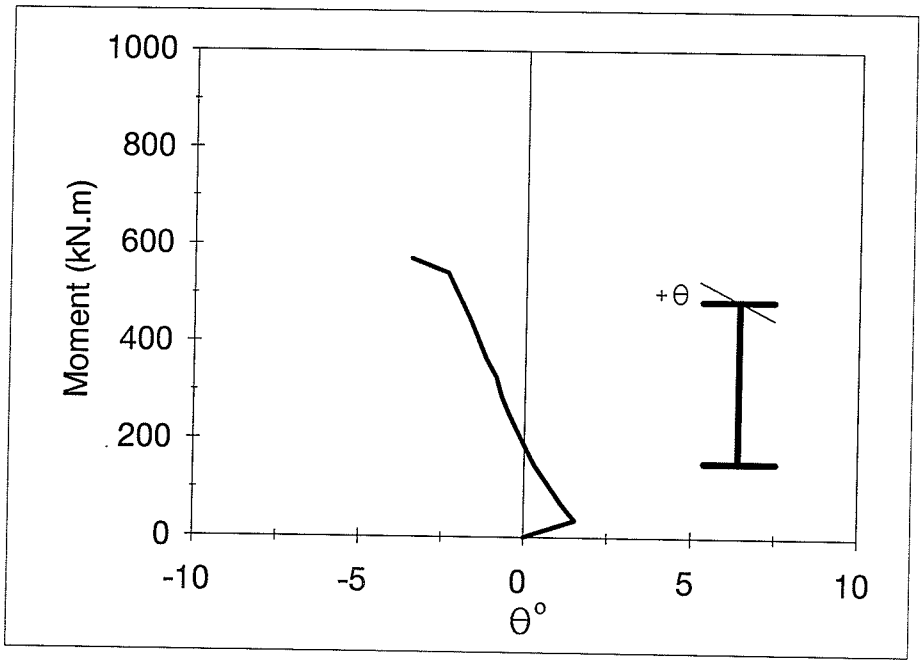

Figure 4.12 Rotation of Tension Flange at Mid-Span of Specimen G4

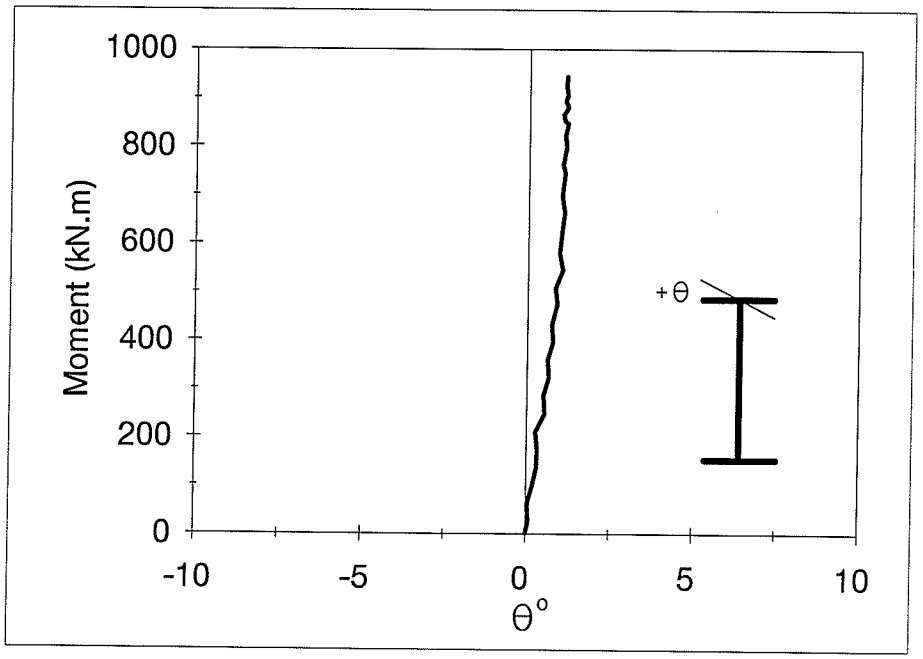

Figure 4.13 Rotation of Tension Flange at Mid-Span of Specimen G9

Figure 4.14 Rotated Tension Flange of Specimen G8

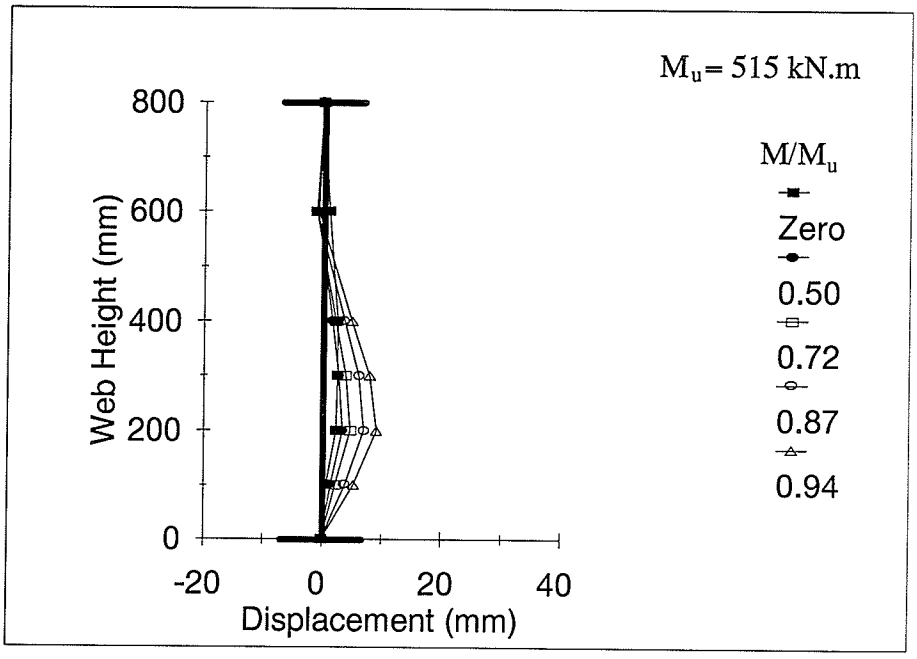

(a) Mid Span

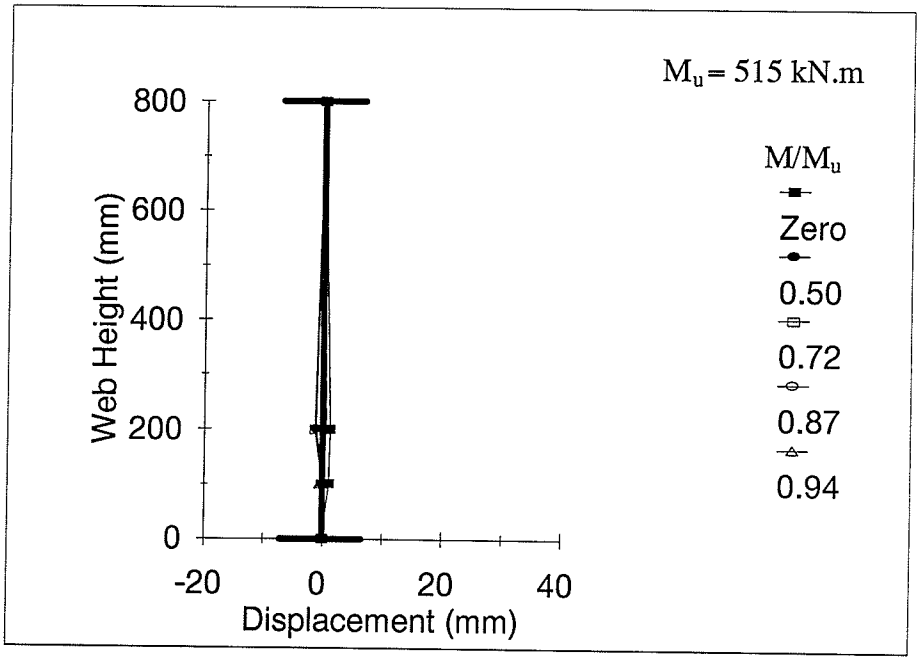

(b) Quarter Span

Figure 4.15 Lateral Displacement of the Web of Specimen G2

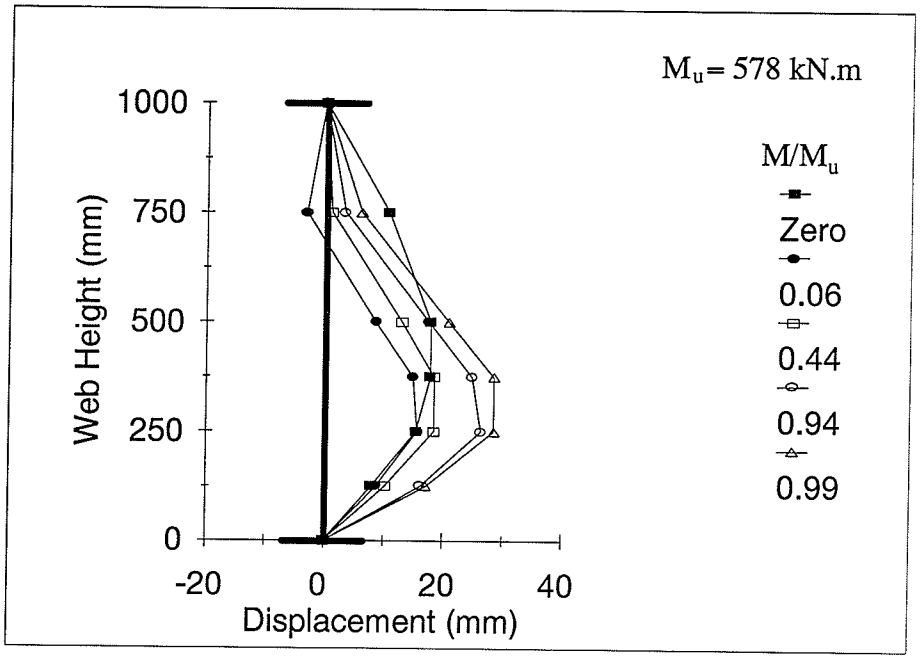

(a) Mid Span

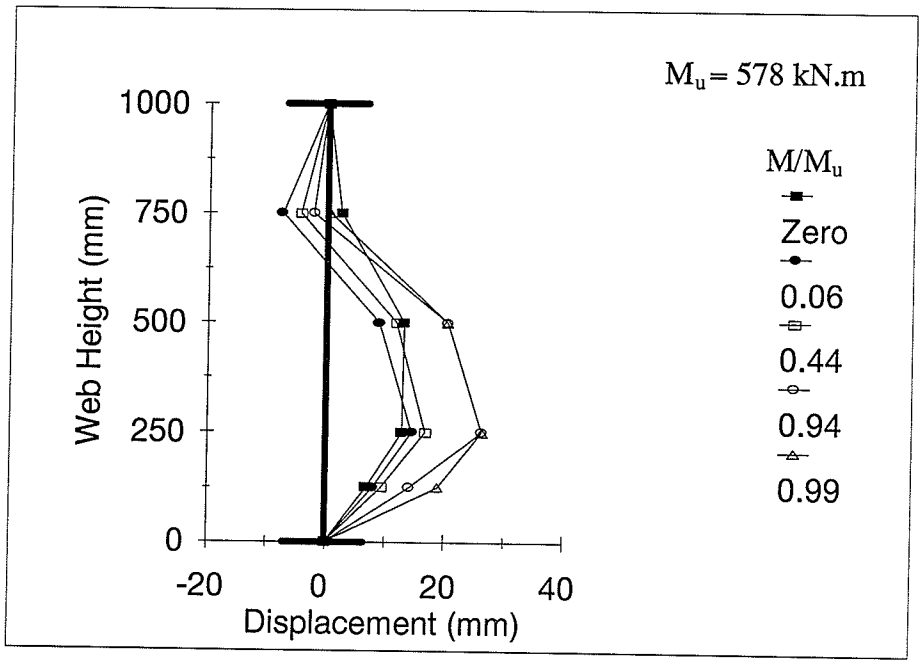

(b) Quarter Span

Figure 4.16 Lateral Displacement of the Web of Specimen G4

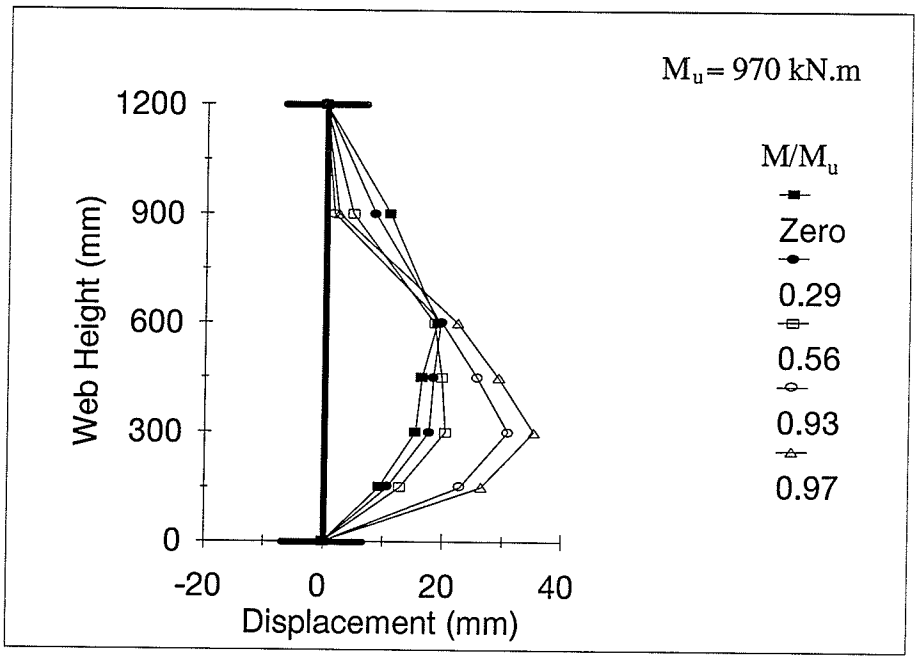

(a) Mid Span

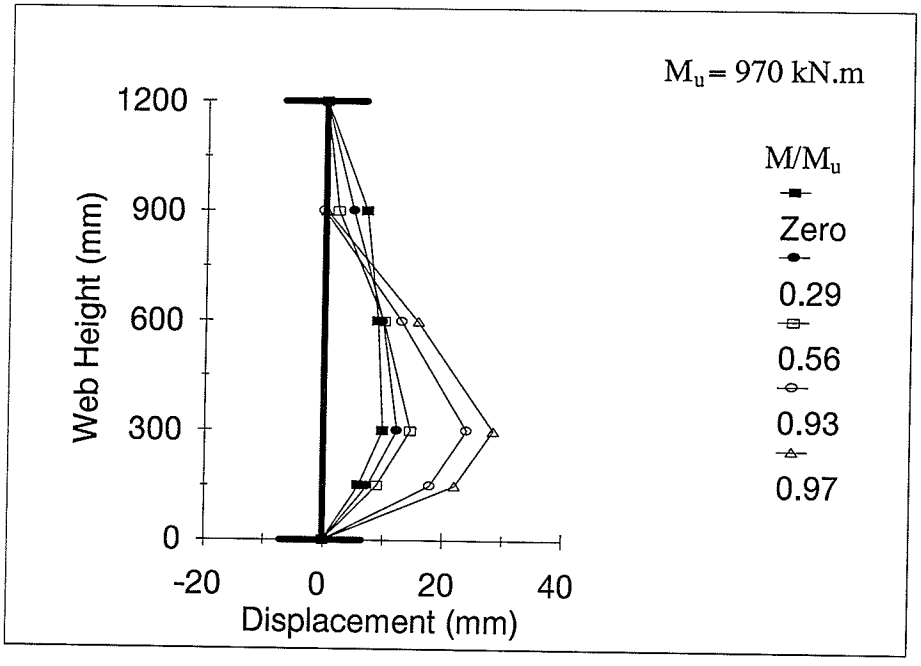

(b) Quarter Span

Figure 4.17 Lateral Displacement of the Web of Specimen G9

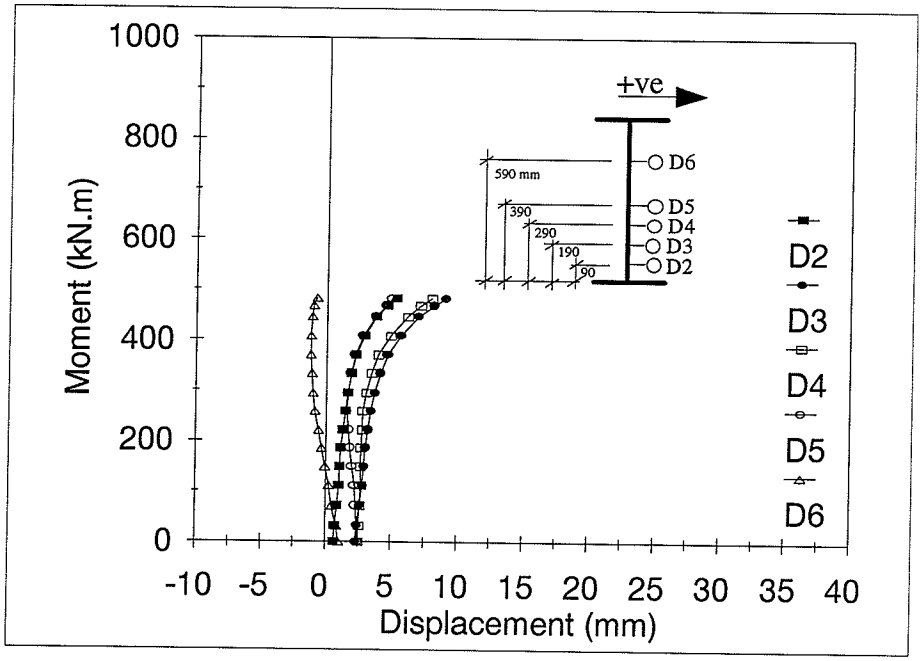

(a) Mid Span

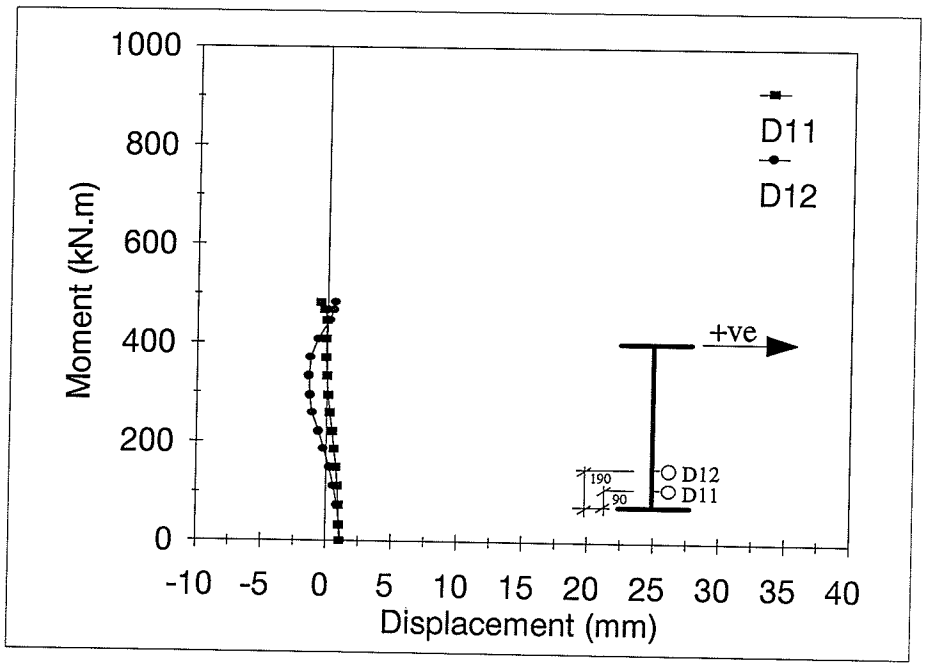

(b) Quarter Span

Figure 4.18 Lateral Displacement Curves of the Web of Specimen G2

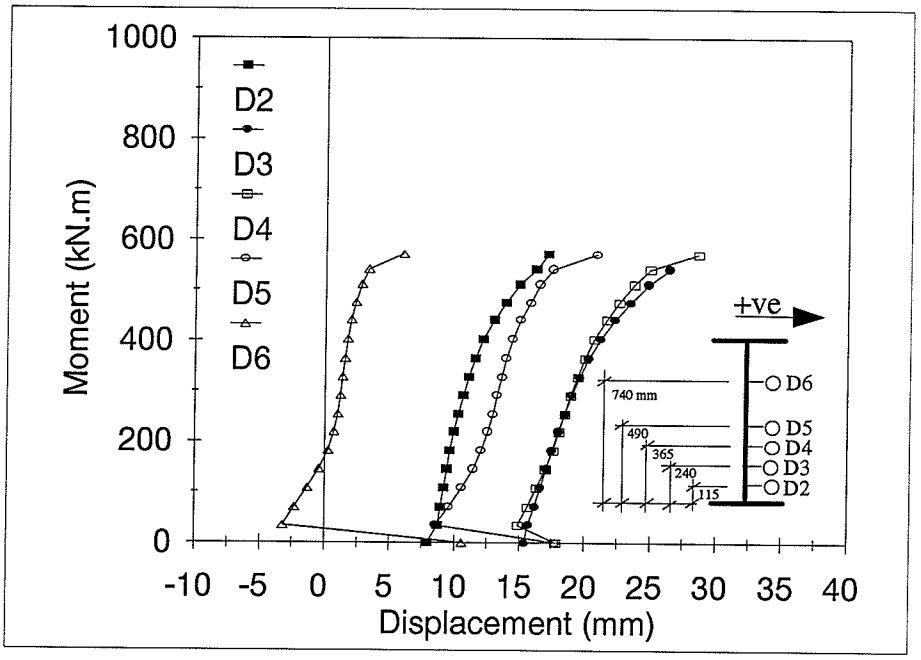

(a) Mid Span

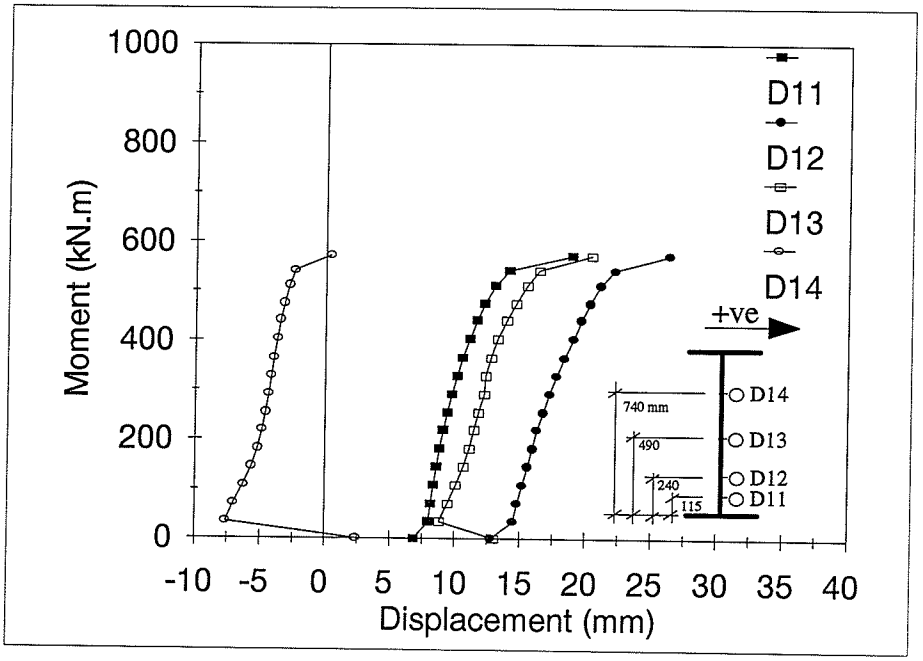

(b) Quarter Span

Figure 4.19 Lateral Displacement Curves of the Web of Specimen G4

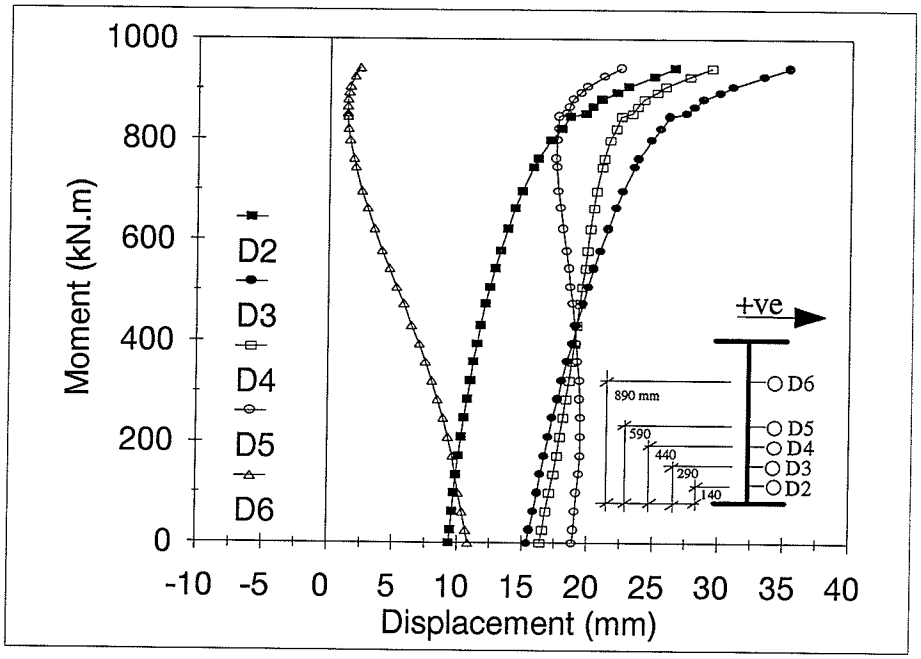

(a) Mid Span

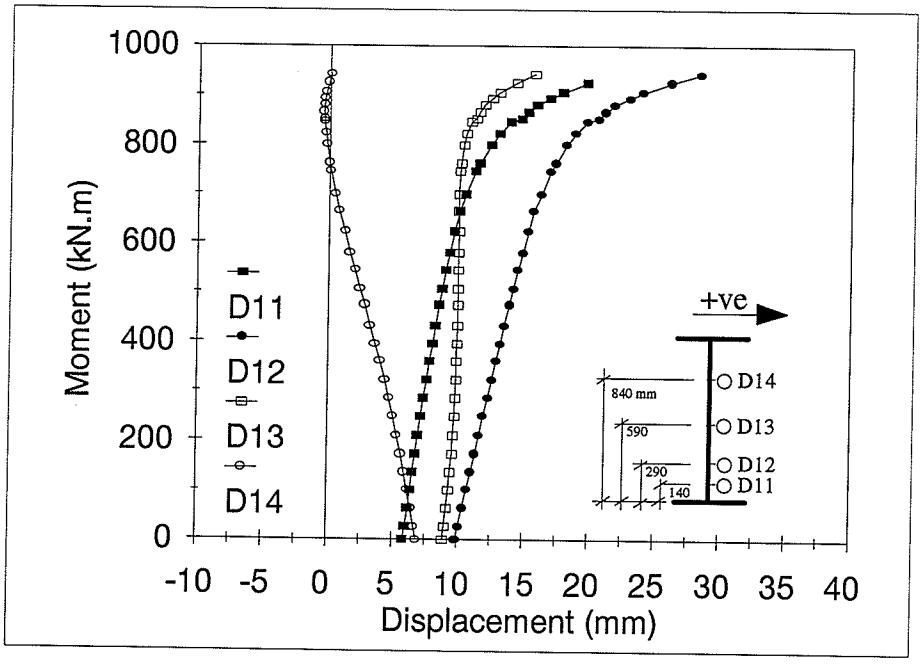

(b) Quarter Span

Figure 4.20 Lateral Displacement Curves of the Web of Specimen G9

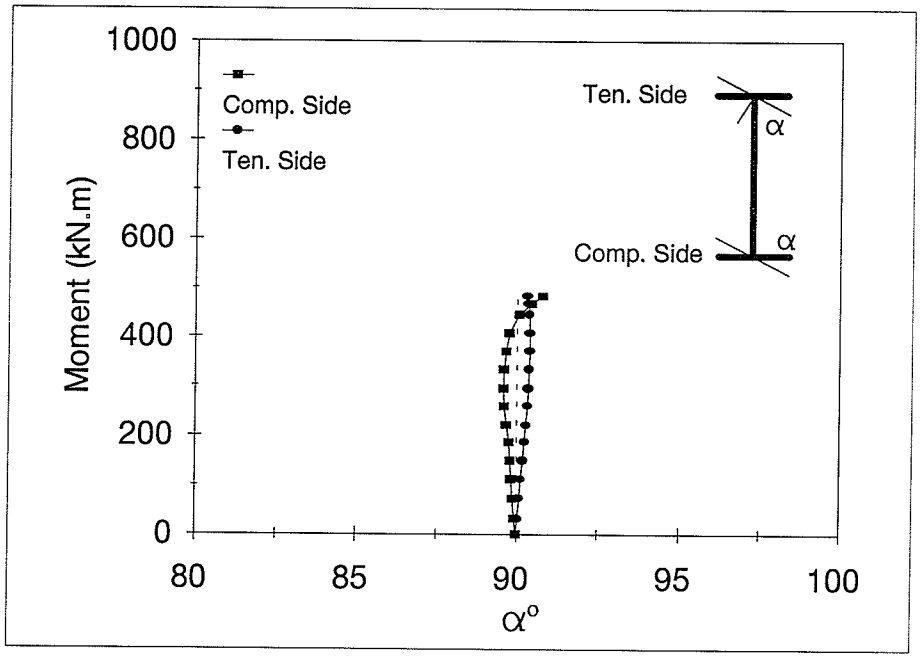

(a) Mid Span

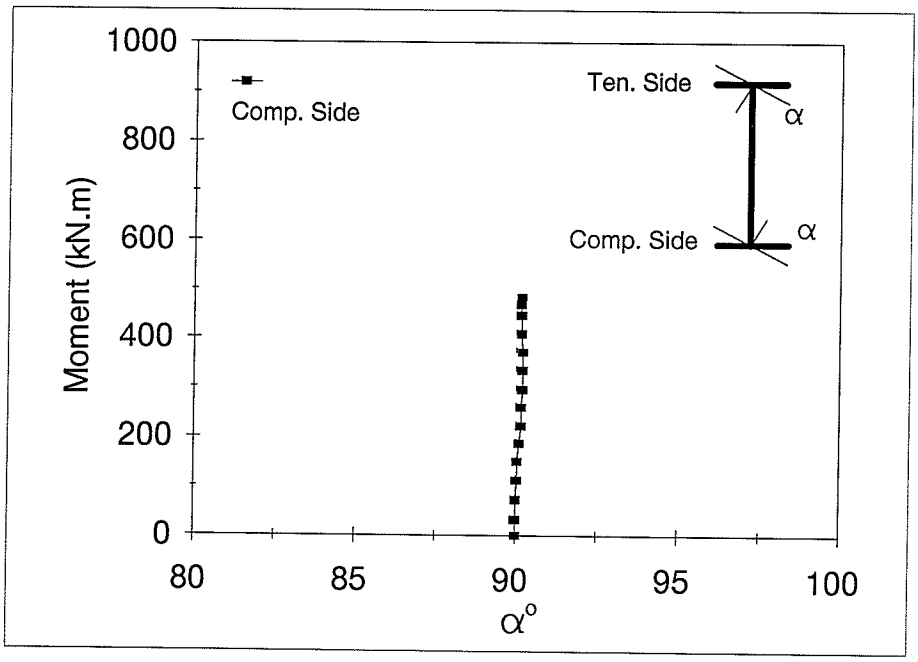

(b) Quarter Span

Figure 4.21 Web-Flange Angle as a Function of Applied Moment of Specimen G2

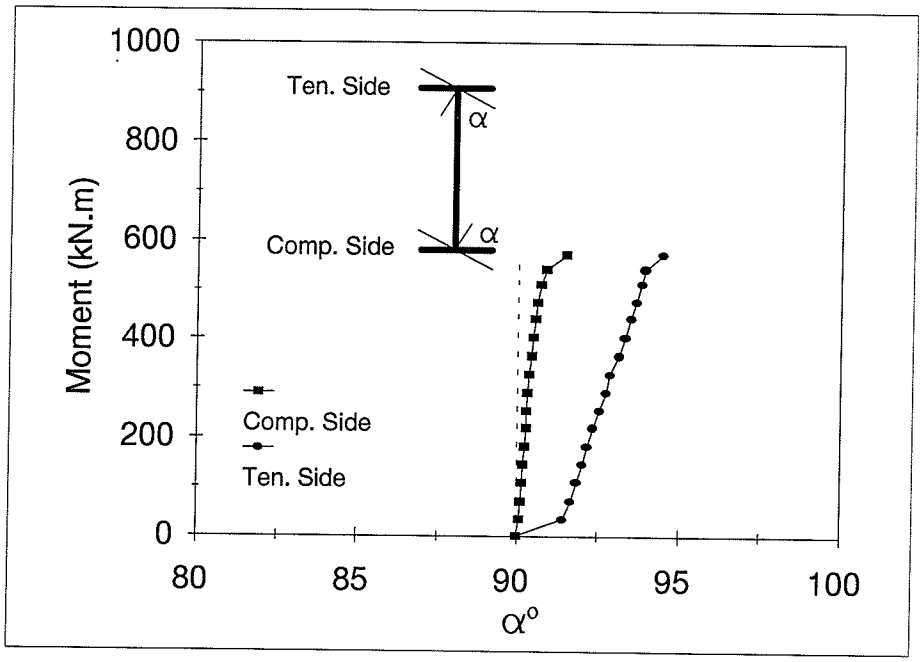

(a) Mid Span

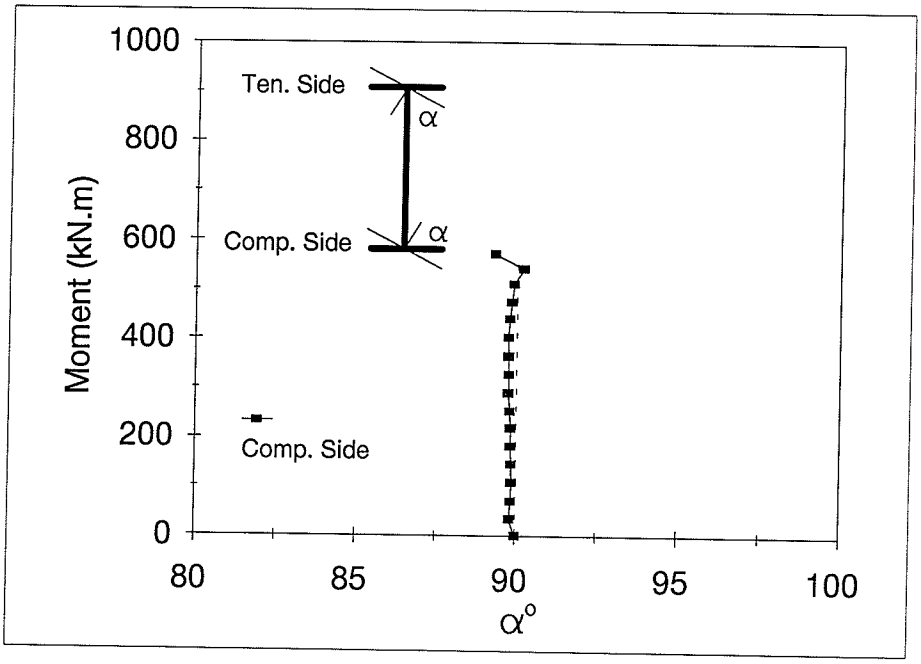

(b) Quarter Span

Figure 4.22 Web-Flange Angle as a Function of Applied Moment of Specimen G4

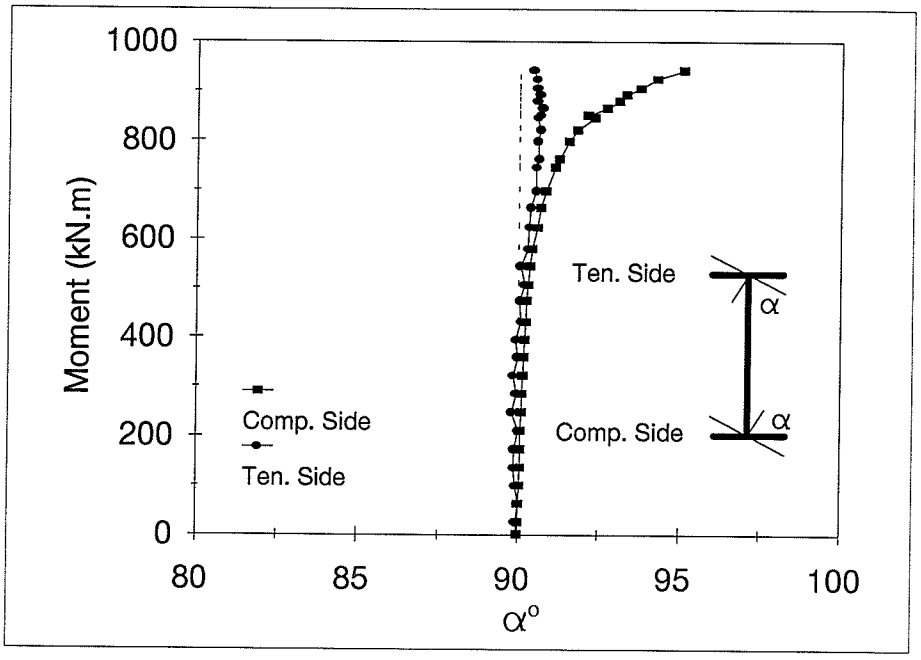

(a) Mid Span

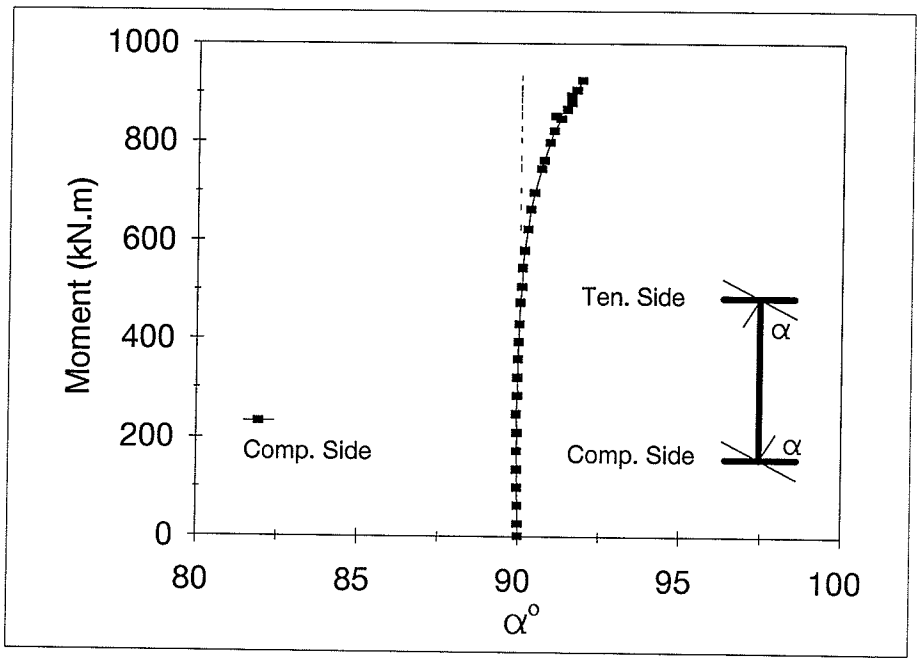

(b) Quarter Span

Figure 4.23 Web-Flange Angle as a Function of Applied Moment of Specimen G9

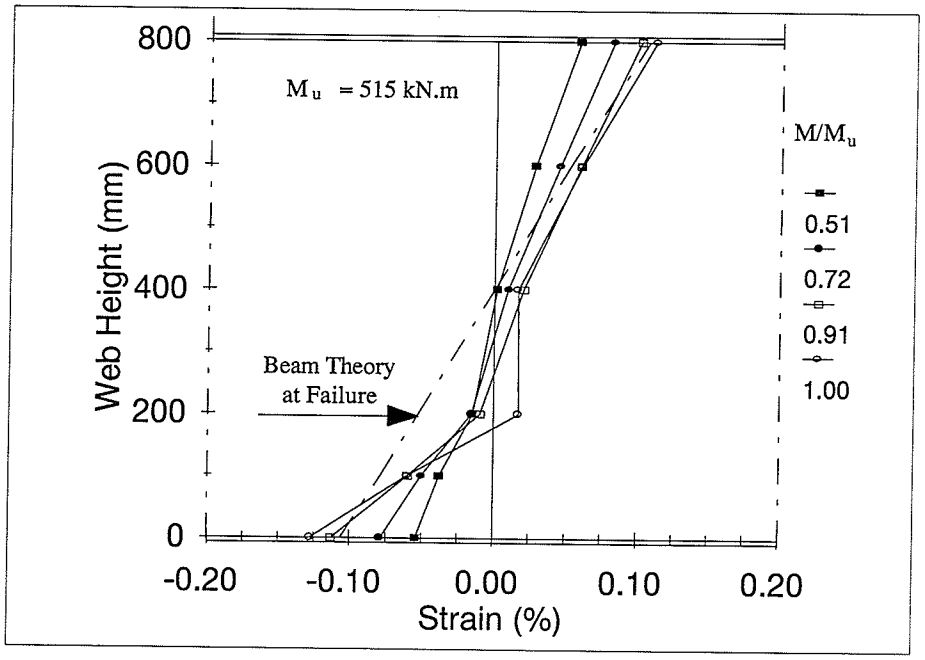

(a) Mid Span

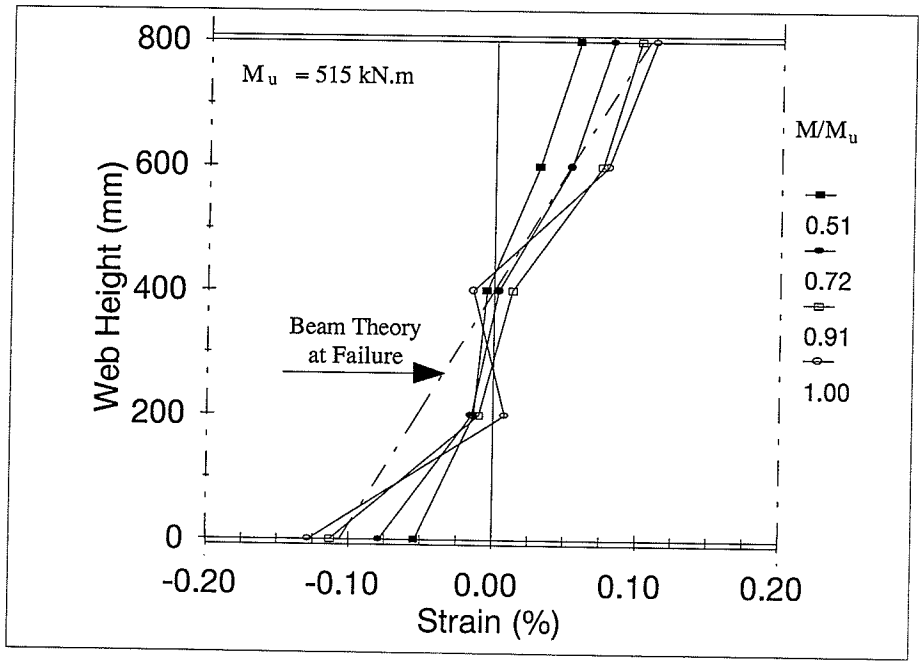

(b) Quarter Span

Figure 4.24 Strain Distribution Along Cross-Sections of Specimen G2

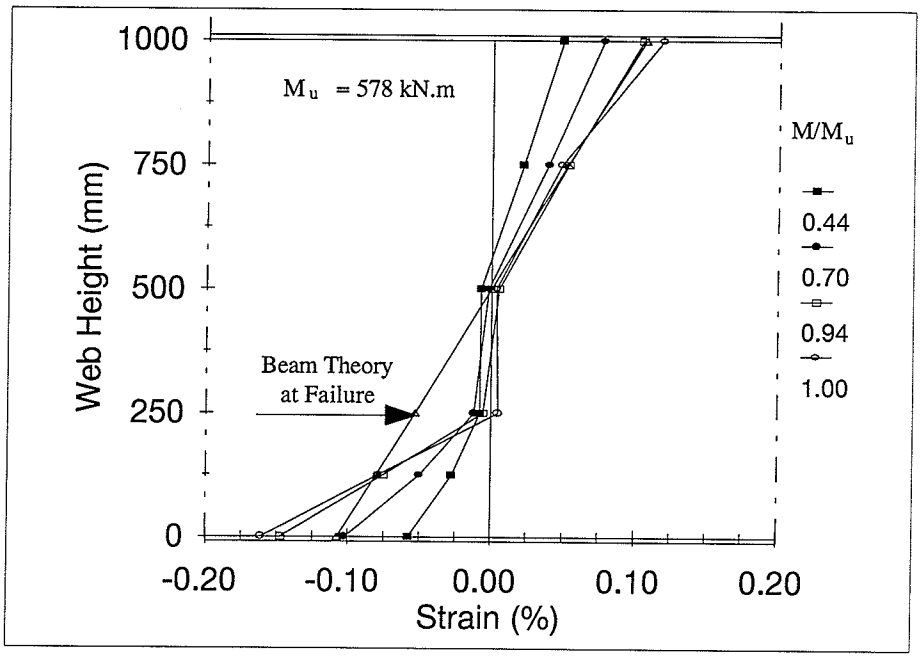

(a) Mid Span

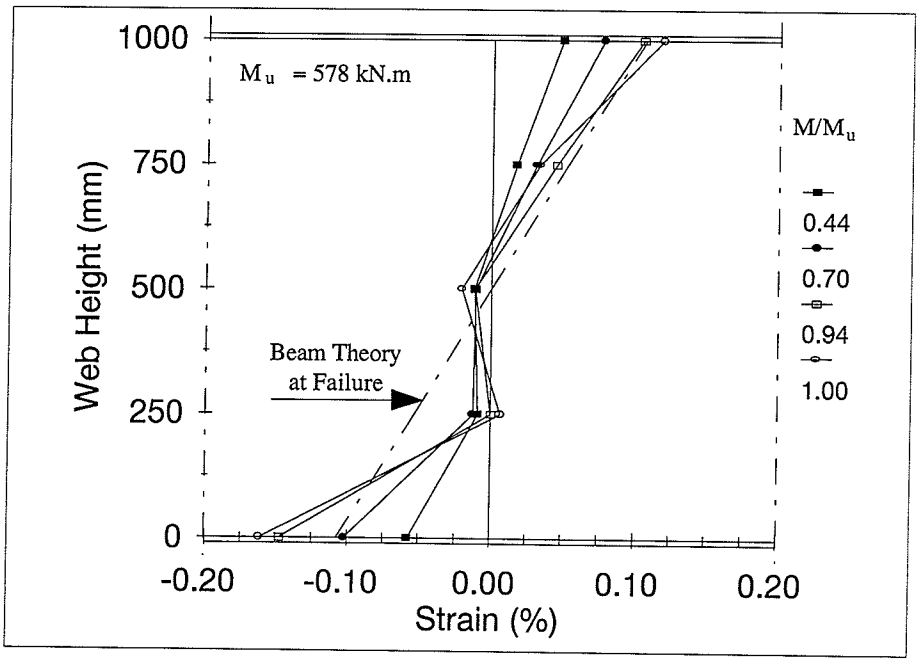

(b) Quarter Span

Figure 4.25 Strain Distribution Along Cross-Sections of Specimen G4

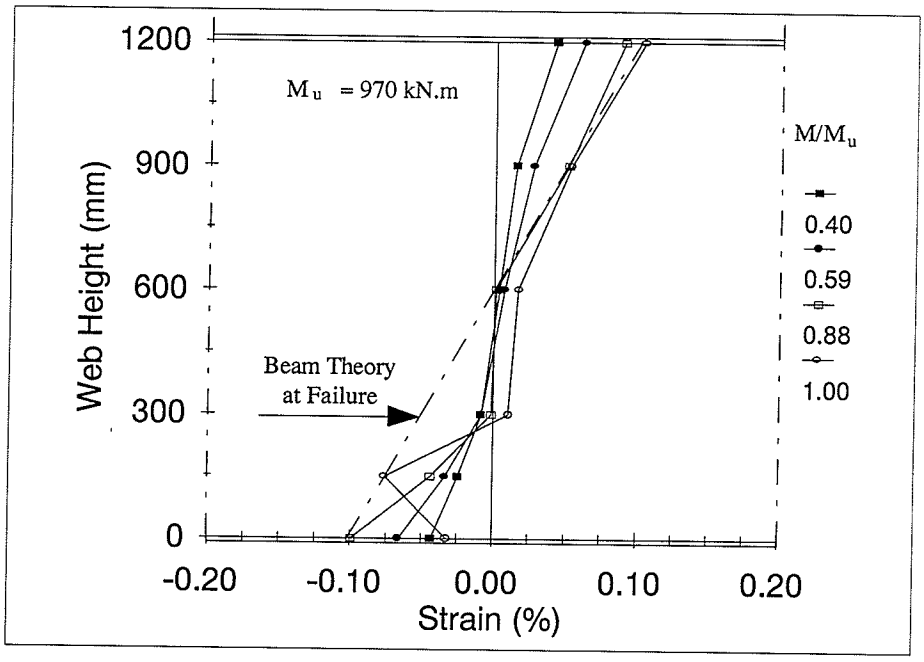

(a) Mid Span

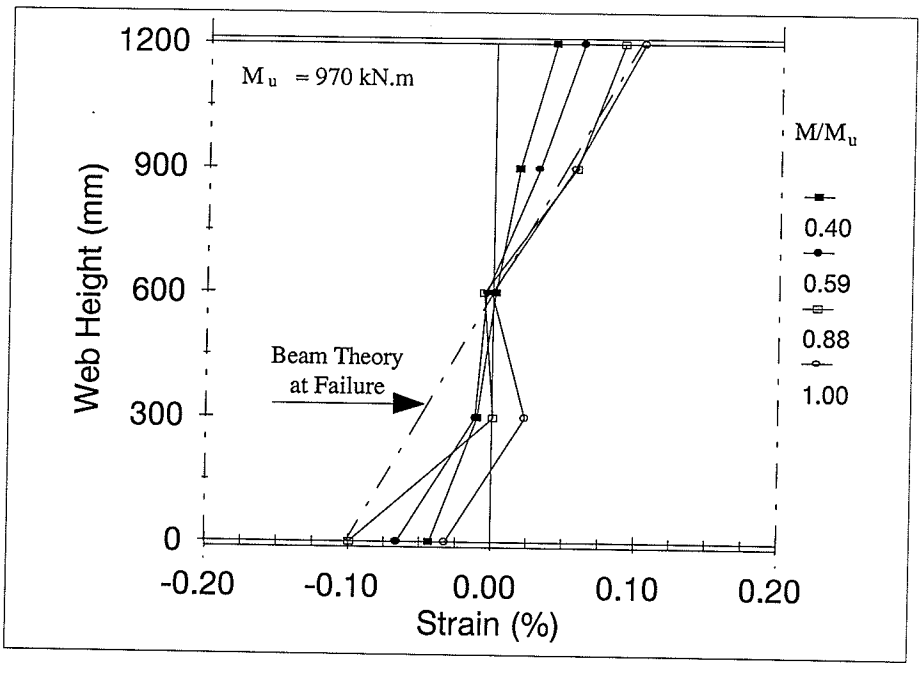

(b) Quarter Span

Figure 4.26 Strain Distribution Along Cross-Sections of Specimen G9

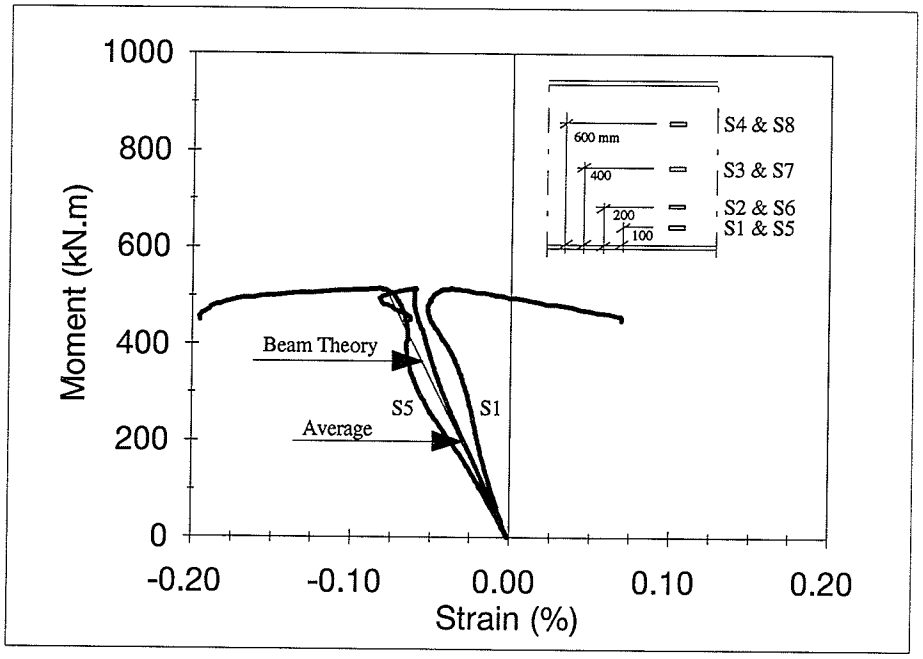

(a) Strain Distribution at S1 & S5

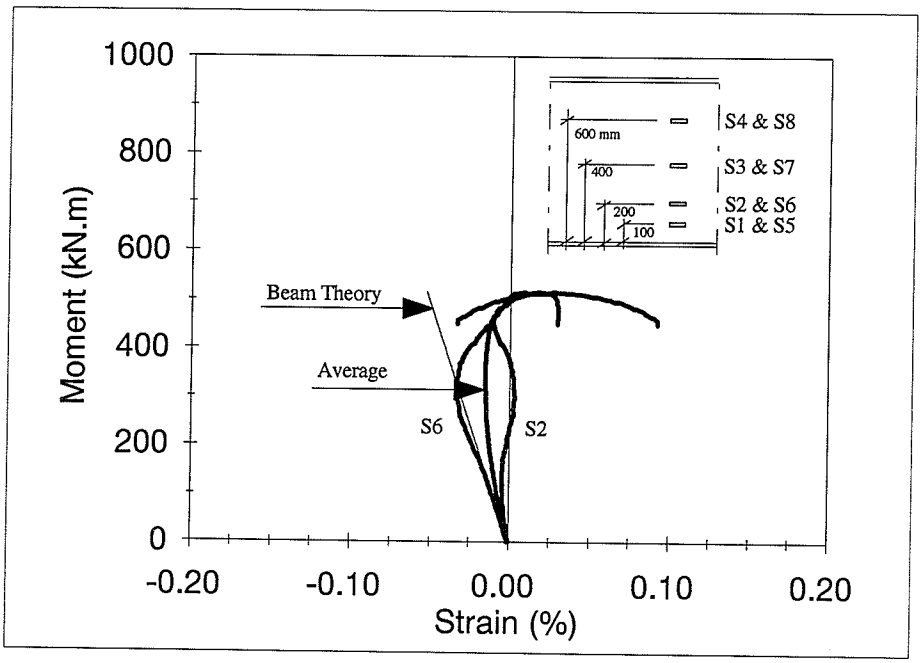

(b) Strain Distribution at S2 & S6

Figure 4.27 Moment-Strain Relationships at Mid-Span Web of Specimen G2

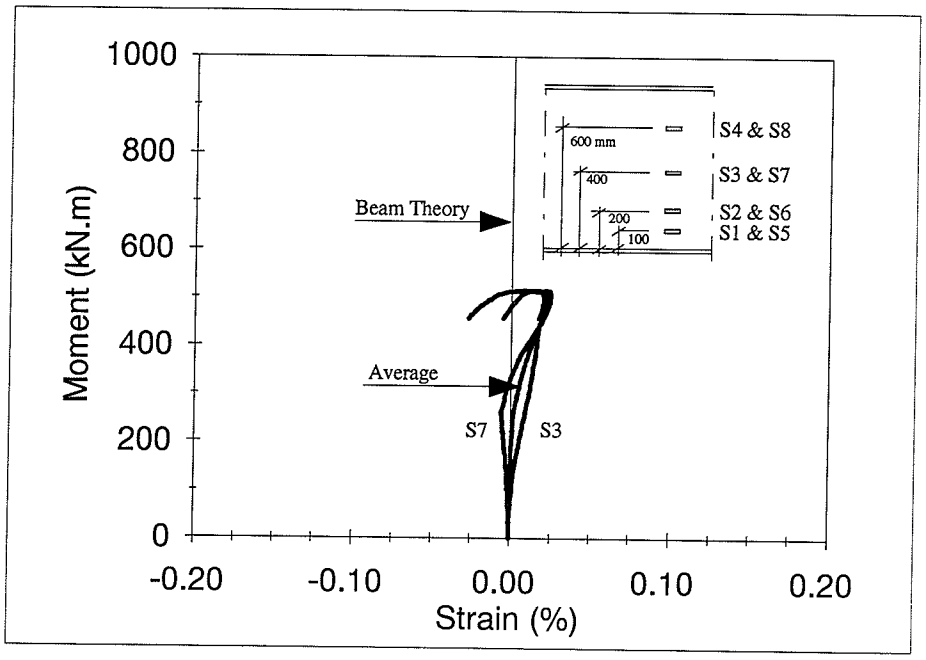

(c) Strain Distribution at S3 & S7

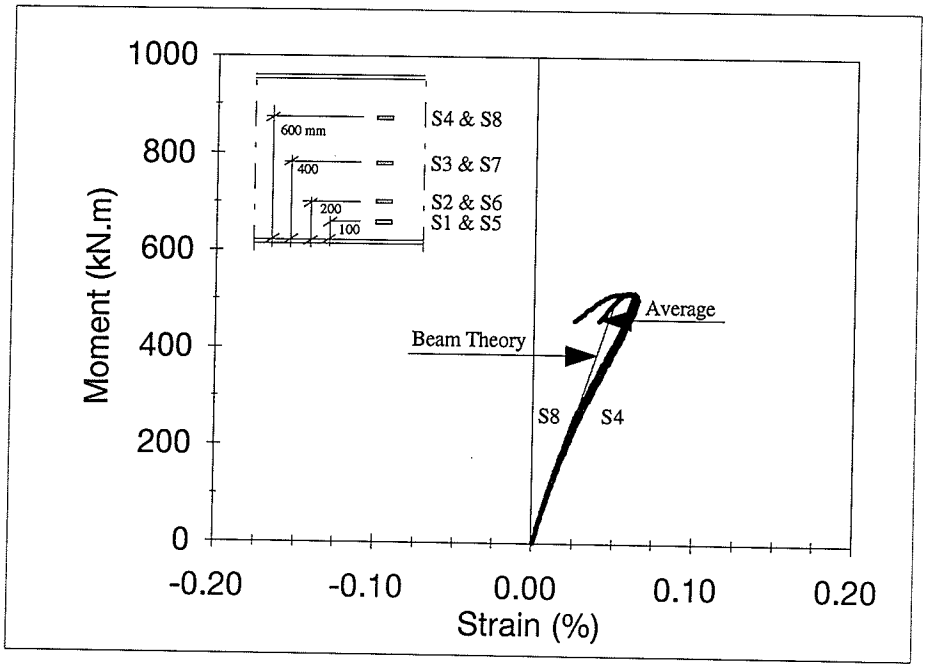

(d) Strain Distribution at S4 & S8

Figure 4.27 Moment-Strain Relationships at Mid-Span Web of Specimen G2

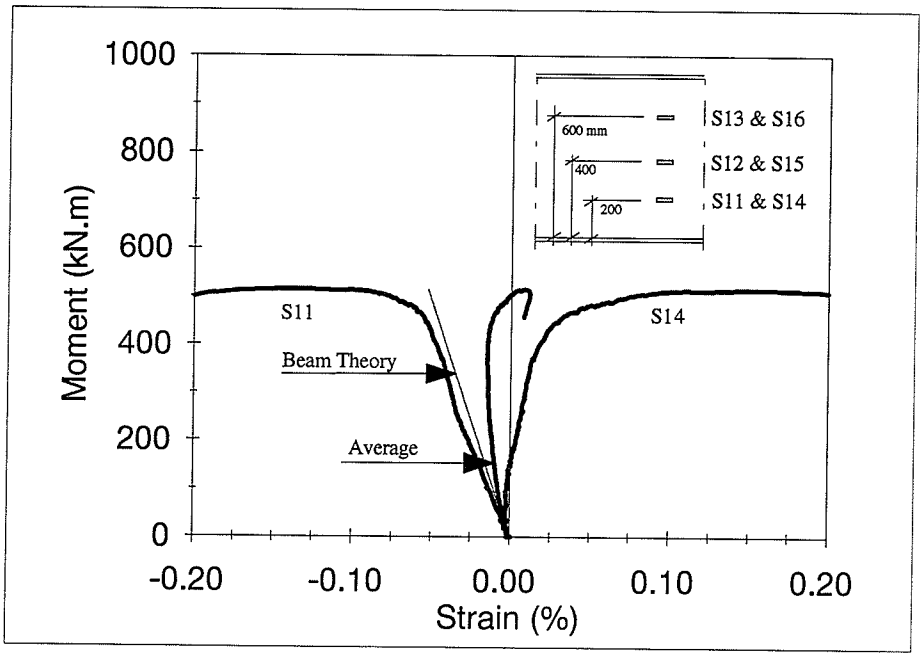

(a) Strain Distribution at S11 & S14

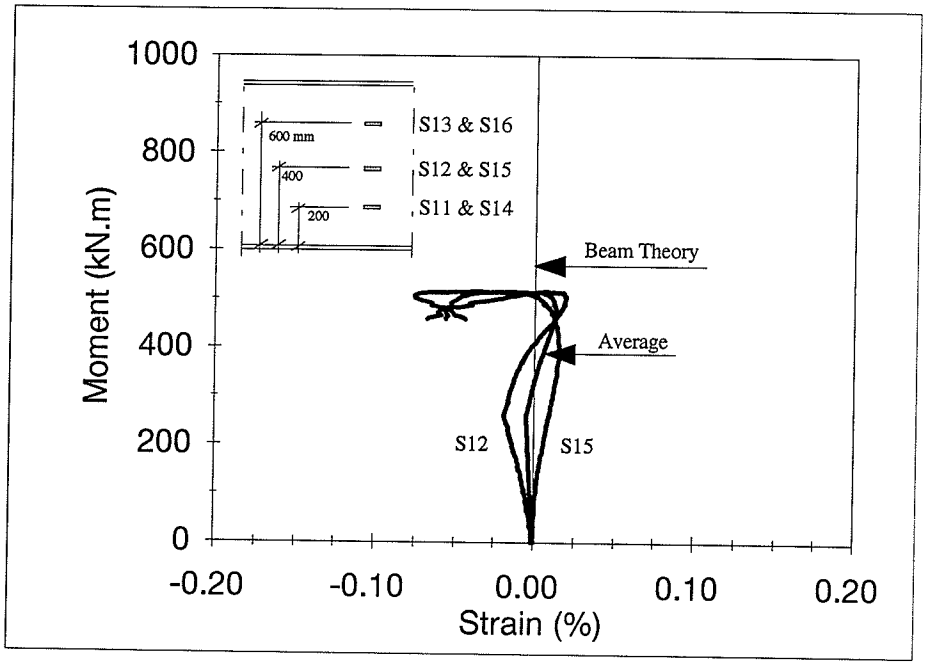

(b) Strain Distribution at S12 & S15

Figure 4.28 Moment-Strain Relationships at Quarter-Span Web of Specimen G2

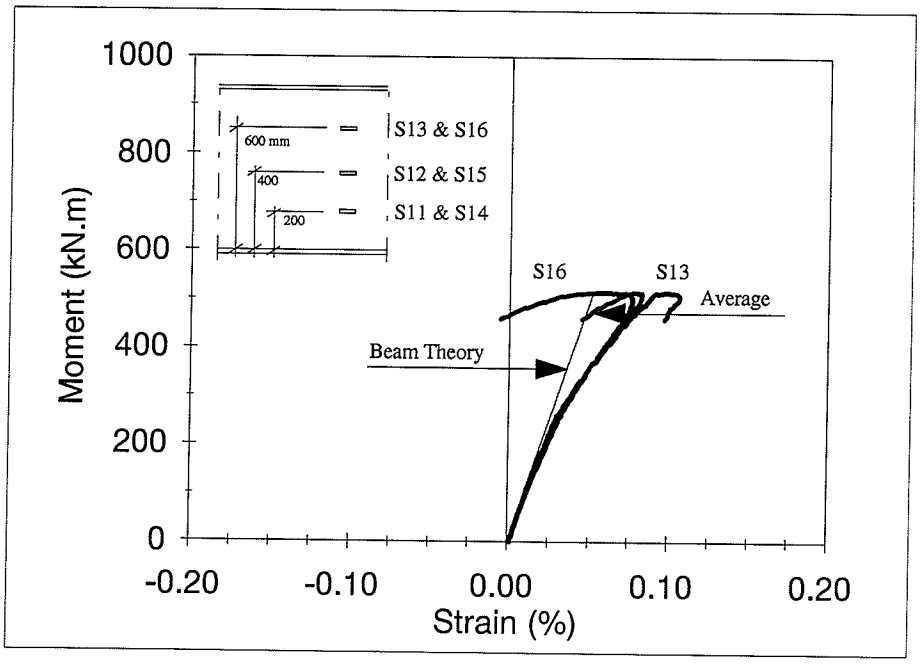

(c) Strain Distribution at S13 & S16

Figure 4.28 Moment-Strain Relationships at Quarter-Span Web of Specimen G2

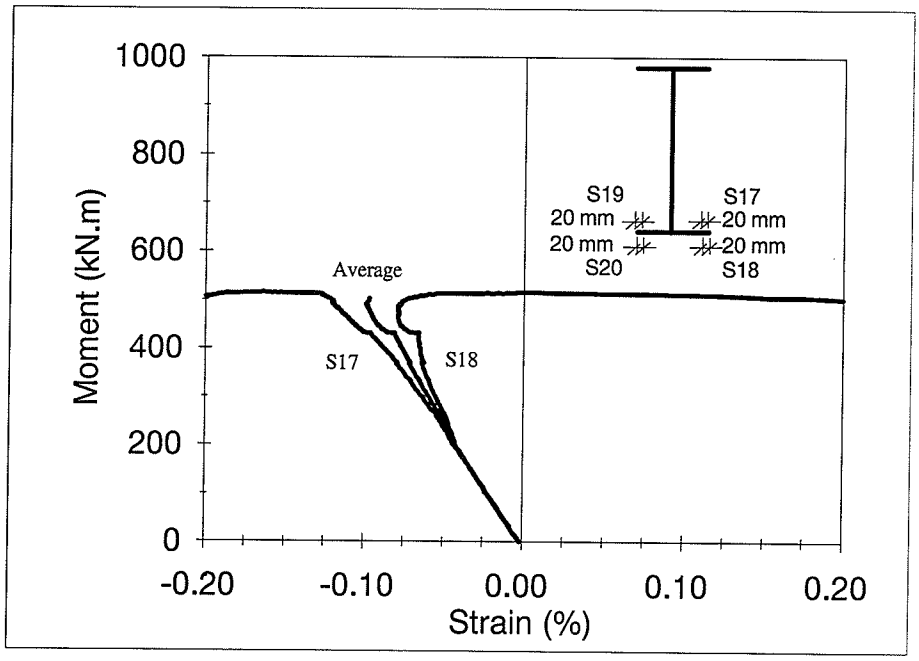

(a) Strain Distribution at S17 & S18

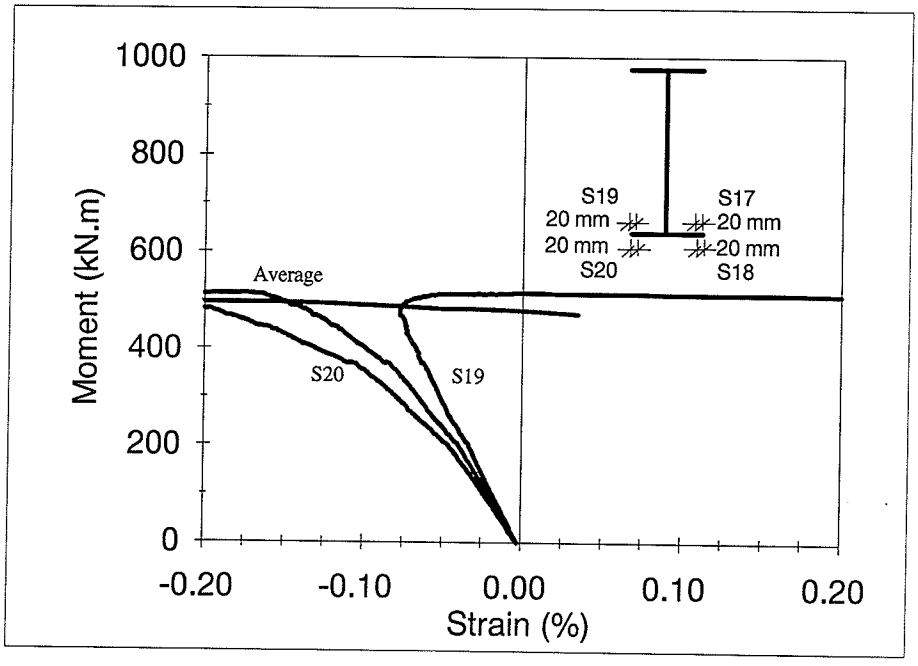

(b) Strain Distribution at S19 & S20

Figure 4.29 Moment-Strain Relationships at Mid-Span Compression Flange of Specimen G2

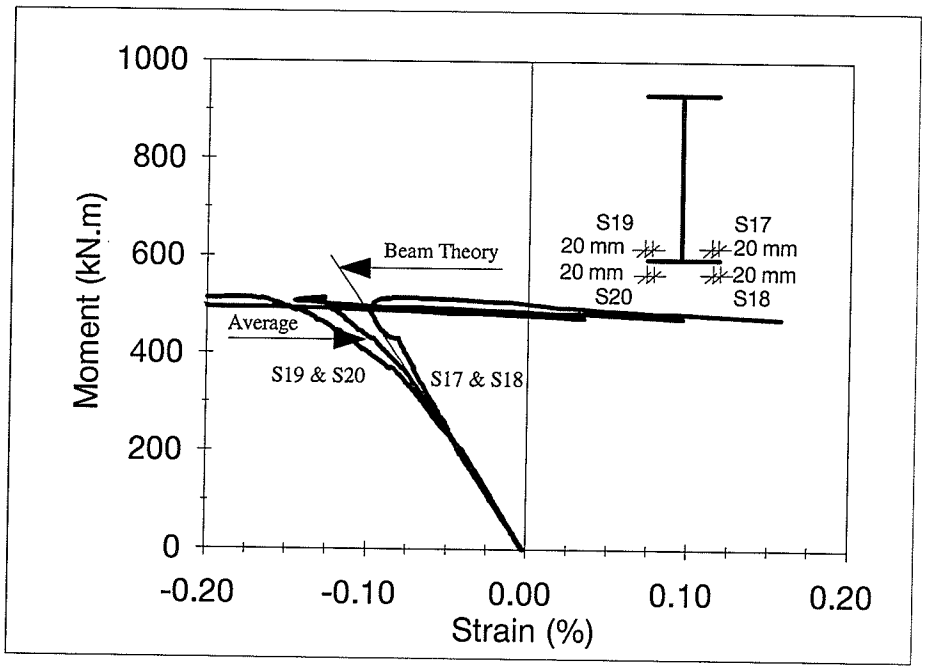

(c) Average Strain

Figure 4.29 Moment-Strain Relationships at Mid-Span Compression Flange of Specimen G2

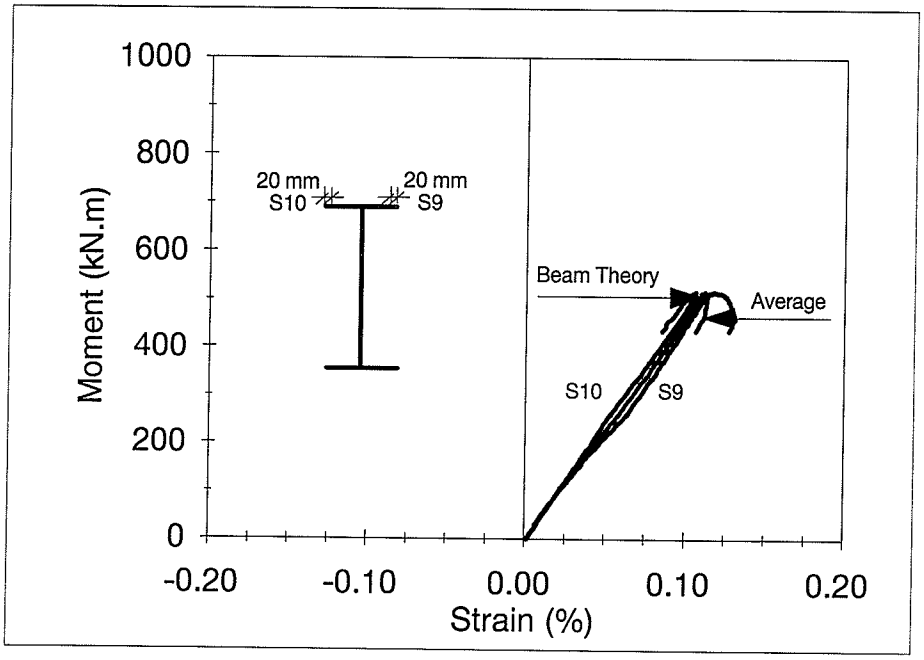

Figure 4.30 Moment-Strain Relationships at Mid-Span Tension Flange of Specimen G2

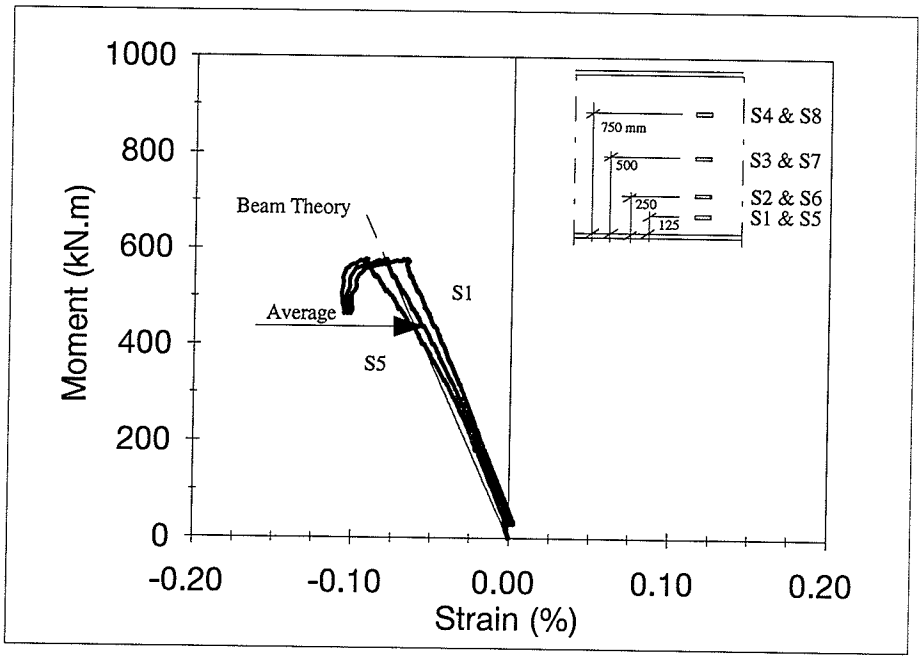

(a) Strain Distribution at S1 &S5

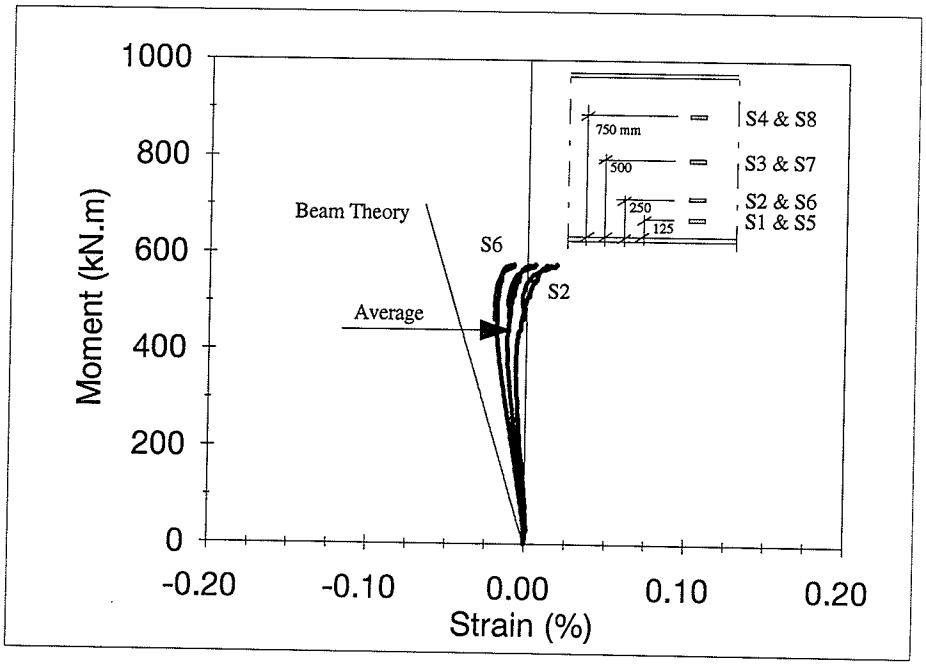

(b) Strain Distribution at S2 &S6

Figure 4.31 Moment-Strain Relationships at Mid-Span Web of Specimen G4

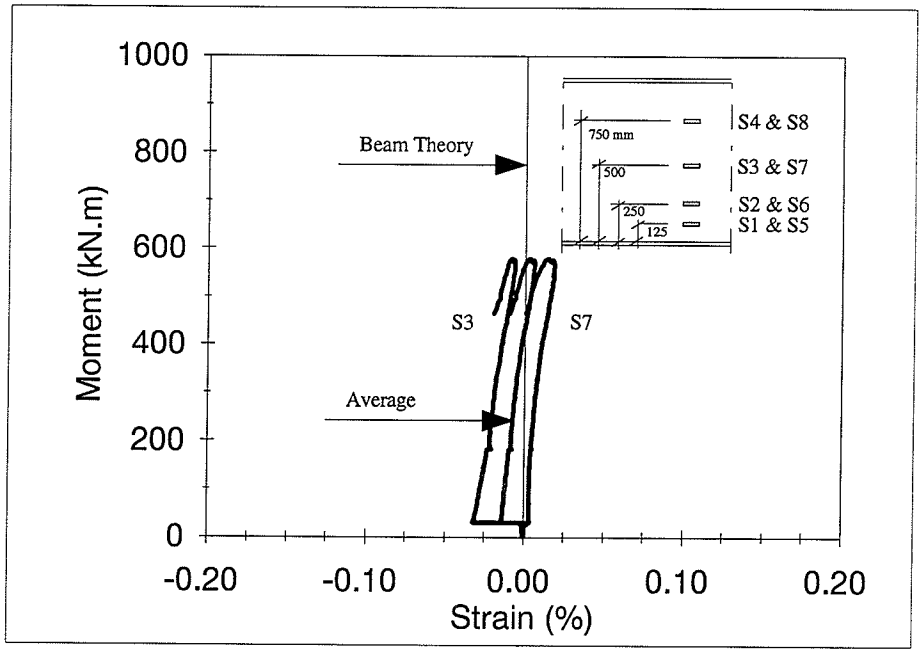

(c) Strain Distribution at S3 &S7

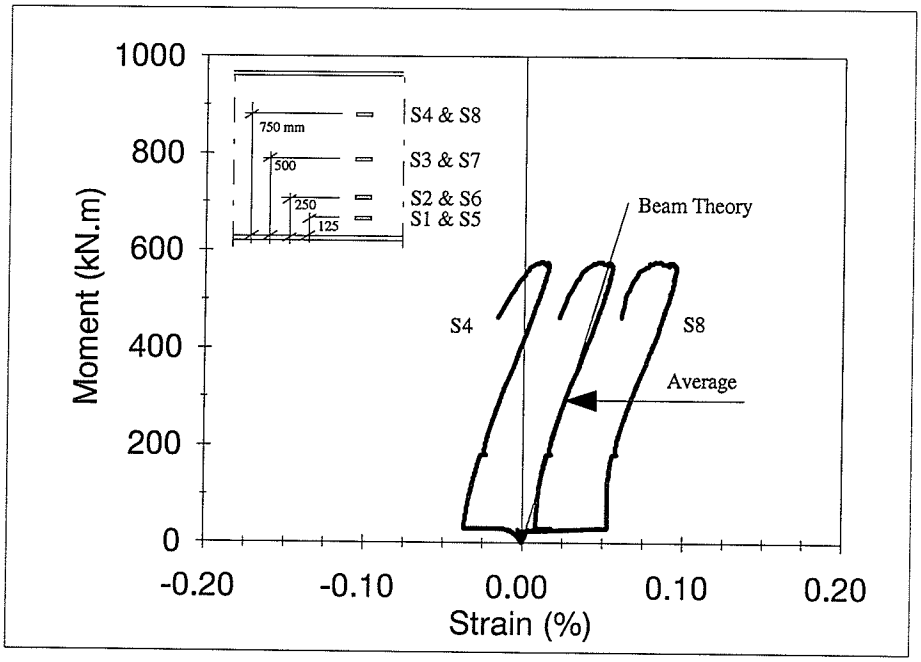

(d) Strain Distribution at S4 &S8

Figure 4.31 Moment-Strain Relationships at Mid-Span Web of Specimen G4

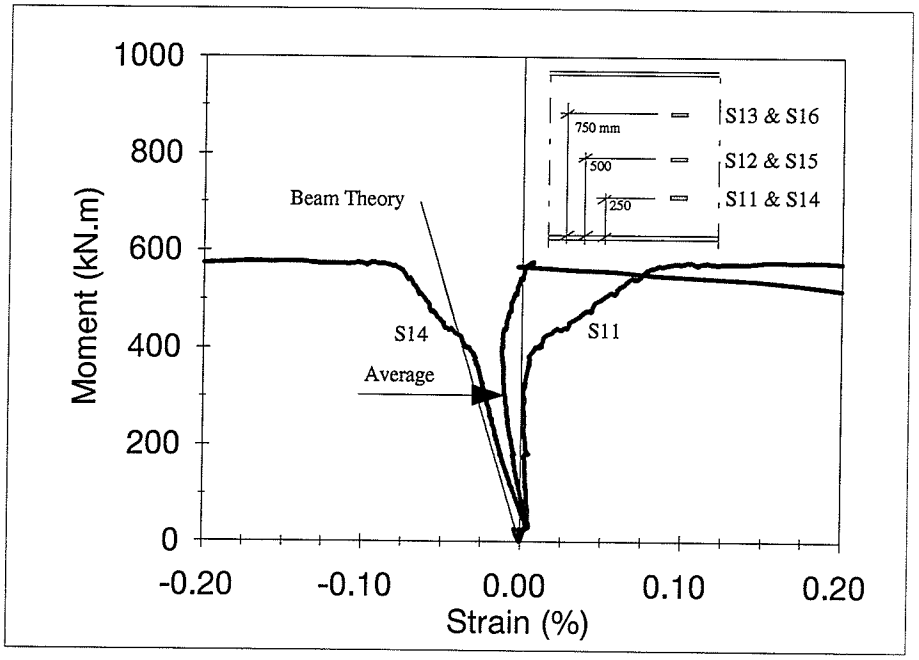

(a) Strain Distribution at S11 &S14

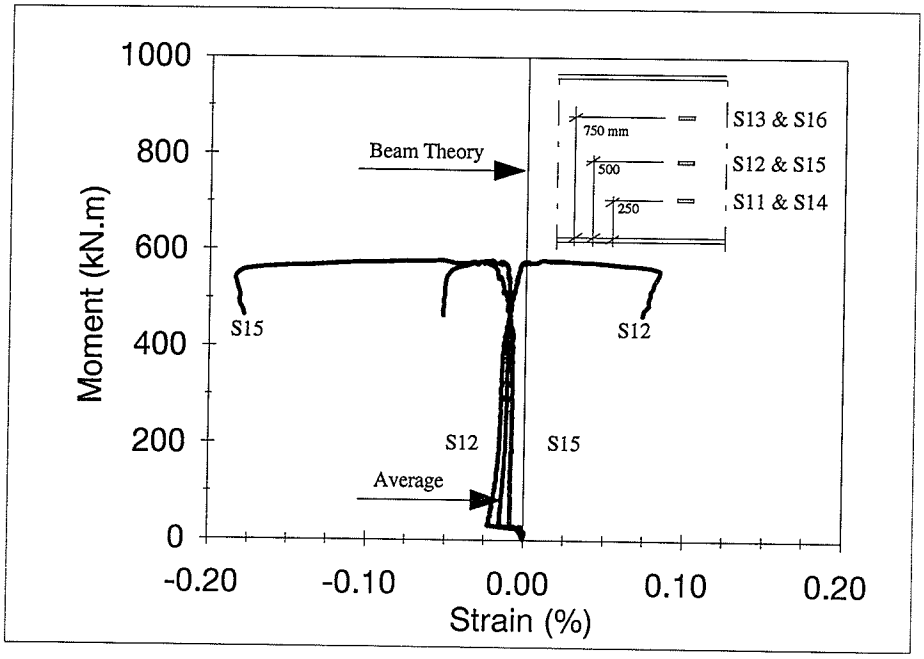

(b) Strain Distribution at S12 &S15

Figure 4.32 Moment-Strain Relationships at Quarter-Span Web of Specimen G4

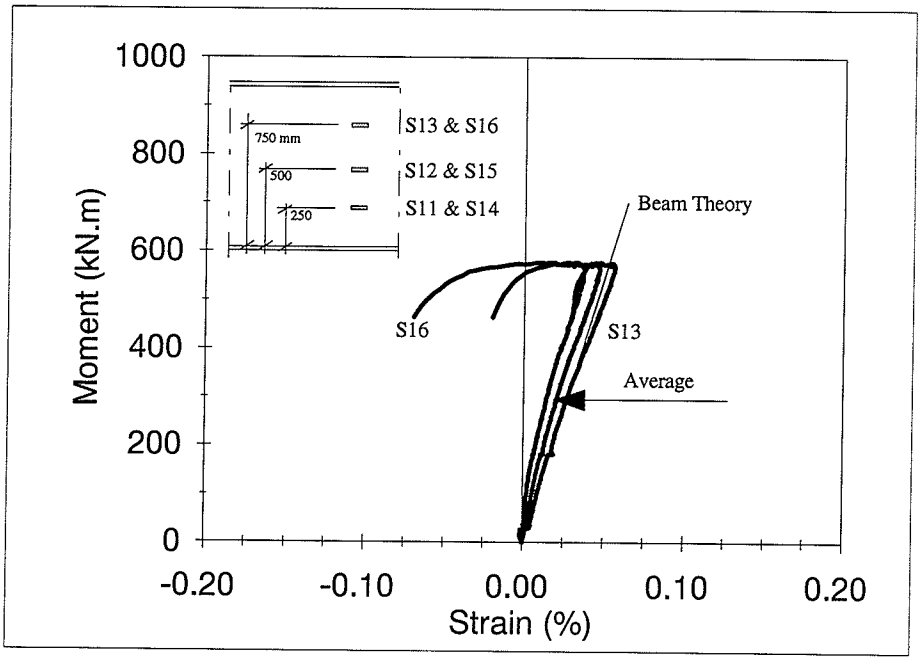

(c) Strain Distribution at S13 & S16

Figure 4.32 Moment-Strain Relationships at Quarter-Span Web of Specimen G4

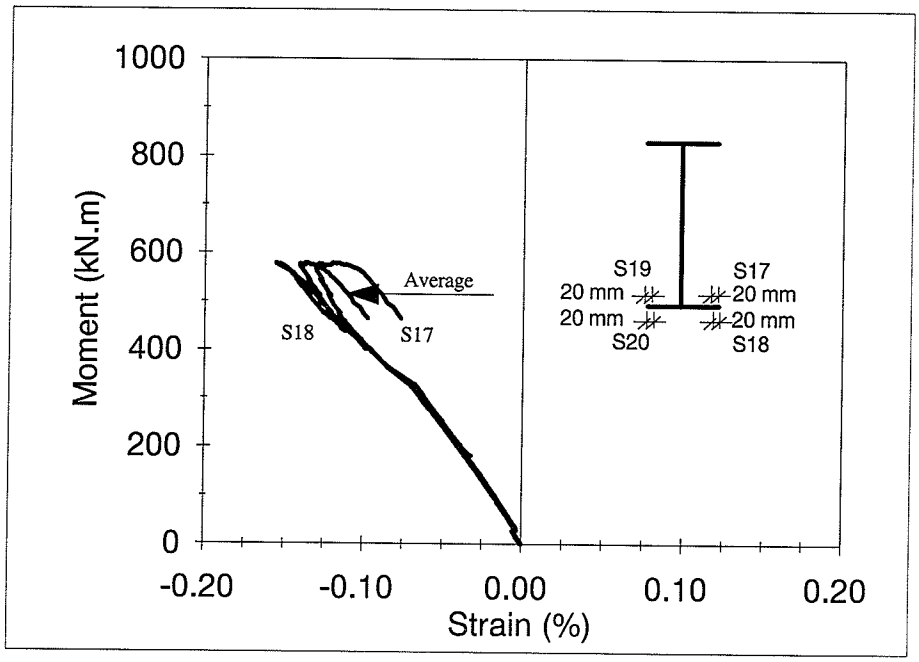

(a) Strain Distribution at S17 & S18

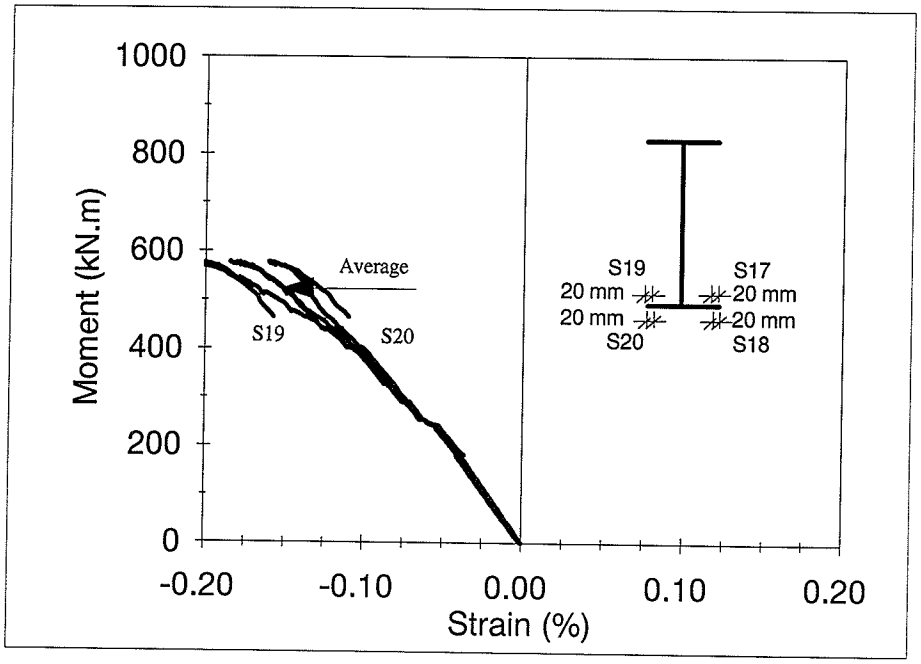

(b) Strain Distribution at S19 & S20

Figure 4.33 Moment-Strain Relationships at Mid-span Compression Flange of Specimen G4

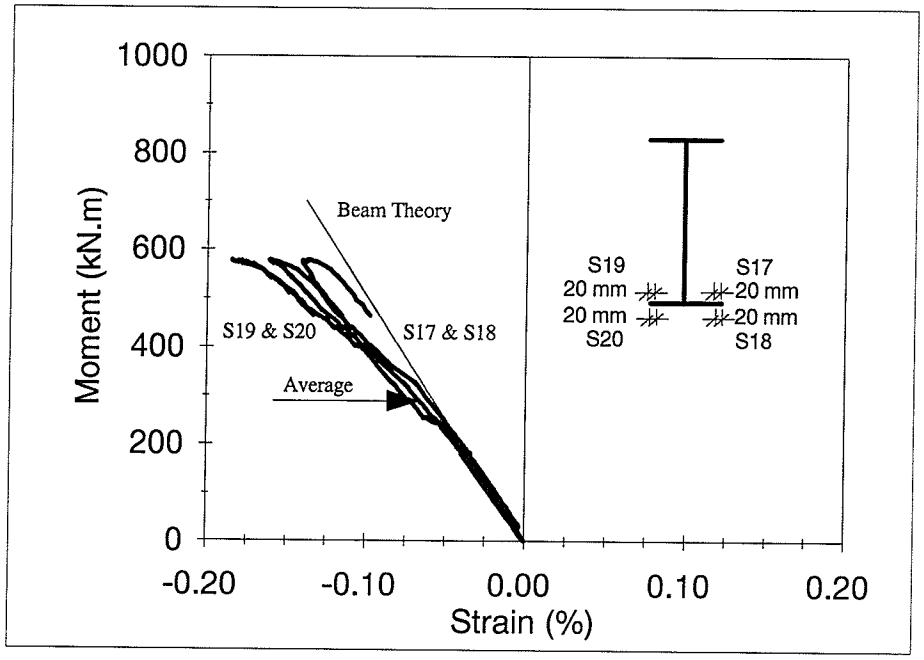

(c) Averagr Strain

Figure 4.33 Moment-Strain Relationships at Mid-Span Compression Flange of Specimen G4

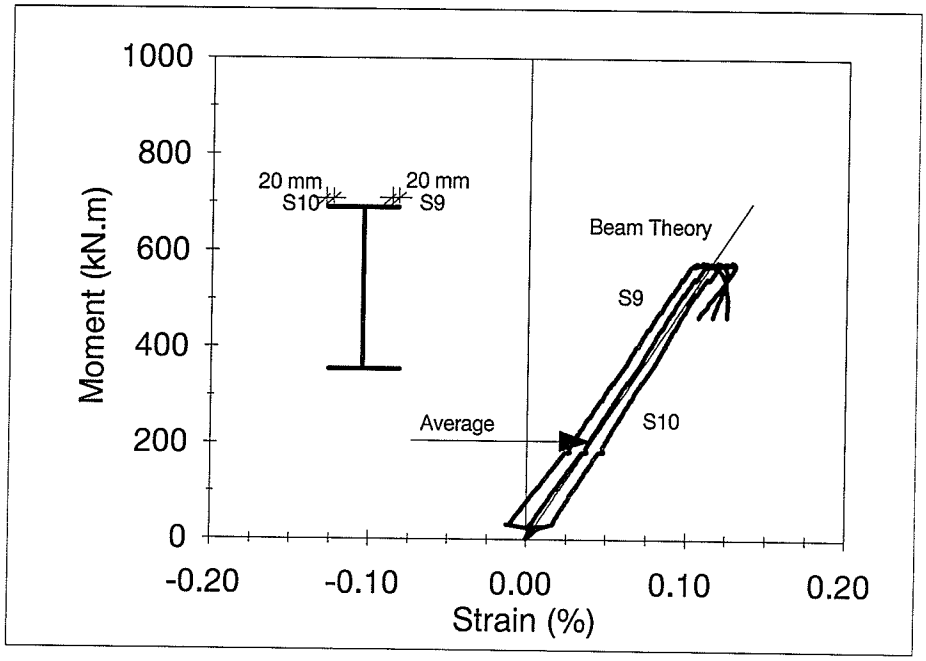

Figure 4.34 Moment-Strain Relationships at Mid-Span Tension Flange of Specimen G4

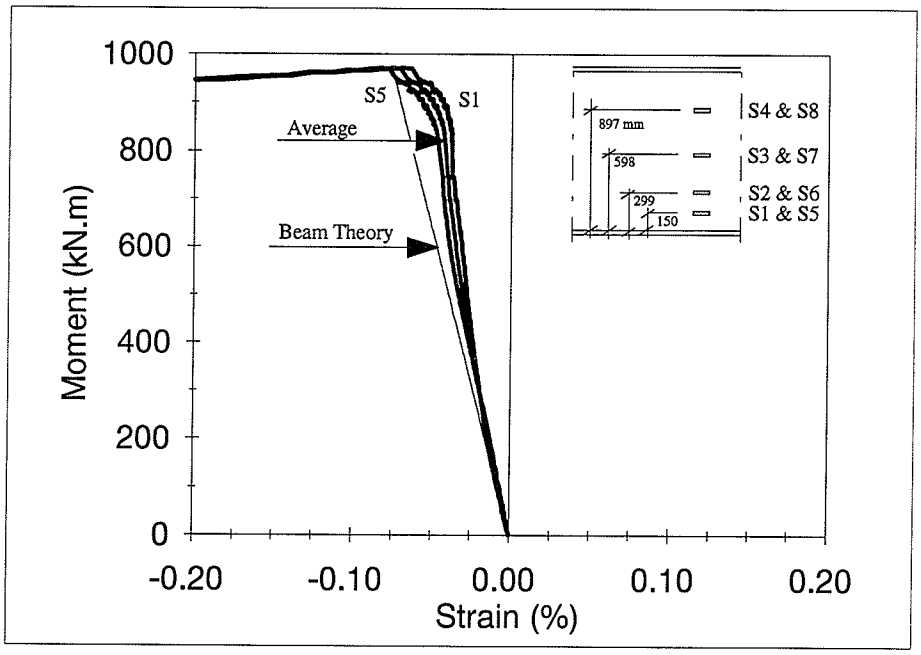

(a) Strain Distribution at S1 & S5

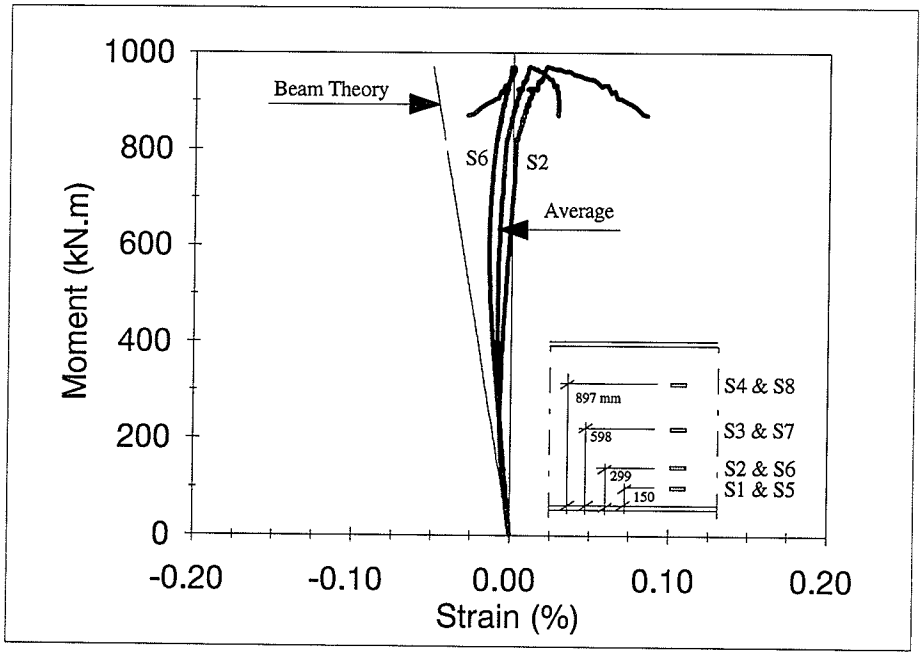

(b) Strain Distribution at S2 & S6

Figure 4.35 Moment-Strain Relationships at Mid-Span Web of Specimen G9

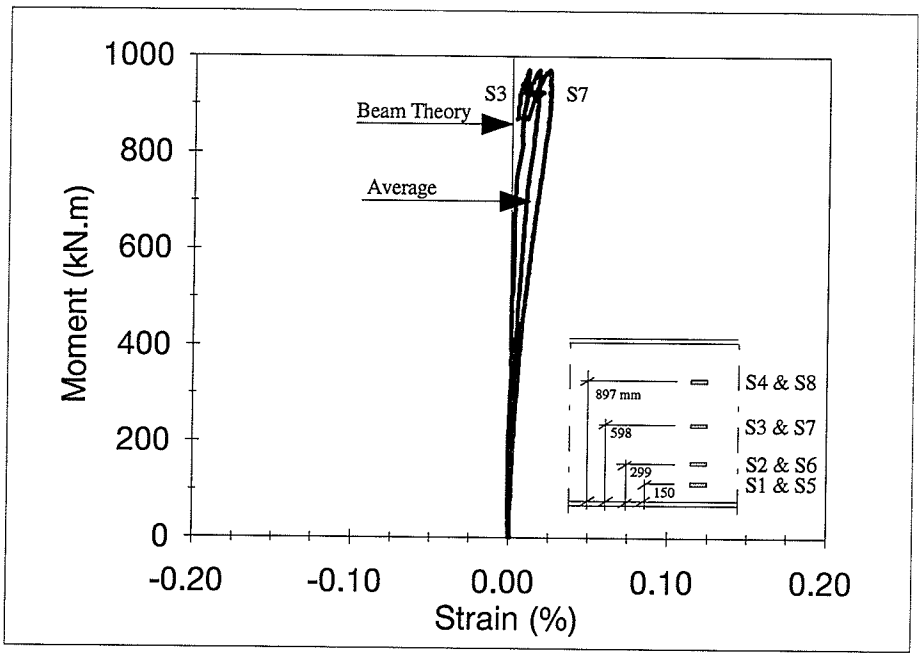

(c) Strain Distribution at S3 & S7

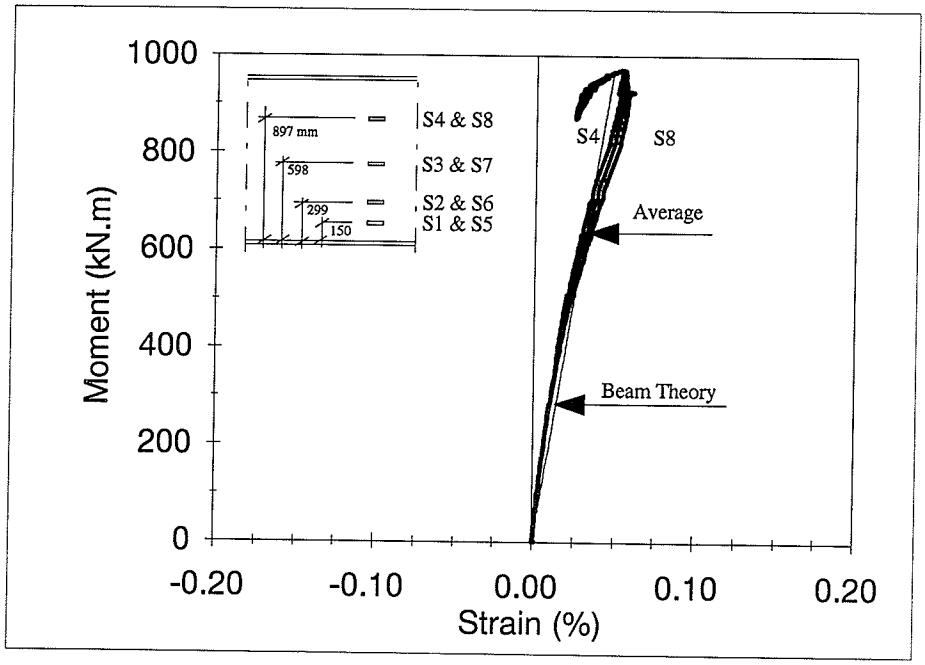

(d) Strain Distribution at S4 & S8

Figure 4.35 Moment-Strain Relationships at Mid-Span Web of Specimen G9

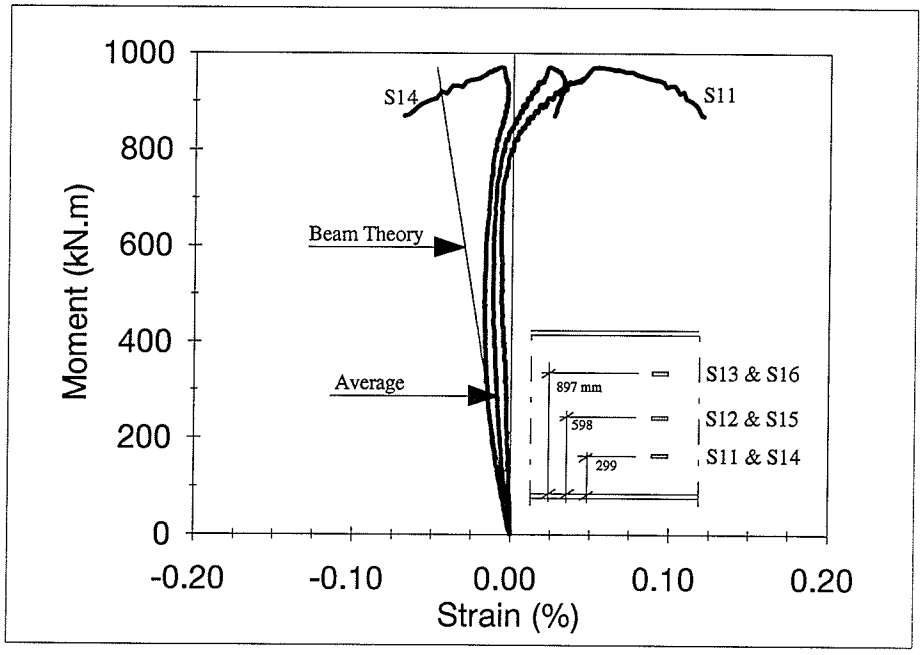

(a) Strain Distribution at S11 & S14

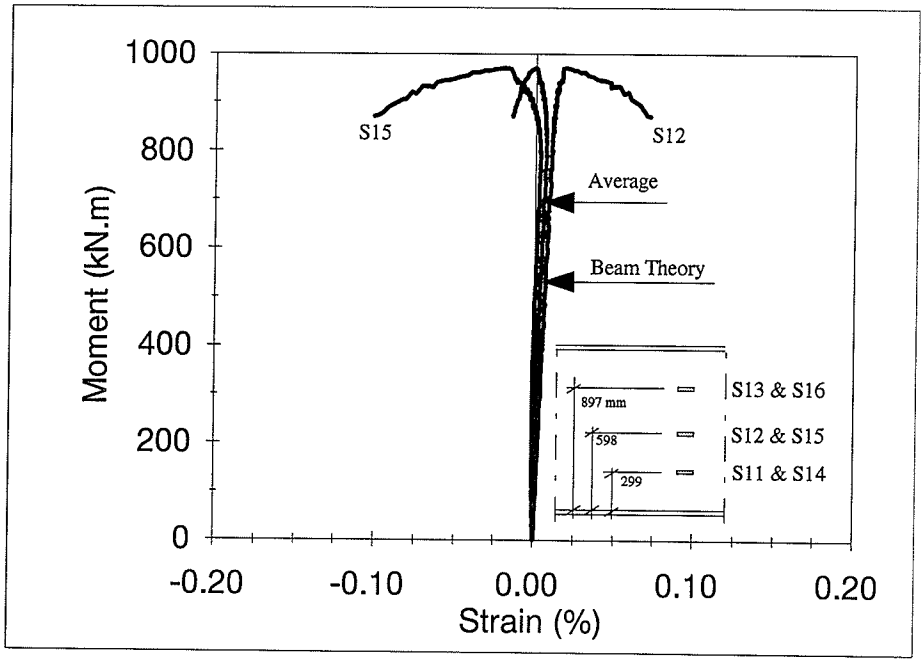

(b) Strain Distribution at S12 & S15

Figure 4.36 Moment-Strain Relationships at Quarter-Span Web of Specimen G9

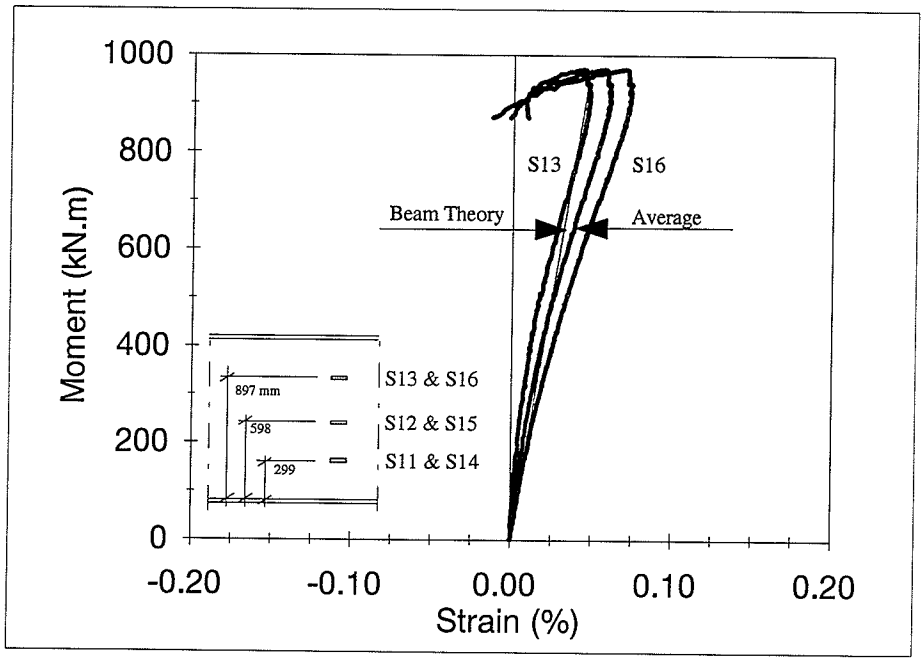

(c) Strain Distribution at S13 & S16

Figure 4.36 Moment-Strain Relationships at Quarter-Span Web of Specimen G9

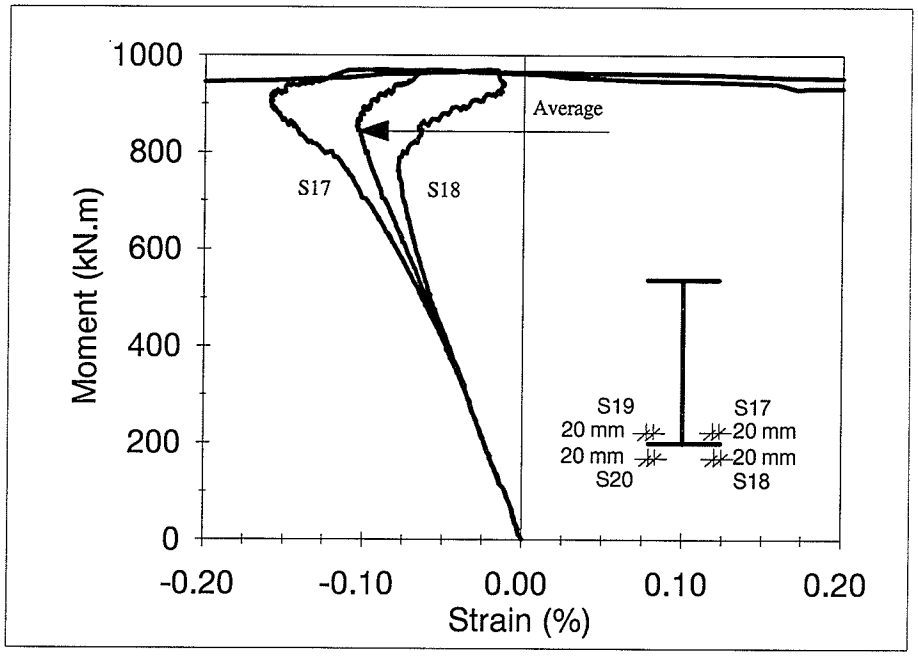

(a) Strain Distribution at S17 & S18

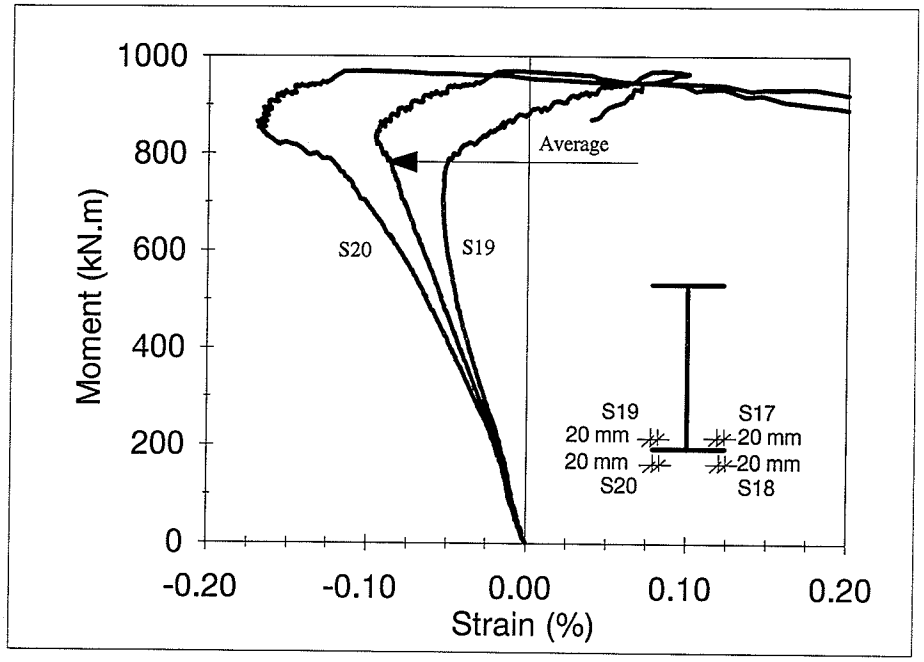

(b) Strain Distribution at S19 & S20

Figure 4.37 Moment-Strain Relationships at Mid-Span Compression Flange of Specimen G9

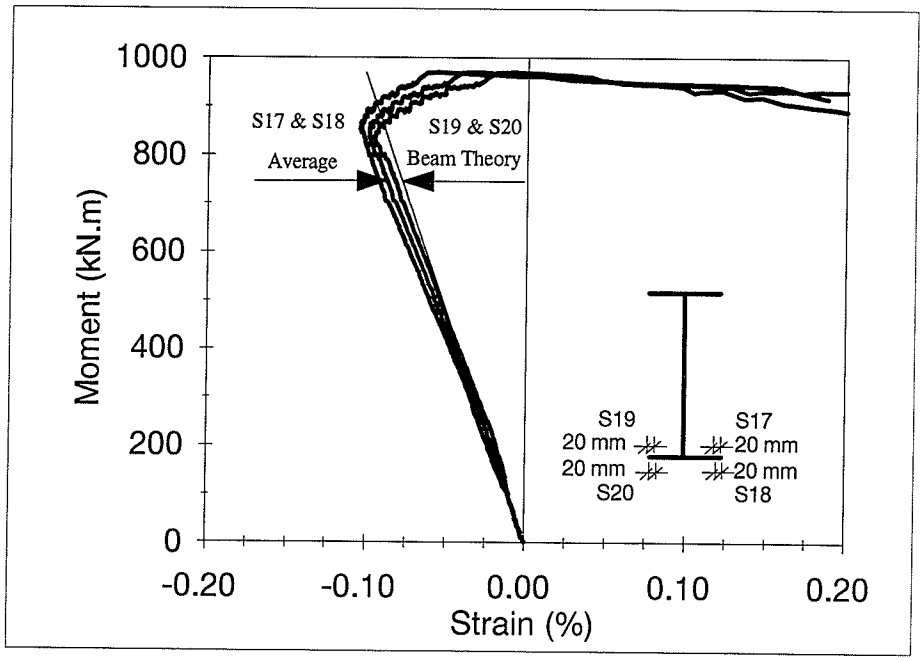

(c) Average Strain

Figure 4.37 Moment-Strain Relationships at Mid-Span Compression Flange of Specimen G9

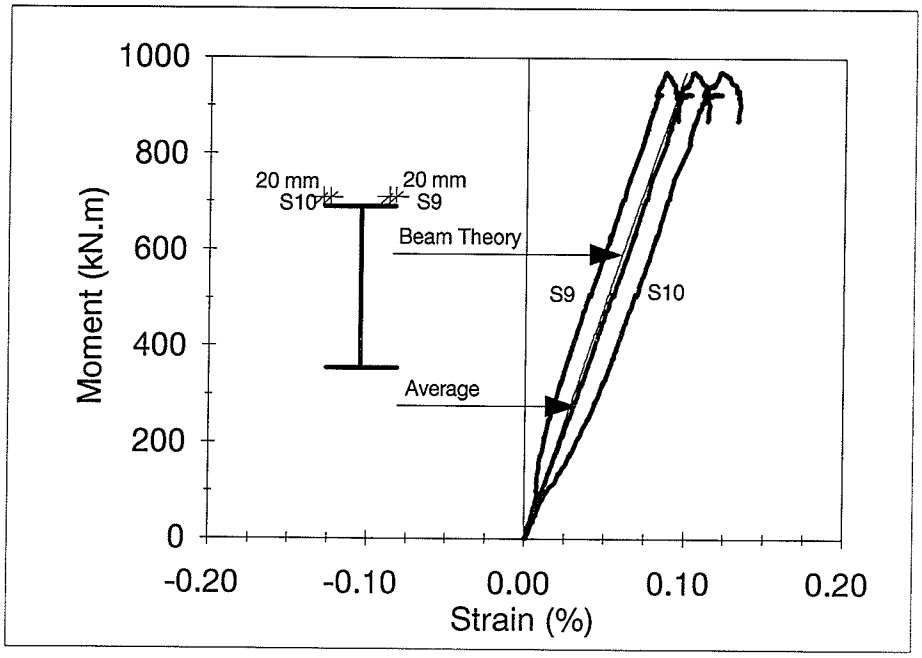

Figure 4.38 Moment-Strain Relationships at Mid-Span Tension Flange of Specimen G9

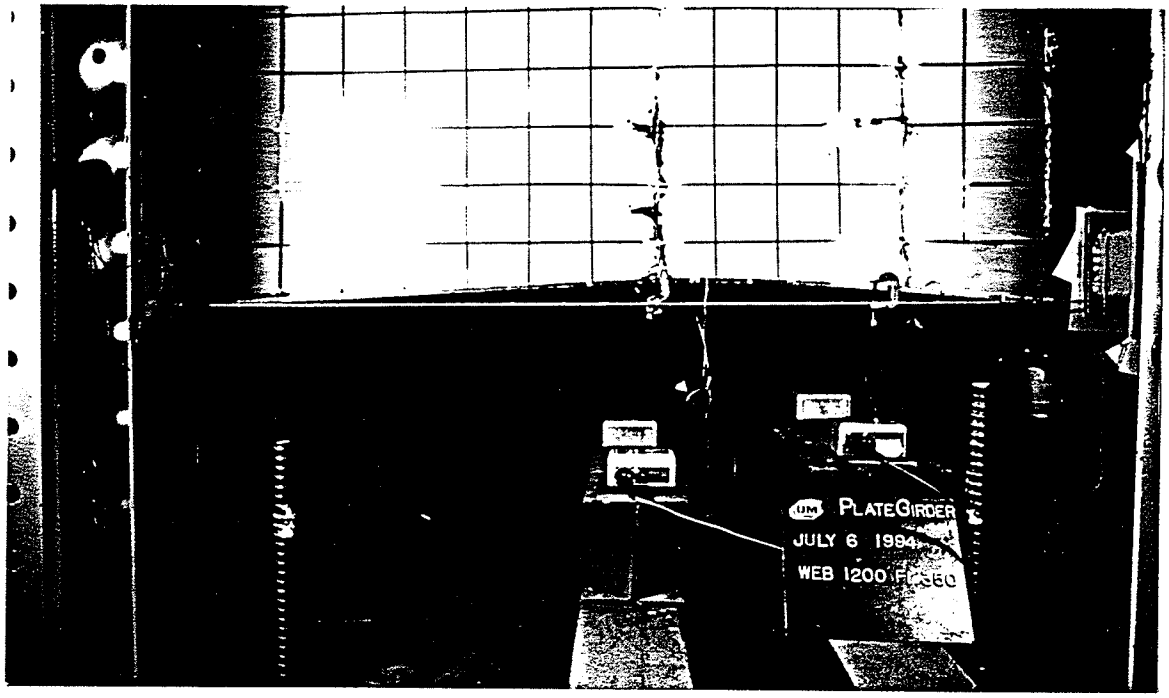

(a) at 450 kN.m Applied Moment

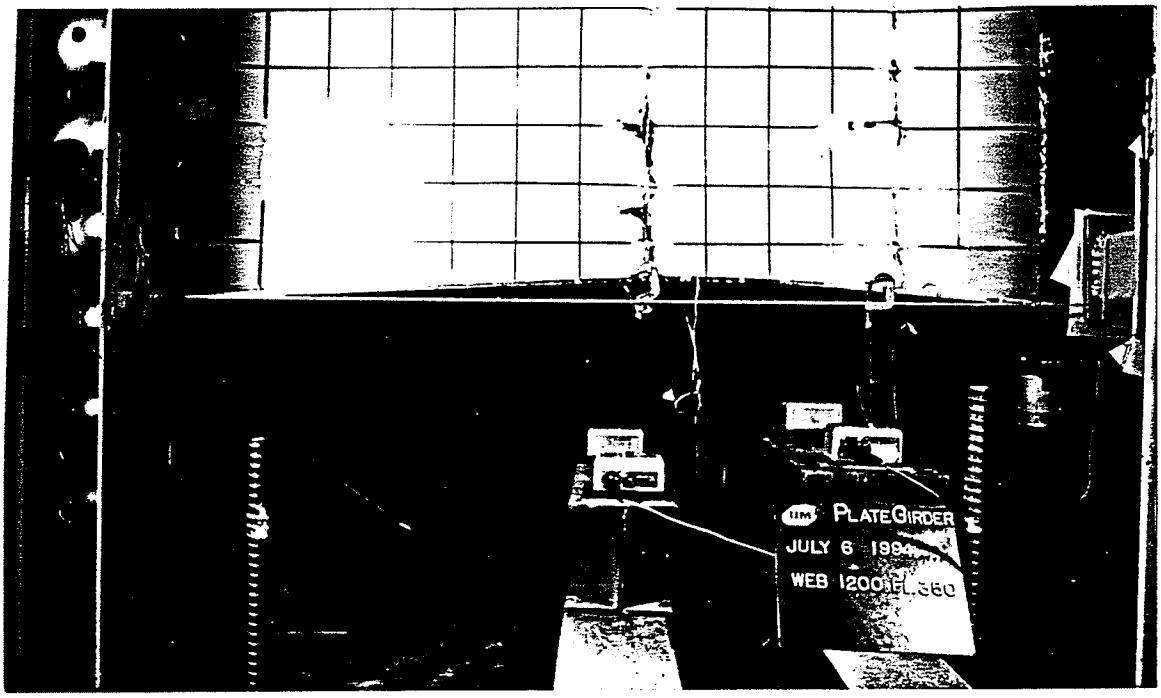

(b) at 825 kN.m Applied Moment

Figure 4.39 Specimen G9 Compression-Flange During Testing

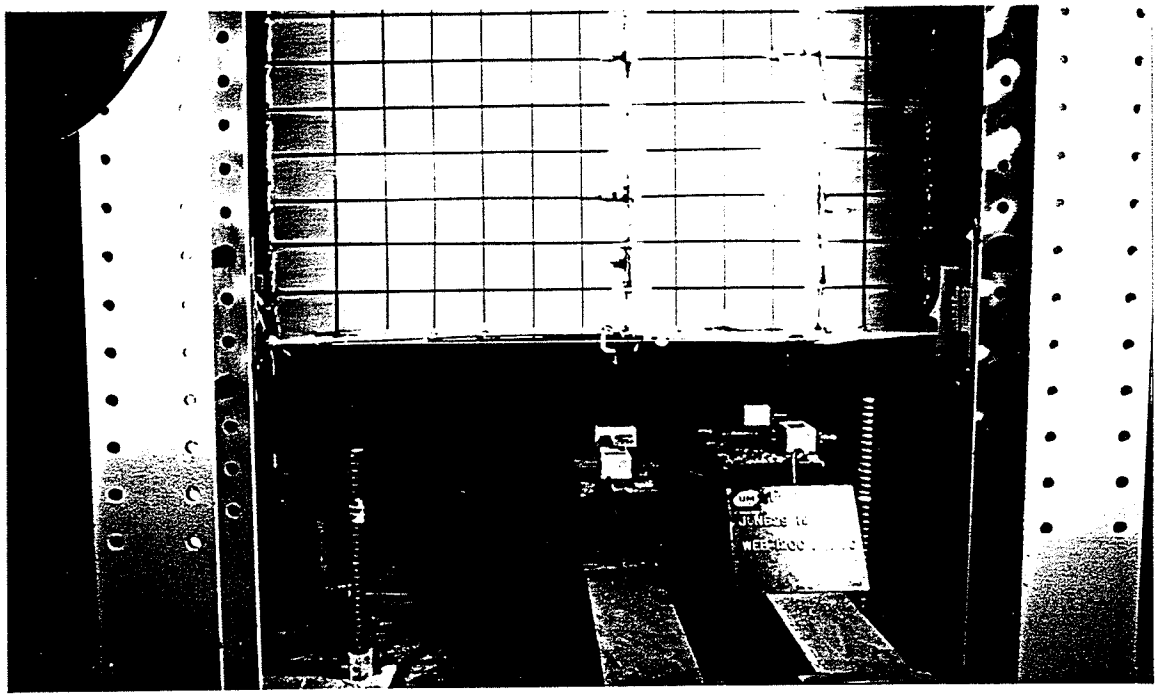

(a) at 408 kN.m Applied Moment

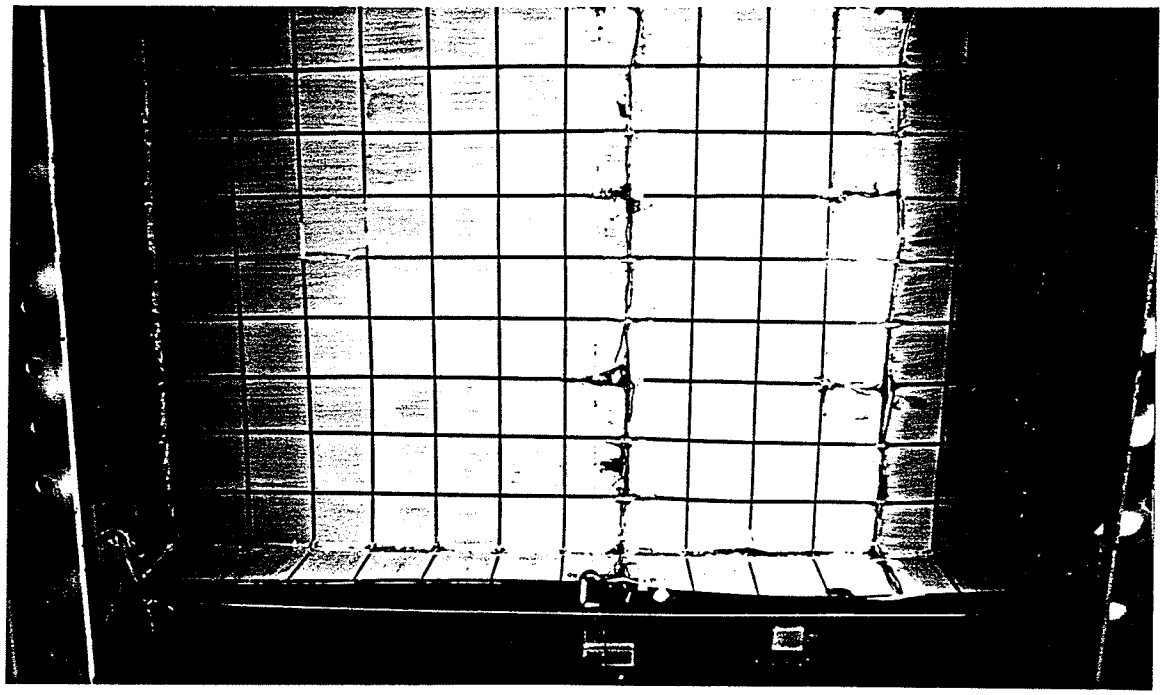

(b) at 713 kN.m Applied Moment

Figure 4.40 Specimen G8 Compression-Flange During Testing

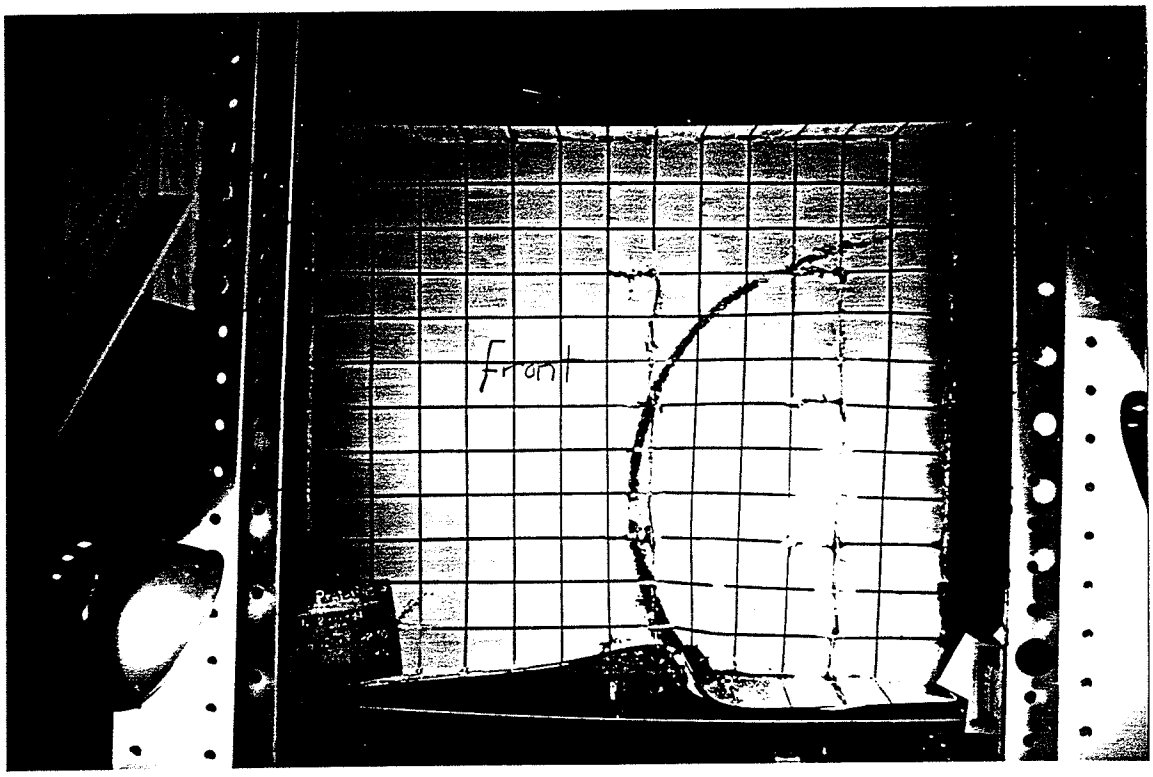

(c) at Failure

Figure 4.40 Specimen G8 Compression-Flange During Testing

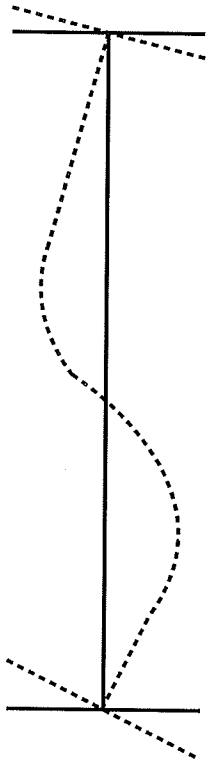

(a) Sine-Wave Pattern

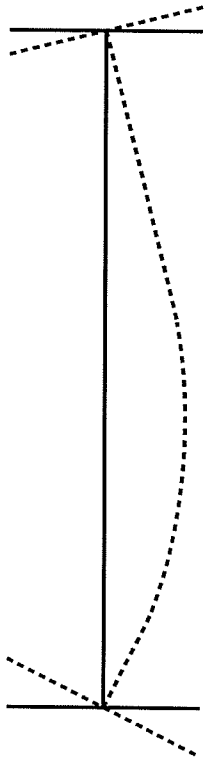

(b) Half Sine-Wave Pattern

Figure 4.41 Buckled Cross-Sections of the Tested Specimens

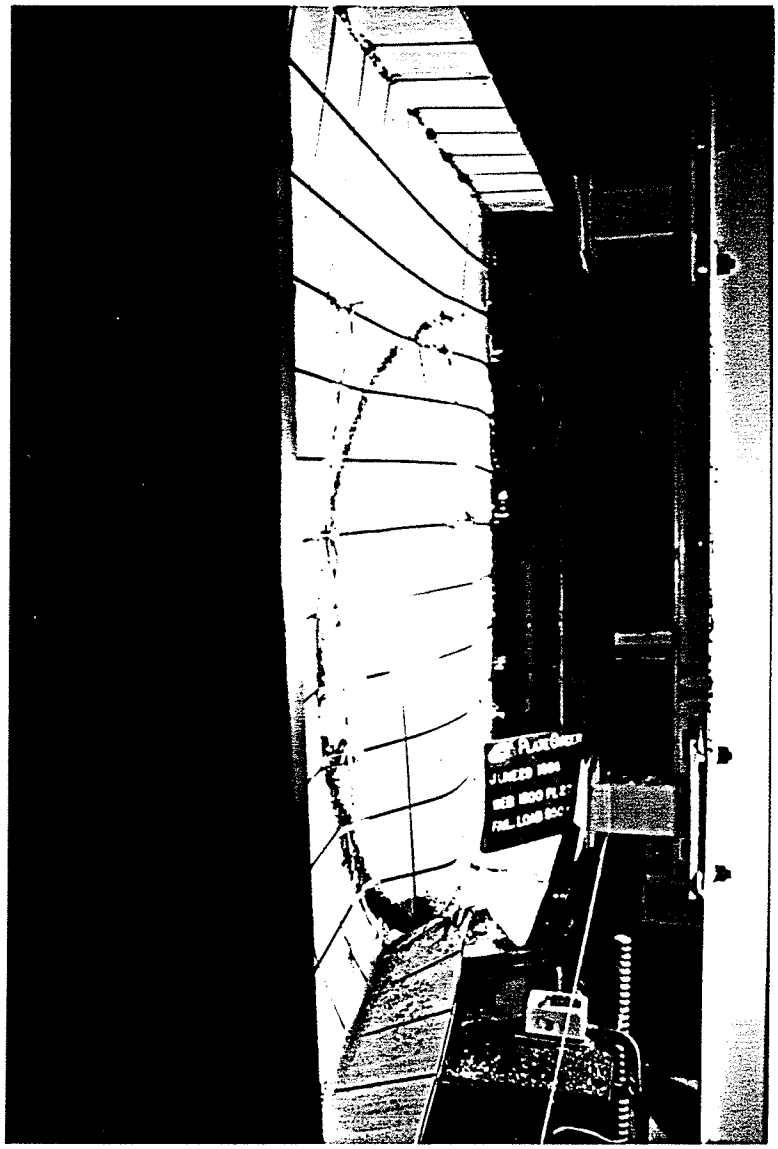

Figure 4.42 Failed Web of Specimen G8

CHAPTER 5

FINITE ELEMENT ANALYSIS

5.1 INTRODUCTION

As evident, none of the discussed techniques in Section 2.5 dealt in depth with the problem of laterally-supported slender plate girders subjected to bending about the major axis. This has led many standards and specifications to recommend or specify that the design of such type of girders may or should be according to the Cold-Formed Steel Structures Members standards or specifications.

In the current study, the finite element method was used to develop a model which could be used adequately in simulating the behaviour of such girders subjected to bending moment about the major axis. The postbuckling behaviour was also included in the analysis.

Eight-node quadrilateral and six-node triangular shell elements were used in the finite element model, each node had six degrees of freedom. One of the reasons of using these shell elements in the model was their capability to represent deformed plates which made the simulation of initially imperfected plates possible. Due to the nonlinearity of the postbuckling behaviour, the Newton-Raphson iterative method was used and the load was applied in increments. A bilinear elasto-plastic stress-strain response of the material was used in the analysis. The effects of the residual stresses were not included in this model for the following

reasons:

i) The effects of residual stresses are more pronounced in stockier plates where overall yielding of the plates governs. For slender plates, practical levels of geometrical imperfections tend to mask the effects of residual stresses (Dubas and Gheri, editors, 1986).

ii) The component plates of the tested specimens were burned mechanically and cut to size, as mentioned in Chapter 3. This process produced longitudinal residual stresses in the opposite direction of those stresses produced by welding the plates, especially in the flange plates.

In addition to these reasons, there was a difficulty of determining the actual distribution of the residual stresses along the cross sections of the tested specimens, and as will be discussed later in this chapter the finite element model results were in excellent agreement with the obtained test results.

Newtonian approach was adopted for the nonlinear analysis using the ANSYS finite element program (Swanson Analysis Systems, Inc., 1992). The main objectives of modelling the problem using the finite element method were as follows:

i) to ascertain the validity of the model by comparing its ultimate moment capacities to those obtained experimentally with a special emphasis to the correlation between the longitudinal stress and strain distributions obtained theoretically and experimentally.

ii) to extend the range of the study, once the validity of the model was verified, to perform a parametric study, which could lead to develop a design model for such girders.

5.2 QUADRILATERAL AND TRIANGULAR SHELL ELEMENTS

As mentioned before, the slender plate girders were modelled, in this study, using quadrilateral and triangular shell elements. The quadrilateral shell element had eight nodes, four-corner nodes and four-mid-side nodes, while the triangular shell element had six nodes, three-corner nodes and three-mid-side nodes, as shown in Figure 5.1. Each node had six degrees of freedom, translations (U_x, U_y, and U_z) in the nodal X, Y and Z directions, respectively, and rotations (Rot_x, Rot_y and Rot_z) about the nodal X, Y and Z axes, respectively.

These shell elements were used to construct the finite element model because of their capability to:

i) include the initial imperfection of plates in the model geometry;

ii) account for plasticity, stress stiffening, large deflection and large strains in the analysis; and

iii) handle the membrane as well as the bending stresses and strains in the process.

In addition, these elements could be used in modelling variable thickness plates by introducing different thicknesses at the element corner-nodes. The thicknesses at mid-side nodes were taken as the average of the corresponding corner-nodes. Over the area of the element, the thickness was varied smoothly.

To adopt nonlinear behaviour of the material in the stiffness matrix of the shell element, five through-the-thickness integration points were used, while only two through-the-thickness integration points were used for the linear material behaviour. Moreover, for in-plane analysis, 2x2 integration points were used for the quadrilateral shell element, while only

three integration points were used for the triangular shell element.

5.3 SOURCES OF NONLINEARITY

Because of the nonlinearity of the postbuckling behaviour problem, two major sources of nonlinearity were taken into account in the current study, the material and the geometric nonlinearity. The nonlinearity due to the flexibility of the connections between the tested specimens and the girder ends was not included in the analysis since these connections were designed to be as rigid as possible and no significant deformations, in these connection regions, were noticed during testing.

An elasto-plastic behaviour was used due to the localized nature of failure, which occurs immediately after local plastification (Klayanaraman and Peköz, 1978). This type of failure was also observed in the specimens tested in this study as evident in Figure 4.40, where local plastification in the compression flange caused the failure of specimen G8. Moreover, the moment-strain curves, presented in Chapter 4, show sudden increase in the longitudinal strains at and close to failure, as shown in Figure 4.35(a) for example.

It has been recognized that the critical buckling load of a plate is not a satisfactory measure of plate strength for design purpose. There are several important parameters that severely modify the critical buckling behaviour of an idealized plate. The most important of these are probably the effect of initial geometric and material imperfections, the effect of plasticity and the effect of postbuckling stability. In order to investigate the true collapse behaviour a of a plate it is necessary to extend the small deflection plate equation to include the effect of out-of-plane deformation on the in-plane stress state of the plate. This essentially

means the inclusion of the large deflection plate membrane actions resulting from stretching of the mid-plane of the plate (Dubas and Gehri, ed., 1986).

As discussed in Chapters 3 and 4, the values of the initial imperfections of the components plates of the specimens were in the order of the magnitude of the plate thickness, thus nonlinear behaviour of the transverse deflections was observed from the onset of loading. Moreover the measured transverse deflections of the component plates of the specimens reached, in many specimens, 4 times the plate thickness. Due to these reasons, the nonlinear geometrical analysis was considered in the theoretical study.

In the nonlinear buckling analysis, the ANSYS program uses an incremental procedure based on the Newton-Raphson method, in which a series of linear iterations converges to the actual nonlinear solution, as shown in Figure 5.2. The solution is converged only if the change from one iteration to the next one is insignificant. The ANSYS program has the capability to include the snap-through in the nonlinear buckling analysis, where the structure reaches a second stable state after buckling if the load continues to increase.

5.3.1 Material Nonlinearity

When the stresses are not proportional to the strains, the material nonlinearity problem exists. The ANSYS program can simulate both nonlinear stress-strain relationships, plasticity and nonlinear elasticity. This is accomplished by using an incremental procedure based on the Newton-Raphson method, in which a series of linear iterations converges to the actual nonlinear solution. The stiffness matrix is updated at each equilibrium iteration to form the tangent stiffness matrix.

The Newton-Raphson equation can be presented as follows:

$$[K_T](\Delta u) = (F^a) - (F^{nr}) \tag{5.1}$$

where,

$[K_T]$ = tangent stiffness matrix;

(Δu) = nodal displacement increment vector;

(F^a) = vector of applied load; and

(F^{nr}) = vector of restoring loads corresponding to the element internal load.

Using the incremental Newton-Raphson method, higher accuracy can be achieved compared to the other iterative procedures.

The ANSYS program accounts for three concepts in the plastic behaviour of the material, the yield criterion, the flow rule and the hardening law. The yield criterion is considered by computing a single equivalent stress. The von Mises criterion is used to predict the yield as follows:

$$\sigma_{eq} = \sqrt{\frac{1}{2}\left[(\sigma_1 - \sigma_2)^2 + (\sigma_2 - \sigma_3)^2 + (\sigma_3 - \sigma_1)^2\right]} \tag{5.2}$$

where,

σ_{eq} = single equivalent stress; and

$\sigma_1, \sigma_2, \sigma_3$ = principle stresses.

The yielding begins when the single equivalent stress (σ_{eq}) reaches the uniaxial yield strength (F_y).

The flow rule is used to predict the direction in which the yielding will occur and it is associated with the von Mises yield criterion so that the plastic strains occur in a direction normal to the yield surface. The associated flow rule is based on the Prandtl-Reuss flow equation:

$$\left(d\epsilon^{pl} \right) = \lambda \left(\frac{\partial Q}{\partial \sigma} \right) \tag{5.3}$$

where,

λ = plastic multiplier determining the amount of plastic straining; and

Q = function of stress termed the plastic potential determining the direction of plastic straining.

Once the material has been loaded into its plastic range, hardening laws determine how the material's yield surface is changed. The ANSYS program uses two kinds of hardening laws, isotropic (work) hardening and kinematic hardening. In the isotropic hardening, the yield surface expands the same in all directions and implies that an increase in the tensile yield stress causes an increase in the compressive yield stress. The kinematic hardening predicts an increase in the tensile stress accomplished with a decrease in the compressive yield stress. Therefore, the material which was initially isotropic will become anisotropic after yielding (Bauschinger effect), which is more realistic, especially for metals.

In the current study, the classical bilinear kinematic hardening procedure was used in the finite element model to simulate the material response of the component plates of the tested specimens taking into account the von Mises criterion, the Prandtl-Reuss flow equation and the kinematic hardening effects. A tangent modulus (E_t) equal to zero was used in this

procedure to simulate the elasto-perfect-plastic response of the material. Since the end girders were designed such that no failure could take a place in their regions, a linear material response was used to simulate the material behaviour of their component plates.

Figure 5.3 shows the elasto-perfect-plastic behaviour of the material used in the current study to simulate the material behaviour of the component plates of the tested specimens. The mechanical properties obtained from the standard tension coupons, listed in Table 3.5, such as yield strength (F_y), elastic modulus (E) and Poisson's ratio (μ), besides shear modulus (G) were used to identify the material behaviour of the specimen component plates. The shear modulus (G) was calculated from the following equation:

$$G = \frac{E}{2(1+\mu)} \tag{5.4}$$

5.3.2 Geometric Nonlinearity

The geometric nonlinearties should be taken into account in the analysis if the change in the structure displacement is significant. As the structure deflects, the large deflection results in a change in the element orientation and consequently a change in the element stiffness matrix. The ANSYS program deals with the large deflection problem by updating the element orientation as the structure deflects. In addition, due to this effect of the large deflection on the stiffness of the element, an iterative method was used to evaluate the change in the stiffness matrix at each iteration. This iterative method, as mentioned before, is based on incremental Newton-Raphson procedure, which depends on updating the tangent stiffness matrix as follows:

$$[K]_{i-1} (\Delta u)_i = (F^a) - (F^{nr})_{i-1} \quad (5.5)$$

where,

$[K]_{i-1}$ = deformed stiffness matrix resulted from the deformed geometry of iteration (i-1);

$(\Delta u)_i$ = nodal displacement increment vector such that:

$$(u)_i = (u)_{i-1} + (\Delta u)_i$$

$(u)_{i-1}$ = displacement vector resulted from iteration (i-1);

$(u)_i$ = displacement vector at the current iteration (i);

(F^a) = applied load vector; and

$(F^{nr})_{i-1}$ = load vector based on the displacement resulted from iteration (i-1).

The large deflection concept assumes that the rotations are large but the mechanical strains, which cause the stresses, are small. At the same time, the stress state of the structure is used by the ANSYS program to calculate a stiffness matrix [S], which is added to the normal stiffness matrix [K]:

$$[[K]+[S]] (u) = (F^a) \quad (5.6)$$

where,

[[K]+[S]] = tangent stiffness based on deformed geometry;

(u) = displacement vector; and

(F^a) = applied load vector.

5.4 FINITE ELEMENT MODEL

The main objective of developing this finite element model was to simulate the actual behaviour of slender plate girders subjected to bending by incorporating all the nodes, elements, material properties, dimensions and boundary conditions, in addition to a suitable analysis method. The following sections present these steps which were used in generating the finite element model.

5.4.1 Solid Modelling

The geometric boundaries of the girder such as flange width, web height, specimen and girder lengths, etc., should be defined as the first step in solid modelling. To simulate the tested specimens geometric boundaries, key points were used to define the corners of the plates in the cartesian coordinates. The main advantage of using such key points was their capability to represent easily the imperfect shapes of the plates. Then lines were generated by the ANSYS program to fit these key points using cubic spline technique, as shown in Figure 5.4. Moreover, a surface was also generated to fit these lines using the same cubic spline technique to form the imperfect surface of the plate. The initial imperfection values of the tested specimens were obtained from the laboratory, as described in Chapter 3.

The end girders' plates (web, flanges and stiffeners) were simulated using perfect rectangular plates. The average measured dimensions of these plates and the component plates of the tested specimens, as listed in Table 3.2, were used in this model.

5.4.2 Discretization Process

Once the geometric shape of the plates was set, a glue command was used to connect these plates at their conjunction lines. The purpose of using this glue command was to create common nodes for these plates along their conjunction lines. Then the discretization process subdivided the structure into an equivalent finite elements system. As known, refining the finite element mesh leads to more accurate results, but it may lead to an expensive process. To minimize this problem fine mesh was used in the regions of the model where failure was expected to take a place, more specifically in the compression flange and the adjacent region of the web of the tested specimens. Gradually the finite element mesh became coarse in two directions, towards the tension flange and the end support section of the girder. This was accomplished by specifying the size of elements in each plate, as shown in Figure 5.5, which presents the generated finite element mesh of specimen G9 (553 element and 1668 node).

Figure 5.6 shows a computer generated plot of the finite element model of the tested specimen G3 which had dimensions (flange width, web height or both) less than those of the girder ends.

5.4.3 Boundary Conditions and Applied Load

Only one-half of the girder was modelled using the advantage of symmetry about the mid-span section. Three degrees of freedom were restrained for all nodes at that section, the translations in the longitudinal direction Z ($U_z = 0$) and the rotations about both X and Y axes ($Rot_x = 0$ and $Rot_y = 0$).

The translation in the Y-direction was restrained along a line at the end-support

section to simulate the vertical support of the girder, as shown in Figure 5.4. Finally the translation in the X-direction of the top and the bottom flanges was restrained at both the end-support and the loaded sections to simulate the lateral supports, as shown in Figure 5.4.

A line load was used to push the bottom flange at the end-plate section of the girder end to simulate the applied load, as shown in Figure 5.4.

5.4.4 Model Analysis

Last step before processing the data using the generated finite element model was to define the type of analysis. In the current study, nonlinear buckling analysis was used, taking into account both the nonlinear response of the material and the nonlinear geometric behaviour of the structure, as discussed earlier in this chapter.

The wavefront (frontal solution) procedure as discussed by Irons (1970) and Melosh and Bamford (1969), was used by the ANSYS program to solve a system of simultaneous linear equations developed by the finite element model.

To determine the ultimate load of the modelled girder, one load step was specified. This load step was automatically divided into unequal substeps searching for the ultimate load. The range of each substep was determined by the program depending on the behaviour of the girder in the previous substep. At the end of each substep, the program adjusted the stiffness matrix to reflect the nonlinear changes in the girder stiffness. The ANSYS program overcame the problem of out-of-equilibrium in the final results at the end of each substep through the use of Newton-Raphson equilibrium iterations, which drove the solution to equilibrium convergence.

5.5 FINITE ELEMENT AND EXPERIMENTAL RESULTS COMPARISON

The main objective of this comparison was to ascertain the validity of the finite element model to simulate the actual behaviour of the slender plate girders subjected to bending, so that it could be used in developing a design model for such girders.

Figures 5.5 and 5.6 show the deformed configurations of the finite element models used to simulate tested specimens G9 and G3, respectively, as typical deformed configurations. As evident in these figures, the compression flange and the adjacent web region of each specimen rotated about their conjunction longitudinal axis. At the same time, a small rotation of the tension flange also occurred. The deformations of specimen G9 were more severe than those of specimen G3, as evident in these figures and shown in Figures 5.7 and 5.8. The figures present the deformed mid-span sections of specimens G9 and G3, respectively, just before failure. The more severe deformations of specimens G9 compared to those of specimen G3, which were obtained from both finite element and experimental analysis, were due to the effect of web height-to-thickness ratio (h/w = 257.2 for specimen G9 and 172.6 for specimen G3) on the girders behaviour.

Slight difference is noticed between the translations obtained from the finite element analysis and those obtained from the experimental testing. This occurred because the simulated finite element model took advantage of the symmetry about the mid-span section, as mentioned before, which was not the actual case, especially for the initial imperfection of the web and the flanges.

As shown in Table 5.1, the difference in predicting the ultimate moment capacities

of specimens G1 to G9 using the finite element model and by obtaining them experimentally, ranged from -4.1% to +6.1%, which emphaszes the validity of the finite element model.

As the determination of the ultimate moment capacities of the slender girders was the most important objective of the finite element analysis, great concern was given to the stress and the strain distributions in the longitudinal direction of such girders. Typical contour figures of these stresses for specimens G9 and G3 are shown in Figures 5.9 and 5.10, respectively. The stress distribution along the compression-flange width was almost uniformly distributed (flange width-to-thickness ratio (b/2t) = 21.81 and 21.63 for specimens G9 and G3, respectively), while it was not the case when this ratio exceeded 22. The stress distribution along the compression flange, in this case, became nonuniform, higher stress values were noticed at the portions adjacent to the web. On the other hand, lower stress values were noticed along the edge regions, as shown in Figure 5.11. The figure shows the stress contours in the longitudinal direction of the slender girder with a flange width of 450 mm and a thickness of 8 mm (b/2t = 28.125) and a web height of 1400 mm and a thickness of 4.68 mm (h/w = 299.1). This may reflect the postbuckling behaviour of the compression flange.

By comparing the stress contours of specimen G9 in Figure 5.9 to that of specimen G3 in Figure 5.10, it is evident that larger web portion of specimen G9, with respect to web height, was not stressed, which is indicated by the green colours in these figures.

Moreover, Figures 5.12 and 5.13 show that the strains obtained from the finite element analysis of specimens G9 and G3, respectively, as functions of the applied moment, were in very good agreement with those strains recorded experimentally, which ascertains the

validity of the finite element model used in this study to simulate the actual behaviour of slender girders in bending. Appendix E presents the strains, obtained from the finite element analysis and recorded experimentally, of the rest of the specimens as function of the applied moment. The differences between the strains obtained experimentally and those of the finite element analysis at or very close to the failure, as shown in these figures, are due to the following:

i) The failure of this type of girder was localized and sometimes the predicted failure by the finite element model took place in a different cross section specimen than the experimentally failed one. This was due to taking advantage of symmetry, with respect to the mid-span section, in the finite element model, which was not the case in the actual tested specimens, especially the initial imperfection of the webs and the compression flanges.

ii) The finite element solution was terminated once the program failed to converge to the solution. This occurred when the maximum moment capacity of the girder was reached. The maximum moment capacity obtained by the finite element model was less than 1% range of the ultimate moment capacity that could have been obtained by more precise analysis.

5.6 PARAMETRIC STUDY

The comparison of the finite element model results with the experimental results indicated a high degree of agreement. Based on this, an extensive parametric study was conducted to investigate the effects of flange width-to-thickness ratio (b/2t) and web height-to-thickness

ratio (h/w) on the behaviour of slender girders subjected to bending about the major axis.

5.6.1 Parametric Study Variables

Two series were investigated in this parametric study. In the first, a flange thickness of 8 mm and a web thickness of 4.68 mm were used, which were the average measured thicknesses of the component plates of the tested specimens. The flange width varied from 200 mm to 650 mm, giving a range in width-to-thickness ratio (b/2t) of 12.5 to 40.6. The web height varied from 650 mm to 2000 mm, giving a range in height-to-thickness ratio (h/w) of 138.9 to 427.4. Figure 5.14(a) presents a layout of this series and its variables.

The second series included eight groups. For each group, both the flange width and the web height were kept constant, while the flange thickness or the web thickness was varied to have the same ranges as the first series. The layout of this series variables, which is presented in figure 5.14(b), shows that each two groups had the same flange width-to-thickness ratio (b/2t) or the same web height-to-thickness ratio (h/w), using different flange or web dimensions, respectively.

The average mechanical properties obtained from testing the standard tension coupons, cut from the component plates of the tested specimens, were used in this parametric study. A yield strength of 330 MPa was used for the flange plates, while a yield strength of 384 MPa was used for the web plates up to 800 mm height and a yield strength of 434 MPa was used for the web plates of 1000 mm height or higher.

The higher yield strength used for the web plates, with respect to that used for the flange plates, had no effect on the results obtained from this study because of using slender

component plates for the studied girders. This was verified by using a 330 MPa yield strength for the component plates, flanges and web, in analyzing girders with low slenderness ratios of the component plates, with respect to the range of this study.

The web initial imperfection was taken into account, as follows:

i) For the girders with web heights up to 800 mm, the initial imperfection mode was assumed to be as those of the tested specimens G1 to G3, shown in Figure 3.4.

ii) For the girders with web heights of 1000 mm or higher, the initial imperfection mode was assumed to be as those of the tested specimens G4 to G9, shown in Figure 3.4.

The values of the web initial imperfection were assumed to be linearly proportional to the web height. The effect of web initial imperfection was investigated by analyzing the same girder with the same initial imperfection mode but the values ranged from one half to double those values used in this study. It was found that the values of the web initial imperfection had an insignificant effect on the ultimate moment capacities of such girders. However, when the same girder was analyzed using different web initial imperfection modes, it was found that these different modes had a significant effect on the ultimate moment capacities of such girders.

The warpage of the flange (c), as shown in Figure 3.3, was taken into account in the analysis, by assuming a linear relationship between this warpage and the flange width. Analyzing the same girders with different values of flange warpage, no effect of this warpage on the ultimate moment capacities of such girders was obtained .

5.6.2 Effect of Flange Width-to-Thickness Ratio (b/2t) and Web Height-to-Thickness Ratio (h/w) on the Behaviour of Slender Girders

Figures 5.15(a) to 5.15(g) and 5.16(a) to 5.16(f) show the longitudinal strain distributions along the web and the compression flange at the mid-span section, respectively, obtained from this parametric study. The flange thickness and the web thickness were kept constant (8 mm and 4.68 mm, respectively), while the flange width varied from 200 mm to 650 mm, giving a range in the width-to-thickness ratio (b/2t) of 12.5 to 40.6 and the web height varied from 650 mm to 2000 mm, giving a range in the height-to-thickness ratio (h/w) of 138.9 to 427.4.

As shown in from Figure 5.15(a) and 5.15(b), the strain distribution was almost linear along the webs of 650 mm and 800 mm height (web height-to-thickness ratio (h/w) = 138.9 to 170.9 and equivalent to $2523/\sqrt{F_{yf}}$ (MPa) to $3105/\sqrt{F_{yf}}$ (MPa) or $961/\sqrt{F_{yf}}$ (ksi) to $1183/\sqrt{F_{yf}}$ (ksi), respectively, where F_{yf} is the compression flange yield strength). However, the nonlinear strain distribution along the web started to take a place when the web height reached 1000 mm (h/w = 213.7 equivalent to $3882/\sqrt{F_{yf}}$ (MPa) or $1478/\sqrt{F_{yf}}$ (ksi), as shown in Figure 5.15(c) to 5.15(g), the mid-height portions of the webs were not sharing in resisting the applied moment, as evident in these unstrained portions. Consequently, the strains at the web portions, adjacent to the flanges, were increased, which may reflect the postbuckling behaviour of such webs. The height of these unstrained portions of the webs were getting larger, with respect to the web height, as the web height-to-thickness ratio (h/w) was increased.

As evident in Figure 5.15(a) to (g), the web height-to-thickness ratio (h/w) had a significant effect on the buckling and postbuckling behaviour of the web plate. On the other

hand, the flange width-to-thickness ratio (b/2t) had a significant effect on the maximum strain (or stress) level at the web portions adjacent to the flanges. This maximum strain (or stress) level increased as the flange width-to-thickness ratio (b/2t) decreased. Also, by comparing Figure 5.15(a) to Figure 5.15(g), for example, it is evident that the flange width-to-thickness ratio (b/2t) had more significant effect on the maximum strain (or stress) levels of girders with low web height-to-thickness ratios (h/w) than those of girders with high web height-to-thickness ratios (h/w). Also, as the web height-to-thickness ratio (h/w) increased, these maximum strain (or stress) levels were decreased, but its effect was not as much as the effect of the flange width-to-thickness ratio (b/2t).

Uniform and linear strain distributions along the compression flanges of width-to-thickness ratios (b/2t) up to 21.9, which is equivalent to $398/\sqrt{F_{yf}}$ (MPa) or $152/\sqrt{F_{yf}}$ (ksi), were obtained, at the mid-span sections, from the finite element analysis, as shown in Figure 5.16(a) to 5.16(c). However, nonlinear strain distributions were obtained when the width-to-thickness ratios (b/2t) of the flanges exceeded the limit of 21.9, as shown in Figure 5.16(d) to 5.16(f), which may reflect the postbuckling behaviour of the compression flange.

The higher strains of one side of the compression flange, with respect to the other side, shown in Figure 5.16(d) to 5.16(f), were only localized at the mid-span region and near the edge, as shown in Figure 5.11. This occurred because of the rotation of the compression flange causing a deflection of this side in the opposite direction to the initial warpage of the compression flange, as evident in the typical Figure 5.17. The figure presents the load-deflection curves in (a) and the stress distribution along the compression flange, at the mid-span section, at different levels of the applied load (P) or moment (M) in (b). It also shows

that the postbuckling behaviour of this compression flange started to take a place at an applied load (P) of 562.4 kN. However, no effect of these local stresses on the ultimate moment capacities of these girders was obtained.

The web height-to-thickness ratio (h/w) had a significant effect on the maximum strain levels of the compression flanges with low width-to-thickness ratios (b/2t). On the other hand, it had an insignificant effect on the maximum strain (or stress) levels of the compression flanges with high width-to-thickness ratios (b/2t), as evident in Figure 5.16. The flange width-to-thickness ratio (b/2t) affected significantly these maximum strain levels, which can be noticed by comparing the strain distributions with the same web height-to-thickness ratio (h/w) in Figure 5.16(a) to 5.16(f) to each other.

As direct results from this parametric study:

i) The yielding moment (M_y) of such girders can be reached if the flange width-to-thickness ratio (b/2t) does not exceed the limit of $250/\sqrt{F_{yf}}$ (MPa) or $95/\sqrt{F_{yf}}$ (ksi) and the web height-to-thickness ratio (h/w) does not exceed the limit of $2523/\sqrt{F_{yf}}$ (MPa) or $961/\sqrt{F_{yf}}$ (ksi), where F_{yf} is the compression flange yield strength. These limits were confirmed by analyzing another girder with a yield strength of 260 MPa, for both flanges and web, using the same finite element model. The girder had a flange width of 350 mm and thickness of 11.3 mm to have a flange width-to-thickness ratio (b/2t) of 15.5 (equivalent to $250/\sqrt{F_{yf}}$ (MPa) or $95/\sqrt{F_{yf}}$ (ksi)), and a web height of 800 mm and a thickness of 5.11 mm to have a web height-to-thickness ratio (h/w) of 156.5 (equivalent to $2523/\sqrt{F_{yf}}$ (MPa) or $961/\sqrt{F_{yf}}$ (ksi)). An ultimate moment capacity equals to the yielding moment (M_y)

of this girder was achieved.

ii) The yield strength has a significant effect on the ultimate moment capacities of the girders whose web height-to-thickness ratios (h/w) lower than $3105/\sqrt{F_{yf}}$ (MPa) or $1183/\sqrt{F_{yf}}$ (ksi) and whose flange width-to-thickness ratios (b/2t) lower than $398/\sqrt{F_{yf}}$ (MPa) or $152/\sqrt{F_{yf}}$ (ksi). This also was verified by analyzing girders with different yield strengths, for both flanges and web. For example, a girder had a flange width of 220 mm and thickness of 8 mm to have a flange width-to-thickness ratio (b/2t) of 13.75 ($250/\sqrt{F_{yf}}$ (MPa) or $95/\sqrt{F_{yf}}$ (ksi) = 11.18), and a web height of 650 mm and thickness of 4.68 mm to have a web height-to-thickness ratio (h/w) of 138.9 ($2523/\sqrt{F_{yf}}$ (MPa) or $961/\sqrt{F_{yf}}$ (ksi) = 112.83). An ultimate moment capacity equivalent to 78.4% of the yielding moment was reached. In the parametric study, where a yield strength of 330 MPa was used, an ultimate moment capacity equivalent to the yielding moment (M_y) was reached.

iii) Girders with web height-to-thickness ratios (h/w) higher than $3882/\sqrt{F_{yf}}$ (MPa) or $1478/\sqrt{F_{yf}}$ (ksi) were analyzed using different yield strength levels for the same girder. The same ultimate moment capacity was achieved for the same girder with different yield levels, which confirms that the yield strength has an insignificant effect on the ultimate moment capacity of these girders.

iv) In addition, other girders with web height-to-thickness ratios (h/w) ranged from $2523/\sqrt{F_{yf}}$ (MPa) or $961/\sqrt{F_{yf}}$ (ksi) to $3105/\sqrt{F_{yf}}$ (MPa) or $1183/\sqrt{F_{yf}}$ (ksi) and whose flange width-to-thickness ratios (b/2t) higher than $398/\sqrt{F_{yf}}$ (MPa) or $152/\sqrt{F_{yf}}$ (ksi), were analyzed using the same finite element model at different yield

strength levels. For each girder, the same ultimate moment capacity was obtained using different yield strengths. This implies that the yield strength has an insignificant effect on the ultimate moment capacity at this range of the study.

v) No failure by vertical buckling of the web was obtained by the finite element analysis, in the range of this parametric study.

However, more studies are required to evaluate the effect of the yield strength on these limits and the ultimate moment capacities of such girders, and they may confirm these limits or modify them according to the used steel type, other than the type investigated in this study.

Table 5.1 Comparison Between the Finite Element Model Results and the Experimental Results

Specimen	$M_{F.E.}$ (kN.m)	M_{exp} (kN.m)	$M_{F.E.}/M_{exp}$
G1	480	465	1.034
G2	507	515	0.984
G3	608	598	1.017
G4	604	578	1.045
G5	730	688	1.061
G6	840	804	1.045
G7	733	752	0.974
G8	840	810	1.038
G9	930	970	0.959

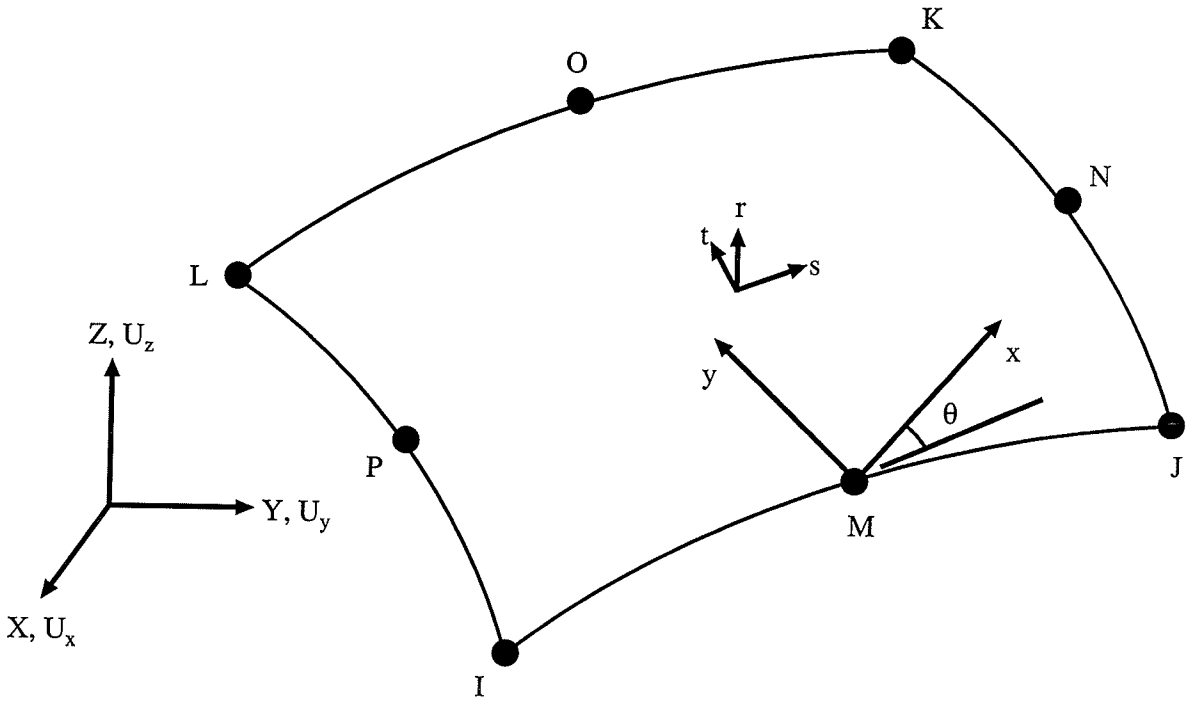

(a) Quadrilateral Shell Element

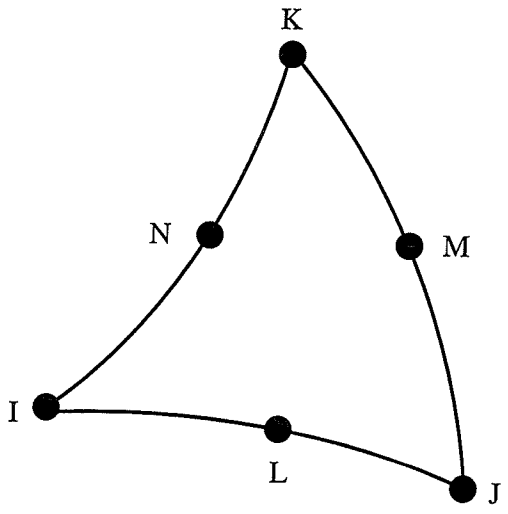

(b) Triangular Shell Element

Figure 5.1 Shell Elements Adopted in the Finite Element Model

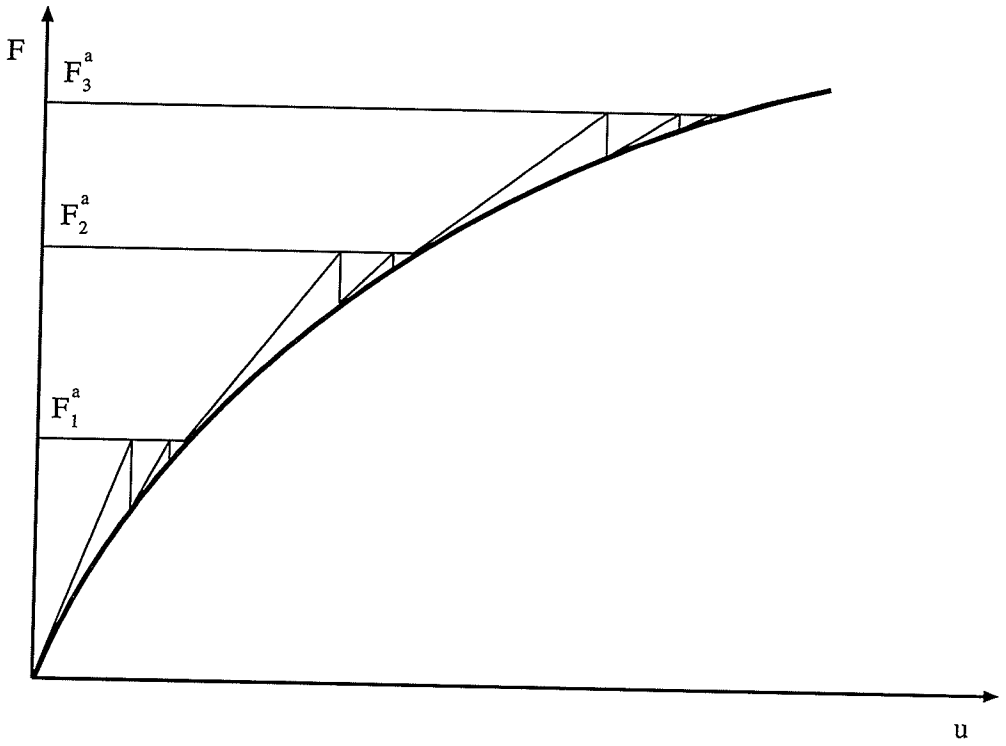

Figure 5.2 Incremental Newton-Raphson Procedure

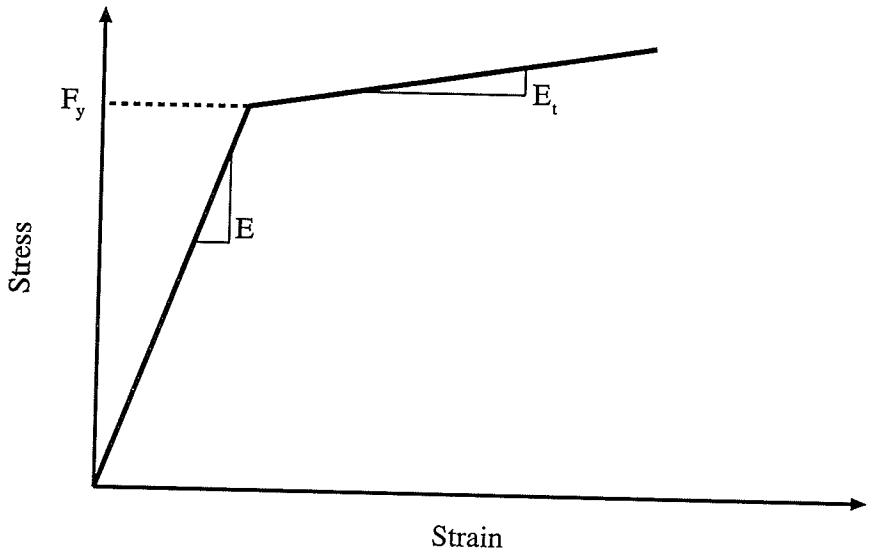

Figure 5.3 Elasto-Plastic Bilinear-Kinematic Hardening Stress-Strain Curve

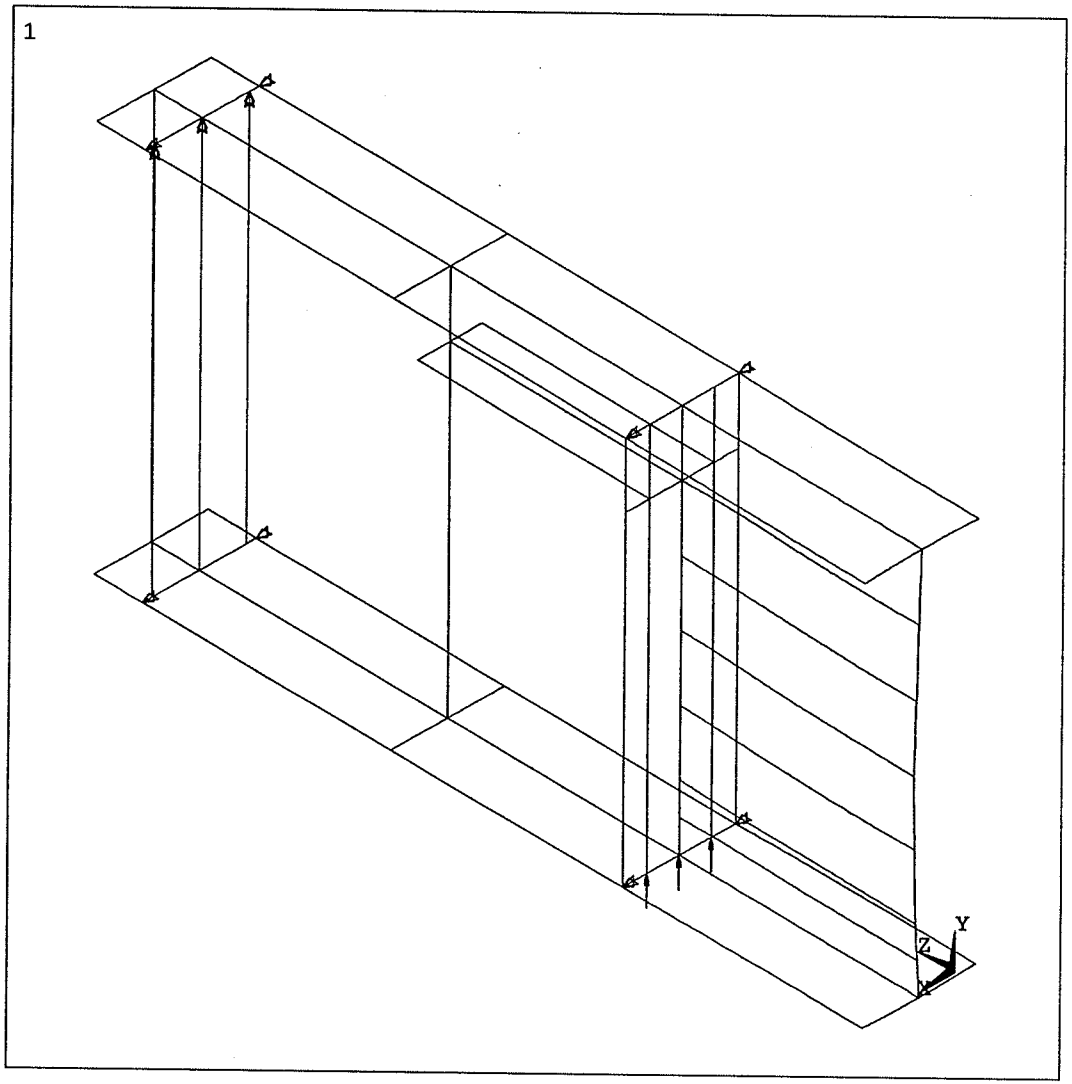

Figure 5.4 Finite Element Model Applied Load and Boundary Conditions

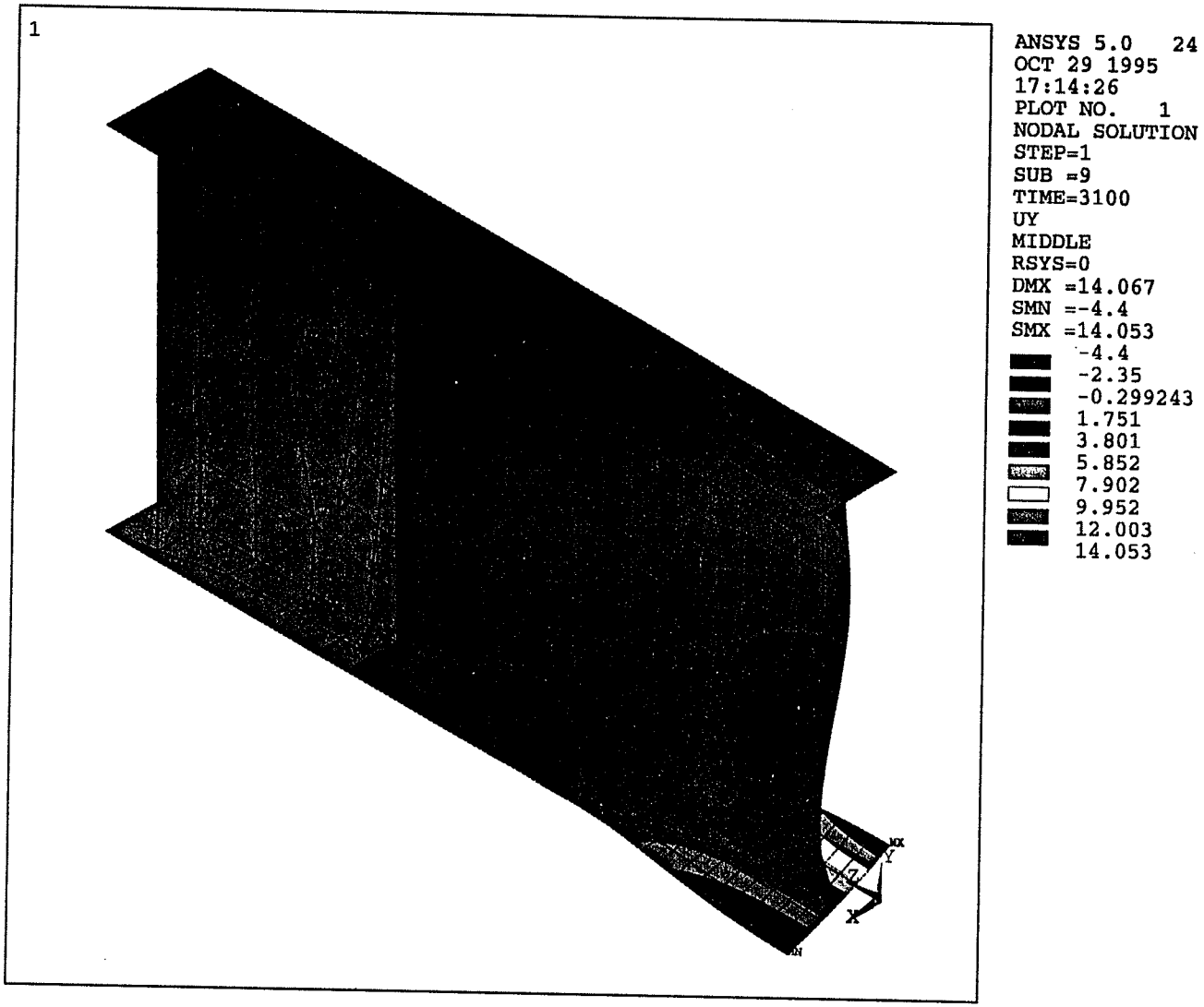

Figure 5.5 Translations in the Global Y-Direction of Specimen G9

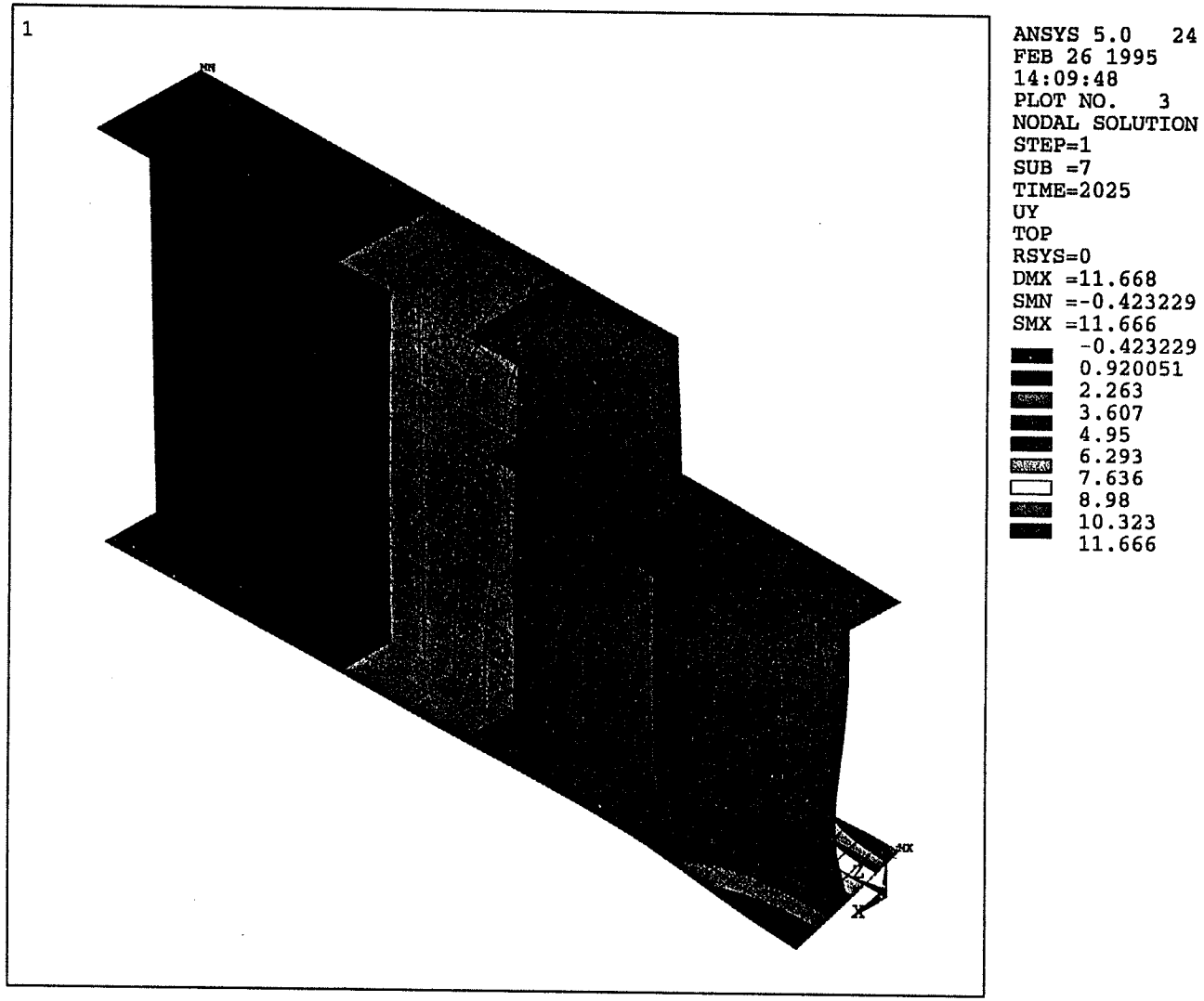

Figure 5.6 Translations in the Global Y-Direction of Specimen G3

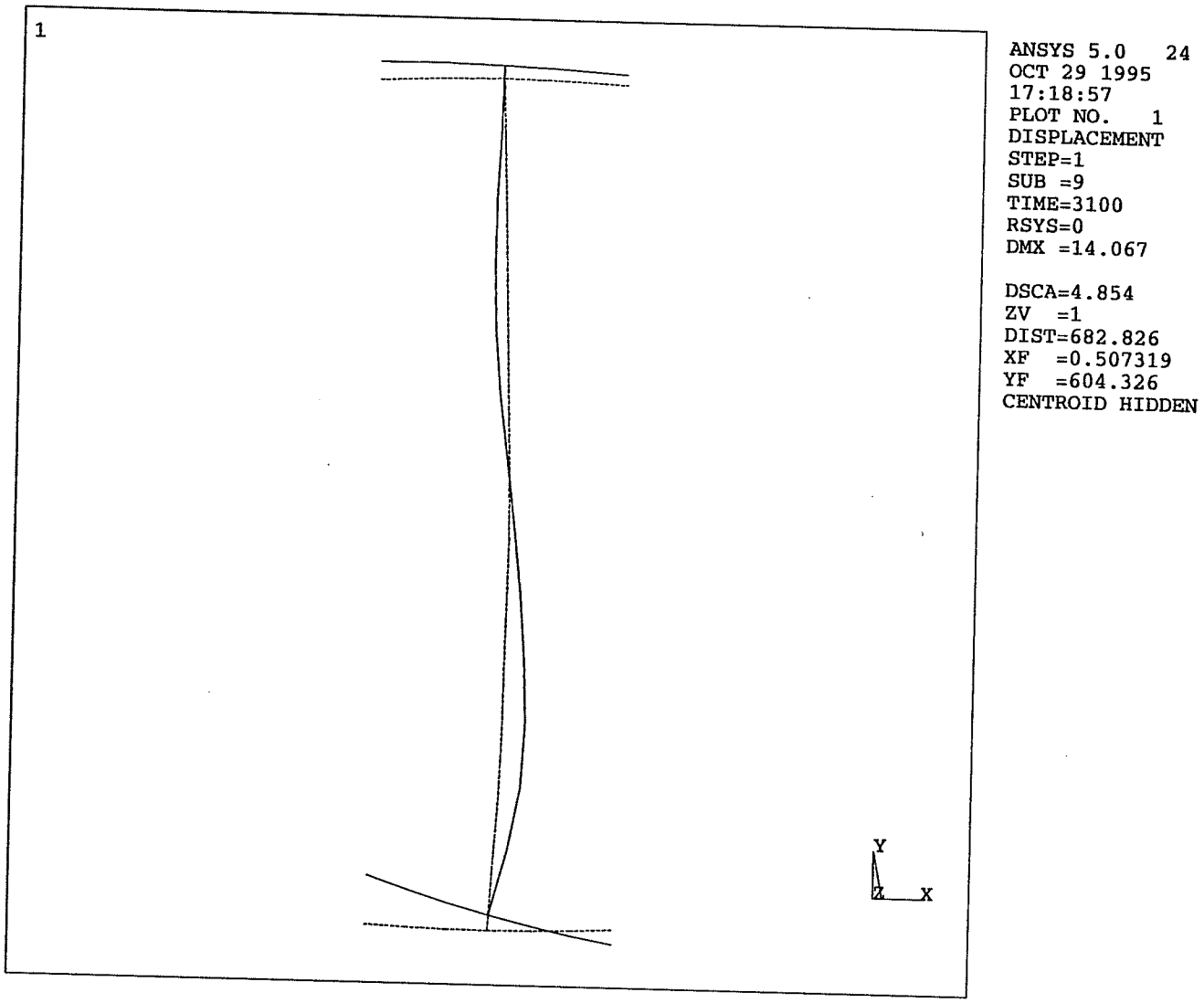

Figure 5.7 Deformed Configuration of the Mid-Span Section of Specimen G9

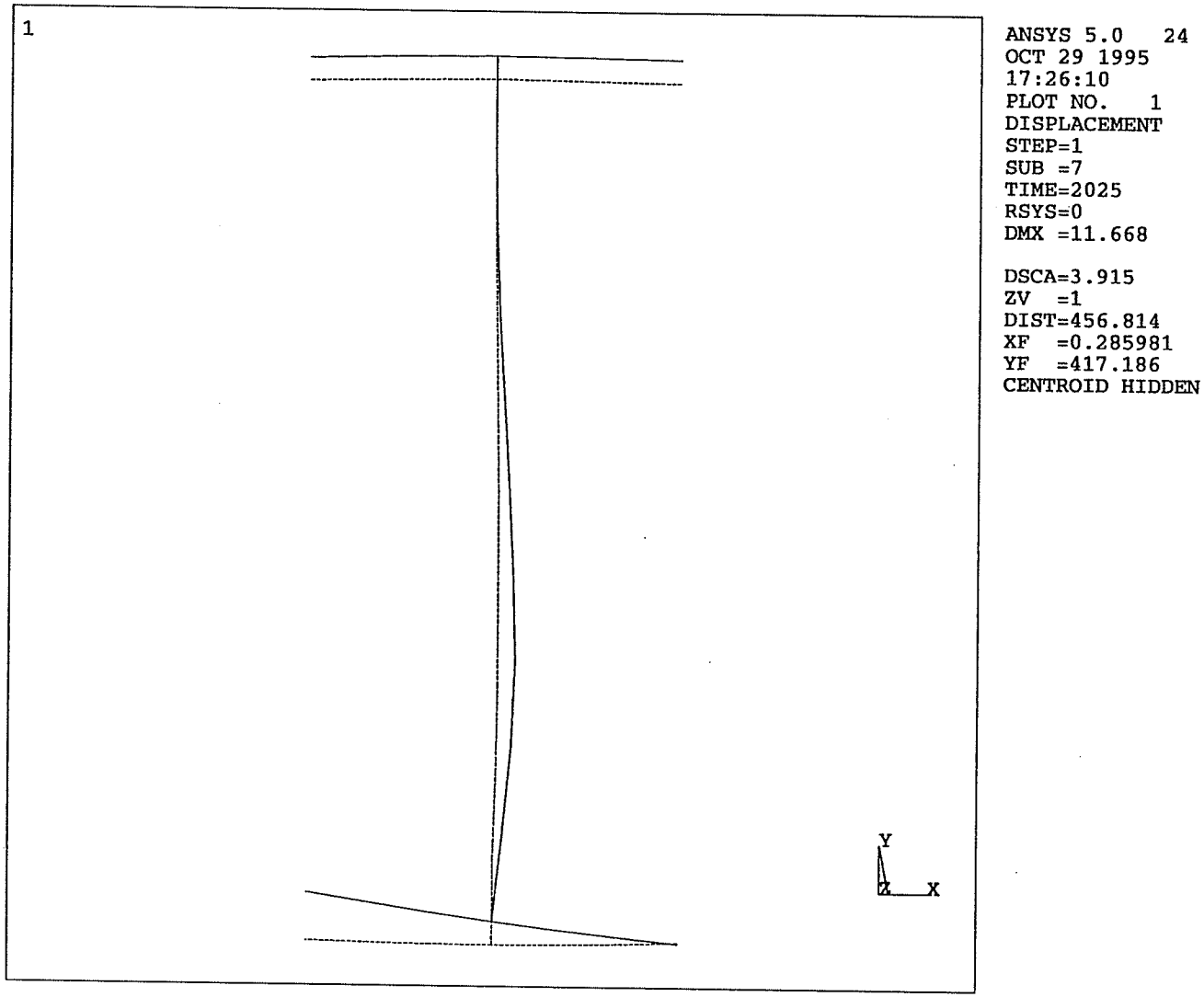

Figure 5.8 Deformed Configuration of the Mid-Span Section of Specimen G3

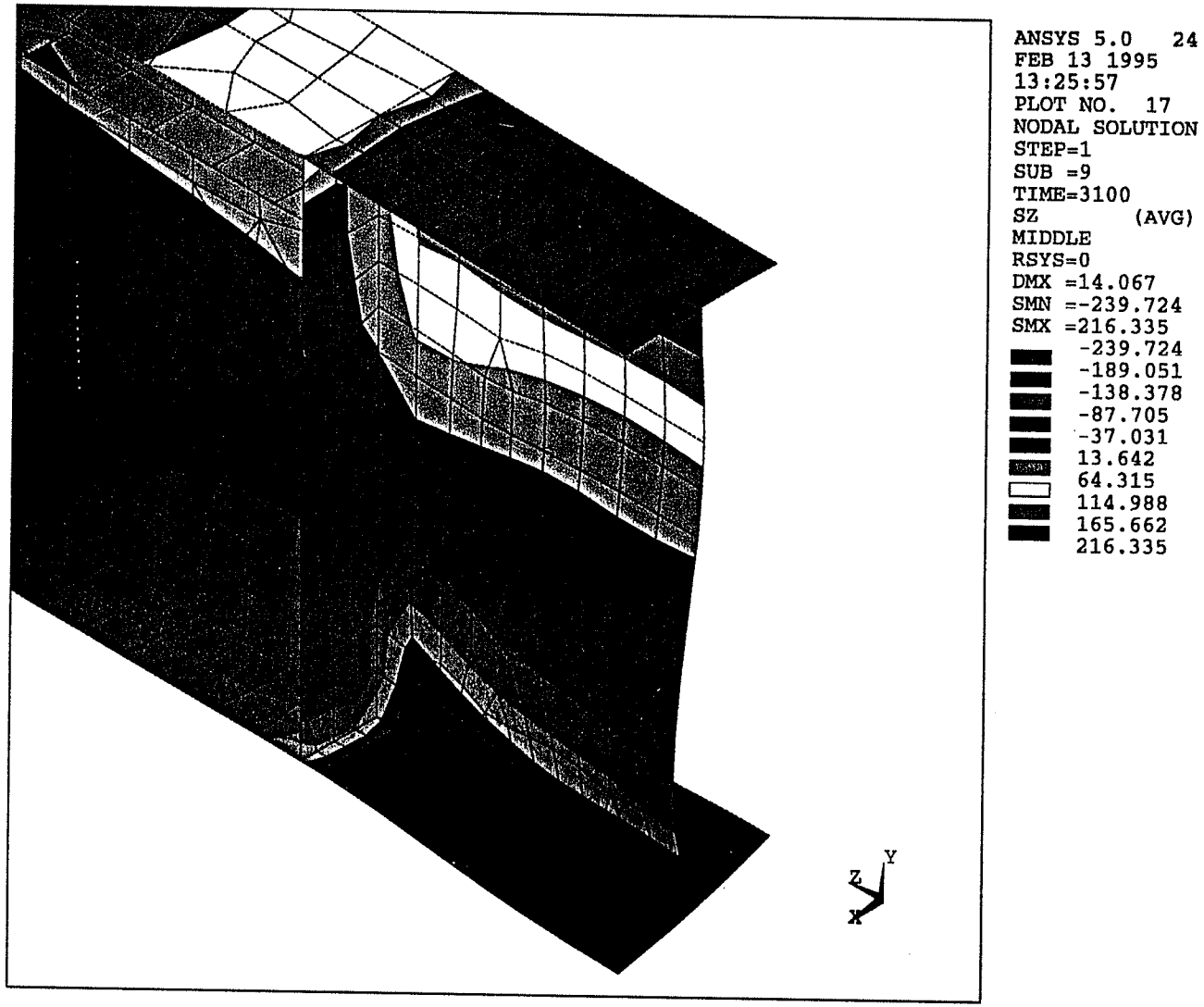

Figure 5.9 Stress Contours in the Longitudinal Direction of Specimen G9

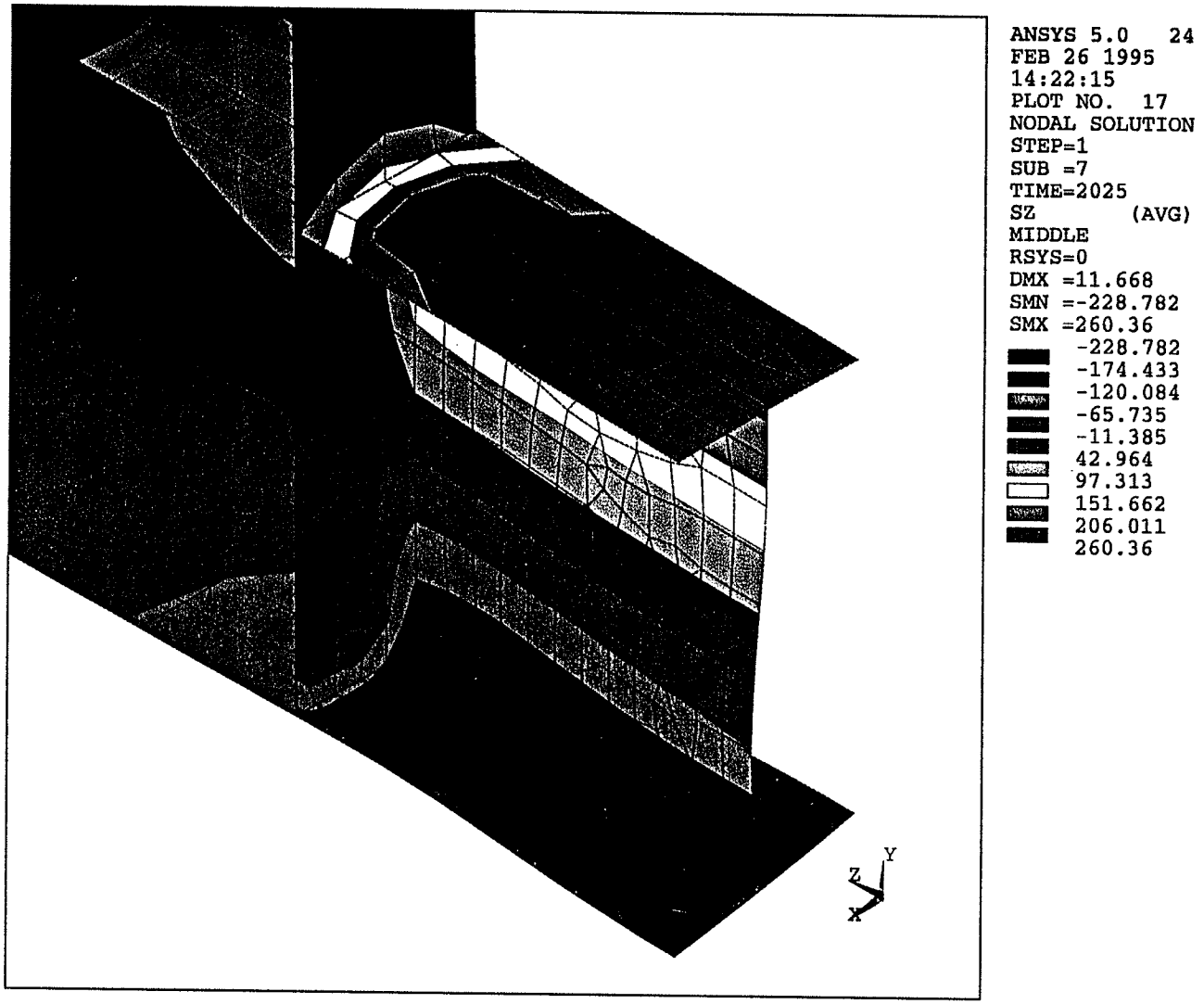

Figure 5.10 Stress Contours in the Longitudinal Direction of Specimen G3

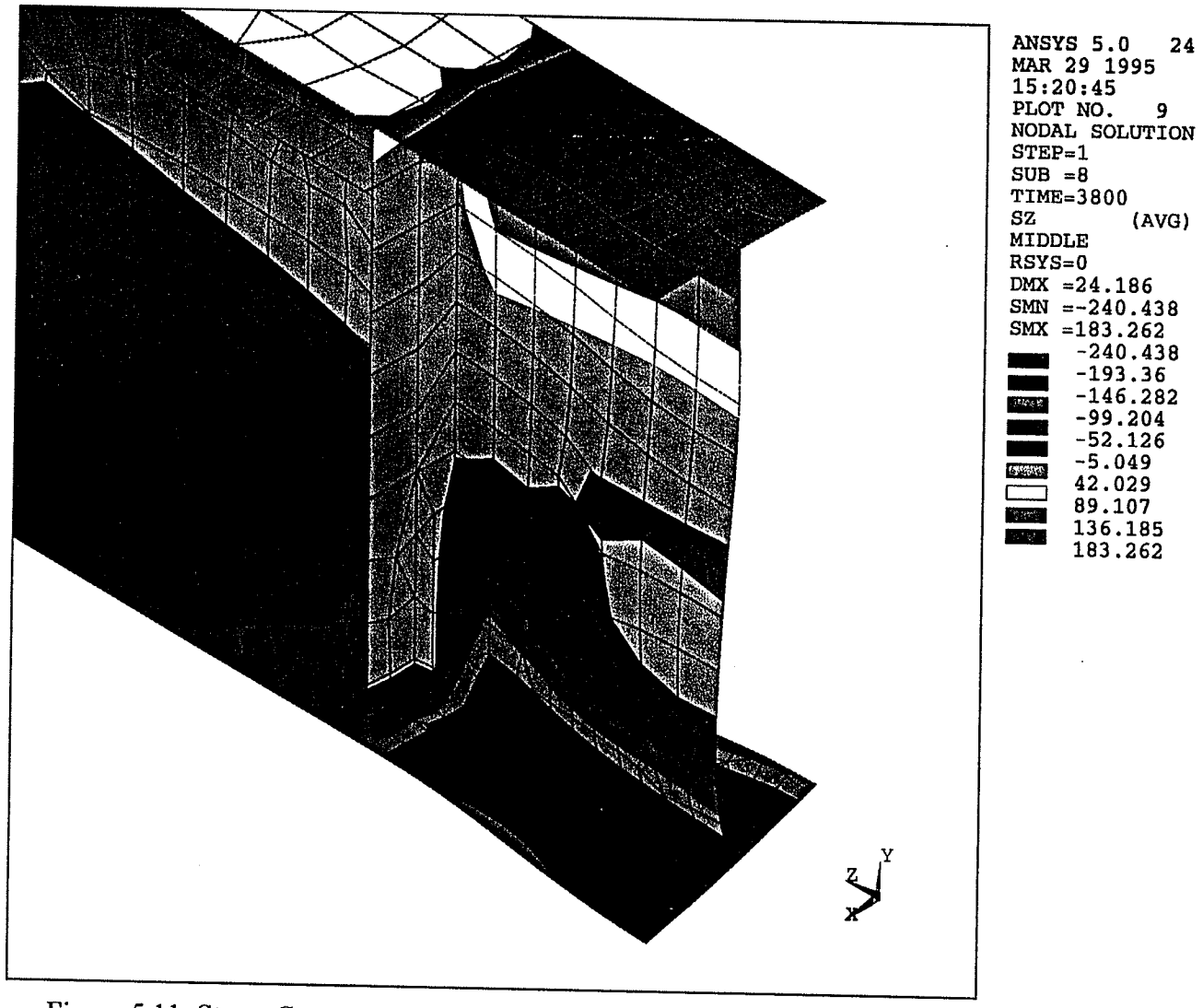

Figure 5.11 Stress Contours in the Longitudinal Direction of Girder with a Flange Width of 450 mm

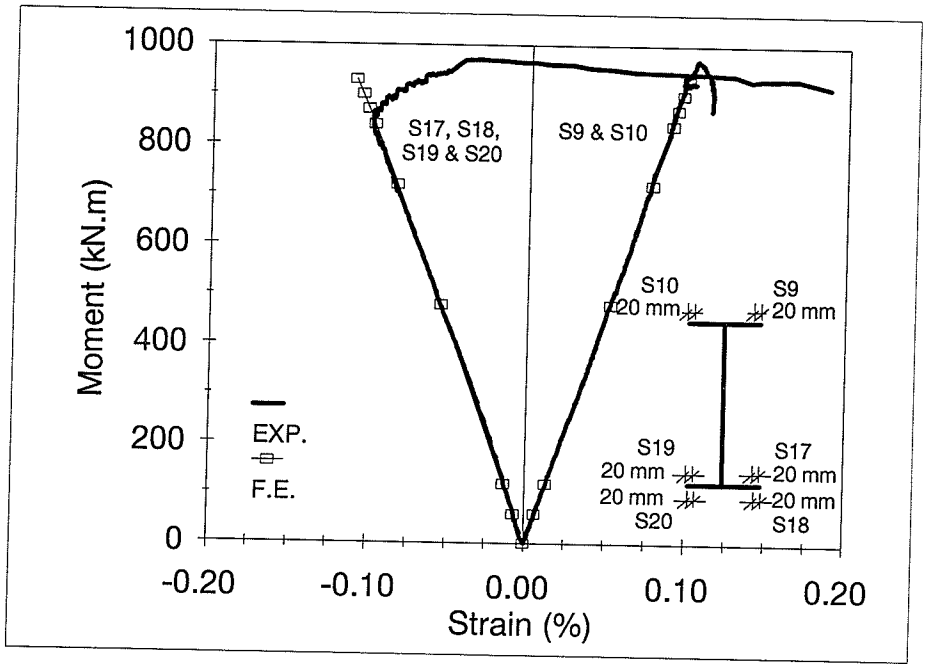

(a) Flanges

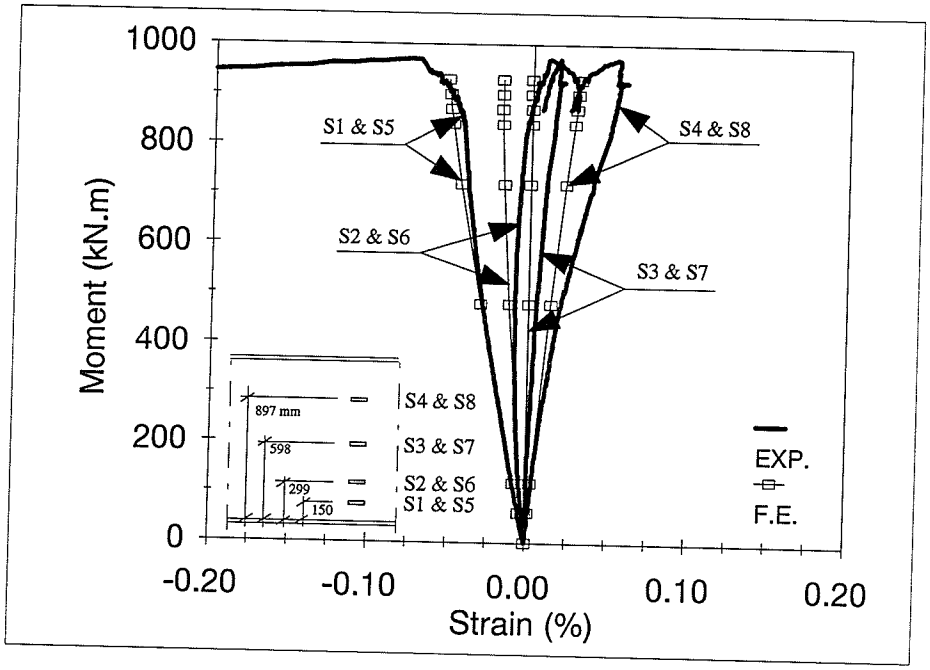

(b) Web

Figure 5.12 Longitudinal Strain as a Function of Applied Moment at Mid-Span Section of Specimen G9

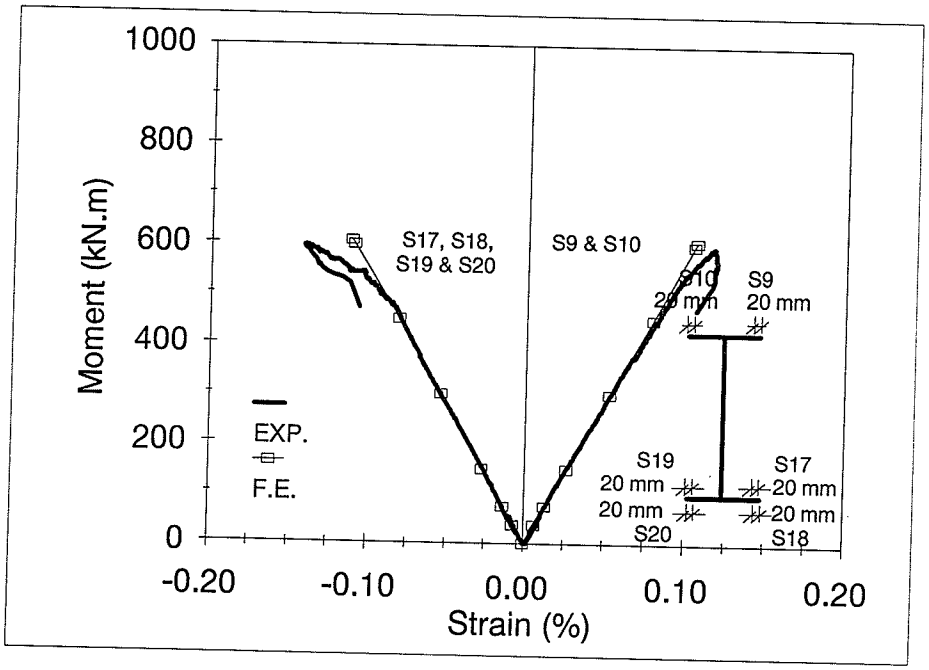

(a) Flanges

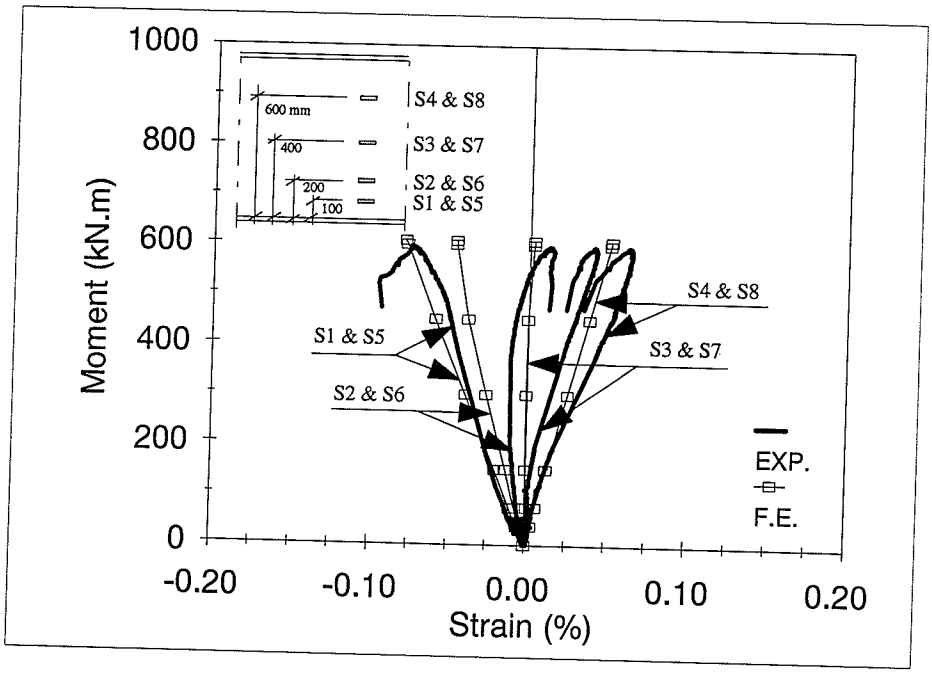

(b) Web

Figure 5.13 Longitudinal Strain as a Function of Applied Moment at Mid-Span Section of Specimen G3

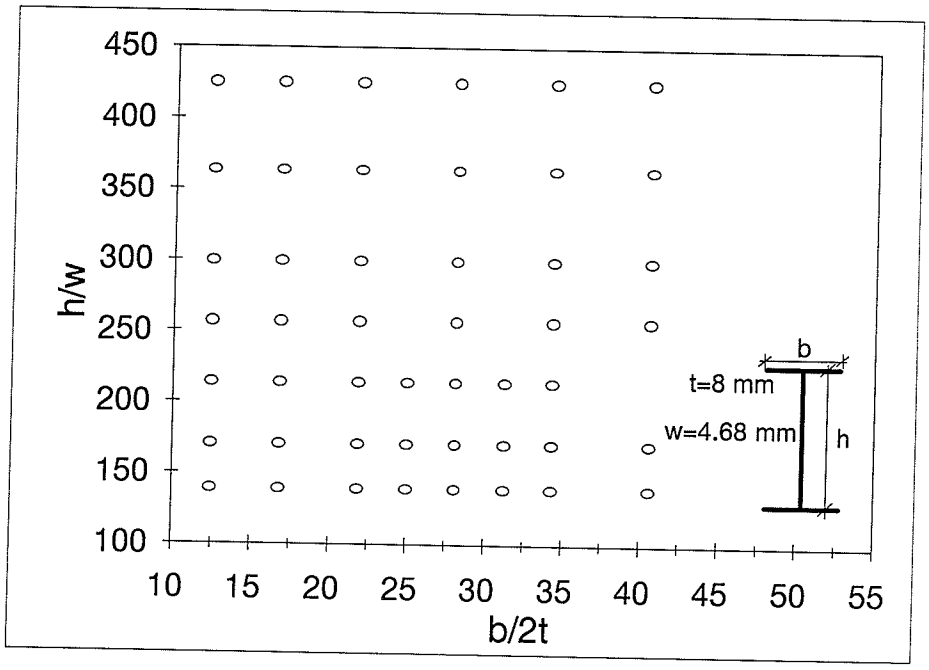

(a) Constant Thicknesses

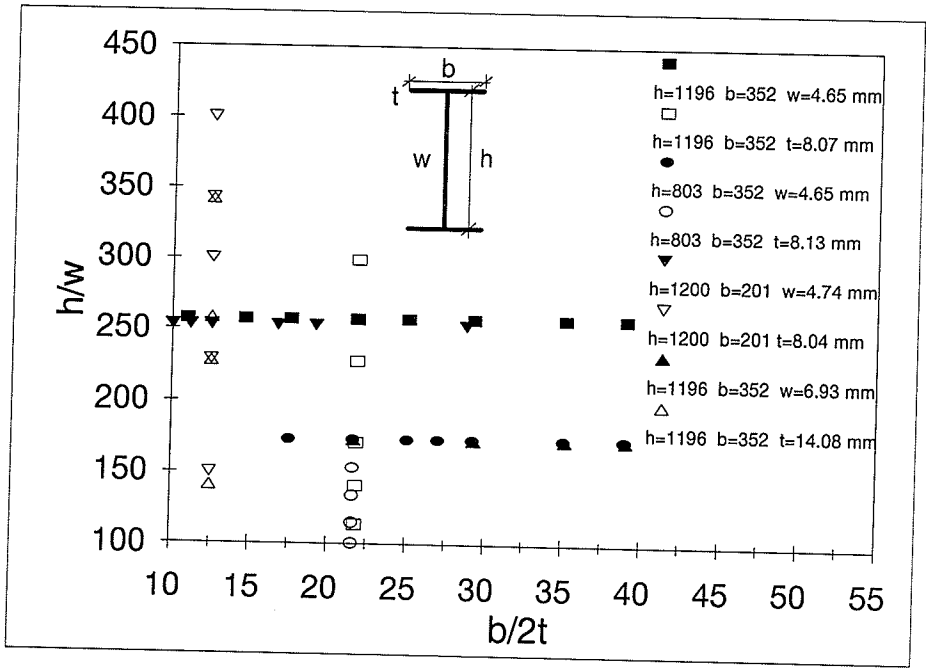

(b) Variable Thicknesses

Figure 5.14 Parametric Study Variables

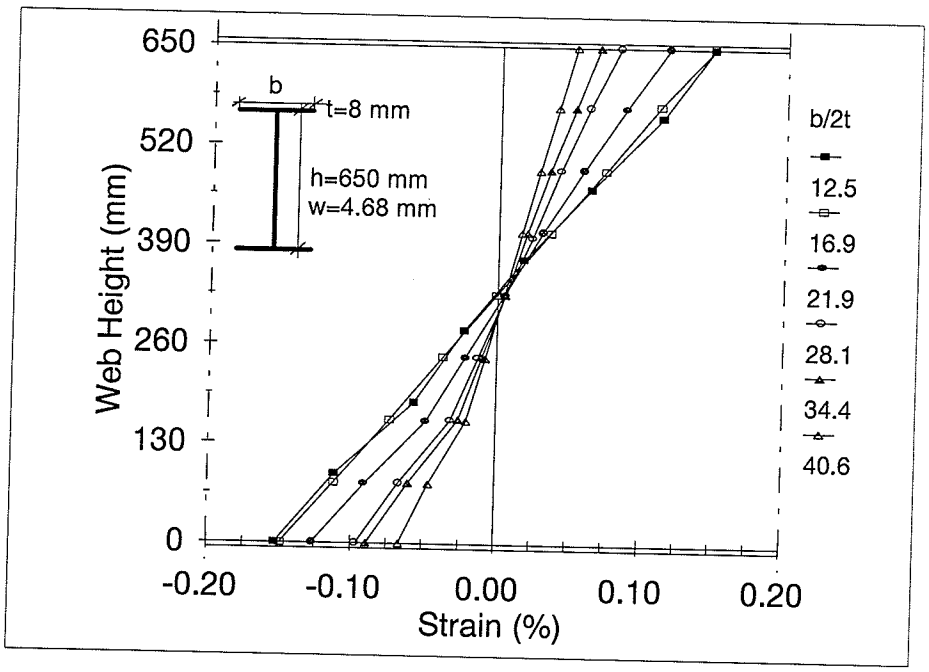

(a) 650-mm Web Height

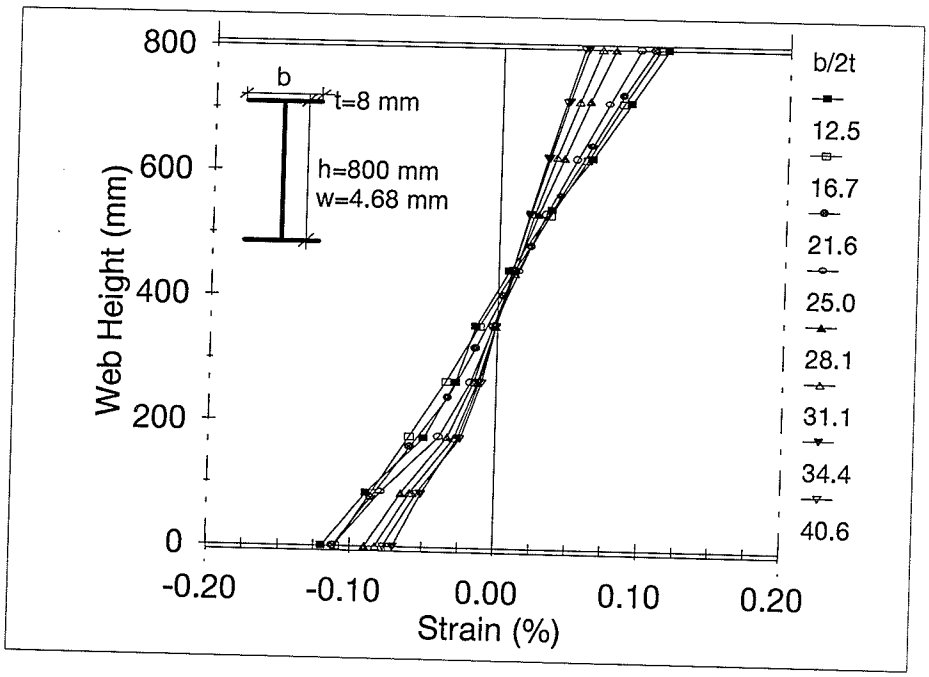

(b) 800-mm Web Height

Figure 5.15 Effect of b/2t on the Strain Distribution Along the Webs at Mid-Span Sections

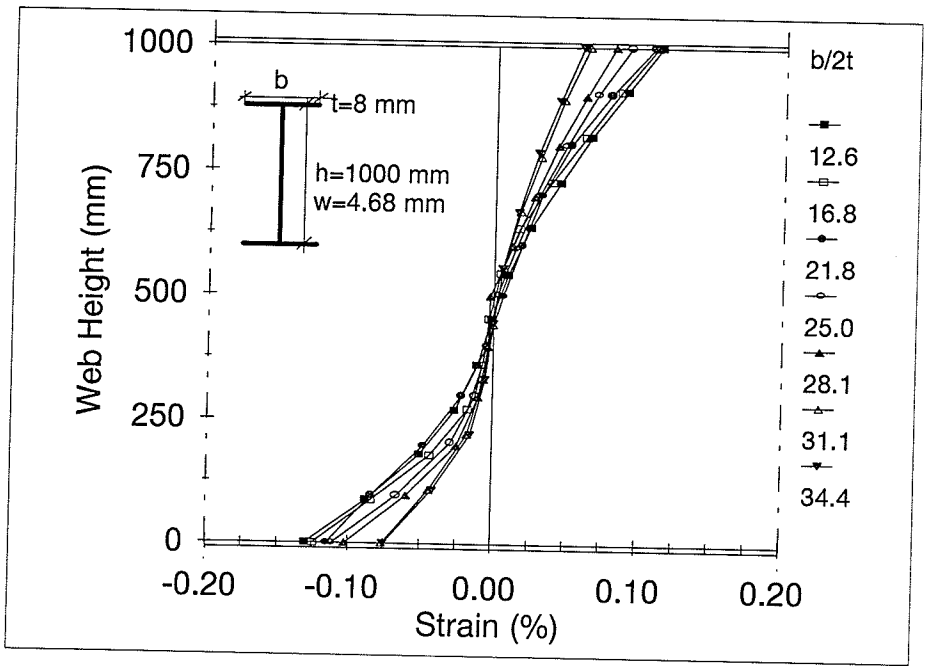

(c) 1000-mm Web Height

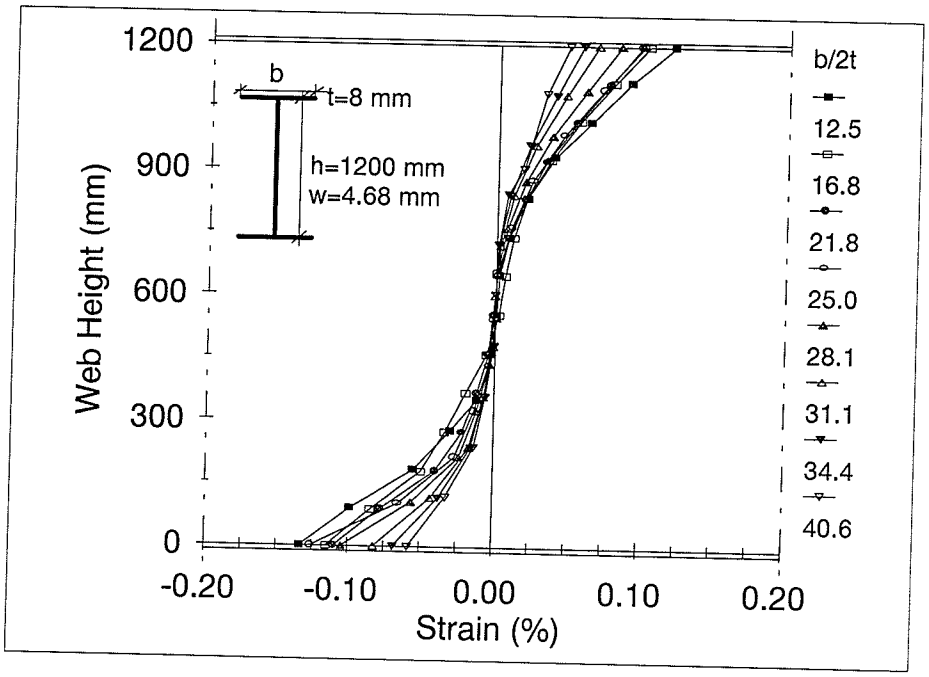

(d) 1200-mm Web Height

Figure 5.15 Effect of b/2t on the Strain Distribution Along the Webs at Mid-Span Sections

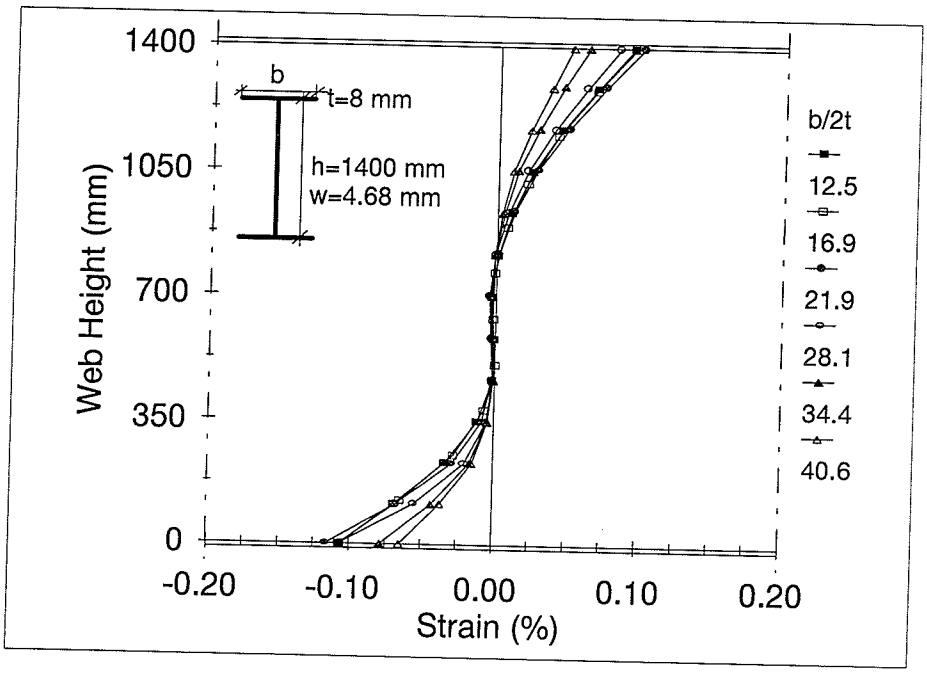

(e) 1400-mm Web Height

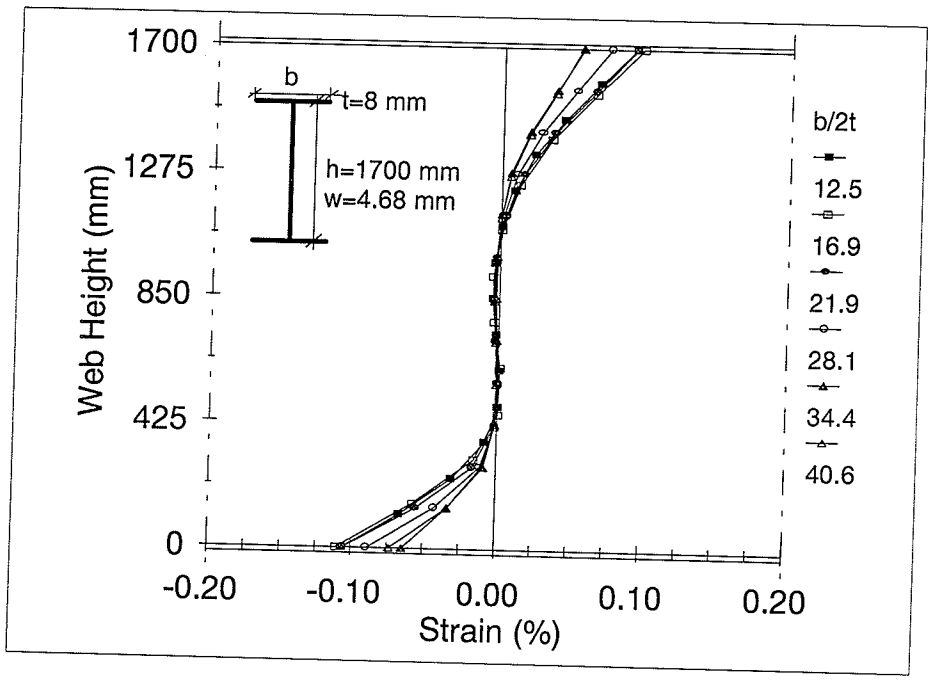

(f) 1700-mm Web Height

Figure 5.15 Effect of b/2t on the Strain Distribution Along the Webs at Mid-Span Sections

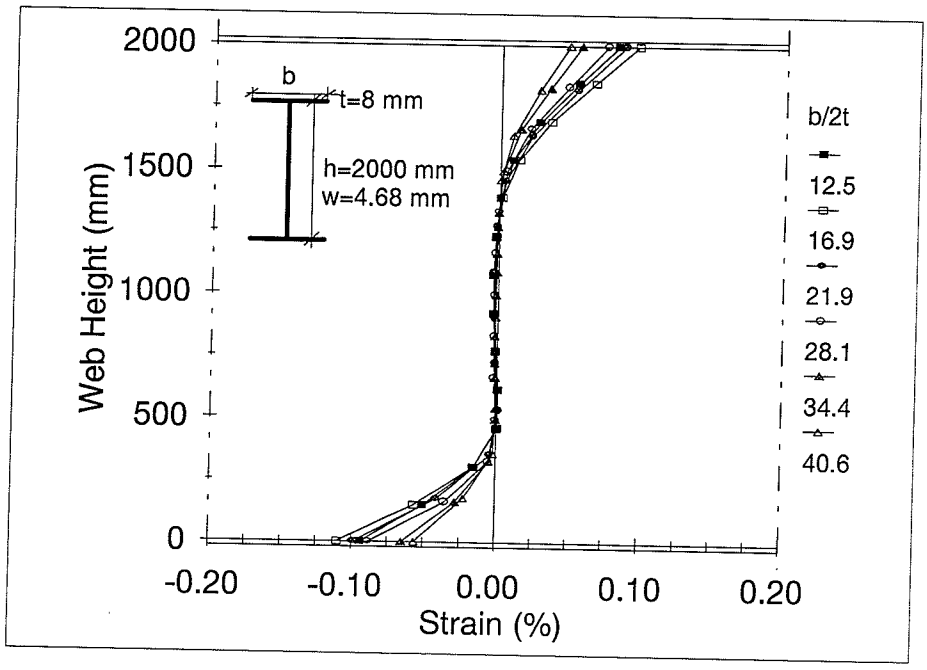

(g) 2000-mm Web Height

Figure 5.15 Effect of b/2t on the Strain Distribution Along the Webs at Mid-Span Sections

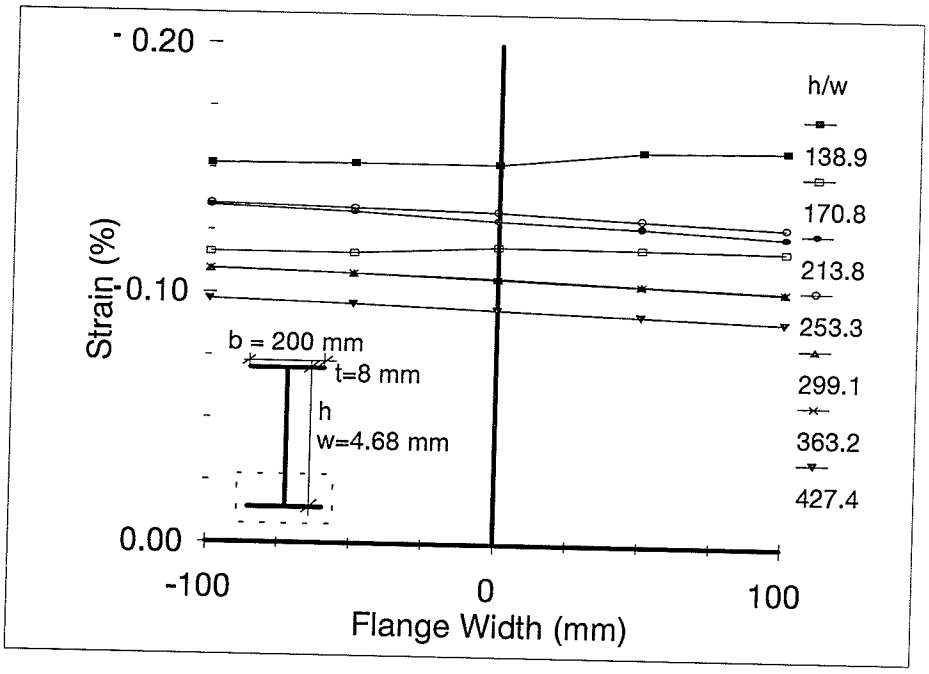

(a) 200-mm Flange Width

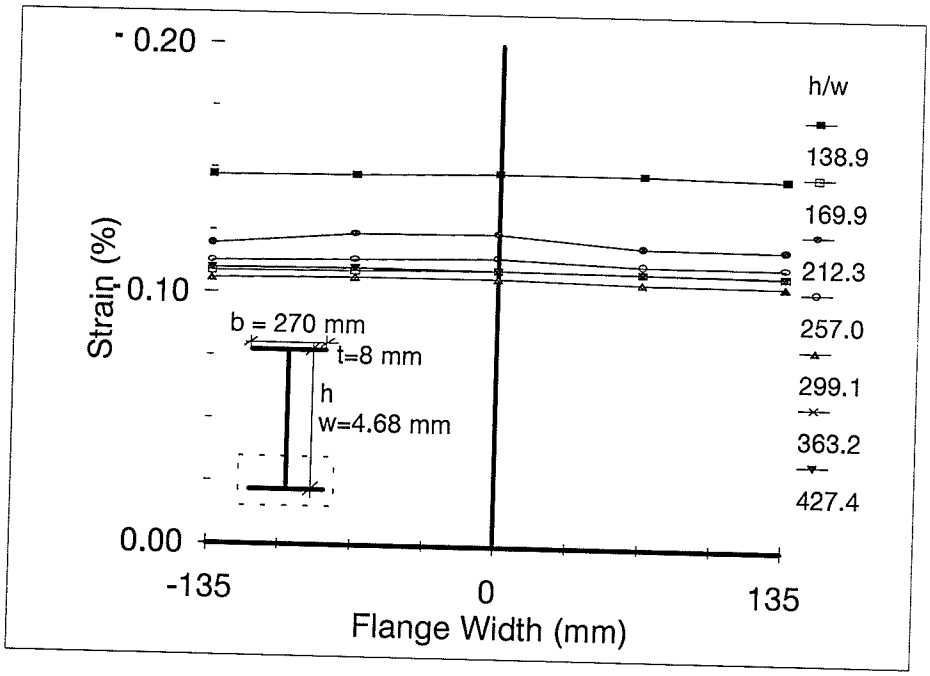

(b) 270-mm Flange Width

Figure 5.16 Effect of h/w on the Strain Distribution Along the Flanges at Mid-Span Sections

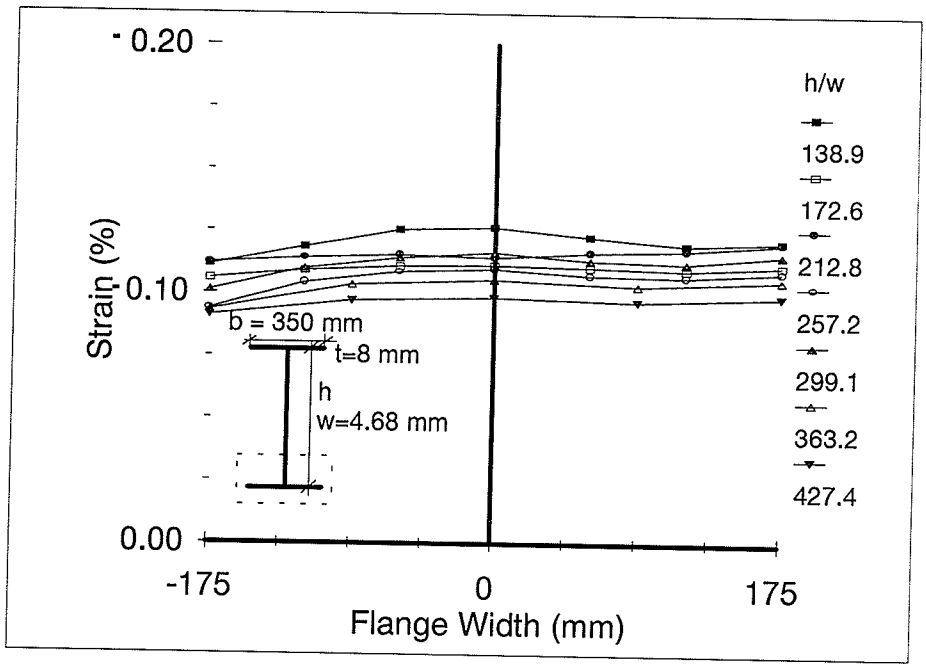

(c) 350-mm Flange Width

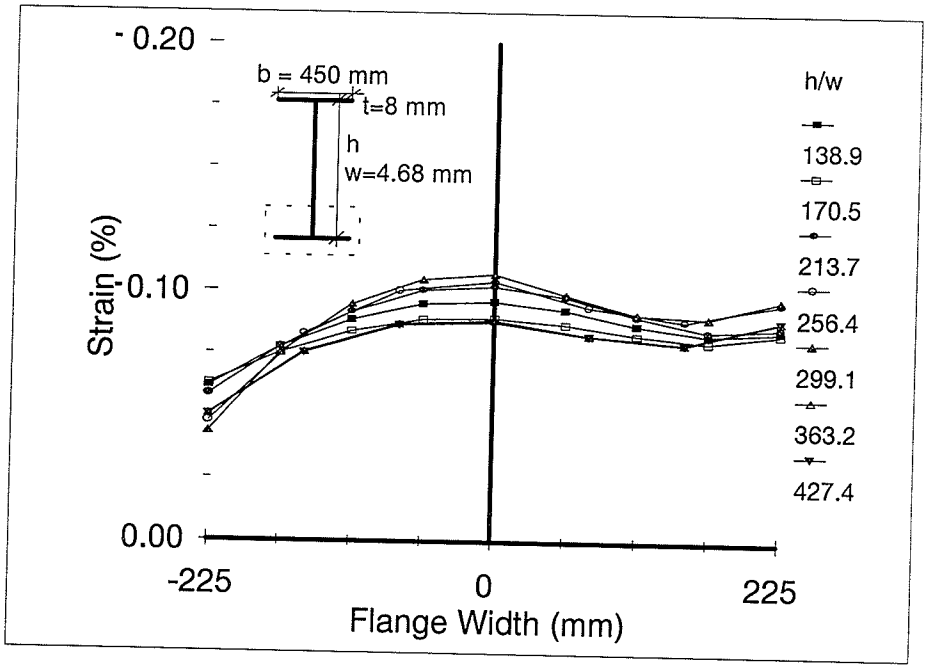

(d) 450-mm Flange Width

Figure 5.16 Effect of h/w on the Strain Distribution Along the Flanges at Mid-Span Sections

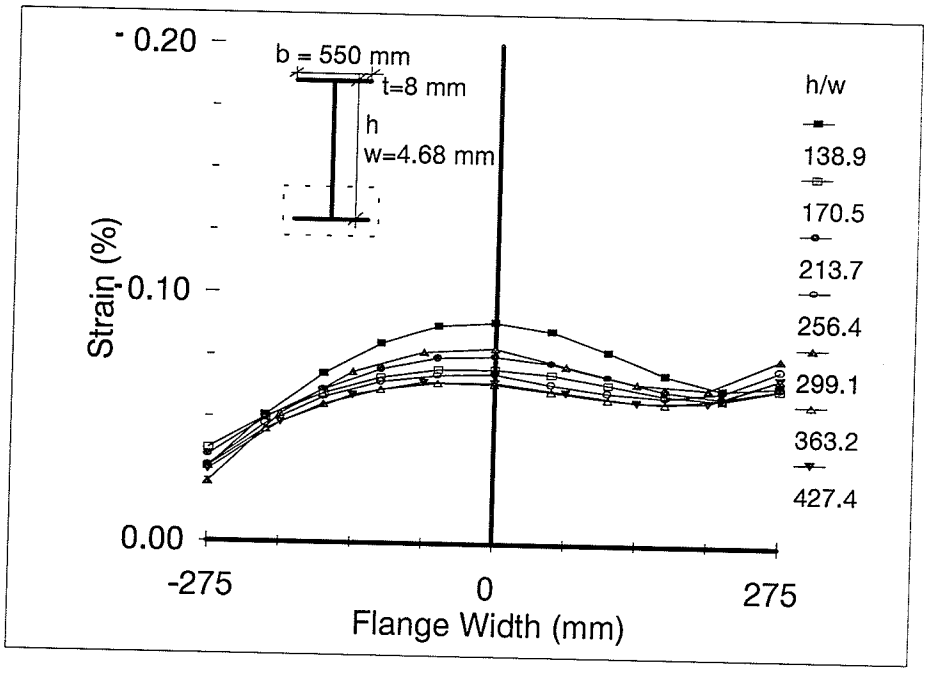

(e) 550-mm Flange Width

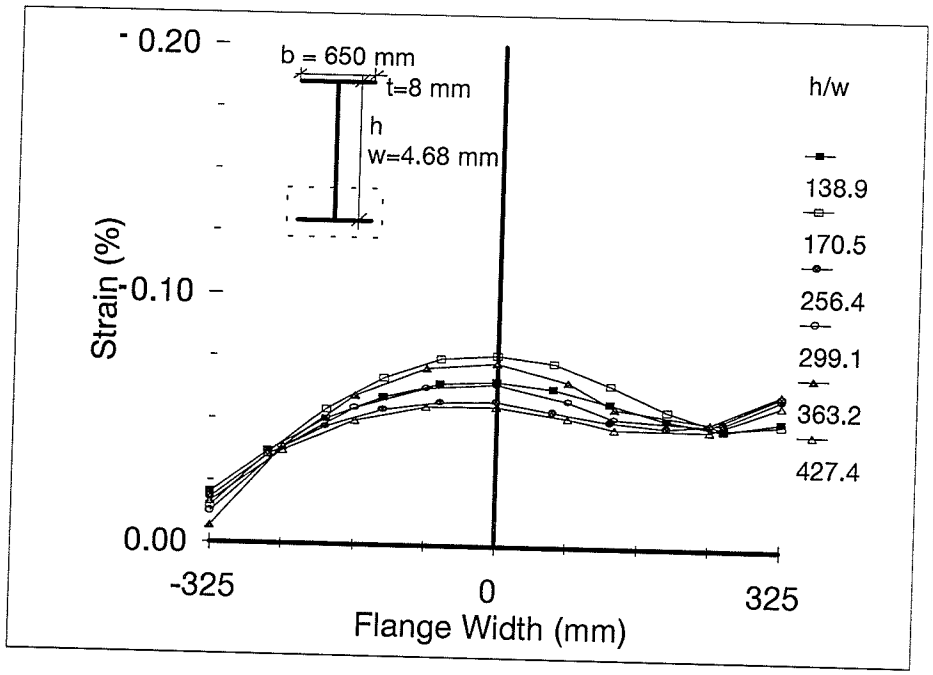

(f) 650-mm Flange Width

Figure 5.16 Effect of h/w on the Strain Distribution Along the Flanges at Mid-Span Sections

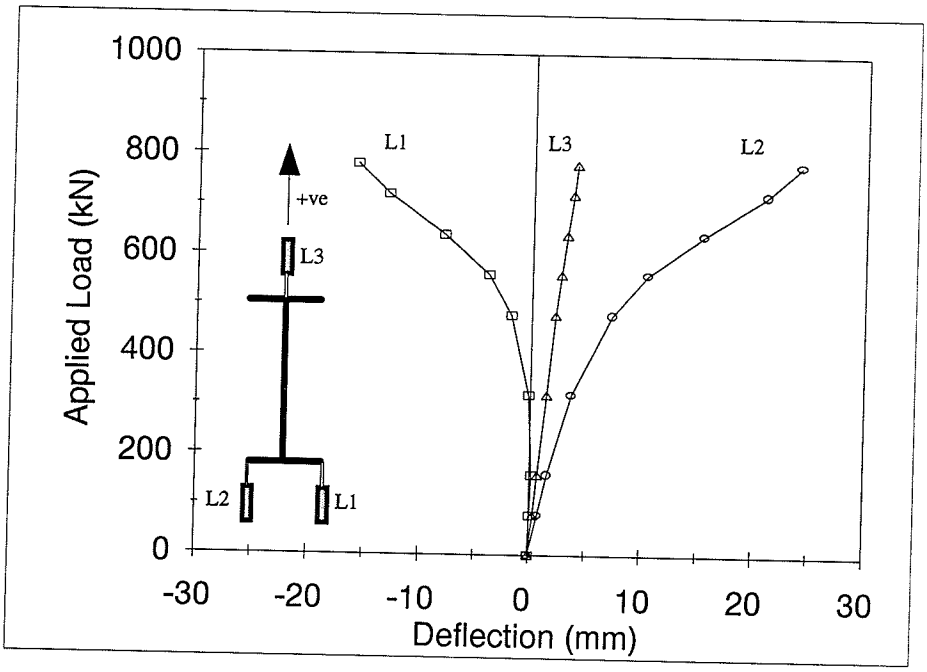

(a) Load-Deflection Curves at Mid-Span Section

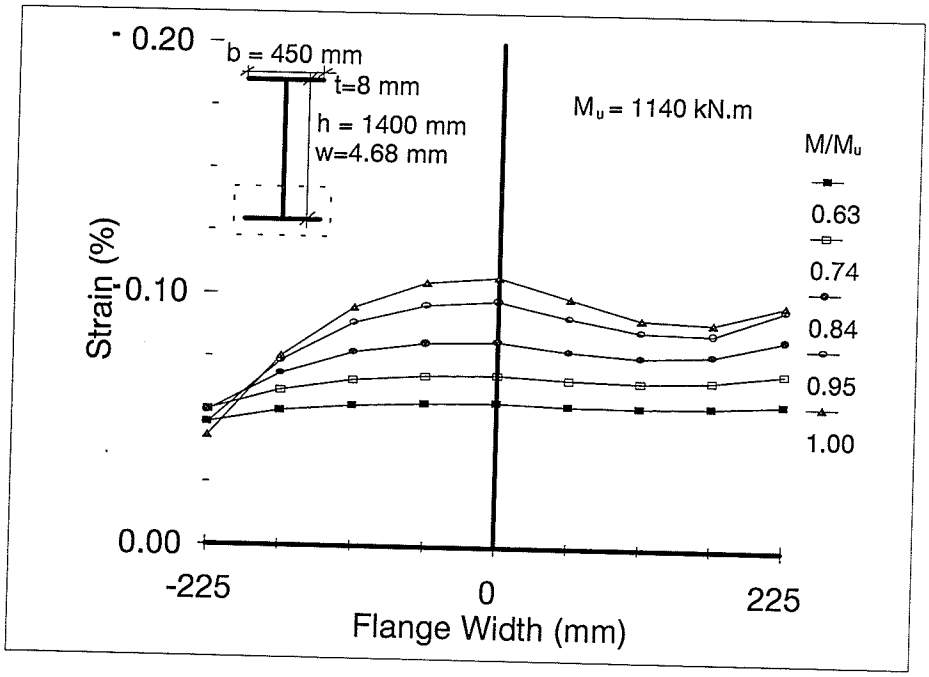

(b) Strain Distrebution Along the Compression Flange at Mid-Span Section at Different Applied Moment Levels

Figure 5.17 Buckling and Postbuckling Behaviour of the Compression Flange

CHAPTER 6

PROPOSED DESIGN MODEL

6.1 INTRODUCTION

A design model for laterally-supported slender plate girders subjected to bending about the major axis is proposed in this chapter. The development of this design model is based on a parametric study performed using the finite element analysis described in Chapter 5. A comparison between the ultimate moment capacity of such girders computed according to the proposed design model and the capacity computed according to various standards and specifications is presented in this chapter. A comparison between the experimental results and the results obtained through the proposed design model is also discussed in this chapter. The following standards and specifications were used in the discussion that follows:

i) CAN/CSA-S16.1-94 Standard (1994), referred to as the S16.1-94 Standard;

ii) ECCS Recommendations (1986); referred to as the ECCS-86 Recommendations;

iii) AISC-LRFD Specification (1986); referred to as the LRFD-86 Specification;

iv) AISC-WSD Specification (1978); referred to as the WSD-78 Specification;

v) AISC-WSD Specification (1989); referred to as the WSD-89 Specification; and

iii) AISC-LRFD Specification (1993); referred to as the LRFD-93 Specification.

The S16.1-94 Standard makes reference to CAN/CSA-S136-94 Standard (1994) for Cold-

Formed Steel Structural Members which, in this discussion, will be referred to as the S136-94 Standard.

The design provisions of these standards and specifications for slender plate girders were discussed in Chapter 2.

In computing the ultimate moment capacity of slender girders, all safety factors and resistance factors were removed. The average measured cross-sectional dimensions of the tested specimens, listed in Table 3.2, and the actual mechanical properties listed in Table 3.5, were used in computing ultimate moment capacities.

6.2 THE PROPOSED DESIGN MODEL

As stated in Chapter 1, the main objective of this study was to develop a design model for computing the ultimate moment capacity of slender girders based on more realistic behaviour than that currently used in design standards. This model must take into account the effect of web-flange buckling interaction as well as the postbuckling strength of both the web and the flange. Such a design model is presented below.

In the proposed design model, the ultimate moment capacity is a function of the dimensions of both the compression flange and the web, as well as the maximum stress in the compression flange. The postbuckling strength is taken into account through the use of effective widths for the compression flange and the web. Expressions for these effective widths are given below.

6.2.1 Effective Width of the Compression Flange

As shown in Figures 5.16(a) to 5.16(c), the strain distribution along the compression flange in girders whose width ranges from 200 mm to 350 mm, is uniform just before failure. This implies that there is no local buckling in the compression flange and the total flange width is effective. The flange thickness in this case is 8 mm. Thus, the b/2t range over which the strain is uniform is from 12.5 to 21.9. Since the yield stress of the compression flange is 330 MPa, this b/2t range can be shown as: $\lambda_{fl} \leq \lambda_f \leq \lambda_{fe}$, where,

$$\lambda_f = \frac{b}{2t} \tag{6.1}$$

$$\lambda_{fl} = \frac{227}{\sqrt{F_{yf}\ (MPa)}} = \frac{86}{\sqrt{F_{yf}\ (ksi)}} \tag{6.2}$$

$$\lambda_{fe} = \frac{398}{\sqrt{F_{yf}\ (MPa)}} = \frac{152}{\sqrt{F_{yf}\ (ksi)}} \tag{6.3}$$

b = width of compression flange;

t = thickness of compression flange; and

F_{yf} = yield strength of compression flange.

Thus, for $\lambda_{fl} \leq \lambda_f \leq \lambda_{fe}$:

$$\frac{b_e}{b} = 1 \qquad (6.4)$$

where,

b_e = effective width of compression flange.

The postbuckling behaviour of the compression flange is evident when $\lambda_f > \lambda_{fe}$ (21.9), as shown in Figures 5.16(d) to 5.16(f). The strain distribution becomes nonuniform when the flange widths are 450 mm, 550 mm and 650 mm. In these girders, local buckling of the compression flange has taken place and the effective width b_e, shown in Figure 6.1, may be used to compute the ultimate moment capacity. This effective width is obtained by equating the area under the actual stress distribution with the area of a rectangular stress distribution which is equal to the maximum stress multiplied by the effective width of this flange.

The best fitting curve technique was used to develop an expression to represent the effective width of slender flanges that accounts for the effect of the web-flange interaction. Thus, for $\lambda_{fe} < \lambda_f \leq \lambda_{fh}$:

$$\frac{b_e}{b} = \frac{1}{\beta}\left(235.7 - 9.02\,\lambda_f - 0.029\,\lambda_w + 0.0043\,\lambda_f\,\lambda_w + 0.1159\,\lambda_f^2 \right.$$

$$\left. - 832.19 \times 10^{-7}\,\lambda_w^{\,2} - 0.986 \times 10^{-7}\,\lambda_f^2\,\lambda_w^2 \right) \leq 1 \qquad (6.5)$$

where,

$$\beta = 59.4 + \frac{105.55}{\left(1 + \left(472.556 \frac{F_{yf}}{E}\right)^{-1.37}\right)} \tag{6.6}$$

$$\lambda_w = \frac{h}{w} \tag{6.7}$$

$$\lambda_{fh} = \frac{738}{\sqrt{F_{yf}\ (MPa)}} = \frac{281}{\sqrt{F_{yf}\ (ksi)}} \tag{6.8}$$

h= height of web; and

w = thickness of web.

The finite element analysis showed that Equations 6.4 and 6.5 are valid for the specified range of λ_f, regardless of the yield strength.

The maximum stress in the compression flange is affected by the dimensions of both the compression flange and the web. As shown in Figure 6.2(a), the effect of the web height-to-thickness ratio (λ_w) on the effective width b_e is more noticeable in girders with relatively high flange width-to-thickness ratios (λ_f). The effective width b_e increases as λ_w increases, reaching a maximum value at $\lambda_w = 300$. Any further increase in λ_w ratio results in a reduction in b_e.

The effect of λ_f on the effective width b_e is quite pronounced when $\lambda_f > \lambda_{fe}$ (21.9), as shown in Figure 6.2(b). The effective width b_e decreases as λ_f increases, reaching a minimum value at $\lambda_f = 36.5$. Beyond this value, the effective width increases with an increase in λ_f.

6.2.2 Effective Width of the Web

As shown in Figures 5.15(a) and 5.15(b), the strain distribution along the height of the web just before failure is almost linear for girders with web height to thickness ratios (λ_w) of 138.9 and 170.9. This implies that no local buckling in the web has taken place in this range of λ_w. The finite element results indicate that the λ_w range over which the web is totally effective is $\lambda_{wl} \leq \lambda_w \leq \lambda_{wp}$, where,

$$\lambda_{wl} = \frac{1864}{\sqrt{F_{yf}\ (MPa)}} = \frac{710}{\sqrt{F_{yf}\ (ksi)}} \tag{6.9}$$

and

$$\lambda_{wp} = \frac{3105}{\sqrt{F_{yf}\ (MPa)}} = \frac{1183}{\sqrt{F_{yf}\ (ksi)}} \tag{6.10}$$

However, a nonlinear strain distribution along the web is evident when λ_w reaches λ_{wr} (= 213.6), as shown in Figures 5.15(c) to 5.15(f), where,

$$\lambda_{wr} = \frac{3882}{\sqrt{F_{yf}\ (MPa)}} = \frac{1478}{\sqrt{F_{yf}\ (ksi)}} \tag{6.11}$$

The best fitting line technique was used to evaluate the effective width of the portion of the web in compression (h_e) for the girders in this range. The following expression for h_e, which accounts for the effect of the web-flange buckling interaction, was developed:

For $\lambda_{wr} \leq \lambda_w \leq \lambda_{wh}$:

$$\frac{h_e}{h} = \left(624 - 7.586\ \lambda_f - 1.013\ \lambda_w + 0.012\ \lambda_f \lambda_w + 0.049\ \lambda_f^2 \right) 10^{-3} \qquad (6.12)$$

where,

h_e = effective width of the web in compression; and

$$\lambda_{wh} = \frac{7763}{\sqrt{F_{yf}\ (MPa)}} = \frac{2957}{\sqrt{F_{yf}\ (ksi)}} \qquad (6.13)$$

The effective width of the web (h_e), shown in Figure 6.1(b), is significantly affected by λ_w. Increasing λ_w results in an increase in h_e, which reaches a maximum value at, approximately, $\lambda_w = 290$, as shown in Figure 6.3(a). Any further increase in λ_w results in a reduction in the value of h_e.

The flange width-to-thickness ratio (λ_f) also affects the effective width of the web, as shown in Figure 6.3(b). An increase in λ_f results in a decrease in h_e, except for the case when λ_w exceeds 363. In this case, h_e reaches a minimum value at approximately $\lambda_f = 33$ for $\lambda_w = 363$ and $\lambda_f = 25$ for $\lambda_w = 427$. Any further increase in λ_f results in an increase in h_e.

According to the proposed design model, the effective width of the web (h_e) ranges from 54w to 76w for $\lambda_w \geq \lambda_{wr}$. The effective width of the web (h_e) in the LRFD-86

Specification, the WSD-78 Specification and the WSD-89 Specification, is assumed to be equal to 30w, irrespective of the web or the flange dimensions.

6.2.3 Ultimate Moment Capacity

Since the ultimate moment capacity of a slender girder depends on both λ_w and λ_f, the discussion that follows is organized into three groups, depending on the value of λ_w. The first range, which covers the range $\lambda_{wl} \leq \lambda_w \leq \lambda_{wp}$, deals with girders that do not experience local buckling of the web but may be subjected to local buckling of the compression flange. Because local buckling of the compression flange depends on the dimensions of this flange and because the stress distribution in the web depends on the effective width of the compression flange, this range has been further divided into three parts. In the first two parts, an expression for the critical stress as a function of the yield strength is given. In the third part, the yield strength has insignificant effect on the critical stress. In this case, an expression for the critical stress as a function of the flange and the web dimensions only is given. To make this parameter dimensionless, the critical stress is divided by the elastic modulus (E).

The second range covers high values of λ_w ($\geq \lambda_{wr}$) where the yield strength has insignificant effect on the capacity.

Finally, the third range ($\lambda_{wp} < \lambda_w < \lambda_{wr}$) covers the transition between the first two ranges.

The various ranges and the corresponding expressions for the ultimate moment capacity are given below and are also shown in Figure 6.4.

(i) $\lambda_{wl} \leq \lambda_w \leq \lambda_{wp}$

As discussed in Chapter 5, the strain distribution along the web in this range is almost linear. Thus, the stress distribution shown in Figure 6.1(a) can be used to compute the ultimate moment capacity of girders whose λ_w ratios are in this range. Alternatively, this capacity can be computed from the following equation:

$$M_u = F_{cr}\ S_{xeff} \qquad \leq \quad M_y \tag{6.14}$$

where,

M_u = ultimate moment capacity;

M_y = yield moment;

S_{xeff} = effective section modulus about the major axis = $I_{xeff}/(h_e + t/2)$;

I_{xeff} = moment of inertia of the effective section; and

F_{cr} = critical stress at the mid-section of compression flange, as shown in Figure 6.1(a), and defined below.

For $\lambda_{wl} \leq \lambda_w \leq \lambda_{wp}$, $\lambda_{fl} \leq \lambda_f < \lambda_{fe}$ **and** $\mathbf{0.0373} \leq \sqrt{F_{yf}/E} \leq \mathbf{0.0411}$:

The finite element analysis showed that the ultimate moment capacity of slender girders is significantly affected by the yield strength of the compression flange in this range.

In this case the critical stress (F_{cr}) is a function of the yield strength (F_{yf}). This stress can be computed from the following expression which takes into account the web-flange buckling interaction.

$$\frac{F_{cr}}{F_{yf}} = \left(297 - 7.27\ \lambda_f - 1.12\ \lambda_w + 0.028\ \lambda_f \lambda_w + 0.0245\ \lambda_f^2 \right) 10^{-2} \quad \leq 1 \qquad (6.15)$$

Equation 6.15 is based on the results obtained from tests where CAN/CSA-G40.21-300W steel with a yield strength of 330 MPa was used. The finite element analysis showed that the same equation can be used for any steel whose $\sqrt{F_{yf}/E}$ is between 0.0373 and 0.0411. However, additional work is required to develop an expression for F_{cr}/F_{yf} out side of this range of $\sqrt{F_{yf}/E}$.

For $\lambda_{wl} \leq \lambda_w < \lambda_{we}$, $\lambda_{fe} \leq \lambda_f \leq \lambda_{fh}$ and $0.0373 \leq \sqrt{F_{yf}/E} \leq 0.0411$:

Equation 6.15 can also be used within this range of λ_f and $\sqrt{F_{yf}/E}$ values, where,

$$\lambda_{we} = \frac{2523}{\sqrt{F_{yf}\ (MPa)}} = \frac{961}{\sqrt{F_{yf}\ (ksi)}} \qquad (6.16)$$

For $\lambda_{we} \leq \lambda_w \leq \lambda_{wp}$, and $\lambda_{fe} \leq \lambda_f \leq \lambda_{fh}$:

The finite element analysis also showed that the yield strength has an insignificant effect on the ultimate moment capacity of slender girders in this range. In this case, Equation 6.14 may also be used to compute the ultimate moment capacity, except that the critical stress at the compression flange is calculated as follows:

$$\frac{F_{cr}}{E} = \left(4566.1 - 111.7\ \lambda_f - 17.166\ \lambda_w + 0.4285\ \lambda_f \lambda_w + 0.3763\ \lambda_f^2 \right) 10^{-6} \qquad (6.17)$$

(ii) $\lambda_{wr} \leq \lambda_w \leq \lambda_{wh}$

As discussed in Section 6.3.2 and Chapter 5, the strain distribution along the web of these girders was nonlinear in this range. Thus, the stress distribution shown in Figure 6.1(b) can be used to compute their ultimate moment capacity. The effective width of the web (h_e) can be obtained from Equation 6.10, while the other terms, shown in Figure 6.1(b), are computed as follows:

$$\frac{F_{cr}}{E} = \left(165 - 0.584\ \lambda_f - 0.1726\ \lambda_w + 0.0046\ \lambda_f\ \lambda_w - 0.0522\ \lambda_f^2 \right) 10^{-5} \qquad (6.18)$$

and

$$\frac{F_t}{E} = \left(162.71 - 1.324\ \lambda_f - 0.1789\ \lambda_w + 0.00507\ \lambda_f\ \lambda_w - 0.0445\ \lambda_f^2 \right) 10^{-5} \qquad (6.19)$$

where,

F_t = tensile stress at the tension flange mid-section.

The finite element analysis showed that the yield strength of the steel has an insignificant effect on the ultimate moment capacity of the girders in this range, as shown in Table 6.3. In this table, results for the ultimate moment capacity of girders obtained from the finite element analysis using two different yield strengths (F_{yf} =330 MPa and 500 MPa) are presented.

(iii) $\lambda_{wp} < \lambda_w < \lambda_{wr}$

A linear transition is used to compute the ultimate moment capacity of slender girders whose

λ_w ratios are in this range, as follows:

$$M_u = M_{sr} + \left(M_{sp} - M_{sr} \right) \left(\frac{\lambda_{wr} - \lambda_w}{\lambda_{wr} - \lambda_{wp}} \right) \leq M_y \qquad (6.20)$$

where,

M_{sp} = ultimate moment capacity when $\lambda_w = \lambda_{wp}$; and

M_{sr} = ultimate moment capacity when $\lambda_w = \lambda_{wr}$;

In the range of parameters considered in this study, the effective width of the compression flange (b_e), shown in Figure 6.1, can be calculated according to the information provided in Section 6.3.1.

6.2.4 Proposed Lower Limits for Class 4 Sections

Values of the web height-to-thickness ratio (λ_w) and the flange width-to-thickness ratio (λ_f) for which a girder can reach its yielding moment capacity (M_y) before any local buckling takes place are defined in the current S16.1-94 Standard as Class 4 limits. They are given as functions of the yield strength only. The results from the present study indicate that these limits should also reflect the interactive effect between the local buckling of the compression flange and the local buckling of the web. The proposed design model is used to develop such limits and they are shown in Figure 6.4. Thus a compression flange is Class 4 if $\lambda_f \geq \lambda_{fe}$ and $\lambda_w \geq \lambda_{wl}$.

For girders with $\sqrt{F_{yf}/E}$ between 0.0373 and 0.0411, an interaction equation is used to determine the lower limit of the web height-to-thickness ratio (λ_w) if the flange width-to-

thickness ratio (λ_f) is lower than λ_{fe}.

Thus, for $\lambda_{fl} \leq \lambda_f < \lambda_{fe}$ and $0.0373 \leq \sqrt{F_{yf}/E} \leq 0.0411$:

$$\lambda_w \geq 175 - 1.226\,\lambda_f - 0.095\,\lambda_f^2 \geq \lambda_{wl} \qquad (6.21)$$

A web is classified as Class 4 web if $\lambda_w \geq \lambda_{we}$ and $\lambda_f \geq \lambda_{fe}$. For girders with $\lambda_{fl} \leq \lambda_f < \lambda_{fe}$ a web is classified as Class 4 if $\lambda_w \geq \lambda_{wr}$.

6.3 EVALUATION OF THE CURRENT STANDARDS AND SPECIFICATIONS USING THE PROPOSED DESIGN MODEL

The discussion that follows focuses on the results obtained through various standards and specifications as well as the proposed design model for the ultimate moment capacity of slender girders. The results are presented in Tables 6.1 and 6.2. For comparison purposes, the computed ultimate moment capacity is examined as a function of three ranges of b/2t: low (b/2t $\approx$ 12.5), intermediate (b/2t $\approx$ 16.8) and high (b/2t $\approx$ 21.8) and is also compared to experimental results.

The results shown in Table 6.2 demonstrate that there is an excellent agreement between the ultimate moment capacities computed according to the proposed design model and those obtained experimentally ($0.954 \leq M_{MOD}/M_{exp} \leq 1.042$).

Using an average yield strength of 330 MPa, the ultimate moment capacities of the specimens computed according to the S16.1-94 Standard and according to the ECCS-86 Recommendations, are also in good agreement with the experimental results ($0.89 \leq M_{CSA}/M_{exp} \leq 1.092$ and $0.913 \leq M_{ECCS}/M_{exp} \leq 1.122$).

The ultimate moment capacities computed according to the S16.1-94 Standard and the ECCS-86 Recommendations, are significantly affected by the yield strength, for all values of flange and web dimensions, as shown in Table 6.3. This table lists the ultimate moment capacities, computed according to various standards and specifications, as well as those computed through the finite element model, using two different yield strengths of the steel (F_{yf} = 330 MPa and 500 MPa). According to the finite element analysis, the yield strength of the compression flange does not affect the ultimate moment capacity of girders with $\lambda_w \geq \lambda_{wr}$ and $\lambda_f \geq \lambda_{fl}$ or with $\lambda_w \geq \lambda_{we}$ and $\lambda_f \geq \lambda_{fe}$, as discussed in Section 6.2 and shown in Table 6.3.

Table 6.4 lists the ratios of the ultimate moment capacities of girders with a yield strength of 330 MPa (M_{y330}) to the ultimate moment capacities of girders with a yield strength of 500 MPa (M_{y500}). This table shows that the M_{y330} /M_{y500} ratio is almost equal to one according to the finite element analysis, while it ranges from 0.76 to 0.79 according to the S16.1-94 Standard and the ECCS-86 Recommendations, indicating that these design guides would give unconservative result in girders with high strength steel.

To verify the proposed model at high yield strengths, the results from an experimental program conducted by Johnson (1985) were used. Some of the results from Johnson's tests are given in Table 6.5. In these specimens, which failed by local buckling, the yield strength of the compression flanges ranged from 407 MPa to 437 MPa (59 ksi to 63.4 ksi), while the h/w ratio ranged from 200.8 to 245.2 and the b/2t ratio was kept constant at 15.5. According to the proposed model these ratios fall between λ_{wr} and λ_{wh} for the web and between λ_{fl} and λ_{fe} for the flange. As shown in Table 6.5, there is an excellent agreement between the ultimate moment capacities obtained through the proposed design model in this study and

those obtained by Johnson (1985) experimentally ($1.000 \leq M_{MOD}/M_{exp} \leq 1.045$). The computed ultimate moment capacities according to the S16.1-94 Standard and the ECCS-86 Recommendations are much higher than those obtained by Johnson (1985) experimentally ($1.154 \leq M_{CSA}/M_{exp} \leq 1.188$ and $1.189 \leq M_{ECCS}/M_{exp} \leq 1.225$).

The ratio between the ultimate moment capacities computed according to various standards and specifications as a function of those obtained through the finite element analysis for two values of yield strength are given in Table 6.6. It is evident in this table that there is a poor correlation between the results computed according to the S16.1-94 Standard and those computed according to the finite element model using a yield strength of 500 MPa ($1.017 \leq M_{CSA}/M_{FE} \leq 1.623$ and $1.061 \leq M_{ECCS}/M_{FE} \leq 1.626$).

The ultimate moment capacities according to the S16.1-94 Standard and the ECCS-86 Recommendations are also function of the flange width-to-thickness ratio (λ_f). As shown in Table 6.3, the capacity of the girder with $F_{yf} = 330$ MPa and $\lambda_w = 256.4$ computed according to the S16.1-94 Standard increased from 756 kN.m when $\lambda_f = 12.5$ to 922 kN.m when $\lambda_f = 34.4$. However, according to the finite element analysis, the capacity is not directly proportional to λ_f. For example, the capacity of the girder with $F_{yf} = 330$ MPa and $\lambda_w = 256.4$ increased from 733 kN.m when $\lambda_f = 12.5$ to a maximum value of 960 kN.m when $\lambda_f = 28.1$. After this value of λ_f, the capacity decreased as λ_f increased. Consequently, higher (M_{CSA}/M_{FE}) and higher (M_{ECCS}/M_{FE}) ratios were obtained at flange width-to-thickness ratios (λ_f) of 12.5 and 34.4 than those obtained at λ_f values of 21.9 and 28.1, as shown in Table 6.6. The main reason for the high M_{CSA}/M_{FE} and M_{ECCS}/M_{FE} ratios shown in Table 6.6 for $\lambda_f = 12.5$ and 34.4, is the omission in the S16.1-94 Standard and the ECCS-86 Recommendations of

the effect of the web-flange interaction, especially on the postbuckling strength of the compression flange.

The ultimate moment capacities computed according to the S16.1-94 Standard, the ECCS-86 Recommendations, the proposed design model and those obtained experimentally, in this study, are shown as functions of the h/w and the b/2t ratios in Figures 6.5(a) to 6.5(m). The average yield strength (330 MPa) and the average elastic modulus (214.8 GPa) obtained from testing standard tension coupons were used to obtain the results shown in these figures. As discussed earlier, there is good agreement between the ultimate moment capacities computed according to these standard and recommendations and those obtained experimentally for these specimens whose yield strength was 330 MPa. However, unconservative ultimate moment capacities are obtained for girders with flange widths of 200 mm ($\lambda_f = 12.5$) and 270 mm ($\lambda_f = 16.9$) when the h/w ratio exceeds 280, as shown in Figures 6.5(a) and 6.5(b). Unconservative results are also obtained for girders with web heights greater than 1000 mm ($h/w \geq 213.7$ or $\lambda_w \geq \lambda_{wr}$) when the b/2t ratio is lower than 15 or higher than 32, as shown in Figures 6.5(I) to 6.5(m).

The WSD-78 Specification yields unconservative estimates of the ultimate moment capacity of the specimens tested in this study by as much as 28%. This specification also gives unconservative estimation of the ultimate moment capacity of the specimens tested by Johnson (1985) by as much as 49.5%, as shown in Table 6.5. This high values of the ultimate moment capacities are a direct result of using a buckling coefficient of 0.7 for the compression flange. The postbuckling strength of the compression flange and the effect of web-flange interaction, however, are ignored in this specification.

The LRFD-86 Specification underestimates the ultimate moment capacity of the specimens with high b/2t ratio by as much as 29.4%, as shown in Table 6.2. At the same time, it overestimates the ultimate moment capacity of Johnson's specimens (1985) experimentally by as much as 14%, as shown in Tables 6.5. Unconservative estimates of the ultimate moment capacity of the girders with low b/2t ratios are also obtained when a yield strength of 500 MPa is used, as shown in Table 6.6. The reason for these unconservative results of the ultimate moment capacity of specimens with low b/2t ratios is the significant role that the yield strength plays in evaluating these capacities, as assumed by this specification regardless of the web dimensions, i.e. ignoring the web-flange interaction. The conservative estimation of the ultimate moment capacity of the specimens with high b/2t ratios is due to ignoring the postbuckling strength of the compression flange, which has a significant effect on the ultimate moment capacity in this range.

In both the WSD-89 and the LRFD-93 Specifications, a buckling coefficient for the compression flange is given as a function of the web height-to-thickness ratio (h/w) only, while this method gives reasonable results for girders with low b/2t ratios, the ultimate moment capacity of the specimens with high b/2t ratios are underestimated, as shown in Tables 6.2 and 6.6. This is due to the fact that the postbuckling strength of the compression flange is ignored. The provisions outlined in this specification are based on the test results obtained by Johnson (1985).

The results given in Tables 6.2 and 6.6 indicate that the ultimate moment capacity of the girders with low b/2t ratios computed according to the AISC Specifications (LRFD-86, LRFD-93, WSD-78 and WSD-89) depend on the yield strength level. The ultimate moment

capacity of the girders with high b/2t ratios is independed of the yield strength, regardless of the web dimensions.

The ultimate moment capacities computed according to the LRFD-86, the LRFD-93, the WSD-78, the WSD-89 Specifications and the proposed design model, along with those obtained experimentally are shown as functions of the h/w ratio and the b/2t ratio in Figures 6.6(a) to 6.6(m). A yield strength of 330 MPa and an elastic modulus of 214.8 GPa were used to obtain the results shown in these figures. The ultimate moment capacities computed according to the LRFD-86, the LRFD-93 and the WSD-89 Specifications are conservative, with respect to those calculated according to the proposed design model, except for low h/w and b/2t ratios, in the range of this study, as shown in Figures 6.6(a), 6.6 (h) and 6.6(i).

Table 6.1 Ultimate Design Moment Capacities as Functions of the Yield Moments

Specimen	h/w	b/2t*	M_u/M_y							
			CSA	ECCS	LRFD-86	LRFD-93	WSD-78	WSD-89	Prop. Model	Exp.
G1	170.8	12.5	0.868	0.892	0.855	0.832	0.966	0.842	0.796	0.795
G2	169.9	16.7	0.736	0.759	0.701	0.644	0.892	0.717	0.726	0.697
G3	172.6	21.8	0.612	0.636	0.502	0.410	0.755	0.443	0.643	0.652
G4	213.8	12.5	0.789	0.801	0.788	0.770	0.892	0.759	0.752	0.731
G5	212.3	16.8	0.720	0.735	0.669	0.616	0.846	0.647	0.721	0.719
G6	212.8	21.8	0.607	0.624	0.490	0.406	0.726	0.399	0.670	0.682
G7	253.3	21.6	0.746	0.752	0.712	0.712	0.800	0.674	0.703	0.740
G8	257.0	16.9	0.680	0.690	0.616	0.568	0.777	0.546	0.680	0.658
G9	257.2	21.9	0.588	0.600	0.464	0.387	0.685	0.354	0.640	0.657

*These dimensions refer to the compression flange.

Table 6.2 Ultimate Design Moment Capacities as Functions of the Experimental Capacities

Specimen	h/w	b/2t*	M_u/M_{exp}						
			CSA	ECCS	LRFD-86	LRFD-93	WSD-78	WSD-89	Prop. Model
G1	170.8	12.5	1.092	1.122	1.075	1.047	1.215	1.059	1.001
G2	169.9	16.7	1.056	1.089	1.006	0.924	1.280	1.029	1.042
G3	172.6	21.8	0.939	0.975	0.770	0.629	1.158	0.679	0.986
G4	213.8	12.5	1.079	1.096	1.078	1.053	1.220	1.038	1.029
G5	212.3	16.8	1.001	1.022	0.930	0.857	1.177	0.900	1.003
G6	212.8	21.8	0.890	0.915	0.718	0.595	1.065	0.585	0.982
G7	253.3	21.6	1.008	1.016	0.962	0.962	1.081	0.911	0.954
G8	257.0	16.9	1.033	1.048	0.936	0.863	1.181	0.830	1.036
G9	257.2	21.9	0.895	0.913	0.706	0.590	1.043	0.539	0.978

*These dimensions refer to the compression flange.

Table 6.3 Ultimate Design Moment Capacities Using Different Yield Strengths

h/w	b/2t	F_{yf} = 330 MPa							F_{yf} = 500 MPa						
		M_u (kN.m)							M_u (kN.m)						
		CSA	ECCS	LRFD-86	LRFD-93	WSD-78	WSD-89	F.E.	CSA	ECCS	LRFD-86	LRFD-93	WSD-78	WSD-89	F.E.
138.9	21.9	456	476	341	279	523	334	551	586	611	341	279	608	334	576
138.9	28.1	474	499	256	210	457	251	489	604	637	256	210	457	251	489
170.9	21.9	567	587	434	355	665	386	608	728	754	434	351	764	386	608
170.9	28.1	589	616	324	265	579	289	570	751	786	324	265	579	289	585
213.6	12.5	624	633	610	597	687	587	604	821	833	775	735	951	753	622
213.6	21.9	716	735	561	464	836	456	840	919	945	561	464	959	456	825
213.6	28.1	744	772	420	344	740	337	788	947	985	420	344	740	337	798
256.4	12.5	756	763	670	700	784	662	733	999	1004	880	858	1070	832	724
256.4	21.9	868	885	671	559	991	513	930	1114	1137	671	559	1133	513	930
256.4	28.1	900	929	522	428	886	386	960	1144	1185	522	428	886	386	972
256.4	34.4	922	959	411	337	725	304	774	1167	1218	411	337	725	304	774
299.1	12.5	890	894	740	779	823	692	724	1175	1177	916	948	1100	843	724
299.1	21.9	1018	1035	764	640	1117	554	1140	1307	1331	764	640	1273	554	1140
299.1	28.1	1057	1086	606	508	1017	434	1140	1347	1386	606	508	1017	434	1152
299.1	34.4	1083	1121	494	404	840	340	983	1371	1425	494	404	840	340	983

Table 6.4 Effect of Yield Strength of Flanges on the Ultimate Design Moment Capacity

h/w	b/2t	M_{y330}/M_{y500}						
		CSA	ECCS	LRFD-86	LRFD-93	WSD-78	WSD-89	F.E.
138.9	21.9	0.778	0.779	1.000	1.000	0.860	1.000	0.957
138.9	28.1	0.785	0.783	1.000	1.000	1.000	1.000	1.000
170.9	21.9	0.779	0.779	1.000	1.011	0.870	1.000	1.000
170.9	28.1	0.784	0.784	1.000	1.000	1.000	1.000	1.000
213.6	12.5	0.760	0.760	0.787	0.812	0.722	0.780	0.971
213.6	21.9	0.779	0.778	1.000	1.000	0.872	1.000	1.018
213.6	28.1	0.786	0.784	1.000	1.000	1.000	1.000	0.987
256.4	12.5	0.757	0.760	0.761	0.816	0.732	0.796	1.012
256.4	21.9	0.779	0.778	1.000	1.000	0.875	1.000	1.000
256.4	28.1	0.787	0.784	1.000	1.000	1.000	1.000	0.988
256.4	34.4	0.790	0.787	1.000	1.000	1.000	1.000	1.000
299.1	12.5	0.757	0.760	0.808	0.822	0.748	0.821	1.000
299.1	21.9	0.779	0.778	1.000	1.000	0.877	1.000	1.000
299.1	28.1	0.785	0.784	1.000	1.000	1.000	1.000	0.990
299.1	34.4	0.790	0.787	1.000	1.000	1.000	1.000	1.000

Table 6.5 Ultimate Moment Capacities of Slender Girders Tested by Johnson (1985)

Specimen	(h/w)	(b/2t)	F_{yf} (MPa)	M_u/M_y							M_u/M_{exp}					
				CSA	ECCS	LRFD	WSD-78	WSD-89	Prop. Model	Exp.	CSA	ECCS	LRFD	WSD-78	WSD-89	Prop. Model
J2	245.2	15.5	428	0.637	0.654	0.605	0.786	0.523	0.550	0.550	1.154	1.189	1.100	1.429	0.951	1.000
J4	236.0	15.4	407	0.655	0.672	0.631	0.808	0.571	0.585	0.564	1.161	1.191	1.119	1.432	1.012	1.037
J5	203.4	15.5	427	0.656	0.680	0.635	0.829	0.592	0.582	0.557	1.183	1.221	1.140	1.488	1.063	1.045
J6	200.8	15.5	437	0.656	0.676	0.628	0.825	0.585	0.572	0.552	1.188	1.225	1.138	1.495	1.059	1.036

Table 6.6 Ultimate Design Moment Capacities as Functions of the Finite Element Capacities

h/w	b/2t	F_{yf} = 330 MPa						F_{yf} = 500 MPa					
		M_u/M_{FE}						M_u/M_{FE}					
		CSA	ECCS	LRFD-86	LRFD-93	WSD-78	WSD-89	CSA	ECCS	LRFD-86	LRFD-93	WSD-78	WSD-89
138.9	21.9	0.828	0.864	0.619	0.506	0.949	0.606	1.017	1.061	0.592	0.484	1.056	0.580
138.9	28.1	0.969	1.020	0.524	0.429	0.935	0.513	1.235	1.303	0.524	0.429	0.953	0.513
170.9	21.9	0.933	0.965	0.714	0.583	1.094	0.635	1.197	1.240	0.714	0.577	1.257	0.635
170.9	28.1	1.033	1.063	0.568	0.465	1.016	0.507	1.284	1.343	0.554	0.453	0.990	0.494
213.6	12.5	1.033	1.048	1.010	0.988	1.137	0.972	1.320	1.339	1.246	1.182	1.529	1.211
213.6	21.9	0.852	0.875	0.668	0.552	0.995	0.543	1.114	1.145	0.680	0.562	1.162	0.553
213.6	28.1	0.944	0.980	0.533	0.437	0.939	0.427	1.187	1.234	0.526	0.431	0.927	0.422
256.4	12.5	1.031	1.041	0.914	0.955	1.070	0.903	1.380	1.387	1.215	1.185	1.478	1.149
256.4	21.9	0.933	0.952	0.722	0.601	1.065	0.552	1.198	1.223	0.722	0.601	1.218	0.552
256.4	28.1	0.938	0.968	0.544	0.446	0.923	0.402	1.177	1.219	0.537	0.440	0.912	0.397
256.4	34.4	1.191	1.239	0.531	0.435	0.937	0.393	1.508	1.574	0.531	0.435	0.937	0.393
299.1	12.5	1.229	1.235	1.022	1.076	1.137	0.956	1.623	1.626	1.265	1.309	1.519	1.164
299.1	21.9	0.947	0.908	0.670	0.561	0.980	0.486	1.146	1.168	0.670	0.561	1.117	0.486
299.1	28.1	0.927	0.953	0.532	0.446	0.892	0.381	1.169	1.203	0.526	0.441	0.883	0.377
299.1	34.4	1.102	1.139	0.503	0.411	0.855	0.346	1.395	1.450	0.503	0.411	0.855	0.360

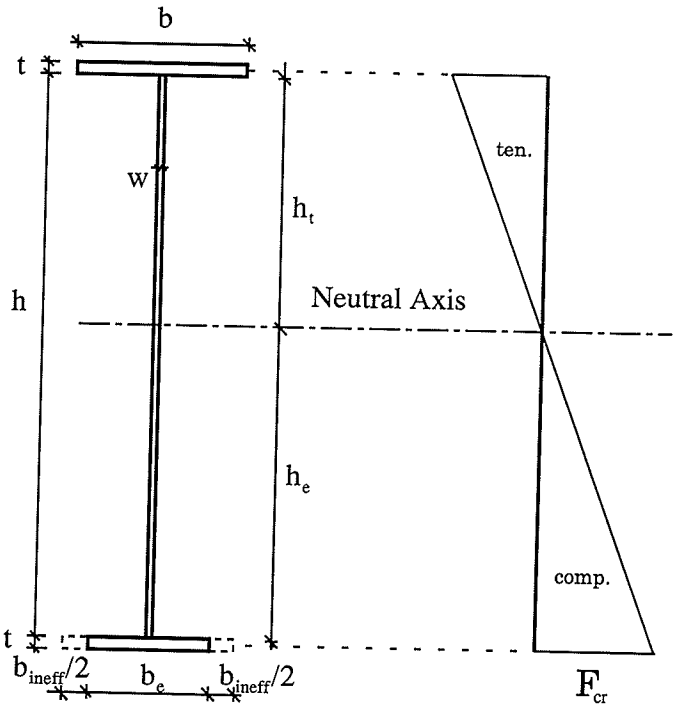

(a) Gross Web

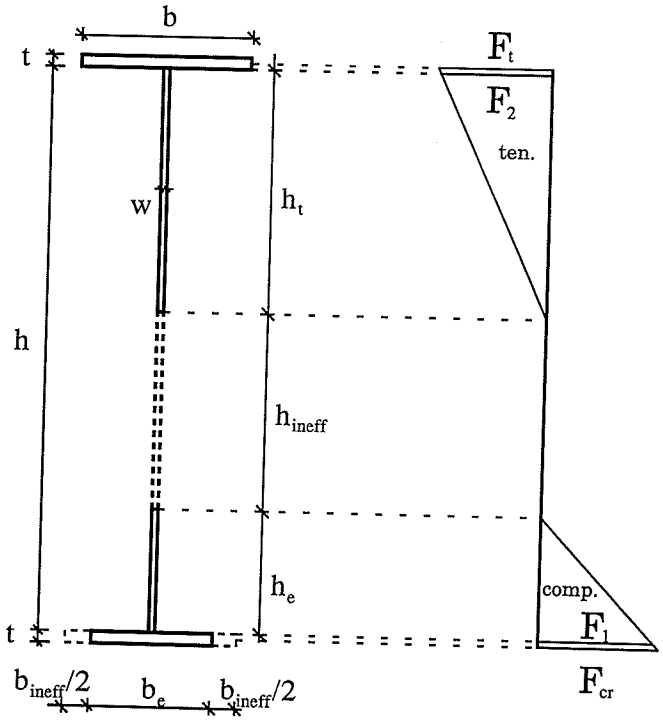

(b) Effective Web

Figure 6.1 Stress Distribution According to the Proposed Design Model

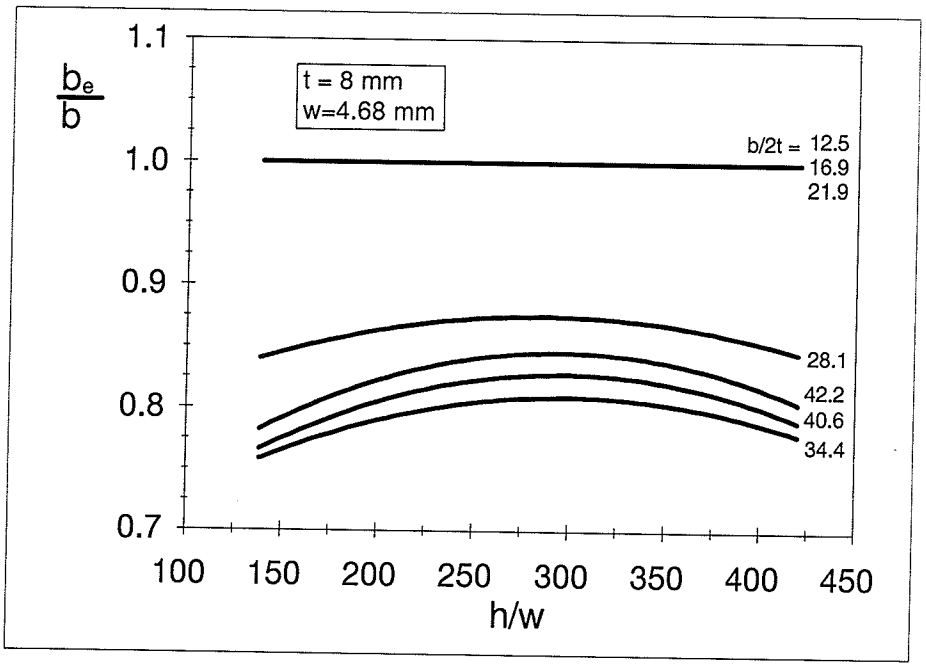

Figure 6.2(a) Effect of h/w on the Effective Width of Compression Flange

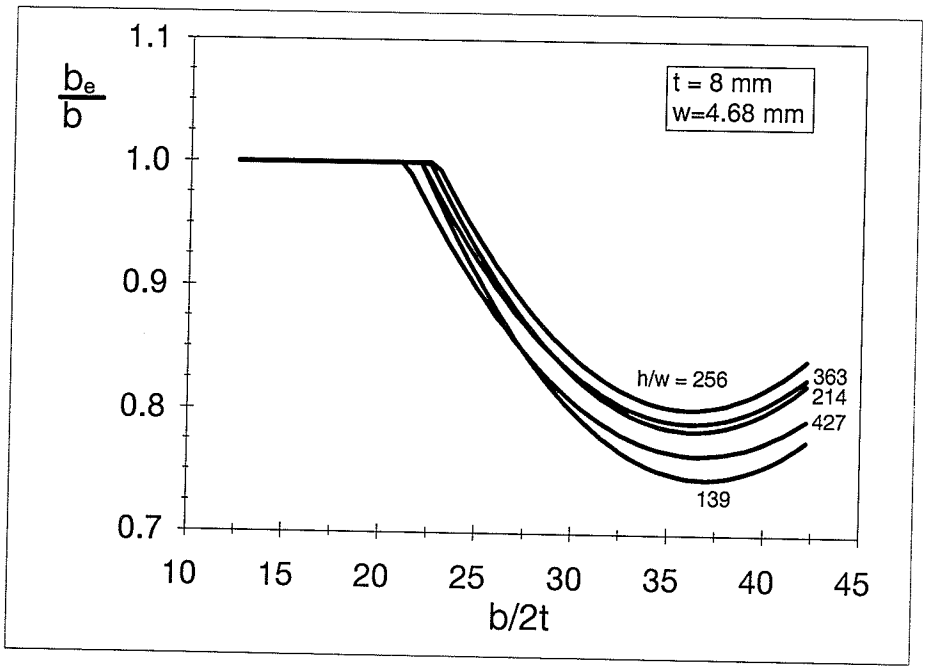

Figure 6.2(b) Effect of b/2t on the Effective Width of Compression Flange

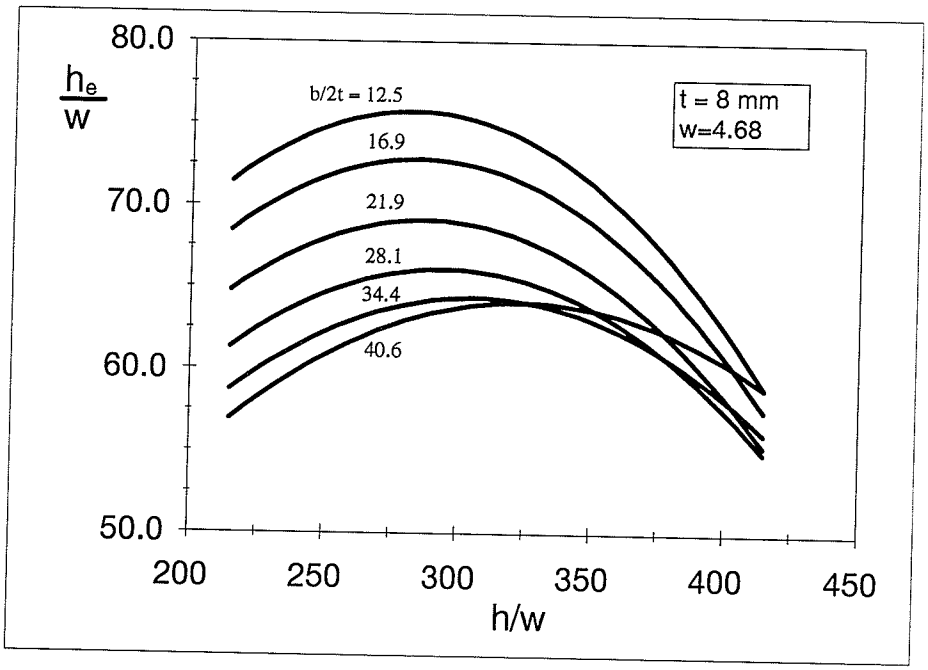

Figure 6.3(a) Effect of h/w on the Web Effective Width in Compression

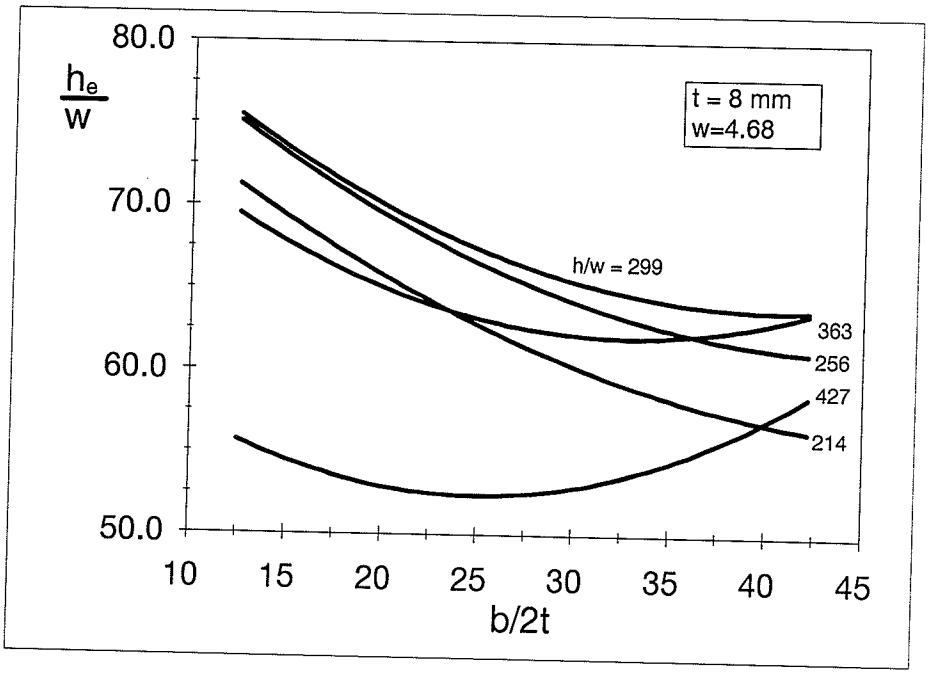

Figure 6.3(a) Effect of b/2t on the Web Effective Width in Compression

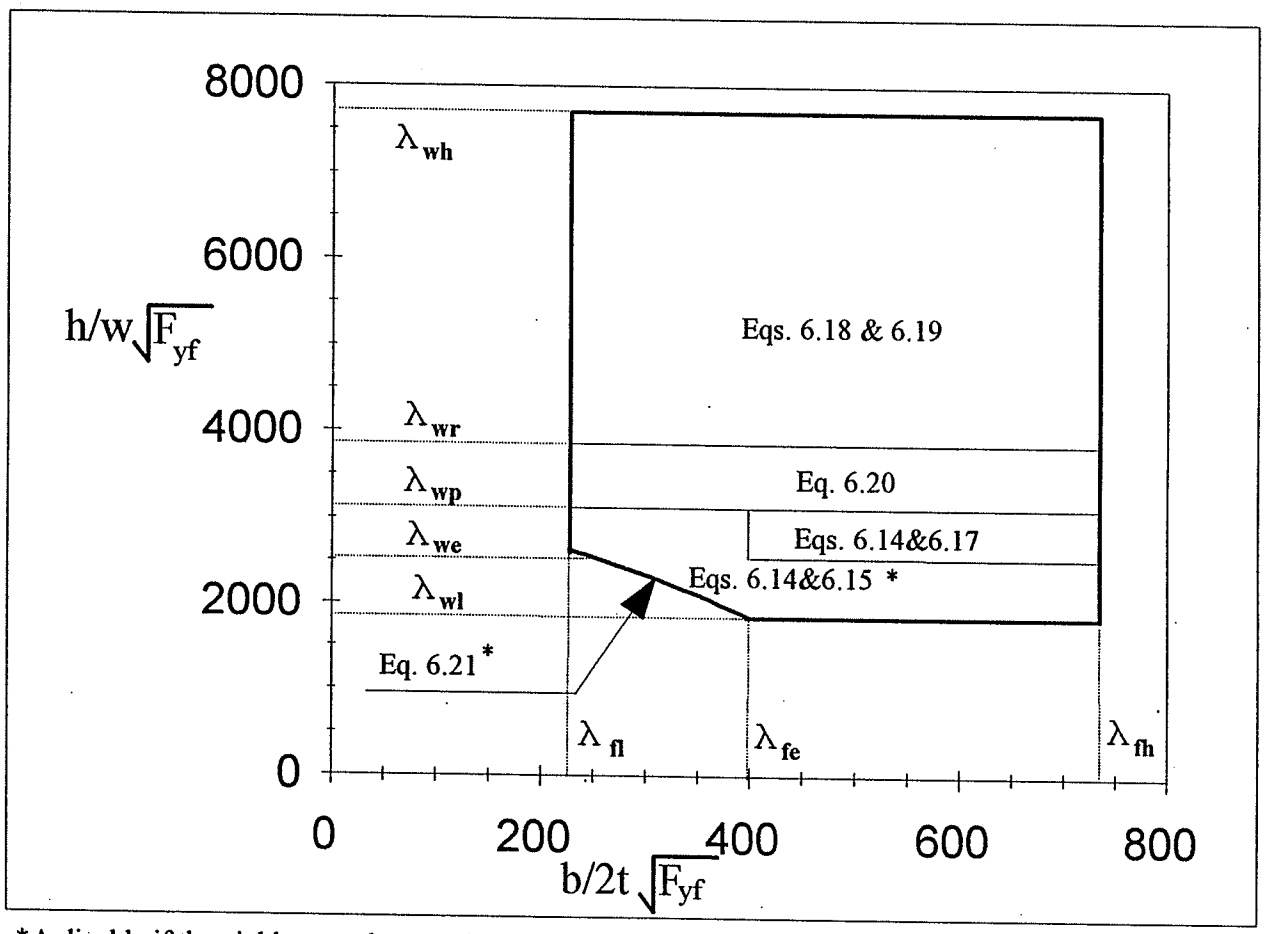

*Aplicable if the yield strength range is between 300 and 360 MPa

Figure 6.4 Class 4 Limits and Design Model Ranges

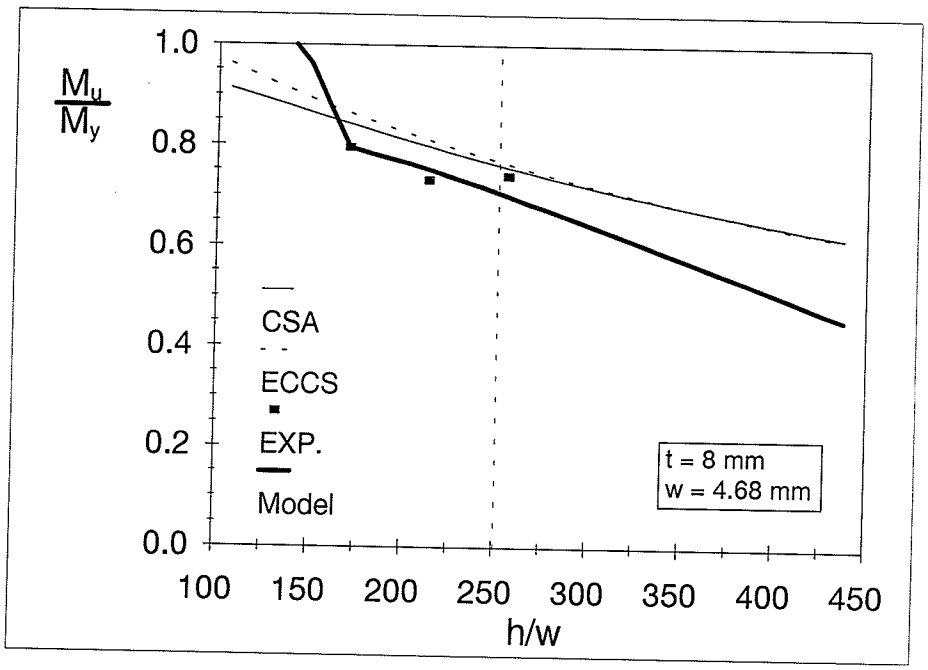

(a) 200-mm Flange Width

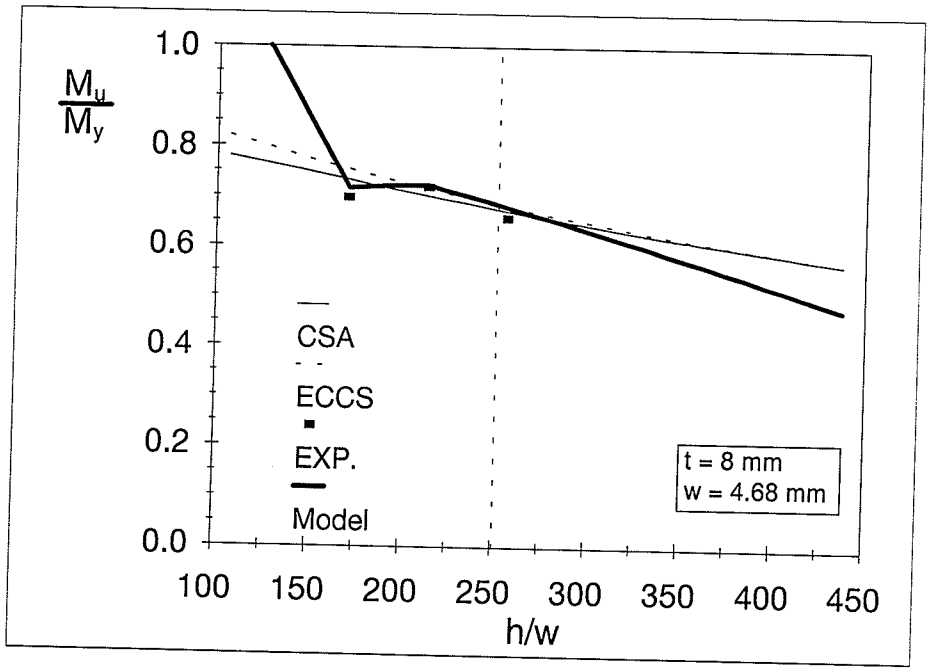

(b) 270-mm Flange Width

Figure 6.5 Comparison Between the CAN/CSA-S16.1-94 Standard (1994), the ECCS Recommendations (1986) and the Proposed Design Model

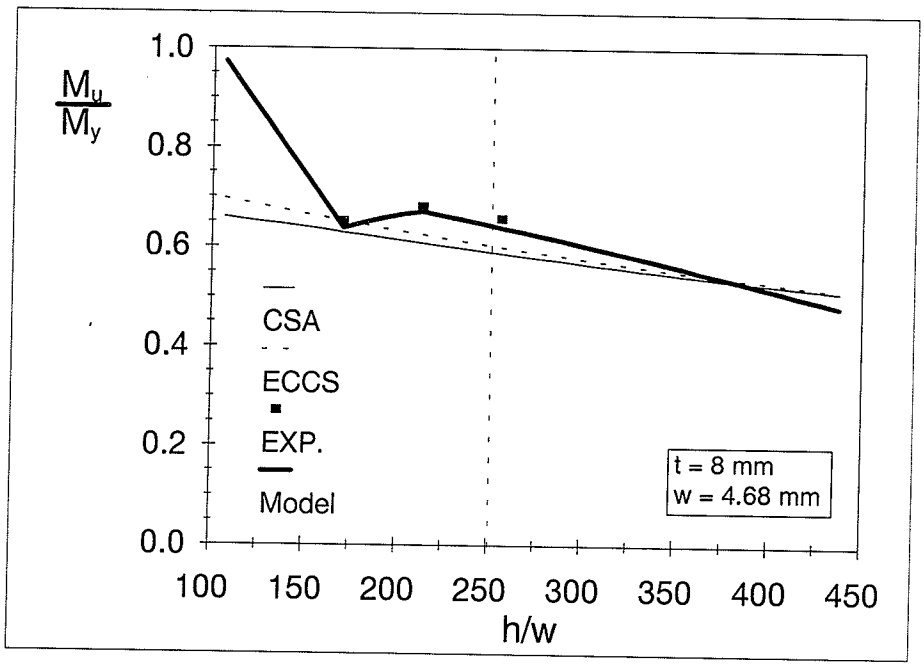

(c) 350-mm Flange Width

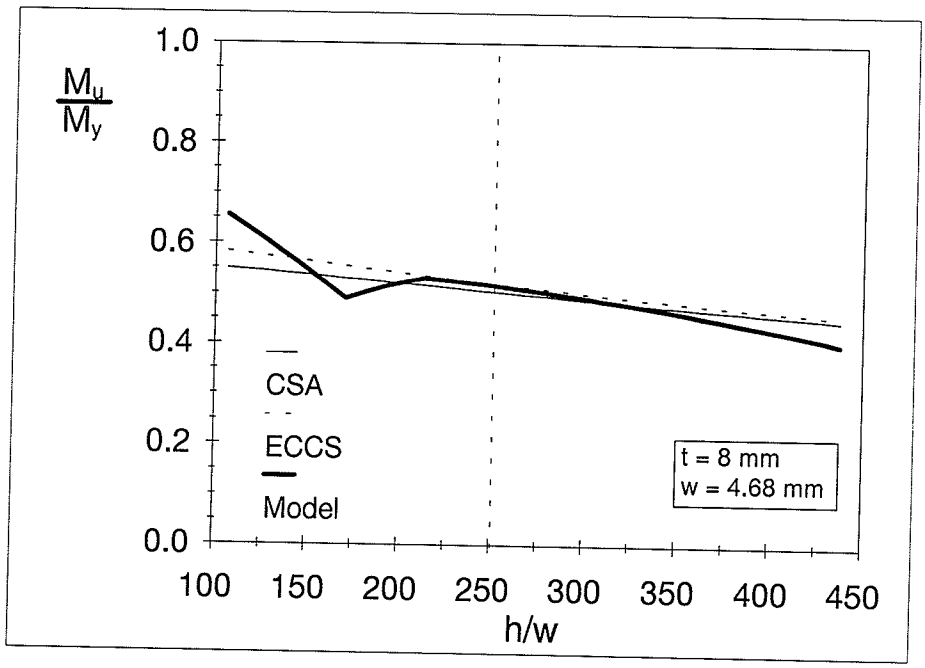

(d) 450-mm Flange Width

Figure 6.5 Comparison Between the CAN/CSA-S16.1-94 Standard (1994), the ECCS Recommendations (1986) and the Proposed Design Model

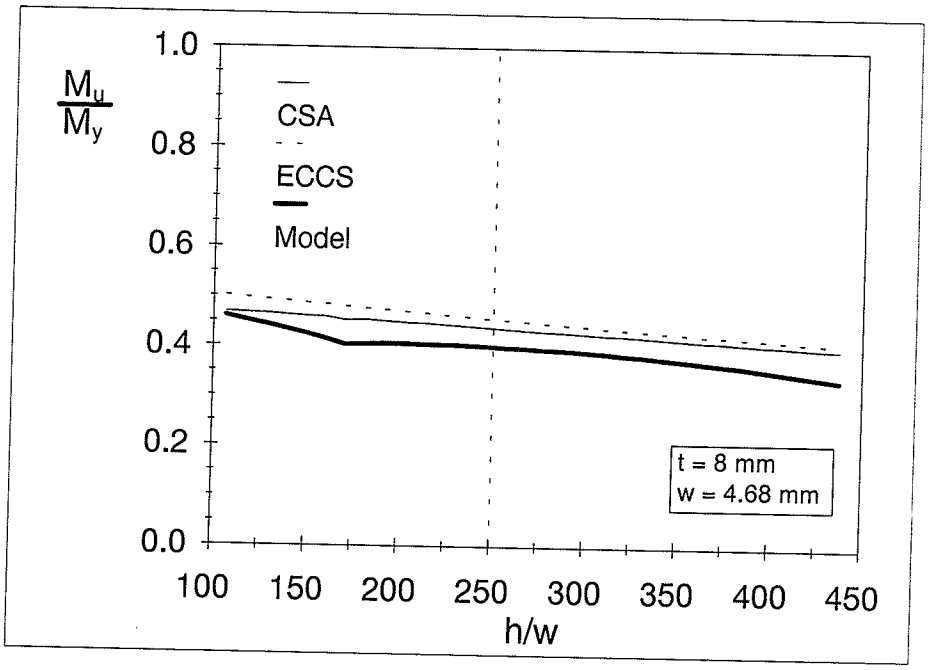

(e) 550-mm Flange width

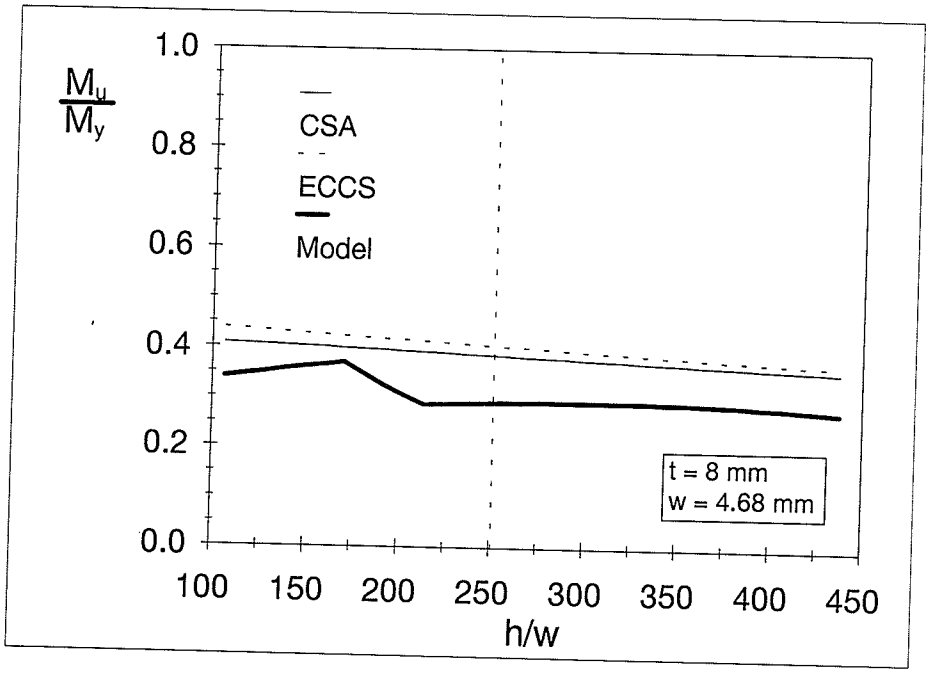

(f) 650-mm Flange Width

Figure 6.5 Comparison Between the CAN/CSA-S16.1-94 Standard (1994), the ECCS Recommendations (1986) and the Proposed Design Model

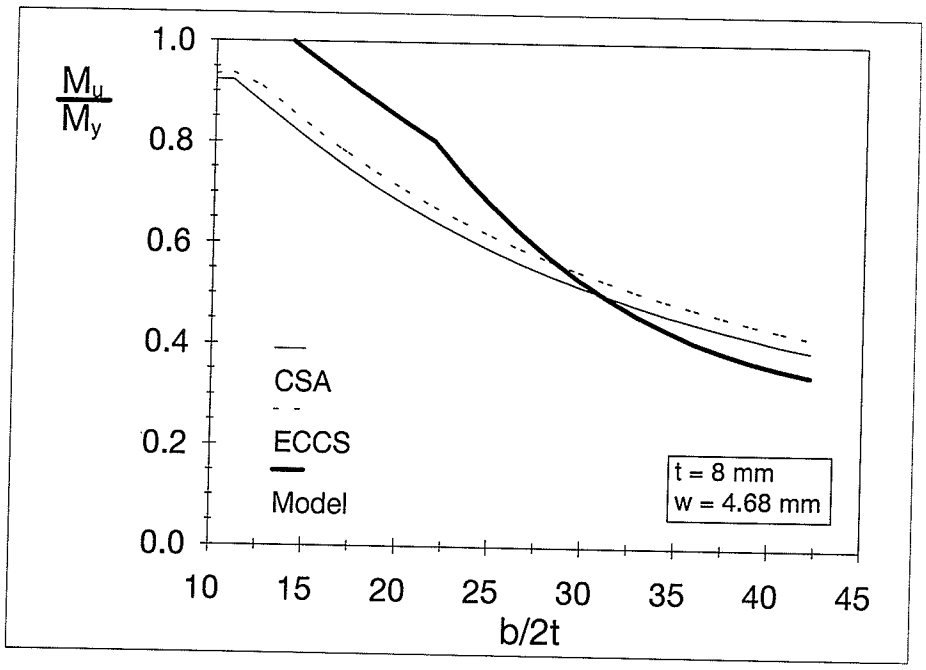

(g) 650-mm Web Height

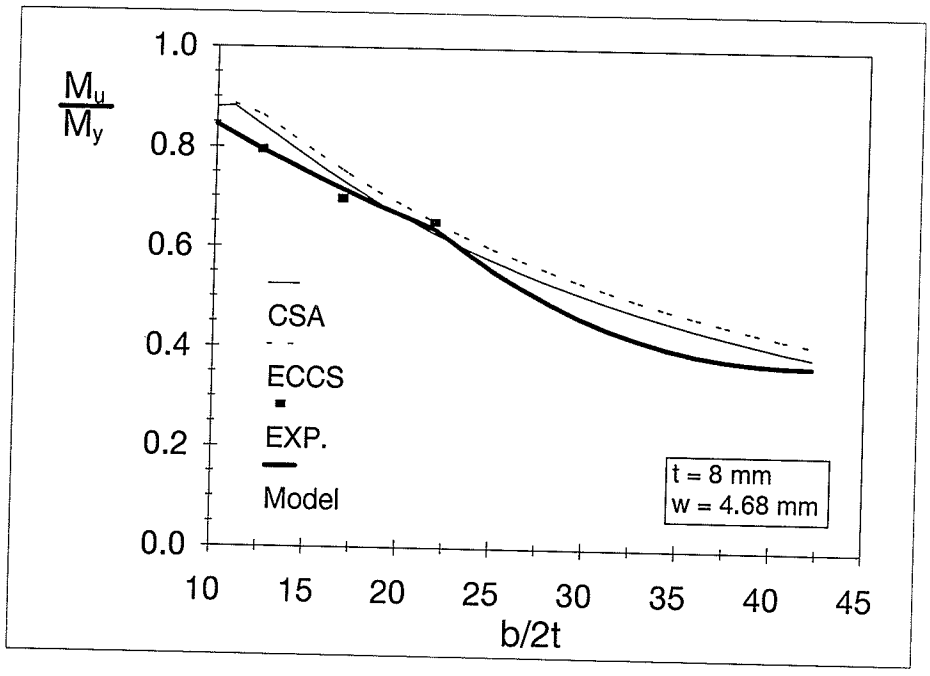

(h) 800-mm Web Height

Figure 6.5 Comparison Between the CAN/CSA-S16.1-94 Standard (1994), the ECCS Recommendations (1986) and the Proposed Design Model

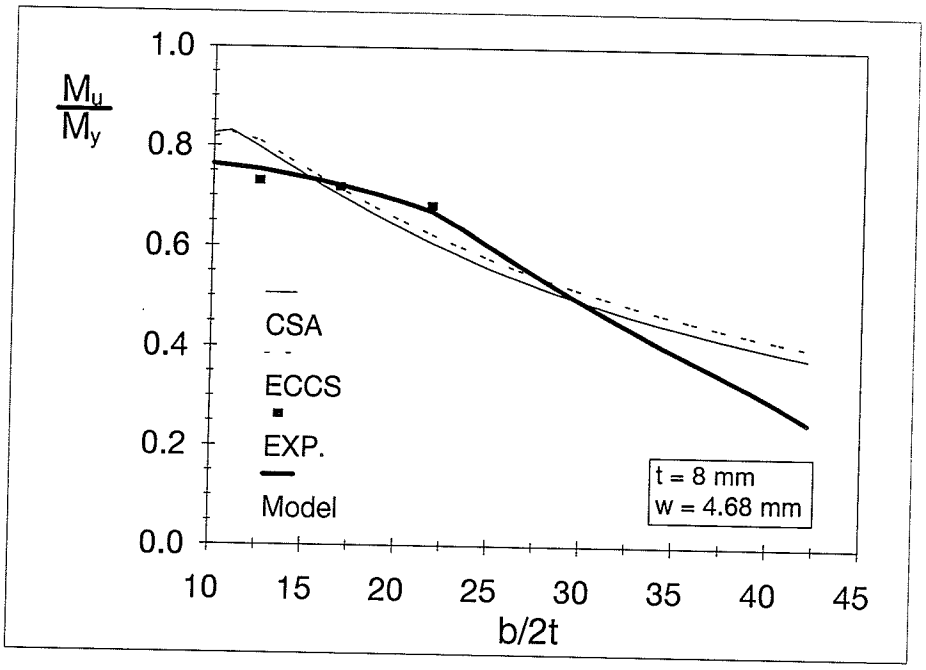

(i) 1000-mm Web Height

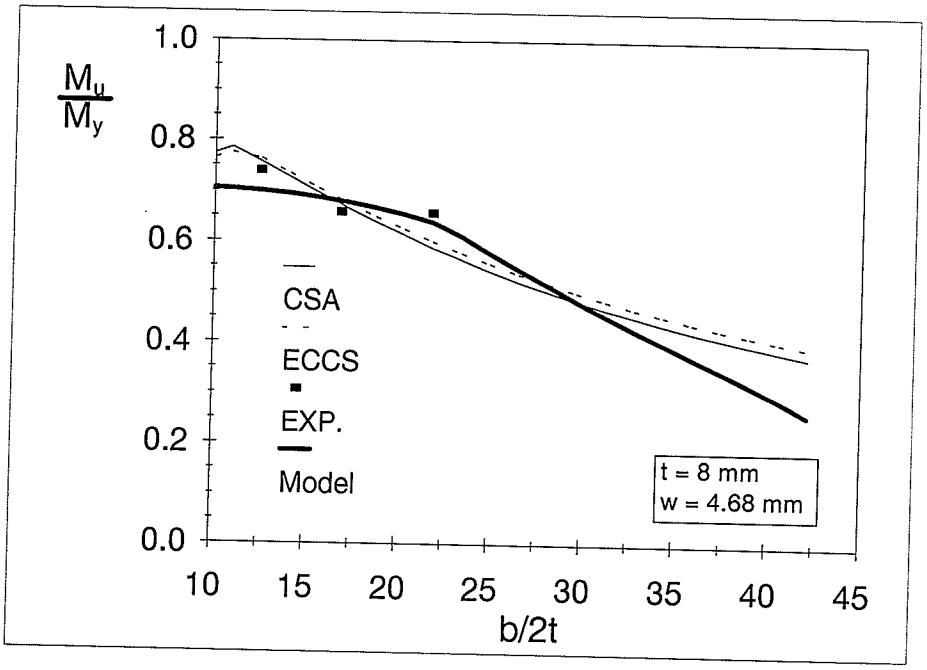

(j) 1200-mm Web Height

Figure 6.5 Comparison Between the CAN/CSA-S16.1-94 Standard (1994), the ECCS Recommendations (1986) and the Proposed Design Model

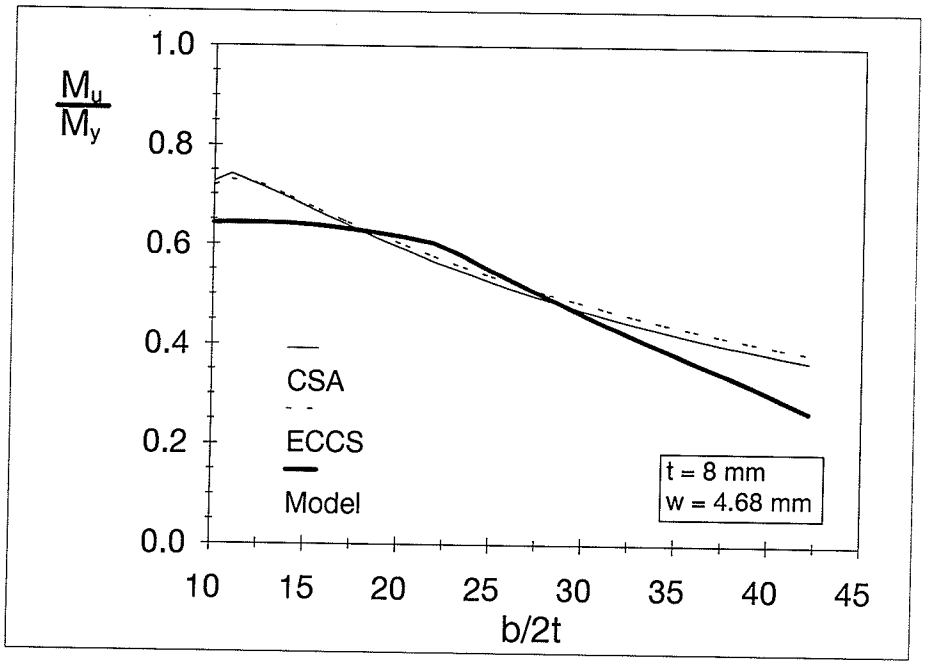

(k) 1400-mm Web Height

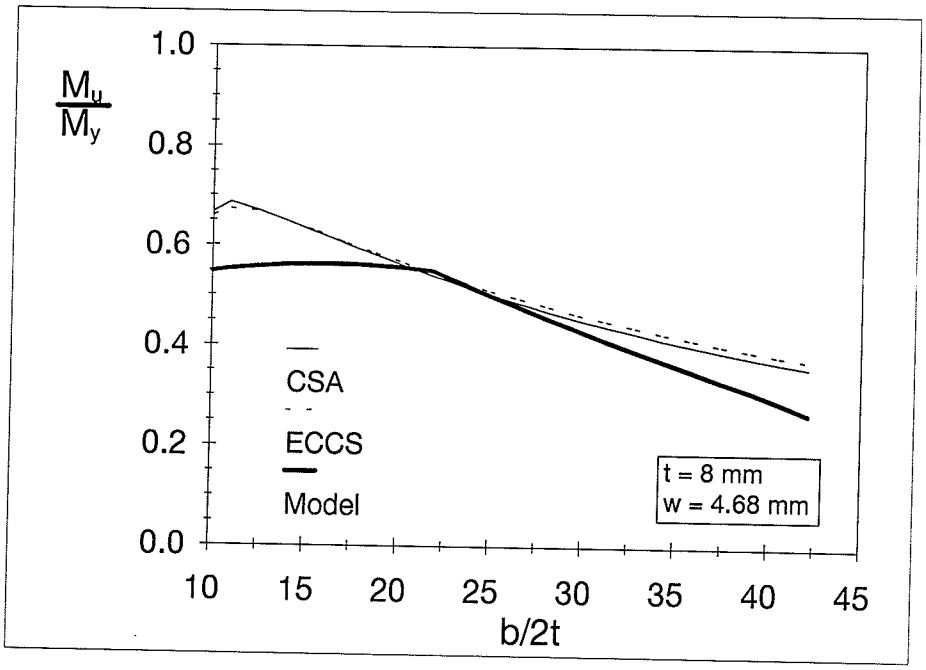

(l) 1700-mm Web Height

Figure 6.5 Comparison Between the CAN/CSA-S16.1-94 Standard (1994), the ECCS Recommendations (1986) and the Proposed Design Model

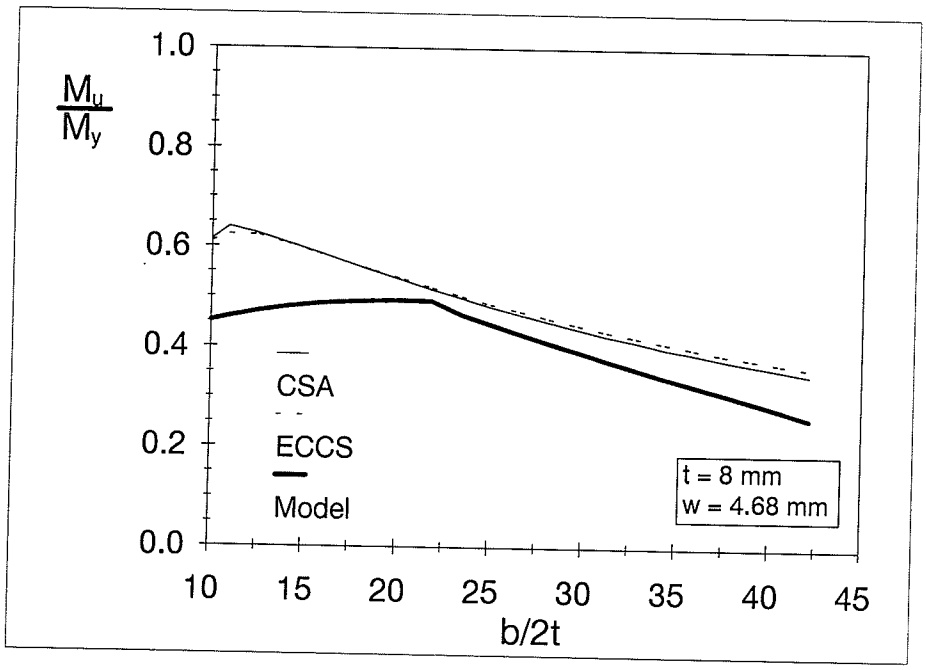

(m) 2000-mm Web Height

Figure 6.5 Comparison Between the CAN/CSA-S16.1-94 Standard (1994), the ECCS Recommendations (1986) and the Proposed Design Model

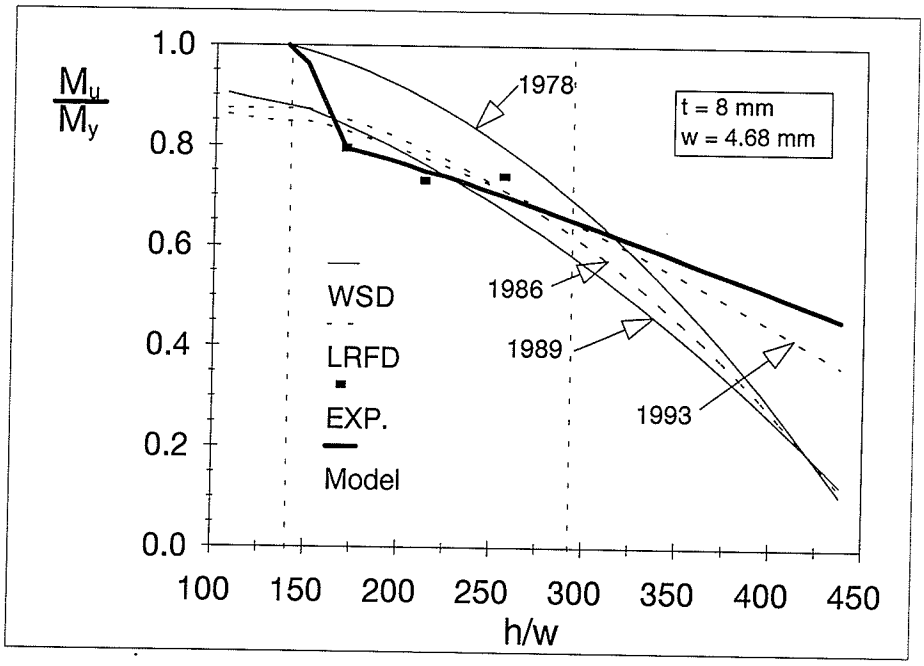

(a) 200-mm Flange Width

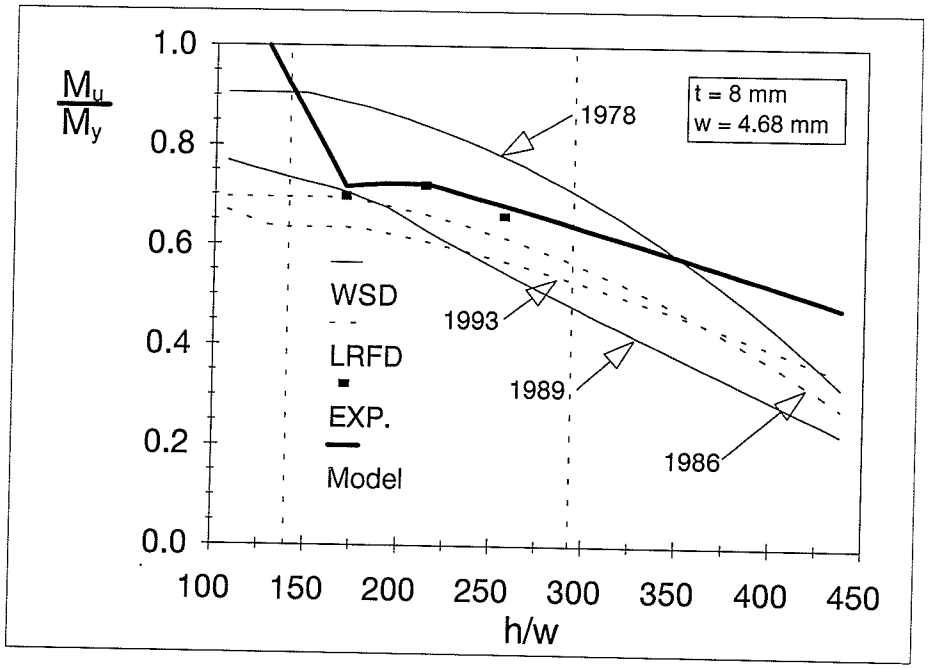

(b) 270-mm Flange Width

Figure 6.6 Comparison Between the AISC-LRFD (1986, 1993), the AISC-WSD (1978, 1989) Specifications and the Proposed Design Model

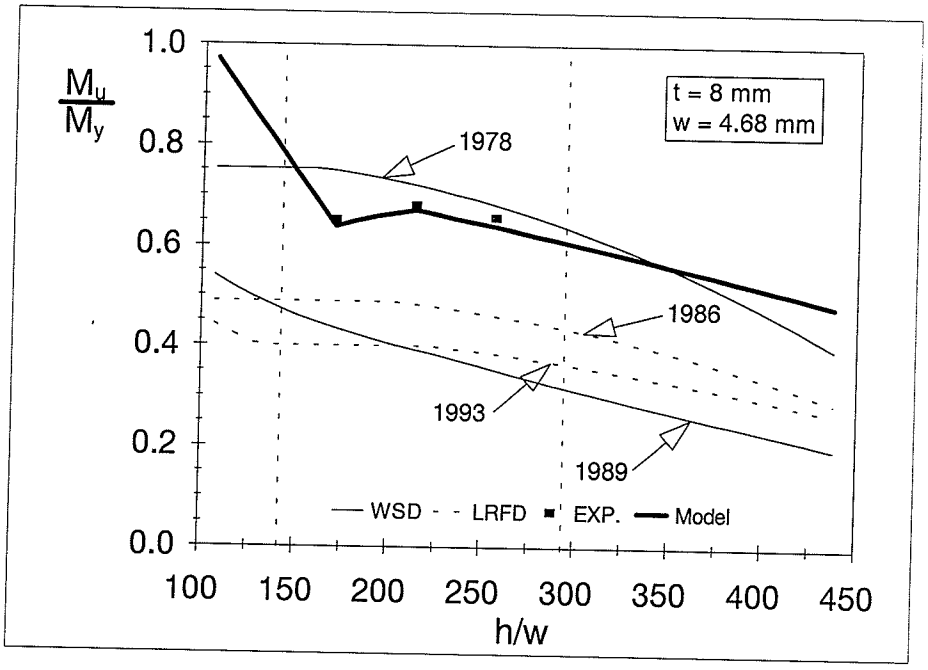

(c) 350-mm Flange Width

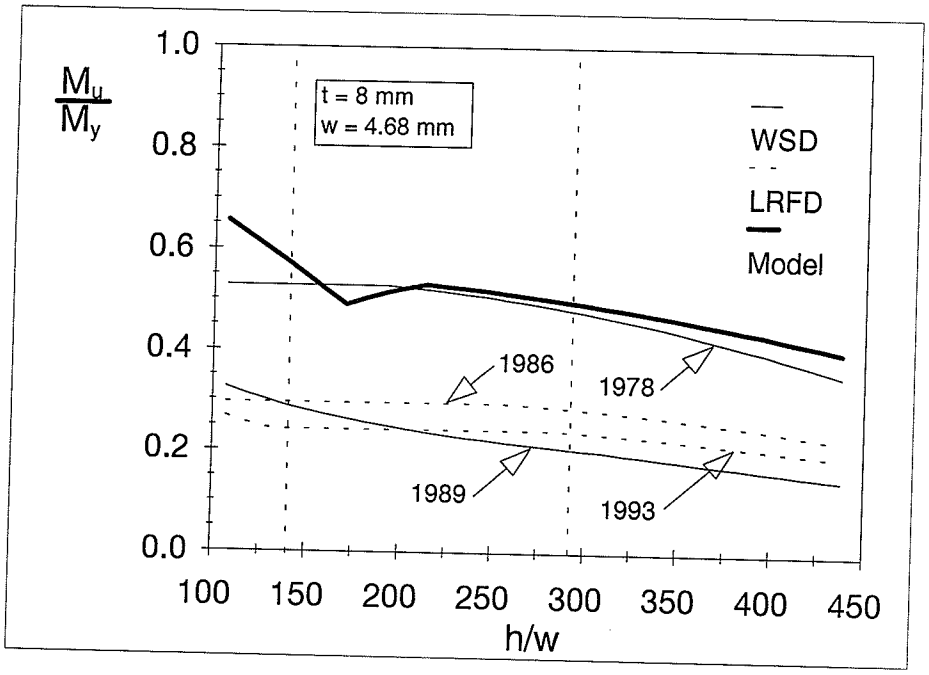

(d) 450-mm Flange Width

Figure 6.6 Comparison Between the AISC-LRFD (1986, 1993), the AISC-WSD (1978, 1989) Specifications and the Proposed Design Model

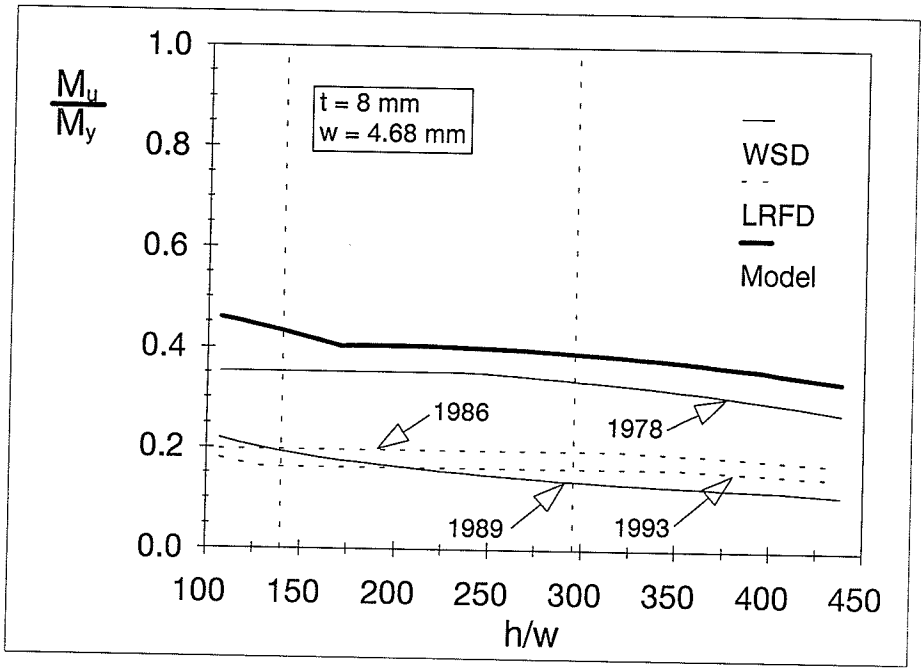

(e) 550-mm Flange Width

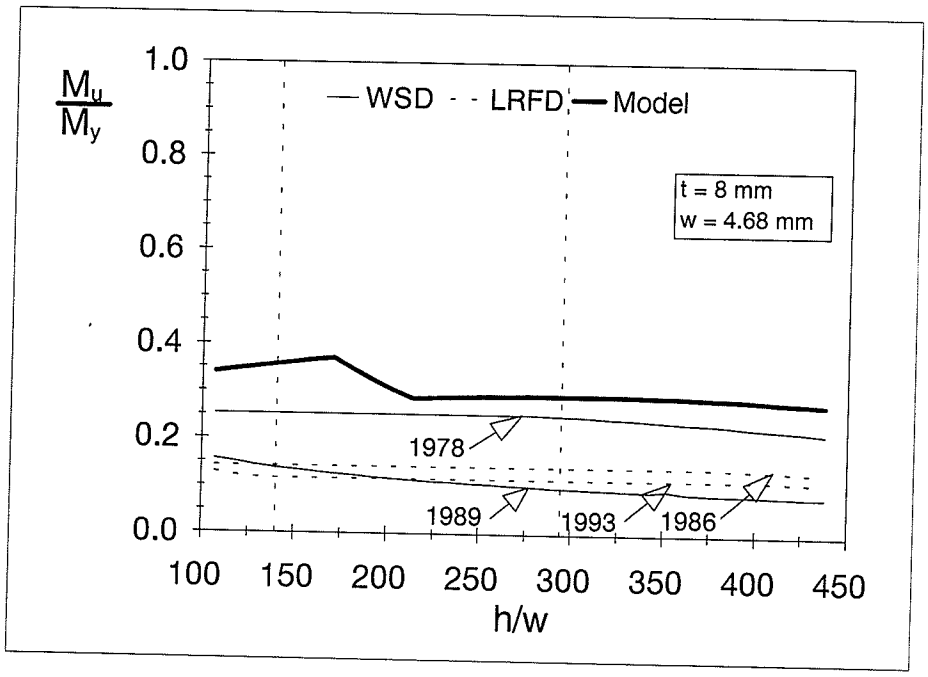

(f) 650-mm Flange Width

Figure 6.6 Comparison Between the AISC-LRFD (1986, 1993), the AISC-WSD (1978, 1989) Specifications and the Proposed Design Model

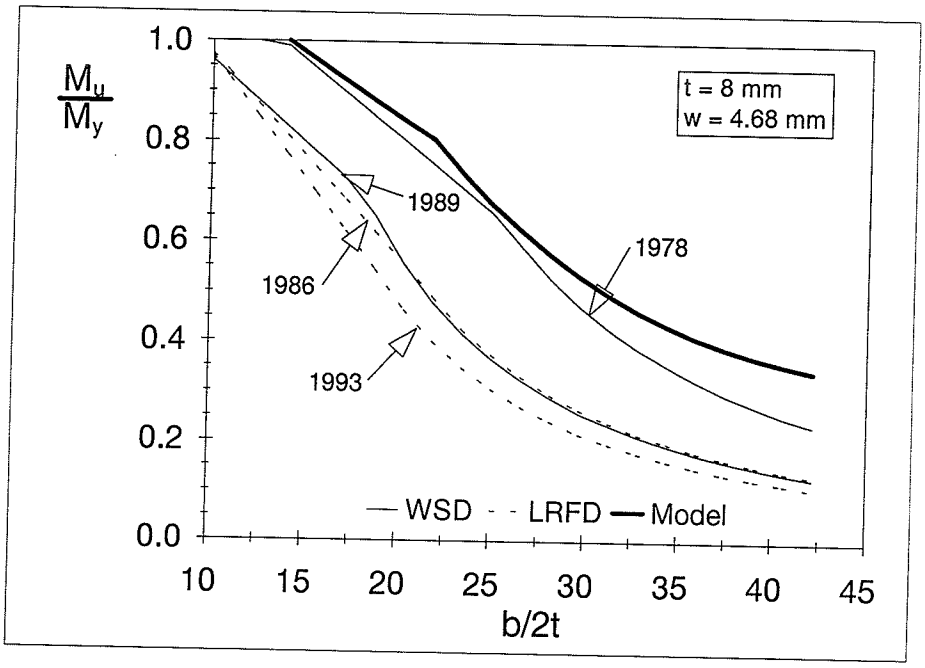

(g) 650-mm Web Height

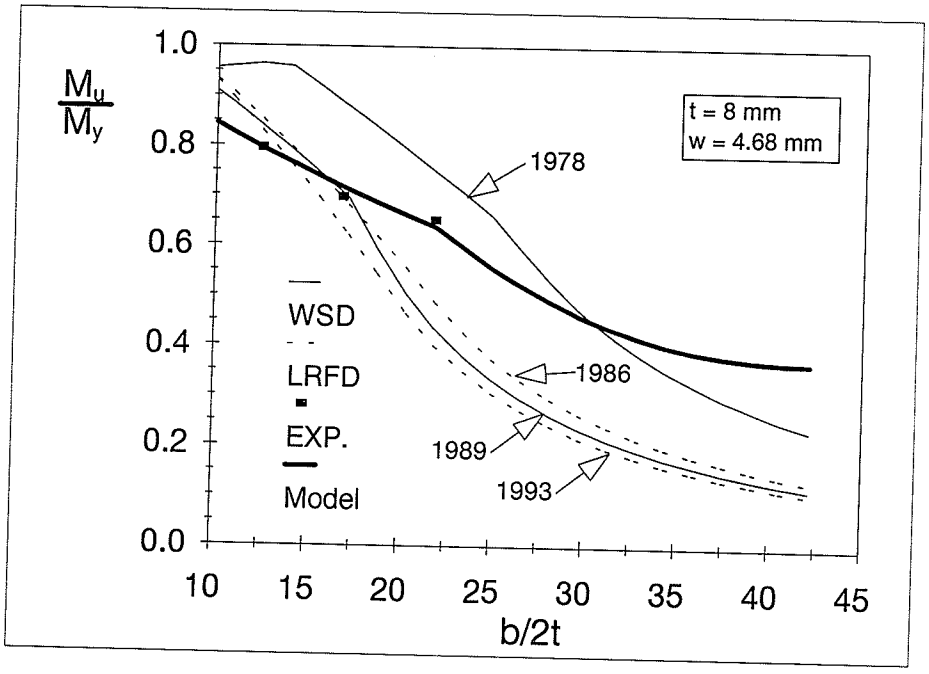

(h) 800-mm Web Height

Figure 6.6 Comparison Between the AISC-LRFD (1986, 1993), the AISC-WSD (1978, 1989) Specifications and the Proposed Design Model

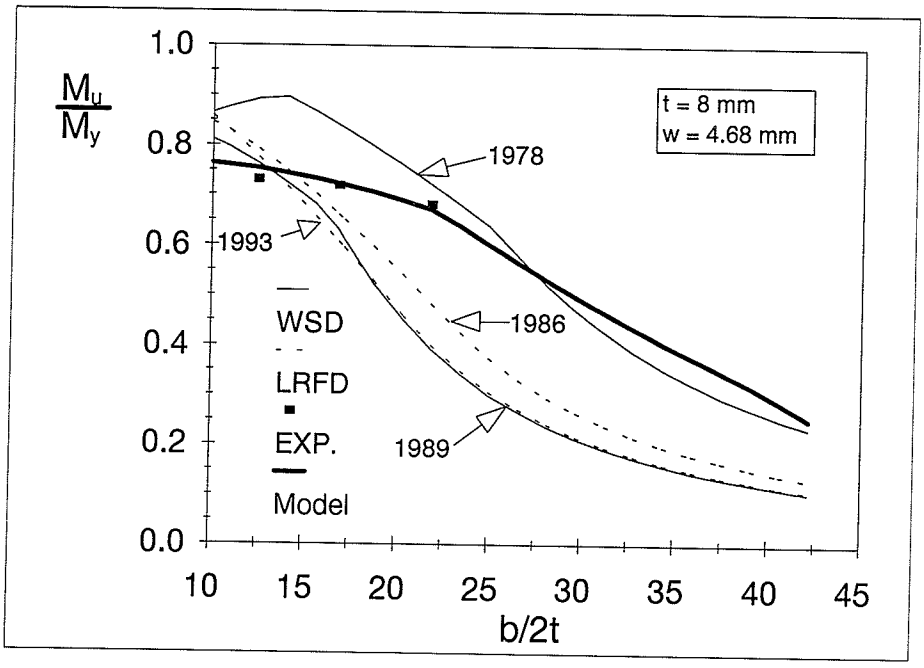

(i) 1000-mm Web Height

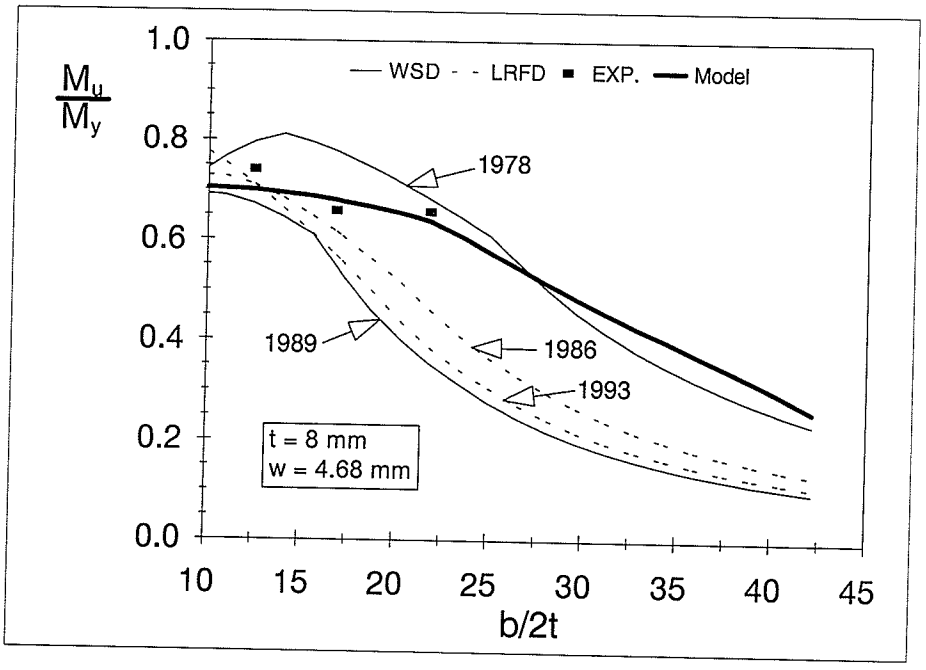

(j) 1200-mm Web Height

Figure 6.6 Comparison Between the AISC-LRFD (1986, 1993), the AISC-WSD (1978, 1989) Specifications and the Proposed Design Model

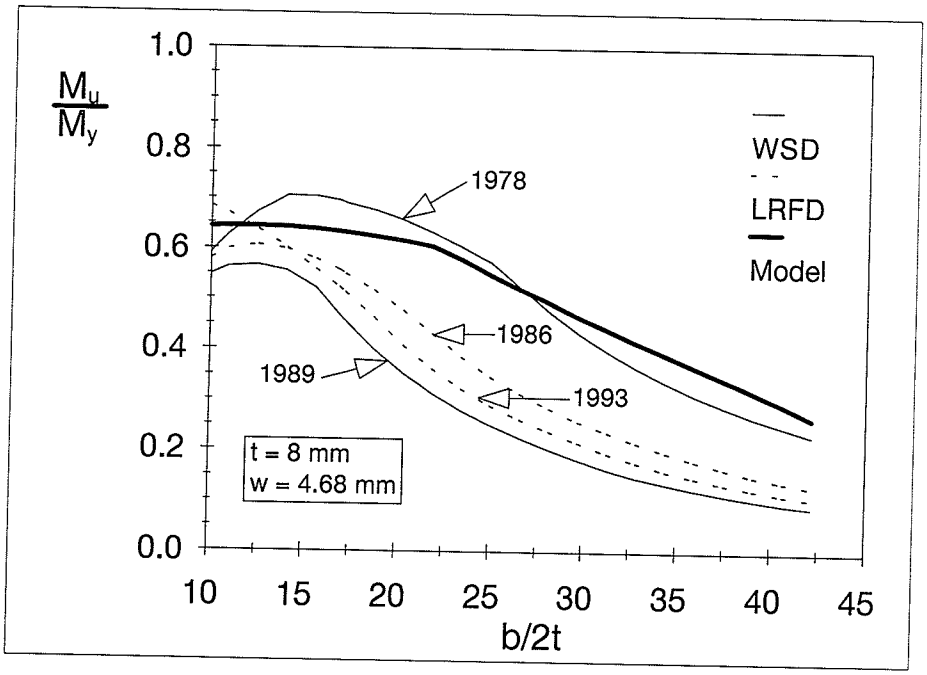

(k) 1400-mm Web Height

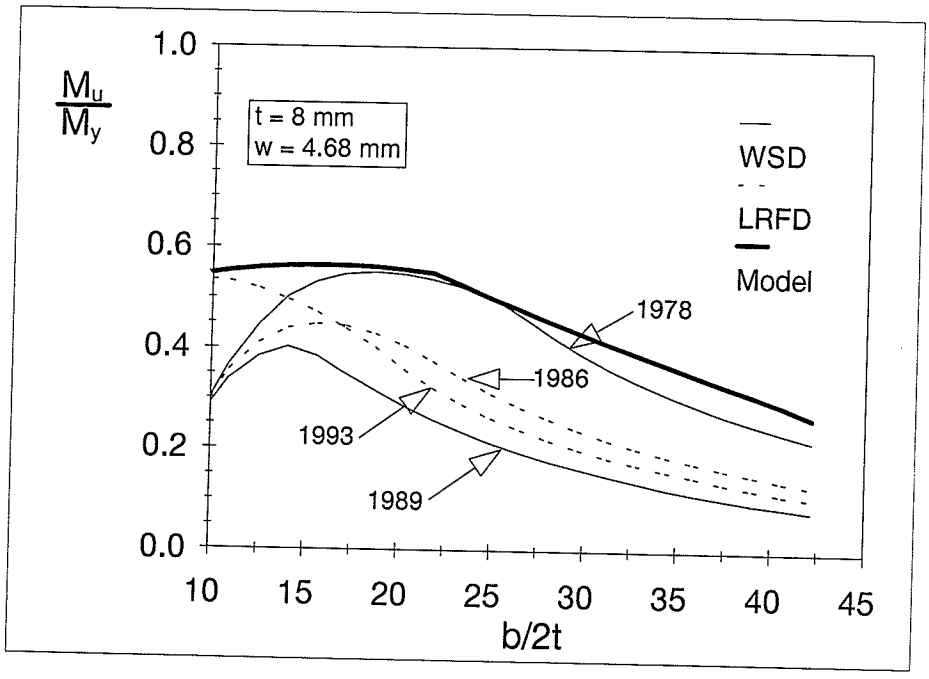

(l) 1700-mm Web Height

Figure 6.6 Comparison Between the AISC-LRFD (1986, 1993), the AISC-WSD (1978, 1989) Specifications and the Proposed Design Model

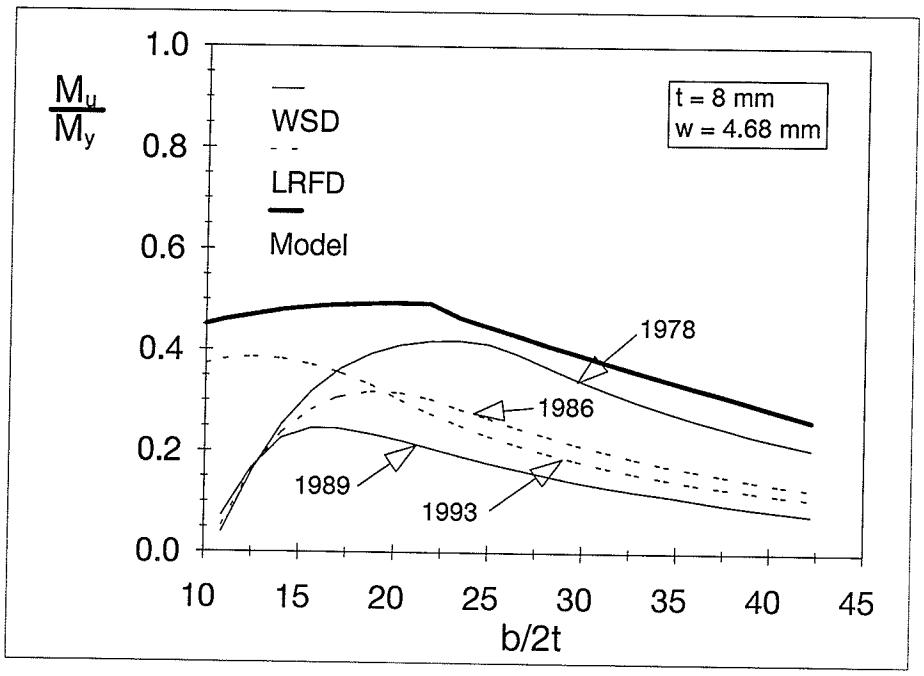

(m) 2000-mm Web Height

Figure 6.6 Comparison Between the AISC-LRFD (1986, 1993), the AISC-WSD (1978, 1989) Specifications and the Proposed Design Model

CHAPTER 7

SUMMARY AND CONCLUSIONS

7.1 SUMMARY

An extensive experimental and theoretical program was conducted to investigate the buckling behaviour of slender plate girders and the effect of web-flange interaction on the bending resistance of these girders. In the experimental phase, nine full-scale girders were tested. The web heights of these specimens ranged from 798 mm to 1200 mm, corresponding to height-to-thickness ratios (h/w) ranging from 170 to 257. The flange widths varied from 201 to 352 mm, corresponding to width-to-thickness ratios (b/2t) ranging from 12.5 to 21.9. The girders were subjected to two concentrated loads applied at the third points of the span causing a uniform bending moment in the central section of the span. The central span constituted of the test specimen whose dimensions varied according to the desired width-to-thickness ratios. The specimens, which were 1.5 m long, were connected to two 1.5 m long stiff end sections for a total girder span of 4.5 m. The end sections were designed for reuse and for failure to occur in the specimen. To prevent failure by lateral-torsional buckling, both the compression and tension flanges were laterally supported at the loaded sections as well as the supports.

Standard tension tests were performed on coupons cut from the component plates of these girders to evaluate the actual mechanical properties, which showed that the flange plates

were made from CAN/CSA-G40.21-300W steel and the web plates were made from different grades of ASTM A607 steel.

In the theoretical phase of this study, a finite element model was developed using the ANSYS finite element program to simulate the behaviour of such tested girders. To include the initial imperfection of the component plates, quadrilateral and triangular shell elements were used in this model. The postbuckling behaviour as well as the interaction between the web and the compression flange were taken into account. To investigate the effect of large displacements on the behaviour, a nonlinear geometric analysis was performed. A bilinear elasto-plastic response of the material was considered. The Newton-Raphson iterative method was used to perform these nonlinear analyses and the load was applied in increments.

The results from the finite element model showed excellent agreement with the experimental results. Once the validity of this model was verified, it was used to conduct a parametric study with the flange width-to-thickness ratio (b/2t) varied from 12.5 to 40.6 and the web height-to-thickness ratio (h/w) varied from 138 to 427.

A design model based on the results developed from the finite element analysis is proposed. The ultimate moment capacities of such girders computed according to different standards and specifications as well as the proposed design model were compared to those obtained experimentally from the tests performed in this study and another study. The comparison showed that the proposed design model results had the strongest correlation with the experimental results. The ultimate moment capacities obtained through the developed model are within 4% of those obtained experimentally. At the same time, the comparison showed that the ultimate moment capacities computed according to the current standards and

specifications varied from overconservative to unconservative depending on the cross-sectional dimensions and the level of yield strength.

7.2 CONCLUSIONS

The results obtained from the experimental phase and the theoretical phase of this study as well as from various standards and specifications are summarized in the following sections.

7.2.1 Observed Behaviour

i) In all tested specimens, failure was due to excessive rotation of the compression flange and the web about the web-flange intersection.

ii) Buckling of the web independent of flange buckling was not observed.

iii) Buckling of the flange independent of web buckling was not observed.

iv) Buckling of the web and the compression flange in the longitudinal direction in either half, one or one and a half sine-waves was observed.

v) Buckling of the web in the transverse direction in either half or one sine-wave was observed.

vi) A sudden change in the web buckling mode took place in early stages of loading for many of the tested girders. This affected the angle of rotation of the flanges as well as the angle between the web and the flange.

vii) No sudden change in the behaviour was observed at the critical buckling loads of the component plates.

viii) In all tested specimens, no failure by vertical buckling of the web was observed.

7.2.2 Current Standards and Specifications

i) The ultimate moment capacity computed according to the CAN/CSA-S16.1-94 Standard (1994) and the ECCS Recommendations (1986) gave good agreement with the test results when a yield strength of 330 MPa was used ($0.89 \leq M_{CSA}/M_{Exp} \leq 1.092$ and $0.913 \leq M_{ECCS}/M_{Exp} \leq 1.122$). However, when higher yield strength levels were used (407 MPa to 437 MPa), unconservative ultimate moment capacities, compared to those obtained experimentally, were computed according to these standard and recommendations ($1.154 \leq M_{CSA}/M_{Exp} \leq 1.188$ and $1.189 \leq M_{ECCS}/M_{Exp} \leq 1.225$). The ultimate moment capacities calculated according to these standards and recommendations were higher than those obtained from the finite element analysis by as much as 62%, when a yield strength of 500 MPa was used.

ii) The AISC-WSD Specification (1978) overestimated the ultimate moment capacity of the tested specimens by as much as 28% when a yield strength of 330 MPa was used and by as much as 48% when a range of yield strength between 407 MPa and 437 MPa was used.

iii) The AISC-LRFD Specification (1986) was conservative in computing the ultimate moment capacity of the tested specimens with 330 MPa yield strength, especially when high flange width-to-thickness ratios (b/2t) were used, by as much as 29%, while it was unconservative in computing the ultimate moment capacity of the tested specimens with a yield strength range of 407 MPa to 437 MPa by as much as 14%. Moreover, the ultimate moment capacity computed according to this specification was higher than that obtained through the finite element analysis when 500 MPa yield

strength was used by as much as 27%, when low flange width-to-thickness ratios (b/2t) were used, while it was conservative when high flange width-to-thickness ratios (b/2t) were used by as much as 50%.

iv) The AISC-WSD Specification (1989) and the AISC-LRFD Specification (1993) were overconservative in computing the ultimate moment capacity of the tested specimens with a yield strength of 330 MPa, especially when high flange width-to-thickness ratios (b/2t) were used, by as much as 46%. However, good agreement between the ultimate moment capacities computed according to these specifications and those obtained experimentally, from testing specimens with a yield strength range of 407 MPa to 437 MPa (these specifications are based on the results of these tests). On the other hand, these specifications overestimated the ultimate moment capacities, compared to those obtained from the finite element analysis using a yield strength of 500 MPa, by as much as 31% when low flange width-to-thickness ratios (b/2t) were used.

7.2.3 Proposed Design Model

i) The ultimate moment capacities computed according to the proposed design model were within 4% of those obtained experimentally using different yield strength levels (These experimental results were obtained through this study program or resulted from other research program in the range of this study).

ii) The lower limit of Class 4 web (slender web) was significantly affected by the flange width-to-thickness ratios (b/2t) and the lower limit of Class 4 flange (slender flange)

was also affected by the web height-to-thickness ratios (h/w), i.e. the web-flange interaction had a significant effect on these limits.

iii) The ultimate moment capacity of slender girders was significantly affected by the yield strength of the compression flange, if low flange width-to-thickness ratios (b/2t) and low web height-to-thickness ratios (h/w) were used, with respect to the studied range. On the other hand, the yield strength had an insignificant effect on the ultimate moment capacity of the girders of high flange width-to-thickness ratio (b/2t) or web height-to-thickness ratios (h/w).

iv) The ultimate moment capacity was insignificantly affected by any change in the flange initial imperfection or the web initial imperfection values.

v) Different modes of web initial imperfection were significantly affecting the ultimate moment capacity of slender girders.

vi) The maximum limit of the web height-to-thickness ratio (h/w) used in most current standards and specifications is a conservative limit.

7.3 RECOMMENDATIONS FOR DESIGN

A design model for slender plate girders subjected to bending about the major axis is proposed. This model is based on experimental results obtained through this research program as well as a parametric study performed using the finite element analysis. In this parametric study, the flange width-to-thickness ratio (b/2t) ranges from 12.5 to 40.7, while the web height-to-thickness ratio (h/w) ranges from 139 to 427 to include more than 100 case of study. The postbuckling strength and the web-flange interaction is considered in the

proposed model. Lower limits for Class 4 web and flange, based on the web-flange interaction, are also proposed.

7.4 RECOMMENDATIONS FOR FURTHER STUDIES

i) The effect of yield strength on the ultimate moment capacity of the girders with low flange width-to-thickness ratios (b/2t) and web height-to-thickness ratios (h/w), with respect to this study range, is recommended to be investigated at different levels, other than the range of 300 MPa to 360 MPa.

ii) The effect of the yield strength on the lower limits of Class 4 girders (slender girders) is suggested to be studied using levels other than that range of 300 MPa to 360 MPa.

iii) More studies are also recommended to evaluate the limits of flange width-to-thickness ratios (b/2t) and web height-to-thickness ratios (h/w), where the yield strength starts to have an insignificant effect on the ultimate moment capacities.

iv) Experimental and theoretical studies are suggested to investigate the effect of different modes of web initial imperfection on the ultimate moment capacity of slender girders.

v) Another experimental and theoretical studies are recommended to investigate the behaviour of hybrid slender girders.

vi) The maximum limit of the web height-to-thickness ratio (h/w) used in most standards and specifications is a conservative limit, more experimental and theoretical studies are suggested to increase this limit, especially when slender flanges are used.

REFERENCES

Akey, H. V., Johnson, C. P., and Will K. M., (1977), "Local and Lateral Buckling of Beams and Frames," Journal of the Structural Division, ASCE, Vol. 103., No. ST9, Proceeding Paper 13226, pp. 1821-1832, September.

American Institute of Steel Construction, (1978), "Working Stress Design," Specifications for Structural Steel Buildings, Chicago, Il.

American Institute of Steel Construction, (1986), "Load and Resistance Factor Design," Specifications for Structural Steel Buildings, Chicago, Il.

American Institute of Steel Construction, (1989), "Working Stress Design," Specifications for Structural Steel Buildings, Chicago, Il.

American Institute of Steel Construction, (1993), "Load and Resistance Factor Design," Specifications for Structural Steel Buildings, Chicago, Il.

American Iron and Steel Institute, (1989), "Specification for the Design of Cold-Formed Steel Structural Members," Part I of Cold-Formed Steel Design Manual, N. W., Washington, D.C.

American Society for Testing and Materials, (1982), "ASTM E 111-82 (Reproved 1988) Standard Test Method for Young's Modulus, Tangent Modulus, and Chord Modulus," Philadelphia.

American Society for Testing and Materials, (1986), "ASTM E 132-86 Standard Test Method for Poisson's Ratio at Room Temperature," Philadelphia.

American Society for Testing and Materials, (1990), "ASTM A 370-90a Standard Test Methods and Definitions for Mechanical Testing of Steel Products," Philadelphia.

American Society for Testing and Materials, (1990), "ASTM A 607-90a Standard Specification for Steel, Sheet and Strip, High-Strength, Low-Alloy, Columbium or Vanadium, or Both, Hot Rolled and Cold Rolled," Philadelphia.

American Society for Testing and Materials, (1990), "ASTM E 8M-90a Standard Methods for Tension Testing of Metallic Materials," Philadelphia.

American Welding Society, (1988), "ANSI/AWS D1.1-88 Structural Welding Code, Steel," Miami, FL.

Basler, K., Yen, B. T., Muller, J. A., and Thürlimann, B., (1960), "Web Buckling Tests on Welded Plate Girders," Weld. Res. Conc. Bult. No. 64.

Basler, K., and Thürlimann, B., (1961a), "Strength of Plate Girders in Bending," Journal of the Structural Division, ASCE, Vol. 87, No. ST6, pp. 153-181.

Basler, K., and Thürlimann, B., (1961b), "Strength of Plate Girders in Bending," Trans. Am. Soc. Civ. Eng., Vol. 128, Part II, pp. 655-686.

Bijlaard, P. P., (1949), "Theory and Tests on the Plastic Stability of Plates and Shells," Journal of Aeronautical Science, V. 16, pp. 529-541, September.

Bliech, F., (1952), "Buckling Strength of Metal Structures," McGraw-Hill Book Co., Inc., New York, N. Y.

Bradford, M. A., and Trahair, N. S., (1981), "Distortional Buckling of I-Beams," Journal of the Structural Division, Proceedings of ASCE, Vol. 107, No. ST2, pp. 355-370, Febraury.

Canadian Standards Association, (1984), "Limit States Design of Steel Structures," CAN/CSA-S16.1-M84 Steel Structures, Rexdale (Toronto), Ontario.

Canadian Standards Association, (1989), "Welded Steel Construction," CAN/CSA-W59-M89 Metal Arc Welding, Rexdale (Toronto), Ontario.

Canadian Standards Association, (1989), "Cold-Formed Steel Structural Members," CAN/CSA-S136-M89 Structural Design, Rexdale (Toronto), Ontario.

Canadian Standards Association, (1989), "Limit States Design of Steel Structures," CAN/CSA-S16.1-M89 Steel Structures, Rexdale (Toronto), Ontario.

Canadian Standards Association, (1992), "Structural Quality Steels," CAN/CSA-G40.21-M92, Rexdale (Toronto), Ontario.

Canadian Standards Association, (1994), "Cold-Formed Steel Structural Members," CAN/CSA-S136-94 Structural Design, Rexdale (Toronto), Ontario.

Canadian Standards Association, (1994), "Limit States Design of Steel Structures," CAN/CSA-S16.1-94 Steel Structures, Rexdale (Toronto), Ontario.

Chou, P. C., and Pango, N. J., (1967), "Elasticity: Tensor, Dyadic and Engineering Approaches," D. Van Nostrand Company, Inc., Princeton, N. J.

Cooper, P. B., (1971), "The Ultimate Bending Moment for Plate Girders," IABSE Coll. Des. Plate Box Girders Ultimate Strength, London.

Culver, C. G., and Nasir, G., (1971), "Inelastic Flange Buckling of Curved Plate Girders," Journal of the Structural Division, ASCE, Vol. 97, No. ST4, pp. 1239-1256.

Dawe, J. L., and Kulak, G. L., (1981), "Local Buckling of W Shapes Used as Columns, Beams, and Beam-Columns," Structural Engineering Report, No. 95, Department of Civil Engineering, University of Alberta, Edmonton, Alberta.

Dawe, J. L., and Kulak, G. L., (1984a), "Plate Instability of W Shapes," Journal of Structural Engineering, ASCE, Vol. 110, No. 6, Paper No. 18955, pp. 1278-1291.

Dawe, J. L., and Kulak, G. L., (1984b), "Local Buckling of W Shapes Columns and Beams," Journal of Structural Engineering, ASCE, Vol. 110, No. 6, Paper No. 18956, pp. 1292-1304.

Drucker, D. C., (1949), "A Discussion of Theories of Plasticity," Readers' Forum, Journal of Aeronautical Sciences, Vol. 16, No. 9, p. 567, September.

Dubas, P., and Gehri, E., ed., (1986), "Behaviour and Design of Steel Plated Structures," European Convention for Constructional Steelwork (ECCS), Technical Committee 8- Structural Stability, Technical Working Group 8.3- Plated Structures.

Dubey, R. N., (1978-79), "Bifurcation in Elastic-Plastic Plates," Transactions, CSME, Vol. 5, No. 2, pp. 79-88.

Faulkner, D., (1977), "Compression Tests on Welded Eccentrically Stiffened Plate Panels," Steel Plated Structures, ed. Dowling, P. J., Harding, J. E., and Frieze, P. A., Crosby Lockwood Staples, pp. 518-617, London.

Fung, Y. C., (1965), "Foundations of Solid Mechanics," Prentice-Hall, Inc., Englewood Cliffs, N. J.

Galambos, T. V., (1968), "Structural Members and Frames," Prentice-Hall, Inc., Englewood Cliffs, N. J.

Galambos, T. V., ed., (1988), "Guide to Stability Design Criteria for Metal Structures," Fourth Edition, John Wiley and Sons, New York, N.Y.

Gallagher, R. H., Lien, S., and Mau, S. T., (1971), "A Procedure for Finite Element Plate and Shell Pre- and Postbuckling Analysis," Conference on Matrix Methods of Structural Mechanics, Wright-Patterson Air Force Base, Ohio, AFFDL-TR-71-160, pp. 857-879.

Gerard, G., (1957), "Compressive Strength of Flat Stiffened Panels," NACA, TN No. 37885.

Goldberg, J. E., Bodanoff, J. L., and Glauz, W. D., (1964), " Lateral and Torsional Buckling of Thin-Walled Beams," Proceedings, International Association for Bridge and Structural Engineering, Vol. 24, pp. 91-100.

Graves-Smith, T. R., and Sridharan, S., (1978), "A Finite Strip Method for the Post-Locally-Buckled Analysis of Plate Structures," International Journal of Mechanical Science, Vol. 20, pp. 833-842.

Haaijer, G., and Thürlimann, B., (1958), "On Elastic Buckling in Steel," Proceedings, Journal of Structural Engineering, ASCE, Vol. 84, No. EM2, April.

Hancock, G. J., (1978), "Local, Distortional and Lateral Buckling of I-Beams," Journal of the Structural Division, Proceedings, ASCE, Vol. 104, No. ST11, pp. 1787-1798, November.

Hancock, G. J., (1981), "Nonlinear Analysis of Thin Section in Compression," Journal of Structural Division, Proceedings of ASCE, Vol. 107, No. ST3, pp. 455-471, March.

Handelman, G. H., and Prager, W., (1948), "Plastic Buckling of a Rectangular Plate Under Edge Thrusts," National Advisory Council for Aeronautics, Technical Notes No. 1530, August.

Höglunt, T., (1973), "Design of Thin Plate I Girders in Shear and Bending with Special Reference to Web Buckling," Institutionen för Byggnadsstatik, KTH Stockholm, Medd., No. 94.

Holtz, N. M., and Kulak, G. L., (1975), "Web slenderness Limits of Non-Compact Beams," Structural Engineering Report, No. 51, Department of Civil Engineering, University of Alberta, Edmonton, Alberta.

Ilyushin, A. A., (1947), "Stability of Plates and Shells Beyond the Proportional Limit," National Advisory Council for Aeronautics, Technical Memorandum, No. 116, October.

Irons, B. M., (1970), "A Frontal Solution Program for Finite Element Analysis," International Journal for Numerical Methods in Engineering, Vol. 2, No. 1, pp. 5-23, January.

Johnson, C. P., and Will, K. M., (1974), "Beam Buckling by Finite Element Procedure," Journal of the Structural Division, ASCE, Vol. 100, No. Set, Proceeding Paper 10432, pp. 669-685, March.

Johnson, D. L., (1985), "An Investigation into the Interaction of Flanges and Webs in Wide Flange Shapes," Proceedings, Structural Stability Research Council, Cleveland, Ohio,

April 16-17, pp. 395-405.

Kulak, G. L., Adams, P. F., and Gilmor, M. I., (1995), "Limite States Design in Structural Steel," Fifth Edition, Universal Offset Limited, Markham, Ontario.

Klayanaraman, V., and Peköz, T., (1978), "Analytical Study of Unstiffened Elements," Journal of the Structural Division, ASCE, Vol. 104, No. ST9, September, pp. 1507-1524.

Lay, M. G., (1965a), "Flange Local Buckling in Wide-Flange Shapes," Journal of the Structural Division, ASCE, Vol. 92, No. ST6, pp. 95-116.

Lay, M. G., (1965b), "Yielding of Uniformly Loaded Steel Members," Journal of the Structural Division, ASCE, Vol. 91, No. ST6, Proceedings Papers 4580, December.

Luckey, A. F., and Adams, P. F., (1969), "Rotation Capacity of Beams Under Moment Gradient," Journal of the Structural Division, ASCE, Vol. 95, No. ST6.

Maeda, Y., (1971), "Ultimate Static Strength and Fatigue Behaviour of Longitudinally Stiffened Plate Girders in Bending," IABSE Coll. Des. Plate Box Girders Ultimate Strength, London.

McDemott, J. F., (1969), "Local Plastic Buckling of A514 Steel Members," Journal of the Structural Division, ASCE, Vol. 95, No. ST9, pp. 1837-1850.

Melosh, R. J., and Bamford, R. M., (1969), "Effective Solution of Load-Deflection Equations, Journal of the Structural Division, ASCE, Vol. 95, No. ST4, Proceeding Paper 6510, pp. 661-676, April.

Onat, E. T., and Drucker, D. C., (1953), "Inelastic Instability and Incremental Theories of Plasticity," Journal of Aeronautical Science, Vol. 20, p. 181, March.

Pi, Y. L., and Trahair, N. S., (1994a), " Nonlinear Inelastic Analysis of Steel Beam-Columns. I-Theory," Journal of Structural Engineering, ASCE, Vol. 120, No. 7, Paper 5709, pp. 2041-2061, July.

Pi, Y. L., and Trahair, N. S., (1994b), " Nonlinear Inelastic Analysis of Steel Beam-Columns. II-Applications," Journal of Structural Engineering, ASCE, Vol. 120, No. 7, Paper 5710, pp. 2062-2085, July.

Polyzois, D., (1990a), "Web-Flange Interaction in Slender Beams," Proceedings, SSRC Annual Conference, April 10-11, pp. 291-303, St. Louis, Missouri.

Polyzois, D., (1990b), "Web-Flange Interaction in Built-up Slender Beams," Proceedings, CSCE Annual Conference, Vol. IV-2 Structures, May 16-18, pp. v-771-v-785, Hamilton, Ontario.

Rajasekaran, S., and Murry, D. W., (1973), "Coupled Local-Buckling in Wide-Flange Beam Columns," Journal of the Structural Division, ASCE, Vol. 99, No. ST6, Proceeding Paper 9774, pp. 1003-1023, June.

Ritz, W., (1908), "Ueber Eine Neue Methode zur Lösung Gawisser Variations Probleme der Mathematischen Physik," Journal für Reine und Angew, Mathematik, Bd 135, pp. 1-101.

Ros, M., and Eichinger, A., (1952), "Reports," 3rd International Congress, Bridge and Structural Engineer, Paris, France.

Schilling, C. G., Chairman (1968), "Design of Hybrid Steel Beams," Report of Subcommittee 1 on Hybrid Beams and Girders, Joint ASCE-AASHO Committee on Flexural Members, Journal of the Structural Division, ASCE, Vol. 104, No. ST9, pp. 1389-1407.

Skaloud, M., and Kristek, V., (1977), "Folded-Plate-Theory Analysis of the Effect of the Stiffener Configuration upon the Buckling of Longitudinally Stiffened Compression Flange," Acta Technical CSAV, pp. 577-601.

Skaloud, M., and Kristek, V., (1981), "Stability Problems of Steel Box-Girders," Transactions of the Gzechoslovak Academy of Sciences, Series "Technical Sciences," No. 1.

Solman, C. G., and Johnson, J. E., (1990), "Steel Structures, Design and Behaviour," Third Edition, Harper & Row, New York, N. Y.

Stowell, E. Z., (1948), "A Unified Theory of Plastic Buckling of Columns and Plates," National Advisory Council for Aeronautics, Technical Notes 1556.

Swanson Analysis Systems Inc., (1992), "ANSYS User's Manual for Revision 5.0 - Volumes I to IV," Houston, PA.

SWEDEN: Kommentarer till Stalbyggnadsorn 70, (1973), Knäckning, Vipping och Buckling; STBK-K2, Statens Stalbyggnadskommitté, Stockholm.

Timoshenko, S. P., and Gere, J. M., (1961), "Theory of Elastic Stability," Second Edition, McGraw-Hill Book Co., Inc., New York, N. Y.

Von-Kármán, T., Scheler, E. E., and Donnell, L. H., (1932), "The Strength of Thin Plates in

Compression," Trans. Am. Soc. Civ. Eng., Vol. 54, APM 54-5.

Wilson, J. M., (1886), "On Specifications for Strength of Iron Bridges," Trans. Am. Soc. Civ. Eng., Vol. 15, Part I, pp. 401-403, 489-490.

Winter, G., (1947), "Strength of Thin Compression Flanges," Trans. Am. Soc. Civ. Eng., Vol. 112, pp. 527-576.

Winter, G., (1968), "Thin-Walled Structures - Theoretical Solution and Test Results," Prelim. Publ., 8th Congress IABSE, New York, N. Y.

APPENDIX A

LOAD-DEFLECTION CURVES

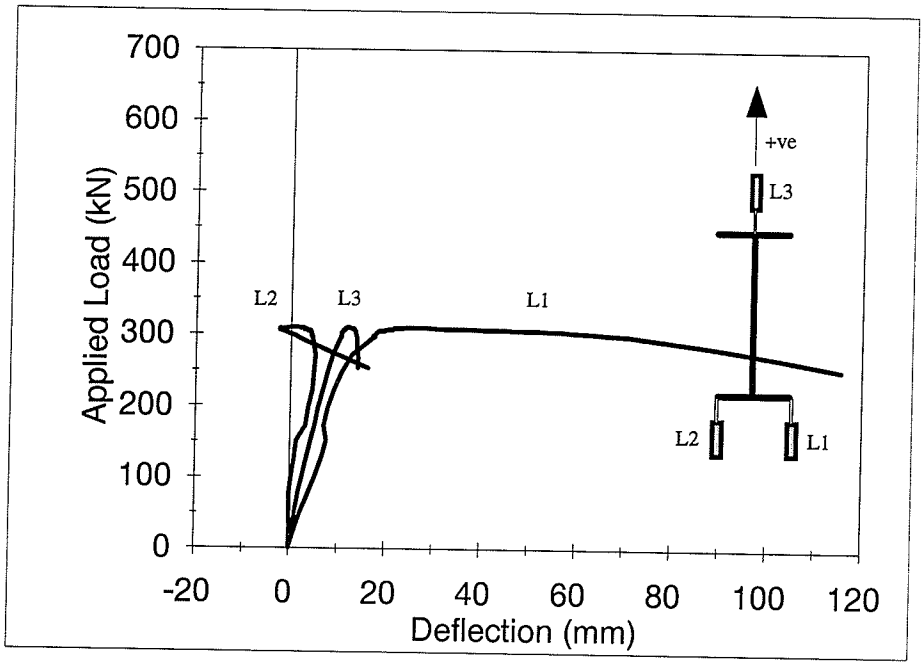

(a) Mid Span

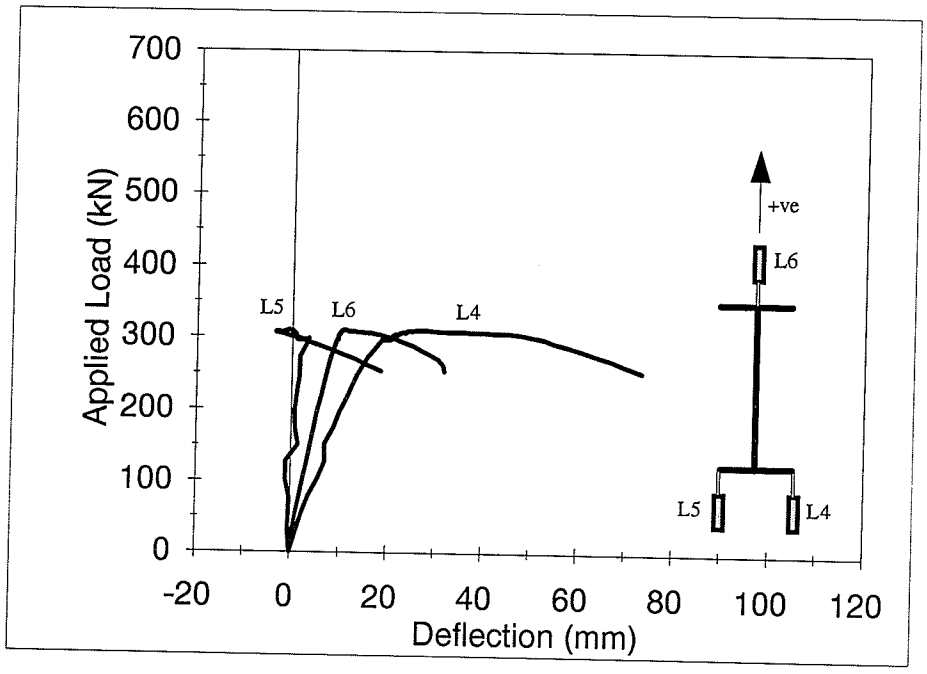

(b) Quarter Span

Figure A.1 Load-Deflection Curves of Specimen G1

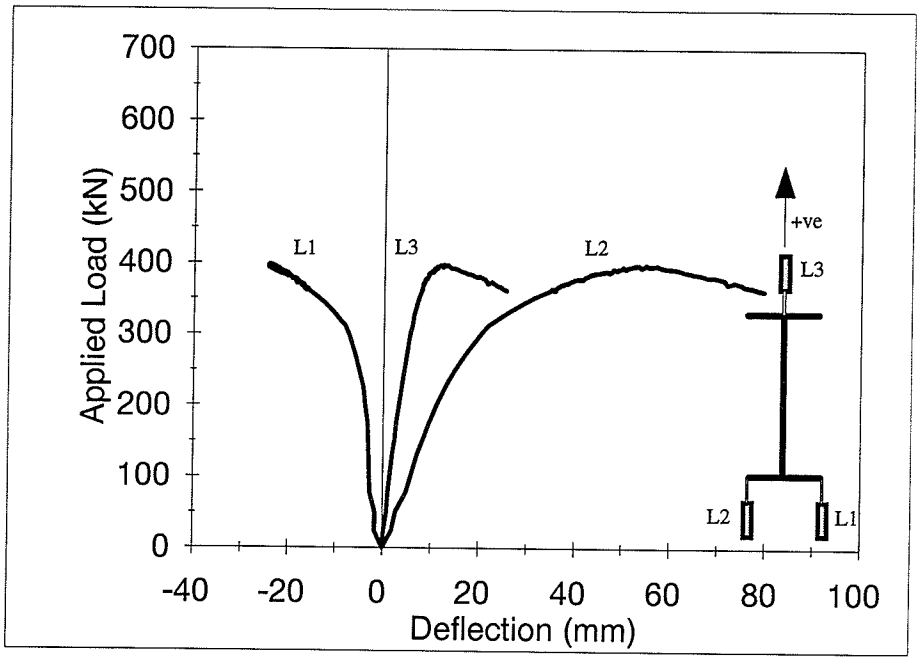

(a) Mid Span

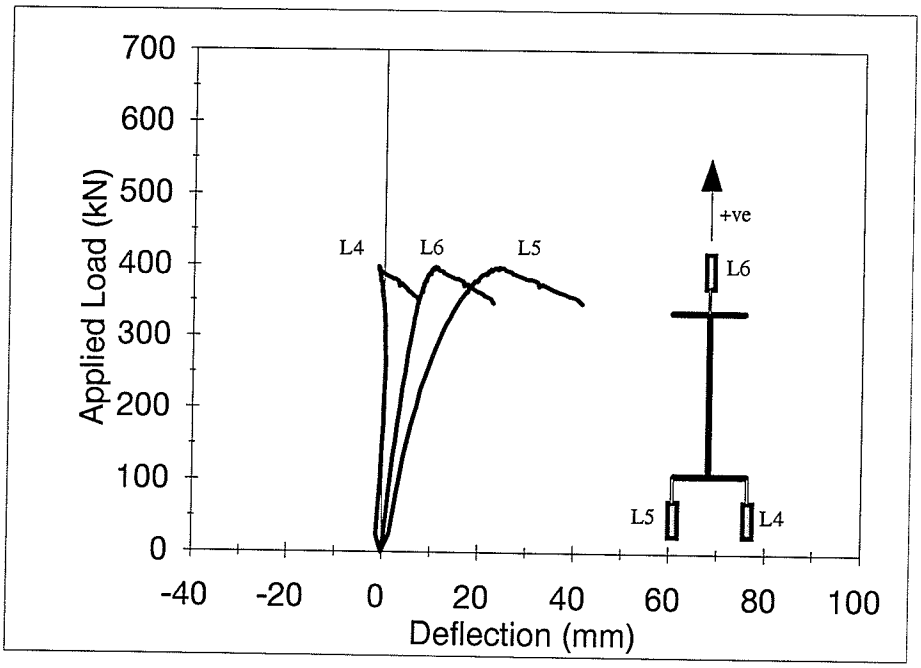

(b) Quarter Span

Figure A.2 Load-Deflection Curves of Specimen G3

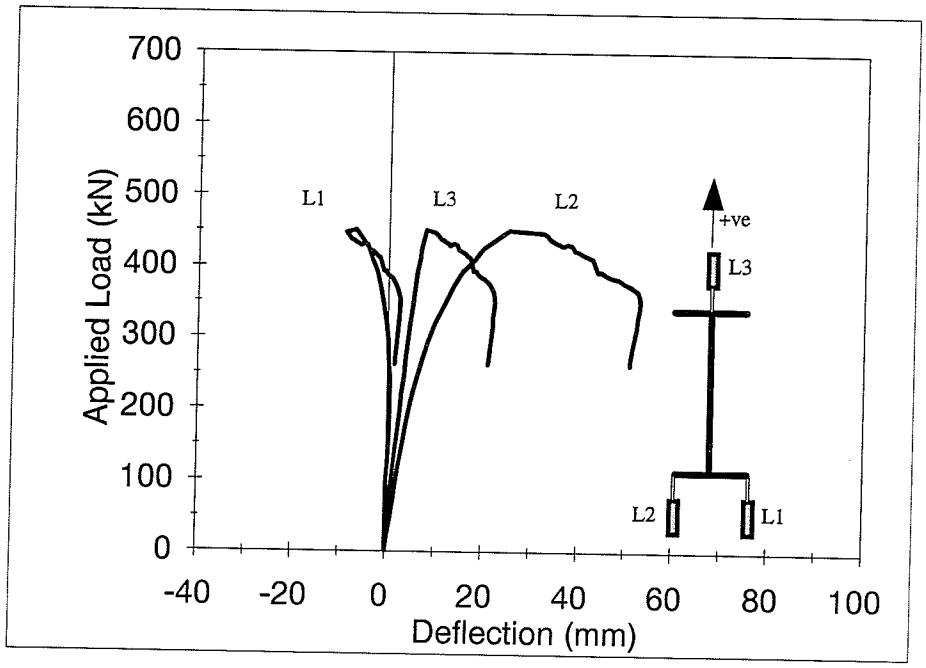

(a) Mid Span

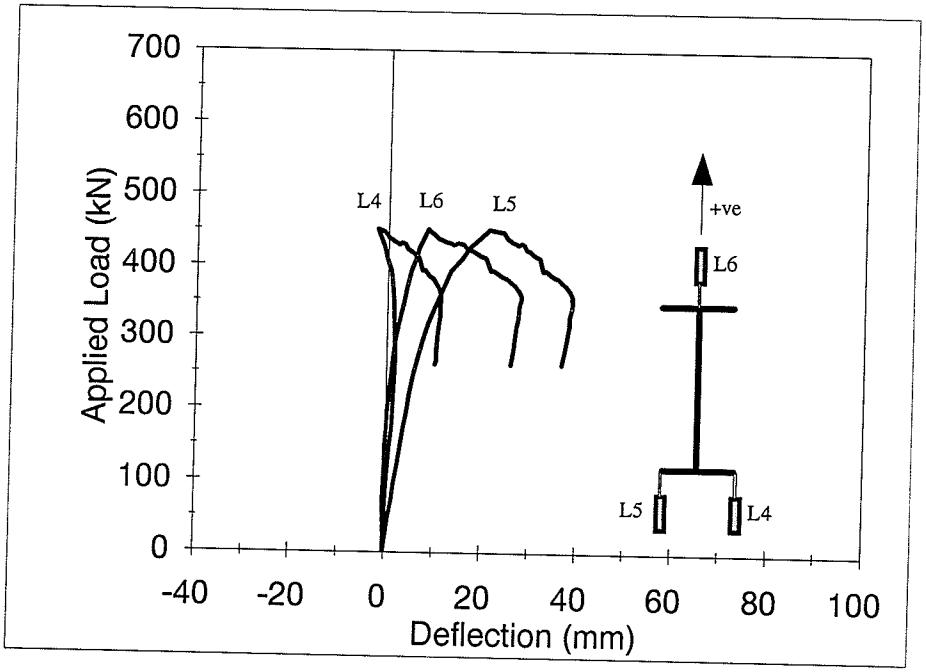

(b) Quarter Span

Figure A.3 Load-Deflection Curves of Specimen G5

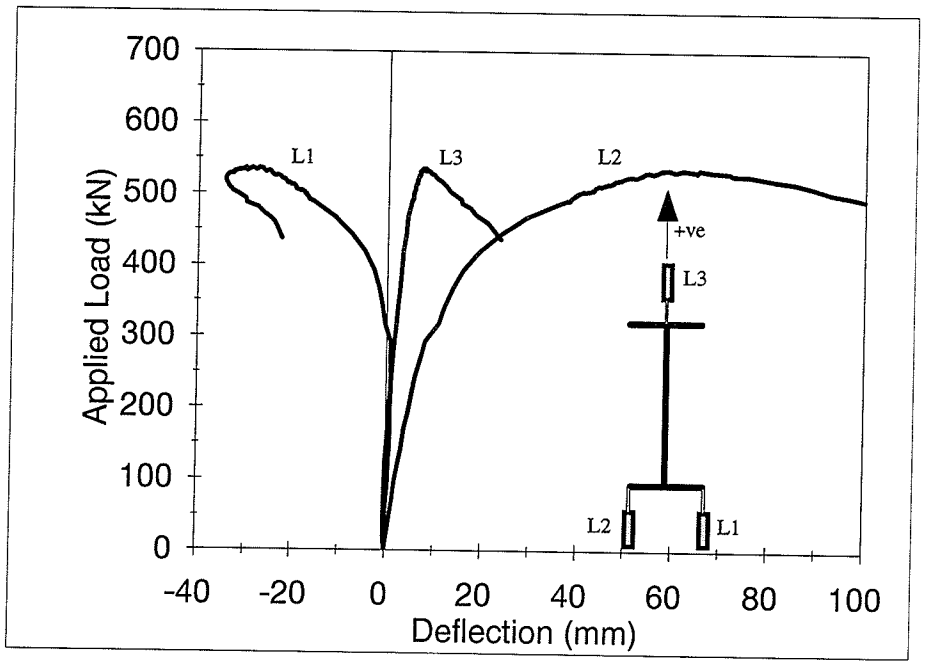

(a) Mid Span

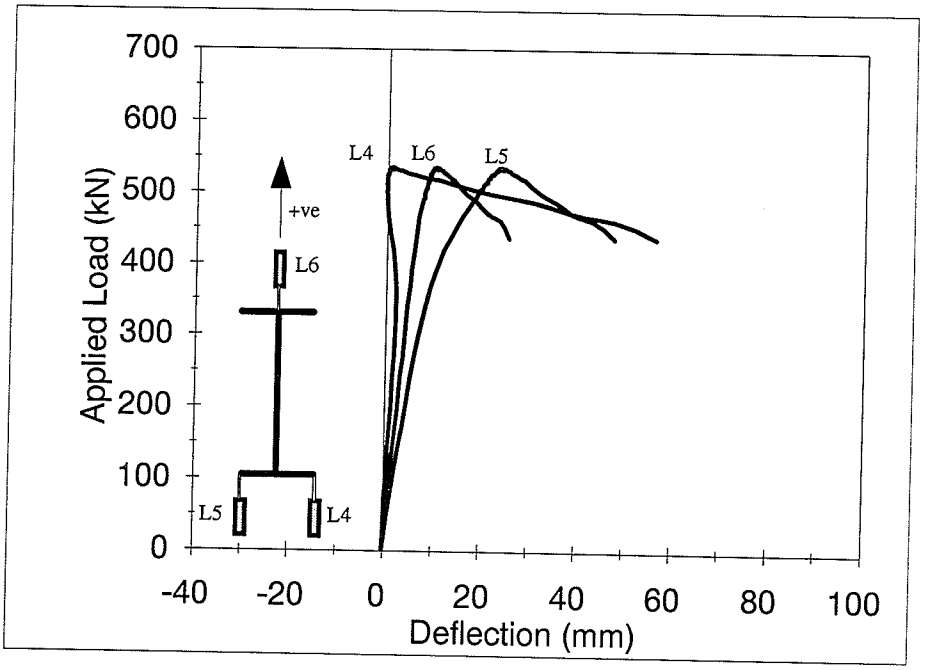

(b) Quarter Span

Figure A.4 Load-Deflection Curves of Specimen G6

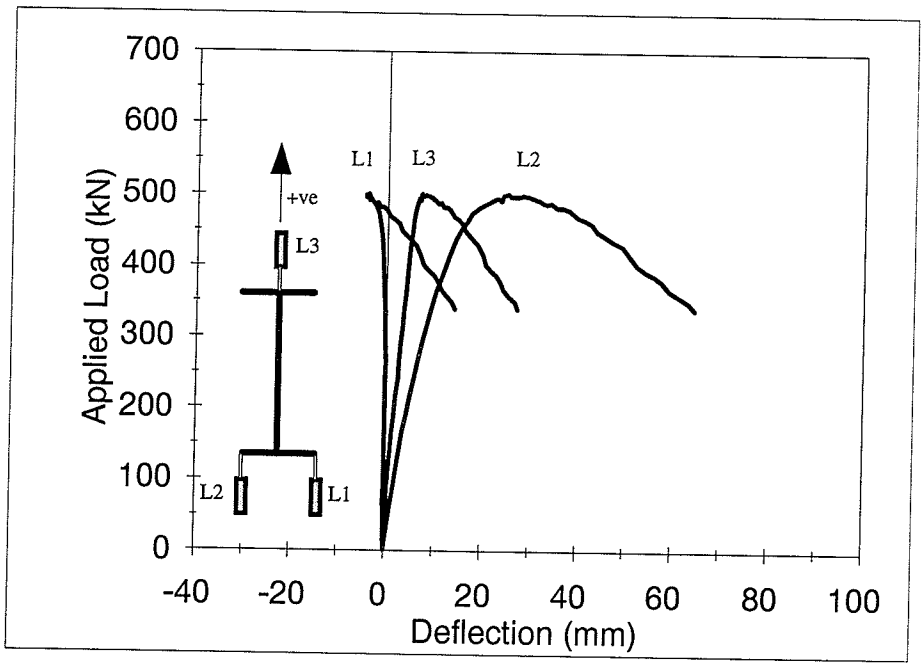

(a) Mid Span

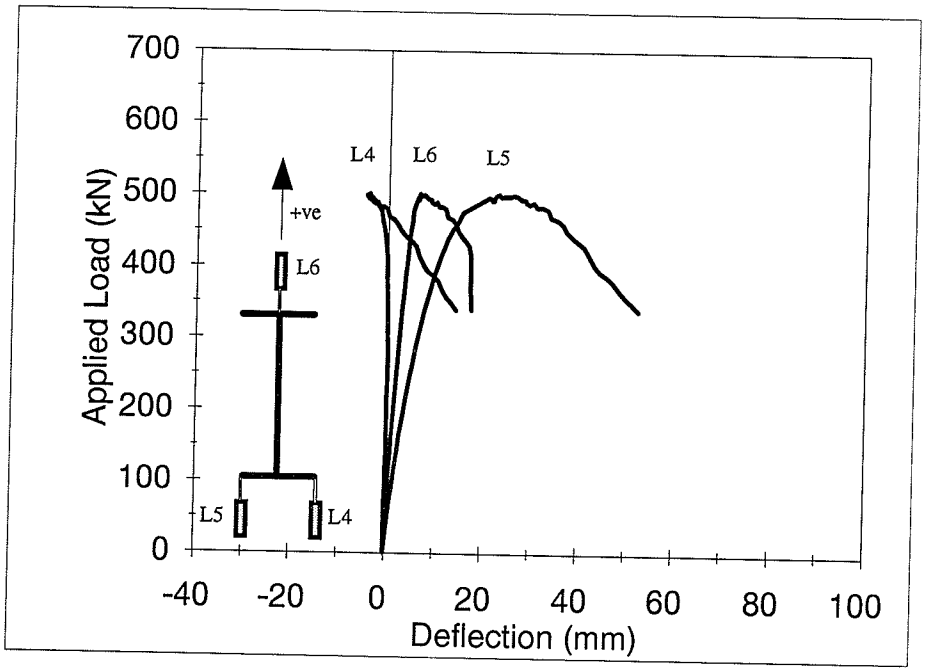

(b) Quarter Span

Figure A.5 Load-Deflection Curves of Specimen G7

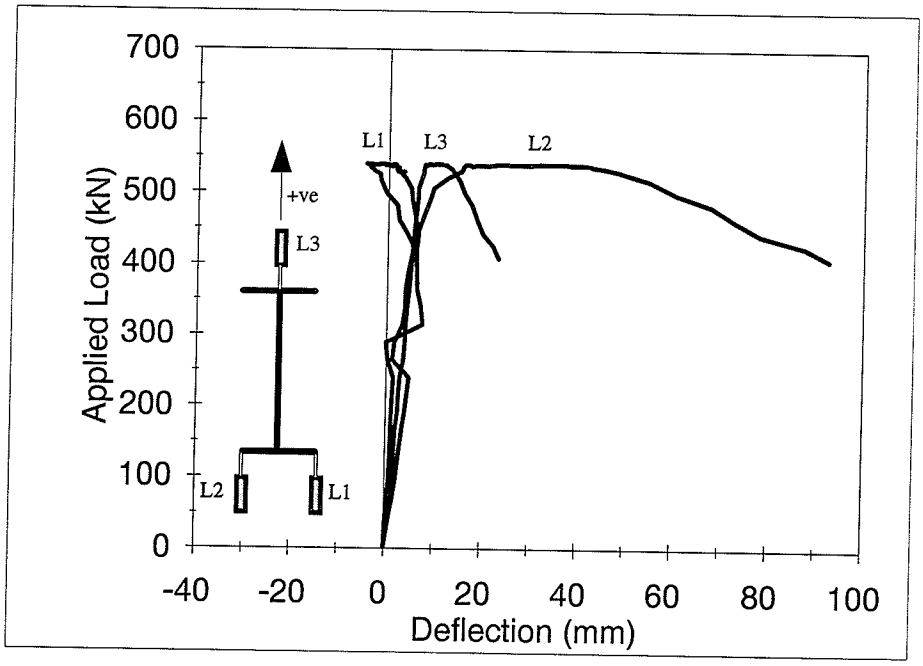

(a) Mid Span

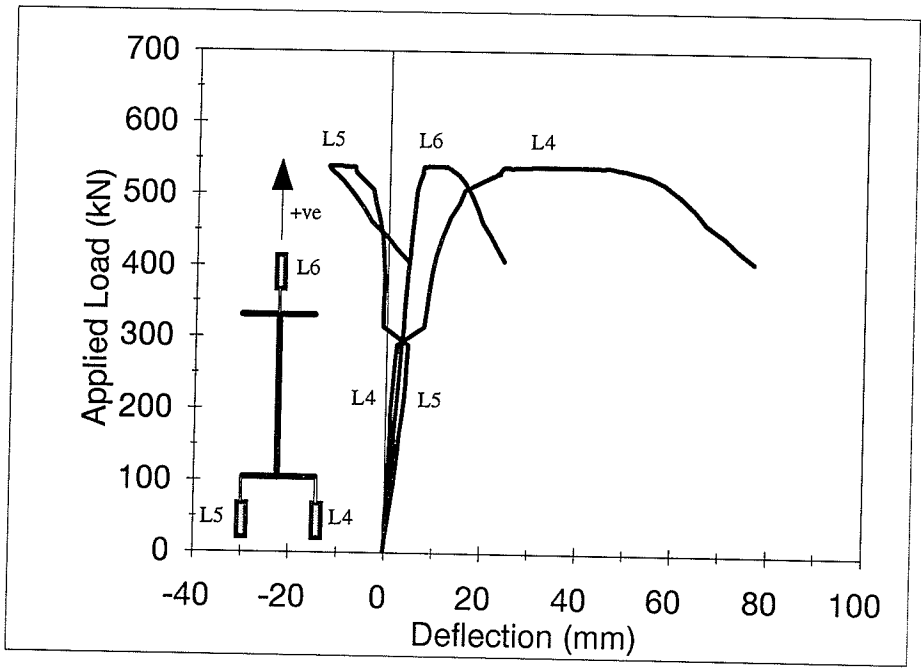

(b) Quarter Span

Figure A.6 Load-Deflection Curves of Specimen G8

APPENDIX B

FLANGE ROTATIONS

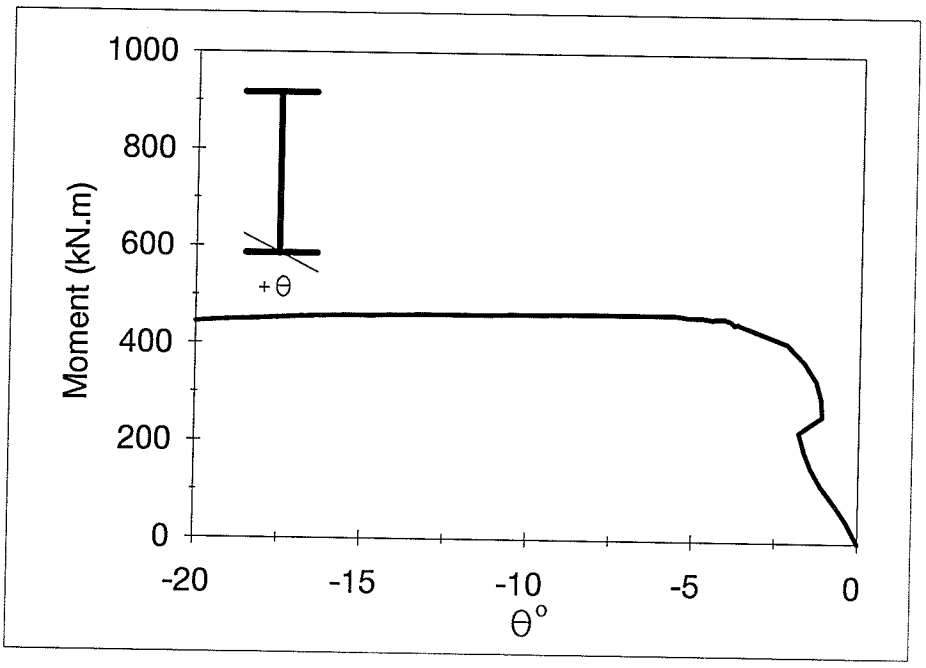

(a) Mid Span

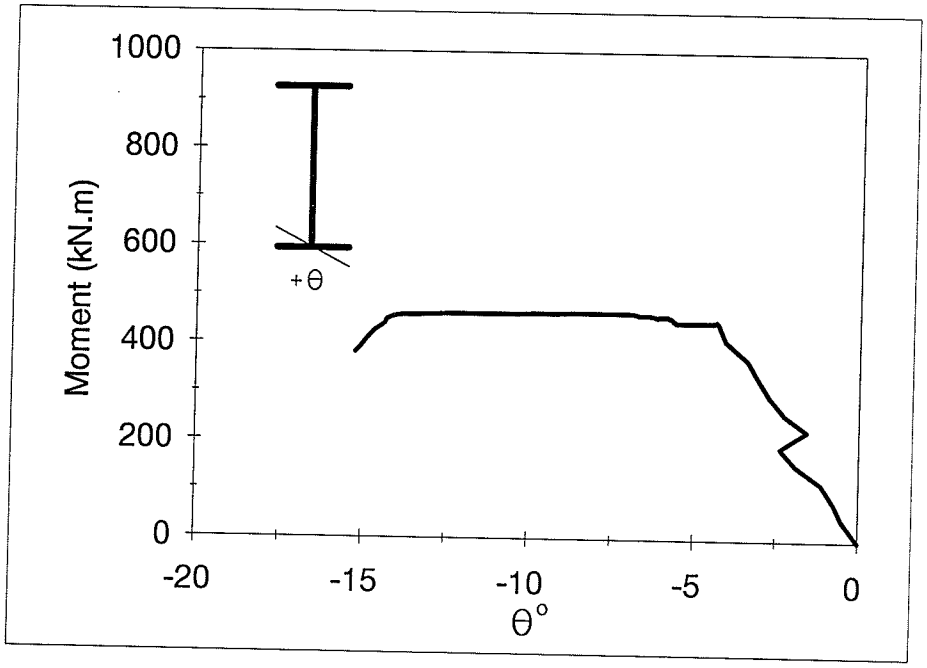

(b) Quarter Span

Figure B.1 Rotation of Compression Flange of Specimen G1

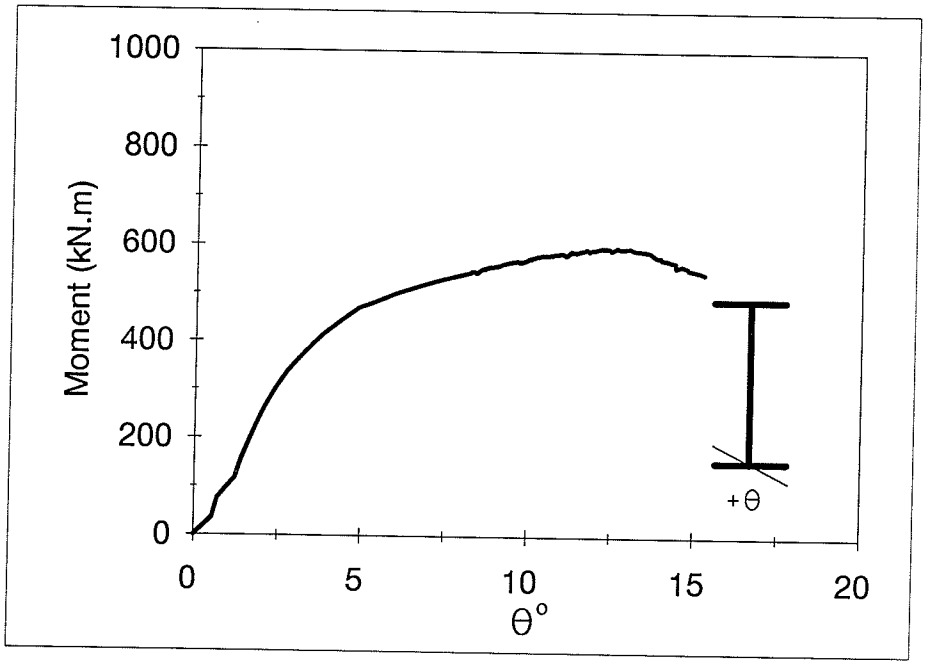

(a) Mid Span

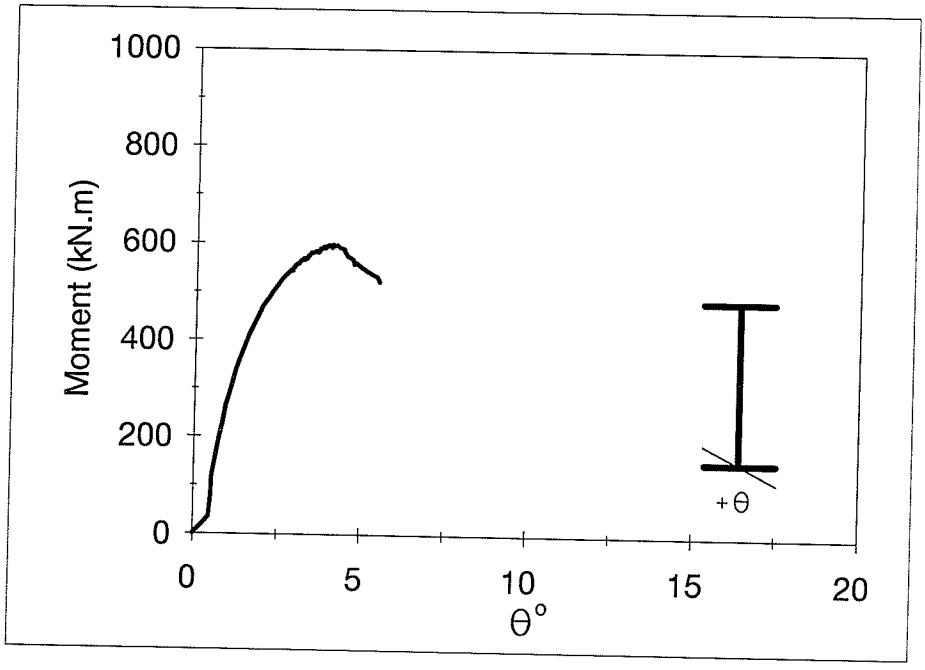

(b) Quarter Span

Figure B.2 Rotation of Compression Flange of Specimen G3

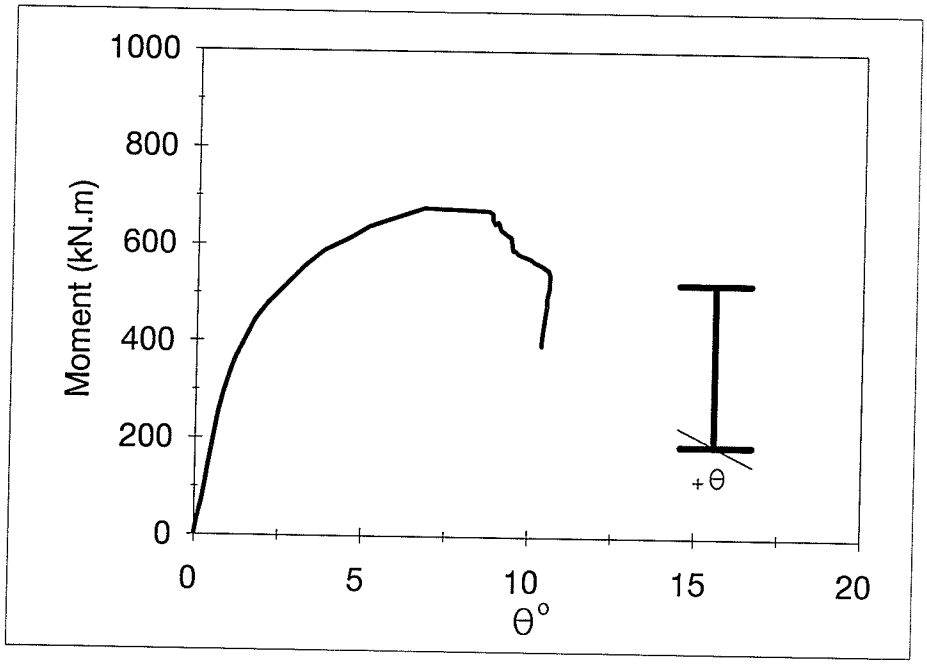

(a) Mid Span

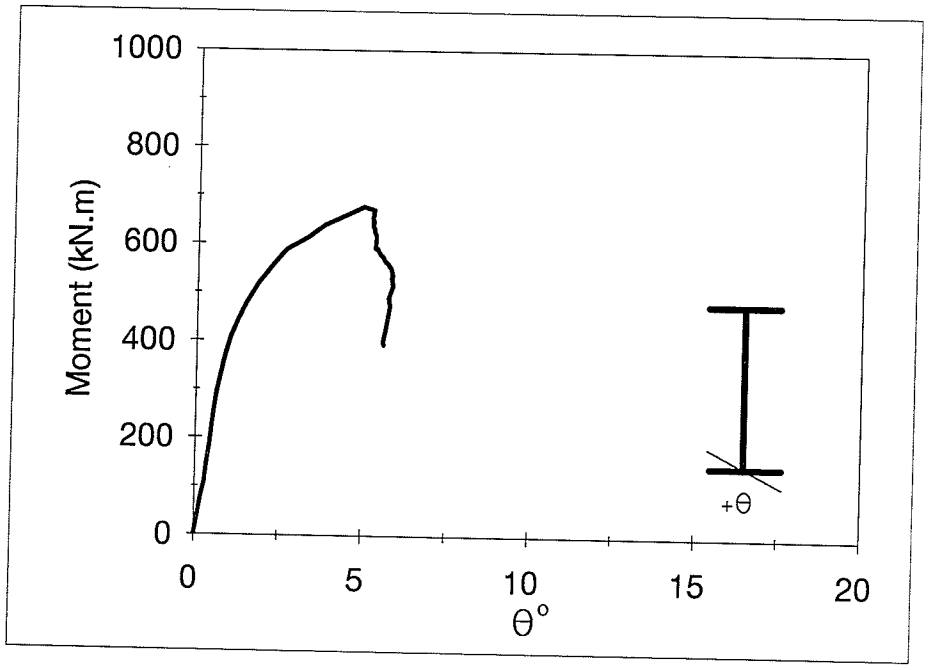

(b) Quarter Span

Figure B.3 Rotation of Compression Flange of Specimen G5

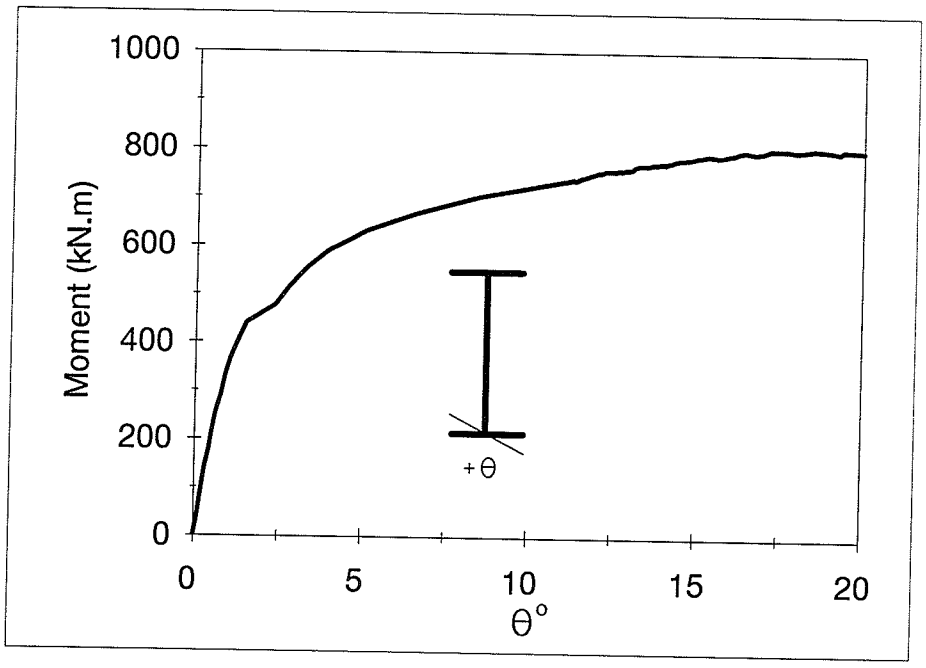

(a) Mid Span

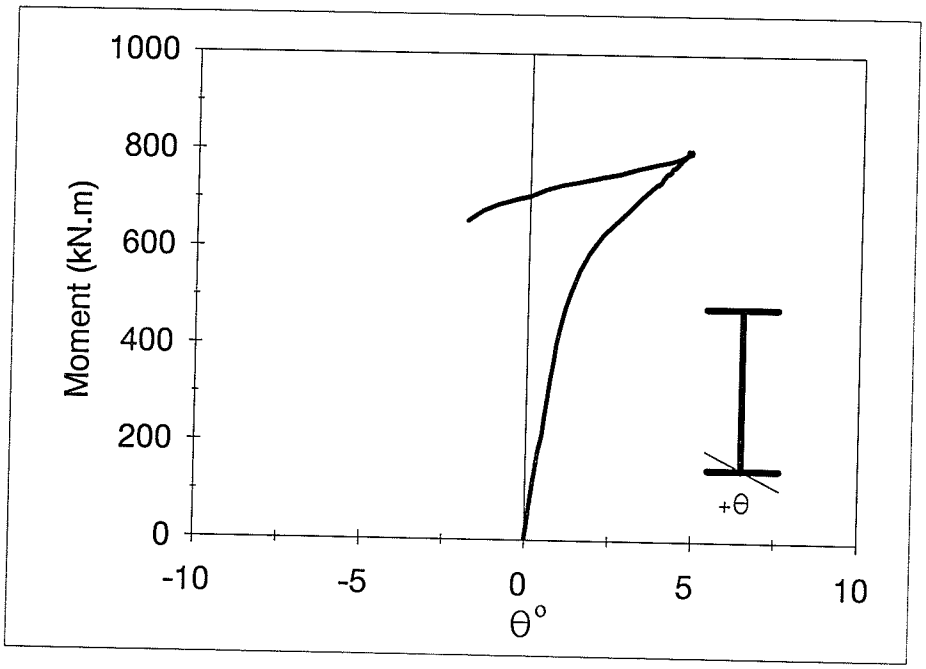

(b) Quarter Span

Figure B.4 Rotation of Compression Flange of Specimen G6

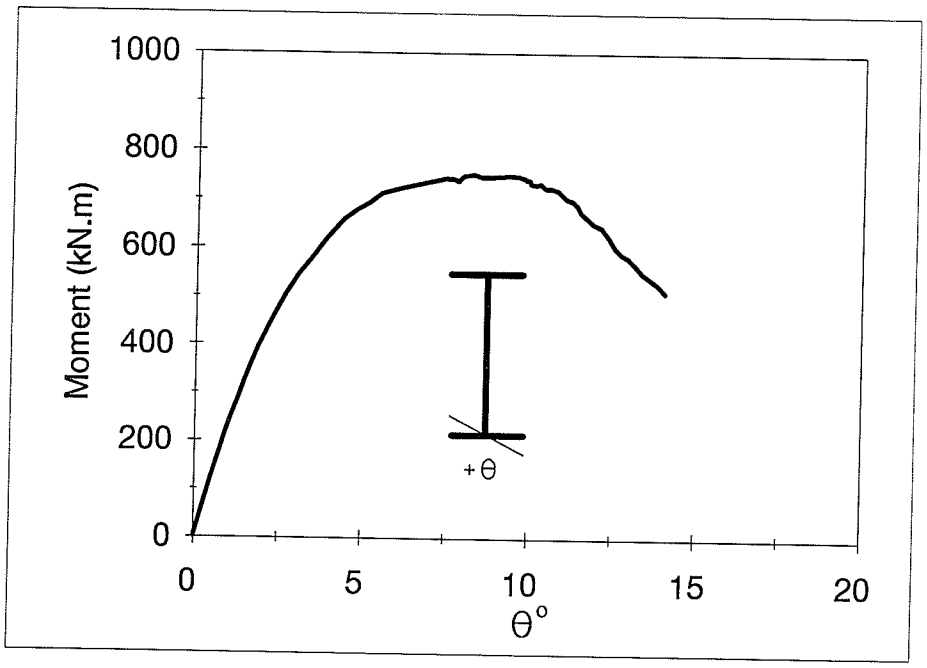

(a) Mid Span

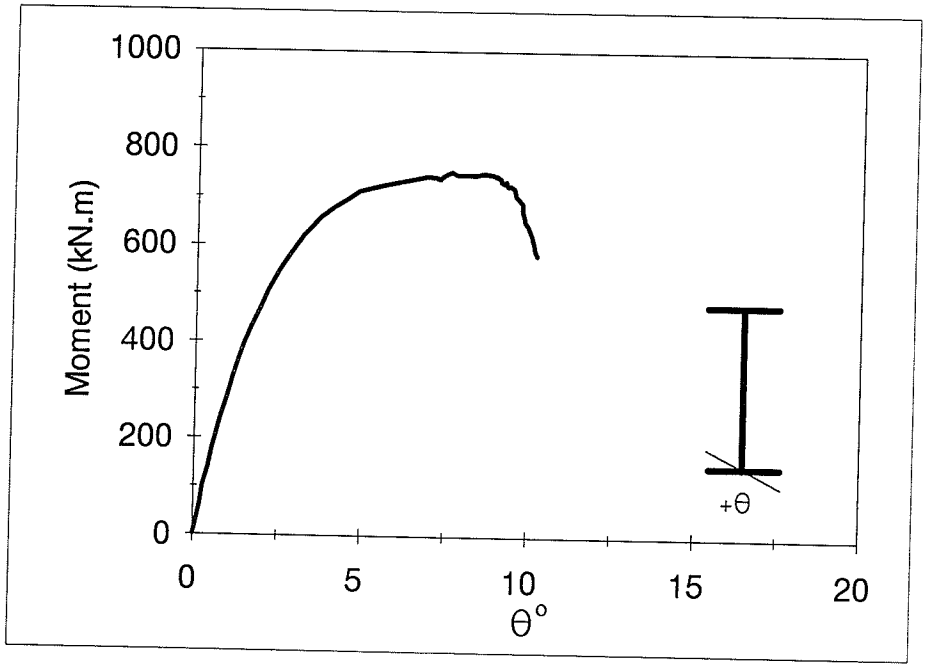

(b) Quarter Span

Figure B.5 Rotation of Compression Flange of Specimen G7

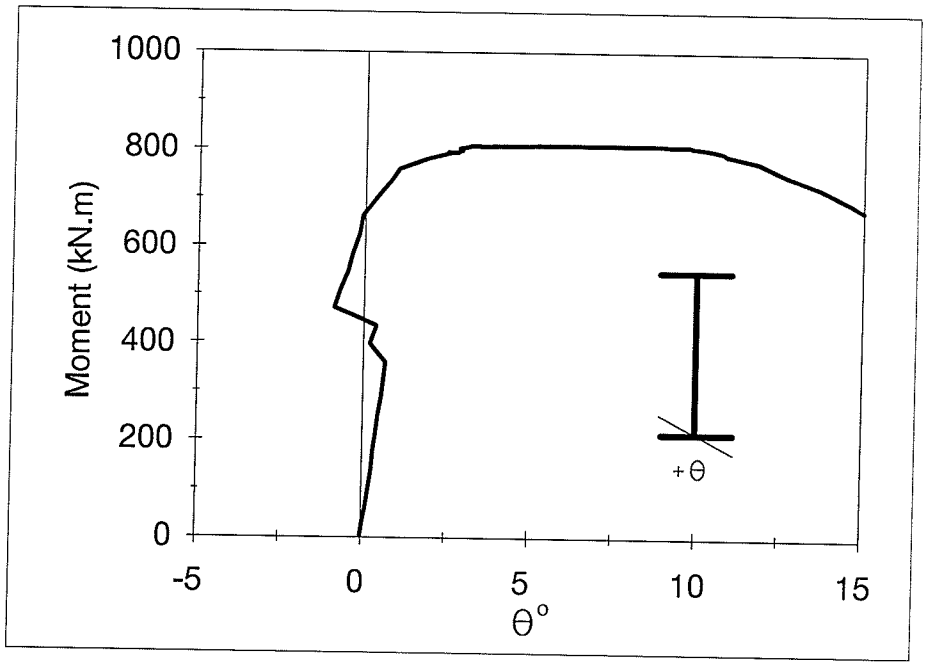

(a) Mid Span

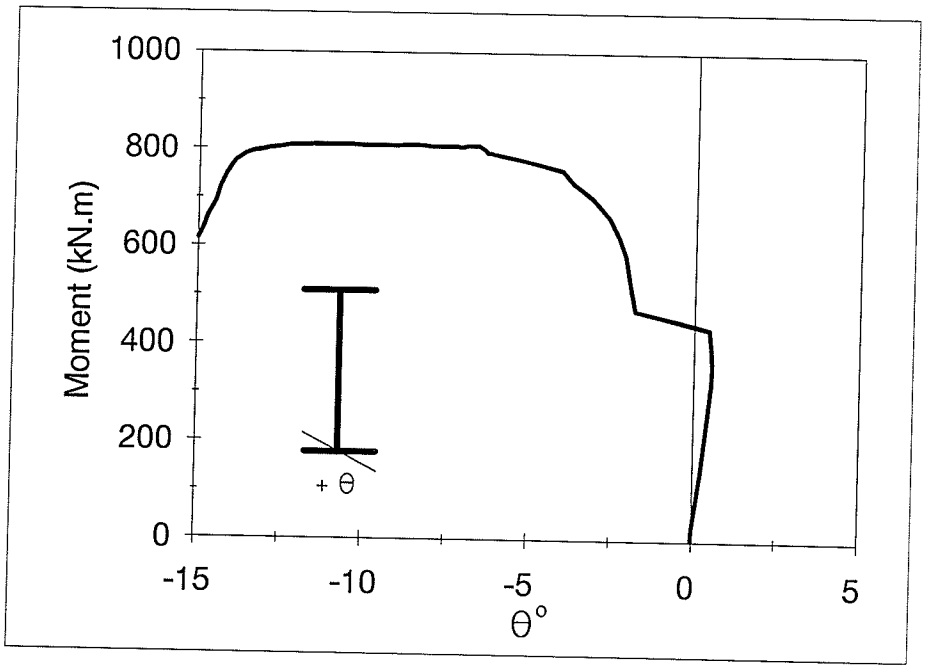

(b) Quarter Span

Figure B.6 Rotation of Compression Flange of Specimen G8

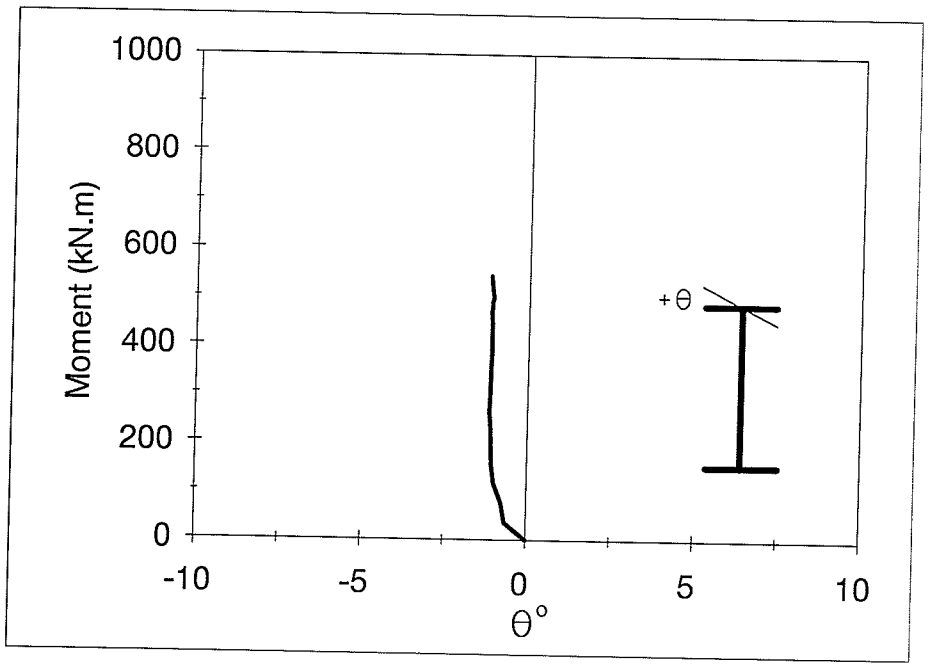

Figure B.7 Rotation of Tension Flange at Mid-Span of Specimen G2

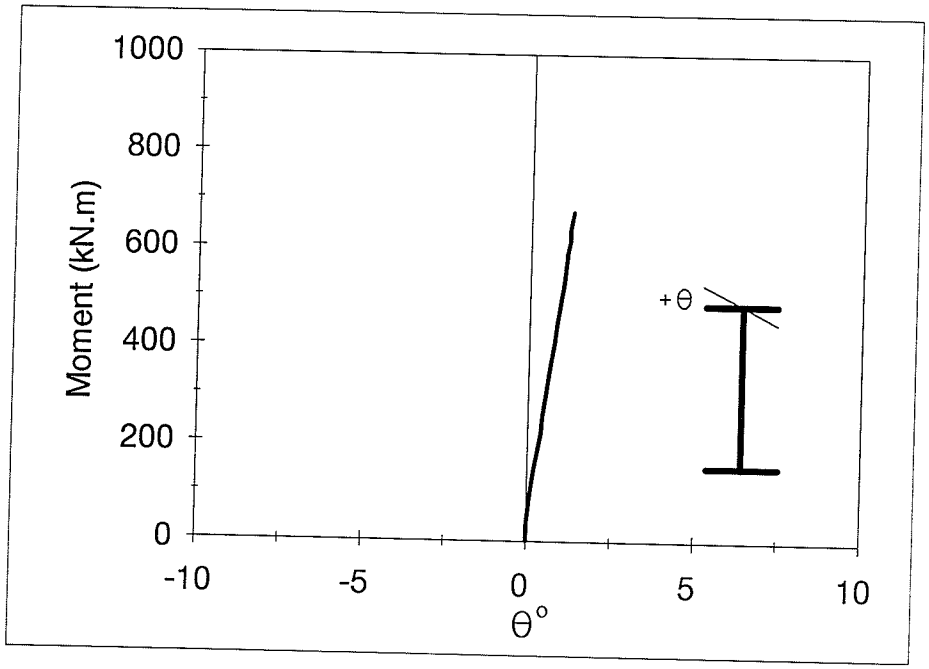

Figure B.8 Rotation of Tension Flange at Mid-Span of Speciemen G5

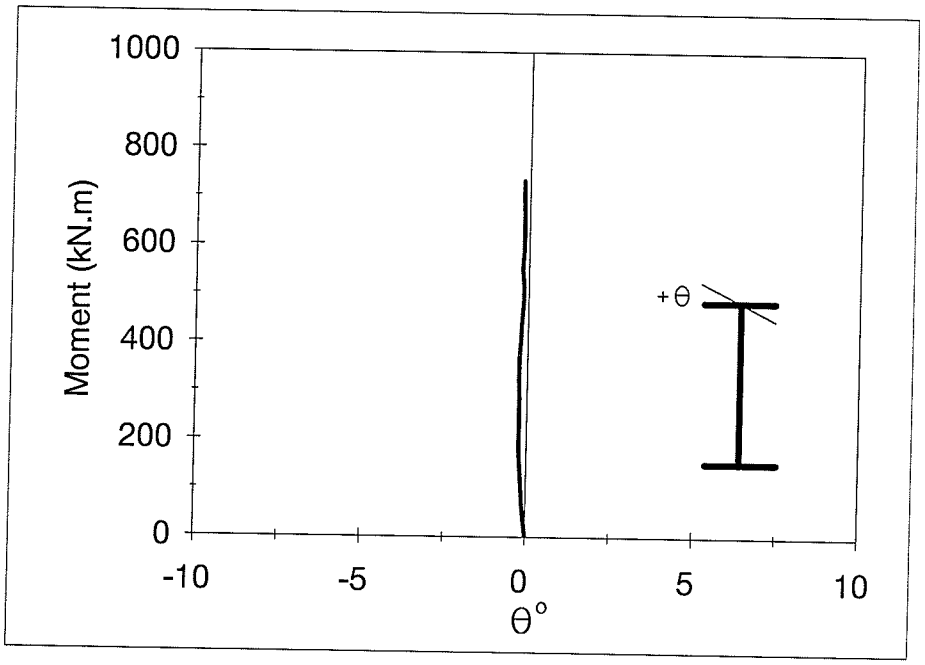

Figure B.9 Rotation of Tension Flange at Mid-Span of Specimen G6

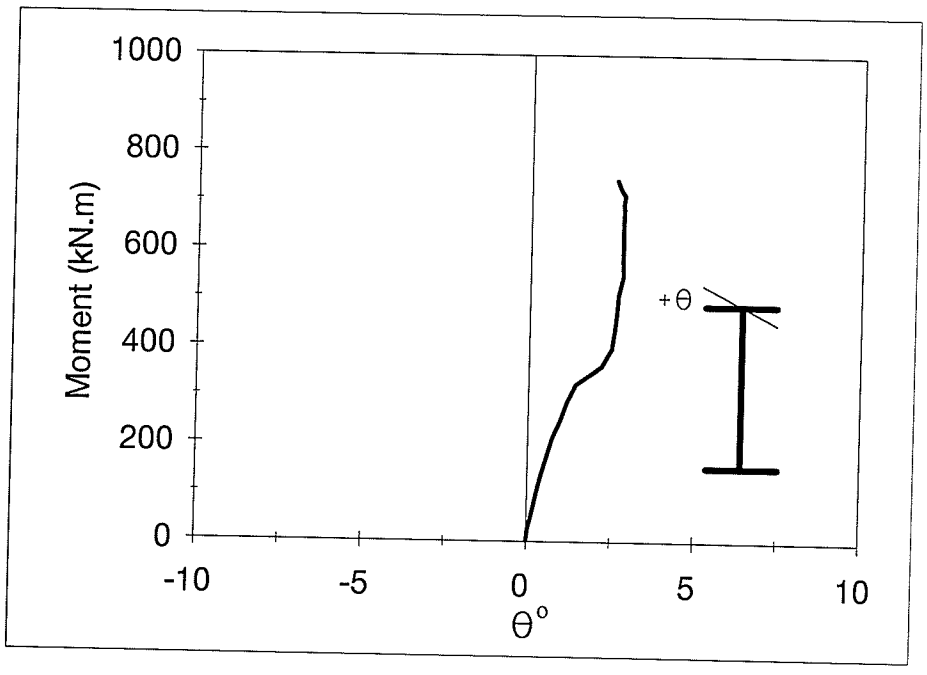

Figure B.10 Rotation of Tension Flange at Mid-Span of Specimen G7

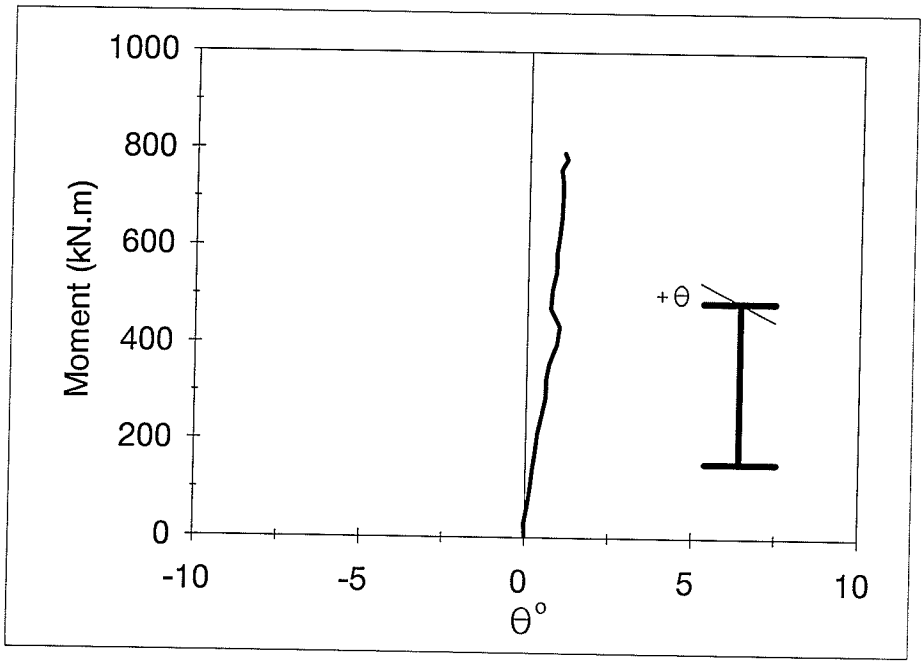

Figure B.11 Rotation of Tension Flange at Mid-Span of Specimen G8

APPENDIX C

WEB LATERAL DISPLACEMENT

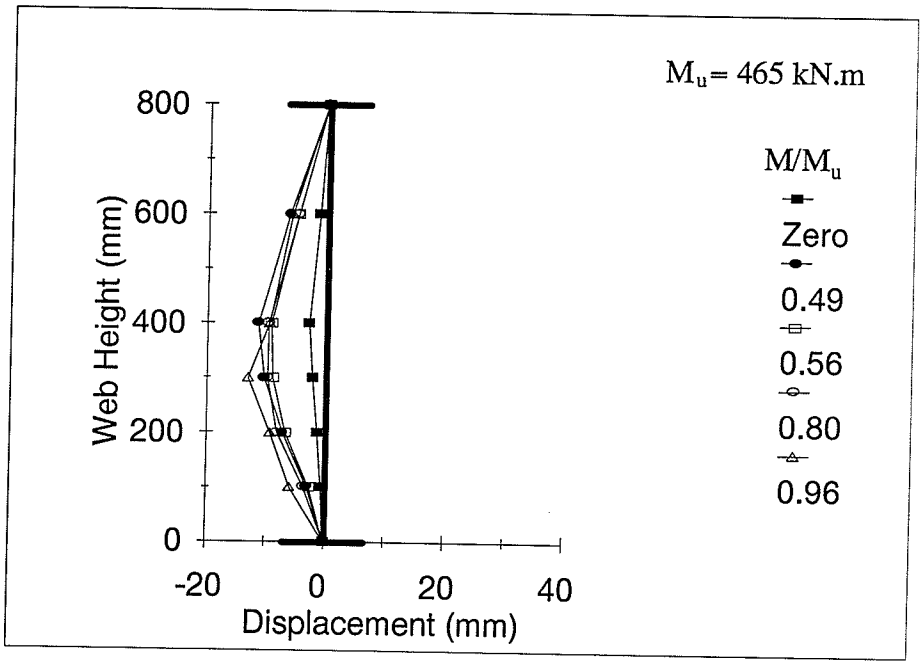

(a) Mid Span

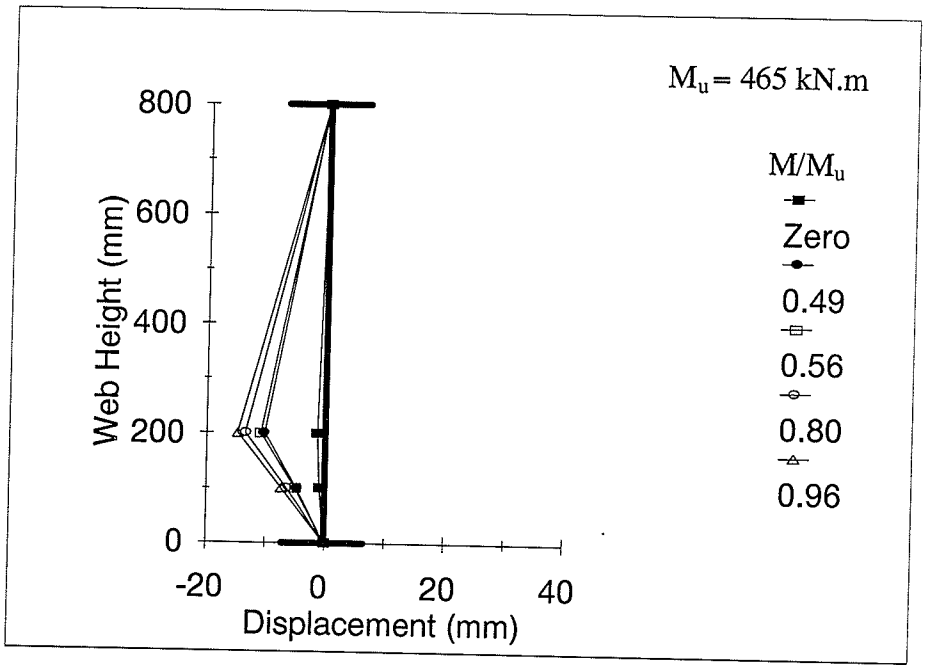

(b) Quarter Span

Figure C.1 Lateral Displacement of the Web of Specimen G1

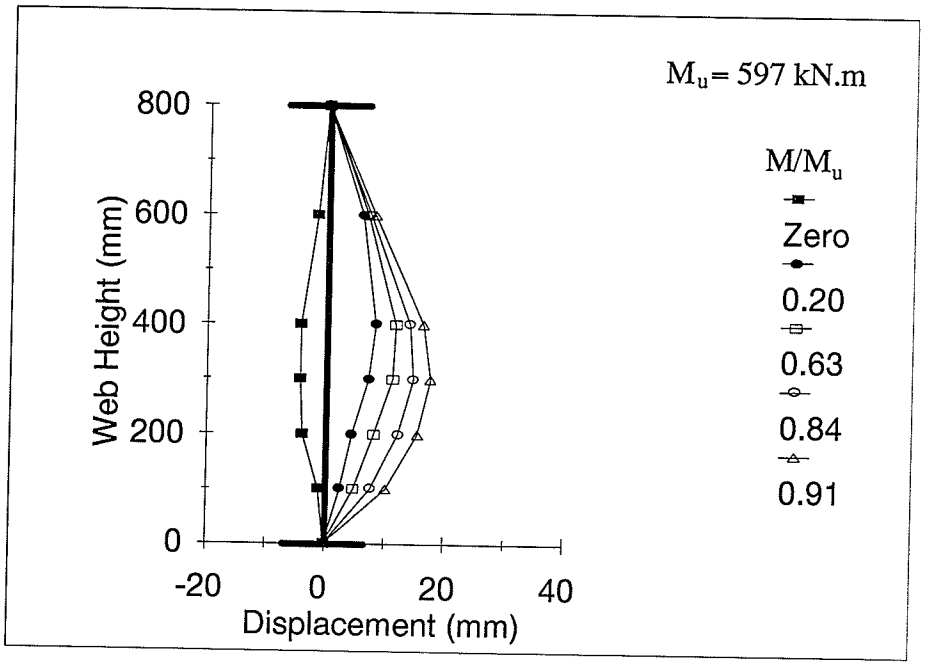

(a) Mid Span

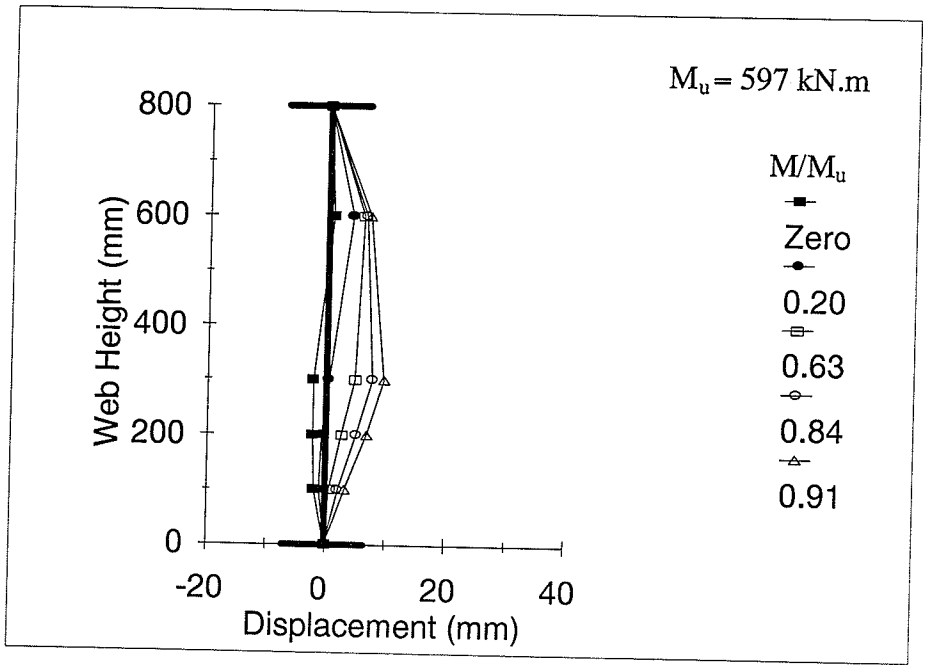

(b) Quarter Span

Figure C.2 Lateral Displacement of the Web of Specimen G3

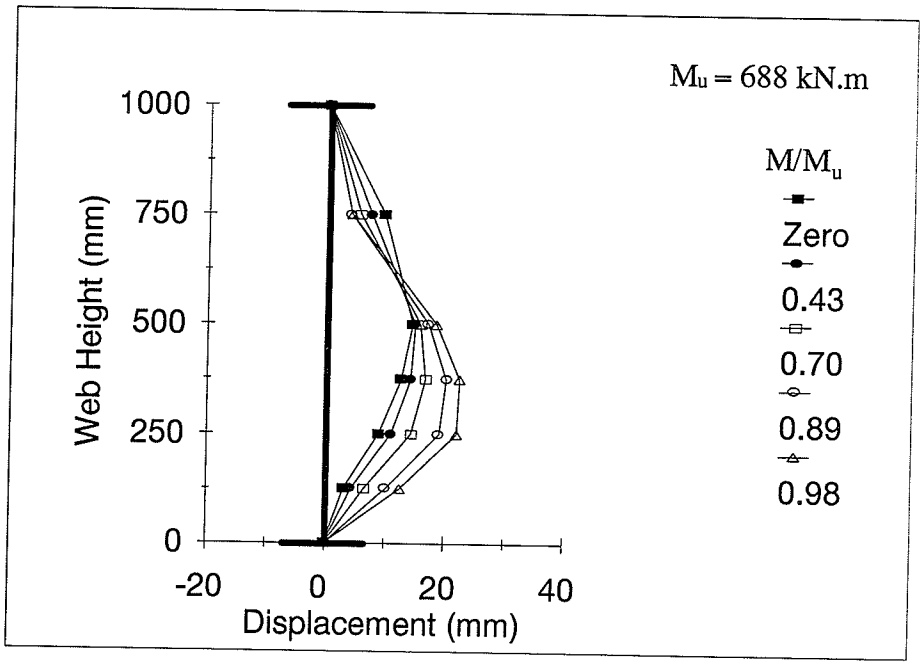

(a) Mid Span

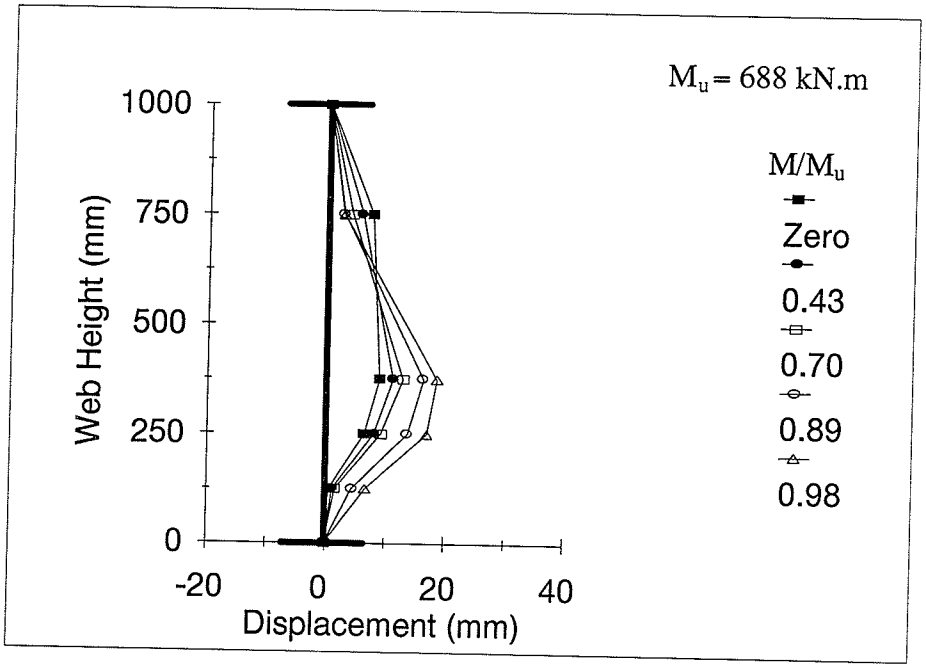

(b) Quarter Span

Figure C.3 Lateral Displacement of the Web of Specimen G5

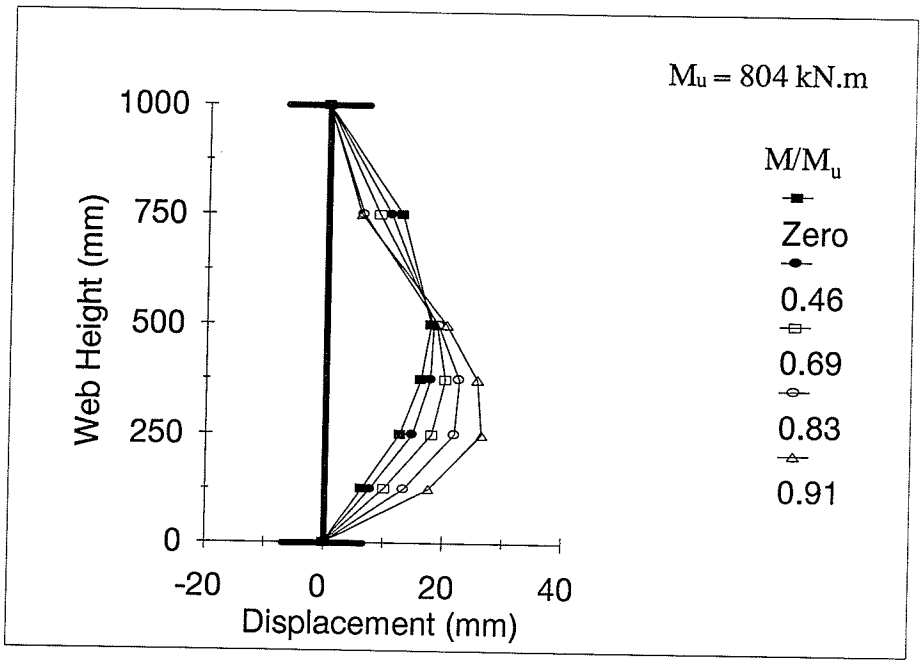

(a) Mid Span

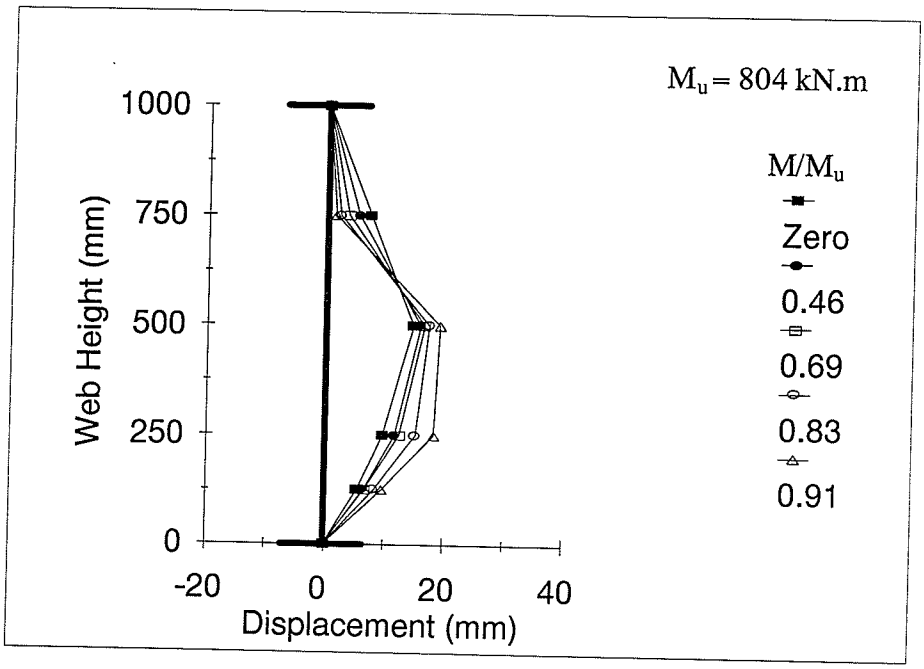

(b) Quarter Span

Figure C.4 Lateral Displacement of the Web of Specimen G6

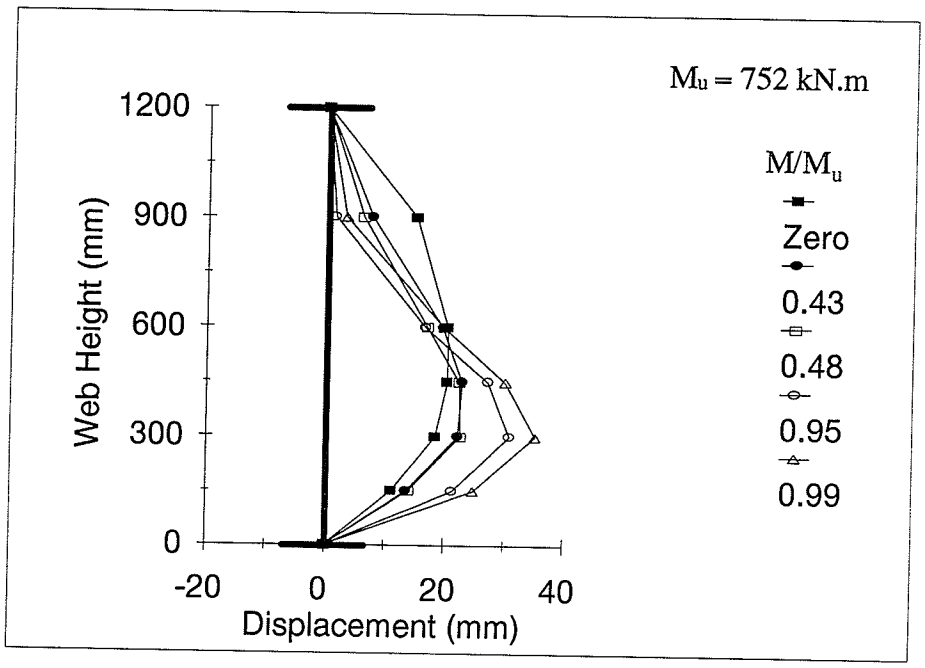

(a) Mid Span

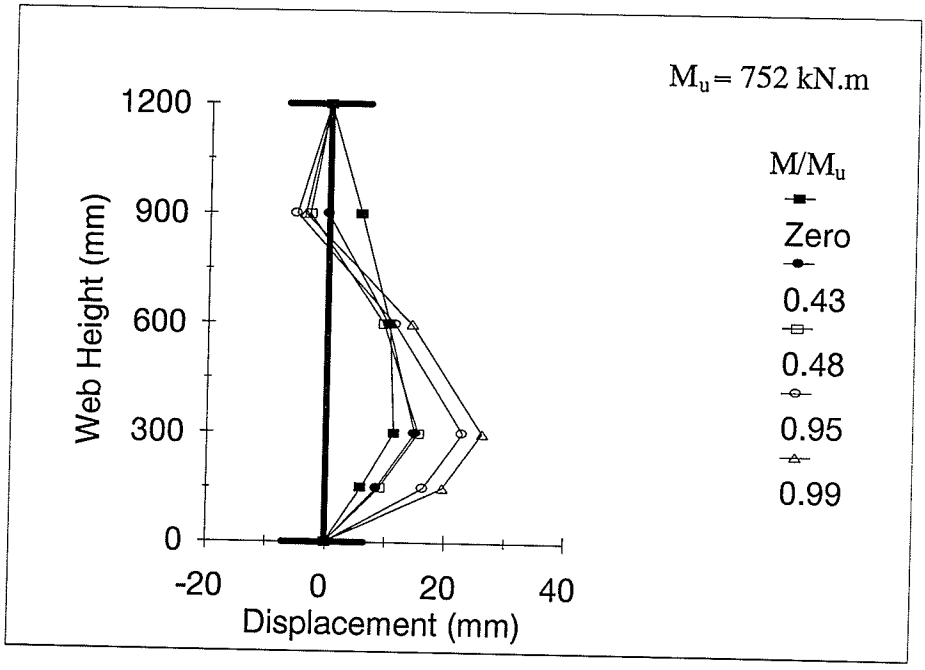

(b) Quarter Span

Figure C.5 Lateral Displacement of the Web of Specimen G7

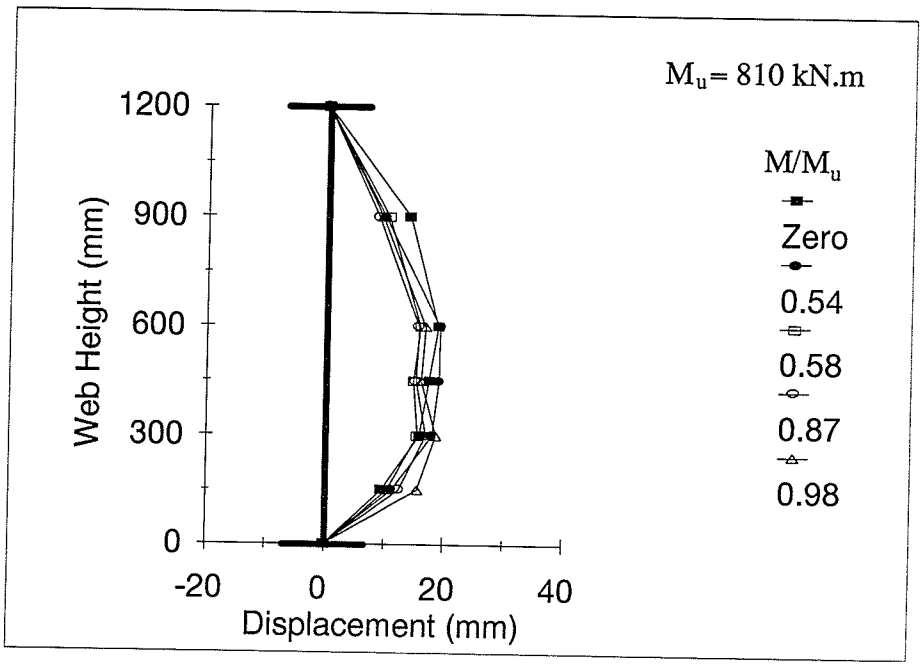

(a) Mid Span

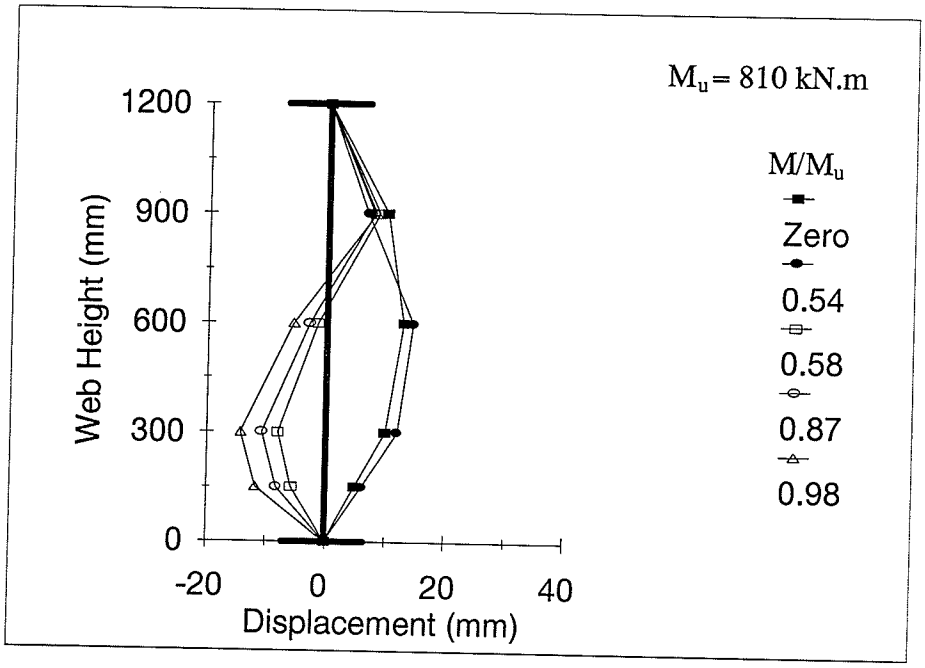

(b) Quarter Span

Figure C.6 Lateral Displacement of the Web of Specimen G8

APPENDIX D

MOMENT-WEB LATERAL

DISPLACEMENT CURVES

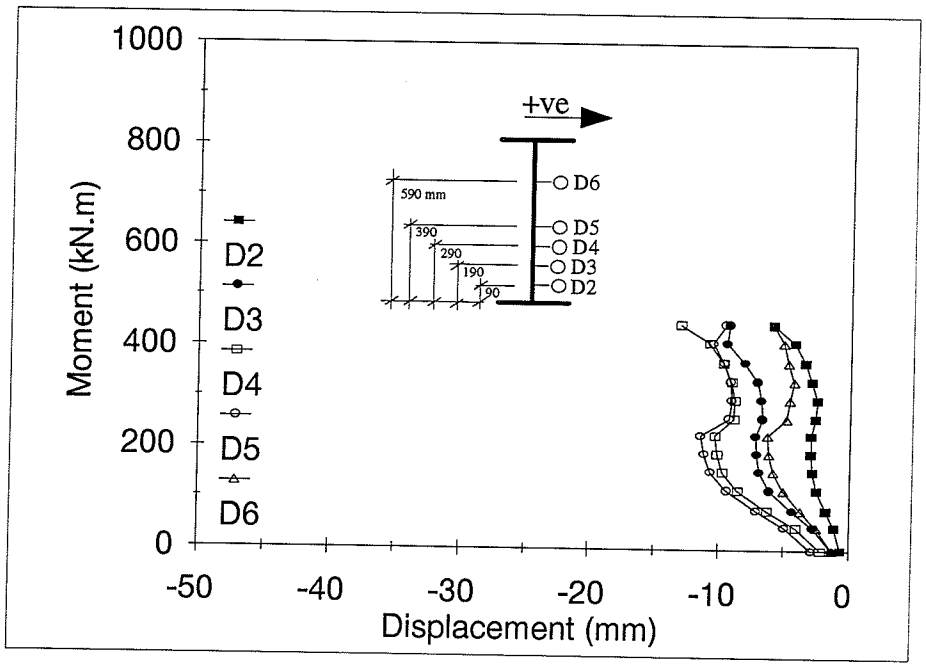

(a) Mid Span

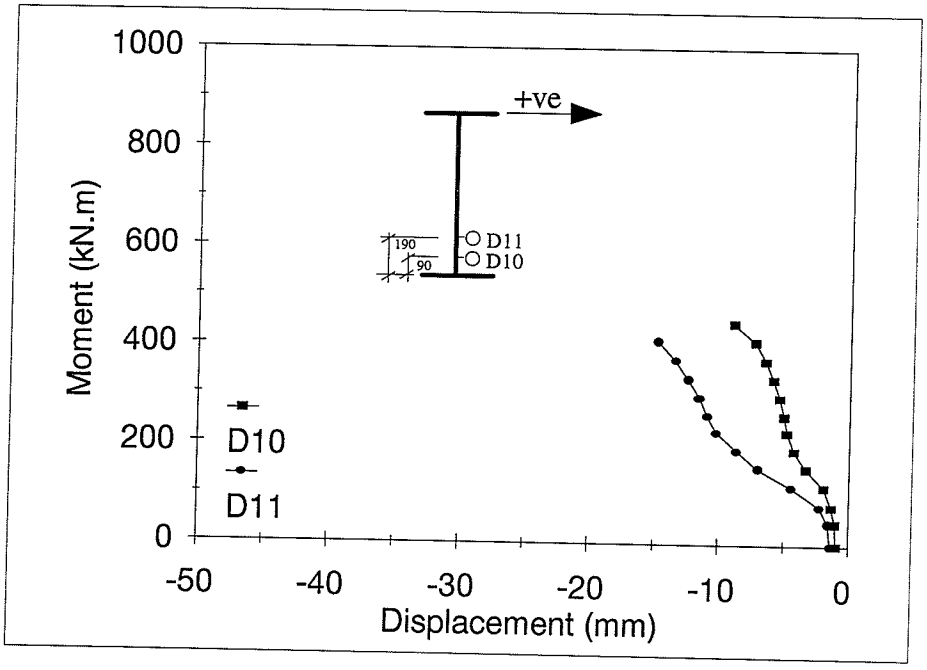

(b) Quarter Span

Figure D.1 Lateral Displacement Curves of the Web of Specimen G1

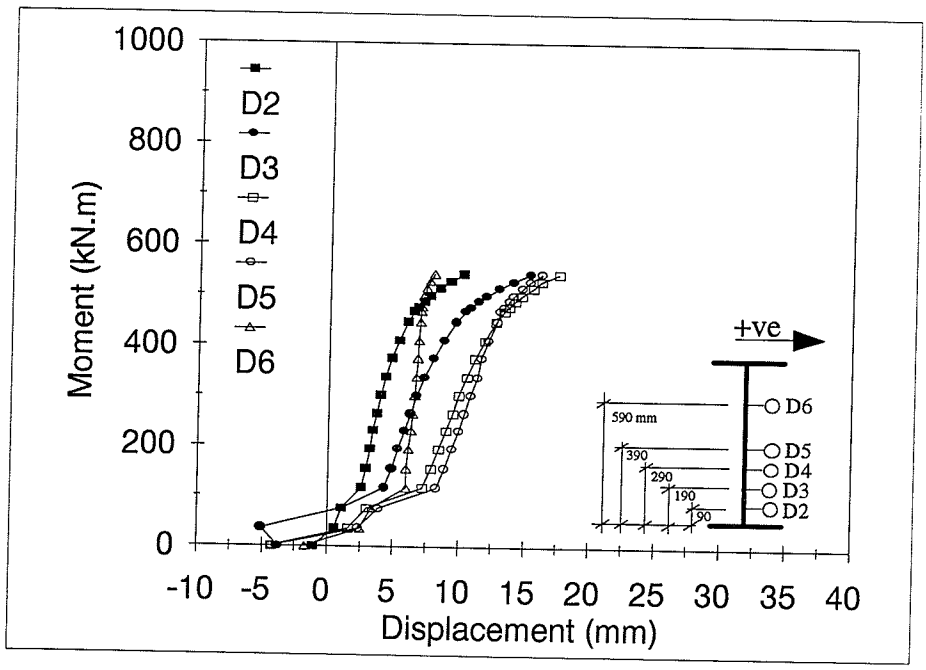

(a) Mid Span

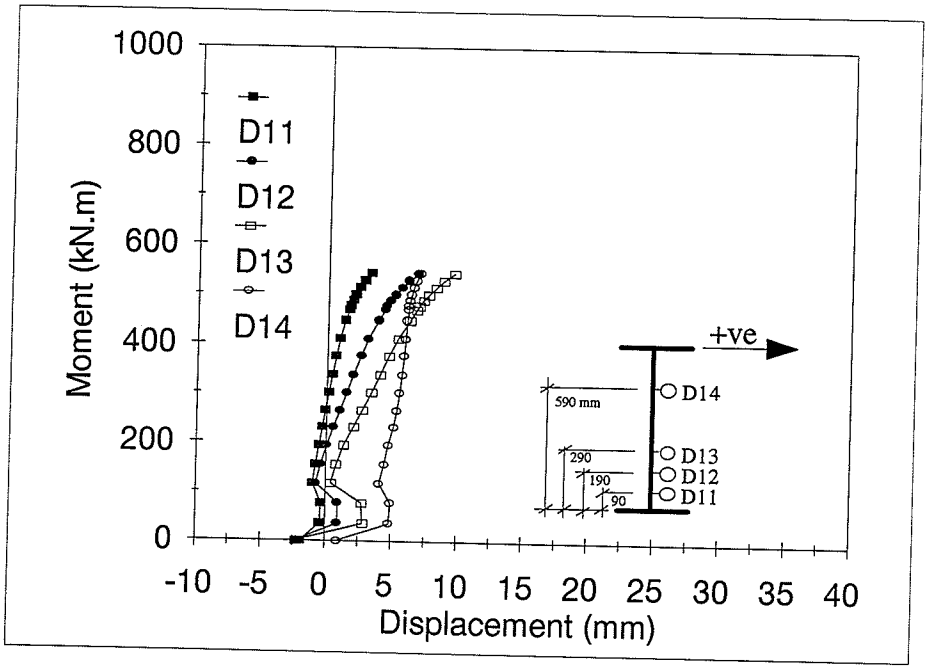

(b) Quarter Span

Figure D.2 Lateral Displacement Curves of the Web of Specimen G3

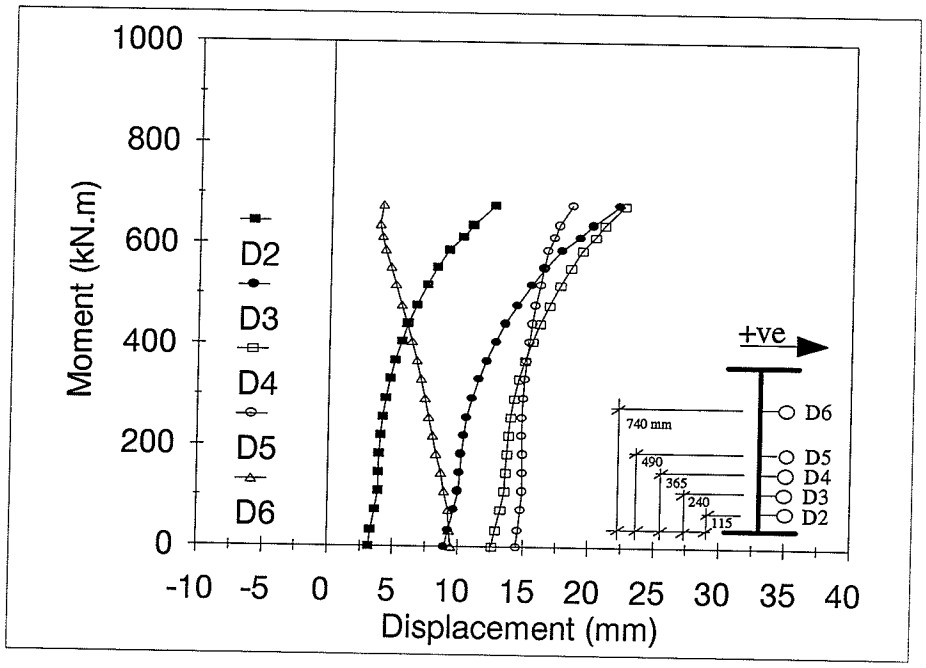

(a) Mid Span

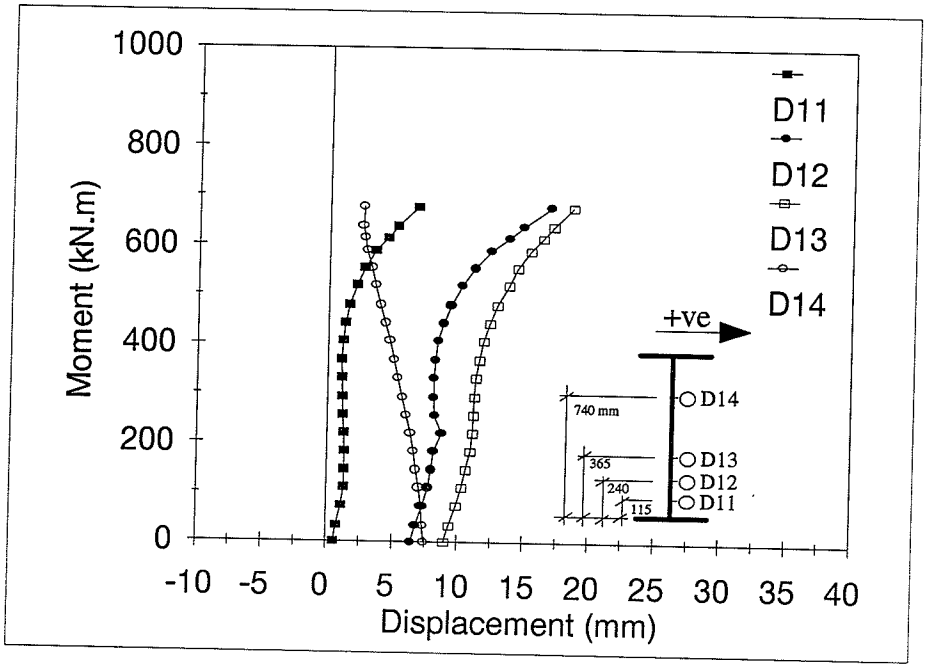

(b) Quarter Span

Figure D.3 Lateral Displacement Curves of the Web of Specimen G5

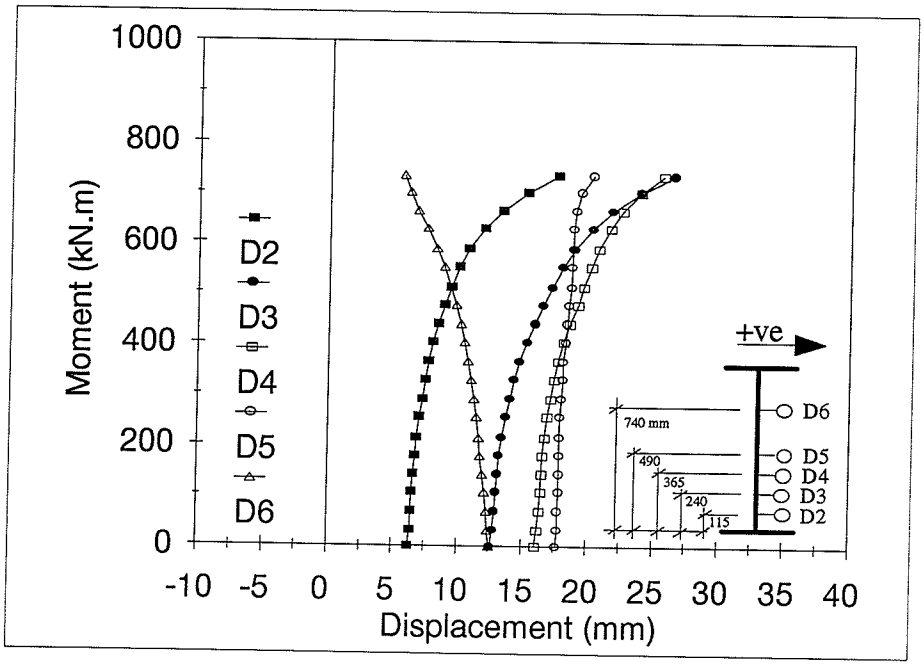

(a) Mid Span

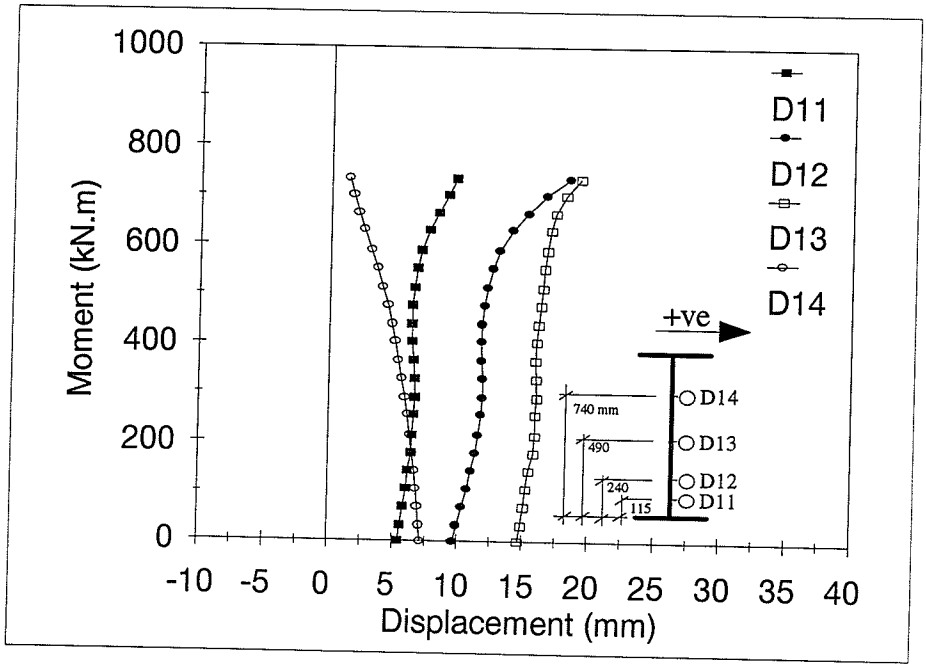

(b) Quarter Span

Figure D.4 Lateral Displacement Curves of the Web of Specimen G6

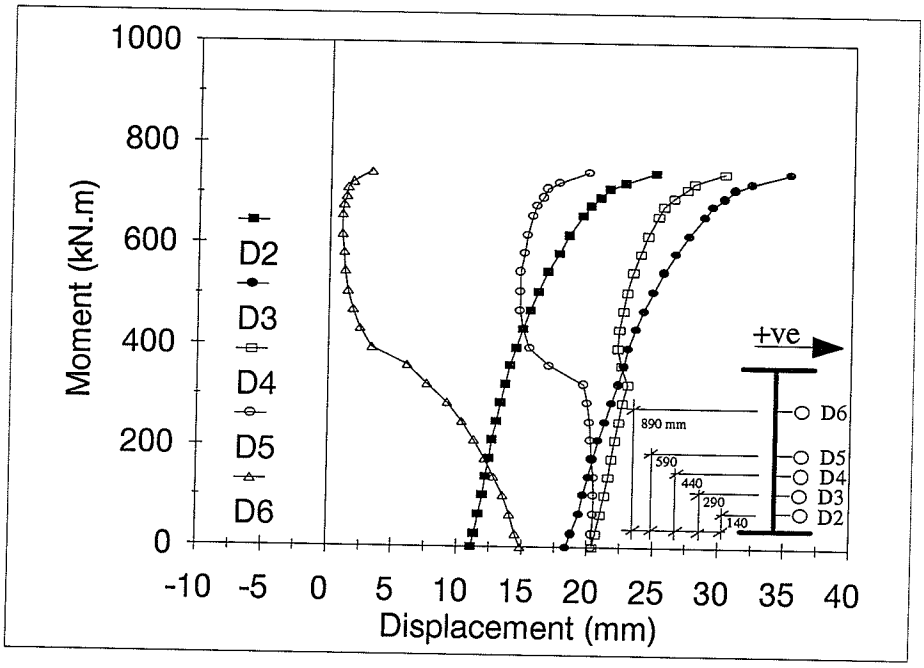

(a) Mid Span

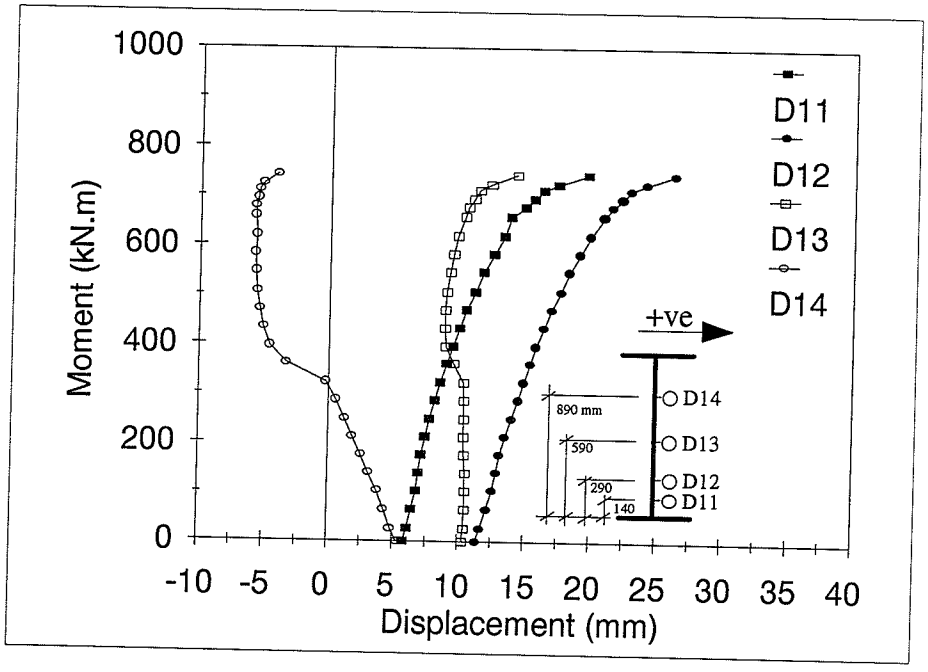

(b) Quarter Span

Figure D.5 Lateral Displacement Curves of the Web of Specimen G7

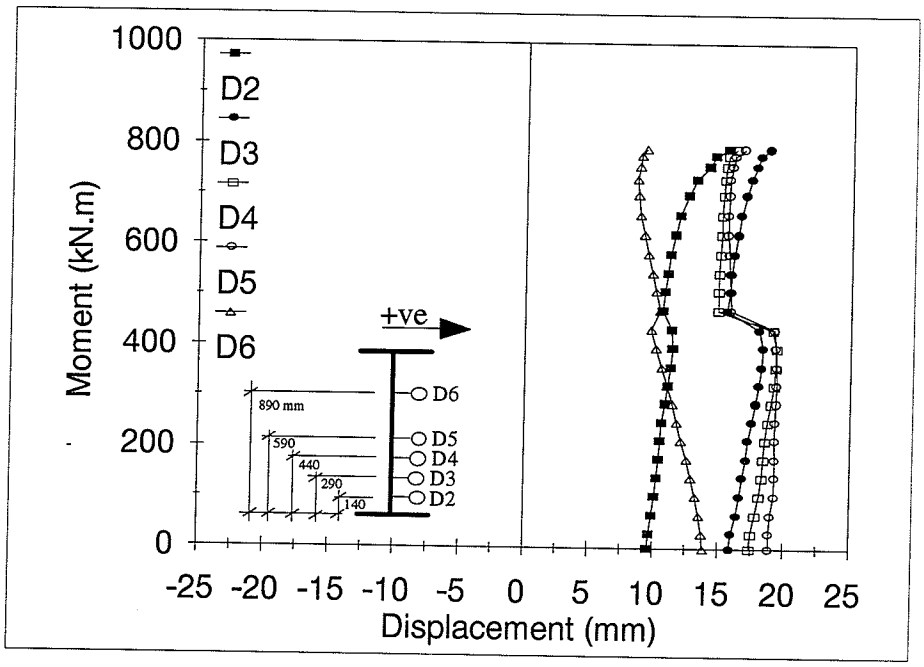

(a) Mid Span

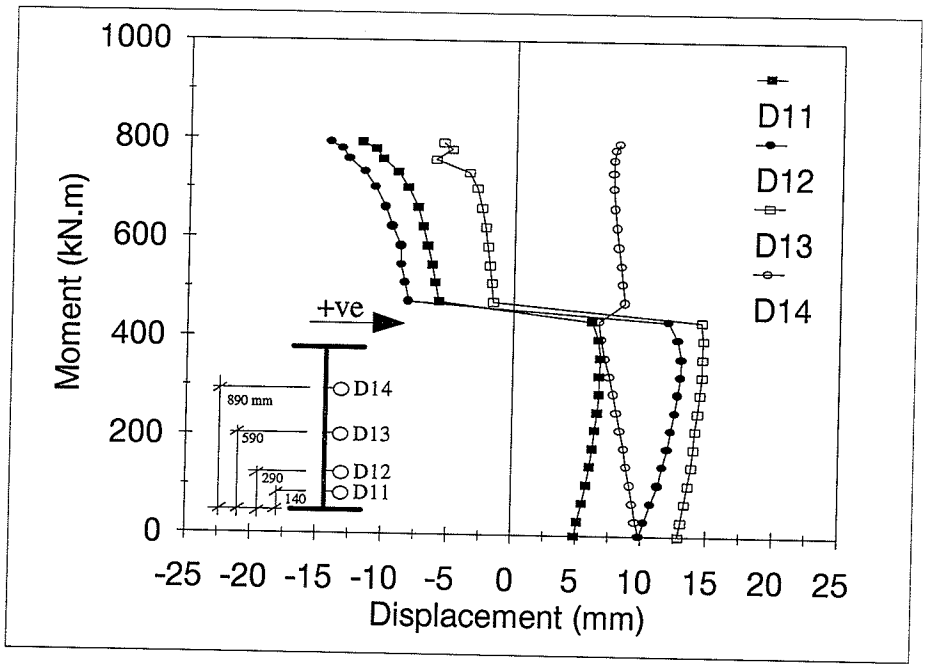

(b) Quarter Span

Figure D.6 Lateral Displacement Curves of the Web of Specimen G8

APPENDIX E

WEB-FLANGE ANGLE

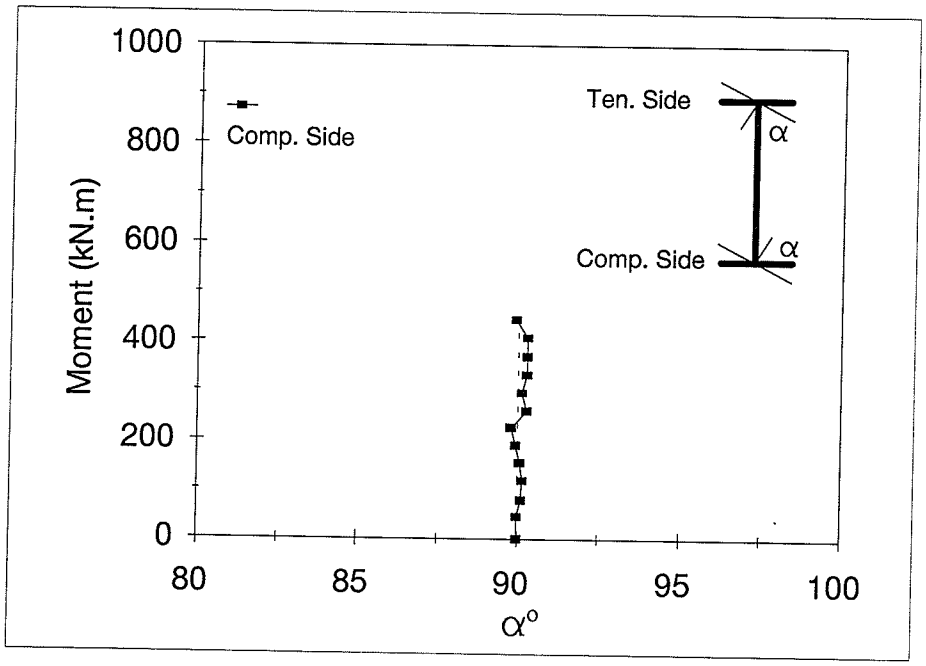

(a) Mid Span

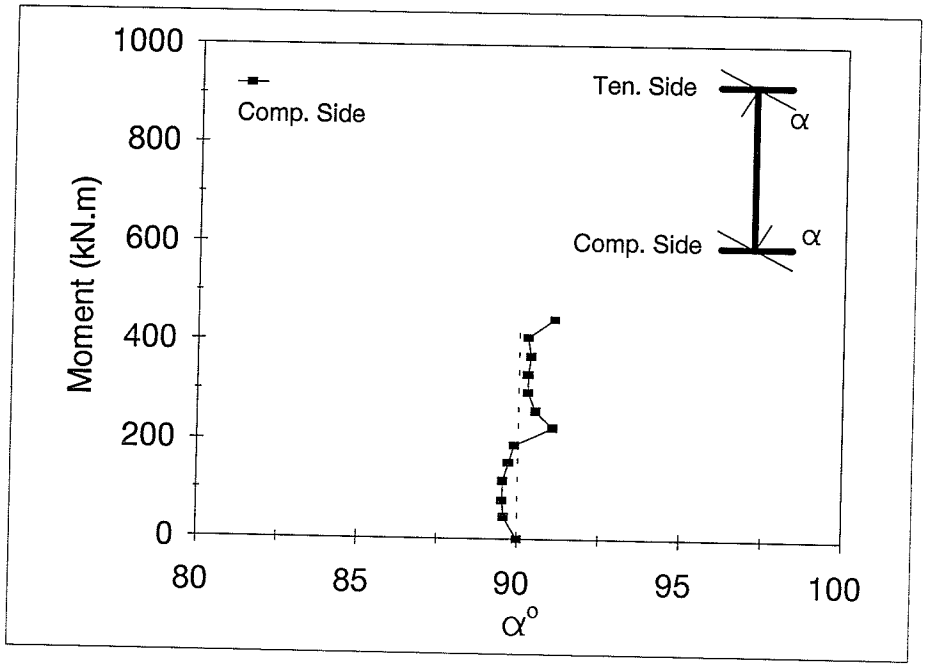

(b) Quarter Span

Figure E.1 Web-Flange Angle as a Function of Applied Moment of Specimen G1

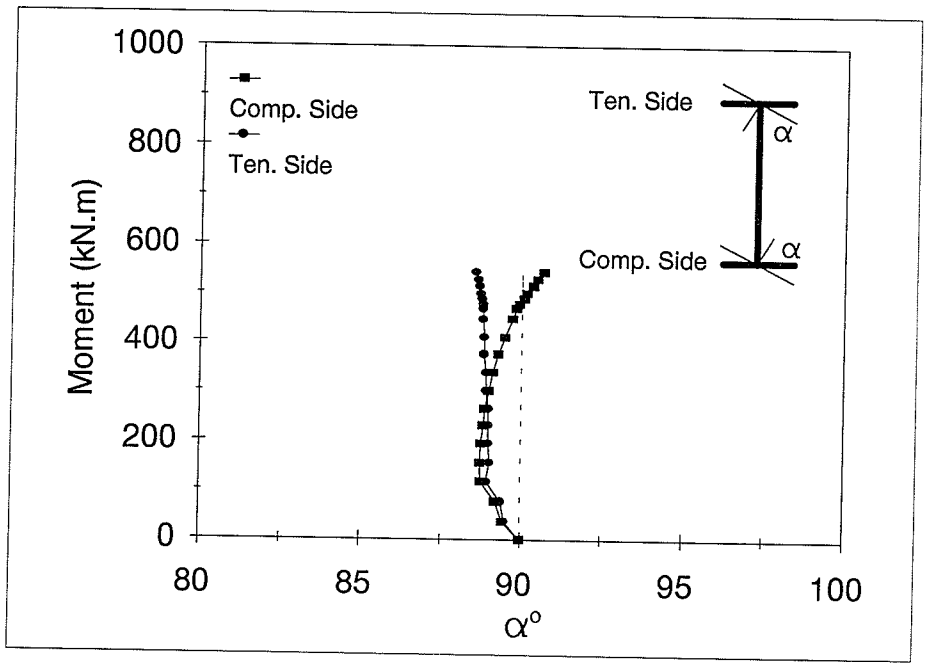

(a) Mid Span

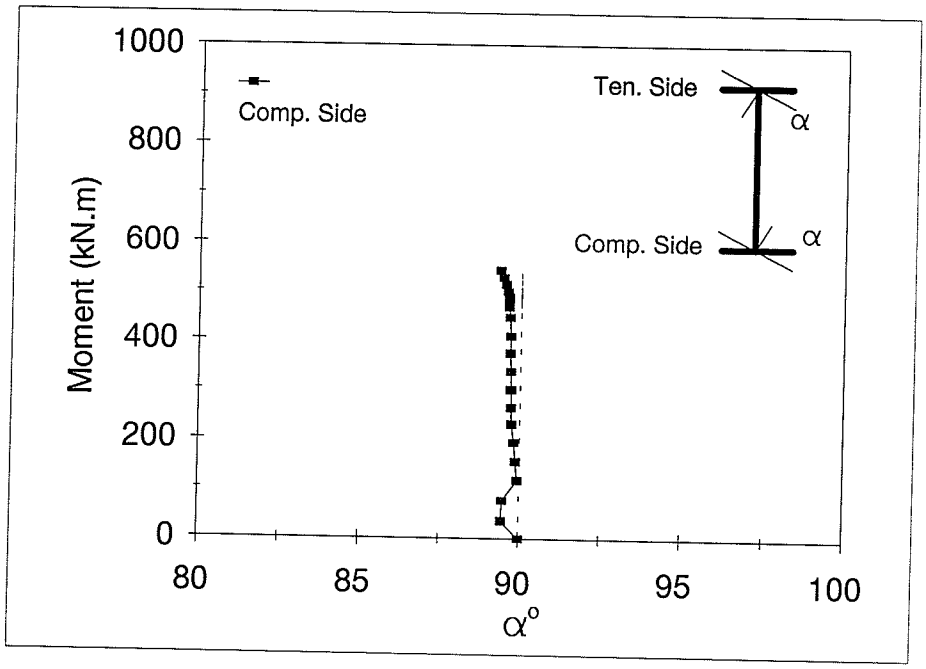

(b) Quarter Span

Figure E.2 Web-Flange Angle as a Function of Applied Moment of Specimen G3

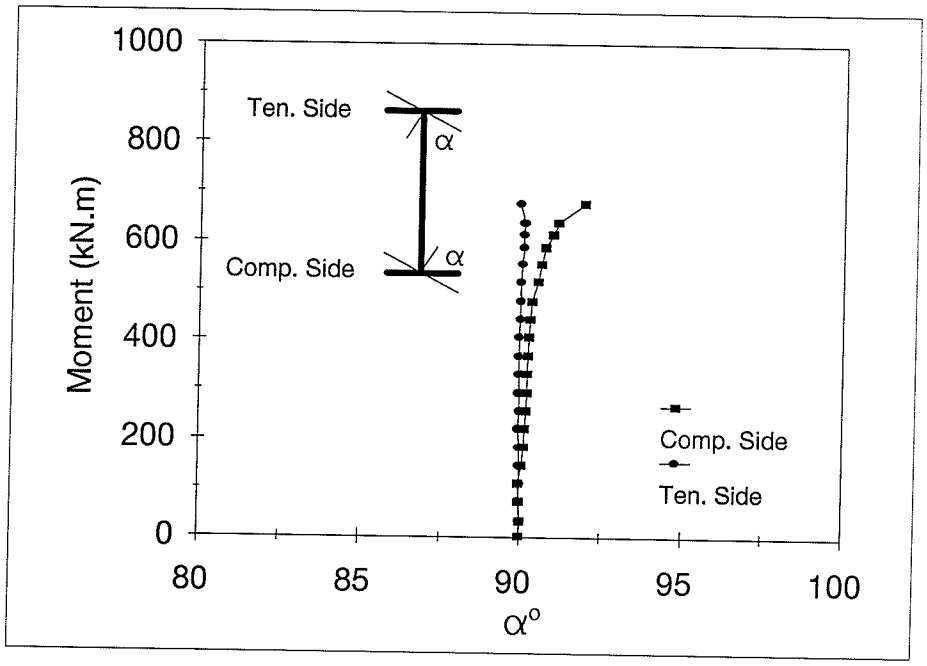

(a) Mid Span

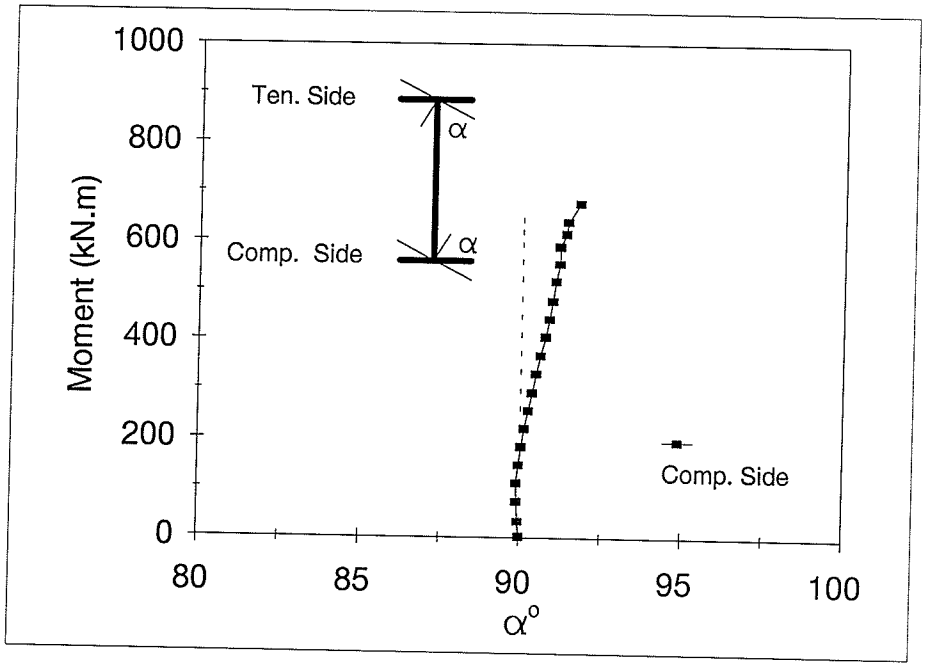

(b) Quarter Span

Figure E.3 Web-Flange Angle as a Function of Applied Moment of Specimen G5

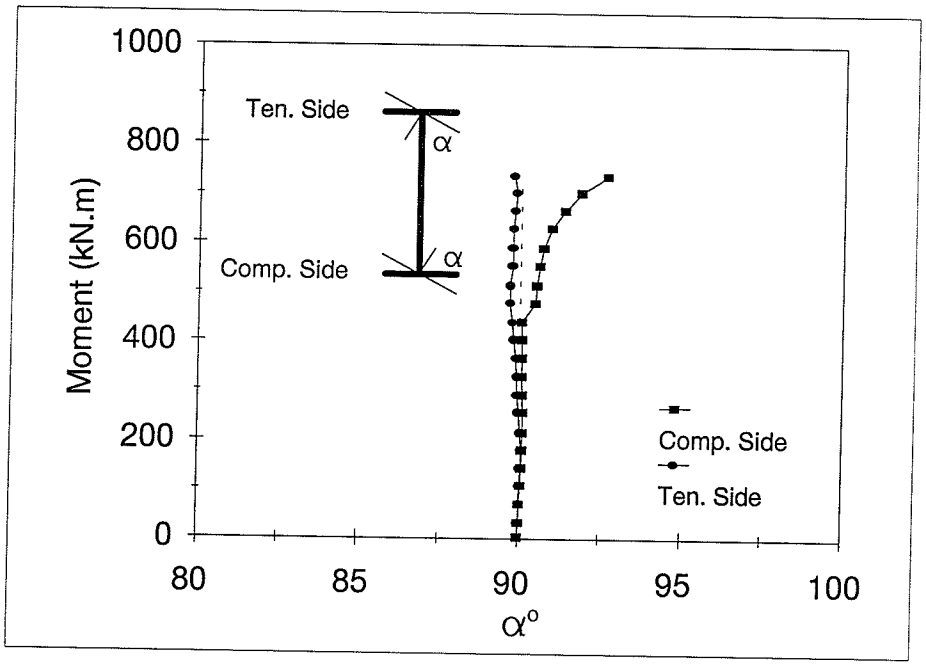

(a) Mid Span

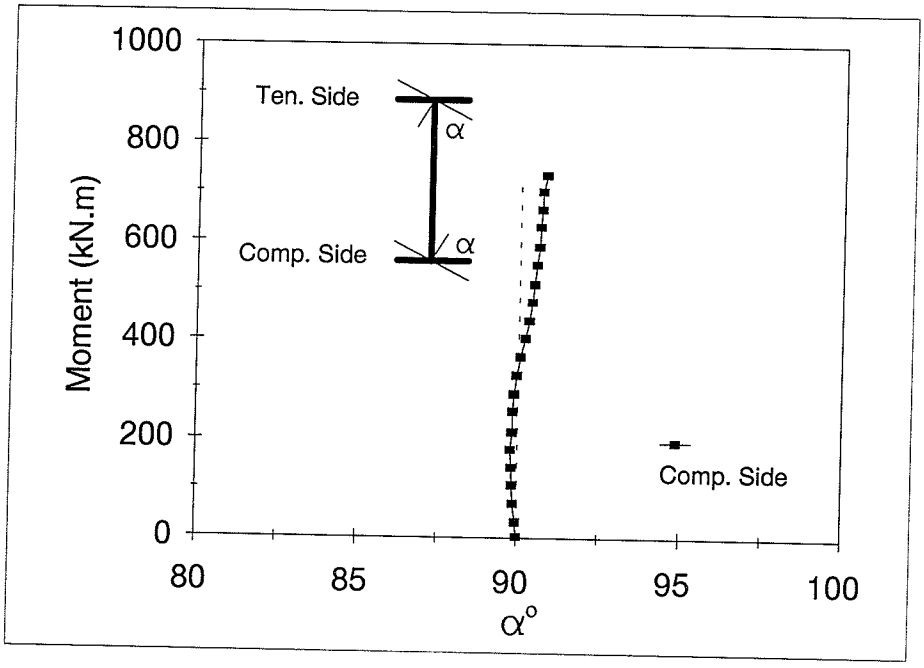

(b) Quarter Span

Figure E.4 Web-Flange Angle as a Function of Applied Moment of Specimen G6

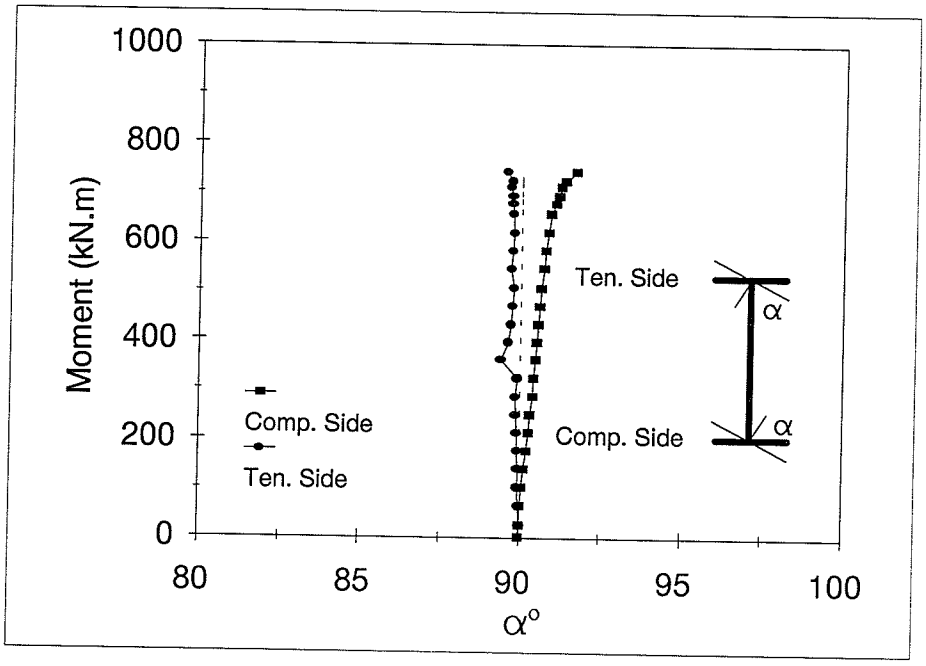

(a) Mid Span

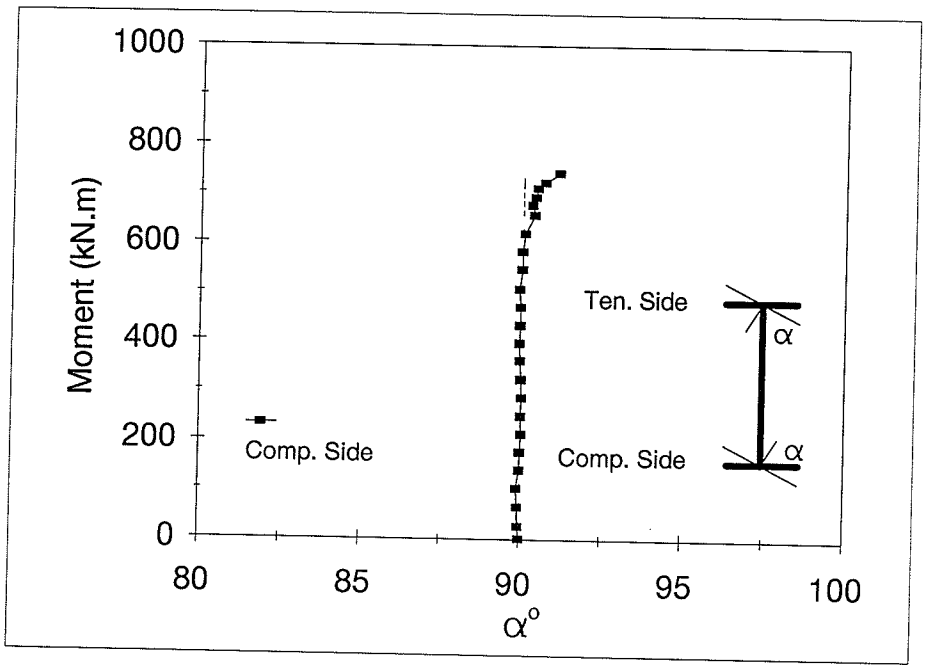

(b) Quarter Span

Figure E.5 Web-Flange Angle as a Function of Applied Moment of Specimen G7

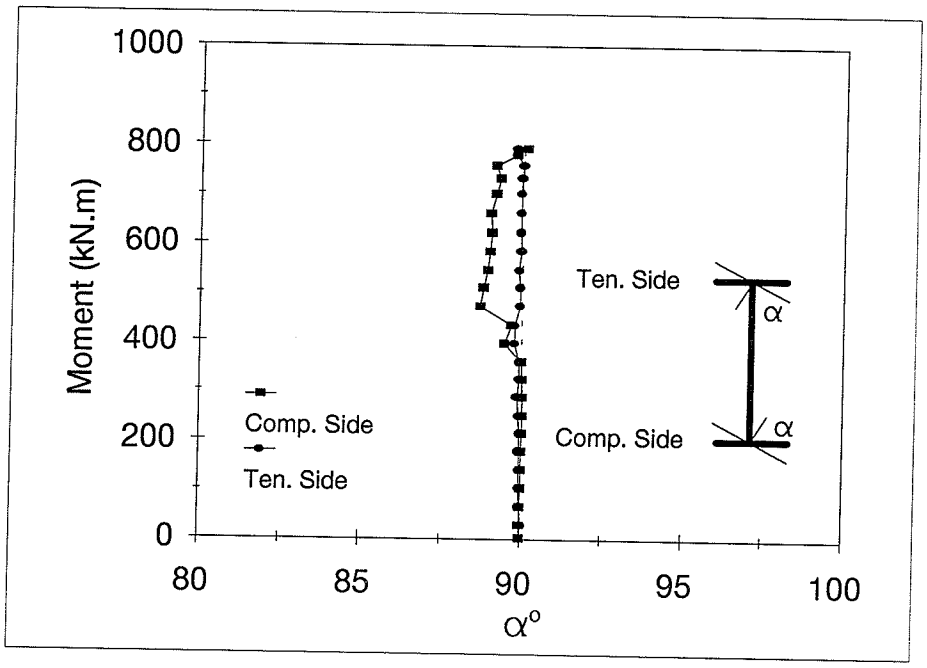

(a) Mid Span

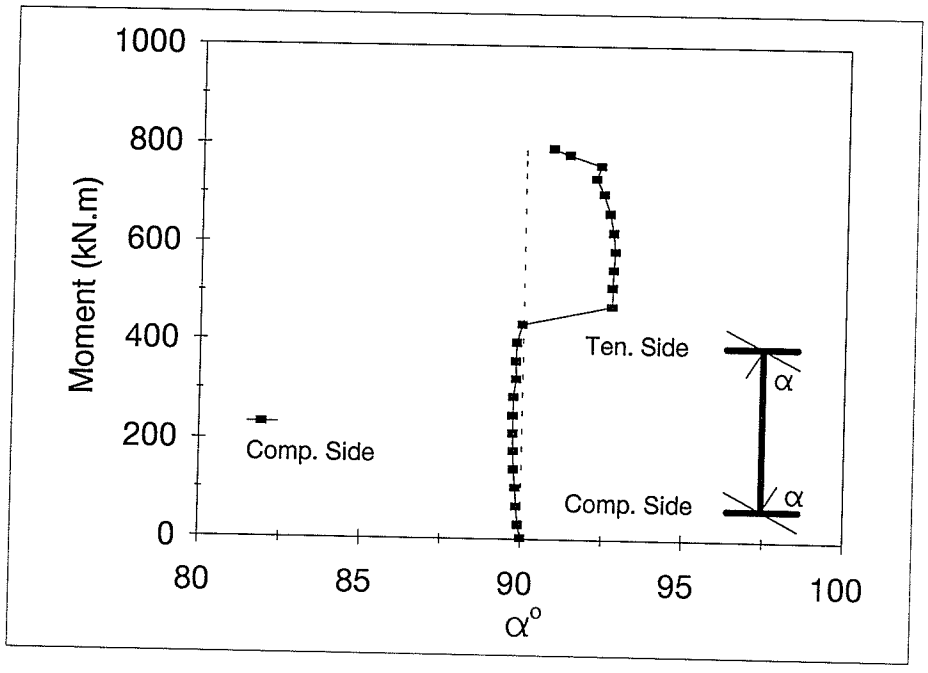

(b) Quarter Span

Figure E.6 Web-Flange Angle as a Function of Applied Moment of Specimen G8

APPENDIX F

STRAIN DISTRIBUTION

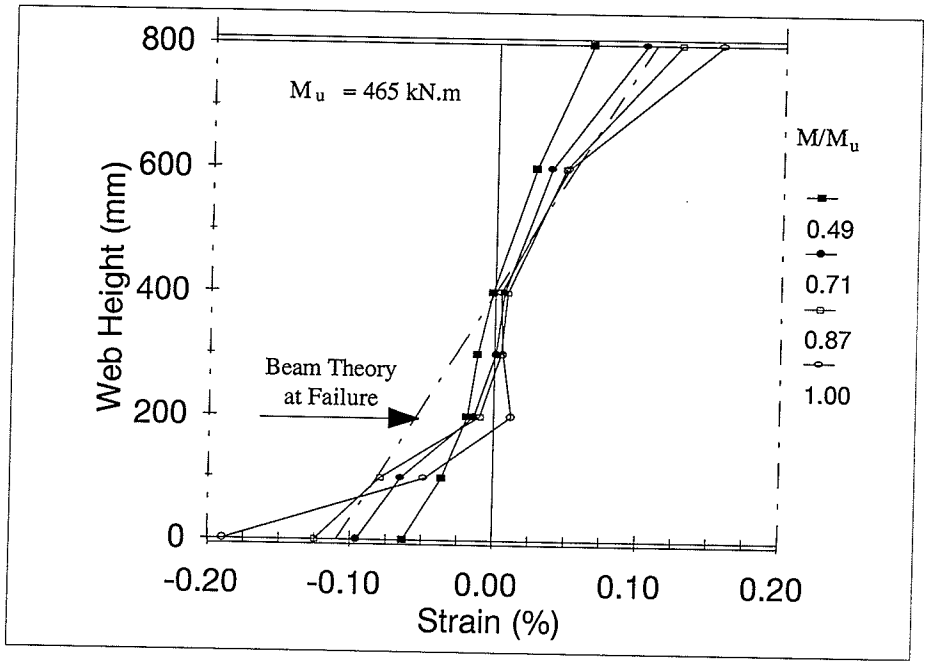

(a) Mid Span

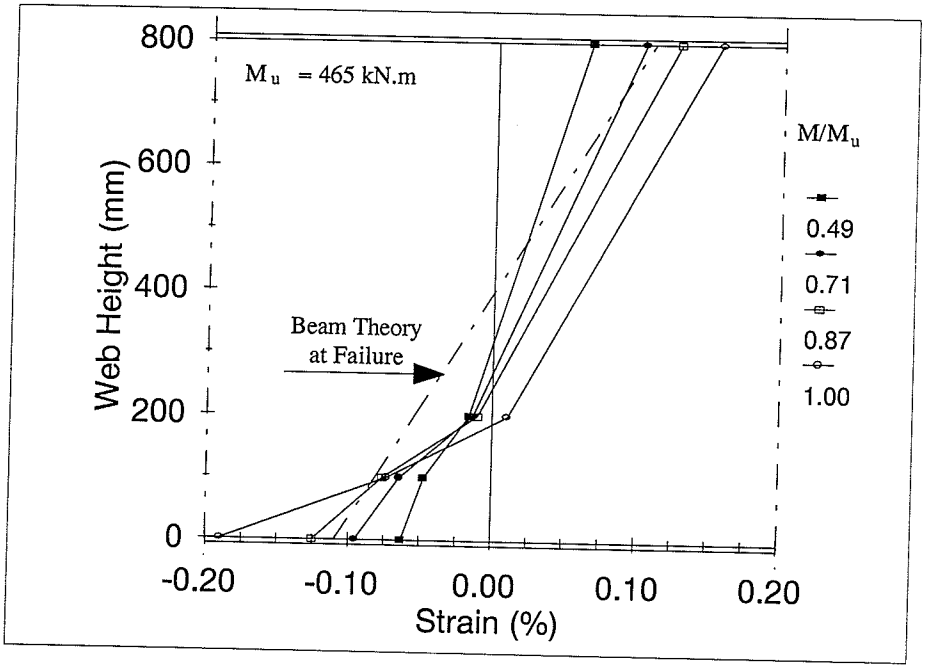

(b) Quarter Span

Figure F.1 Strain Distribution Along Cross-Sections of Specimen G1

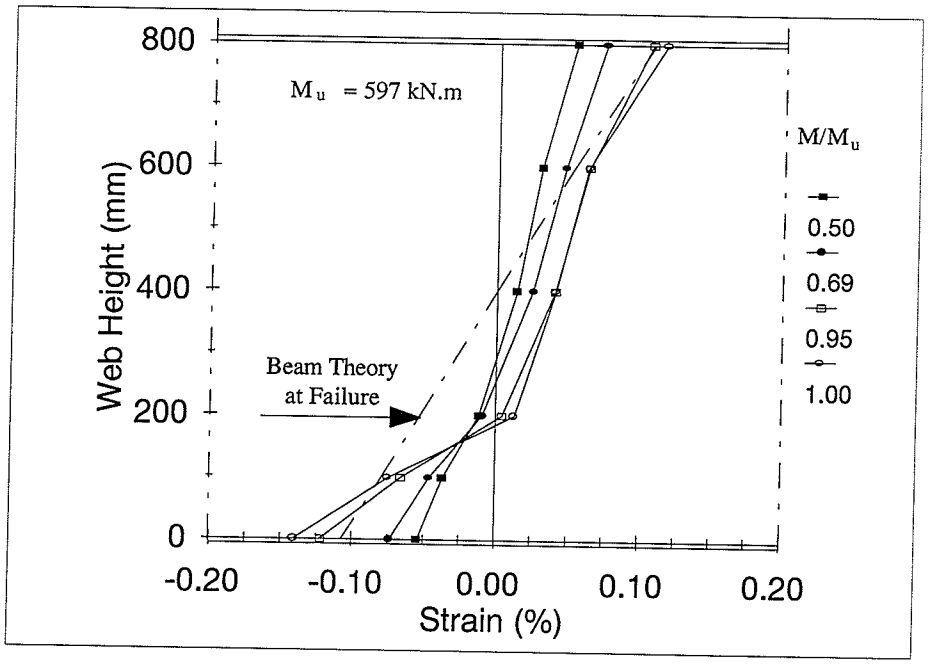

(a) Mid Span

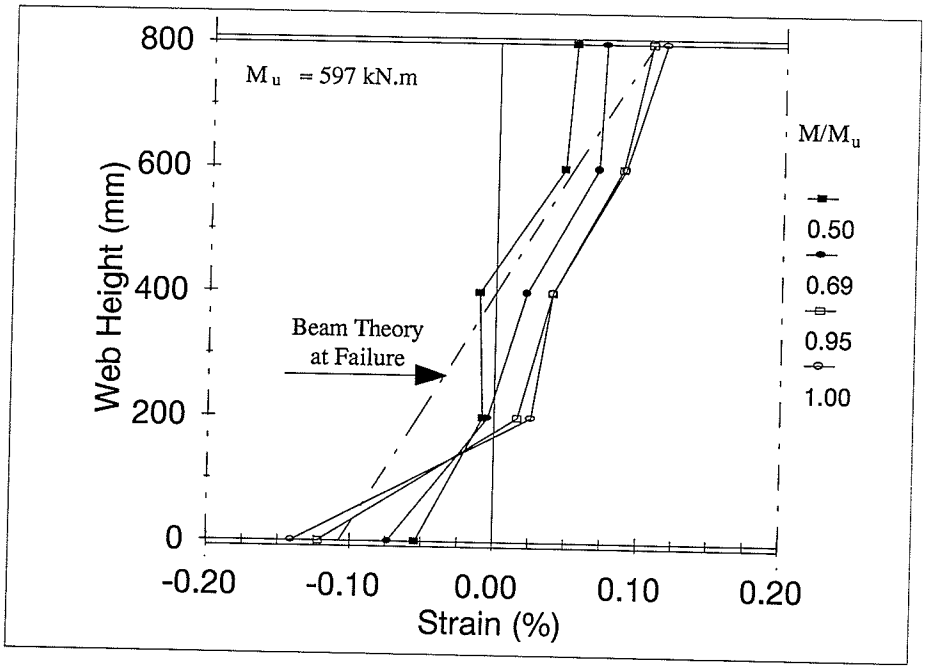

(b) Quarter Span

Figure F.2 Strain Distribution Along Cross-Sections of Specimen G3

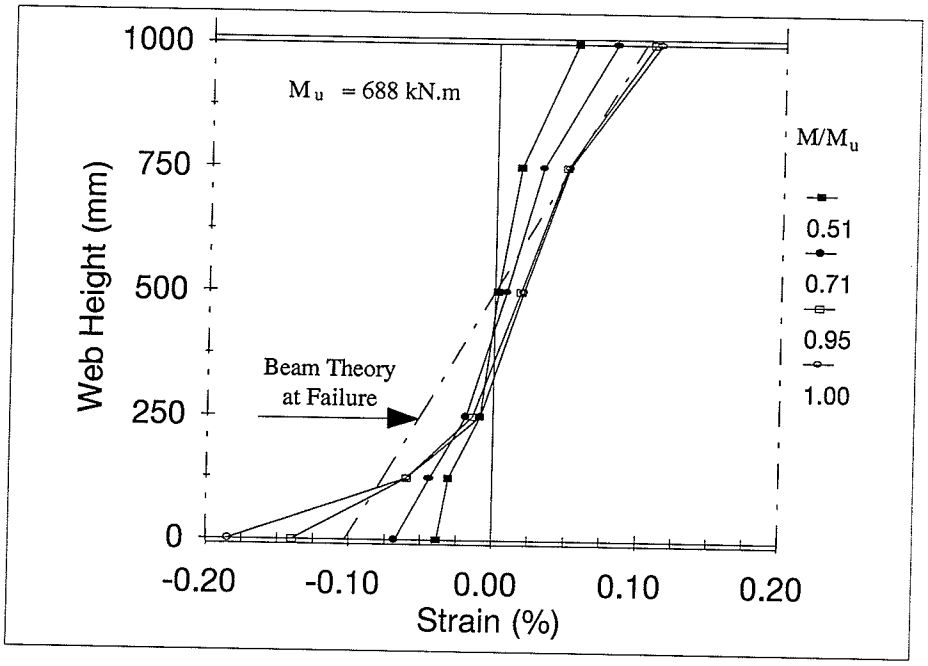

(a) Mid Span

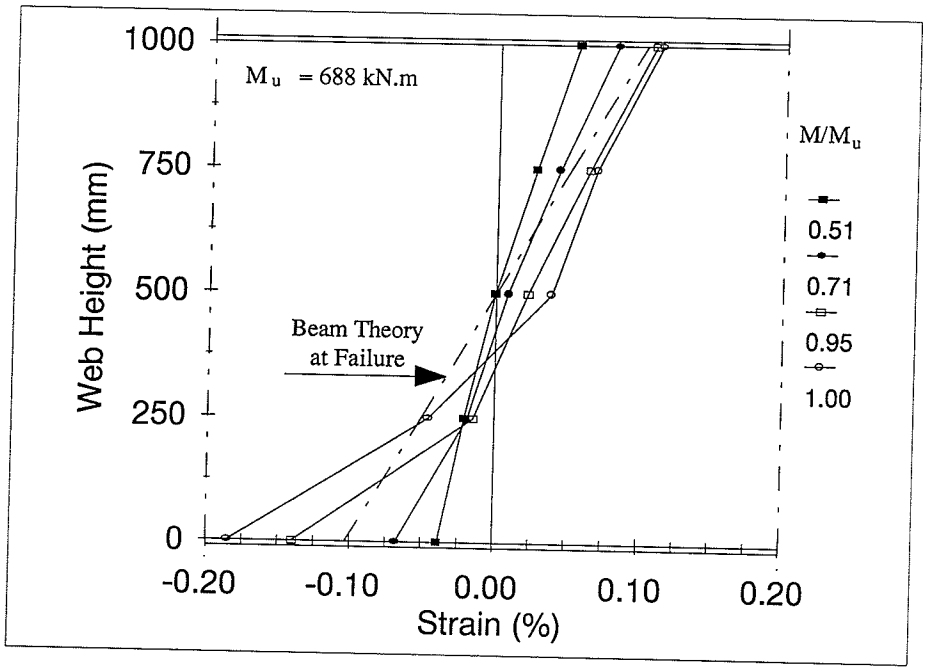

(b) Quarter Span

Figure F.3 Strain Distribution Along Cross-Sections of Specimen G5

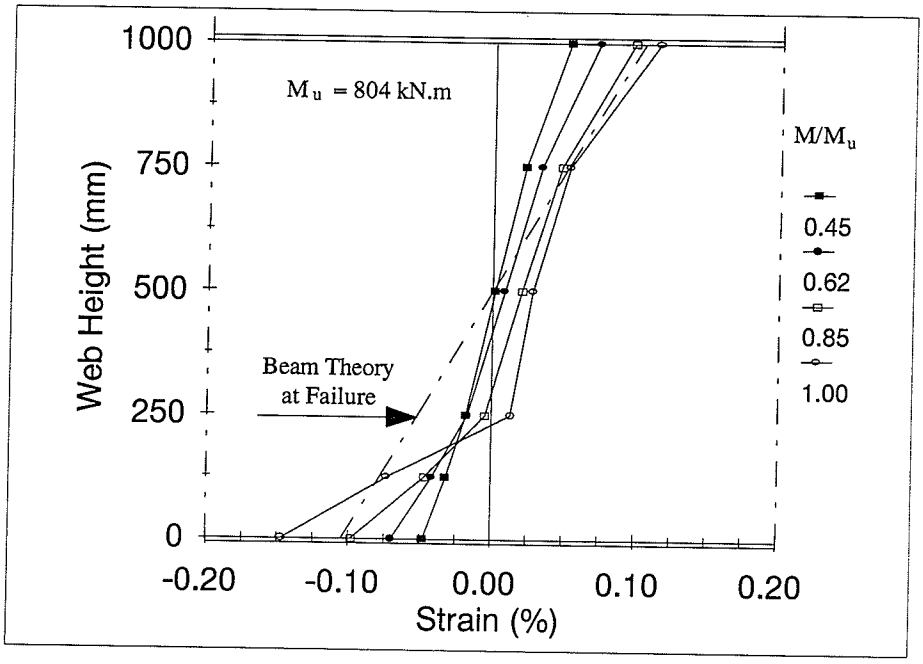

(a) Mid Span

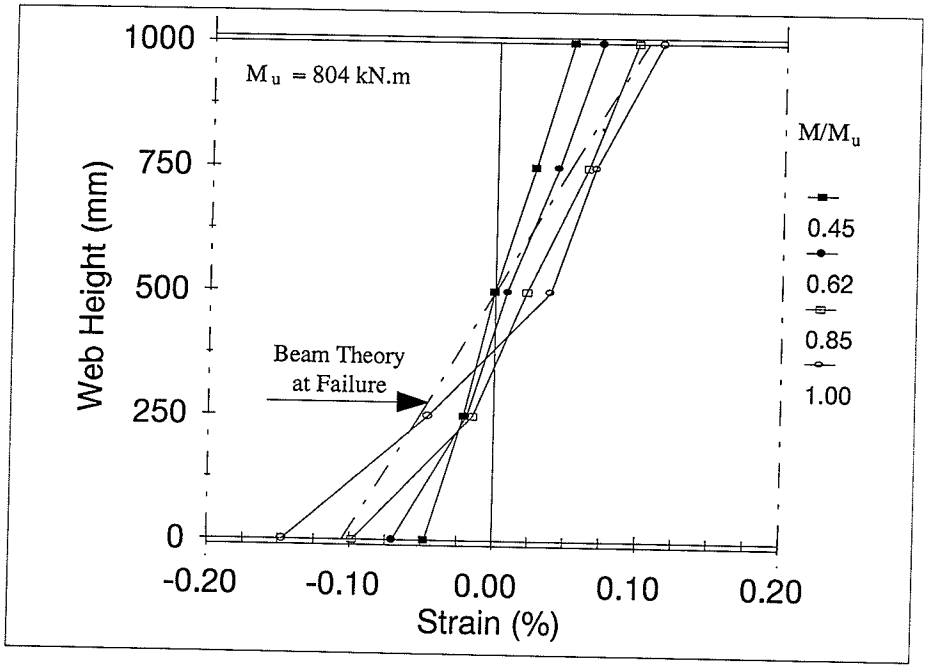

(b) Quarter Span

Figure F.4 Strain Distribution Along Cross-Sections of Specimen G6

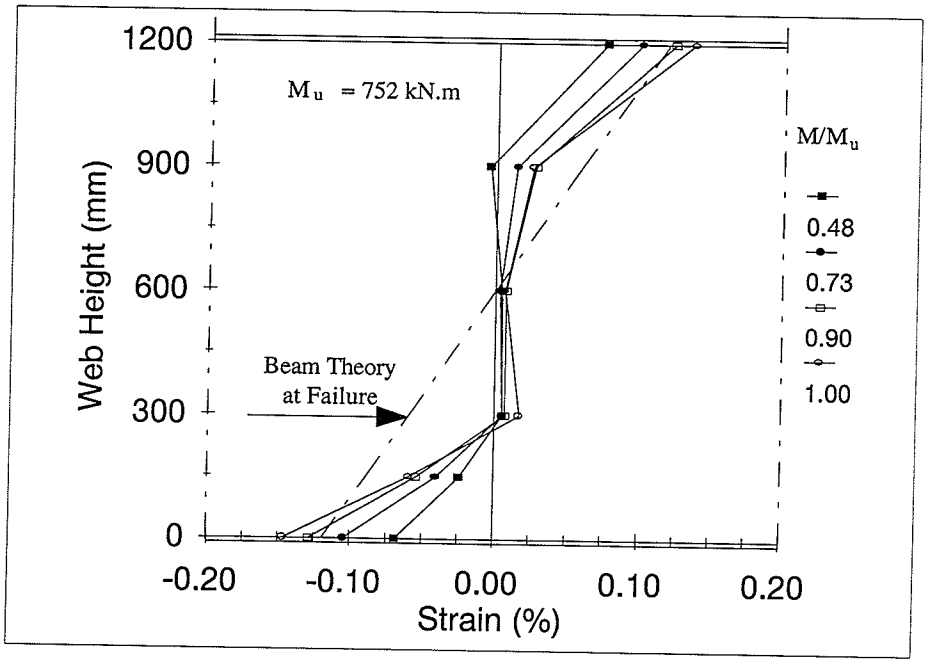

(a) Mid Span

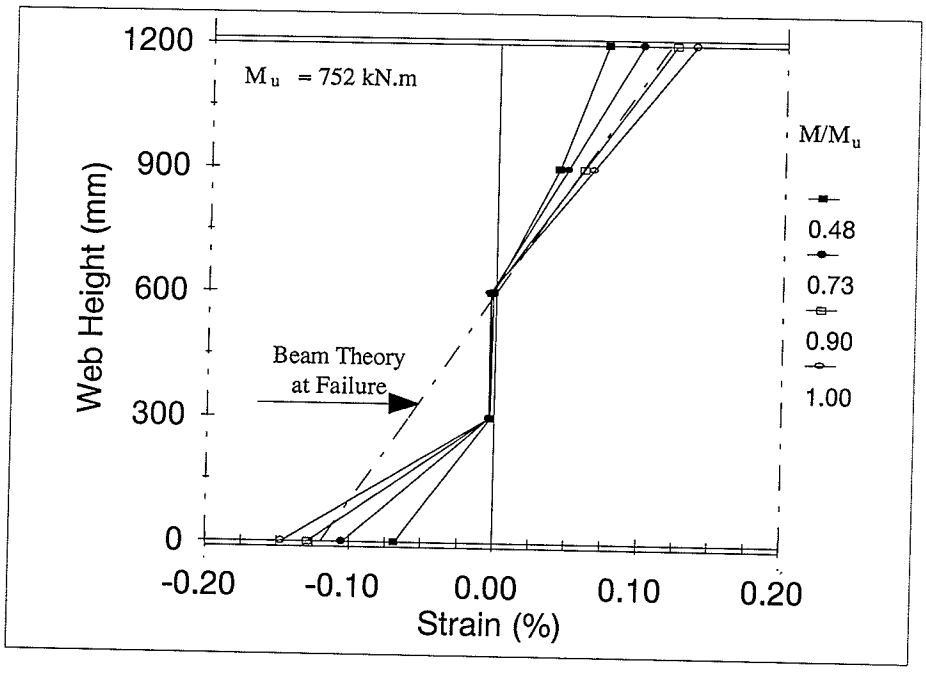

(b) Quarter Span

Figure F.5 Strain Distribution Along Cross-Sections of Specimen G7

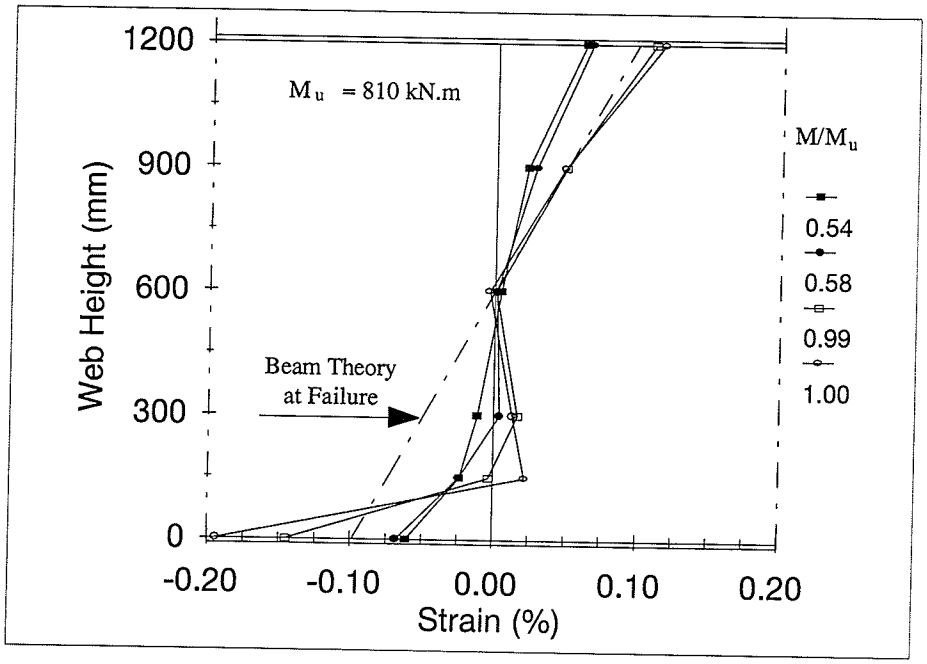

(a) Mid Span

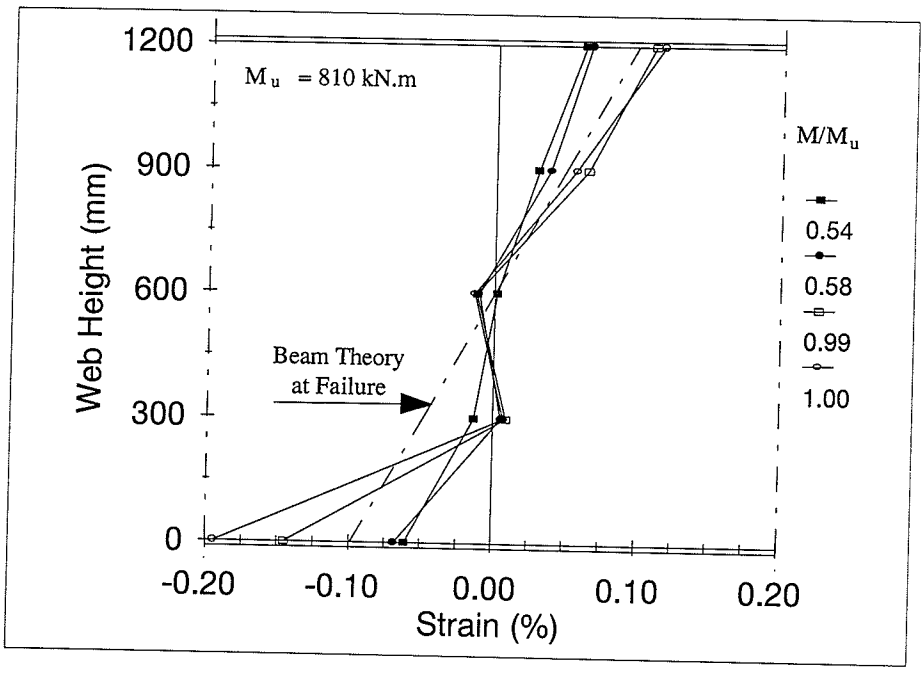

(b) Quarter Span

Figure F.6 Strain Distribution Along Cross-Sections of Specimen G8

APPENDIX G

MOMENT-STRAIN CURVES

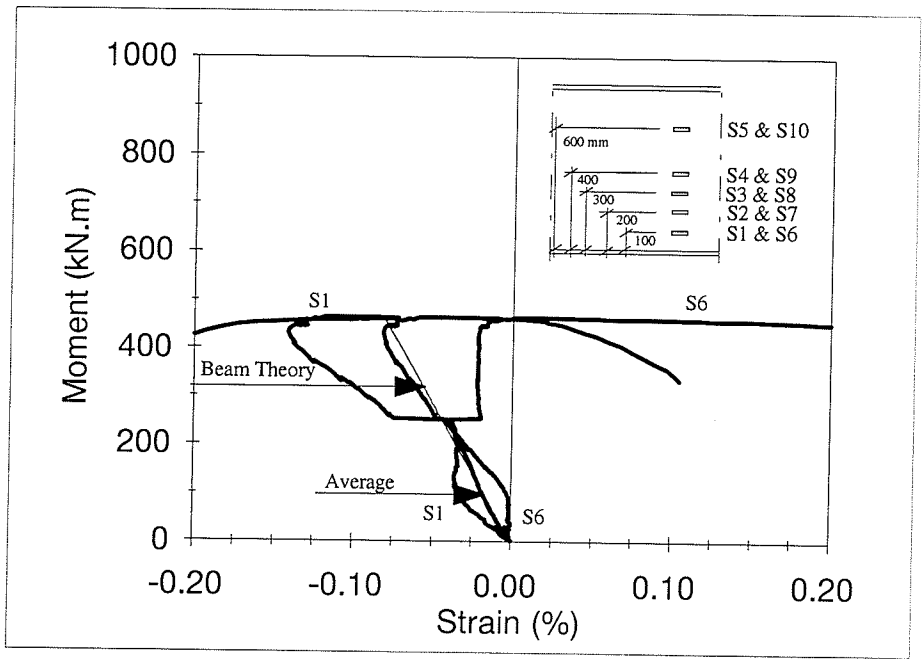

(a) Strain Distribution at S1 & S6

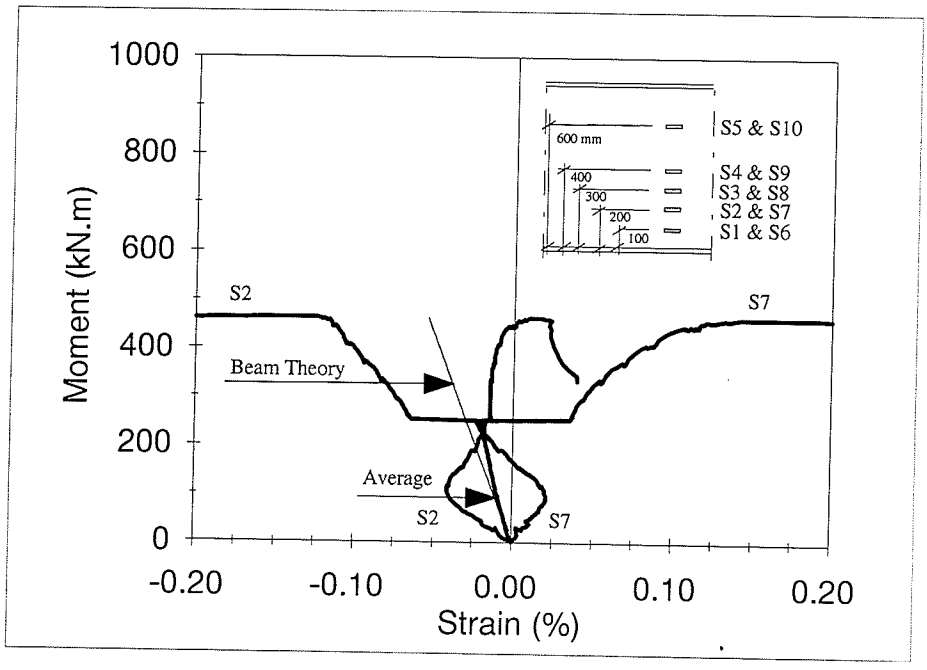

(b) Strain Distribution at S2 & S7

Figure G.1 Moment-Strain Relationships at Mid-Span Web of Specimen G1

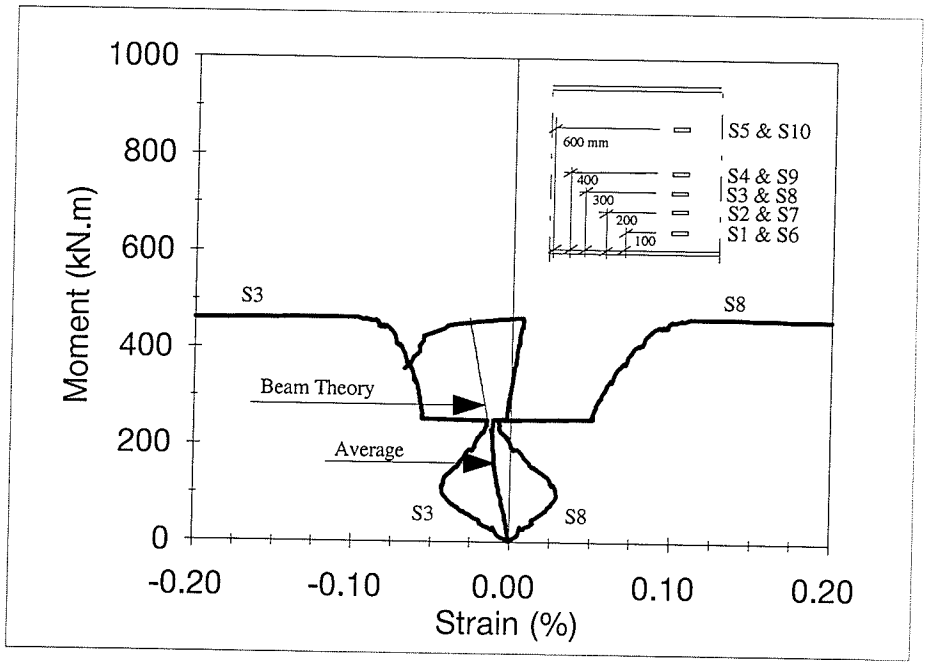

(c) Strain Distribution at S3 & S8

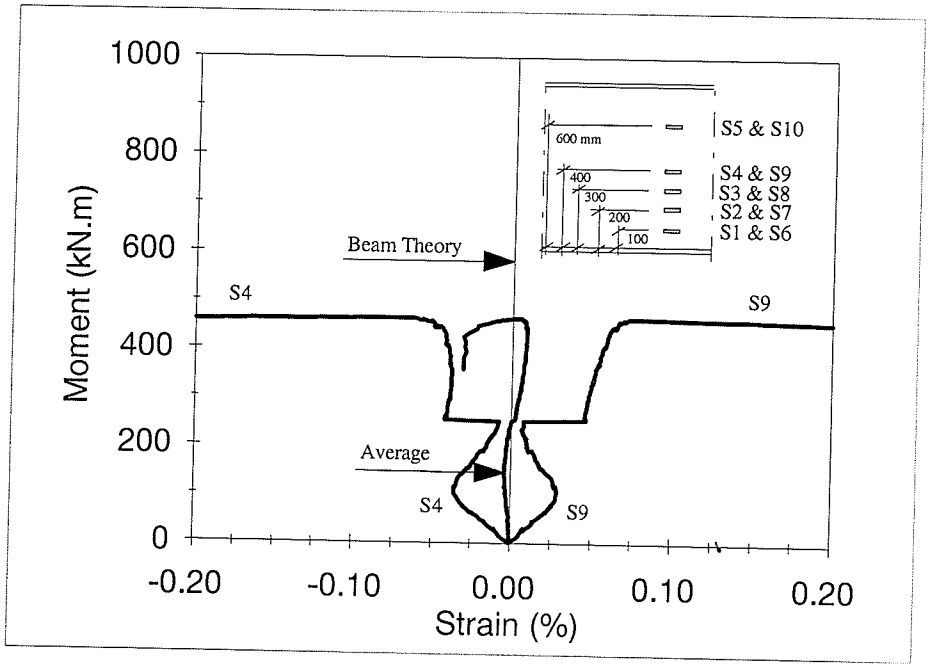

(d) Strain Distribution at S4 & S9

Figure G.1 Moment-Strain Relationships at Mid-Span Web of Specimen G1

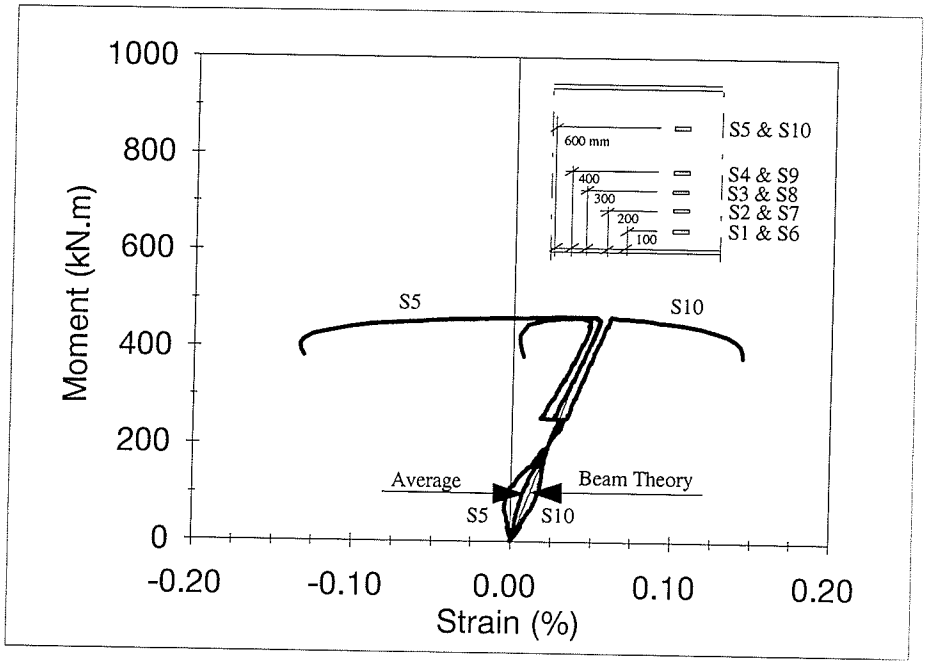

(e) Strain Distribution at S5 & S10

Figure G.1 Moment-Strain Relationships at Mid-Span Web of Specimen G1

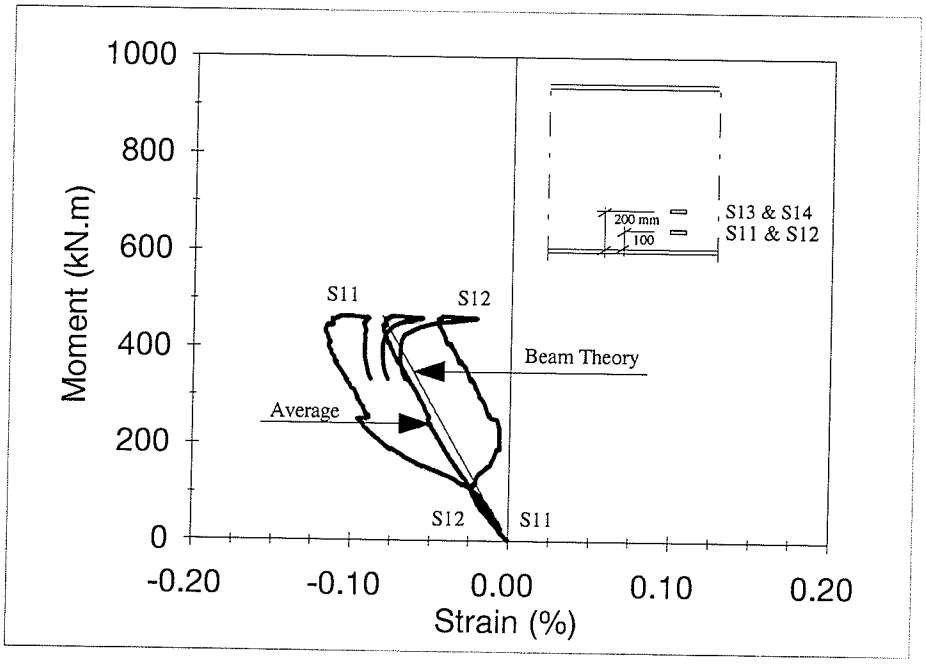

(a) Strain Distribution at S11 & S12

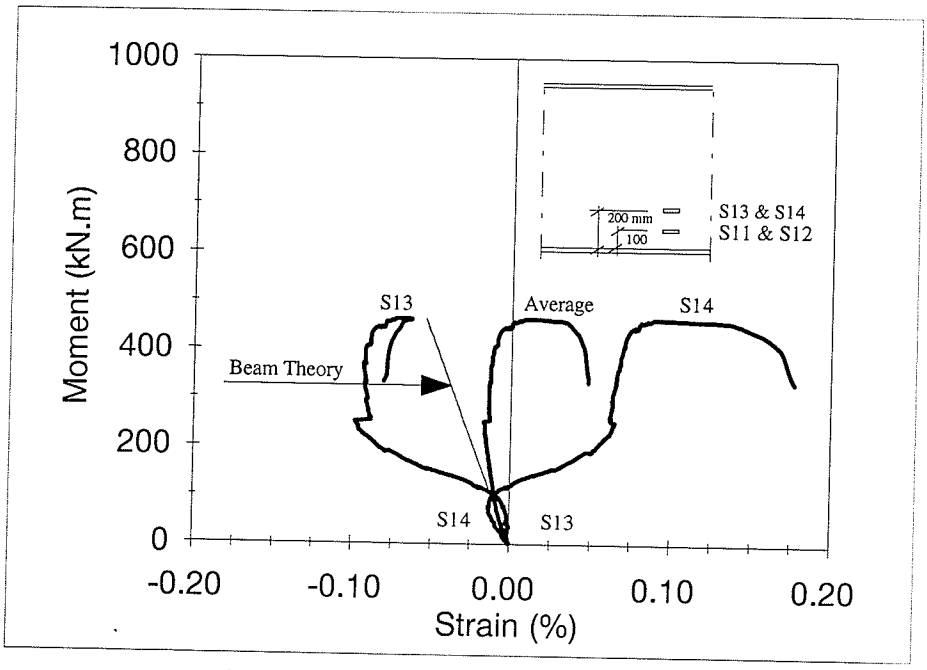

(b) Strain Distribution at S12 & S14

Figure G.2 Moment-Strain Relationships at Quarter-Span Web of Specimen G1

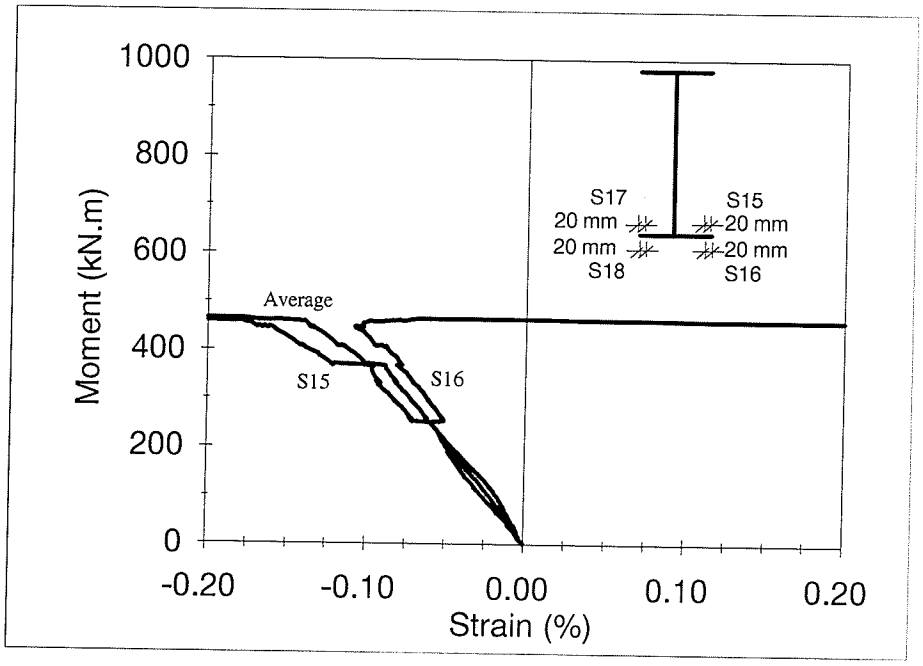

(a) Strain Distribution at S15 & S16

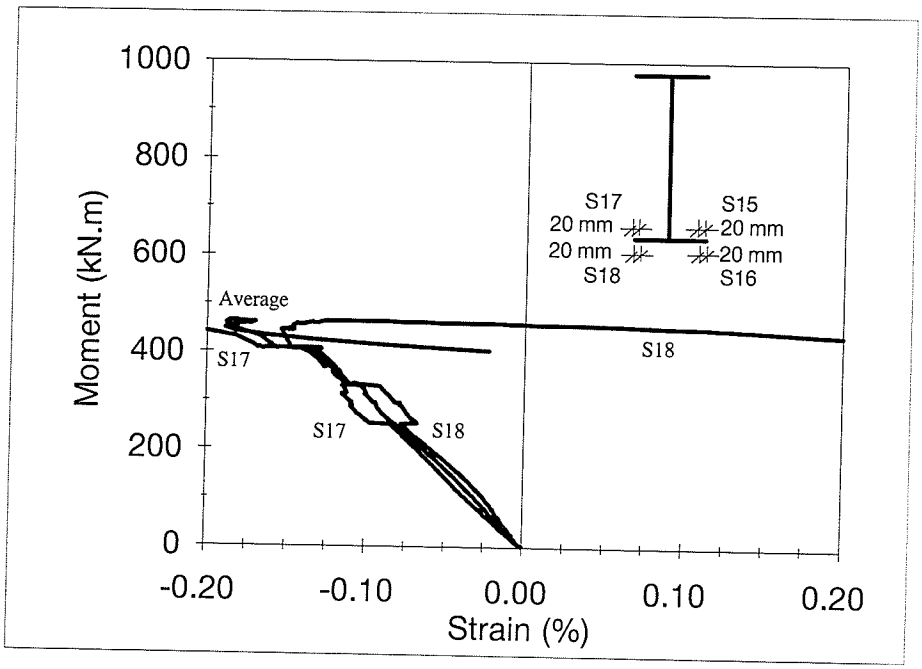

(b) Strain Distribution at S17 & S18

Figure G.3 Moment-Strain Relationships at Mid-Span Compression Flange of Specimen G1

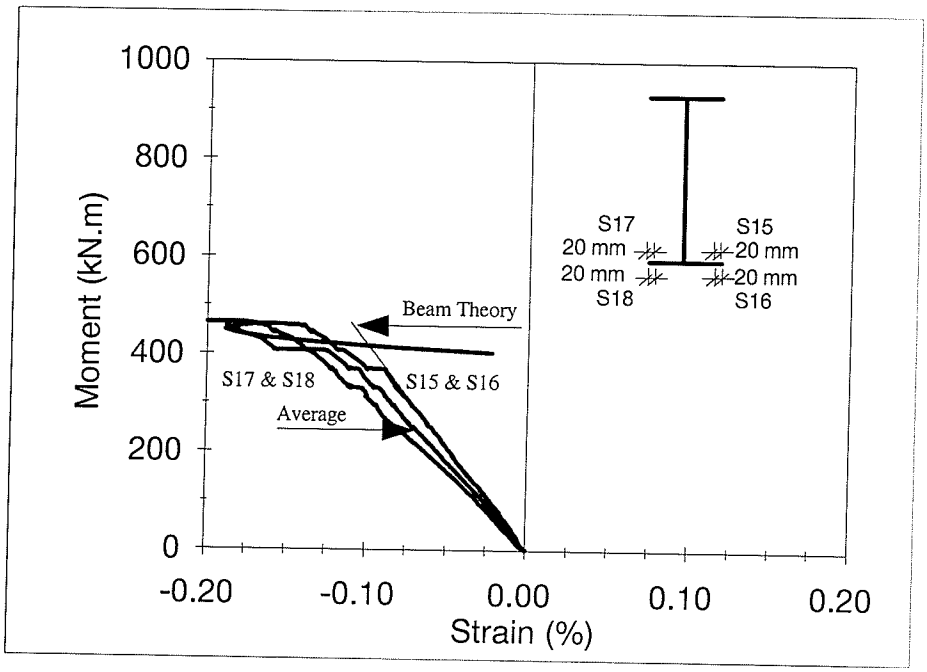

(c) Average Strain

Figure G.3 Moment-Strain Relationships at Mid-Span Compression Flange of Specimen G1

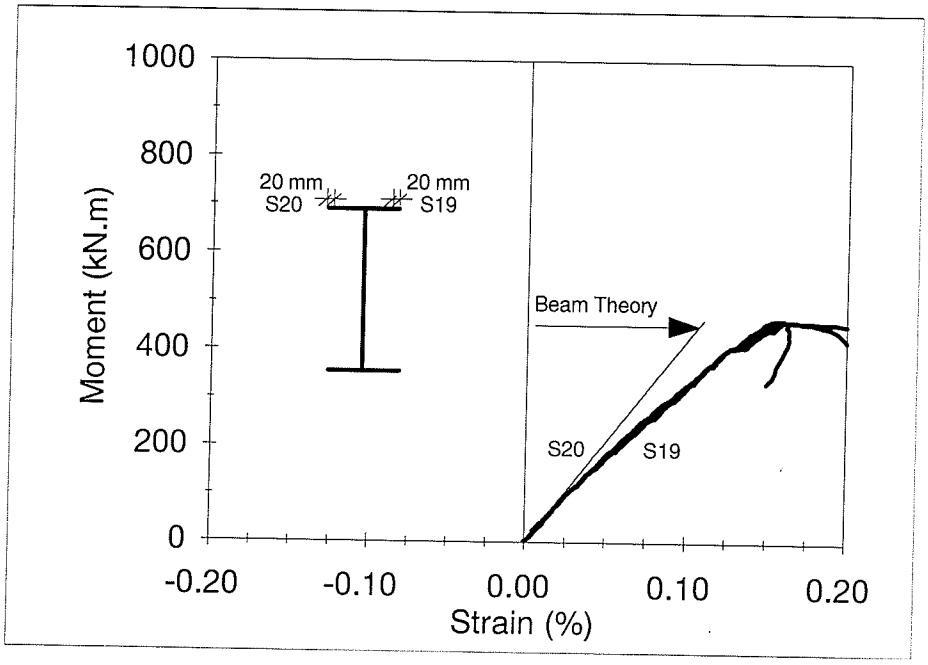

Figure G.4 Moment-Strain Relationships at Mid-Span Tension Flange of Specimen G1

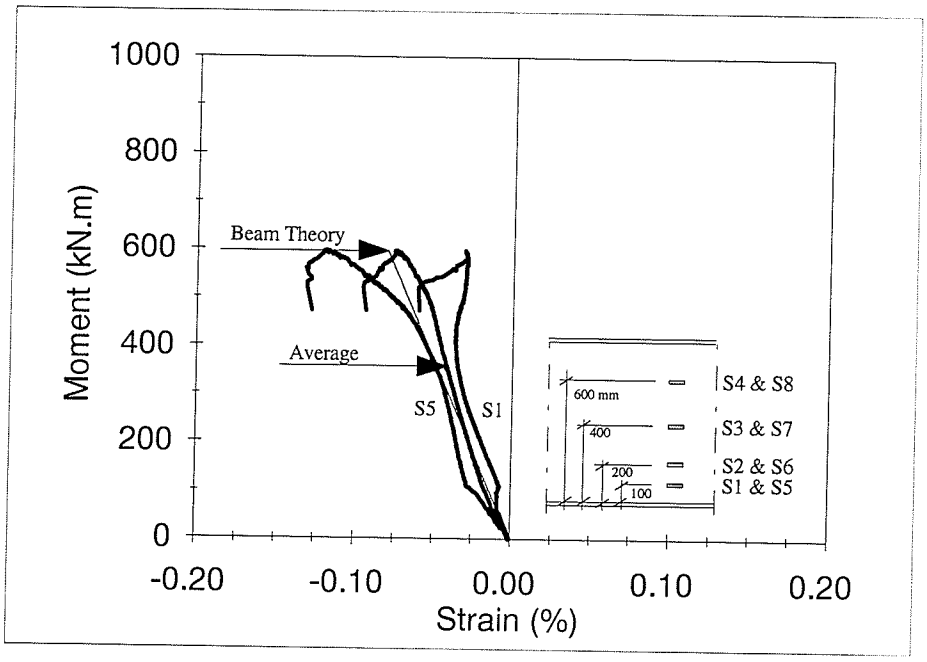

(a) Strain Distribution at S1 & S5

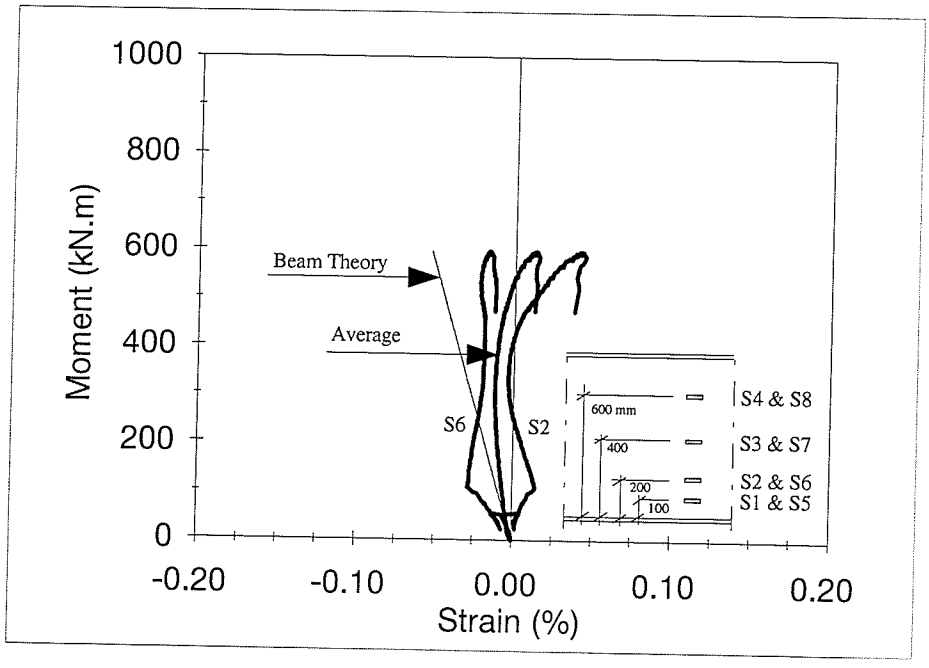

(b) Strain Distribution at S2 & S6

Figure G.5 Moment-Strain Relationships at Mid-Span Web of Specimen G3

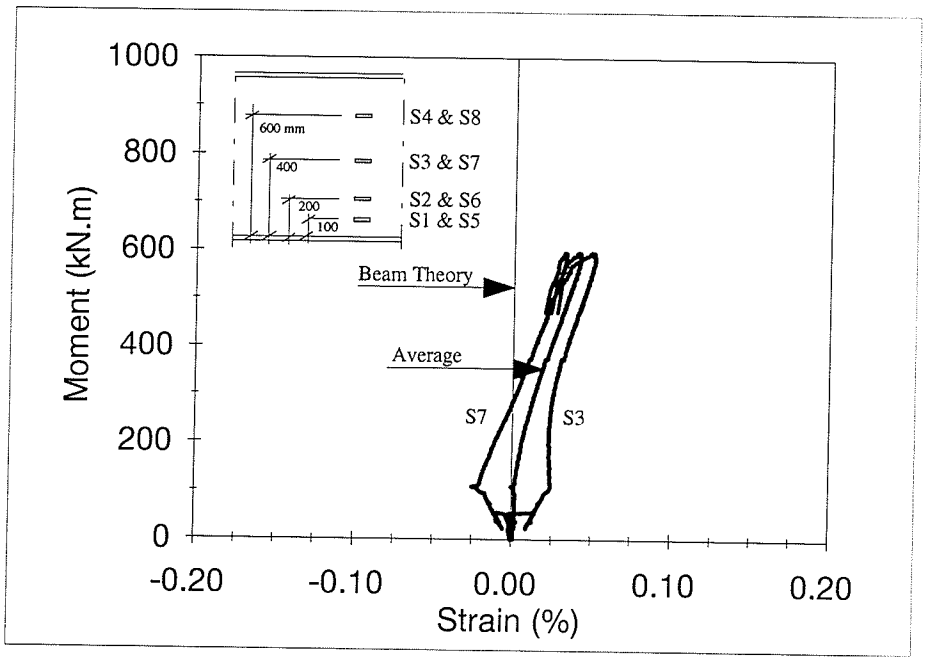

(c) Strain Distribution at S3 & S7

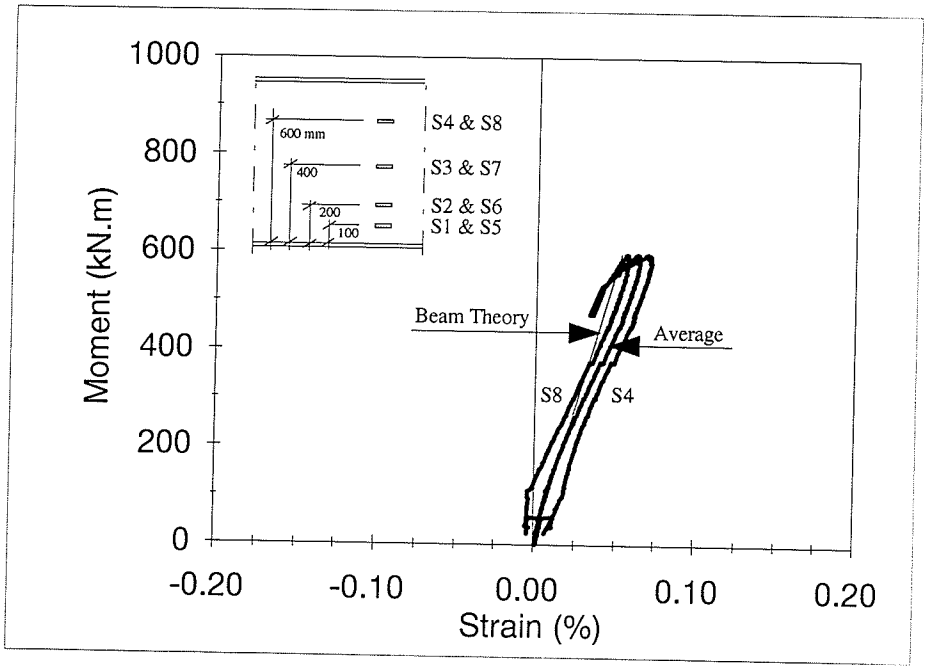

(d) Strain Distribution at S4 & S8

Figure G.5 Moment-Strain Relationships at Mid-Span Web of Specimen G3

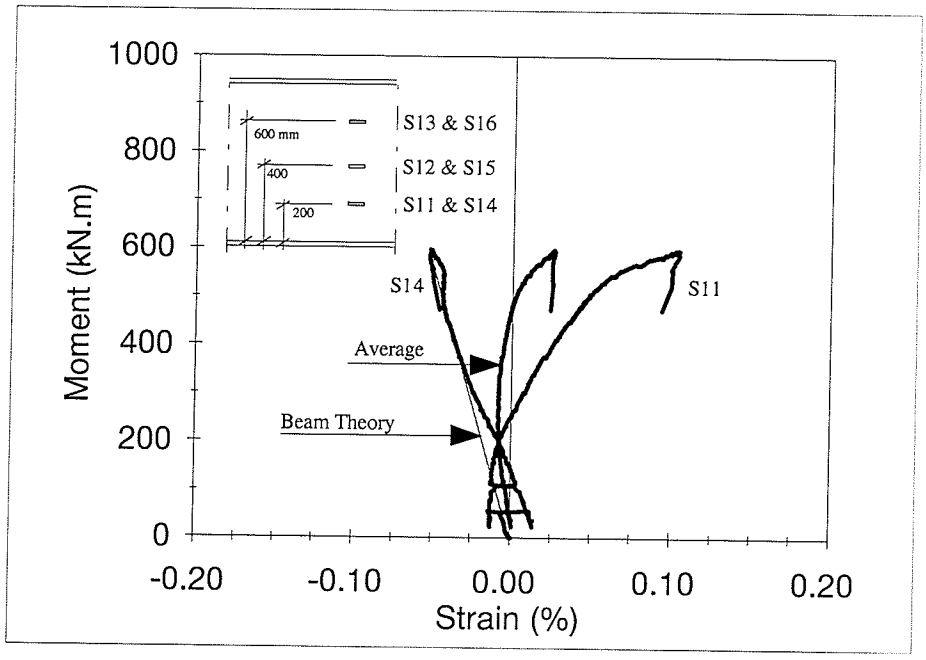

(a) Strain Distribution at S11 & S14

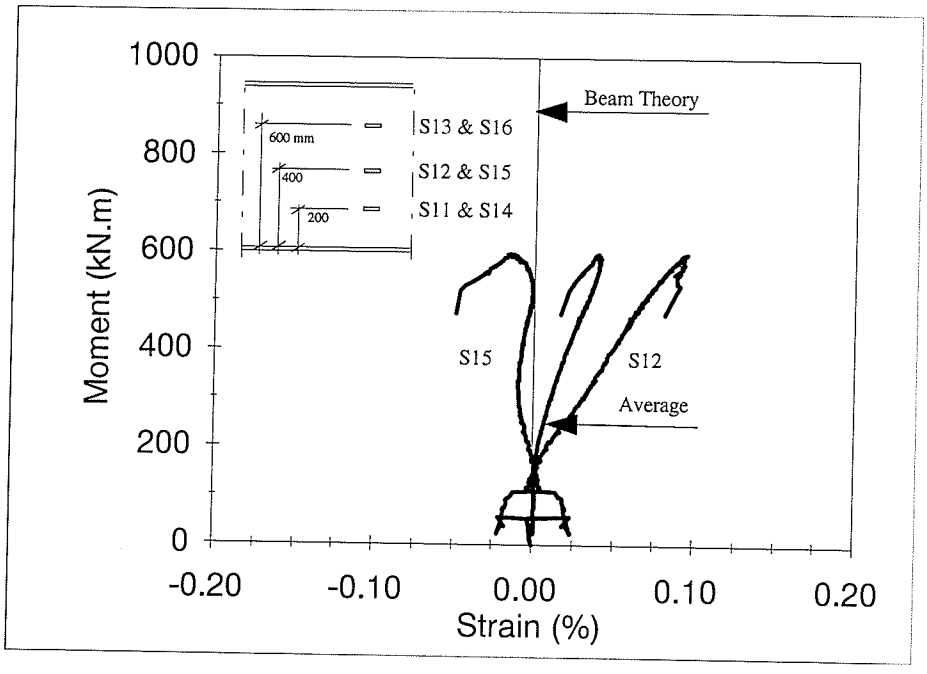

(b) Strain Distribution at S12 & S15

Figure G.6 Moment-Strain Relationships at Quarter-Span Web of Specimen G3

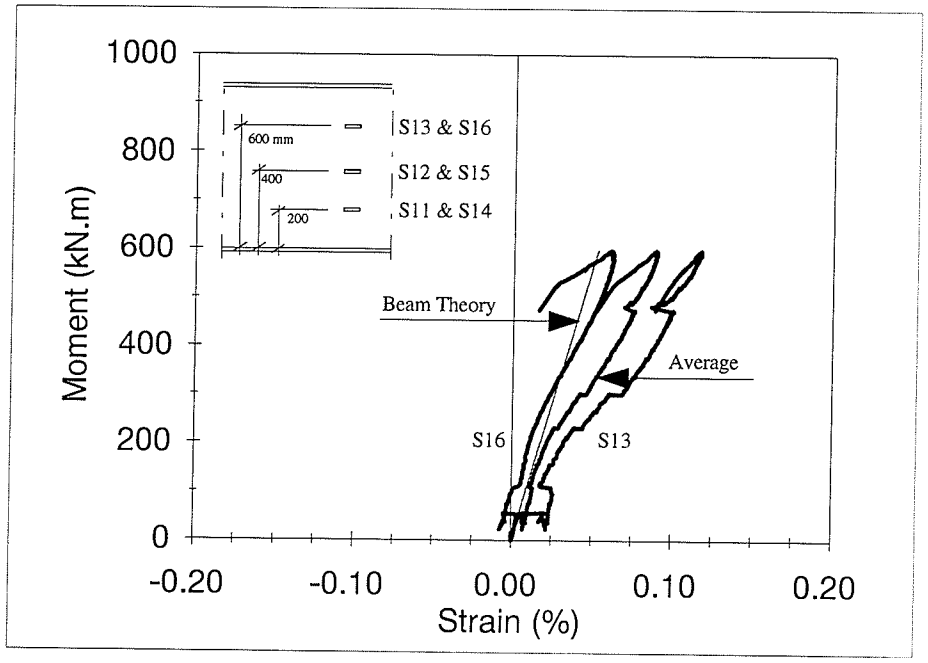

(c) Strain Distribution at S13 & S16

Figure G.6 Moment-Strain Relationships at Quarter-Span Web of Specimen G3

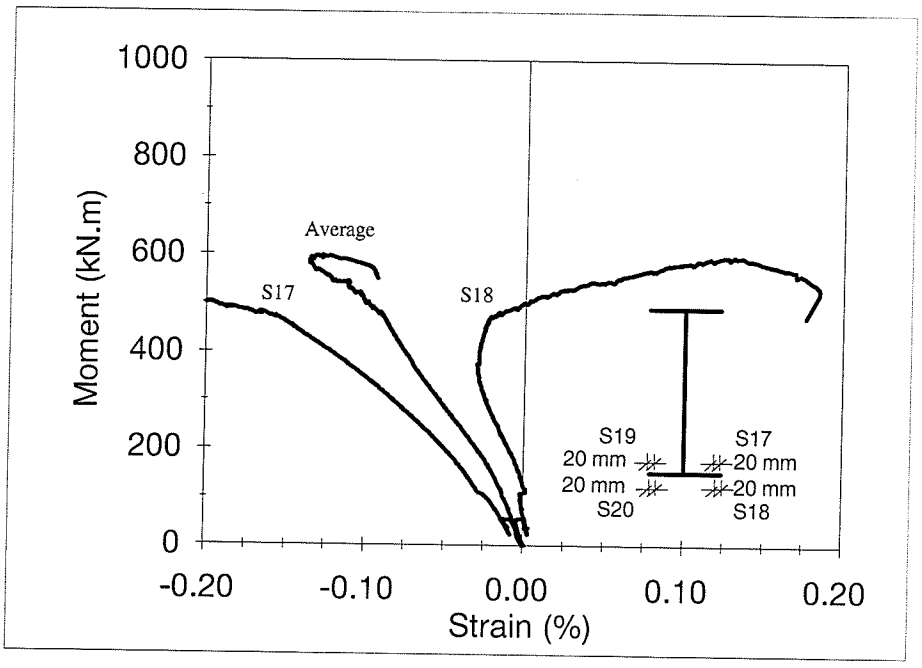

(a) Strain Distribution at S17 & S18

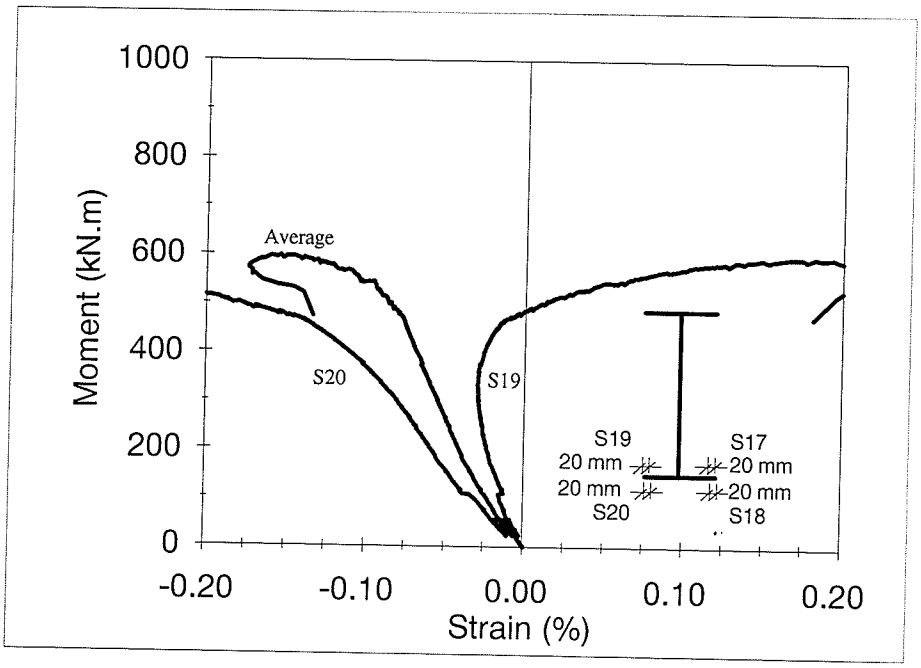

(b) Strain Distribution at S19 & S20

Figure G.7 Moment-Strain Relationships at Mid-Span Compression Flange of Specimen G3

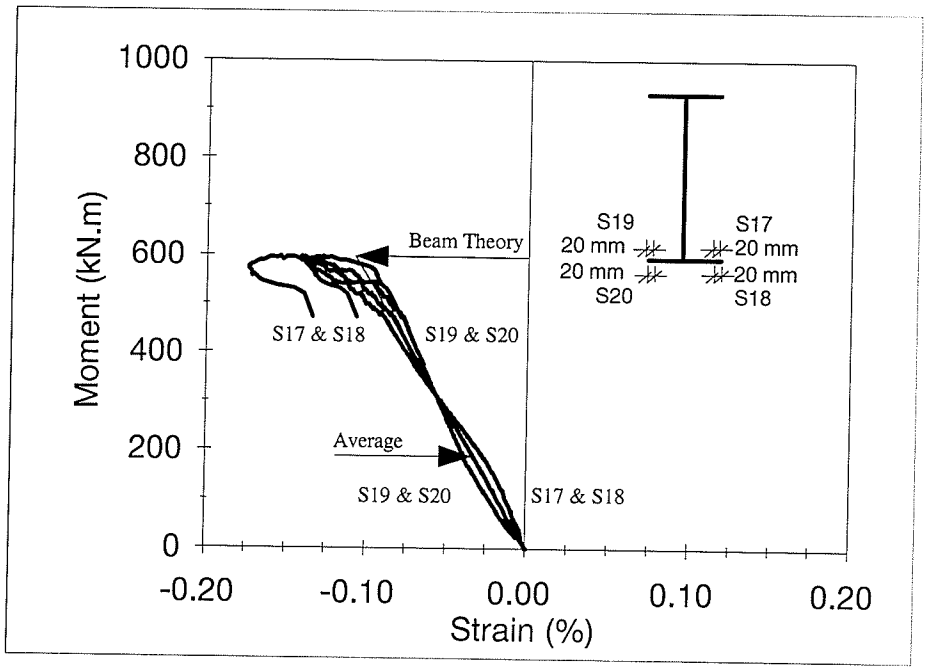

(c) Average Strain

Figure G.7 Moment-Strain Relationships at Mid-Span Compression Flange of Specimen G3

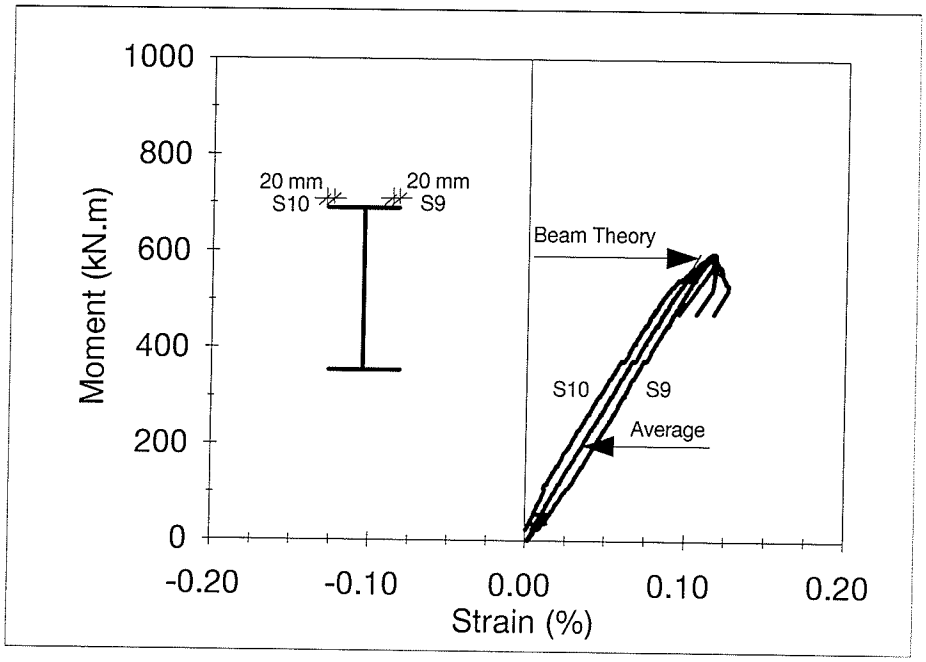

Figure G.8 Moment-Strain Relationships at Mid-Span Tension Flange of Specimen G3

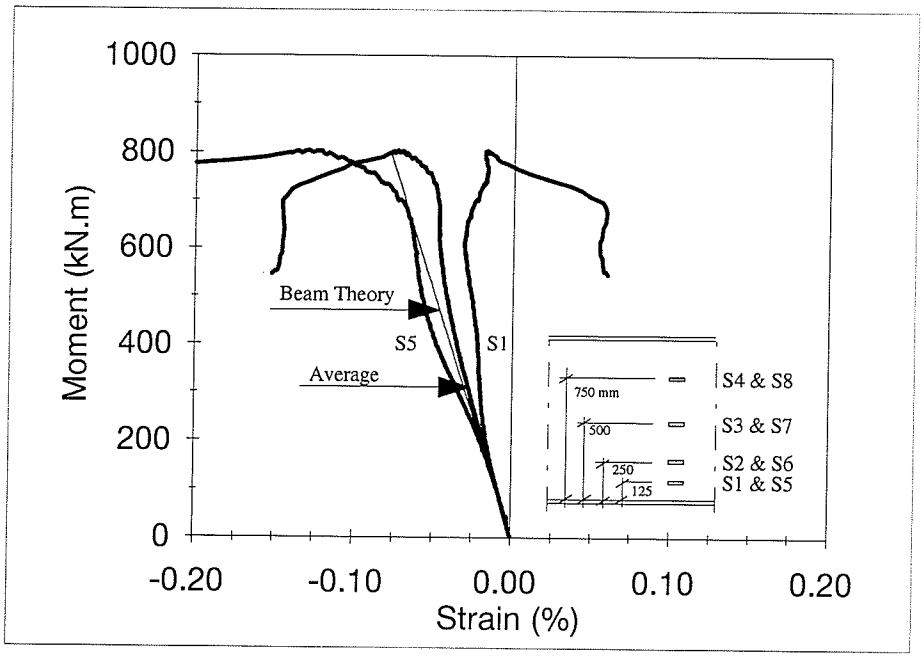

(a) Strain Distribution at S1 & S5

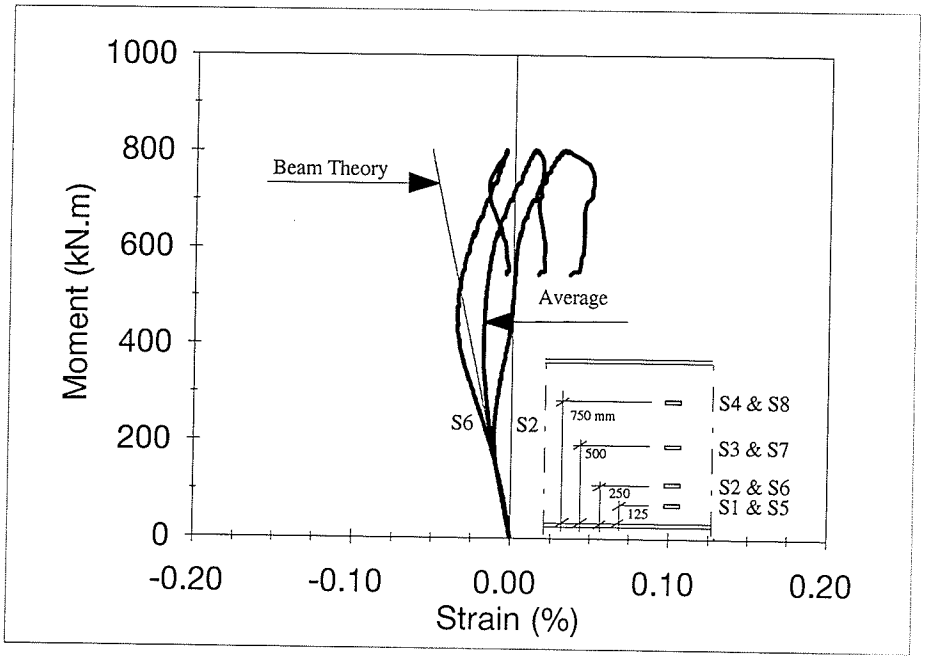

(b) Strain Distribution at S2 & S6

Figure G.9 Moment-Strain Relationships at Mid-Span Web of Specimen G6

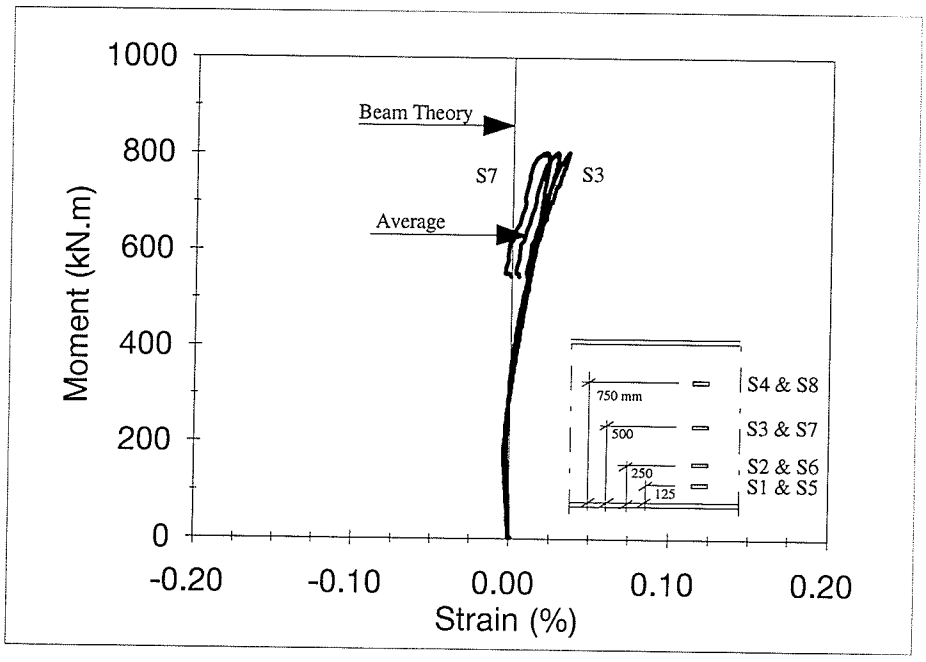

(c) Strain Distribution at S3 & S7

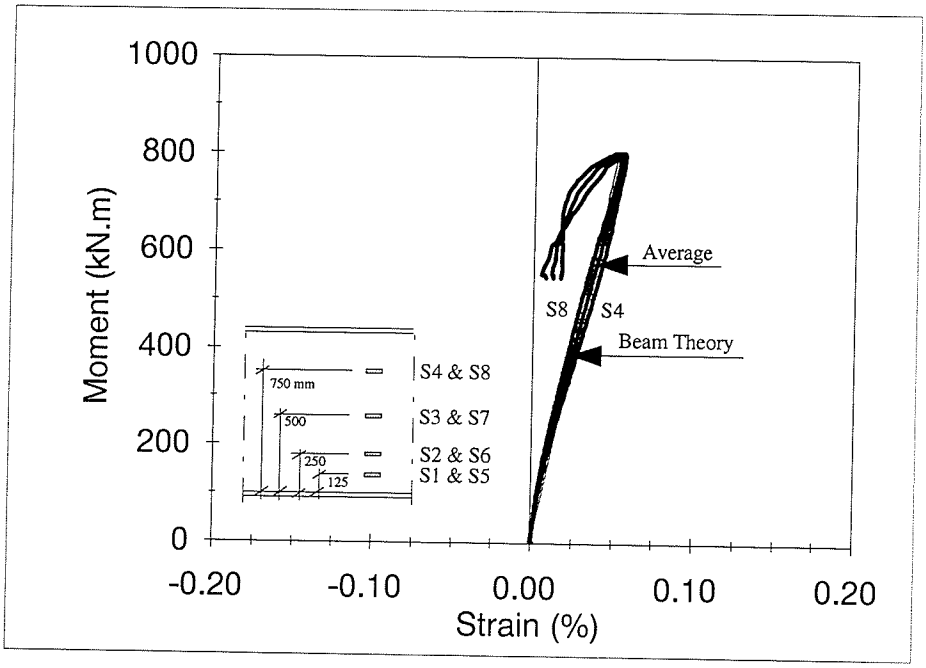

(d) Strain Distribution at S4 & S8

Figure G.9 Moment-Strain Relationships at Mid-Span Web of Specimen G6

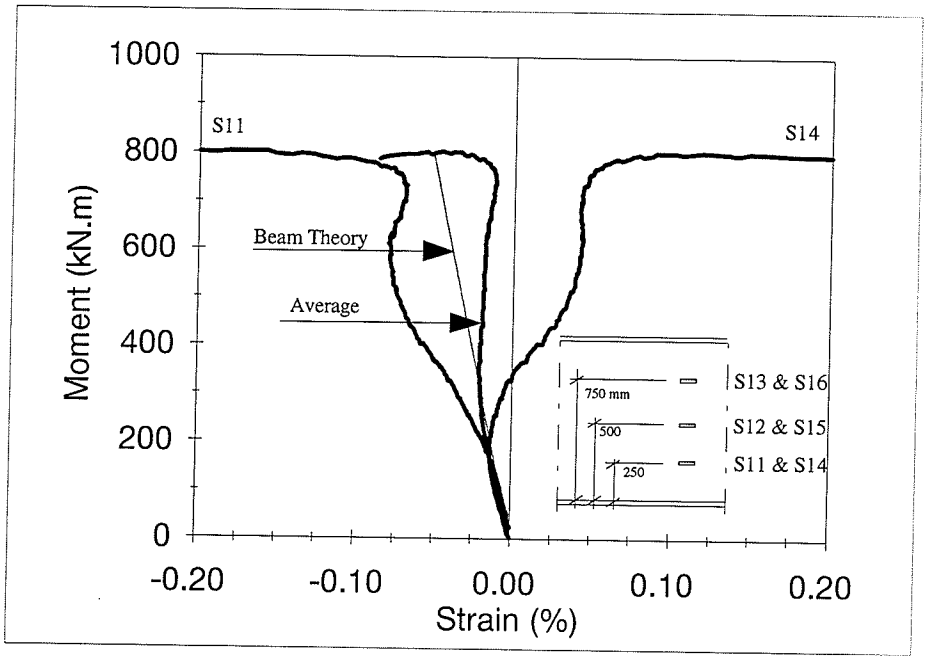

(a) Strain Distribution at S11 & S14

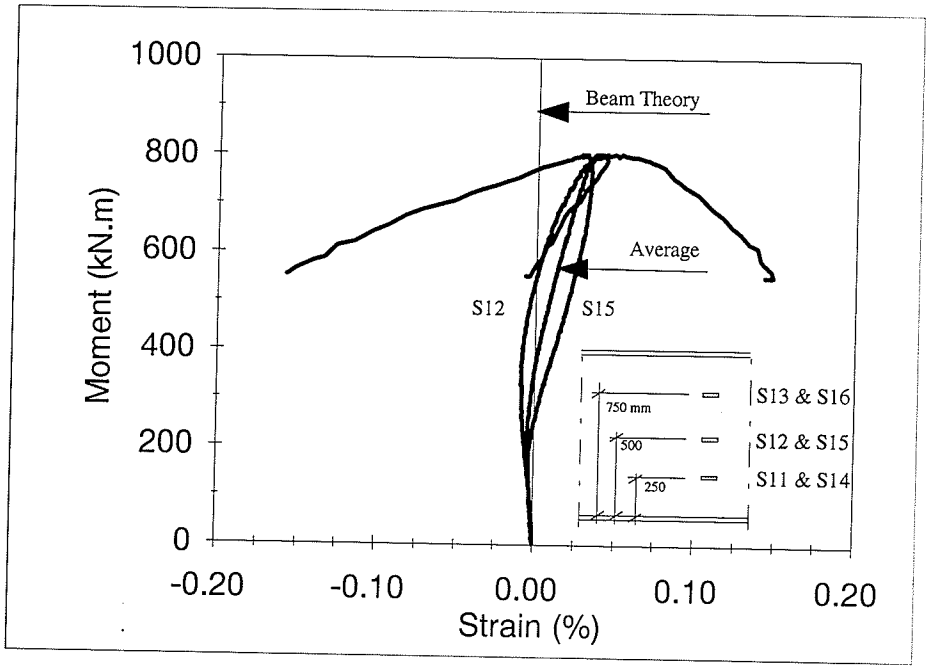

(b) Strain Distribution at S12 & S15

Figure G.10 Moment-Strain Relationships at Quarter-Span Web of Specimen G6

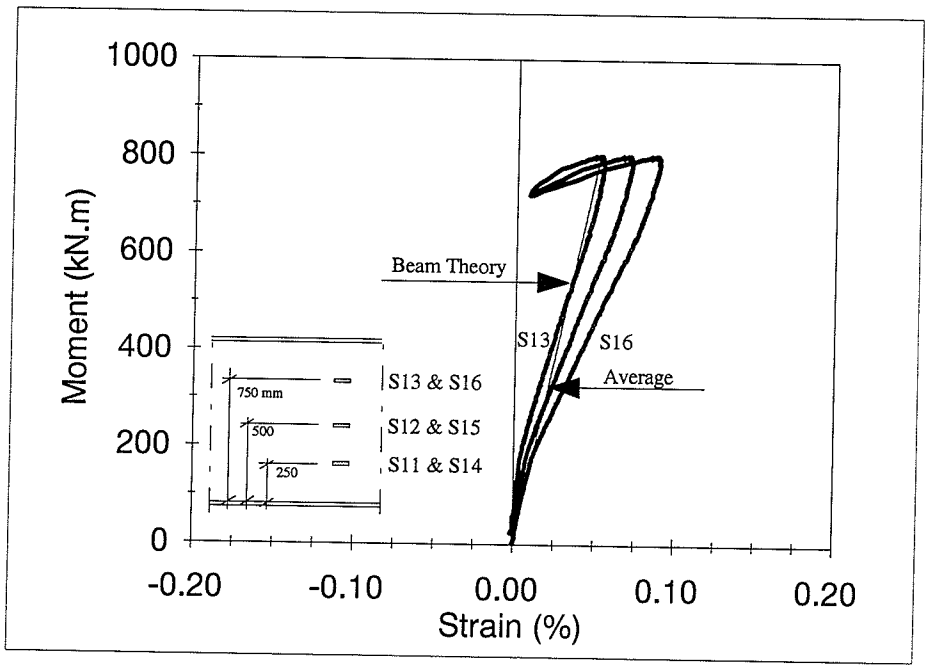

(c) Strain Distribution at S13 & S16

Figure G.10 Moment-Strain Relationships at Quarter-Span Web of Specimen G6

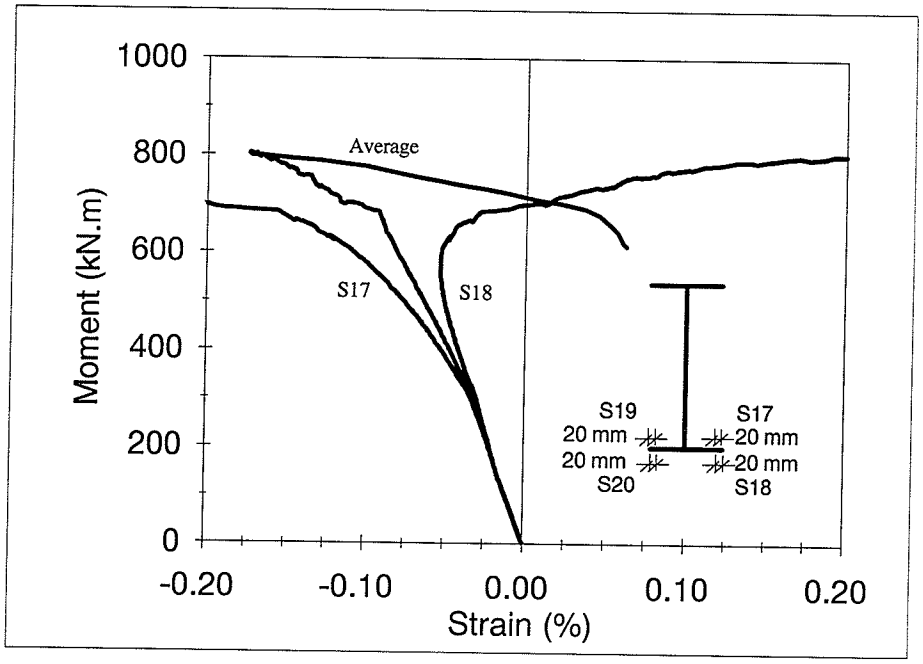

(a) Strain Distribution at S17 & S18

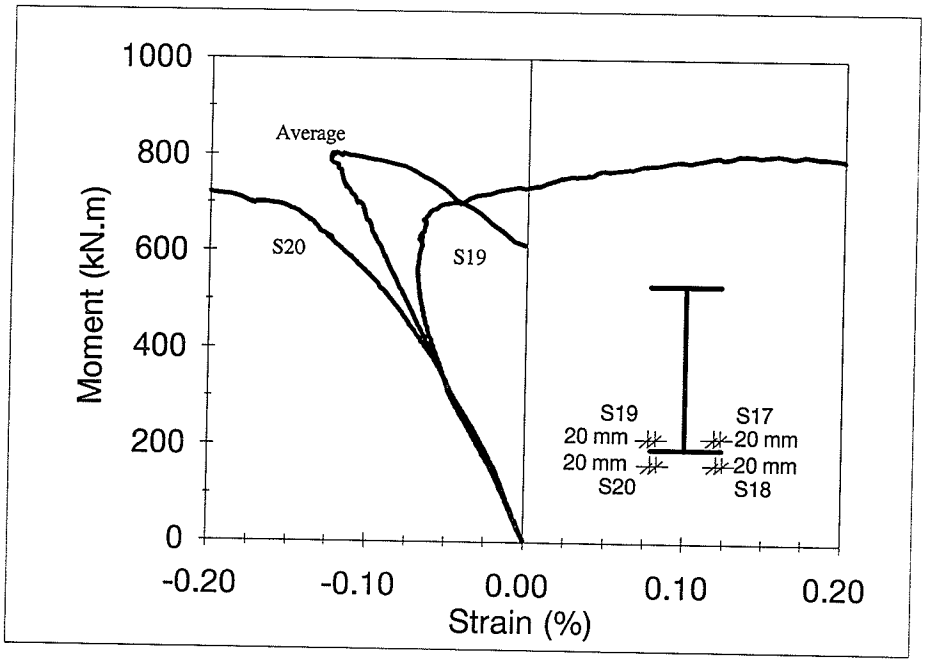

(b) Strain Distribution at S19 & S20

Figure G.11 Moment-Strain Relationships at Mid-Span Compression Flange of Specimen G6

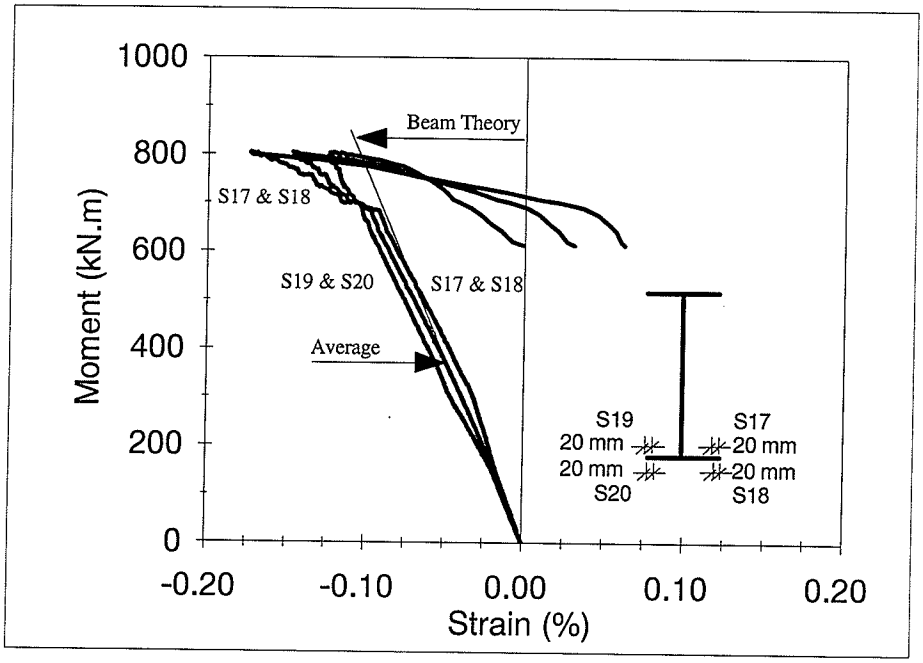

(c) Average Strain

Figure G.11 Moment-Strain Relationships at Mid-Span Compression Flange of Specimen G6

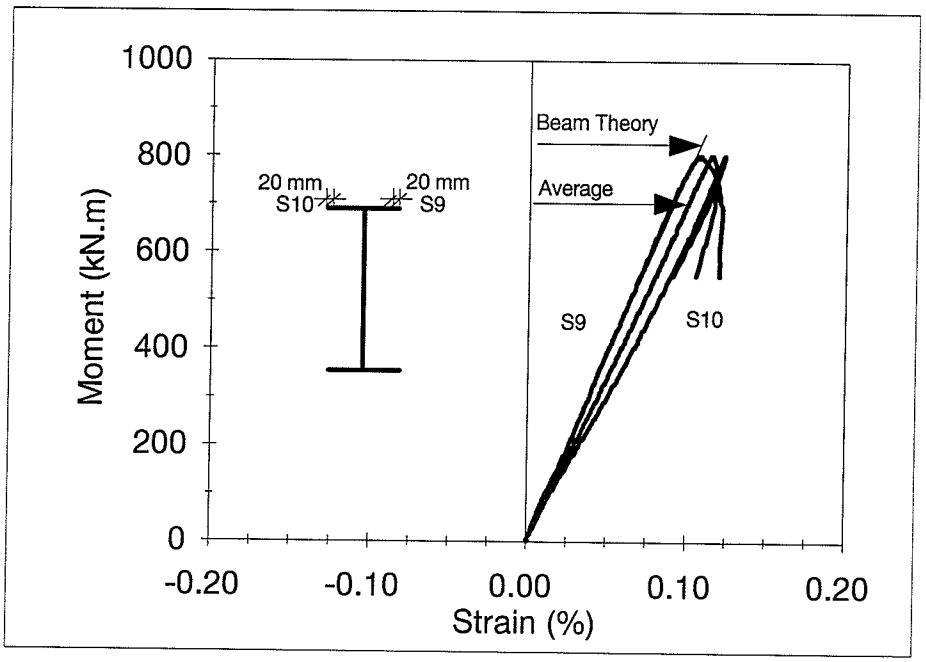

Figure G.12 Moment-Strain Relationships at Mid-Span Tension Flange of Specimen G6

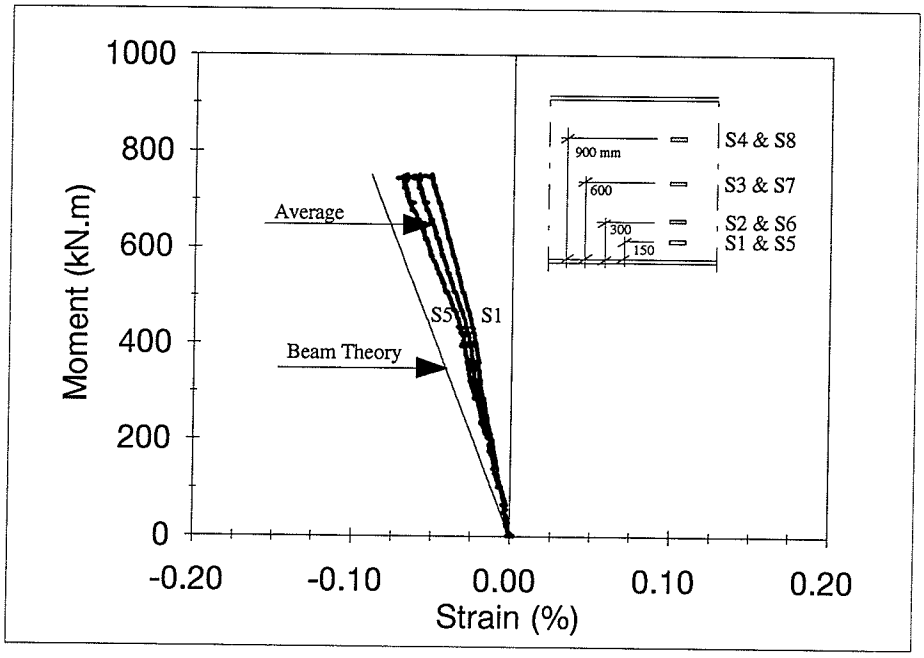

(a) Strain Distribution at S1 & S5

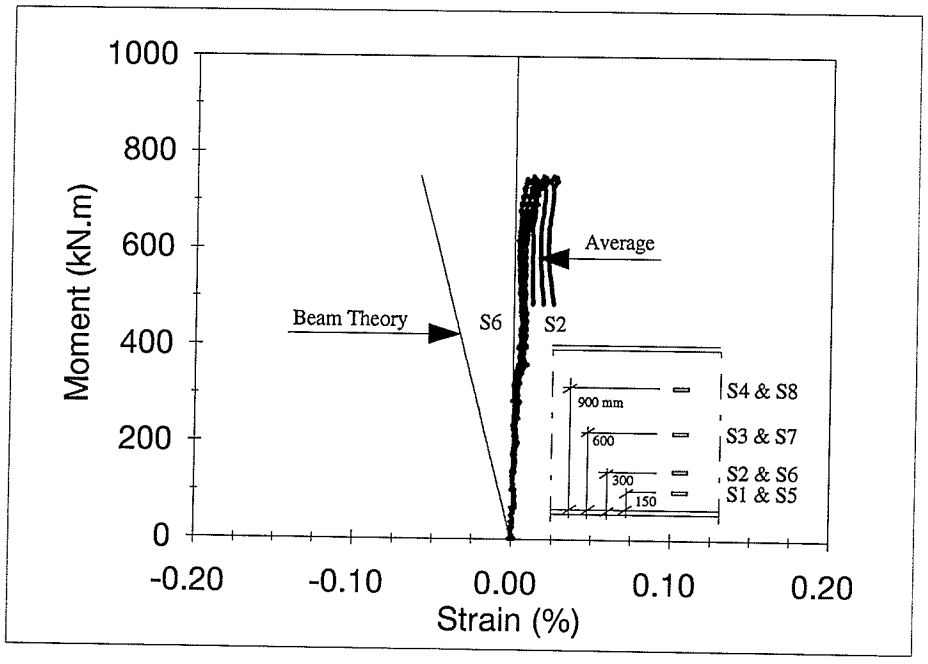

(b) Strain Distribution at S2 & S6

Figure G.13 Moment-Strain Relationships at Mid-Span Web of Specimen G7

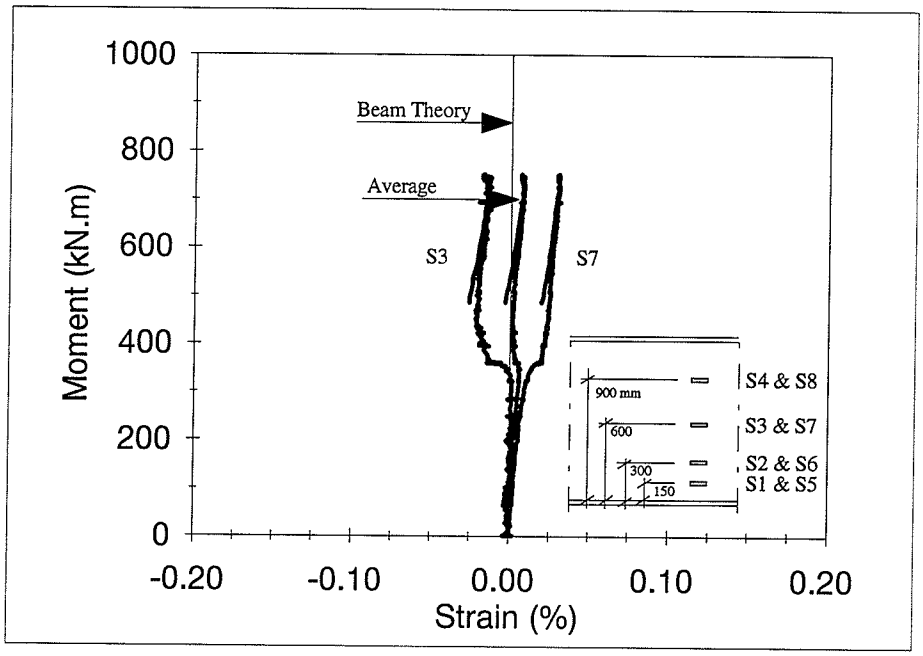

(c) Strain Distribution at S3 & S7

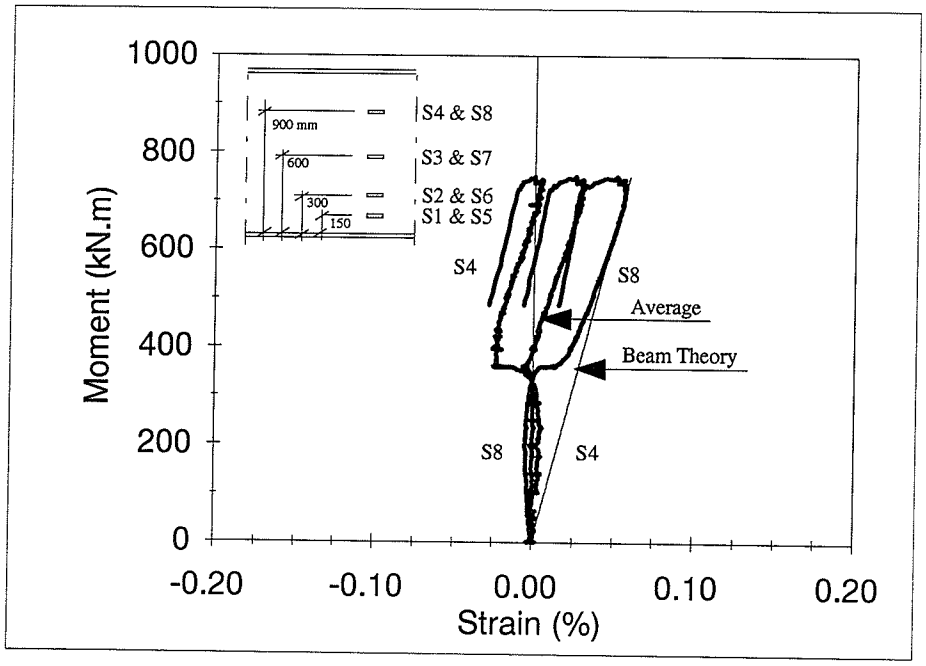

(d) Strain Distribution at S4 & S8

Figure G.13 Moment-Strain Relationships at Mid-Span Web of Specimen G7

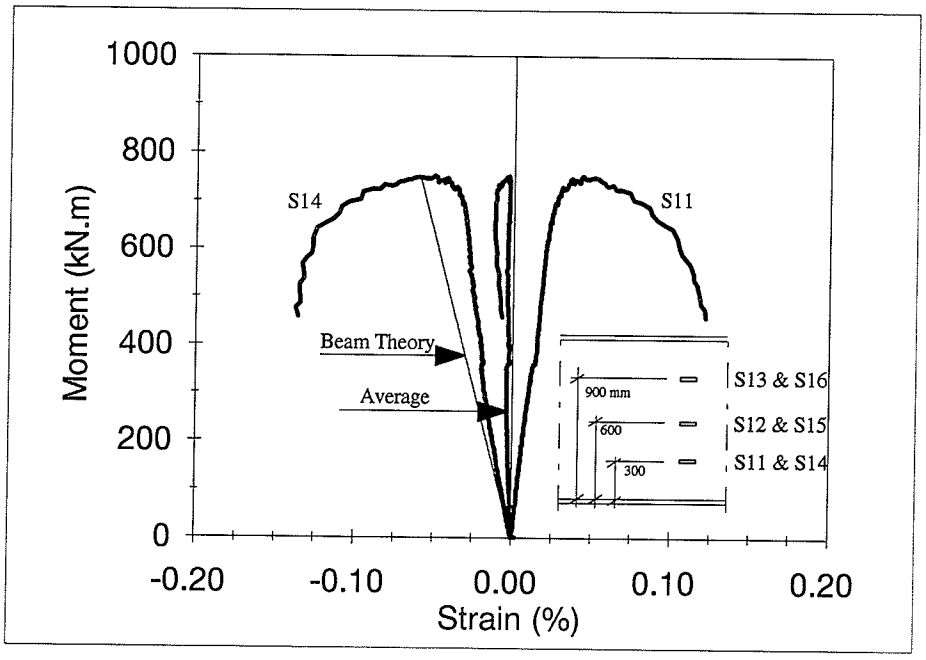

(a) Strain Distribution at S11 & S14

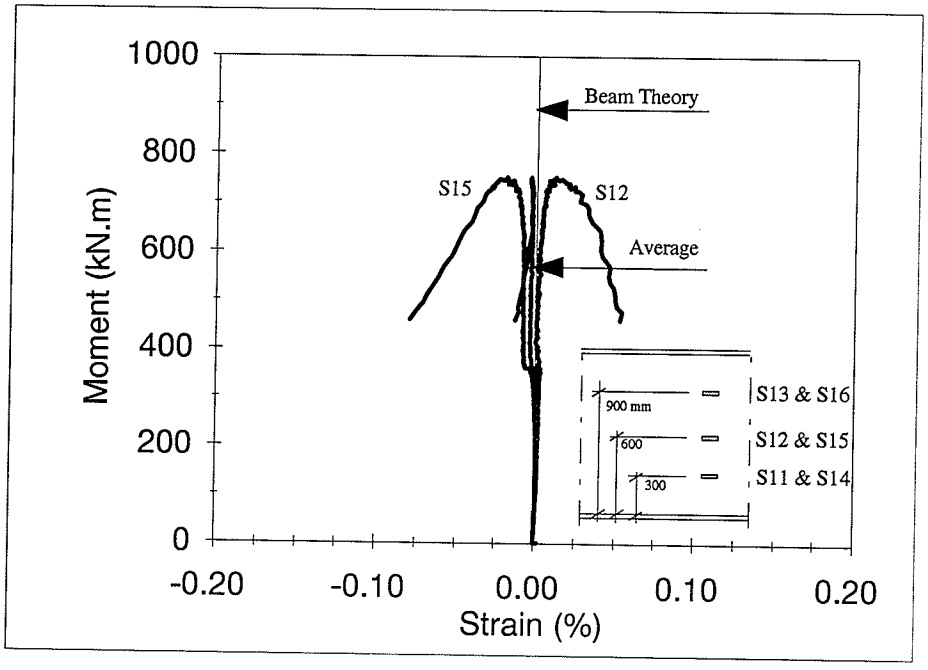

(b) Strain Distribution at S12 & S15

Figure G.14 Moment-Strain Relationships at Quarter-Span Web of Specimen G7

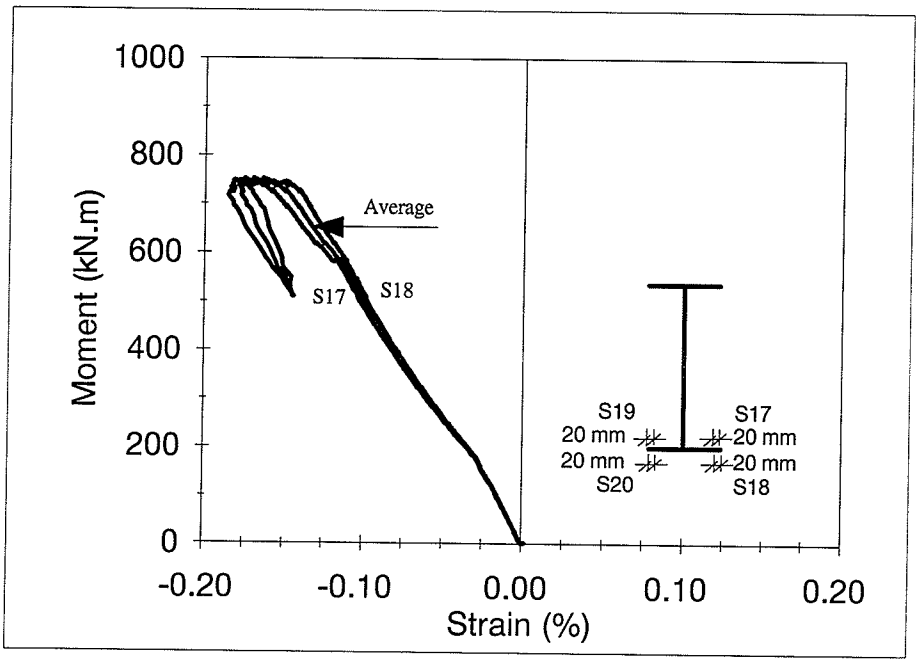

(a) Strain Distribution at S17 & S18

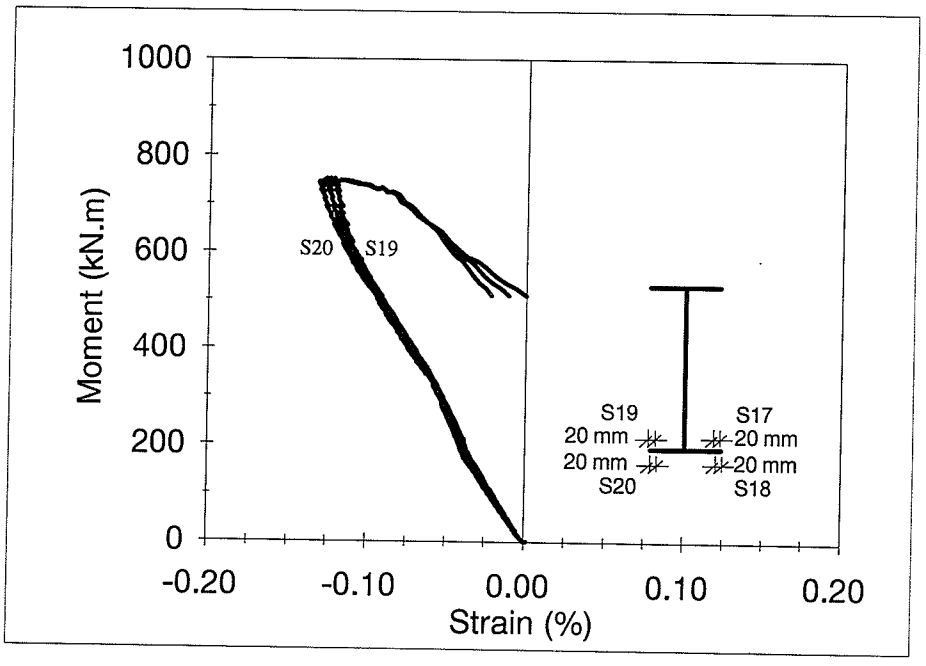

(b) Strain Distribution at S19 & S20

Figure G.15 Moment-Strain Relationships at Mid-Span Compression Flange of Specimen G7

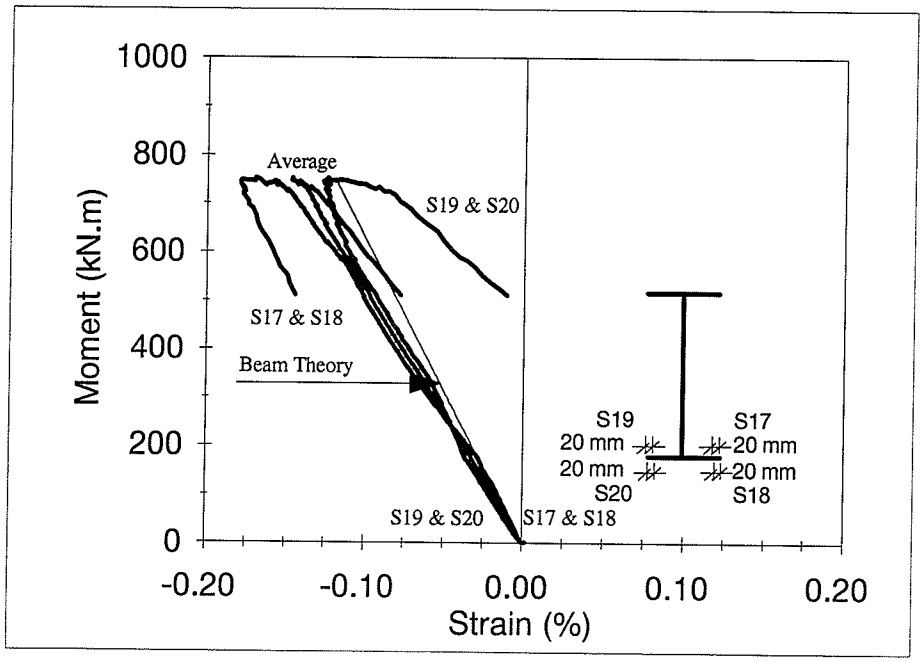

(c) Average Strain

Figure G.15 Moment-Strain Relationships at Mid-Span Compression Flange of Specimen G7

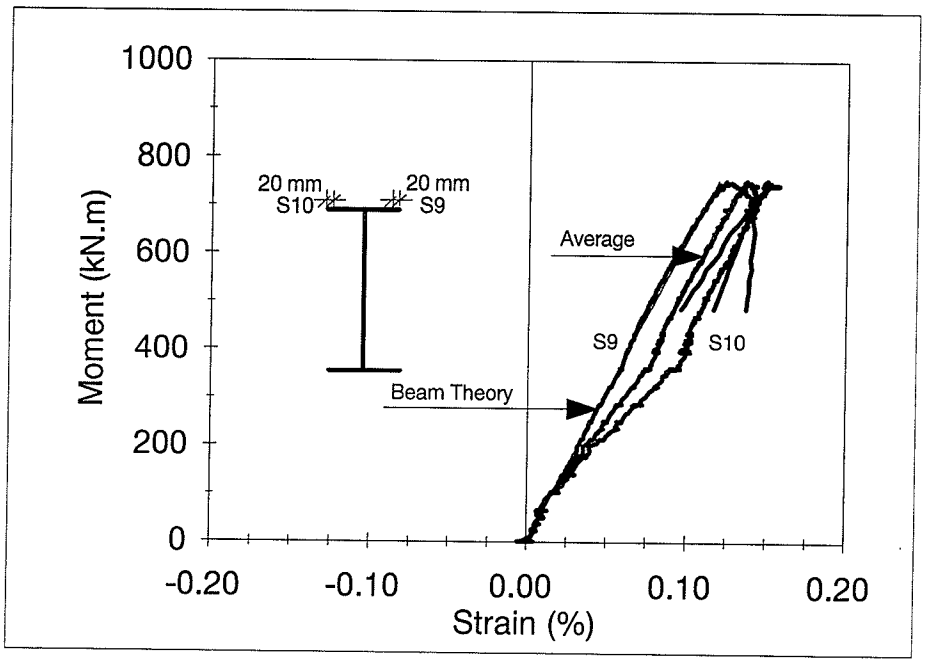

Figure G.16 Moment-Strain Relationships at Mid-Span Tension Flange of Specimen G7

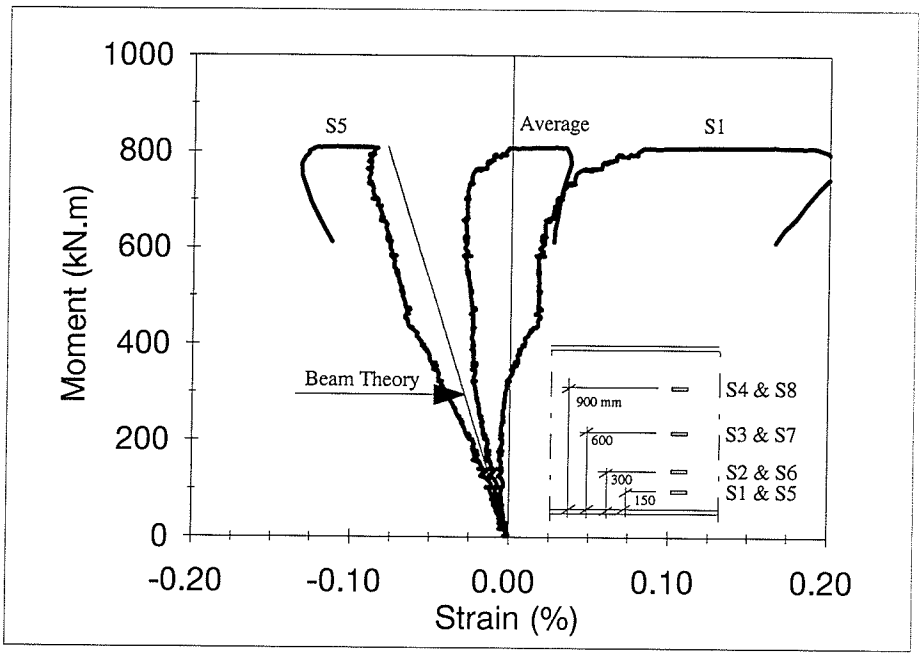

(a) Strain Distribution at S1 & S5

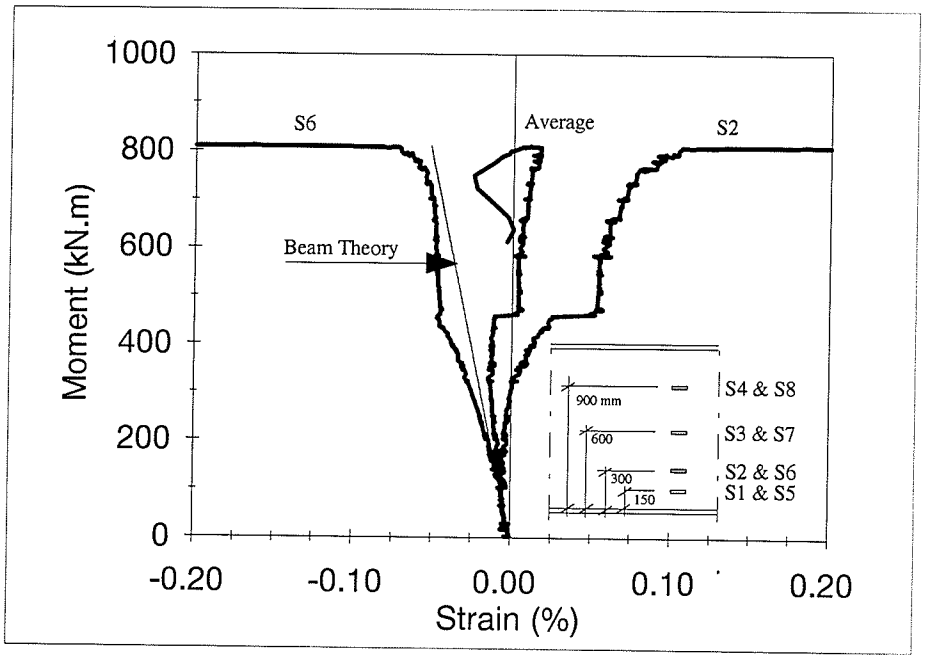

(b) Strain Distribution at S2 & S6

Figure G.17 Moment-Strain Relationships at Mid-Span Web of Specimen G8

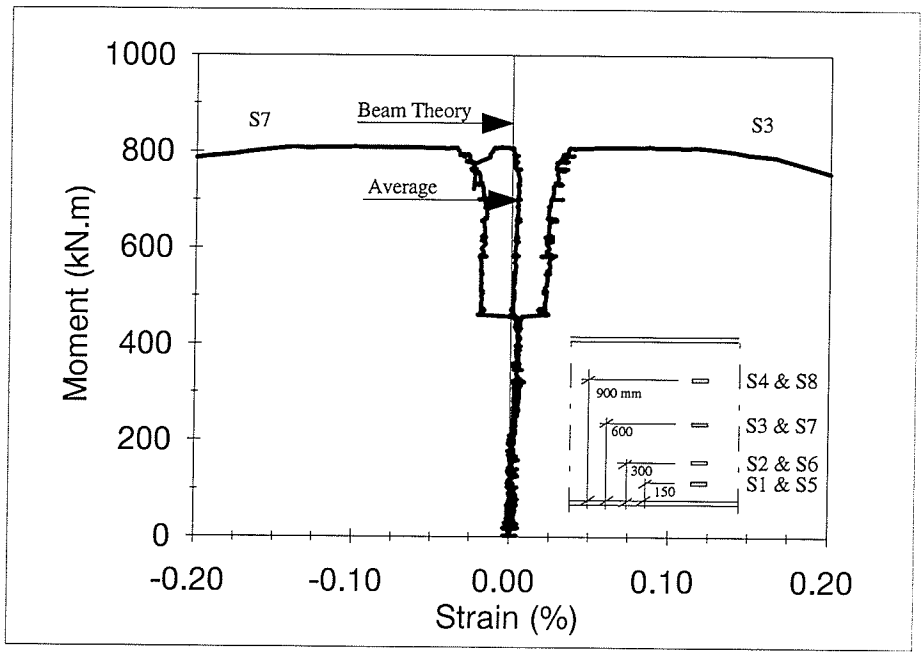

(c) Strain Distribution at S3 & S7

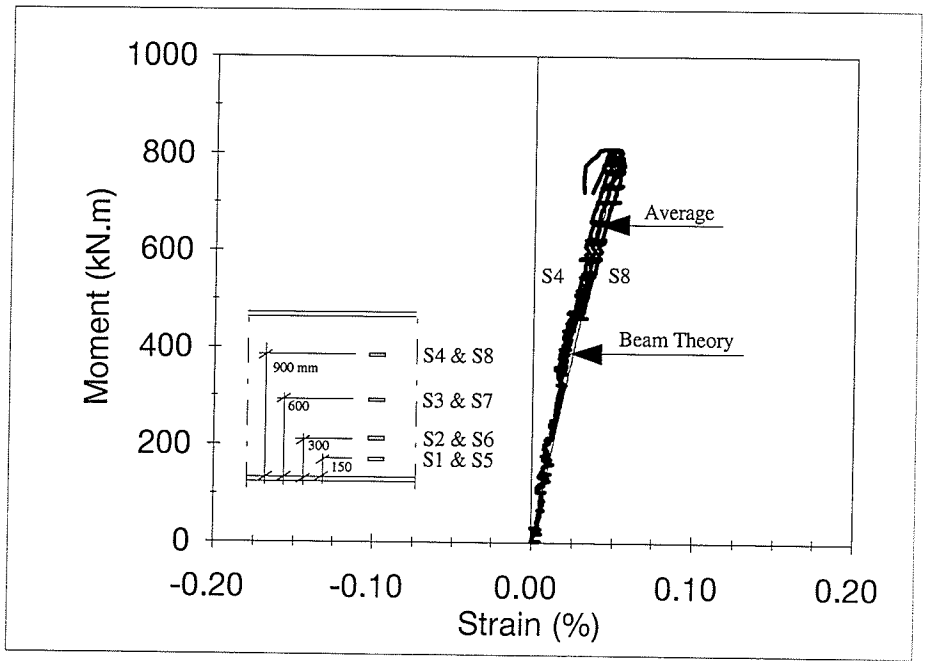

(d) Strain Distribution at S4 & S8

Figure G.17 Moment-Strain Relationships at Mid-Span Web of Specimen G8

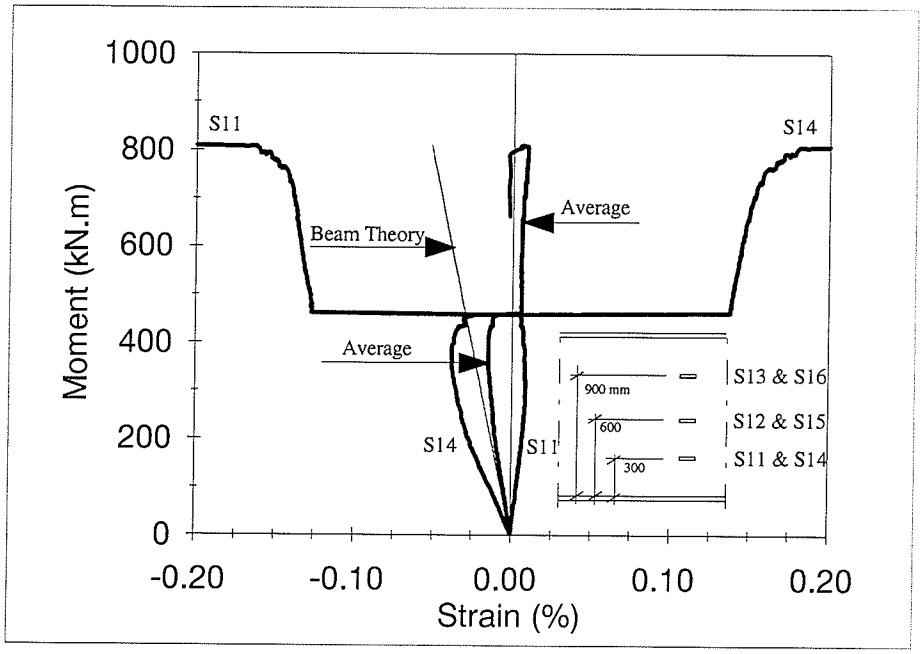

(a) Strain Distribution at S11 & S14

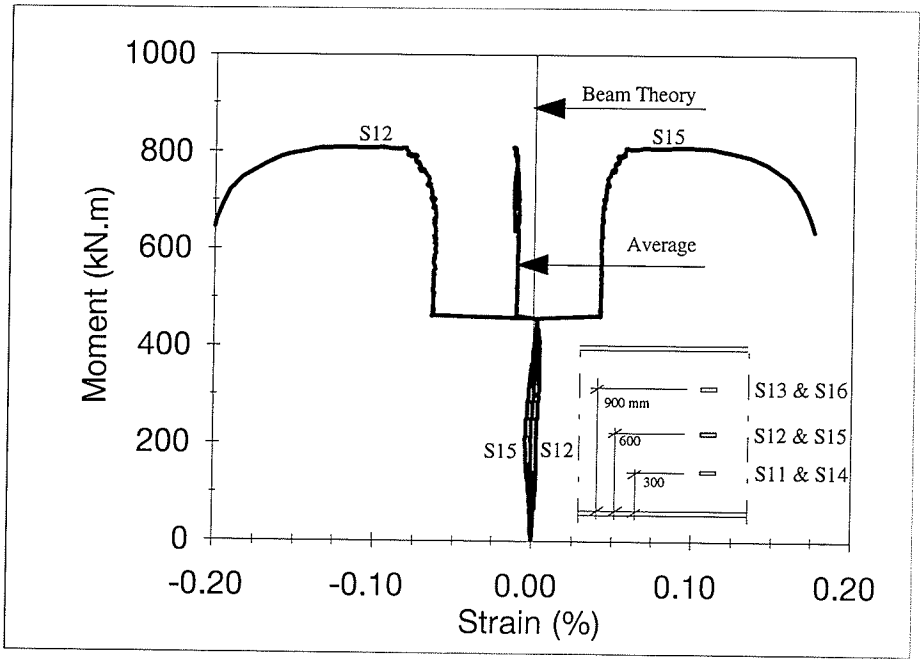

(b) Strain Distribution at S12 & S15

Figure G.18 Moment-Strain Relationships at Quarter-Span Web of Specimen G8

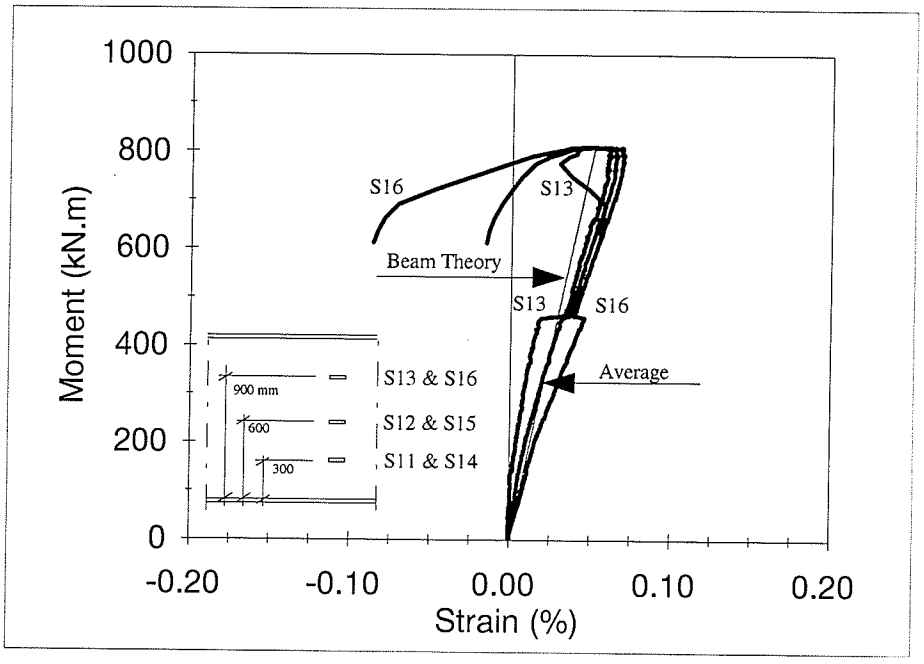

(c) Strain Distribution at S13 & S16

Figure G.18 Moment-Strain Relationships at Quarter-Span Web of Specimen G8

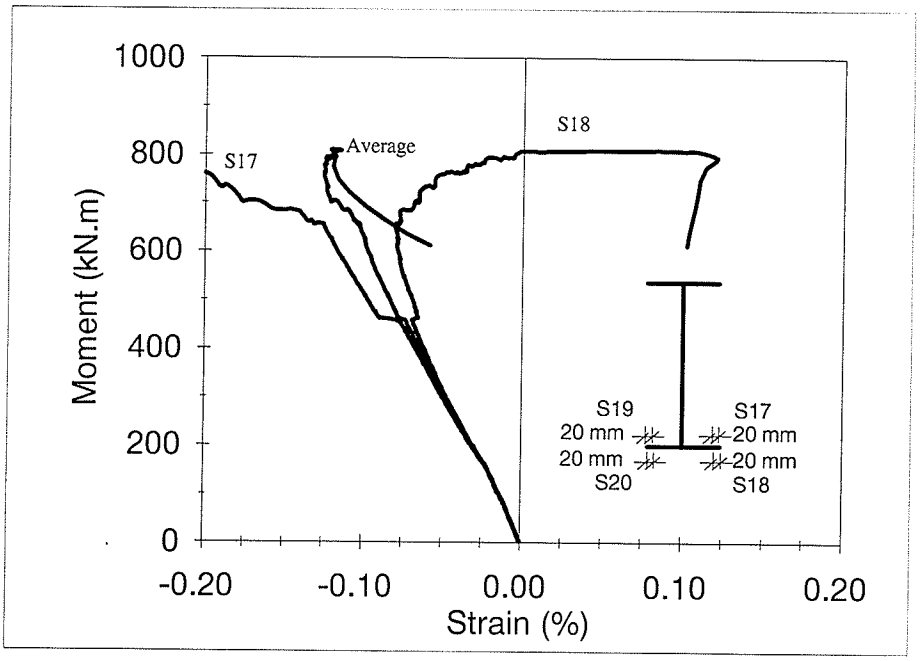

(a) Strain Distribution at S17 & S18

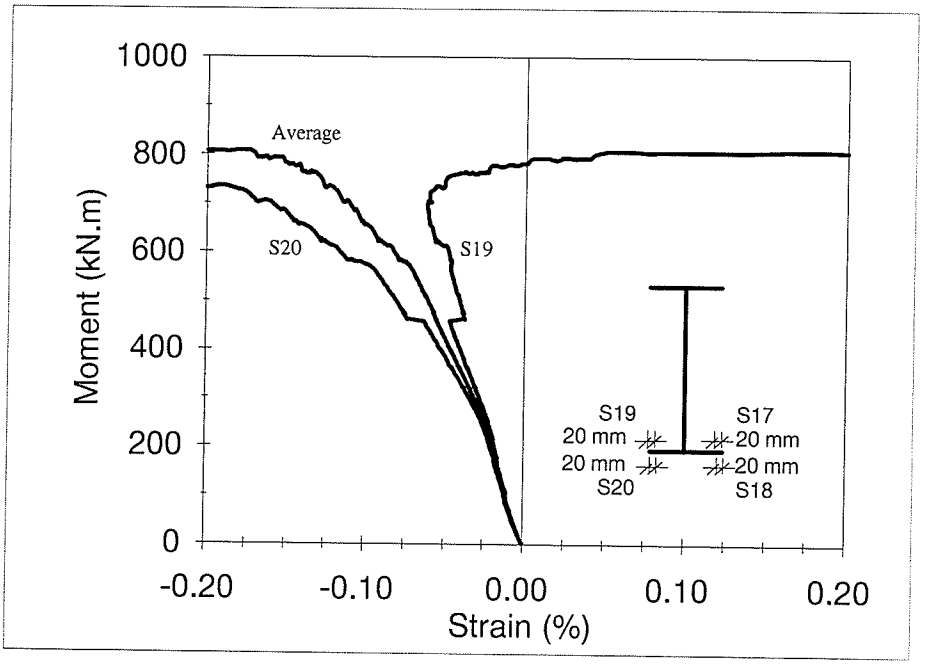

(b) Strain Distribution at S19 & S20

Figure G.19 Moment-Strain Relationships at Mid-Span Compression Flange of Specimen G8

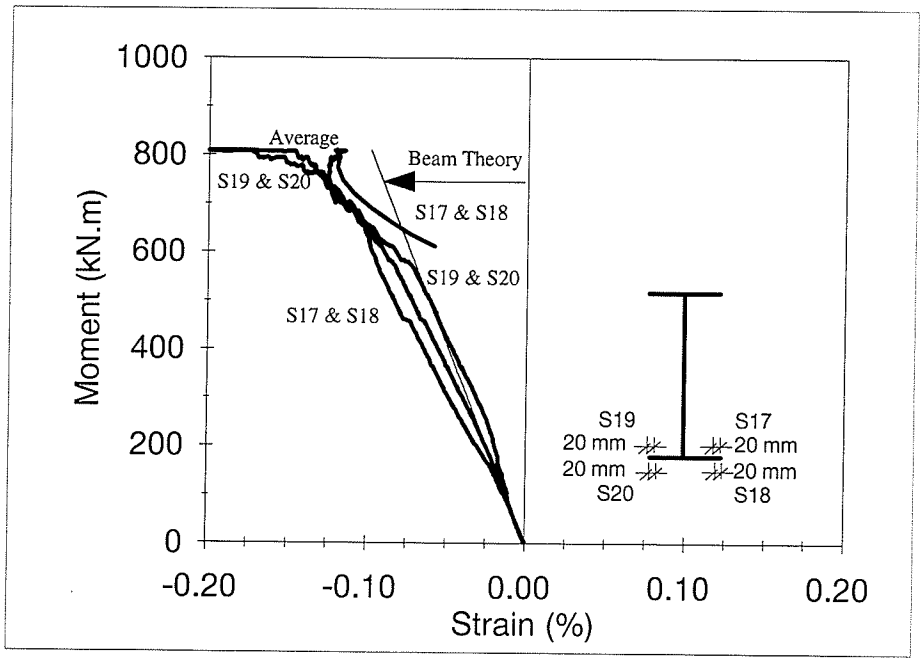

(c) Average Strain

Figure G.19 Moment-Strain Relationships at Mid-Span Compression Flange of Specimen G8

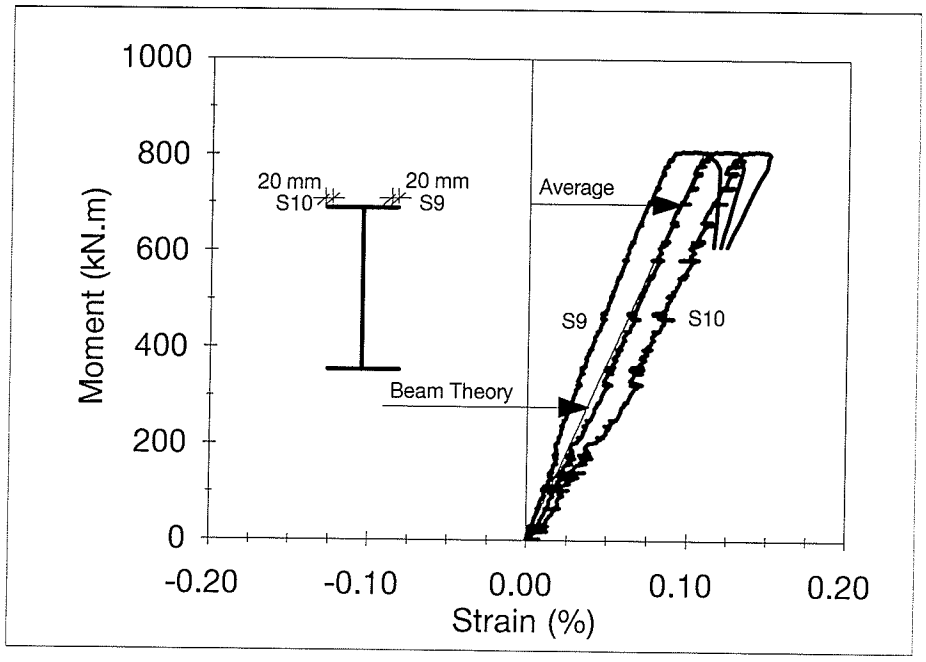

Figure G.20 Moment-Strain Relationships at Mid-Span Tension Flange of Specimen G8

APPENDIX H

FINITE ELEMENT-EXPERIMENTAL

RESULTS COMPARISON

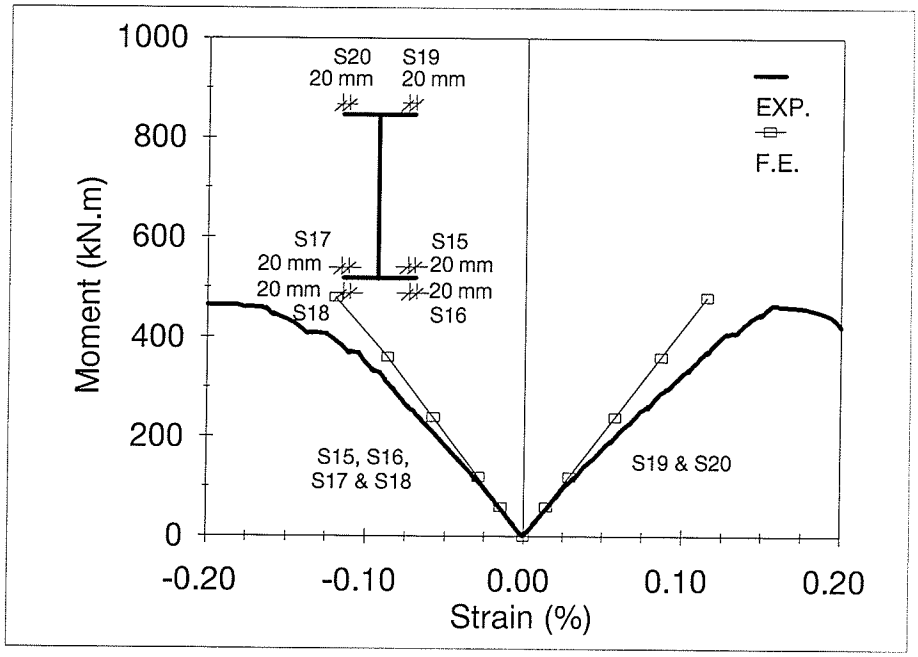

(a) Flanges

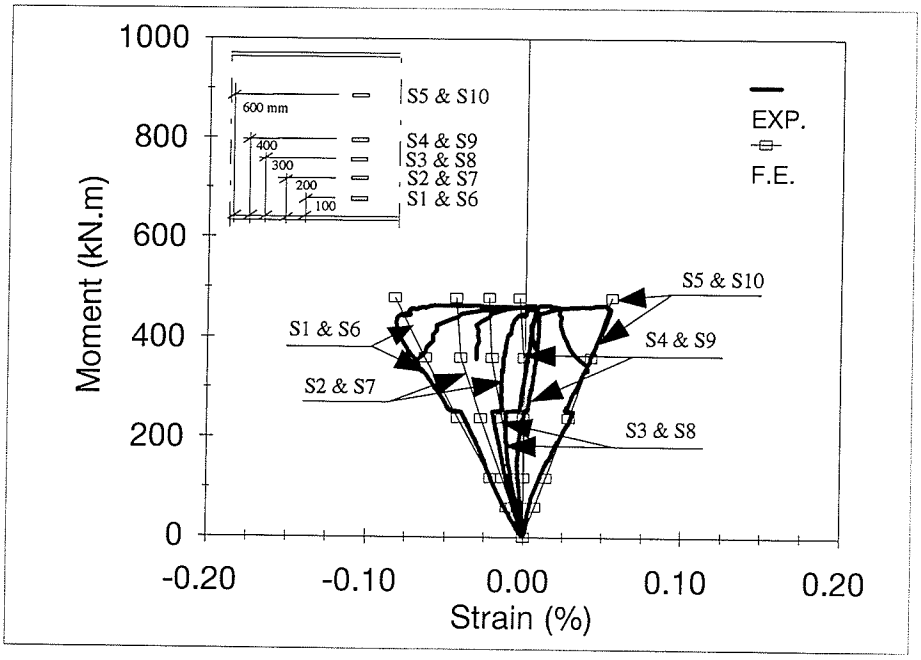

(b) Web

Figure H.1 Longitudinal Strain as a Function of Applied Moment at Mid-Span Section of Specimen G1

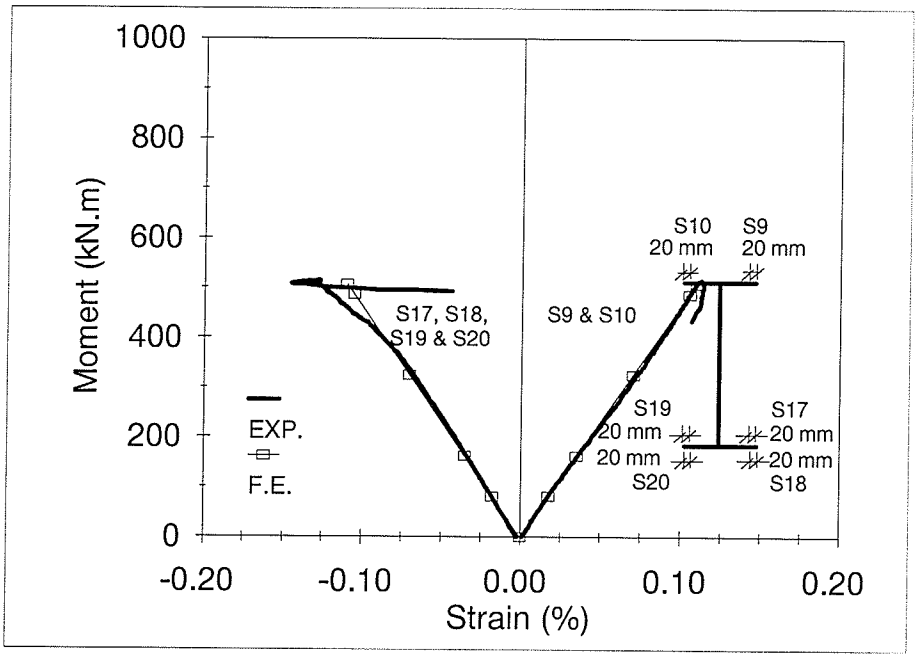

(a) Flanges

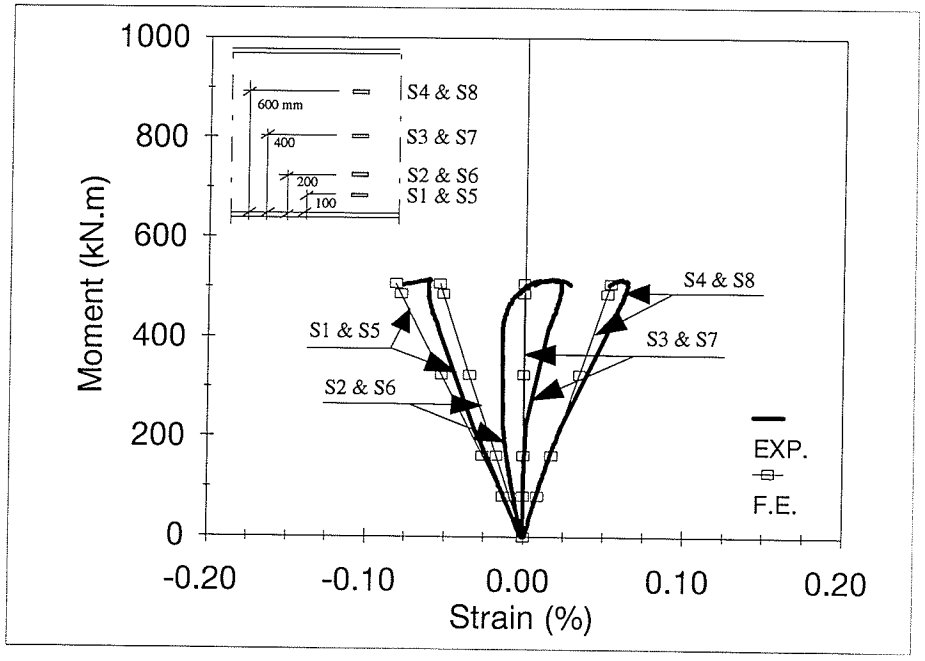

(b) Web

Figure H.2 Longitudinal Strain as a Function of Applied Moment at Mid-Span Section of Specimen G2

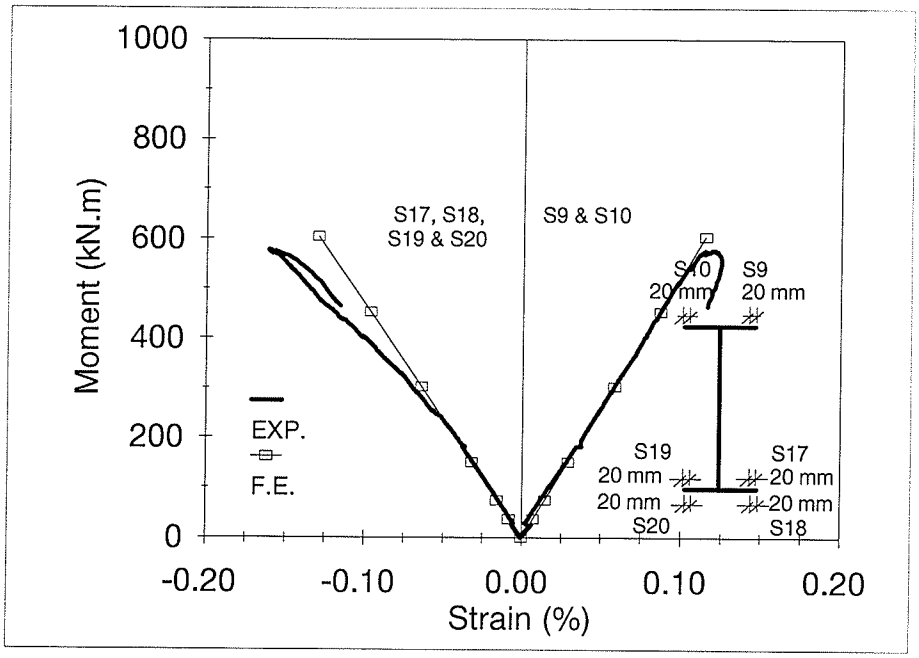

(a) Flanges

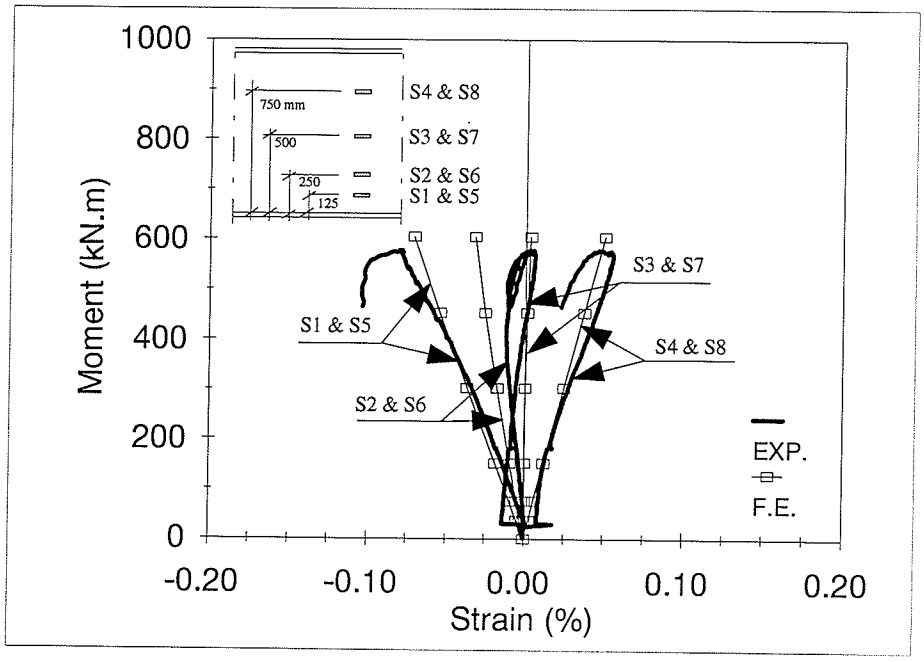

(b) Web

Figure H.3 Longitudinal Strain as a Function of Applied Moment at Mid-Span Section of Specimen G4

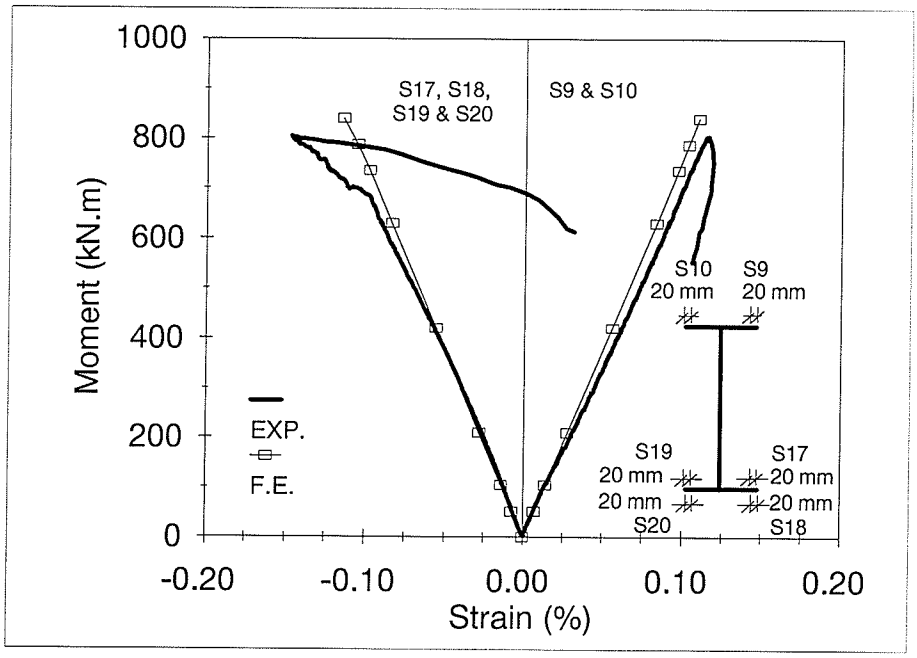

(a) Flanges

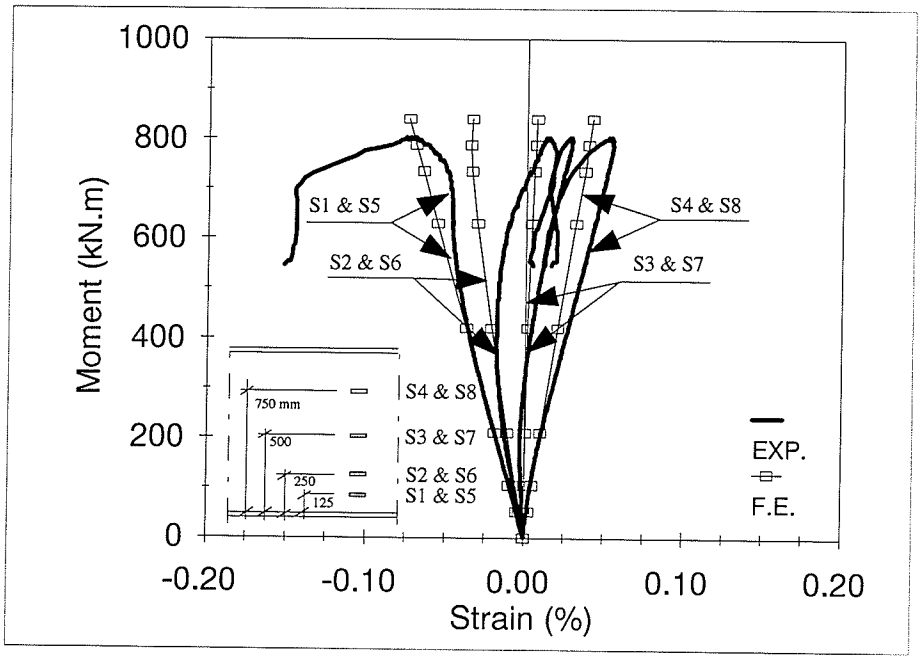

(b) Web

Figure H.4 Longitudinal Strain as a Function of Applied Moment at Mid-Span Section of Specimen G6

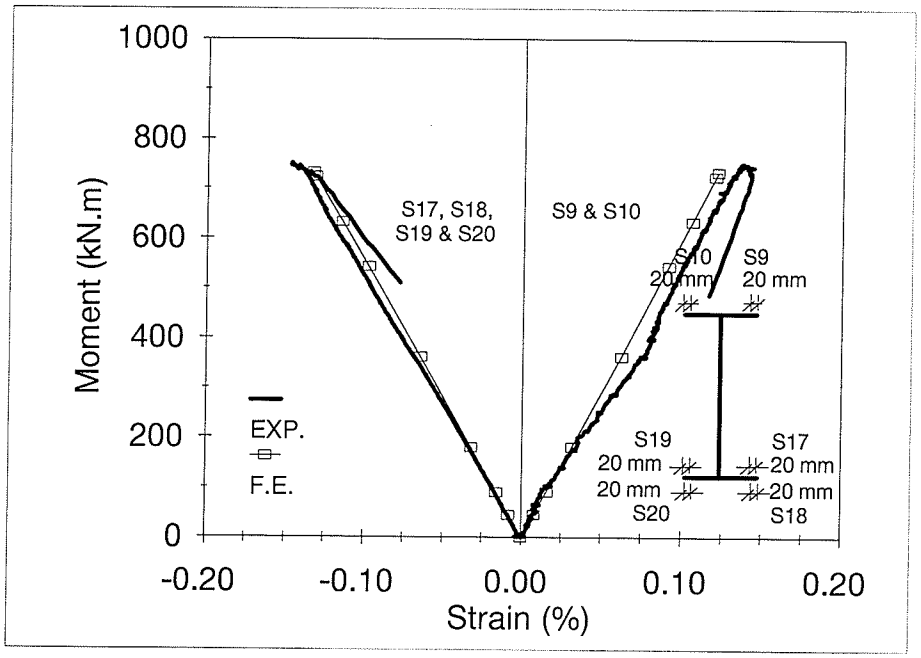

(a) Flanges

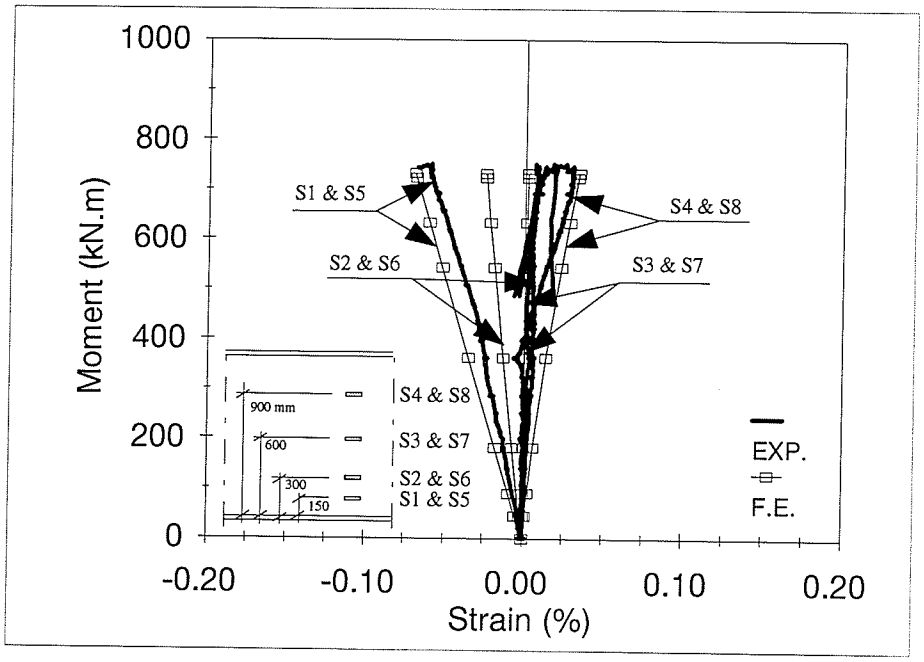

(b) Web

Figure H.5 Longitudinal Strain as a Function of Applied Moment at Mid-Span Section of Specimen G7

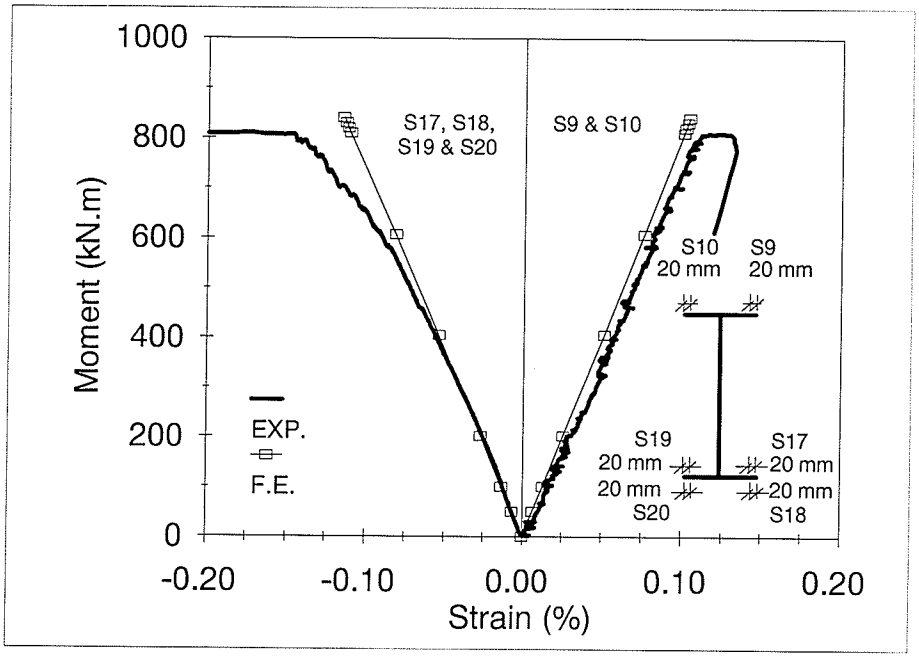

(a) Flanges

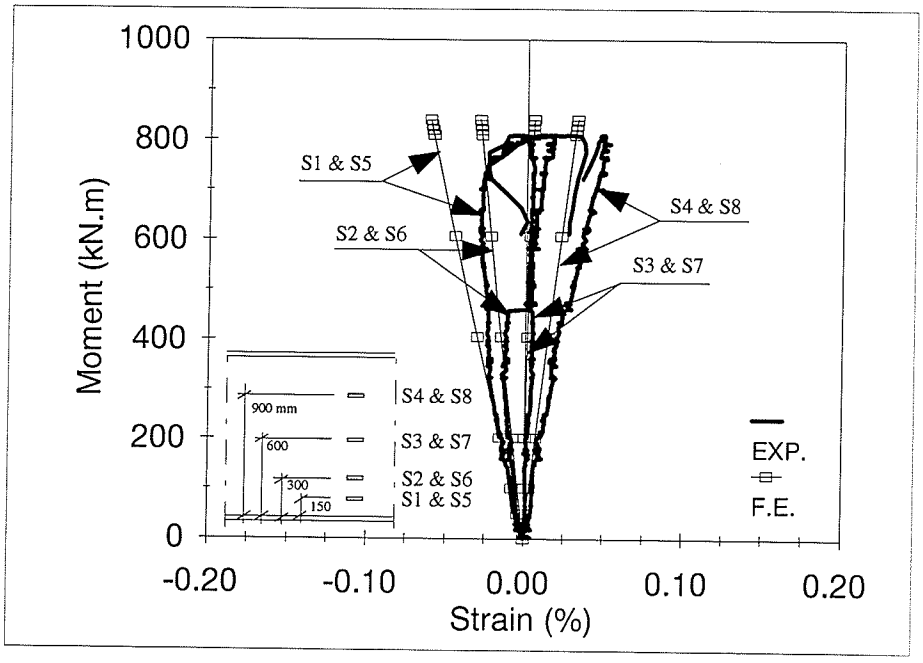

(b) Web

Figure H.6 Longitudinal Strain as a Function of Applied Moment at Mid-Span Section of Specimen G8

APPENDIX I

FINITE ELEMENT-

PROPOSED MODEL COMPARISON

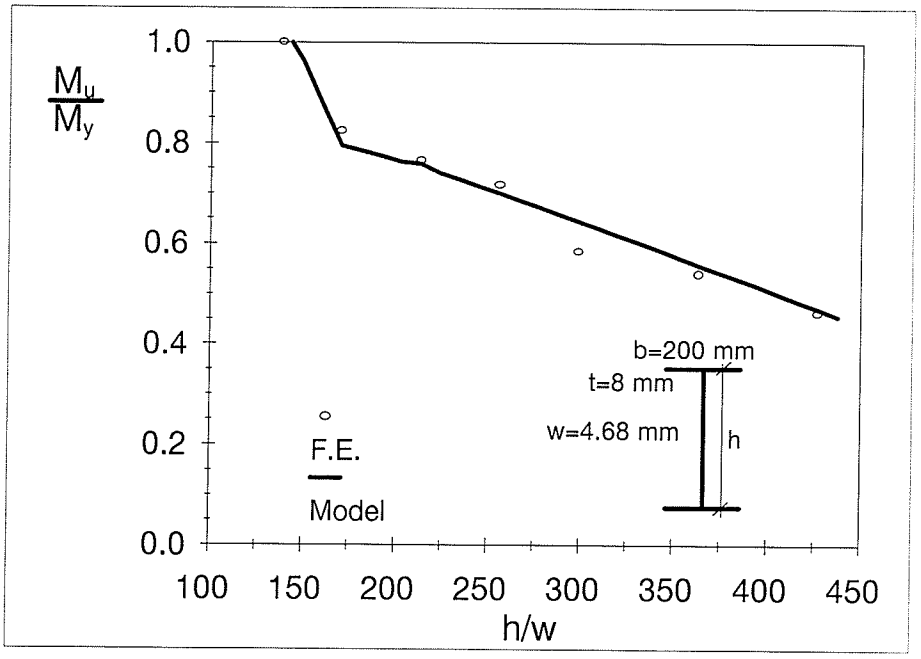

(a) 200-mm Flange Width

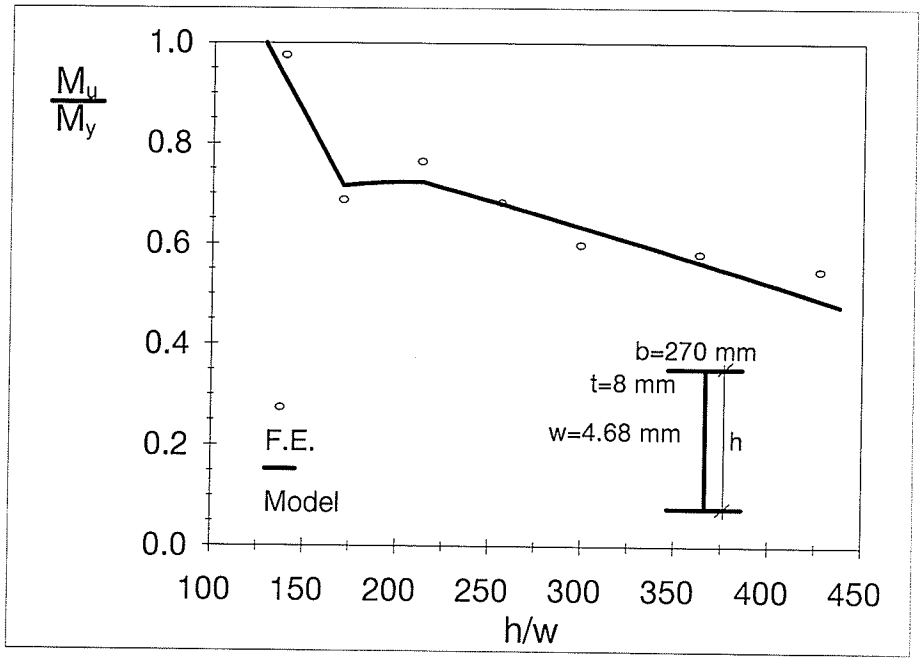

(b) 270-mm Flange Width

Figure I.1 Effect of h/w on the Ultimate Moment Capacity

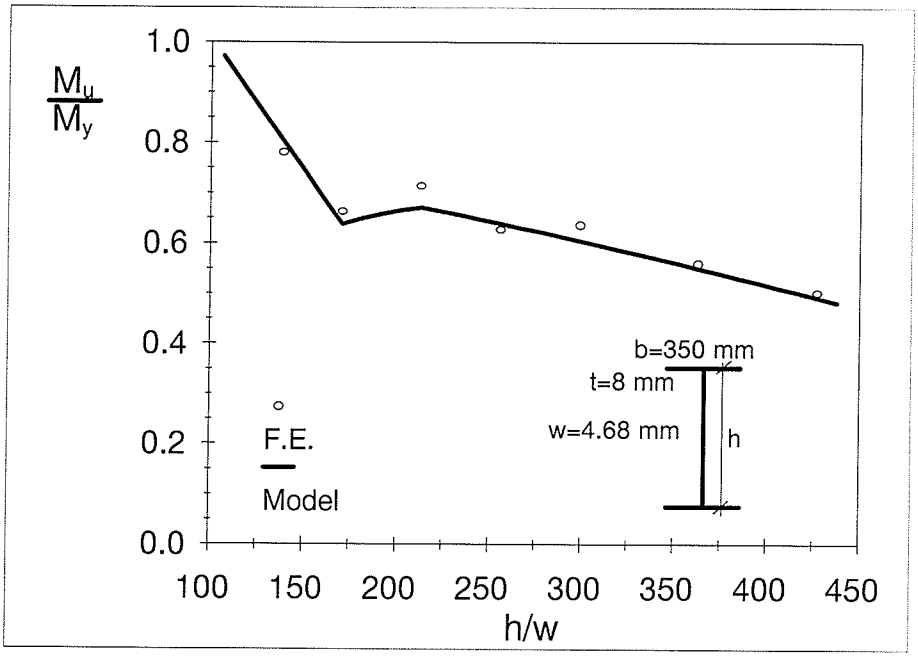

(c) 350-mm Flange Width

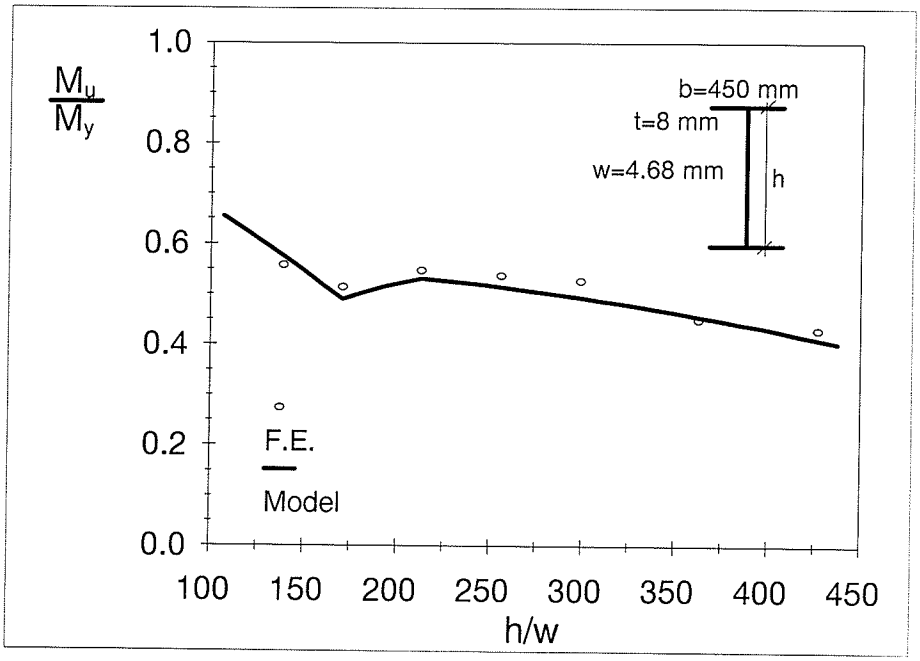

(d) 450-mm Flange Width

Figure I.1 Effect of h/w on the Ultimate Moment Capacity

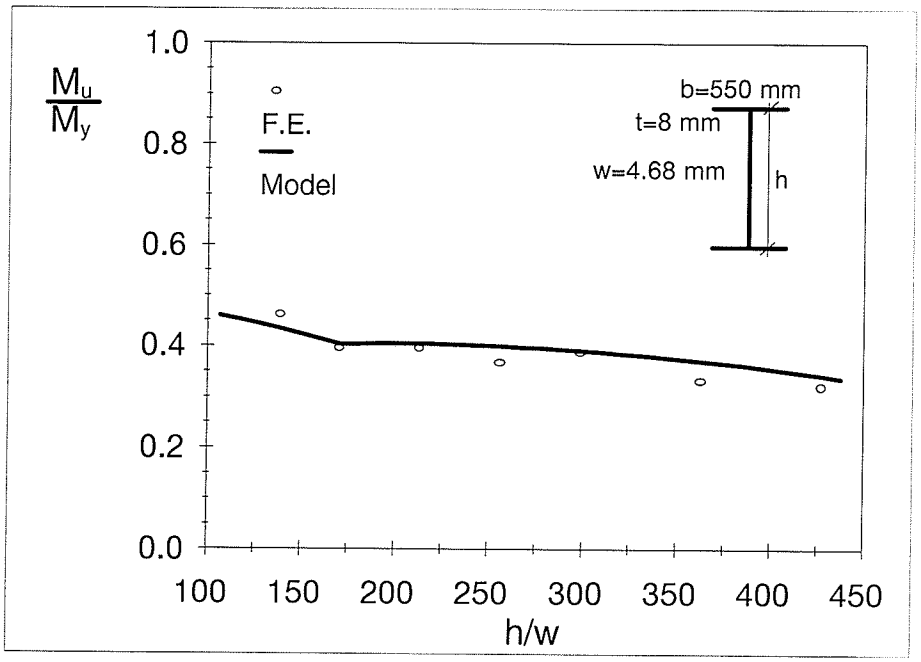

(e) 550-mm Flange Width

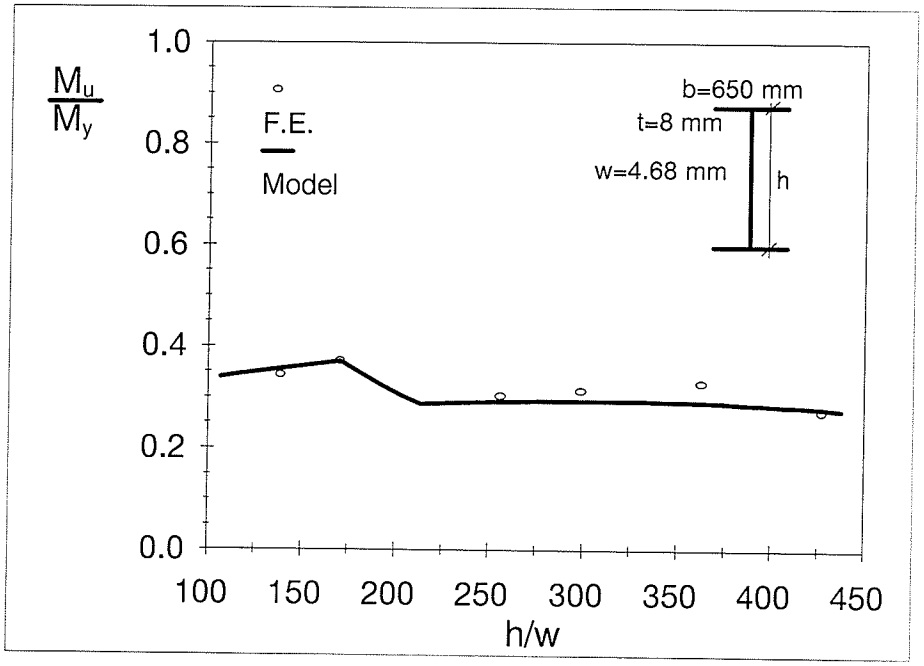

(f) 650-mm Flange Width

Figure I.1 Effect of h/w on the Ultimate Moment Capacity

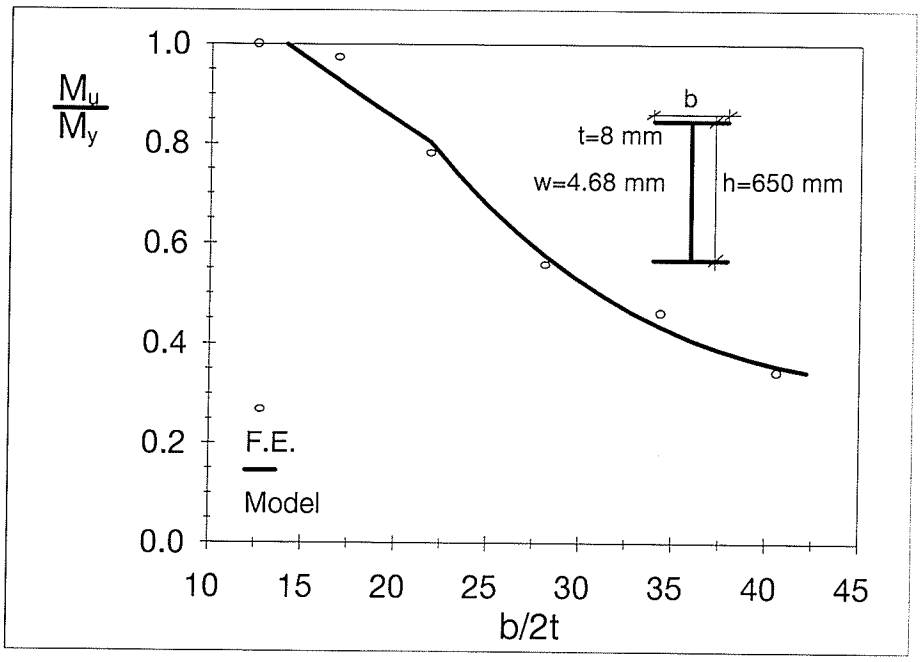

(a) 650-mm Web Height

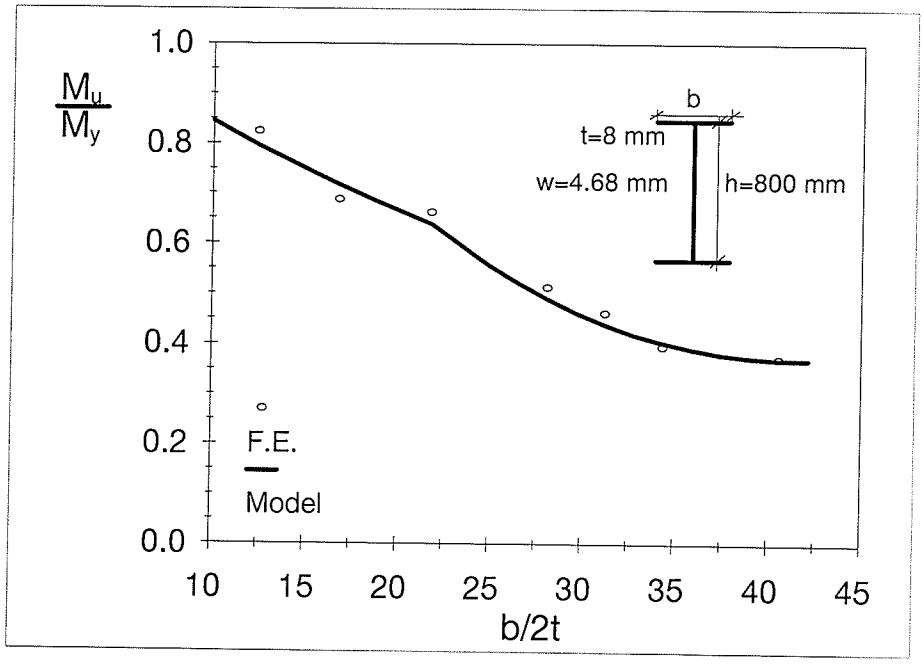

(b) 800-mm Web Height

Figure I.2 Effect of b/2t on the Ultimate Moment Capacity

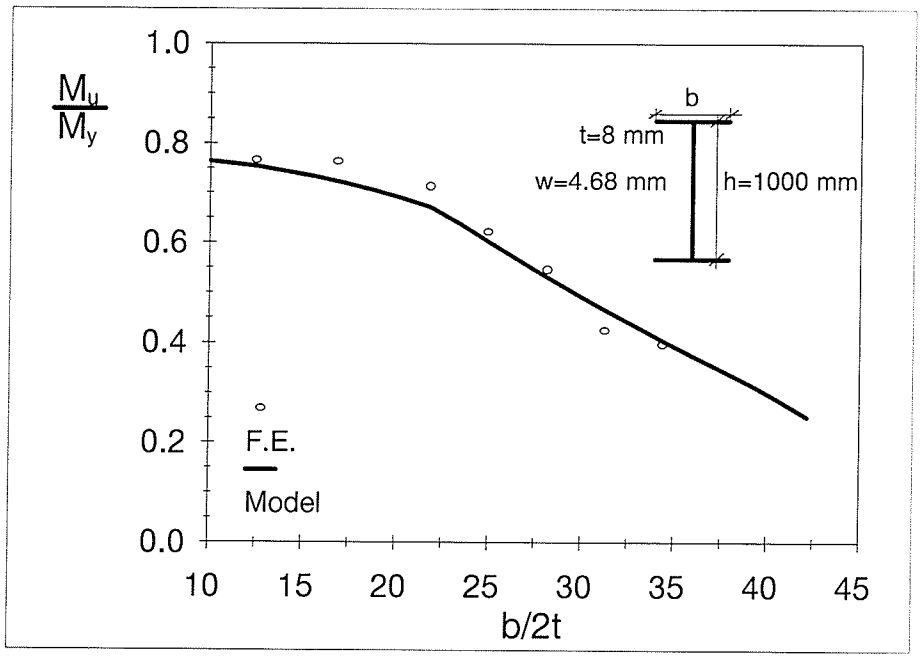

(c) 1000-mm Web Height

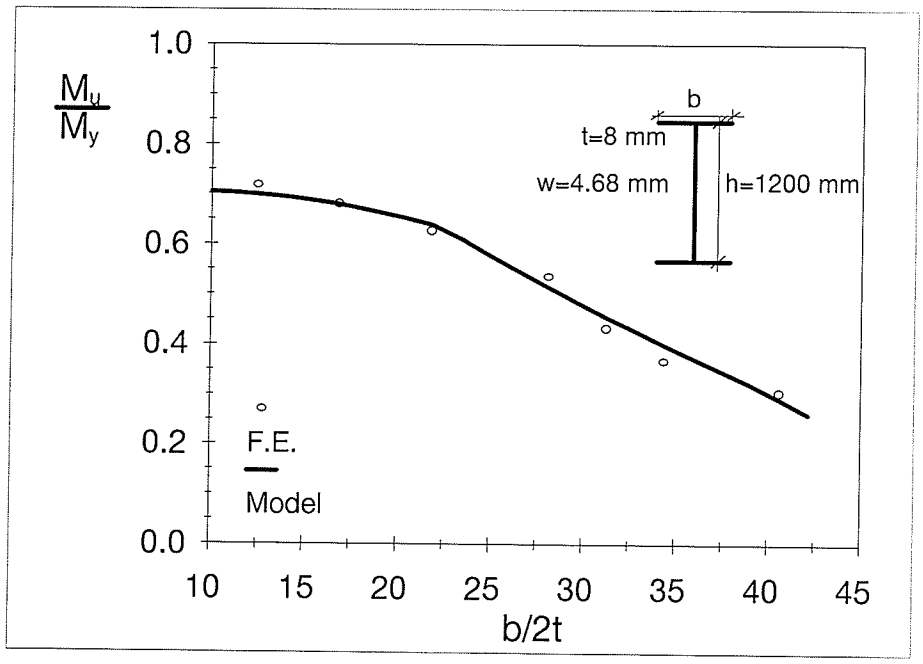

(d) 1200-mm Web Height

Figure I.2 Effect of b/2t on the Ultimate Moment Capacity

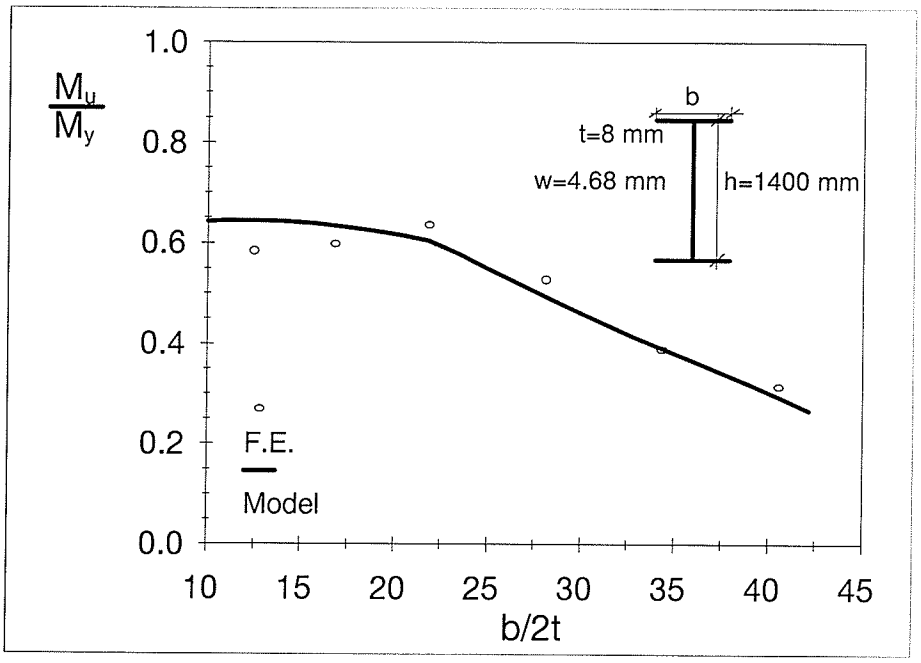

(e) 1400-mm Web Height

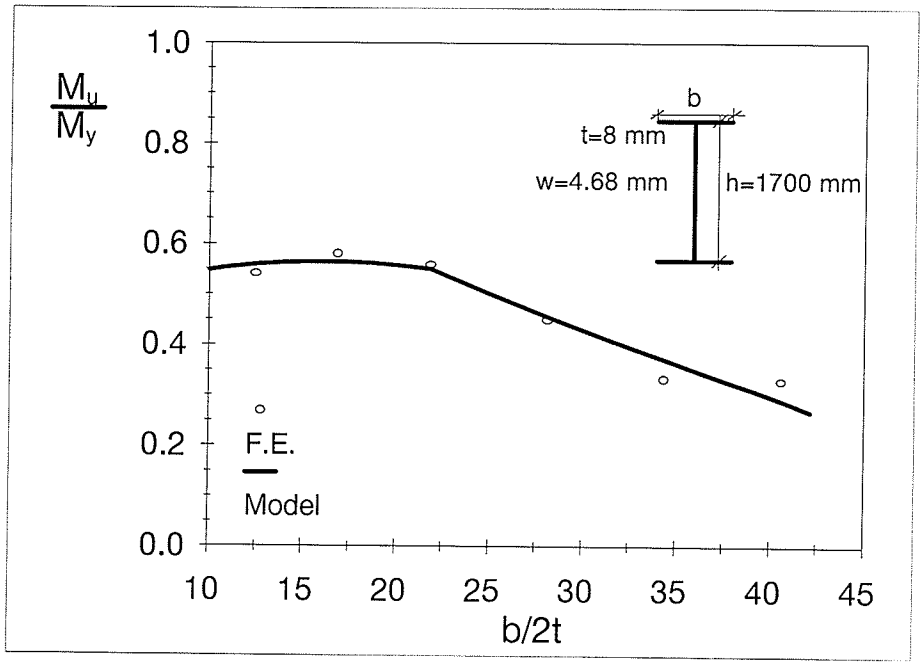

(f) 1700-mm Web Height

Figure I.2 Effect of b/2t on the Ultimate Moment Capacity

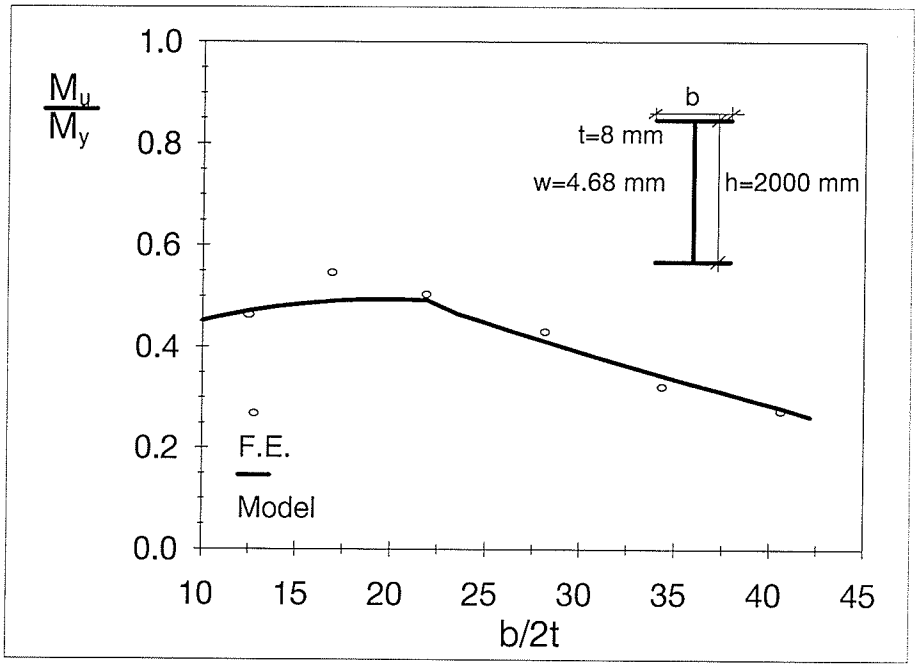

(g) 2000-mm Web Height

Figure I.2 Effect of b/2t on the Ultimate Moment Capacity